

THÈSE

En vue de l'obtention du

DOCTORAT DE L'UNIVERSITÉ DE TOULOUSE

Délivré par :

Institut National Polytechnique de Toulouse (Toulouse INP)

Discipline ou spécialité :

Dynamique des fluides

Présentée et soutenue par :

M. MAEL HARNIEH

le lundi 20 janvier 2020

Titre :

Prédiction de la génération des pertes des écoulements compressibles anisothermes appliquée aux distributeurs hautes pressions de turbine avec les simulations aux grandes échelles

---

Ecole doctorale :

Mécanique, Energétique, Génie civil, Procédés (MEGeP)

Unité de recherche :

Centre Européen de Recherche et Formation Avancées en Calcul Scientifique (CERFACS)

Directeur(s) de Thèse :

M. LAURENT GICQUEL

M. FLORENT DUCHAINE

Rapporteurs :

M. ERIC LAMBALLAIS, UNIVERSITE DE POITIERS

M. STEPHANE AUBERT, ECOLE CENTRALE DE LYON

Membre(s) du jury :

Mme EVA DORIGNAC, UNIVERSITE DE POITIERS, Président

M. CHARLIE KOUPPER, GROUPE SAFRAN, Invité

M. FLORENT DUCHAINE, CERFACS, Membre

M. LAURENT GICQUEL, CERFACS, Membre

M. THOMAS GROSNICKEL, GROUPE SAFRAN, Invité

M. TONY ARTS, UNIVERSITE CATHOLIQUE DE LOUVAIN, Membre

Remerciements

J'entame ici la rédaction des dernières pages de mon manuscrit. Après ces remerciements, il sera temps pour moi de tourner la page, aussi bien au sens propre qu'au sens figuré. C'est donc le moment pour ma part de réaliser un bilan de ces 4 années passées au CERFACS en compagnie de l'équipe CFD.

Je tiens tout d'abord à remercier le CERFACS pour m'avoir permis de découvrir le monde de la recherche et de la simulation numérique. Cette aventure Cerfacsienne a commencé avec Eléonore Riber et Bénédicte Cuenot, qui m'ont pris en stage durant 6 mois. Merci donc à Eléonore et Bénédicte pour m'avoir fait confiance et intégré à l'équipe CFD. Ces premiers mois au CERFACS m'ont permis de découvrir ce fameux code AVBP, dont je n'avais même pas encore idée qu'il allait mettre à rude épreuve ma ténacité, mon courage et ma détermination. Suite à ce stage, j'ai pu enchaîner avec cette thèse qui allait m'occuper au minimum 3 ans (en réalité 4 ans... en prenant en compte une année de rédaction).

Suite à ces 4 années de simulation, de crash, de post-traitement et de réflexion, un manuscrit de thèse est né. Je voudrais ainsi remercier les rapporteurs de mes travaux de thèse, M. Aubert et M. Lamballais, pour avoir lu en détail les 260 pages de mon manuscrit. Je remercie aussi les examinateurs, Mme Dorignac, M. Arts et M. Giauque pour m'avoir écouté durant la soutenance. La discussion qui a suivi était fort enrichissante et pertinente. Merci enfin à l'ensemble du jury pour m'avoir élevé au rang de docteur.

Cette thèse, financée à travers le projet CASCADE, a été réalisée en collaboration étroite avec Safran Helicopter Engines (SHE). Je tiens donc à remercier SHE et plus particulièrement mon encadrant industriel, Charlie Koupper, pour les diverses discussions et questions durant ces nombreux points thèses. Merci aussi à Charlie pour m'avoir permis de réaliser une immersion d'un mois sur le site à Bordes situé entre les Pyrénées, Pau et la campagne verdoyante des Pyrénées-Atlantiques. Ce fut pour moi une expérience intéressante et enrichissante de travailler au sein même d'une grande entreprise. Merci aussi à l'ensemble de l'équipe MO de SHE pour ces longues discussions pendant les points thèses industriels qui se sont toujours déroulées juste avant de manger le midi. Ces discussions ont aussi permis de faire avancer mes travaux.

Ensuite, ce paragraphe sera consacré spécialement aux "parrains" de ces travaux thèse, c'est-à-dire, mon directeur et co-directeur de thèse, ainsi nommé Laurent Gicquel et Florent Duchaine. Vous m'avez encadré durant ces 4 années, parfois décadré et recadré afin que mes travaux de thèse puissent rentrer dans le cadre d'un doctorat. Tout d'abord, merci à toi Laurent, pour ces discussions, ces nombreuses questions et ta volonté que je sois "carré" dans ma tête pour améliorer ma rigueur scientifique. Je me rappelle aussi que tu m'as accompagné et défendu pendant les réunions CASCADE dans toute la France. Enfin, merci pour ces nombreux conseils durant les répétitions de présentations et de points thèses. Merci aussi à

toi Florent, pour avoir pointé maintes et maintes fois les coquilles, les fautes et les imprécisions que je tentais de cacher pendant mes points thèses. Merci à vous deux pour m'avoir appris à répondre aux différentes critiques sur mes travaux pendant mes présentations et pour rédiger les réponses aux reviewers. Même si cette dernière année de rédaction fut un peu plus longue que les trois premières années, un manuscrit de thèse dense et de qualité est né, en partie grâce à vous.

Un remerciement spécial à Rudolf Clausius pour avoir inventé cette notion d'entropie et de perte en turbomachine, qui a sauvé mes travaux de thèse et m'a permis d'écrire un manuscrit original. Un autre remerciement spécial à Navier, Stokes, Smagorinsky et l'ensemble des personnes que j'ai cité dans mon manuscrit, pour avoir initier ces longs travaux de recherche sur la mécanique des fluides et qui ont donc crée indirectement de nombreux emplois !

Évidemment, je ne peux pas oublier dans ces remerciements les équipes admin. et support informatique CSG. En effet, c'est aussi grâce à vous que cette thèse a été menée à son terme. Merci à Chantal, Marie et Michelle pour l'organisation des déplacements et leurs précieuses aides pour utiliser l'imprimante de l'étage. Merci aussi à la nouvelle venue, Jade, qui a organisé ma soutenance de thèse. Merci aussi à l'équipe CSG, notamment Fred, Gérard et Fabrice qui m'ont toujours apporté leur aide quand j'en avais besoin.

Je ne peux pas non plus oublier mes anciens collègues thésards pour la bonne humeur de l'équipe CFD et Aéro. Merci à mes anciens co-bureaux, Laura, Quentin et Martin pour avoir supporté mes petits bruits, mes coups de pieds et mes discussions solitaires. Au passage, ces discussions avec moi-même m'ont vraiment permis de prendre du recul et d'avoir de nouvelles idées ! Un merci particulier à Martin qui m'a donné l'accès au toilette plusieurs fois par jour lors de notre immersion à Pau (Oui, je n'avais pas le bon badge pour aller au petit coin...). Merci aussi aux thésards de l'étage pour ces discussions, à la fois scientifiques et culturelles, qui pouvaient se poursuivre autour d'un verre (hors CERFACS bien sûr...). Merci aussi à la team du midi, Quentin, Simon, Fabien, Fred, Charlélie, Queguineur et Soizic pour m'avoir surveillé si je terminais mon assiette...

Enfin, il est important pour moi de remercier mes amis Normands, Jacques, Jeff, Kévin, Laure, Etienne et Alexandre pour ces moments passés autour d'un verre lorsque je remontais en Normandie pour retrouver ma pluie natale. Un remerciement particulier pour mes amis qui sont venus spécialement me voir pour ma soutenance. Merci aussi au chat que j'ai récupéré dans ma voiture qui m'a aussi soutenu pendant ma préparation de soutenance. Enfin, un remerciement particulier à mes parents, Papa et Maman, et mes grands-parents, Papy et Mamye, pour m'avoir soutenu et encouragé durant toutes ces années. Merci aussi à la famille pour m'avoir envoyé autant de messages d'encouragements avant le jour J.

Il est temps pour moi de refermer ce manuscrit afin d'écrire une nouvelle histoire...

Résumé en français

Afin d'améliorer l'efficacité des moteurs aéronautiques, une des solutions envisagées par les industriels est d'augmenter la température d'entrée de la turbine. Cependant, ces hautes températures induisent de fortes contraintes thermiques sur les pales de turbine ce qui réduit leur durée de vie. Pour surmonter ces problèmes thermiques, des systèmes de refroidissement efficaces sont nécessaires. Afin d'évaluer la performance de ces systèmes, une prédiction précise de la température de paroi des pales de turbine et des pertes générées par ces systèmes est requise. Profitant de l'opportunité de récents développements d'outils de prédiction haute-fidélité, cette thèse financée par Safran Helicopter Engines à travers le projet FUI CASCADE, a pour but de valider la prédiction de la température de paroi des pales de turbine refroidie et des pertes générées par ces systèmes avec la Simulation aux Grandes Echelles (SGE). Pour atteindre ces objectifs, différentes configurations académiques et industrielles refroidies par film de refroidissement ont été simulées et étudiées. Les résultats obtenus dans cette thèse montrent que la SGE est capable de prédire l'aérodynamique et l'environnement thermique pour de tels systèmes. Pour faciliter l'utilisation de la SGE dans l'industrie et limiter le coût CPU lié à la résolution de l'écoulement dans le système de refroidissement des pales, un modèle de jets de refroidissement a été proposé et évalué dans ce travail. Les résultats montrent que ce modèle permet de reproduire l'aérodynamique des jets de refroidissement et la température de paroi des pales sans mailler le système de refroidissement. Pour évaluer les pertes dans ce contexte, l'approche Second Law Analysis (SLA) est adoptée. Contrairement aux bilans de température et pression totales, cette approche donne directement accès aux champs de perte 3D qui sont construits à partir des termes sources de l'entropie résolus sur le maillage. Ainsi, le mécanisme de génération de perte peut être localement étudié et ne requière pas de procédure de moyenne contrairement aux modèles de perte 1D. Ces champs de perte sont décomposés en deux contributions : une contribution aérodynamique et une contribution thermique liée au mélange chaud-froid. L'étude de ces champs montre que les pertes aérodynamiques sont principalement générées dans les régions de fort cisaillement (couche limite et de mélange) alors que les pertes de mélange sont générées dans les films de refroidissement et dans le sillage des pales. Des analyses avancées des champs de perte mettent en évidence que les fluctuations turbulentes dominent la génération des pertes pour ces systèmes. Ce dernier résultat met en évidence les bénéfices de l'approche Second Law Analysis pour prédire les pertes à partir des champs obtenus avec la SGE. En effet et contrairement aux approches RANS, les contributions turbulentes des pertes sont directement résolues sur le maillage avec la SGE et ne requiert aucune stratégie de modélisation. La principale conclusion de cette thèse est que l'approche Second Law Analysis couplée avec la SGE est une méthodologie très prometteuse et pertinente pour la prédiction des écoulements et des pertes pour les futurs designs de pale de turbine industriel.

Abstract

To improve the efficiency of aeronautic engines, the turbine entry temperature has strongly increased in recent years. Such high temperatures induce high thermal stresses for the turbine blades and vanes which reduces the blade lifetime. To overcome this thermal issue, efficient turbine cooling systems need to be designed. To do so, the accurate prediction of blade wall temperature and losses generated by these systems is required. Taking the opportunity of recent developments of high-fidelity predictions, this PhD thesis funded through the FUI project CASCADE with the support of Safran Helicopter Engines (SHE), aims to evaluate the prediction of blade wall temperature and losses for cooled high-pressure vanes with Large Eddy Simulations (LES). To do so, academic and complex anisothermal configurations featuring film cooling are investigated. Results obtained in the present work show that LES is able to predict the flow aerodynamics and blade wall temperature for all configurations studied. The prediction is clearly improved if the mesh is sufficiently refined in high dynamic regions and if turbulent fluctuations are taken into account at the inlet of the computational domain especially for cases presenting separation bubbles. To ease the use of LES in an industrial context and reduce the CPU effort associated to the resolution of the flow in the cooling system of turbine blades and vanes, a new coolant ejection model is introduced and evaluated. This model is shown to well reproduce the coolant jets aerodynamics and provides a good prediction of the wall temperature without meshing the cooling system. To accurately evaluate and investigate the losses in this context of turbine blade cooling, the approach Second Law Analysis (SLA) is adopted. Contrary to total temperature and total pressure balances, SLA directly gives access to 3D loss maps which are constructed from the entropy source terms resolved on mesh. As a result, the loss generation mechanism can be locally investigated and does not require any averaging procedures contrary to 1D loss models. These loss maps are split in an aerodynamic contribution and a mixing contribution which is linked to mixing process between hot and cold flows. The study of these loss maps shows that aerodynamics losses are generated in high sheared regions (boundary and mixing layers) while mixing losses are produced in the film cooling and in the wake of the vanes. Advanced analysis of loss maps indicate that turbulent fluctuations dominate the loss generation mechanism. This last finding evidences the benefits of SLA to predict losses from LES fields. Indeed and contrary to RANS, the turbulent contributions to losses are directly resolved on mesh with LES and do not require any modelling strategies. As a consequence of this PhD work, SLA coupled to LES is shown to be a very promising methodology to predict the flow aerodynamics and losses for the design of future geometries of industrial turbine vanes and blades.

Nomenclature

Acronyms

ACL	Axial Chord Length
$AITEB$	Aerothermal Investigations on Turbine Endwalls and Blades
CFD	Computational Fluid Dynamics
CPU	Central processing unit
DES	Detached Eddy Simulation
DNS	Direct Numerical Simulation
DP	Design Point
$FACTOR$	Full Aerothermal Combustor Turbine interactiOns Research
HPC	High Performance Computing
LE	Leading Edge
LES	Large Eddy Simulation
NGV	Nozzle Guide Vane
PS	Pressure Side
$RANS$	Reynolds-Averaged Navier-Stokes
SGS	Sub-Grid Scale
SLA	Second Law Analysis
SS	Suction Side
TE	Trailing Edge
TET	Turbine Entry Temperature
$WALE$	Wall-Adapting Local Eddy-viscosity
$WMLES$	Wall-modelled LES
$WRLES$	Wall-resolved LES

Greek letters

δ	Boundary layer thickness	$[m]$
δ^*	Displacement thickness	$[m]$
δ_f	Film thickness	$[m]$
η	Adiabatic film effectiveness	[-]
η_t	Isentropic turbine efficiency	[-]
η_{th}	Thermal engine efficiency	[-]
γ	Ratio of specific heat	[-]
λ	Thermal conductivity	$[W/m/K]$
μ	Dynamic viscosity	$[kg/m/s]$
ν	Kinematic viscosity	$[m^2/s]$
ω	Vorticity	$[s^{-1}]$
ρ	Density	$[kg/m^3]$
τ_w	Wall shear stress	$[Pa]$
$\tau_{i,j}$	Viscous shear stress tensor	$[Pa]$
θ	Momentum displacement thickness	$[m]$
θ^*	Energy displacement thickness	$[m]$
ξ	Loss coefficient	[-]
u_τ	Shear velocity	$[m/s]$

Operators

$< \Phi >$	Surface-averaged
$\bar{\Phi}$	Time-averaged
$\breve{\Phi}$	Favre filter (LES)
$\check{\Phi}$	Favre average (RANS)
$\widehat{\Phi}$	LES filter
$\widetilde{\Phi}$	Mass-flow averaged

Subscripts

$1, in$	Inlet condition
$2, ex$	Outlet condition
40	Plane 40
41	Plane 41
∞	Freestream condition

$c, cool$	Coolant flow
$film$	Film condition
is	Isentropic
$mean$	Mean condition
RMS	Root Mean Square
sgs	Sub-grid scale
$shaft$	Shaft condition
t	Total or turbulent state
tan	Tangential to the wall
$turb$	Turbulent condition
$wall$	Wall condition

Variables

$\mathbf{v}$	Velocity magnitude	$[m/s]$
$\dot{S}$	Entropy production	$[W/K]$
$\dot{s}$	Local entropy production	$[W/m^3/K]$
c	Chord length	$[m]$
C_D	Discharge coefficient	[-]
C_d	Dissipation coefficient	[-]
C_f	Friction coefficient	[-]
C_P	Pressure coefficient	[-]
C_p	Heat capacity per mass unit at constant pressure	$[J/kg/K]$
DR	Density ratio	[-]
H	Shape factor	[-]
h	Sensible enthalpy	$[J]$
J	Impulse ratio	[-]
k	Turbulent kinetic energy	$[m^2/s^2]$
L	Characteristic length	$[m]$
M	Blowing ratio	[-]
Ma	Mach number	[-]
n	Normal wall distance	$[m]$
P	Pressure	$[Pa]$
P_k	Local turbulent kinetic energy production	$[m^2/s^3]$
P_m	Aerodynamic loss	$[W/m^3]$
P_q	Mixing loss	$[W/m^3]$
Pr	Prandtl number	[-]
Pr_k	Normalized turbulent kinetic energy production	[-]
Q	Heat	$[W]$
q	Dynamic pressure	$[Pa]$
$Q_m, \dot{m}$	Mass flow rate	$[kg/s]$
Q_{crit}	Q-criterion	$[s^{-2}]$
r	Perfect gas constant	$[= 287\, J/kg/K]$
R_c	Curvature radius	$[m]$
Re	Reynolds number	[-]
s	Sensible entropy	$[J/K/kg]$
s_c	Curvilinear coordinate	$[m]$
s_m	Local aerodynamic entropy production	$[W/m^3/K]$
s_q	Local mixing entropy production	$[W/m^3/K]$
S_{ij}	Symmetric part of strain rate tensor	$[s^{-1}]$
T	Temperature	$[K]$
u, v, w	Velocity vector components	$[m/s]$
W	Work	$[W]$
x, y, z	Cartesian coordinates	$[m]$
y^+	Wall normal unit	[-]
$Y_{coolant}$	Coolant mass fraction	[-]

Table of contents

Remerciement ii

Résumé en français iv

Abstract v

Nomenclature viii

Table of contents ix

General introduction and motivations 1

Part I Overview of high-pressure turbine flows and loss modelling 19

Chapter 1 Overview of flow physics in film cooled high-pressure turbines 23

1.1 Flow aerodynamics of high-pressure turbines . . . 24
1.2 Near wall flow region . . . 25
1.2.1 Laminar boundary layer . . . 26
1.2.2 Turbulent boundary layer . . . 27
1.2.3 Turbulent transition of the boundary layer . . . 29
1.3 Flow structure of film cooling systems . . . 33
1.4 Heterogeneities of the inflow from the combustor . . . 37
1.5 Secondary flows . . . 38
1.6 Mesh and numerical property requirements . . . 39

Chapter 2 Loss modelling 41

2.1 Thermodynamic representation of losses . . . 42
2.2 Losses in 1D flows . . . 47
2.2.1 Loss coefficients . . . 48
2.2.2 Review of 1D loss models . . . 49
2.3 Extension of 1D balances to LES data . . . 56
2.3.1 Data reduction by the means of averaging procedures . . . 56
2.3.2 Total enthalpy and entropy balance with LES . . . 57
2.4 Second Law Analysis . . . 60
2.4.1 Second Law Analysis applied to fluid mechanics . . . 60
2.4.2 Second Law Analysis adapted to LES . . . 61

2.5 Chapter conclusions 63

Part II LES of academic blades 65

Chapter 3 Loss prediction of the academic uncooled T120 blade 69
3.1 Review of the T120 academic blade 70
3.1.1 Introduction of the AITEB II project 70
3.1.2 Experimental set up and operating point 71
3.1.3 Aerodynamic measurements 72
3.1.4 CFD prediction of the T120 uncooled blade 75
3.2 Methodology and numerics 78
3.2.1 Methodologies to inject fluctuations at the inlet of a LES computation 78
3.2.2 Numerical set up and LES modelling 80
3.3 LES predictions of the uncooled blade T120 84
3.3.1 Validation of the synthetic turbulence injection 84
3.3.2 Impact of freestream turbulence on the flow prediction and validations 86
3.3.3 Investigation of the boundary layers 95
3.3.4 Investigation of losses 107
3.4 Chapter conclusions 121

Chapter 4 Loss prediction of the academic cooled blade T120D 123
4.1 Review of the T120D academic cooled blade 124
4.1.1 Introduction of the T120D blade 124
4.1.2 Cooling system and operating condition 124
4.1.3 Available experimental measurements 127
4.1.4 CFD predictions of the T120D blade 131
4.2 Methodology and numerics 133
4.3 LES prediction of the T120D cooled blade 137
4.3.1 LES results and validations 137
4.3.2 Investigation of the mixing process in the film 157
4.3.3 Investigation of the losses 162
4.4 Chapter conclusions 175

Part III LES of an industry-oriented cooled vane 177

Chapter 5 Loss prediction for an industry-oriented geometry of high-pressure vanes 181
5.1 Review of the NGVs of the FACTOR project 182
5.1.1 Presentation of FACTOR project and test rig 182
5.1.2 Design of the NGVs 183
5.1.3 Experimental operating point 185
5.1.4 Experimental measurements 187

5.1.5 Literature review of CFD prediction . . . 189
5.2 Numerics and modelling . . . 191
5.3 LES results . . . 196
5.3.1 Flow description and validations . . . 196
5.3.2 Investigation of the losses . . . 214
5.4 Chapter conclusions . . . 223

Chapter 6 Develoment of a coolant model to perform LES of realistic NGVs 225
6.1 Review of coolant injection modelling . . . 226
6.2 Coolant ejection modelling in the context of turbine blade cooling . 227
6.3 Numerical set up of the hole-modelled LES . . . 230
6.4 Impact of the coolant model on the flow prediction . . . 233
6.4.1 Impact of the coolant model on operating point . . . 233
6.4.2 Impact of the coolant model on large scale structures . . . 236
6.4.3 Impact of the coolant model on mean flow structure . . . 237
6.4.4 Adiabatic film effectiveness predictions . . . 241
6.4.5 Analysis of the mixing process in the coolant film . . . 243
6.4.6 Impact of the coolant model on the loss prediction . . . 249
6.5 Chapter conclusions . . . 253

General conclusions and perspectives 255

Appendix A LES governing equations of non-reactive compressible flows 261
A.1 Governing equations of non-reactive compressible flows . . . 261
A.2 LES governing equations . . . 262
A.3 AVBP solver . . . 264

Appendix B Effect of the formalism used for γ on the computation of the stagnation variables 265

Appendix C Averaging operator to compute the balance of an extensive variable 269

Appendix D Sentivity of Large Eddy Simulations to the operating point of the T120 blade. 273

Appendix E LARGE EDDY SIMULATIONS OF A HIGHLY LOADED TRANSONIC BLADE WITH SEPARATED FLOW 287

Appendix F Sensitivity of resolved turbulence and wall temperature to mesh adaptation process 301

Bibliography 320

General introduction and motivations

To reduce the impact of the aeronautic industry on the environment, the efficiency of aeronautic engines needs to be improved. One solution is to optimize the design of turbine vanes and blades to maximise the work recovered by the turbine. To qualify the designs of turbine vanes and blades, the identification of loss locations and mechanisms in turbulent flows is required. However, the keywords "Turbomachinery" , "Losses" and "Turbulence" rise a lot of questions and generate even a bit of anxiety for the researchers when they meet together. Indeed, these concepts are very complex because they involve several branches of science such as fluid mechanics, thermodynamic and chaotic systems. Nevertheless, a better understanding of turbulent flow physics has been possible through the use of Computational Fluid Dynamics (CFD). Taking the opportunity of recent developments of high-fidelity prediction tools, this PhD thesis funded through the FUI project CASCADE with the support of Safran Helicopter Engines, aims to contribute to the understanding of the loss generation mechanisms in turbine flows. First off all, the industrial and scientific context of the PhD thesis is recalled.

Impact of aeronautic industry on environment

Aeronautic industry plays a key role in our modern society and globalization. An illustration of its increasing importance appears through the study of future world annual aeronautic traffic prediction by the Airbus' Global Market Forecast (GMF) and the International Civil Aviation Organization (ICAO) plotted in Fig. 1. From



Figure 1 – World annual aeronautic traffic prediction by (GMF, 2018).

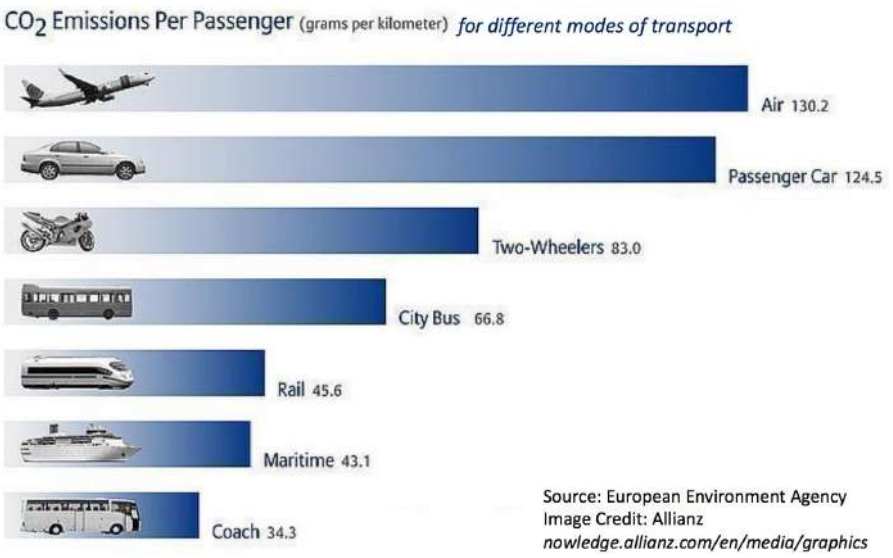

Figure 2 – CO_2 emitted per passenger per kilometer for different transport modes.

this study, world annual air traffic is expected to strongly increase in future years by doubling every 15 years. However, aviation has a strong impact on environment and human health through pollutant emissions such as nitrogen oxide (NO_x), carbon monoxide (CO), sulfur dioxide (SO_2) and fine particles (Kampa and Castanas, 2008). Despite aircraft is the most convenient transport for long distances, a large quantity of carbon dioxide CO_2 is also emitted compared to other modes of transportation for a passenger by kilometer as indicated on Fig. 2. To reduce the environmental impact of aeronautic industry and to comply with Paris Agreement goals on climate change, objectives of reduction of CO_2, NO_x, fine particles and noise have been established by the ICAO and can be found in (ICA, 2016). They should be met by the aeronautic industry and one way of reaching the objectives from an engineering perspective is to design more efficient aircraft's. As a result, the efficiency of gas turbine engines has to be improved. To better understand the constrains of gas turbine optimization, the working principle of gas turbine engine is recalled in the next section.

Gas turbine engine generalities

Gas turbine engines convert chemical energy of fuel by means of combustions into mechanical work or to provide thrust. Due to excellent power to weight ratio, gas turbines find a wide range of applications. Three typical gas turbine engines are today used by aircraft (Fig. 3):

- In turbofans (Fig. 3 (a)), thrust is produced from the suction and ejection of fresh gases through a fan located at the inlet of the engine and from the expansion of hot gases in a nozzle located at the outlet of the engine.
- In turboprops (Fig. 3 (b)), thrust is mainly produced from a inducted propeller located at the inlet of the engine which has a larger diameter compared



(a) (b) (c)

Figure 3 – Examples of the different types of aeronautical engines. (a) Turbofan, *Honda* engine from General Electric (GE). (b) Turboprop, *Dart* engine from Rolls-Royce taken (RR). (c) Turboshaft, *Ardiden* from Safran Helicopter Engine (SHE).

to turbofans. As a result, the by-pass ratio, defined as the bypass stream to the mass flow rate entering the engine core, is higher than turbofans which increases the engine efficiency (Mattingly et al., 2002). However, turboprops can only run at low and medium Mach number due to mechanical stresses on the propeller.

- In turboshafts (Fig. 3 (c)), a mechanical work is recovered by a free turbine to supply a powered shaft to drive the helicopter main rotor.

This last class of engine applied to helicopter engines is of particular interest in this document. Indeed, this thesis has been funded with the support of *Safran Helicopter Engines (SHE)*.

To better explain the inner working of this class of engine, a scheme of a turboshaft and its associated Brayton cycle are presented on Fig. 4. The engine

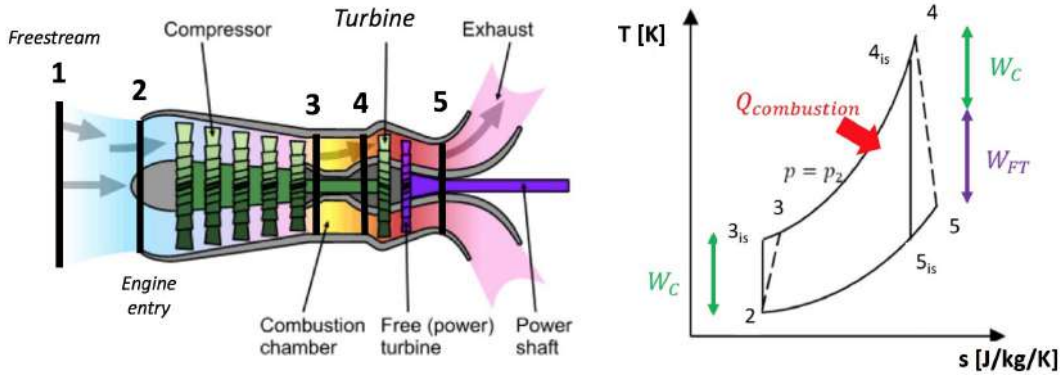

(a) (b)

Figure 4 – Turboshaft engine scheme (a) and associated temperature - entropy (T-s) cycle (b). 1: Freestream condition. 2: Engine inlet. 3: Combustion chamber inlet. 4: Turbine Inlet 5: Exit of the engine. The ideal cycle is represented by the subscript is. The combustion energy supplied to the system is noted $Q_{combustion}$ and the work recovered by the high-pressure turbine (W_T) is supplied to the compressor ($W_C = W_T$). The useful work is retrieved by the free turbine (W_{FT}).

is split into different parts separated by stations corresponding to axial planes to shaft axis as shown on Fig. 4 (a). The working principles is summarized between the stations for an ideal cycle as represented on the Brayton cycle on Fig. 4 (b):

- Station 1 corresponds to freestream ambient conditions.
- From station 1 to 2, the air enters in the engine through the air intake.
- From station 2 to 3, the air is isentropically compressed through a multi-stage compressor to increase the gas pressure and temperature. To do so, the compressor supplies a work W_C to the flow. This multi-stage compressor is usually composed of low-pressure (LP) and high-pressure (HP) stages.
- From station 3 to 4, the fuel is injected and mixed with fresh air to produce a chemical reaction in the combustion chamber at constant pressure. This increases the total energy of burnt gases thanks to chemical energy of fuel released by combustion reactions $Q_{combustion}$. As a result, highly hot gases are obtained at the exit of the combustion chamber.
- From station 4 to 5, burnt gases are isentropically expanded in the turbine. The turbine is usually composed of a high-pressure turbine (HPT) stage and a low-pressure turbine (LPT) stage. The work recovered by the HPT and LPT stages W_T is use to supply work to the compressor, i.e, $W_C = W_T$. Finally, the free turbine recovers useful mechanical work W_{FT} which is then transmitted to the powered shaft.

To evaluate the efficiency of such a cycle, the thermal efficiency η_{th} is defined as,

$$\eta_{th} = \frac{W_{FT}}{Q_{combustion}}, \tag{1}$$

where W_{FT} is the work recovered by the free turbine and $Q_{combustion}$ is the heat supplied by combustion. Assuming constant heat capacity ratio γ , 0D analysis of the cycle is performed to express the thermal efficiency through the use of total pressure P_t and total temperature T_t at stations 2 and 4 yielding (Boyce, 2012),

$$\eta_{th} = \frac{\eta_t \frac{T_{t,4}}{T_{t,2}} \left(1 - \frac{1}{\pi^{\frac{\gamma}{\gamma-1}}}\right) - \frac{\pi^{\frac{\gamma}{\gamma-1}}-1}{\eta_c}}{\frac{T_{t,4}}{T_{t,2}} - \left(1 + \frac{\pi^{\frac{\gamma}{\gamma-1}}-1}{\eta_c}\right)}, \tag{2}$$

where η_t and η_c are respectively the isentropic efficiency of the turbine and of the compressor; π is the compression ratio of the compressor defined as $\pi = \frac{P_{t,3}}{P_{t,2}}$; $T_{t,2}$ represents the total temperature at the inlet of the compressor and only depends on flight conditions of the aircraft; $T_{t,4}$ represents the Turbine Entry Temperature (TET) and depends on the compression ratio and combustion process. If the compressor properties, i.e, π and η_c are assumed fixed, the thermal efficiency η_{th} can be plotted against turbine efficiency η_t and TET $T_{t,4}$ on Fig. 5. Improving efficiency of such an engine can hence be obtained through the increase of the

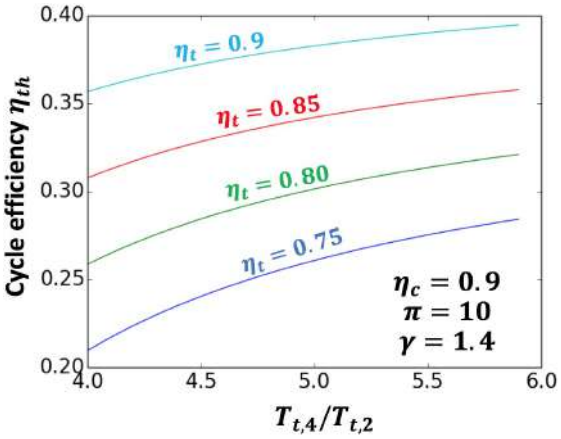

Figure 5 – Cycle efficiency η_{th} [-] against total temperature ratio $\frac{T_{t,4}}{T_{t,2}}$ [-] for different turbine efficiencies. Other parameters are fixed at $\pi = 10$, $\eta_c = 0.9$, and $\gamma = 1.4$.

TET and η_t. Thus, the TET of industrial engines has significantly increased since the first designs of gas turbine. To illustrate this increase, the evolution of the TET over the year for different aeronautic engines is provided in Fig. 6. From this graph, a clear trend is deduced showing an increase of the TET of $10K$ a year. In recent engines, the TET is found to approach 1800 K. As a consequence, the high-pressure turbine located downstream the combustor suffers from a very harsh thermal environment. To illustrate the impact of such high temperatures issued from the combustor on stator and rotor turbine blades, a scheme of the first stage of

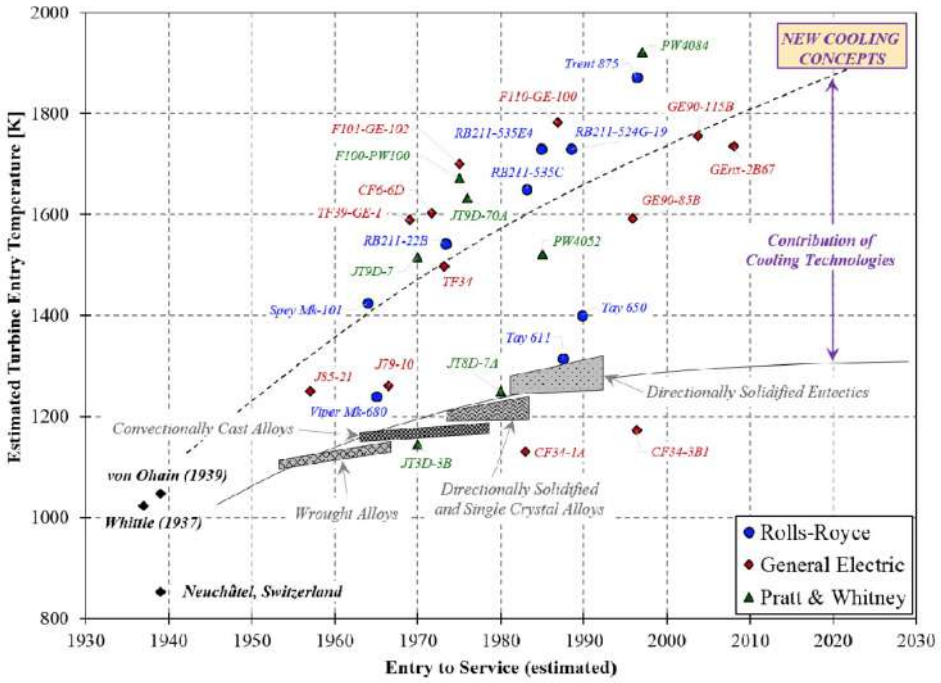

Figure 6 – Temporal evolution of the Turbine Entry Temperature (TET) [K] for different aeronautic engines. Extracted from (Terzis, 2014).

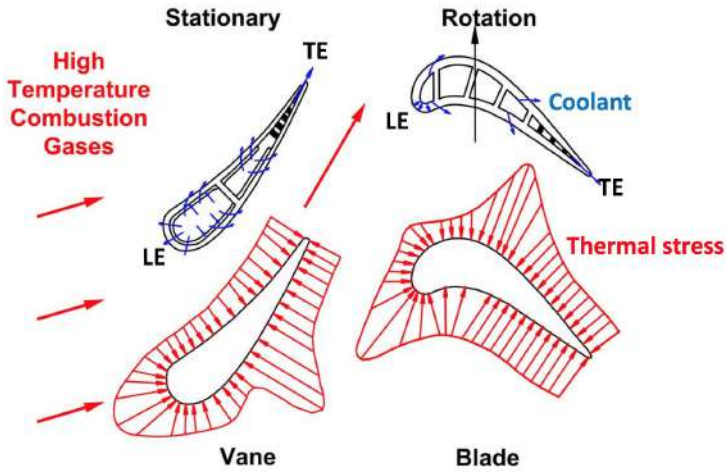

Figure 7 – Scheme of stator and rotor stages of a turbine adapted from (Han and Rallabandi, 2010). Leading edge (LE) and trailing edge (TE).

the turbine is provided on Fig 7. The first stage of turbine is composed of a stator vane, called Nozzle Guide Vane (NGV), which accelerates, deviates and aligns the flow on the rotor blades. Downstream, the rotor blades rotate around the axis of the engine and extract mechanical work from the fluid. The blades are bounded by their leading edge (LE) and trailing edge (TE). Due to their positions in the engine, both stator vanes and rotor blades are exposed to high temperature levels. However, the maximum capacity of turbine material lies around 1300 K despite the use of new alloys and thermal barrier coating (Caron and Khan, 1999). Aside the maximum temperature, large temperature gradients in the blade can also induce high mechanical stresses which can degrade turbine blades (Brandt and Wesorick, 1994; Montomoli et al., 2012). To obtain an acceptable blade lifetime, maximum temperature on the blade as well as temperature gradients must be limited. To do so, cooling systems have been implemented for turbine blades and vanes and are addressed in the next section.

Turbine cooling systems

The ability of a cooling system to limit the blade temperature is crucial for engine design. Indeed, efficient cooling systems allows to increase the allowable gas temperature at the turbine inlet which improves the thermal efficiency of the engine. Cooling systems consist in extracting air from the compressor which is around 600 - 800 K. Then, this air is transported to turbine stages through the secondary air system of the engine. Finally, the air which is colder than hot gases exiting the combustor is re-injected inside the vane through the internal cooling system and around the vane through the external cooling system to limit the wall temperature. A scheme of a cooled turbine blade is provided on Fig. 8. For the internal cooling system, Fig. 8 (a), coolant is injected though interior channels to evacuate excess of heat. Thermal exchange between the solid and the coolant can be improved by the presence of impingement jets and ribs in the channels to increase

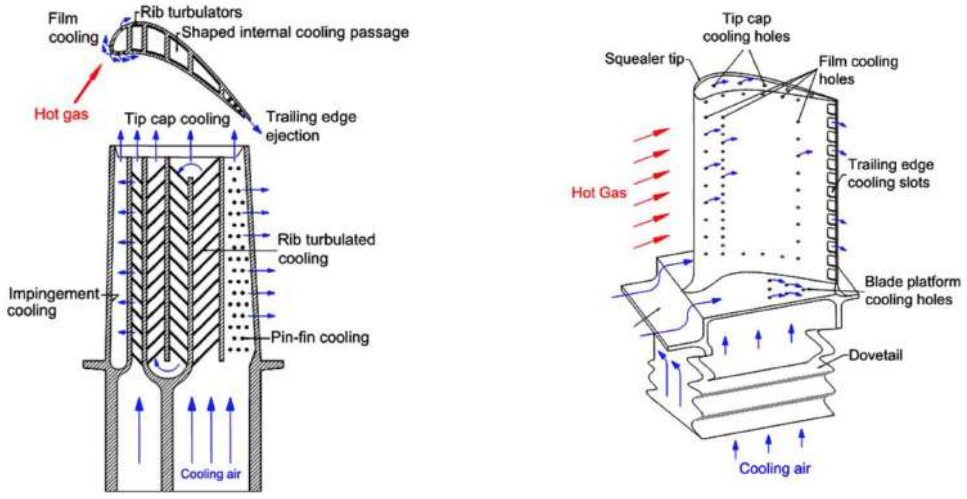

(a) (b)

Figure 8 – Scheme of cooling systems of a turbine blade extracted from (Han and Rallabandi, 2010). Internal cooling system (a) and external cooling system (b).

heat exchange surfaces and turbulence (Han and Ekkad, 2001). Then, coolant is ejected around the blade through coolant holes drilled on the blade surface to form a coolant film which corresponds to the external cooling system, Fig. 8 (b). It is important to note that coolant is mainly ejected at the leading edge of the blade where hot gases are expected to impact this region of the vane. Coolant is also ejected at the trailing edge of the vane where the thickness of the wall is small and then expected to suffer from high thermal stresses.

However, cooling systems were shown to degrade the thermal efficiency of the engine (Horlock et al., 2001; Wilcock et al., 2005). Indeed, when the air is extracted from the compressor and transported to turbine stages, the coolant flow suffers from pressure losses through the secondary air system. Then, when the coolant is then ejected around the vane, the coolant mixes with the hot stream coming from the combustor. This mixing process generates aerodynamic and mixing losses which degrades the turbine efficiency η_t. This mixing process is also expected to decrease total temperature of the main stream which decreases the work recovered by rotor blades.

As a consequence of the previous discussions, the main industrial challenge in the context of turbine blade cooling is to improve the efficiency of turbine cooling systems while limiting the losses generated by the flow aerodynamics. To overcome such challenges, one solution is to qualify the designs of turbine blades and vanes through the prediction of the blade wall temperature and the evaluation of losses in such complex systems.

Contributions of the thesis to industrial challenges

Taking the opportunity of recent developments of high-fidelity prediction tools, the accurate prediction of blade wall temperature and losses is addressed in this PhD thesis. To quantify the losses in such complex systems, current methodologies used in the industry are mainly based on analytical loss models (Denton, 1993). These loss models are generally based on a 1D evolution of the flow properties constructed from simple configurations which neglects the local complexity of the flow physics. Furthermore, the majority of the loss models are initially built for isothermal configurations, i.e, without temperature difference. **As a result to evaluate the losses in the context of turbine blade cooling, a new context of work is proposed in this thesis.** With this new context of work, the loss generation locations and mechanisms issued by the flow aerodynamics and by the mixing process taking place between the hot and the coolant streams will be investigated. To simplify the study, the framework of the thesis will be limited to cooled turbine vanes featuring only film cooling systems.

To precisely evaluate the losses, an accurate prediction of the flow physics is nevertheless required. In an industrial context, Reynolds numbers generally lies between 10^5 and 10^6 and transonic Mach numbers are observed at the trailing edge of turbine vanes. The flow physics present in such configurations is then expected to be compressible and highly turbulent. Since the difference of temperature between the hot and coolant gases is high ($\approx 1000\ K$), the flow is considered strongly anisothermal with variable heat capacity ratio. To predict such a flow, the compressible Navier-Stokes equations (recalled in Appendix A.1) need to be solved. Since the flow is expected to be highly turbulent, generalities on turbulent flows are recalled in the next section.

Generalities on turbulent flows

Turbulence has been observed for a long time as indicated on Fig 9. To characterise

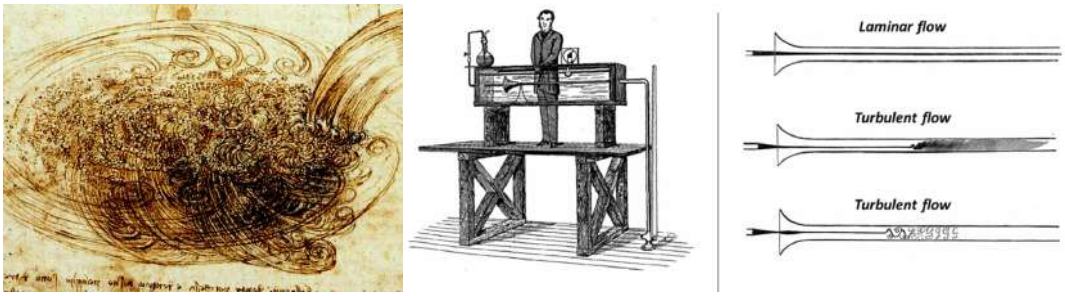

(a) (b)

Figure 9 – Turbulence sketched and experimented by Leonard Da Vinci around 1510 (a) and experiment of Reynolds (b) in 1883.

turbulent flows, Reynolds introduced in 1883 the Reynolds number Re so that,

$$Re = \frac{V_0 L}{\nu_0}, \tag{3}$$

built from a reference velocity V_0, a characteristic length L and a reference kinematic viscosity ν_0. The Reynolds number represents the ratio between the convective term and the viscous term in the momentum equation of the Navier-Stokes equations. When the Reynolds number remains low, the viscous term dominates and damps instabilities in the flow. However above a critical value of Re, the non-linear term dominates the viscous term and instabilities can develop in the flow creating turbulent structures which are highly unsteady, 3D presenting a stochastic behaviour (Pope, 2000). In 1922, (Richardson, 1922) assumed that the size of turbulent structures are of a wide range assimilated to eddies. He postulated that turbulence is produced in the large eddies and then transmitted to smaller eddies, where turbulence is dissipated by viscous effects. In 1941, (Kolmogorov, 1941) proposes a theory to investigate the energy transfer in the turbulent structures assuming homogeneous isotropic turbulence for large Reynolds numbers. He represented the energy transfer between the eddies of different sizes by the Kolmogorov cascade represented on Fig. 10. The largest scales are characterized by the integral length scale l_t where the production of turbulence dominates. Assuming a small perturbation in the velocity field in the Navier-Stokes equations, (Kolmogorov, 1941) shows that the non-linear term produces more perturbations of smaller scale for high Reynolds numbers. It results in an energy transfer from the large eddies to smaller eddies in the inertial range. Experiments confirm that this energy transfer in the inertial range is characterized by the famous -5/3 slope against the size of turbulent structures in the frequency space. Finally, the viscous dissipation domi-

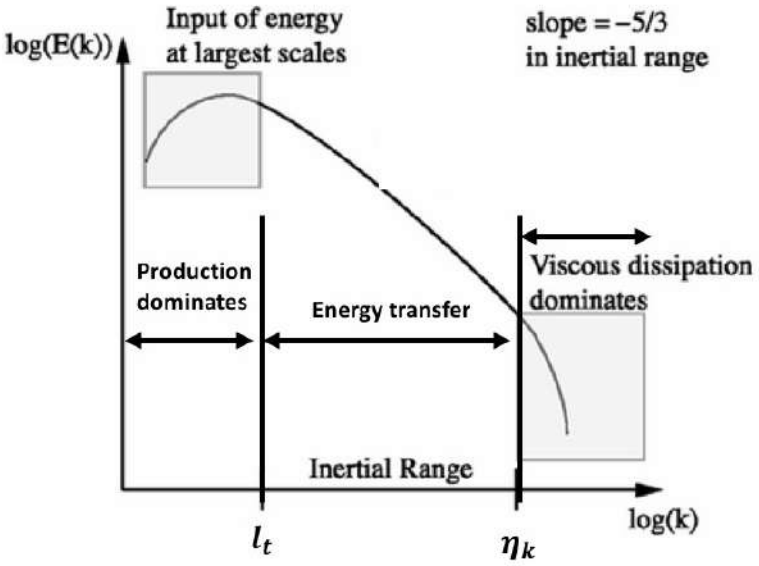

Figure 10 – Kolmogorov cascade of the energy transfer of turbulent eddies. $E(k)$ represents the power spectral density for each wave number k.

nates for the smallest eddies characterized by the Kolmogorov scale η_k. Performing a non-dimensional analysis, (Kolmogorov, 1941) estimated that the ratio between l_t and η_k is mainly dictated by the Reynolds number reading,

$$\frac{l_t}{\eta_k} \sim Re^{\frac{3}{4}}. \tag{4}$$

As a result for a given integral length scale, the higher the Reynolds number is, the smaller the Kolmogorov scale is. If applying to turbomachinery, taking a Reynolds number around $Re \sim 10^6$ and an integral scale of the size of the chord of a typical NGV, i.e, $l_t \sim 100mm$, the Kolmogorov scale is estimated to be around $\eta_k \sim 1\mu m$. To deal with such a wide of range, various modelling approaches have been constructed to yield numerical predictions of turbulent flows. The most common modelling approaches for the prediction of turbulent flows are presented in the next section.

Numerical prediction of turbulent flows

To predict the flow of complex systems as in turbomachinery, the turbulence can be either resolved or modelled according to 3 methods: Direct Numerical Simulation (DNS), Reynolds Average Navier-Stokes (RANS) and Large Eddy Simulations (LES). These notions of modelling rely on the energy transfer in the turbulent flows represented by the Kolmogorov cascade and are summarized on Fig. 11.

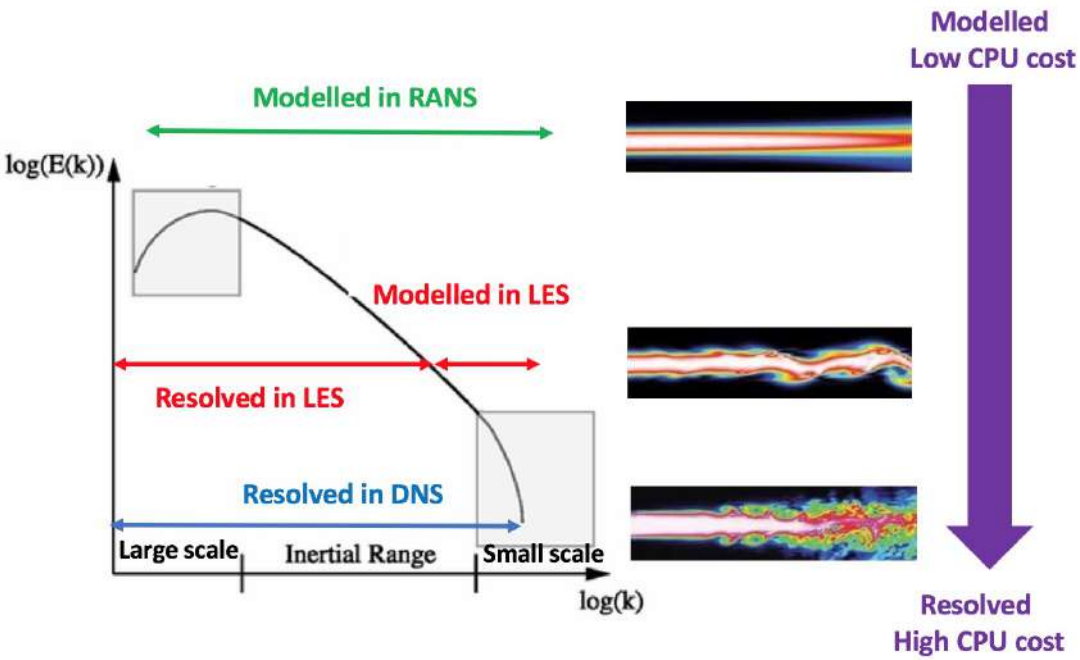

Figure 11 – Strategies to deal with numerical turbulent flow prediction and associated represented of a turbulent jet. Adapted from (Laidlaw and Vilanova, 2012).

Direct Numerical Simulation (DNS) DNS consists in resolving all the range of turbulence on the mesh. This method requires that the mesh size is sufficiently small to resolve the Kolmogorov scale. High order numerical schemes are also necessary to avoid numerical dissipation of small wave lengths of turbulence which induces very CPU intensive simulations. For this reason, DNS are usually performed in the context of fundamental research. However, due to the constant increasing of the CPU resources, DNS of limited span wise blade begin to be accessible (ZAKI et al., 2010; Sandberg et al., 2015; Wheeler et al., 2017). Nonetheless, it remains very expensive for high Reynolds number flow and complex geometries.

Reynolds Average Navier Stokes (RANS) RANS consists in modelling the entire field of turbulence to access only to the statistical mean flow properties. To do so, the (Favre, 1969) averaging is applied to the compressible Navier-Stokes equations and the effect of the turbulence on the mean flow is reduced in the Reynolds stress tensor. By observing that the main effect of turbulence on the mean field is the increase of the mixing and of the diffusion in the flow, (Boussinesq, 1877) proposed a turbulent viscosity closure to model the Reynolds stress tensor. From this Boussinesq hypothesis, several methods are described in the literature to close the turbulent viscosity (Pope, 2000). RANS has been used for a long time for the prediction of the flow in complex systems of turbomachinery since the computational time and associated CPU effort are low compared to others modelling approaches. However, RANS suffers from limitations for highly unsteady flows and is very sensitive to the turbulence modelling as well as to the mesh resolution (S. Lardeau, 2005). When addressing anisothermal flows, RANS suffers from lack of accuracy to predict the mixing process between hot and coolant streams (Dyson et al., 2012; Ravelli and Barigozzi, 2017; Dickhoff et al., 2018).

Large Eddy Simulations (LES) LES aims at resolving the most energetic turbulent structures on mesh while the smaller turbulent structures supposed to be more universal, i.e, independent of the geometry, are modelled (Sagaut, 2000). Theoretically, this is obtained by applying a low pass filter (here noted $\widehat{\bullet}$) to the governed equations with a filter size Δ_f. The filtered equations can be found in Appendix A.2. Ideally, the grid size Δx is recommended to satisfy $\Delta x = \frac{\Delta_f}{2}$ to ensure that the smallest resolved structures are correctly discretized by the mesh and to avoid numerical issues (Lele, 1992). However in practise, $\Delta_f \approx \Delta x$ to limit the computational cost. In that case, it is important that numerical schemes have good spectral properties to preserve the smallest resolved structures. Taking advantage of the energy distribution of the turbulent structures, the majority of turbulent energy will be resolved on the mesh. The effect of unresolved turbulence on resolved fields is represented by the filtered residual stress tensor $\widehat{u_i'' u_j''}$, where u_i'' is the residual velocity with respect to resolved field. To close this term, a common approach is to use the Boussinesq approximation (Boussinesq, 1877) which introduces an eddy viscosity model through the use of a sub-grid scale turbulent viscosity ν_t. Note that this approach assumes that sub-grid turbulence has a purely dissipative effect on the resolved field. Others more sophisticated models

have been introduced (Bardina et al., 1983; Germano, 1992; Zang et al., 1993) but will not be here detailed.

If compared to DNS, the mesh size is less constrained with LES thanks to the filtering which gives access to simulation of higher Reynolds number. Contrary to RANS, LES is less sensitive to the turbulence modelling if 80% of the turbulent kinetic energy is resolved on mesh (Pope, 2000). For these reasons, LES is well appropriated for the flow prediction in turbomachinery (Tucker, 2011a; Tyacke and Tucker, 2014). With the increase of computer power and using High Performance Computing (HPC) facilities, LES can predict high Reynolds number flows in complex geometries (Gourdain et al., 2009b; Gicquel et al., 2012). As a result, this specific approach is the CFD method retained in this work.

In the context of turbine blade cooling, the flow in the cooling system is bounded by walls and the mixing process between the hot and coolant flows occurs in the near wall flow region of the blade. However, turbulence in the near wall flow region is known to strongly impact the mixing process and wall fluxes, i.e, wall shear tress and wall heat flux (Pope, 2000). The treatment of the turbulence in the near wall region is then highly critical in LES and needs to be specifically addressed. To deal with such a flow when dealing with LES, two approaches can be adopted.

One first solution aims to directly resolve turbulent structures on the mesh which corresponds to a Wall-Resolved LES (WRLES). In this case, the mesh design near the wall is strongly constrained to ensure that turbulent structures are resolved on mesh. To evaluate the near wall mesh resolution with respect to the flow physics, a non-dimensional mesh resolution is used and corresponds to a Reynolds number based on a friction velocity u_τ so that,

$$u_\tau = \sqrt{\frac{\tau_w}{\rho}}, \tag{5}$$

where τ_w is the wall shear stress. From this friction velocity, the non-dimensional normal mesh resolution is given through the evaluation of Δy^+ so that,

$$\Delta y^+ = \frac{\Delta y u_\tau}{\nu}, \tag{6}$$

where Δy is the mesh resolution normal to the wall and ν is the kinematic viscosity. Note that a similar definition can be used to define the non-dimensional streamwise mesh resolution Δx^+ and non-dimensional span-wise mesh resolution Δz^+. To predict the correct wall shear stress, one off-wall point must be included in the viscous sub-layer of the turbulent boundary layer, i.e, $\Delta y^+ < 5$ (Tyacke and Tucker, 2014). To resolve the anisotropic wall turbulent structures in this region, the mesh resolution is also constrained in the span-wise direction Δz^+ and stream-wise direction Δx^+ so that $50 < \Delta x^+ < 130$ and $10 < \Delta z^+ < 30$ (Tyacke and Tucker, 2014). This approach is then costly for high Reynolds number flows

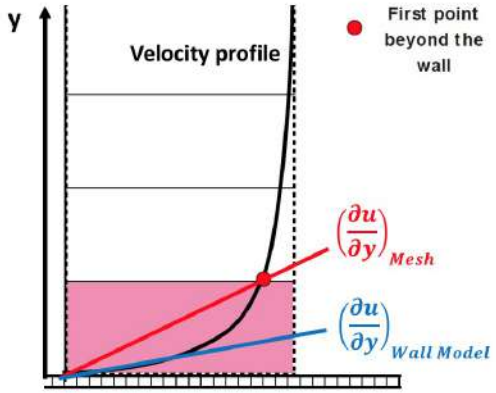

Figure 12 – Turbulent boundary layer velocity profile along wall normal distance y and the resulting velocity gradient $\frac{\partial u}{\partial y}$ with and without wall models.

and usually used for academic vanes on a limited-span-wise extent. Nevertheless, if the first off-wall point is not located in the viscous sub-layer of the boundary layer, the predicted wall shear stress is over-estimated as shown on Fig. 12.

To recover the wall shear stress in such cases, wall models have been introduced resulting in a Wall-Modelled LES (WMLES). It is important to note that the majority of wall models are only valid for attached flows. The main families of wall models are here summarized:

- *Analytical wall law or equilibrium model.* In this approach, the wall shear stress is deduced from an analytical law. The first analytical wall law was proposed by (Von Karman, 1930) and is known as the logarithmic law of the wall. For this wall law, a turbulent boundary layer developing on a flat plate is considered and only the mean flow is treated. For an incompressible flow with no streamwise pressure gradient in the boundary layer and an equilibrium between the viscous and Reynolds stresses, the wall shear stress can be analytically deduced from the properties of the fluid and the distance of first off-wall point in terms of Δy^+. Note that in this approach, the Reynolds stress tensor is closed with a mixing length model. More sophisticated wall laws have been introduced to take into account compressibility effects in the boundary layer for high Mach number flows (Driest, 1951; Huang and Coleman, 1994) and streamwise pressure gradient term (Mcdonald, 1969; Huang and Bradshaw, 1995). In terms of mesh design, since the viscous sub-layer is modelled, the first off-wall point can be included in the inertial zone of the turbulent boundary layer, i.e, $\Delta y^+ > 30$. To resolve turbulent structures in this region, the mesh resolution is also constrained in the span-wise direction Δz^+ and the stream-wise direction Δx^+ so that $100 < \Delta x^+ < 600$ and $100 < \Delta z^+ < 300$ (Tyacke and Tucker, 2014).

- *Integral Wall Model LES* (IWMLES) (Catchirayer et al., 2018). In this approach, the turbulent boundary layer equations are integrated from the wall

to the first off-wall point. Then the velocity profile is approximated by a polynomial function. The coefficient of the polynomial function is deduced from the integral boundary layer properties to reconstruct the velocity profile. The wall shear stress can be deduced from the resulting velocity profile. In this approach, pressure gradient and compressibility effects are then taken into account in the integral equations. However, it also requires numerical methodologies to solve the integrated equations which increases the CPU cost of the near wall region treatment.

- *ODE / PDE based models.* In this approach, the mean turbulent boundary layer equations (TBLE) (Schlichting and Gersten, 2000) are resolved in a wall-modelled layer defined from the wall to a normal distance located in the LES mesh (Bodart and Larsson, 2011). If neglecting streamwise terms in the mean TBLE, fields only depends on the normal direction and the mean TBLE can be then reduced to a set of Ordinary Differential Equations (ODE). Taking a model to close the Reynolds stress tensor, the set of ODEs can be numerically solved on an 3D implicit grid defined in the wall-modelled layer. In terms of boundary conditions for the TBLE, no-slip condition is taken at wall and informations from the LES mesh is imposed at the top of the wall-modelled layer. This implies a weak interaction between the wall-modelled and the external layer of the boundary layer. From this numerical resolution, the velocity profile is obtained and so the wall shear stress can be deduced. If taking into account streamwise terms, the TBLE corresponds to a set of Partial Differential Equations (PDE) which should also be numerical solved to obtain the wall shear stress (Bodart and Larsson, 2011). Note that this approach is only limited to attached flows since boundary layer hypothesis should be satisfied. As a result, difficulties are encountered for the definition of the wall-modelled layer for cases featuring separations.

- *Detached Eddy Simulation (DES)* (Spalart et al., 1997). With this method, RANS is performed in the near wall region where the flow is attached. Otherwise, LES is used far from the wall or in the wall region where the flow is detached. Contrary to the ODE / PDE model approaches, the interface between RANS and LES is not explicitly defined on mesh and is determined by the turbulent model adopted for the numerical resolution. The exchange of informations between the two zones requires a special treatment which increases the CPU effort of such methodologies. Note that zonal DES's have been introduced where the interface LES/RANS is explicitly defined on mesh by the user (Spalart, 2009).

In the present work, both approaches will be used:

- WRLES for academic vanes configurations to give access to the near wall flow region.

- WMLES for industry-oriented applications to limit the CPU effort inherent in the resolution of the near wall physics. For simplicity, the analytical logarithm law of the wall will be adopted.

Scientific objectives of the thesis

To overcome the industrial challenges discussed above, the main objective of this PhD work is to evaluate and investigate the loss generation locations and mechanisms in the context of turbine blade cooling for industrial purposes with LES. To evaluate the losses in such complex systems, 1D analytical loss models are generally used. These loss models assumes that the flow is stationary, uniform for each axial section of the engine (fully mixed) with constant heat capacity ratio. However, the hypotheses used to derive 1D loss models are not verified for turbine blade cooling where the flow is 3D, unsteady and anisothermal with variable heat capacity ratio. To overcome the limitations inherent in 1D loss models and to evaluate losses in the context of turbine blade cooling, a loss modelling is proposed and high-fidelity methodologies are introduced in this PhD work. The first methodology is to evaluate the losses generated between two stations of the flow through balances of total variables, i.e, total pressure P_t and total temperature T_t (Denton, 1993). To reduce the LES data to a 1D steady evolution, an averaging procedure is introduced in the present work. The second methodology is to study loss maps through the use of *Second Law Analysis* (SLA) (Bejan, 1982). In this approach, loss maps are constructed from the local entropy source terms. The main advantage of this approach is that losses can be locally investigated through the study of loss maps and does not require any averaging procedures contrary to 1D loss models. With this approach, the loss generation locations and mechanisms issued by the flow aerodynamics and by the mixing process taking place between hot and coolant flows will be investigated. A particular attention will be paid to the losses generated in the near wall flow region (i.e, boundary layer regions).

To investigate the loss generation mechanism, an accurate prediction of the flow with LES is nevertheless required. When addressed LES to turbomachinery, this approach has proved its capacity to predict the flow aerodynamics for academic configurations (Collado, 2012; Papadogiannis, 2015; Koupper, 2015; Segui Troth, 2017; Pichler et al., 2017; Harnieh et al., 2018). However, when extended to aerothermal configurations, only isolated cooling systems have been simulated (Duchaine et al., 2009b; Fransen, 2013; Simiriotis, 2016; Aillaud, 2017; Grosnickel, 2019). Very few LES studies representing full span-wise extent of 3D cooled turbine vanes have been reported in the literature (Ling and Guoliang, 2011; Ravelli and Barigozzi, 2017). **As a result of the previous discussion, the second objective of this thesis is to validate the capacity of LES to predict the flow aerodynamics, the blade load distribution and the blade wall temperature in the context of turbine blade cooling.** For the flow prediction, the LES solver AVBP co-developed at CERFACS (Toulouse, France) and at IFPEN (Rueil-Malmaison, France) is chosen. A brief presentation of AVBP can be found in Appendix A.3.

To achieve the different scientific objectives cited above, LES of academic high-pressure vanes and blades of increasing complexity are performed. The configura-

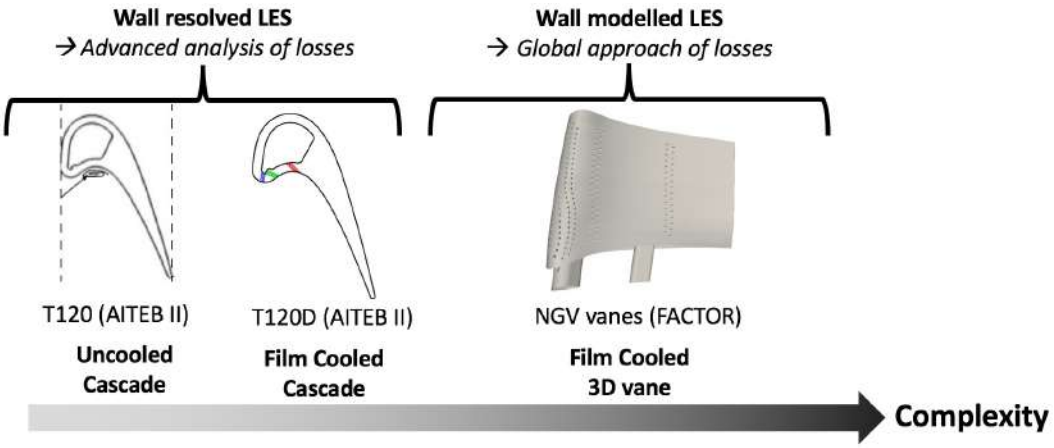

Figure 13 – Configurations studied in the thesis.

tions studied in this present work are presented on Fig. 13. The first configuration is the academic uncooled highly-loaded cascade blade *T120* experimentally studied in the European Aerothermal Investigations on Turbine Endwalls and Blades (AITEB) project. The second configuration is the academic film-cooled blade *T120D* which is based on the *T120* design and experimentally studied in the same project. For these two academic configurations, the capacity of LES to predict the blade load distribution and the adiabatic wall temperature will be validated through the comparison with experimental results. Then, the loss generation mechanisms issued by the flow aerodynamics and mixing process between the hot and coolant flows will be investigated. To do so, WRLES will be performed to obtain accurate predictions of the near wall flow physics. The third configuration studied in this work is the industry-oriented configuration corresponding to the 3D film-cooled high-pressure vanes of the European Full Aerothermal Combustor Turbine interactiOns Research (FACTOR) project. The capacity of LES to predict the blade load distribution, the adiabatic wall temperatures as well as the losses for such a complex configuration will be evaluated. Due to the configuration complexity, a global approach of losses is adopted. To do so, a WMLES will be performed to avoid the overall cost imposed by the near wall flow resolution for an industrial context. However, such a simulation still requires lot of CPU efforts to resolve the flow in the cooling system of the vanes. To alleviate this CPU issue, the coolant can be directly ejected on the vane surfaces without meshing the cooling system through the use of a coolant ejection model. To ease the use of LES in an industrial context, a new coolant ejection model is introduced in this PhD work. The capacity of the coolant ejection model to reproduce the adiabatic wall temperature and losses is finally assessed on the high-pressure vanes of the FACTOR project.

For all configurations, the losses are investigated through the use of the different methodologies introduced in this work. More specifically, the capacity of SLA to evaluate the losses in strongly anisothermal flows is discussed.

Organization of the manuscript

Based on the described objectives, the manuscript is organized as follows:

Part I In Chapter 1, an overview of the flow aerodynamics observed in film cooled high-pressure turbine flows is provided to evidence the region of interests for the prediction of the blade wall temperature and losses. Following this discussion and to accurately predict such a flow, mesh and numerical property requirements are discussed. In Chapter 2, the loss modelling is addressed and the methodologies to evaluate the losses with LES are introduced.

Part II In this part, the academic *T120* and *T120D* cascade blades are addressed. In Chapter 3, the WRLES of the uncooled *T120* cascade blade is addressed. In Chapter 4, the WRLES of the cooled *T120D* cascade blade is presented.

Part III In this part, the industry-oriented configuration of the NGVs of the FACTOR project is addressed. In Chapter 5, the WMLES of the NGVs of FACTOR is presented. In Chapter 6, the coolant ejection model is introduced and assessed on the NGVs of FACTOR.

Note finally that a part of this work has been published in international conferences and journals:

- ***M. Harnieh**, L. Gicquel, and F. Duchaine. Sensitivity of large eddy simulations to inflow condition and modeling if applied to a transonic high-pressure cascade vane. In Proceedings of the ASME Turbo Expo 2017: Turbine Technical Conference and Exposition, GT2017-64686, Charlotte, USA, 2017.*

- ***M. Harnieh**, L. Gicquel, and F. Duchaine. Large eddy simulations of a highly loaded transonic blade with separated flow. In Turbomachinery Technical Conference and Exposition 2018, GT2018-75730, Oslo, Norway, 2018.*

- ***Harnieh, M.**, Thomas, M., Bizzari, R., Gicquel, L. Y. M. and Duchaine, F. (2018) Assessment of a coolant injection model on cooled high-pressure vanes in Large Eddy Simulation, 12th International Symposium on Engineering Turbulence Modelling and Measurements (ETMM12). Montpellier, France, 9 2018, ERCOFTAC.*

- ***Harnieh, M.**, Thomas, M., Bizzari, R., Gicquel, L. Y. M. and Duchaine, F. Assessment of a coolant injection model on cooled high-pressure vanes with Large Eddy Simulation. Flow Turbulence and Combustion (2019).*

- *N. Odier; A. Thacker; **M. Harnieh**; G. Staffelbach; L. Gicquel; F. Duchaine; N. G. Rosa, PhD; J. Mueller. A mesh adaptation strategy for complex wall-modeled turbomachinery LES, Computers and Fluids, 2019.*

- ***M. Harnieh***, *N. Odier, J. Dombard, F. Duchaine and L. Gicquel. Loss predictions in the high-pressure film-cooled turbine blade cascade T120D by mean of Wall-resolved Large Eddy Simulation. In Turbomachinery Technical Conference and Exposition 2020, GT2020-14231, London, England, 2020.*

- ***M. Harnieh***, *N. Odier, J. Dombard, F. Duchaine and L. Gicquel. Loss predictions in the high-pressure film-cooled turbine vane of the FACTOR project by mean of Wall-modeled Large Eddy Simulation. In Turbomachinery Technical Conference and Exposition 2020, GT2020-14232, London, England, 2020.*

Part I

Overview of high-pressure turbine flows and loss modelling

Outline of Part I

In this first part of the PhD work, the flow physics observed in film cooled high-pressure turbines and loss modelling are addressed. In Chapter 1, an overview of the flow physics of high-pressure turbines is presented to evidence the regions of interest for the prediction of the blade wall temperature and losses. In Chapter 2, a loss thermodynamic modelling is proposed and the different methodologies to evaluate the losses in this work are introduced.

Chapter 1

Overview of flow physics in film cooled high-pressure turbines

Contents

1.1 Flow aerodynamics of high-pressure turbines **24**

1.2 Near wall flow region **25**

1.2.1 Laminar boundary layer 26

1.2.2 Turbulent boundary layer 27

1.2.3 Turbulent transition of the boundary layer 29

1.3 Flow structure of film cooling systems **33**

1.4 Heterogeneities of the inflow from the combustor **37**

1.5 Secondary flows **38**

1.6 Mesh and numerical property requirements **39**

In this chapter, an overview of the physics of film cooled high-pressure turbines is provided. The aim of this chapter is to identify the critical regions and parameters governing the flow aerodynamics, the blade wall temperature as well as the losses. To do so, the flow aerodynamics around high-pressure turbine vanes is first presented in Section 1.1. A specific focus of the near wall flow region is given in Section 1.2. Next, a description of the flow dynamic observed in film cooling systems is presented in Section 1.3. Afterwards, the effect of temperature heterogeneities coming from the combustor on the thermal environment of high-pressure turbine vanes is addressed in Section 1.4. Finally, secondary structures observed around 3D high-pressure vanes are presented in Section 1.5. From this overview of the flow physics, mesh and numerical property requirements are discussed in Section 1.6 to finely predict such a flow with LES.

1.1 Flow aerodynamics of high-pressure turbines

To illustrate the flow aerodynamics observed around high-pressure vanes, instantaneous Mach number, numerical Schlieren and wall shear stress maps obtained for the academic high-pressure vane LS89 issued from the work of (Collado, 2012; Segui-Troth et al., 2017) are provided on Fig. 1.1. From the Mach number map, Fig. 1.1 (a), the high-pressure vane is observed to deviate and to accelerate the flow. The acceleration of the flow is induced by the local curvature of the vane which generates a normal pressure gradient to the wall. Since the curvature of the vane is different on its both sides, the acceleration is stronger on the suction side (SS) than the pressure side (PS). The flow presents very localized features as represented on Fig. 1.1 (b). Upstream the vanes, freestream turbulent structures coming from the combustor are transported through the flow passage between the vanes, zone 1. Downstream the vanes, a wake presenting a deficit of velocity is observed in zone 2. The wake originates from the shear generated by the velocity difference of the streams coming from both pressure and suction side of the vane and depends on the shape of the vane trailing edge. The wake is generally observed to be turbulent in turbine flows and contains large coherent structures which break into smaller structures. The disturbances generated by the wake produce acoustic waves which impact the other vanes as shown in zone 3. On the suction side of the vane, the acceleration of the flow can lead to a supersonic region when the Mach number overcomes 1. Downstream this supersonic region, shock waves interacting with the wake are noticed, zone 4. Finally, a low velocity region is observed in the near wall flow region, zone 5. This specific region is known to generate the majority of losses in turbine flows (Denton, 1993). A closer look of the flow structure in this region is then given in the next section.

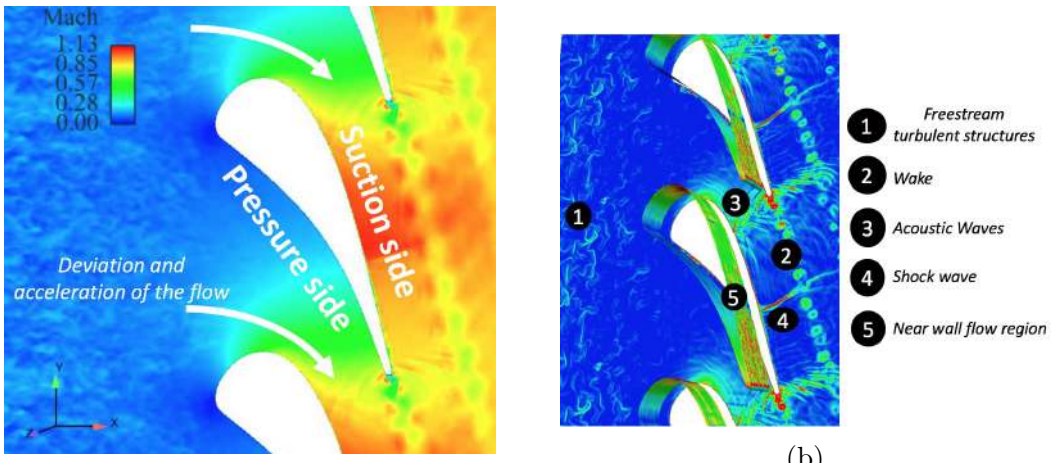

(a) (b)

Figure 1.1 – Instantaneous Mach number Ma [-] (a), numerical Schliren $\frac{\|\nabla\rho\|}{\rho}$ $[m^{-1}]$ and wall shear stress τ_w $[Pa]$ maps (b) for the high-pressure vane LS89. Adapted from (Collado, 2012; Segui-Troth et al., 2017).

1.2 Near wall flow region

The near wall flow region is characterized by a strong sheared flow due to the velocity difference between the freestream flow and the no-slip wall condition. To describe this specific region of the flow, (Prandtl, 1905) introduced the theory of *boundary layers*. The main characteristics of boundary layers are presented on Fig. 1.2. The boundary layer region is mainly dominated by viscous effects. The boundary layer is characterized by its thickness δ which grows along a wall in the streamwise direction. Normal profile of the streamwise velocity $u(y)$ lies between the freestream velocity U_∞ and no-slip condition at wall $u(y = 0) = 0$. Wall shear stress τ_w corresponds to the momentum diffusion due to viscous effects and expresses as,

$$\tau_w = \mu \frac{\partial u}{\partial y}, \tag{1.1}$$

where μ is the dynamic viscosity. To model the evolution of the flow properties in the boundary layer, the boundary layer equations can be derived from the Navier-Stokes (NS) equations following some hypothesis recalled here (Schlichting, 1955):

- The wall curvature radius R_c is small compared to the characteristic length of the wall L so that $\frac{R_c}{L} >> 1$. In that case, the wall can be considered as a flat plate.
- The thickness of the boundary layer δ is very small compared to the characteristic length of the wall L, so that $\frac{\delta}{L} << 1$.

From these hypotheses a dimensional analysis of the NS equations can be realized which leads to the following conclusions:

- Normal velocity v is negligible compared to tangential velocity u so that, $v << u$.

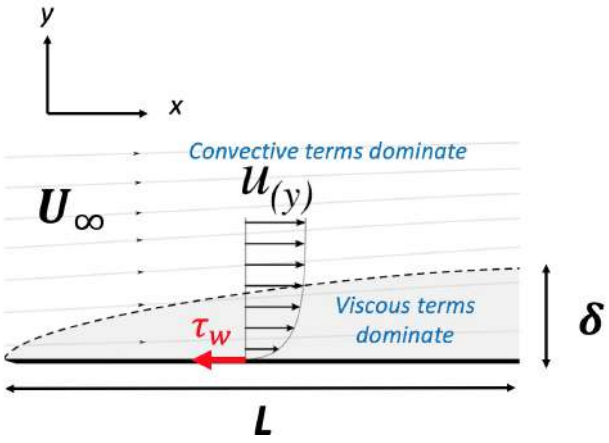

Figure 1.2 – Scheme of a boundary layer. Characteristic length of the wall is represented by L, thickness of the boundary layer δ, streamwise velocity u, freestream velocity U_∞ and wall shear stress τ_w. Tangential and normal directions to the wall are given by x and y.

- Normal gradients dominate streamwise gradients, so that, $\frac{\partial}{\partial y} >> \frac{\partial}{\partial x}$. Streamwise pressure gradient $\frac{\partial P}{\partial x}$ is then considered independent with respect to normal direction to the wall in the boundary layer thickness and only depends on freestream flow.

- Normal pressure gradient $\frac{\partial P}{\partial y}$ is very small compared to normal shear stress τ_{xy} so that, $\frac{\partial P}{\partial y} << \tau_{xy}$.

By introducing these assumptions in the NS equations, the boundary layer equations are obtained and can be retrieved in the majority of fluid mechanic books (Schlichting, 1955; Chassaing, 2000; Greitzer., 2004). Boundary layers are observed to be in two different states presenting different behaviour of the flow and correspond to laminar and turbulent state. The flow physics involved in both states is hereafter described.

1.2.1 Laminar boundary layer

Laminar boundary layer is mainly driven by viscous effects. For a steady flow, laminar boundary layer equations become a set of PDE which can be analytically solved. For a 2D incompressible boundary layer developing on a flat plate with no streamwise pressure gradient, (Blasius, 1908) derives analytical solutions using self-similar variables known as Blasius profiles. Later, to deal with high Mach number flows, compressible effects have been taken into account using the transformation of (Howarth, 1948). Finally, the effect of streamwise pressure gradient can be taken into account by resolving the Falkner-Skan equations. To do so, the freestream velocity is assumed to follow a power law with respect to the streamwise coordinate x so that, $U_\infty = Cx^m$ where C is a constant and m a parameter representing the streamwise pressure gradient. The analytical solutions obtained from the resolution of the Falkner-Skan equations for different pressure gradient parameter m are presented in Fig. 1.3. Naturally, if $m = 0$, the Blasius profile is recovered. If $m > 0$, the pressure gradient is positive which accelerates the flow in the boundary layer. Otherwise, if $m < 0$, the pressure gradient is adverse in the boundary layer which decelerates the flow. This deceleration necessary implies an inflexion point in the boundary layer profile. If the adverse pressure gradient is sufficiently strong, the sign of the streamwise velocity in the profile can be locally reversed. In that case, the boundary layer detaches off the wall which leads to a creation of a recirculation bubble as represented on Fig. 1.4. The separation point of the boundary layer is defined when $\tau_w = 0$, i.e, $\left(\frac{\partial u}{\partial y}\right)_{y=0} = 0$. Downstream the separation point, the boundary layer layer thickness strongly increases and becomes not negligible compared to the characteristic length of the wall, which breaks the boundary layer hypotheses. To reattach the boundary layer to the wall, an acceleration of the flow is required to recover a positive wall shear stress.

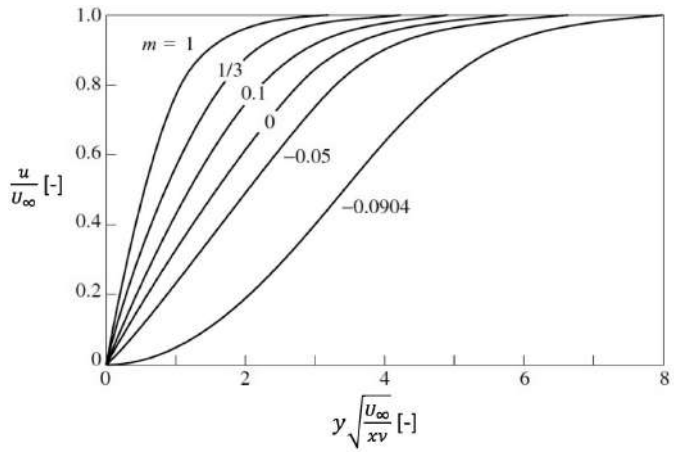

Figure 1.3 – Analytical solutions of Falkner-Skan equations for different pressure gradient parameter m. Extracted from (Cebeci and Bradshaw, 1977).

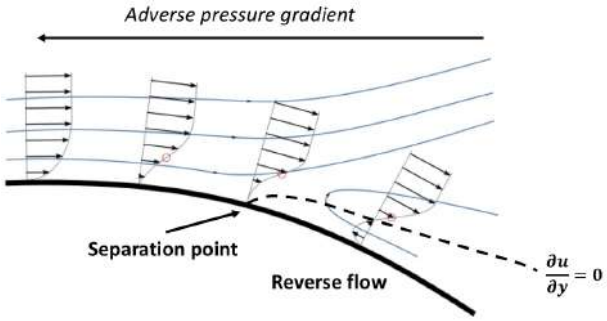

Figure 1.4 – Effect of the adverse pressure gradient on the boundary layer.

1.2.2 Turbulent boundary layer

Turbulent boundary layer is mainly characterized by the generation of turbulent fluctuations. Turbulent fluctuations are associated to turbulent structures present in the boundary layer which are highly stretched in the streamwise direction. These turbulent structures are composed of 3D vortices looking like hairpins and elongated streaks near the wall as shown on Fig. 1.5. Turbulent fluctuations are

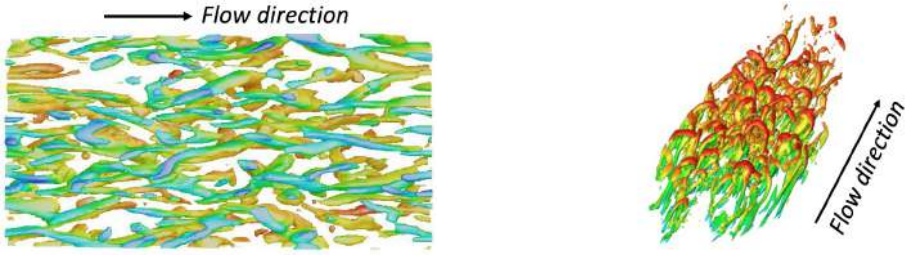

(a) (b)

Figure 1.5 – View of streaks near the wall (a) and hairpin vortices (b).

.

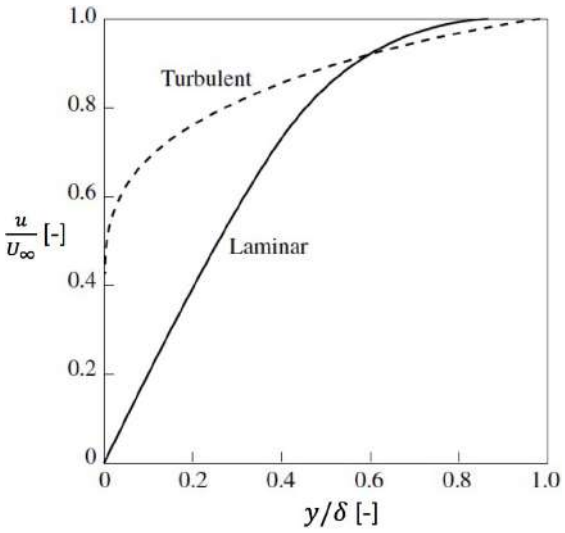

Figure 1.6 – Comparison between a laminar and a turbulent velocity profile. Extracted from (Greitzer., 2004).

known to increase the shear stress in the boundary layer. This results in a higher wall shear stress and a sharper mean velocity profile compared to a laminar one as represented on Fig. 1.6. The mean velocity profile of a turbulent boundary layer can be split in different regions as shown on Fig. 1.7. In the inner region, the flow is mainly dominated by both viscous effects and Reynolds stresses while in the outer region, Reynolds stresses dominate the flow. The delimitation between the inner and outer region depends on the Reynolds number of freestream flow and generally lies around $y/\delta \approx 0.1 - 0.2$. In the inner region, different sub-layers are

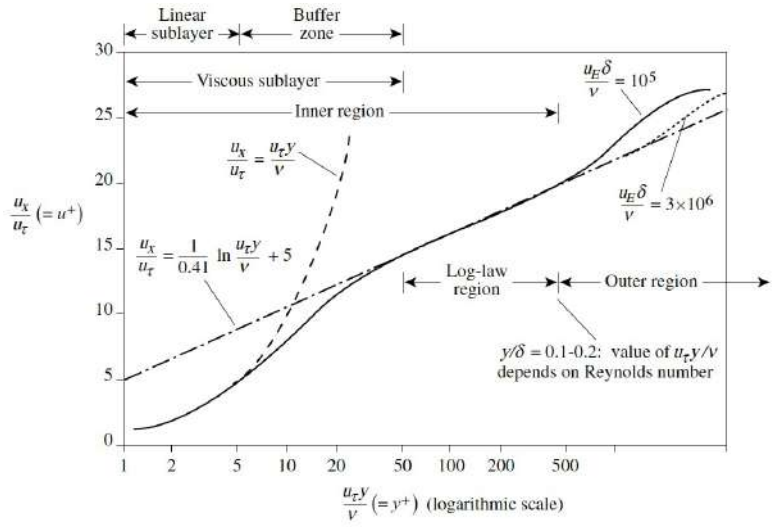

Figure 1.7 – Normalized mean velocity $u^+ = \frac{u}{u_\tau}$ [-] profile against the no-dimensional wall unit distance y^+ [-] for a turbulent boundary layer with no pressure gradient. Extracted from (Cebeci and Bradshaw, 1977).

.

defined according to the normalized wall unit y^+ defined as,

$$y^+ = \frac{yu_\tau}{\nu}, \tag{1.2}$$

where y is the wall normal distance, u_τ the friction velocity defined by Eq. (5) and ν the kinematic viscosity. In the linear sub-layer, i.e for $y^+ < 5$, only viscous effects dominate the flow which necessary implies a linear relation of the velocity profile with respect to y^+. When increasing y^+ and approaching the freestream flow, Reynolds stresses become predominant with respect to viscous stresses. Indeed, in the log-law region, i.e for $y^+ > 50$, the stresses weakly depend on the laminar viscosity. If taking a mixing length model to close Reynolds stresses, the velocity profile in this region follows a logarithm law. Finally, in the buffer zone, i.e for $5 < y^+ < 50$, the flow involves both viscous and inertial stresses.

Turbulent boundary layer originates from laminar boundary layer which has suffered from a turbulent transition. The transition process from laminar to turbulent state of boundary layers is hereafter described.

1.2.3 Turbulent transition of the boundary layer

The turbulent transition process of a boundary layer is mainly characterized by a loss of coherency of the flow. To illustrate this process, a view of a turbulent boundary layer transition on a blade is provided in Fig. 1.8. During the transition process, unsteadiness appear and develop in the boundary layer. This region is associated to a strong increase of turbulence generation. Downstream the transition region, turbulence generation decays in a non-equilibrium region whose the position can vary in time. Finally, a fully turbulent boundary layer is obtained where turbulence generation is stabilized. Different modes of transition are found in the literature (summarized in (Mayle, 1991)) and are hereafter described:

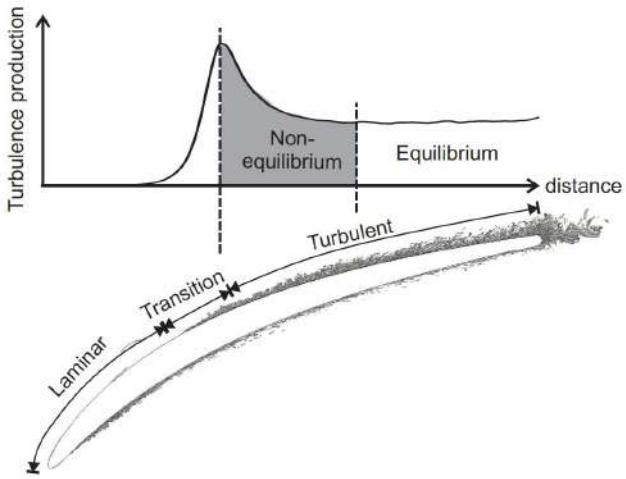

Figure 1.8 – Example of the transition of the boundary layer at the suction side of a compressor blade. Taken from (Wheeler et al., 2017).

Natural transition This mode of transition was found and investigated by (Emmons, 1951; Schlichting and Gersten, 2000) and is widely admitted in the literature. The different steps of the natural transition are summarized on Fig. 1.9. In absence of freestream turbulence or entropy waves impacting the boundary layer, the natural transition process occurs when the Reynolds number of the boundary is sufficiently large. For a boundary layer, the Reynolds number is based on the momemtum thickness of the boundary layer $\theta = \int_0^\delta \left(1 - \frac{u(y)}{U_\infty}\right) \frac{u(y)}{U_\infty} dy$ so that $Re_\theta = \frac{U_\infty \theta}{\nu}$. Above a critical value of Re_θ, non-linear processes become predominant in the flow and disturbances received by the boundary layer (such as acoustics waves) grow and develop in the boundary layer. These disturbances generate 2D instability waves in the boundary layer, called Tollmien-Schlichting (TS) waves. Then, the TS waves grow and break into 3D stochastic structures involving abrupt variations of the velocity fields (spikes). Afterwards, stochastic structures continue to grow merging localized turbulent spots near the wall. Turbulent spots spatially extends, overlaps each other and finally lead to a fully turbulent flow.

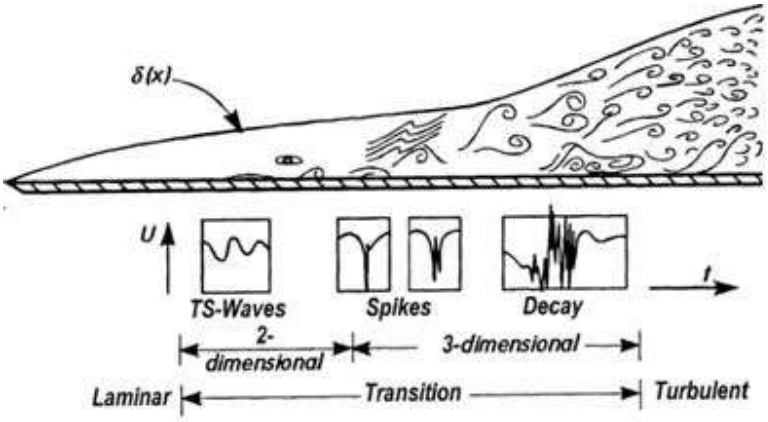

Figure 1.9 – Sketch of the natural transition of a boundary layer. Extracted from (Emmons, 1951).

By-pass transition In this case, the development and breakdown of 2D instabilities is by-passed so that turbulent spots are directly obtained in the boundary layer. Turbulent spots are generated from external disturbances of the boundary layer such as freestream turbulence or turbulent wake. External disturbances penetrate the boundary layer and form elongated streaks which are highly stretched in the streamwise direction. Then, streaks destabilize the flow and generate turbulent spots due non-linear processes. Note that the transition process generally occurs upstream the position where natural transition would have happened without the presence of external disturbances. Indeed, freestream turbulence is observed to decrease the critical value of Re_θ for a flat plate with no pressure gradient as shown on Fig. 1.10. It is important to notice that for a freestream turbulent intensity above 3-4%, the beginning of the transition become insensitive to the value of freestream turbulent intensity. This corresponds to a minimum value of Reynold number around $Re_\theta \approx 300$. For typical medium-sized gas tur-

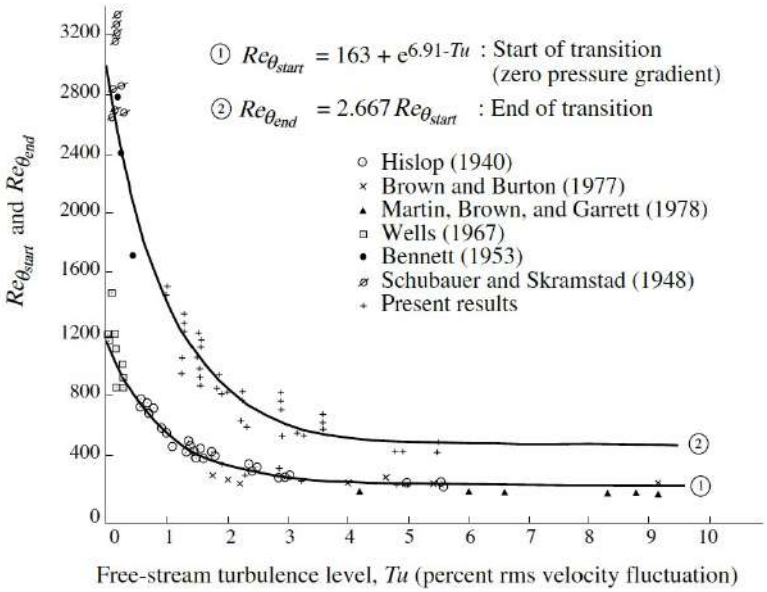

Figure 1.10 – Start and end of a turbulent transition with respect to Reynolds number Re_θ and freestream turbulence intensity TU from different experiments. $Re_{\theta,start}$, start of the transition and $Re_{\theta,end}$ end of the transition. Extracted from (Abu-Ghannam and Shaw, 1980).

.

bine engines, $Re_\theta \approx 100 - 1000$ are generally observed with a freestream turbulent intensity around 5 - 10% (Mayle, 1991). As a consequence, the transition process is expected to be mainly of by-pass type for turbine flows in industrial engines.

Separated flow transition The separated flow transition occurs when a region of adverse pressure gradient is present in the vane boundary layer. As previously explained, the adverse pressure gradient can generate a recirculation bubble. The flow physics involved in a steady recirculation bubble has been investigated in the literature (Lee et al., 2014; Uzun and Malik, 2017; Cadieux et al., 2014) and is presented on Fig. 1.11. Downstream the separation point, the first part of the bubble

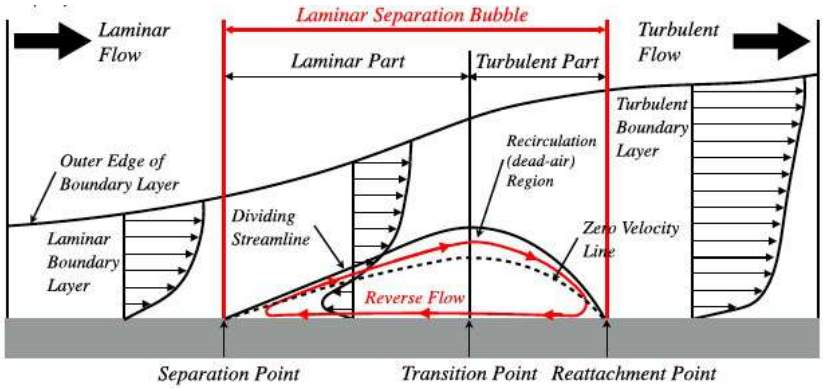

Figure 1.11 – Flow dynamic of a recirculation bubble from (Lee et al., 2014).

is laminar. At the edge of the bubble, a strong shear is created from the difference of velocity between the reversed flow within the bubble and freestream flow. If the bubble length and Reynolds number are sufficiently large, disturbances created at the edge at the bubble destabilize the flow due to non-linear processes. Then, disturbances grow and become 3D stochastic structures which initiate a turbulent transition process. Unsteady fluctuations generated from this process increase the wall shear stress which reattaches the boundary layer to the wall. Downstream the reattachment point, a fully turbulent flow is thus obtained. It is important to note that this transition process is observed to be highly sensitive to freestream turbulence (Burgmann and Schroder, 2008; Zilli et al., 2017) which tends to reduce the bubble size.

The last point shows that an adverse pressure gradient in the boundary layer can induce a transition process. Otherwise, a favourable pressure gradient is also observed to impact the transition process. The effect of the pressure gradient on the transition mechanism is hereafter addressed.

Effect of streamwise pressure gradient To evaluate the effect of streamwise pressure gradient on the transition process, the acceleration parameter K is used and is defined so that:

$$K = \frac{\nu}{U_\infty}\frac{dU_\infty}{dx}. \tag{1.3}$$

The combined effects of K with freestream turbulent intensity on the turbulent transition process was investigated in (Mayle, 1991) and is shown on Fig. 1.12. Naturally, separated flow occurs for negative acceleration parameters which corresponds to an adverse pressure gradient. When increase freestream turbulence

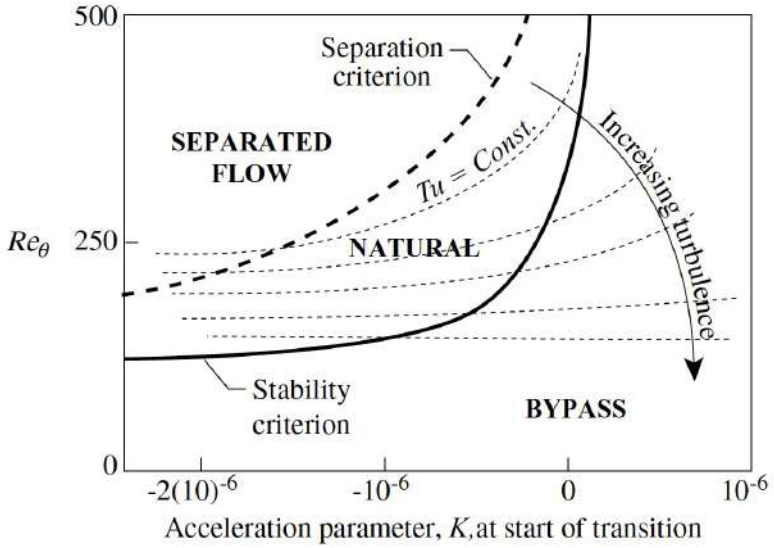

Figure 1.12 – Effect of the acceleration parameter and freestream turbulence on the turbulent transition process of a boundary layer. Extracted from (Mayle, 1991).

intensity, natural and by-pass transitions are encouraged because freestream turbulence is observed to reduce and even vanish the bubble (Burgmann and Schroder, 2008; Zilli et al., 2017). When K is strictly positive, only the by-pass transition process is possible. Indeed, the acceleration of the flow in the boundary layer stretches and damps the TS waves which makes impossible the natural transition. Note that for the specific value of $K > 3.10^{-6}$, a reverse transition (from a turbulent to a laminar state) was observed in experiments (Mayle, 1991). Indeed for such values of K, the acceleration of the flow strongly stretches and fully dissipates the turbulent structures which relaminarizes the flow in the boundary layer.

Independently of the mode of transition, the transition to turbulence is observed to increase the loss generation (Denton, 1993; Wheeler et al., 2017). To evaluate the losses associated to boundary layer regions, an accurate evaluation of the position of the boundary layer turbulent transition is then required.

1.3 Flow structure of film cooling systems

In this section, a brief description of the flow structure observed in film cooling systems is presented. First off all, an illustration of a film cooling system is provided on Fig. 1.13. Hot stream is defined by freestream density ρ_∞, velocity U_∞ and temperature T_∞. Cold stream is defined by coolant density ρ_c, velocity U_c and temperature T_c. To characterize the coolant film through the pipes with respect to freestream flow, density ratio DR, blowing ratio M and impulse ratio J are defined so that,

$$DR = \frac{\rho_c}{\rho_\infty}, \tag{1.4}$$

$$M = \frac{\rho_c U_c}{\rho_\infty U_\infty}, \tag{1.5}$$

$$J = \frac{\rho_c U_c^2}{\rho_\infty U_\infty^2}, \tag{1.6}$$

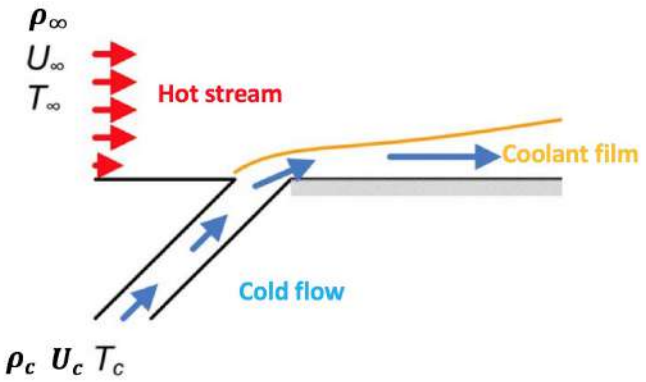

Figure 1.13 – Illustration of a coolant film system. Adapted from (Han and Rallabandi, 2010).

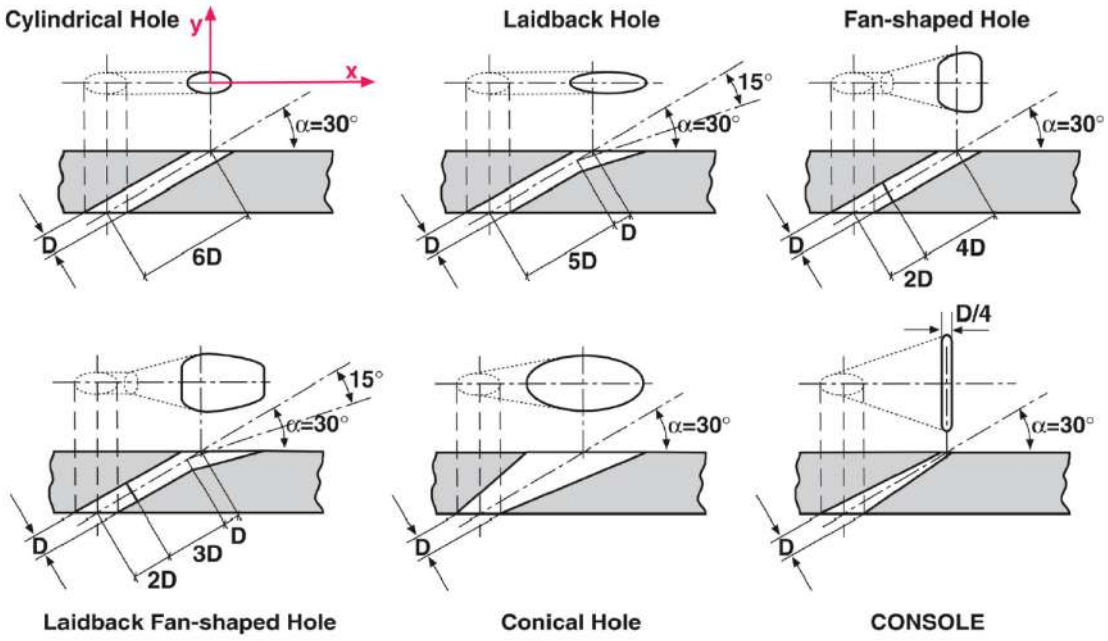

Figure 1.14 – Typical hole design. Extracted from (Saumweber and Schulz, 2012).

where the subscript c refers to cooling flow properties at the exit section of the cooling hole and ∞ to local freestream conditions. M represents the ratio between coolant and freestream mass fluxes and J the ratio of kinetic energy. Note that J can be retrieved from DR and M by $J = \frac{M^2}{DR}$. In the context of turbine blade cooling, typical values of M and J lie around 0.5 - 2 (Han and Ekkad, 2001). To eject the coolant, holes should be drilled on the vane surface. The shape of holes is shown to strongly impact the cooling system performance (Goldstein et al., 1974). The main hole shapes which can be found in the literature are presented in Fig. 1.14. The most common shape found in the industry is the cylinder hole because this is the simplest and cheapest hole shape to manufacture. The exit ejection surface is generally elliptical. However, this specific shape induces a jet detachment off the wall when the flow is ejected, leaving a part of the wall without cooling (Goldstein et al., 1974). To help the jet to remain attached to the wall, fan shaped-holes have been designed. Shaped-holes are characterized by an expansion of the flow passage section to reduce the momentum flux as well as the jet penetration. With this specific feature, fan shaped-holes are observed to improve the performance of cooling systems compared to classical cylindrical holes (Gritsch et al., 1998). However, the manufacturing cost of shaped-holes is increased compared to cylindrical holes. As a result, cylindrical holes are still mainly used in the industry. To illustrate the typical flow structure observed in cylindrical holes, contours of mean velocity magnitude for a cylindrical hole are plotted on Fig. 1.15. The flow velocity map is very heterogeneous in the coolant pipe. A recirculation bubble is observed to originate at the inlet of the coolant hole and extends in the pipe. This low momentum region acts as a blockage effect which accelerates the flow out of the bubble. This specific flow structure results in a strong sheared-flow at the exit plane of the hole. Indeed, the velocity map presents

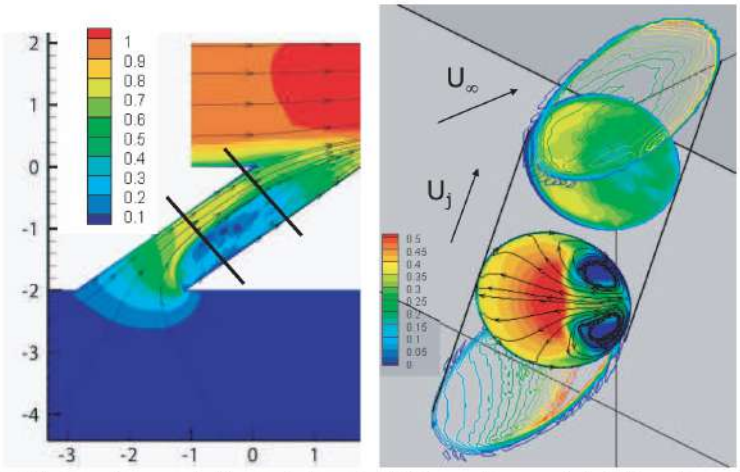

(a) Contours of mean velocity magnitude and streamlines in the center-plane.

(b) Contours of mean vertical velocity and streamlines in the cross-sections perpendicular to the hole centerline.

Figure 1.15 – Contours of mean velocity magnitude normalized by freestream velocity $\overline{\mathbf{v}}/U_\infty$ [-] for a cylindrical hole. Extracted from (Peet, 2006).

a high velocity region (red) located near the center of the section and low velocity regions associated to recirculation regions (blue). In the sheared flow regions, high levels of turbulent fluctuations are observed (Peet, 2006). Downstream the coolant hole, the coolant flow is ejected on the blade surface and interacts with the flow from the combustion chamber corresponding to a jet in cross-flow. The flow structure of jets in cross-flow is quite complex and was experimentally studied in (Fric and Roshko, 1994; New et al., 2003). To illustrate the flow structure of jets in cross-flow, the sketches of the flow structure issued from the experiment of (Fric and Roshko, 1994) are presented in Fig. 1.16. First of all, the jet is observed to be detached off the wall. The jet detachment and penetration is observed to be linked to the blowing ratio M (Goldstein et al., 1974). Several vortices are observed inside and around the jet, Fig. 1.16 (a). First, horse-shoe vortices are observed around

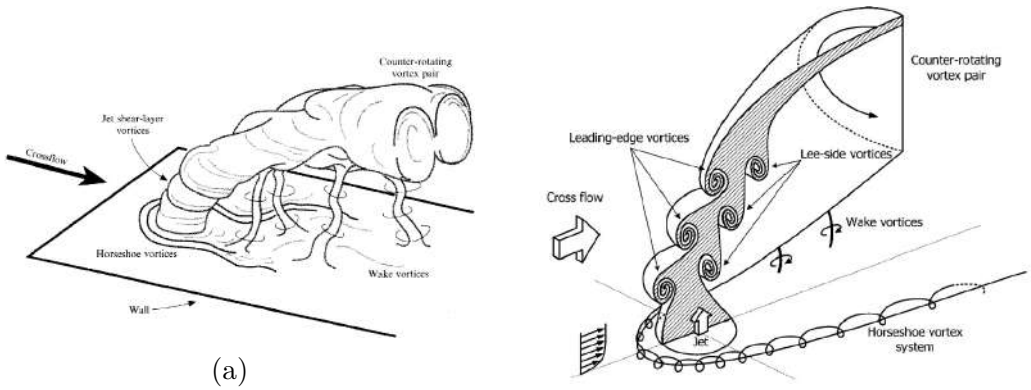

(a)

(b)

Figure 1.16 – Flow structure of a cross-flow jet from (Fric and Roshko, 1994). 3D views (a) and view of a cut plane through the center line of the jet (b).

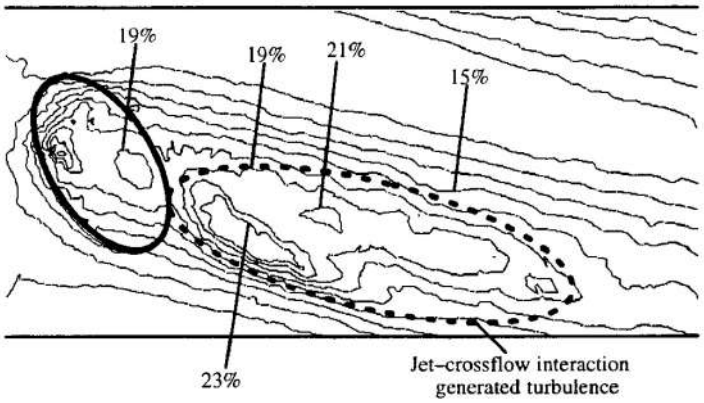

Figure 1.17 – Contours of turbulence intensity TU [-] of a jet in cross-flow. Extracted from (McGovern and Leylek, 2000).

the jet and originate from the 3D separation of the inflow boundary layer. Indeed, the jet acts as an obstacle which induces a strong potential effect and adverse pressure gradient on the inflow. Then, a counter-rotating vortex pair (CRVP) is observed to be generated from the base of the jet and to propagate along the jet direction. These vortices are generated from the shear between the coolant flow and the inflow. This interaction also generates shear layer vortices (leading edge and lee-side vortices) as observed on Fig. 1.16 (b). Finally, normal vortices to the wall are noticed between the jet and the wall. Such a flow structure is observed to be associated with strong turbulent fluctuations as shown on Fig. 1.17. Turbulent fluctuations are mainly generated in the interaction region between the inflow and coolant flow. Turbulent fluctuations are known to strongly affect the mixing process between hot and cold streams and thus the cooling performance of the film. To characterize the efficiency of a film cooling system, the adiabatic film effectiveness η is defined so that,

$$\eta = \frac{T_{aw} - T_\infty}{T_c - T_\infty} \tag{1.7}$$

where T_{aw} is the adiabatic wall temperature. To illustrate typical spatial distribution of η downstream a coolant jet, contours of adiabatic film effectiveness η issued from (McGovern and Leylek, 2000) are presented on Fig. 1.18. Near the hole position, η is observed not to be equal to 1 because the jet is detached from the

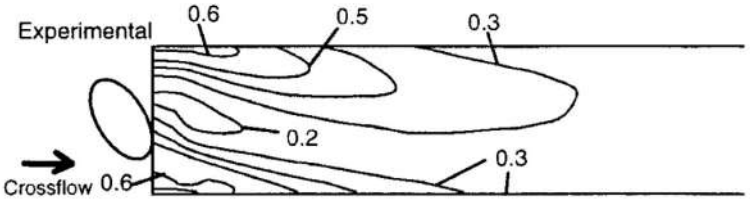

Figure 1.18 – Contours of adiabatic film effectiveness η [-] on a wall downstream a coolant jet. Extracted from (McGovern and Leylek, 2000).

wall. Downstream, the jet reattaches to the wall and η decreases due to the mixing process between the hot and cold streams. This mixing process is enhanced by the generation of turbulent fluctuations in jets. This mixing process is also shown to be enforced with the presence of freestream turbulence (Bons et al., 1996; Ekkad et al., 1997).

The previous discussion shows that adiabatic film effectiveness and blade wall temperature depend on the coolant operating point, turbulence generated in the jet as well as freestream turbulence. As a consequence to predict the blade wall temperature and losses from the mixing process, an accurate evaluation of the coolant flow aerodynamics and associated turbulent fluctuations is required.

1.4 Heterogeneities of the inflow from the combustor

In real engines, the flow issued from the combustion chamber is highly non-uniform. A typical temperature map at the turbine entry is presented on Fig. 1.19. High temperature levels are concentrated in hot spots located at the center of the plane. Hot spots are created in the combustion chamber from the injectors. The migration of hot spots through high-pressure vanes has been widely investigated in the FACTOR project (Bacci et al., 2015; Koupper, 2015; Thomas et al., 2017). To illustrate the impact of the hot spot propagation on the thermal environment of high-pressure vanes, a radial cut of total temperature located at mid-height of the FACTOR NGVs is provided on Fig. 1.20. The hot spot is observed to impact the NGV. Downstream, the hot spot is stretched by the flow acceleration in the flow passage between the vanes. The position of the hot spot with respect to NGVs is shown to impact the blade wall temperature (Koupper, 2015). The inflow can also exhibit large scale structures coming from the combustor. These large scale structures are observed to impact the mixing process with the coolant (Thomas et al., 2018) and thus the blade wall temperature.

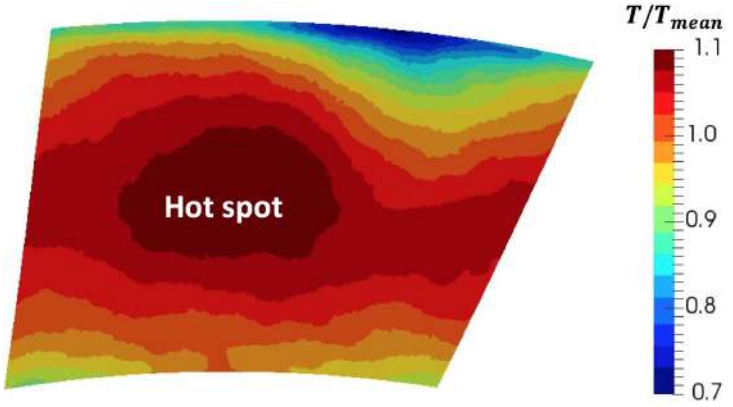

Figure 1.19 – Typical temperature map normalized by the temperature spatial averaged T/T_{mean} [-] at turbine entry.

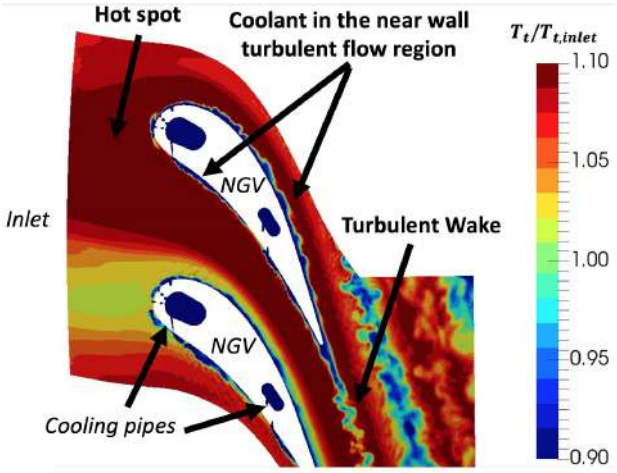

Figure 1.20 – Total temperature normalized by the inlet spatial averaged temperature $T_t/T_{t,inlet}$ [-] map at mid-height of the NGVs of the FACTOR project.

1.5 Secondary flows

When dealing with 3D turbine vanes, 3D vortices are experimentally observed near the end-walls, i.e, near the hub and shroud. A schematic view of the secondary flows for a 3D turbine vane is provided in Fig. 1.21. These 3D structures, called secondary flows, originate from the separation of the inflow boundary layer. Indeed, the leading edge of the vane generates an adverse pressure gradient on the inflow boundary layer. This adverse pressure gradient produces a 3D separation of the inflow boundary layer and generates horse-shoe vortices which propagates through the flow passage between the turbine vanes. The vortex located on the pressure side of the vane migrates to the suction side of the other vane due to the blade to blade pressure gradient and is thus called *passage vortex*. When reaching the suction side of a vane, the passage vortex merges with the suction side

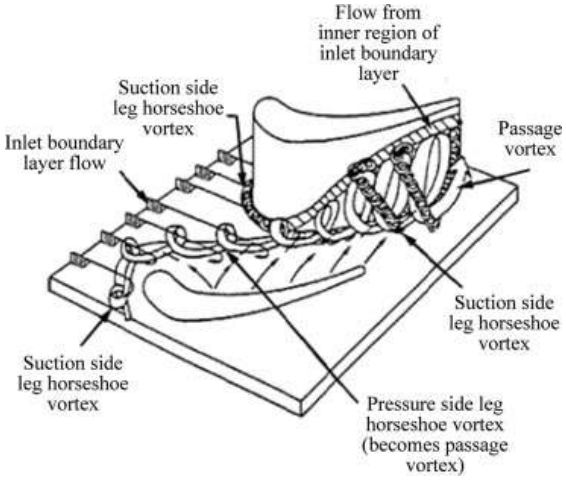

Figure 1.21 – Sketch of secondary structures observed in turbine flows. Extracted from (Attia et al., 2013).

horse-shoe vortex. These secondary flows are shown to highly generate losses in turbine flows (Harrison, 1990; Denton, 1993; Zlatinov, 2011). Indeed, kinetic energy contained in secondary flows is dissipated through viscous effects and then corresponds to a loss of energy for the system.

To sum up this section, the flow observed in high-pressure vanes is complex and presents very localized structures characterized by strong velocity and temperature gradients. An accurate prediction of all these regions presented above is needed to study the losses associated to the flow aerodynamics and mixing process. To predict such a flow with LES, mesh and numerical property requirements are discussed in the next section.

1.6 Mesh and numerical property requirements

To obtain an accurate prediction of the blade wall temperature and losses, the flow dynamic in the regions presented above needs to be properly captured. To do so, a fine mesh resolution is required in high dynamic regions as in turbulent wake, coolant jets, mixing regions between hot and coolant streams as well as in near wall flow regions (Tucker, 2011a). A fine mesh resolution is also needed in the freestream region of the flow from the inlet to the flow passage between the vanes to properly transport the heterogeneities imposed at the inlet of the computational domain (Koupper, 2015). To ensure a proper transport of the resolved finest structures in these regions, a low-dispersion and dissipation numerical scheme is nevertheless required. Such numerical properties are complied with the use of Taylor-Galerkin (TG) schemes (Colin and Rudgyard, 2000; Donea and Huerta, 2003). Indeed, TG schemes are shown to be well adapted for LES in the context turbomachinery in the PhD of (Lamarque, 2007). Finally, the effect of sub-grid scale (SGS) turbulent fluctuations on the resolved field is represented through the use of eddy viscosity models introducing a turbulent viscosity ν_t. The choice of the SGS model will be hereafter discussed for each computation realized in this work.

In the next chapter, the loss modelling is addressed to link the flow physics described here with the loss generation mechanism.

Chapter 2

Loss modelling

Contents

2.1 Thermodynamic representation of losses **42**

2.2 Losses in 1D flows **47**

2.2.1 Loss coefficients 48

2.2.2 Review of 1D loss models 49

2.3 Extension of 1D balances to LES data **56**

2.3.1 Data reduction by the means of averaging procedures . 56

2.3.2 Total enthalpy and entropy balance with LES 57

2.4 Second Law Analysis **60**

2.4.1 Second Law Analysis applied to fluid mechanics 60

2.4.2 Second Law Analysis adapted to LES 61

2.5 Chapter conclusions **63**

The aim of this chapter is to introduce a new context of work to identify the loss location and mechanisms for turbine flows. In this new context of work, different methodologies are proposed for the loss evaluation of cooled turbine blades and vanes. To do so, a loss thermodynamic modelling is first proposed in Section 2.1. From this thermodynamic analysis, a review of the 1D loss models used in the literature is presented in Section 2.2. To overcome the limitations inherent in these 1D loss models, two high-fidelity methodologies are introduced to extent the loss evaluation to 3D anisothermal flows. The first methodology is based on the use of balance of total variables between two stations of the flow and is presented in Section 2.3. The second methodology relying on the use of the Second Law Analysis with LES is presented in Section 2.4. The capacity of both methodologies to identity the losses in this PhD work is discussed.

2.1 Thermodynamic representation of losses

A rigorous definition of losses is quite complex to give. The definition of losses depends on the objective of the studied system. For instance, the objective of a helicopter engine is to supply a work on a powered shaft thanks to a turbine. In this specific case, the losses can be considered as work which is not recovered by the turbine, in other words, a work lost for the powered shaft. To evaluate this work lost, a thermodynamic modelling of the system is required. To do so, basic thermodynamic laws are applied to the turbine part of the engine, i.e, between stations 4 and 5 of the engine (Fig. 4). It is important to note that such a thermodynamic analysis assumes that the flow evolution is steady and purely 1D, i.e, the flow is considered uniform for each axial section of the engine (fully mixed). To link a 1D steady flow evolution and 3D unsteady data obtained with LES, a specific procedure will be proposed later in this chapter.

Prior to applying thermodynamic principles, the system considered here must be accurately defined. The system studied here is the turbine part of the engine. It is assumed to be bounded by the inlet plane of the turbine, here noted *in*, the exit plane of the engine, here noted *ex* and turbine walls including blade and vane walls as well as shroud and hub. To simplify the analysis, the framework is first limited to uncooled turbines. The extension to cooled turbines will be later addressed in the work. The thermodynamic representation of such a system is shown on Fig. 2.1. The control volume delimiting the system is represented by the red box. The turbine extracts a work from the fluid W_{shaft} arbitrary defined positive. The heat flux Q passing through the turbine walls is supposed to be fully evacuated in an environment at temperature T_0. Note that by convention, Q is here defined positive when it goes from the system to the environment. The environment is here complex to define. Indeed, in a real turbo-shaft engine, the

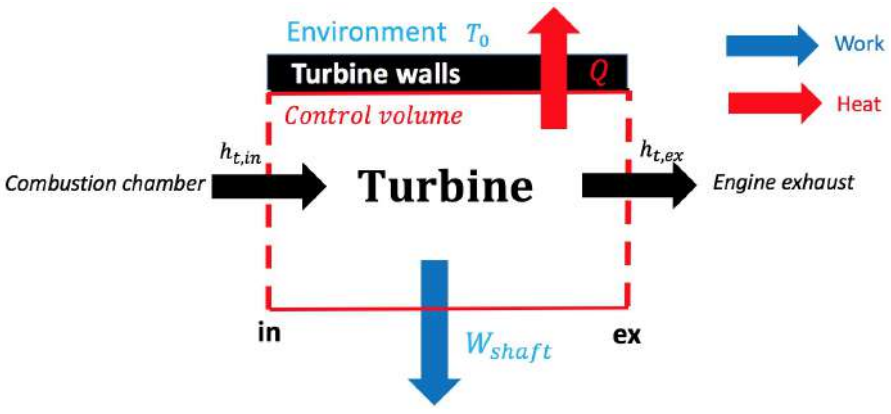

Figure 2.1 – Thermodynamic representation of the turbine. The system is delimited by the axial planes *in*, *ex* and by the turbine walls (blade walls, shroud/hub walls...). Sensible total enthalpy h_t at inlet and outlet. The heat flux Q passing through the turbine walls is supposed to be evacuated in an environment at temperature T_0. The work extracted from the fluid is noted W_{shaft}.

turbine is surrounded by the engine components such as secondary systems or the by-pass stream of the engine. To take into account the engine environment, more complex thermodynamic analysis should be performed and can be found in (Bejan, 1982; Horlock, 2013). For simplicity, if assuming that the heat flux passing through the turbine walls is fully evacuated in the atmosphere through the engine components, the environment can be here considered as the atmosphere (Greitzer., 2004). For such a system, the work shaft recovered by the turbine is given by a 1D steady balance of sensible total enthalpy h_t between stations in and ex so that (Greitzer., 2004; Dixon and Hall, 2010),

$$W_{shaft} = \dot{m}\left(h_{t,in} - h_{t,ex}\right) - Q, \tag{2.1}$$

where $\dot{m}$ is the mass flow rate entering in the turbine. Equation (2.1) shows that the work recovered by a turbine depends on the capacity of the system to extract total enthalpy from the fluid while limiting the heat flux losses Q through the walls. The heat flux Q can be expressed with respect to the sensible entropy s of the fluid through the use of the second principle so that,

$$\dot{m}\left(s_{ex} - s_{in}\right) = -\frac{Q}{T_0} + \dot{S}, \tag{2.2}$$

where $\dot{S}$ is the entropy generated within the flow due to irreversible processes between stations in and ex. According to the second principle, this term is necessary strictly positive. If combining Eq. (2.1) with Eq. (2.2), the work recovered by the turbine per mass flow unit is,

$$\frac{W_{shaft}}{\dot{m}} = \left(h_{t,in} - h_{t,ex}\right) + T_0\left(s_{ex} - s_{in}\right) - \frac{T_0\dot{S}}{\dot{m}}. \tag{2.3}$$

Equation (2.3) shows that the work depends on the variation of total sensible enthalpy and sensible entropy between the inlet and outlet planes as well as irreversibilities generated in the system. Note that the last term of the RHS is necessary negative according to the second principle. As a result, irreversibility processes taking place in the flow can only degrade the work recovered by the turbine. From this observation, (Denton, 1993) proposes to define the losses as all irreversible phenomena taking place in the flow. Furthermore, if heat is lost through the turbine walls, the second term of the RHS is also negative according to Eq. (2.2) which means that heat loss also degrades the work. As a result, to evaluate the performance of a turbine, the ideal reference is taken as the isentropic transformation (adiabatic $Q = 0$ and reversible $\dot{S} = 0$) through the use of the isentropic efficiency of the turbine η_t:

$$\eta_t = \frac{W_{shaft}}{W_{shaft,is}}, \tag{2.4}$$

where $W_{shaft,is}$ is the work recovered by the turbine if the expansion is isentropic. To express $W_{shaft,is}$, the total inlet enthalpy $h_{t,in}$ and the mass flow rate entering

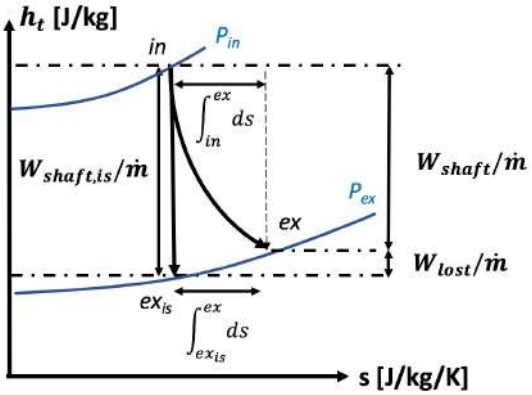

Figure 2.2 – h_t - s diagram of the expansion of the turbine between the inlet of the turbine, station in and the exit of the turbine, station ex. Isentropic expansion is represented by $_{is}$.

in the turbine $\dot{m}$ are assumed not to be impacted by the losses. In that case, $W_{shaft,is}$ is given by,

$$\frac{W_{shaft,is}}{\dot{m}} = \left(h_{t,in} - h_{t,ex_{is}}\right), \tag{2.5}$$

where $h_{t,ex_{is}}$ is the total enthalpy obtained at the outlet plane of the turbine through an isentropic expansion. If the walls are assumed adiabatic, W_{shaft} and $W_{shaft,is}$ can be represented on the total enthalpy - entropy diagram h_t - s plotted on Fig. 2.2. The expansion of the flow in the turbine is supposed to lie between two isobars (static pressure) P_{in} and P_{ex}. Since the station ex is taken as the exit plane of the engine, the final pressure of the expansion P_{ex} can be taken as the atmosphere pressure. This pressure is then considered not to be impacted by any transformation taking place in the turbine. On this graph, two transformations are represented: the real transformation defined between in and ex and an isentropic (ideal) transformation defined between in and ex_{is} . This diagram clearly illustrates that any entropy positive variation decreases the work retrieved by the turbine. The work lost can be then naturally defined as,

$$W_{lost} = W_{shaft,is} - W_{shaft}. \tag{2.6}$$

Note that W_{lost} is here defined positive when work is lost in the real transformation. To express W_{lost} with respect to the flow properties, Eq. (2.3) and Eq. (2.5) are re-injected in Eq. (2.6) while using integral form for more clarity giving,

$$\frac{W_{lost}}{\dot{m}} = \int_{ex_{is}}^{ex} dh_t - T_0 \int_{in}^{ex} ds + \frac{T_0 \dot{S}}{\dot{m}}. \tag{2.7}$$

The first term on the RHS represents the loss of total enthalpy along the path ex - ex_{is} as shown on Fig. 2.2. The second and third term on the RHS depend on entropy variation and creation between stations in and ex. To simplify the expression of the first term of the RHS, total enthalpy variation can be split into static enthalpy variation dh and kinetic energy variation dK:

$$\int_{ex_{is}}^{ex} dh_t = \int_{ex_{is}}^{ex} dh + \int_{ex_{is}}^{ex} dK. \tag{2.8}$$

The impact of losses on kinetic energy is generally assumed very small compared to static enthalpy variation (Denton, 1993) and can be neglected giving, $\int_{ex_{is}}^{ex} dh_t \approx \int_{ex_{is}}^{ex} dh$. The variation of static enthalpy can be expressed as system temperature T and static pressure variation dP using the Gibbs equation,

$$\int_{ex_{is}}^{ex} dh = \int_{ex_{is}}^{ex} Tds + \int_{ex_{is}}^{ex} \frac{dP}{\rho}. \tag{2.9}$$

Since the pressure along ex and ex_{is} is taken as constant, the last term of the RHS cancels. If re-injecting Eq. (2.9) in Eq. (2.7) and after rearrangement the different terms, the work lost can be expressed as,

$$\frac{W_{lost}}{\dot{m}} = \int_{ex_{is}}^{ex} Tds - T_0 \int_{in}^{ex} ds + \frac{T_0 \dot{S}}{\dot{m}}. \tag{2.10}$$

The second term of the RHS corresponding to the entropy variation between stations in and ex can be also expressed between stations ex and ex_{is} as clearly illustrated on Fig. 2.2, i.e, $\int_{in}^{ex} ds = \int_{ex_{is}}^{ex} ds$. After rearrangement of the different terms, the lost work per unit mass flow rate is given by the following relation:

$$\frac{W_{lost}}{\dot{m}} = \underbrace{\frac{T_0 \dot{S}}{\dot{m}}}_{\text{Losses generated within the flow}} + \underbrace{\int_{ex_{is}}^{ex} (T - T_0)\, ds}_{\text{Potential work lost at the exhaust}} . \tag{2.11}$$

At the end of the day, the work lost can be divided into two contributions. The first term of the RHS represents the losses due to irreversibilities generated within the flow. The second term represents the work lost due to the difference of temperature between T and T_0 along the path ex - ex_{is}. To understand the meaning of this last term, it is represented on the diagram T - s in Fig. 2.3. If assuming that $T > T_0$, it means that the flow at the turbine outlet still contains thermal energy depending on the temperature difference $T - T_0$. If the final pressure at the

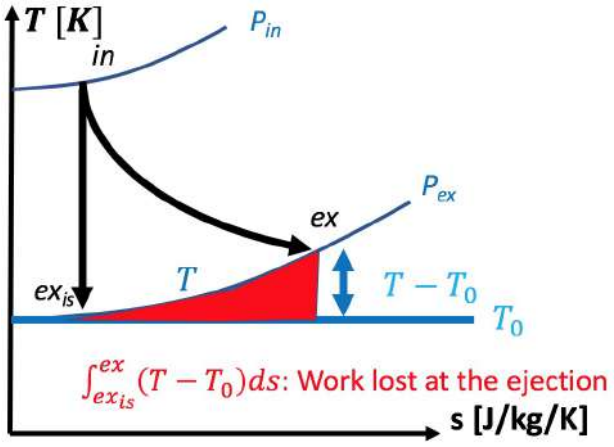

Figure 2.3 – T - s diagram of the flow expansion in the turbine between stations in and ex. Isentropic expansion is represented by $_{is}$. The work lost due to difference of temperature between T and T_0 is shown in red.

turbine outlet P_{ex} corresponds to the atmosphere pressure, this energy can not be extracted through another expansion process. This thermal energy can only be recovered using an hypothetical Carnot cycle located at the nozzle of the engine as explained in (Greitzer., 2004; Horlock, 2013). However, such systems are quite complex to implement at the exhaust of an engine due to geometry constraints and costs. If assuming that the temperature along the path ex_{is} - ex lies around the atmosphere temperature T_0, the last term of the RHS of Eq. (2.11) can be neglected with respect to the first term in Eq. (2.11). As a consequence of the previous hypothesis, the work lost is shown to be directly proportional to entropy creation within the flow so that,

$$W_{lost} = T_0 \dot{S}. \tag{2.12}$$

It is worth to note that this last expression recovers the theorem of Gouy-Stodola for adiabatic systems (Bejan, 2013; Pal, 2017). To comply with the loss modelling presented in this section, the walls of the configurations studied in this PhD work will be considered adiabatic.

When extended the analysis to cooled turbines, the coolant contribution is represented as an additional inlet of the system. From this hypothesis, the 1D steady balance of total enthalpy through the turbine should include the contribution of the coolant total enthalpy $h_{t,c}$ so that,

$$W_{shaft} = Q_{m,exit}\left(h_{t,in} - h_{t,ex}\right) - Q_{m,cold}\left(h_{t,in} - h_{t,c}\right), \tag{2.13}$$

where $Q_{m,hot}$ is the mass flow rate coming from the combustor, $Q_{m,cold}$ the coolant mass flow rate and $Q_{m,exit}$ the mass flow rate leaving the system which is determined from a steady mass balance so that, $Q_{m,exit} = Q_{m,hot} + Q_{m,cold}$. If assuming that the coolant contributions $h_{t,c}$ and $Q_{m,exit}$ are not impacted by the losses, the expression for W_{shaft} is the same between a real and an isentropic transformation. As a result, the expression of the work lost for adiabatic cooled turbines remains unchanged to coolant ejection. It can be surprising that the effect of the coolant ejection around the turbine blades on the work recovered by the turbine is not explicitly given in Eq. (2.12). Actually, this effect is "hidden" in the entropy creation term $\dot{S}$ through the creation of entropy by mixing of hot and cold streams (Denton, 1993).

Aside this thermodynamic analysis, the definition of work lost is shown to be multiple in the literature as shown in (Struchtrup and Rosen, 2002). More sophisticated aerodynamics analysis can be performed using the concept of *exergy* which will not be here detailed and can be found in (Miller, 2013; Fiore, 2019). Nevertheless, for a system with adiabatic walls, all these thermodynamic analyses are shown to be equivalent and lead to the same expression for the work lost, Eq. (2.12). It is important to note that the work lost expression includes the temperature environment T_0 generally taken as the atmosphere temperature. However, T_0 is not clearly defined in the literature, e.g, it may be the atmosphere temperature or the exit turbine temperature depending on the thermodynamic

representation. Nevertheless, in this work, the choice of T_0 is not essential to investigate the loss location and mechanisms. Indeed, T_0 is a constant inherent of the thermodynamic modelling. To investigate the losses, the entropy production $\dot{S}$ will be further addressed in this PhD work.

As a consequence of the previous discussion, any entropy creation in the flow through both stator and rotor stages degrades the work recovered by the rotor stages. According to (Denton, 1993), losses can be seen as smoke produced by each stage of the turbine (stator and rotor) which can not be destroyed and propagates to the exhaust of the engine. If walls are assumed adiabatic, entropy creation $\dot{S}$ can be related to entropy variation Δs according to the second law of thermodynamic. Based on this thermodynamic analysis, the loss evaluation in the literature is generally based on a steady 1D evolution of the flow to recover thermodynamic modelling. The measure of losses in 1D flows is then addressed in the next section.

2.2 Losses in 1D flows

To evaluate the losses in 1D flows, entropy variation should be measured between two stations of the flow. In experiments and simulations, entropy variation is measured from the evaluation of total temperature T_t and total pressure P_t between two stations of the system. The definition of total variables is well known if $\gamma = cst$ and can be found in most of compressible fluid mechanic books as in (Shapiro, 1953). However, this assumption is not fully verified for turbine flows where large temperature differences are expected between the static and total state. As a result, the variability of γ can affect the computation of total variables. This specific point is addressed in Appendix B. For convenience, γ will be assumed constant for the following derivations.

As previously stated, entropy variation can be expressed as variation of total temperature T_t and pressure P_t assuming $\gamma = cst$ between 2 stations of the flow i and j through the following relation (Denton, 1993),

$$\Delta s = s_j - s_i = C_p Ln\left(\frac{T_{t,j}}{T_{t,i}}\right) - rLn\left(\frac{P_{t,j}}{P_{t,i}}\right), \tag{2.14}$$

where r is the perfect gas constant. This equation shows that entropy variation is non-linear with respect to the variation of the total enthalpy T_t and the total pressure P_t between two stations. The sign of the first term $Ln\left(\frac{T_{t,j}}{T_{t,i}}\right)$ depends on heat fluxes and work extracted from the flow. The sign of $Ln\left(\frac{P_{t,j}}{P_{t,i}}\right)$ is not known in the general case of compressible anisothermal flows. In this specific case of a stationary adiabatic vane, the total temperature within the flow is conserved, i.e, $T_{t,i} = T_{t,j}$ (Greitzer., 2004). Injecting the Meyer relation, $r = C_p\frac{\gamma-1}{\gamma}$ in Eq. (2.14), entropy variation is given by,

$$\frac{\Delta s}{C_p} = -\frac{\gamma-1}{\gamma} Ln\left(\frac{P_{t,j}}{P_{t,i}}\right). \tag{2.15}$$

This last relation shows that entropy variation is directly related to total pressure evolution for a stationary adiabatic vane. Assuming that variation of P_t between station i and j is very low compared to $P_{t,j}$, a Taylor expansion can be used to simplify the logarithmic term so that, $Ln\left(\frac{P_{t,ex}}{P_{t,in}}\right) \approx \frac{P_{t,ex}-P_{t,in}}{P_{t,ex}}$. Since entropy can only increase in an adiabatic system, total pressure P_t necessary decreases for a stationary adiabatic vane. A simple consequence of the previous discussion is that losses can be evaluated through the measurement of total pressure between two stations of the flow for adiabatic vanes. In the literature, entropy and total pressure 1D variations are generally given using loss coefficients. A brief description of the loss coefficient is hereafter provided.

2.2.1 Loss coefficients

In the literature, many loss coefficients are defined and a complete review can be found in (Brown, 1972). These loss coefficients are based on 1D evolution of entropy, total enthalpy or total pressure between two stations of the flow here noted i and j.

The first loss coefficient used in the literature is the entropy loss coefficient ξ_S defined such as,

$$\xi_S = \frac{T_0 \left(s_j - s_i\right)}{K_j}, \tag{2.16}$$

where K_j is the kinetic energy at station j. ξ_S represents the work lost with respect to the kinetic energy at the exit of the turbine stage. For incompressible flow, kinetic energy variation is small and the loss coefficient can be built only from variation of static enthalpy so that,

$$\xi_h = \frac{h_j - h_i}{K_j}. \tag{2.17}$$

For a stationary adiabatic vane, the most used loss coefficient is based on the variation of total pressure generally noted ξ,

$$\xi = \frac{P_{t,i} - P_{t,j}}{q_j}, \tag{2.18}$$

where q_j is the dynamic pressure measured at station j. Note that ξ is equivalent to ξ_S for stationary adiabatic vanes since entropy variation links to total pressure variation if total temperature T_t is conserved between two stations of the flow.

By choosing carefully balance planes in the system, the losses generated by specific regions of the flow can be evaluated. For instance, to evaluate the losses generated by a turbine stage, 1D balances are generally performed between the inlet and outlet stations of the turbine stage. From such an analysis, 1D loss models are built to evaluate the losses generated by each region of turbine flows (wake, boundary layer, shock...). An overview of these 1D loss models is provided in the next section.

2.2.2 Review of 1D loss models

In the literature, losses generated by a stationary adiabatic vane are split into different contributions: profile loss, shock loss and secondary loss (Howell, 1945; Ainley et al., 1951). Profile loss is associated to shear flow regions for 2D vanes, i.e, boundary layers developing on vanes and wakes downstream the trailing edge. Secondary loss corresponds to the losses generated by the secondary flows and the boundary layers developing on end-walls for 3D vanes. To evaluate the losses in these regions from the flow properties, 1D loss models are used in the literature assuming a steady 1D state of the flow. To build these loss models, entropy balance is performed on simple configurations representative of each region of turbine flows so that, boundary layers, wakes, shocks... A complete review of these loss models can be found in (Denton, 1993). In the following, a brief description of 1D loss models is provided.

Boundary layers Boundary layers are known to be responsible for total pressure loss and drag in wall bounded flows. To build a loss model for this context, a 2D incompressible boundary layer developing on an adiabatic flat plate without pressure gradient is first considered. Then, an entropy balance is performed in the boundary layer thickness δ giving (Denton, 1993),

$$\frac{d}{dx}\int_0^{\delta(x)} \rho u(s - s_{\delta(x)})dy = \dot{S}_\delta, \tag{2.19}$$

where ρ is the density, u is the streamwise velocity, $\dot{S}_\delta$ is the integrated entropy creation per unit volume in the boundary layer thickness, x streamwise coordinate and y wall normal coordinate. For boundary layers, the integrated entropy creation in the boundary layer thickness $\dot{S}_\delta$ is shown to be (Greitzer., 2004)

$$\dot{S}_\delta = \int_0^{U_\infty(x)} \frac{1}{T}\tau_{xy}du, \tag{2.20}$$

where τ_{xy} is the normal shear stress. Equation (2.19) shows that losses generated in a boundary layer depend on the work of the viscous forces and the local temperature. To evaluate this loss with respect to freestream flow, a local dissipation coefficient C_d can be introduced so that,

$$C_d = \frac{T\dot{S}_\delta}{\rho U_\infty^3}, \tag{2.21}$$

where U_∞ is the freestream velocity. C_d represents the local loss production with respect to flux of kinetic energy in the freestream flow. By performing a kinetic energy balance in the boundary layer thickness, C_d is shown to be linked to the energy displacement thickness θ^* of the boundary layer defined as (Greitzer., 2004),

$$\theta^* = \int_0^\delta \left(1 - \frac{u^2}{U_\infty^2}\right)\frac{u}{U_\infty}dn, \tag{2.22}$$

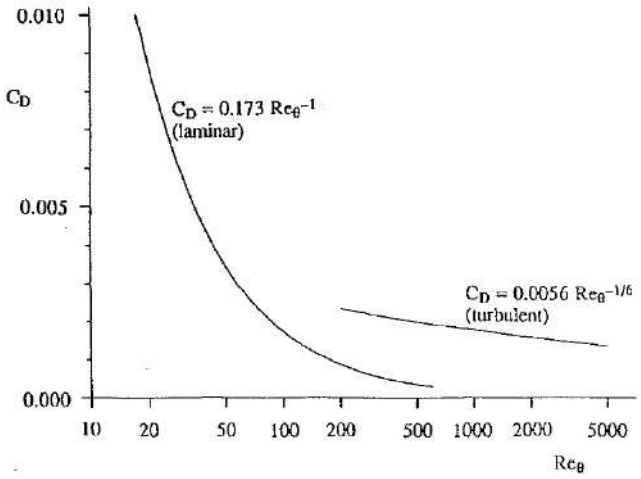

Figure 2.4 – Dissipation coefficient evolution against the momentum thickness Reynolds number Re_Θ for laminar and turbulent boundary layers. Extracted from (Denton, 1993). Correlations from (Schlichting, 1955).

where U_∞ is the freestream velocity and n the wall normal distance. θ^* is a measure of the kinetic energy dissipation in the boundary layer and its axial evolution is directly proportional to C_d so that (Greitzer., 2004),

$$\frac{d\theta^*}{dx} = 2C_d. \tag{2.23}$$

In that respect, θ^* is a measure of the losses for an incompressible adiabatic boundary layer. The evolution of the dissipation coefficient C_d can be plotted against the momentum thickness Reynolds number Re_Θ for laminar and turbulent boundary layers on Fig. 2.4. C_d is observed to be higher in laminar boundary layer if compared to a turbulent boundary layer. Note that the evolution of C_d is very similar to the skin friction coefficient C_f (Greitzer., 2004). Indeed, irreversibilities taking place in the boundary layer are shown to be associated to the wall shear stress. To link the dissipation coefficient C_d and the skin friction coefficient C_f, (Wheeler et al., 2017) proposed the following modelling for a turbulent boundary layer without pressure gradient,

$$C_d = \frac{C_f}{2} U_s + c_\tau \left(1 - U_s\right), \tag{2.24}$$

where U_s is an effective normalized slip velocity determined from Re_Θ and $c_\tau = \frac{\overline{u'v'}}{U_\infty}$ is the Reynold stress coefficient. This model allows to estimate the dissipation coefficient C_d from the measure of the skin friction coefficient C_f but such a model strongly depends on the Reynold stress modelling in the boundary layer.

When addressing the turbulent transition process of boundary layers, loss generation is more complex to investigate. Indeed, in the transition range, the boundary layer exhibits a non equilibrium state featuring high unsteady effects (Mayle, 1991). These unsteady effects lead to a sudden increase of the boundary layer

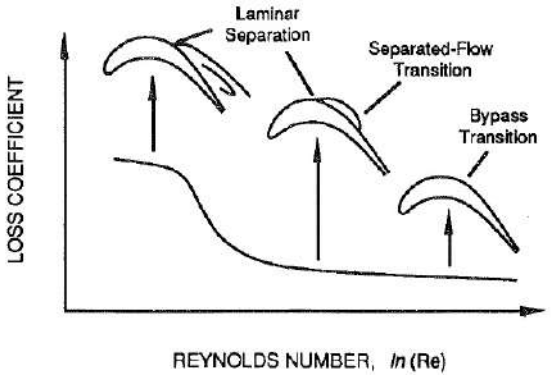

Figure 2.5 – Loss coefficient against the Reynolds number and the mode of transition. Extracted from (Mayle, 1991).

energy thickness generating more losses (Wheeler et al., 2017). The mode of the transition is also observed to strongly impact the loss generation (Mayle, 1991) as shown in Fig. 2.5. At low Reynolds number, the separation of the boundary layer generates losses due to the shear produced at the edge of the recirculation bubble. For higher Reynolds number, losses are mainly generated from apparition of turbulent spots in the boundary layer. Finally, when turbulence is fully developed in the boundary layer, (Dawes, 1990) showed that about 90 % of the loss generation is mainly localized in the inner layer of the boundary layer, whose 50 % is the viscous sub-layer and 40 % in the logarithmic layer.

Wake The wake mixes the two streams coming from both pressure and suction sides of the vane downstream the trailing edge. (Denton, 1993) proposes a general expression to determine the losses generated by a wake for a 2D blade. Using a momentum balance between the trailing edge plane of the blade and an imaginary plane far from the trailing edge where the flow is uniform (as represented on Fig. 2.6), the loss coefficient ξ can be expressed as,

$$\xi = -\frac{C_{pb}t}{w} + \frac{2\theta}{w} + \left(\frac{\theta^* + t}{w}\right)^2, \tag{2.25}$$

where θ^* and θ are respectively the displacement and momemtum boundary layer thickness, t the trailing edge thickness, w the blade to blade distance and C_{pb} the pressure coefficient at the trailing edge. The full demonstration of the formula can

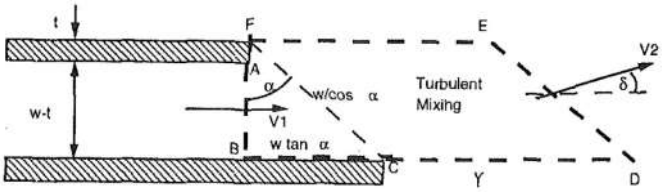

Figure 2.6 – Sketch of the control volume used by (Denton, 1993) to compute the loss generated by a wake.

be found in (Denton, 1993). The first term of the RHS represents the effect of the boundary layer separation at the trailing edge. The second term of the RHS represents the mixing of the boundary layers coming from the pressure and suction side of the blade. The third term of the RHS represents the blockage effect due to the thickening of boundary layers in the flow passage between the vanes. This last term is large if the boundary layer exhibits a separation upstream the trailing edge. In the literature, Eq. (2.25) is still widely used to quantify the losses in wakes as shown in the recent work of (Hammer et al., 2018). However, such a model is only valid for 2D anisothermal flows. A more sophisticated methodology is needed to evaluate the losses in the wakes of 3D cooled turbine vanes. This specific point will be later addressed in this work.

Shock The main difficulty with shock waves is the sharp evolution of the flow fields across the shock. Such variations can be evaluated using balance of energy upstream and downstream the shock and using the Rankine Hugoniot jump conditions. By expanding entropy variation in terms of Mach Number Ma, entropy increase across a normal shock is shown to be (Shapiro, 1953),

$$\Delta s = C_v \frac{2\gamma(\gamma-1)}{3(\gamma-1)^2}(Ma^2-1)^3, \tag{2.26}$$

where C_v is heat capacity at constant volume. As a result, the losses generated by a shock depends strongly on the Mach Number Ma. Indeed, the more the Mach number is, the more velocity gradients in shock are. However, shock waves in the turbine are generally not strictly normal to the flow. More sophisticated models were developed to give a better prediction of the losses generated by discontinuities in a more general case and can be retrieved in (Denton and Xu, 1990).

Film cooling In film cooling systems, two streams of different temperature mixes which generates entropy. To evaluate this entropy generation in this context, a simple configuration representing a coolant flow ejection in a hot stream is addressed as shown on Fig. 2.7. A mixing plane located far downstream the

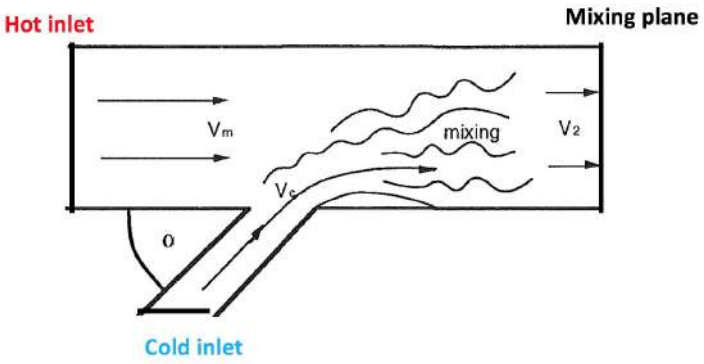

Figure 2.7 – Mixing of a hot and cold stream. Adapted from (Denton, 1993).

mixing region where streams are considered fully mixed is defined. Then, entropy balance is realized between the mixing plane and the hot and cold inlets. To simplify the balance, (Shapiro, 1953) assumes that the coolant mass flow rate is small compared to hot mass flow rate. Assuming a 1D evolution of the flow, (Shapiro, 1953) showed that entropy variation Δs is expressed as,

$$\Delta s = C_p \frac{Q_{m,c}}{Q_{m,h}} \left[\left(1 + \frac{\gamma - 1}{2} M_h^2 \right) \frac{T_{t,c} - T_{t,h}}{T_{t,h}} + (\gamma - 1) M_h^2 \left(1 - \frac{V_c cos\alpha}{V_h} \right) \right], \quad (2.27)$$

where $Q_{m,c}$ and $Q_{m,h}$ are respectively the coolant and hot mass flow rate, M_h the hot inlet Mach number, $T_{t,c}$ and $T_{t,h}$ respectively the total temperature of coolant and hot streams, V_c the velocity of coolant stream, V_h velocity of hot stream and α the angle formed between the hole and the main stream. In this case, entropy variation depends on the total temperature differences between hot and cold streams and velocity differences between the two streams. However, such a model is only valid if balance planes are located far from the mixing region. In a real cooled turbine, the hot and cold streams around the vane are not fully mixed. The local complexity of the flow then needs to be taken into account to evaluate the mixing losses in real cooled turbines. This specific point will be later addressed in this work.

Measurement of cumulated losses downstream a cascade vane The overall losses generated by an adiabatic cooled vane can be evaluated by performing a global balance between two stations of the flow respectively located upstream and downstream the vane. To do so, the spatial distribution of total pressure $P_t(y, z)$ is measured in an axial plane (defined by the coordinate y and z) located in the wake downstream the trailing edge of a vane as illustrated on Fig. 2.8. By measuring

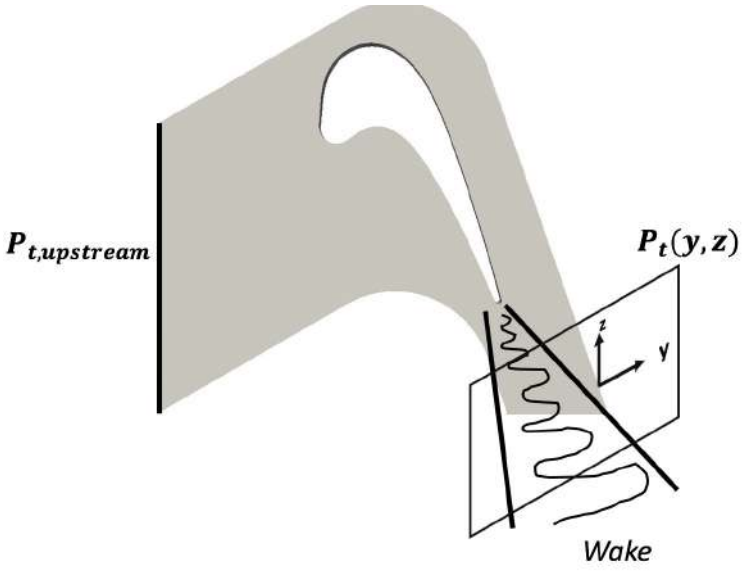

Figure 2.8 – Measurement planes used to obtain overall losses for an adiabatic vane.

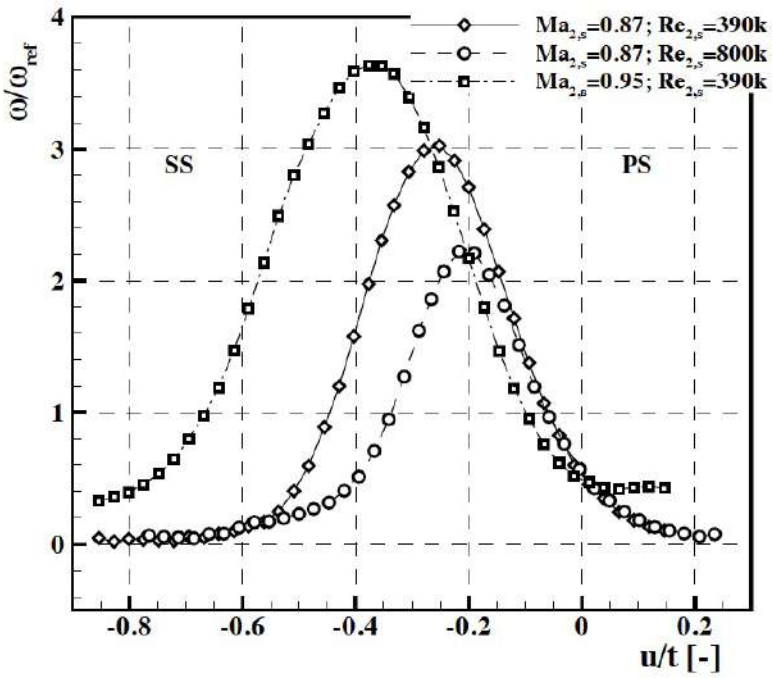

Figure 2.9 – Typical loss coefficient profile $\xi(\frac{u}{t})$ [-] for a 2D transonic cascade along the blade to blade direction $\frac{u}{t}$ [-]. Adapted from (Gomes and Araujo, 2010).

the difference between the total pressure $P_t(y,z)$ downstream the vane and the total pressure upstream the vane $P_{t,upstream}$, a loss profile is obtained through the total pressure loss coefficient ξ such as,

$$\xi = \frac{P_{t,upstream} - P_t(y,z)}{q_{ex}}, \tag{2.28}$$

where q_{ex} is the dynamic pressure measured in the exit plane of the turbine stage. One example of a loss coefficient profile of a linear cascade taken at mid-span of a vane is shown on Fig. 2.9. The shape of the profile depends on the losses generated upstream the measurement axial plane. If the loss profile tends to be asymmetric, it means that the loss generation between the pressure and suction side is also asymmetric. For example, if the boundary layer on the pressure side of a vane suffers from a separation followed by a turbulent transition, a higher value of ξ toward the pressure side is obtained. The resulting value of ξ is also observed to be sensitive to the Mach and Reynolds numbers of the vane (Mee et al., 1992). To illustrate this, the contribution of each flow region of a 2D transonic cascade to losses against the exit Mach number was evaluated by (Mee et al., 1992) as shown on Fig. 2.10. For low Mach number flows, there is no losses generated by shock waves because the flow does not exhibit supersonic zones. The boundary layer produces about 65 % of the total losses and the wake about 35 % of the overall losses. But if increasing the Mach number above 1, the global loss generation strongly increases due the interactions between boundary layers, shocks and wake.

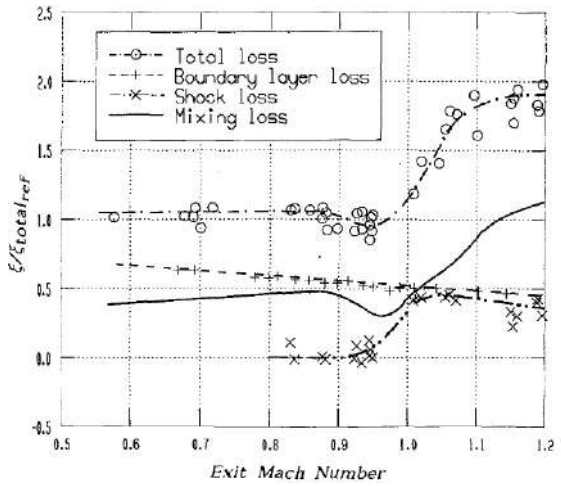

Figure 2.10 – Loss contribution between near wall, mixing process and shock loss against the exit Mach number of a 2D turbine extracted from (Mee et al., 1992).

Secondary flow To evaluate the losses generated by secondary flows, 2D loss coefficient maps ξ can be investigated in an axial plane located downstream the trailing edge of the vane. One example of the impact of the end-walls on the loss coefficient profile of a transonic blade measured in an axial plane downstream the blade is presented in Fig. 2.11. The loss coefficient map is observed to be strongly marked by secondary flows. The different vortices observed in secondary flows are well marked by the loss generation. Secondary losses represent about 1/3rd of the overall losses generated by a turbine blade (Denton, 1993). Since the secondary flows are induced by the separation of the boundary layers end-walls, the optimization of the shape of end-walls can lead to a reduction of 25 % of the secondary losses as shown in the work of (Kumar and Govardhan, 2011).

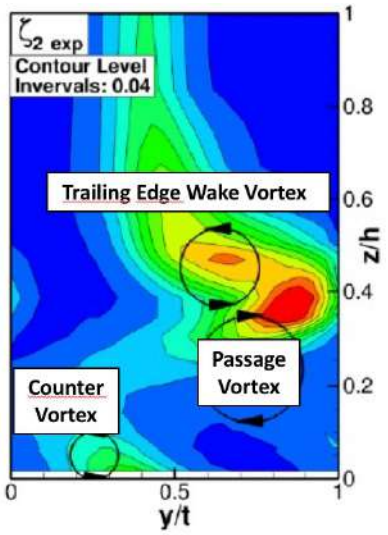

Figure 2.11 – Secondary loss coefficient of a transonic blade downstream the blade near the end wall. Extracted from (Ciorciari et al., 2018).

To sum up this section, the loss models presented here are based on simple geometries assuming a steady 1D evolution of the flow. However, such assumptions are not verified in turbine flows where the flow is 3D unsteady. When addressing film cooling systems, the hot and coolant streams are also not fully mixed around the vane in the film region which breaks hypotheses used in 1D loss models. As a result, a new methodology is needed to quantify the losses generated between two stations of the flow for 3D unsteady anisothermal flows. To overcome the limitations inherent to 1D loss models, one solution is to evaluate 1D entropy balance directly from the LES flow fields. To do so, 1D balances need to be extended to LES fields. This last point is specifically addressed in the next section.

2.3 Extension of 1D balances to LES data

In this section, a methodology to perform 1D balances with LES is proposed. To link 3D unsteady LES data and 1D steady state, a LES data reduction is needed. To do so, one solution is to use averaging procedures which are hereafter discussed.

2.3.1 Data reduction by the means of averaging procedures

This specific issue of averaging techniques has been widely studied in the literature (Pianko and Wazelt, 1983; Greitzer., 2004; Cumpsty and H. Horlock, 2006). It is however note worthy to recall as stated by (Pianko and Wazelt, 1983), *"No uniform flow exists which simultaneously matches all the significant stream fluxes, aerothermodynamic and geometric parameters of a non-uniform flow."* Based on this observation, (Cumpsty and H. Horlock, 2006) investigated the effect of different averaging procedures on the conservation of the fluxes, and work recovered by a turbine. Among the procedure tested, the mixed out averaging introduced by (Amecke, 1967) allows to reconstruct a 1D steady state by fully mixing the flow on several axial planes representing different stations of the flow. This approach is however found to increase the entropy of the obtained 1D flow compared to the entropy existing in the 3D flow. Another averaging procedure called the work average was introduced by (Pianko and Wazelt, 1983) which conserves the work obtained between the 3D flow and 1D model, but does not conserve entropy fluxes. In the following, the averaging procedure to be derived will aim at conserving work and fluxes between the 3D and 1D states so that losses can be adequately evaluated. To build such an averaging operator, the transport of a variable ϕ is addressed in a compressible unsteady flow. Here, ϕ can be any extensive variables (entropy, enthalpy...) and is assumed to be governed by a generic transport equation so that,

$$\rho \frac{d\phi}{dt} = \frac{\partial(\rho\phi)}{\partial t} + \frac{\partial(\rho U_i \phi)}{\partial x_i} = \dot{S}_\phi, \tag{2.29}$$

where ρ is the density, U_i the velocity vector and $\dot{S}_\phi$ is the local source term of ϕ. If the time average operator $\overline{\bullet}$ is applied to Eq. (2.29) and assuming that the time

average operator commutes with derivative operators, the unsteady term on the LHS cancels which gives,

$$\frac{\partial(\overline{\rho U_i \phi})}{\partial x_i} = \overline{\dot{S}_\phi}. \tag{2.30}$$

If Eq. (2.30) is integrated over a control volume bounded by an inlet section S_1, an outlet section S_2 and walls elsewhere and using the Green Ostrogradsky theorem, one can obtain,

$$\iint_{S_1} (\overline{\rho U_i \phi}) n_i dS + \iint_{S_2} (\overline{\rho U_i \phi}) n_i dS = \iiint_V \overline{\dot{S}_\phi} dV. \tag{2.31}$$

Ah this point of the demonstration, it is worth to define a *mass flow averaging* on surface S so that,

$$\widetilde{\phi}_S = \frac{< \overline{\rho U_i n_i \phi} >_S}{< \overline{\rho U_i n_i} >_S}, \tag{2.32}$$

where $< \bullet >_S$ is the spatial averaged operator on the surface S and n_i the normal surfaces pointing outward of the control volume. This averaging operator applied to Eq. (2.32) allows to obtain a 1D evolution for the variable ϕ so that,

$$Q_m \left(\widetilde{\phi}_{S_2} - \widetilde{\phi}_{S_1} \right) = \iiint_V \overline{\dot{S}_\phi} dV, \tag{2.33}$$

where Q_m is the time averaged mass flow rate passing through the system. The full demonstration of the formula can be found in Appendix C. Equation (C.12) shows that the averaging operator $\widetilde{\bullet}_S$ allows to reconstruct a 1D evolution of ϕ between two stations of the flow. As a result, this averaging operator is a powerful tool to link 1D steady state and 3D unsteady data for instance obtained from LES. It is important to note that such an averaging procedure can be applied to any transport equation following the generic form of a transport equation for a scalar. In the following, this specific averaging procedure will be applied to total enthalpy h_t, total temperature T_t and total pressure P_t to link the 1D thermodynamic modelling of losses with the 3D unsteady data obtained from LES.

2.3.2 Total enthalpy and entropy balance with LES

To recover the thermodynamic modelling of work, the total enthalpy evolution needs to be addressed. The transport equation of the total enthalpy has been derived in lot of studies for unsteady, compressible and no reactive flows (Greitzer., 2004),

$$\rho \frac{dh_t}{dt} = \frac{\partial \left(U_i \tau_{ij} \right)}{\partial x_j} + \frac{\partial P}{\partial t} - \frac{\partial q_i}{\partial x_i}, \tag{2.34}$$

where q_i is the heat flux and τ_{ij} the viscous stress tensor. To integrate this equation, a control volume must be first defined. The control volume chosen here corresponds to a turbine stage bounded by an inlet S_{in}, an outlet S_{ex}, moving walls S_{blade} (rotor) and stationary walls S_w (stator and end-walls). If Eq. (2.34) is integrated in such a control volume and using the mass flow averaging operator $\widetilde{\bullet}_S$ previously

introduced, the 1D evolution of h_t between stations S_{in} and S_{ex} is obtained through the following relation,

$$Q_m\left(\widetilde{h_{tS_{ex}}}-\widetilde{h_{tS_{in}}}\right)=\underbrace{-\iint_{S_{blade}}\overline{PU_i}n_i dS}_{\text{Work shaft}}\underbrace{-\iint_{S_w\cup S_{blade}}\overline{q_i}n_i dS}_{\text{Heat flux}}\underbrace{+\iint_{S_{ex}\cup S_{in}}\overline{U_i\tau_{ij}}n_j dS}_{\text{Work of viscous forces}}. \tag{2.35}$$

The first term of the RHS recovers the 1D steady work W supplied to rotor blades, $W=\iint_{S_{blade}}\overline{PU_i}n_i dS$. The second term recovers the 1D steady heat flux Q lost through the walls, $Q=\iint_{S_w\cup S_{blade}}\overline{q_i}n_i dS$. The third term corresponds to the work of viscous forces which is generally neglected in 1D analysis. As a consequence of the application of the mass flow averaging operator $\widetilde{\bullet}_S$ to total enthalpy, the 1D thermodynamic analysis is fully recovered,

$$Q_m\left(\widetilde{h_{tS_{ex}}}-\widetilde{h_{tS_{in}}}\right)=-W-Q. \tag{2.36}$$

Note that if $C_p=cst$, the balance can be expressed in terms of total temperature variation so that,

$$Q_m C_p\left(\widetilde{T_{tS_{ex}}}-\widetilde{T_{tS_{in}}}\right)=-W-Q. \tag{2.37}$$

For an adiabatic stator vane, h_t (and also T_t) is shown to be naturally conserved between S_{in} and S_{ex}. Note that if C_p is not constant, only total enthalpy should be considered to evaluate the work recovered by rotors. In the following, the mass flow averaging is applied to the entropy balance for the loss prediction.

Starting from the Gibbs equation expressed as infinitesimal variations of total temperature T_t and pressure P_t for $C_p=cst$,

$$ds=C_p\frac{dT_t}{T_t}-r\frac{dP_t}{P_t}, \tag{2.38}$$

multiplying the LHS and RHS by $\rho\frac{\bullet}{dt}$ and using the logarithm derivative, a transport equation for the sensible entropy s can be derived,

$$\rho\frac{ds}{dt}=\rho C_p\frac{dLn\left(T_t\right)}{dt}-r\rho\frac{dLn\left(P_t\right)}{dt}. \tag{2.39}$$

One can notice that each term in both LHS and RHS corresponds to the particle derivative through the generic expression $\rho\frac{d\bullet}{dt}$. Since C_p and r are thermodynamic constants, the mass flow averaging operator $\widetilde{\bullet}_S$ can be applied on each term of Eq. (2.39) to make appear a 1D variation of entropy, total temperature and total pressure. To do so, the same control volume as the one used above (for total enthalpy) is chosen. If Eq. (2.39) is integrated in such a control volume and using the mass flow averaging operator $\widetilde{\bullet}_S$ is applied, one can derive a 1D evolution of entropy between stations S_{in} and S_{ex} so that,

$$Q_m\left(\widetilde{s_{ex}}-\widetilde{s_{in}}\right)=Q_m C_p\left(\widetilde{Ln\left(T_{t,ex}\right)}-\widetilde{Ln\left(T_{t,in}\right)}\right)-Q_m r\left(\widetilde{Ln\left(P_{t,ex}\right)}-\widetilde{Ln\left(P_{t,in}\right)}\right). \tag{2.40}$$

This equation shows that the 1D entropy evolution can be retrieved from 1D balances of the logarithm total temperature and total pressure between two stations of the flow. It is important to note that the logarithm operator Ln is included in the averaging expression. For stationary adiabatic blade, $\widetilde{T_{tin}} = \widetilde{T_{tex}}$ using Eq. (2.37). For this specific case, the entropy balance is reduced to the evolution total pressure P_t. Using the Meyer relation, the 1D loss thermodynamic modelling for stationary adiabatic blade given by Eq. (2.15) is recovered:

$$\frac{(\widetilde{s_{ex}} - \widetilde{s_{in}})}{C_p} = -\frac{\gamma - 1}{\gamma}\left(\widetilde{Ln\,(P_{t,ex})} - \widetilde{Ln\,(P_{t,in})}\right). \tag{2.41}$$

As a result of the application of the mass flow averaging operator $\widetilde{\bullet}_S$ to entropy, the 1D thermodynamic analysis is also fully recovered. If neglecting the commutation error between the averaging operator $\widetilde{\ }$ and the logarithm operator Ln, the loss coefficient ξ can be reconstructed so that,

$$\xi = \frac{\widetilde{P_{t,in}} - \widetilde{P_{t,ex}}}{q_{ex}}, \tag{2.42}$$

where q_{ex} is the reference dynamic pressure measured downstream the blade. 1D loss coefficients can be then recovered from LES data through the use of the mass flow averaging $\widetilde{\bullet}_S$. However, it is note worthy to recall that total pressure drop only represent the losses in anisothermal flows, i.e, if the total temperature is conserved. Indeed, increase of total pressure has been observed for 3D viscous flows and has been investigated by (Williams et al., 2016). To understand such a behaviour of total pressure in viscous flows, he derived a transport equation for the total pressure and showed that the total pressure can locally increase thanks to the work of viscous forces in particular cases. Although this results is counter-intuitive, it is worth to recall that 1D thermodynamic analysis does not take into account these viscous effects. As a consequence, total pressure is not fully representative of losses for viscous anisothermal flows. To evaluate the losses in cooled turbine flows where the flow is strongly anisothermal, total pressure can not be used and another methodology is required.

To sum up this section, the mass flow averaging operator $\widetilde{\bullet}_S$ is shown to be powerful tool to recover the thermodynamic modelling of work and losses for turbine flows. For a system bounded by adiabatic walls, the entropy balance in a control volume bounded by an inlet *in* and outlet *ex* can be also expressed as local entropy generation $\dot{s}$ per unit volume so that,

$$Q_m\,(\widetilde{s_{ex}} - \widetilde{s_{in}}) = \int_V \overline{\dot{s}} dV. \tag{2.43}$$

A simple consequence of this last expression is that the losses can be also investigated through the study of the entropy source term $\dot{s}$. The study of the entropy source term corresponds to the *Second Law Analysis* methodology. This specific methodology is hereafter addressed and detailed in the next section.

2.4 Second Law Analysis

The Second Law Analysis (SLA) was initially introduced by (Bejan, 1982) to study the losses for energetic systems. As previously stated, the main idea of this methodology is to directly investigate the entropy source term in the flow. The main advantage of SLA is that the source of losses is directly studied in the flow without introducing any averaging procedures which greatly simplifies the loss evaluation. To use such a methodology, the entropy source term expression should be first addressed in the context of compressible fluid mechanics.

2.4.1 Second Law Analysis applied to fluid mechanics

For a compressible anisothermal flow, the entropy source term expression can be demonstrated from the comparison of an entropy balance applied to an infinitesimal fluid volume to the second law of thermodynamic. The demonstration can be found in many fluid mechanic books as in (Chassaing, 2000) and will not be detailed here. The entropy source term $\dot{s}$ is shown to be split in two contributions so that,

$$\dot{s} = s_m + s_q, \tag{2.44}$$

where,

$$s_m = \frac{1}{T}\tau_{ij}\frac{\partial U_i}{\partial x_j}, \tag{2.45}$$

$$s_q = \frac{-q_i}{T^2}\frac{\partial T}{\partial x_i}, \tag{2.46}$$

where τ_{ij} is the shear stress tensor, q_i the heat flux vector, U_i the velocity vector and T the static temperature. From these expressions, s_m is shown to be associated to velocity gradients, shear and local temperature while s_q is associated to heat flux and temperature gradients. In a general case, the flux terms need to be closed. Assuming a Newtonian fluid, τ_{ij} is given by the following relation,

$$\tau_{ij} = 2\mu\left(S_{ij} - \frac{1}{3}S_{ll}\delta_{ij}\right), \tag{2.47}$$

where μ is the dynamic viscosity, $S_{ij} = \frac{1}{2}\left(\frac{\partial U_i}{\partial x_j} + \frac{\partial U_j}{\partial x_i}\right)$ is the symmetric part of the strain-rate tensor and δ_{ij} the Kronecker symbol. To model the heat flux q_i, a Fourier law is adopted through the introduction of a thermal conductivity λ so that,

$$q_i = -\lambda\frac{\partial T}{\partial x_i}. \tag{2.48}$$

If re-injecting Eq. (2.47) in Eq (2.45) and Eq. (2.48) in Eq. (2.46), the entropy source terms are expressed with respect to local flow properties so that,

$$s_m = \frac{1}{T}2\mu\left(S_{ij} - \frac{1}{3}S_{ll}\delta_{ij}\right)S_{ij}, \tag{2.49}$$

$$s_q = \frac{\lambda}{T^2}\frac{\partial T}{\partial x_i}\frac{\partial T}{\partial x_i}. \tag{2.50}$$

It is worth to note that if compressibility effects are neglected, i.e, $S_{ll} = 0$, both entropy source terms are strictly positive. This confirms that both terms correspond to irreversibilities generated within the flow. To evaluate the work lost by local entropy generation, loss maps are constructed so that,

$$P_m = Ts_m = 2\mu \left(S_{ij} - \frac{1}{3} S_{ll} \delta_{ij} \right) S_{ij}, \tag{2.51}$$

$$P_q = Ts_q = \frac{\lambda}{T} \frac{\partial T}{\partial x_i} \frac{\partial T}{\partial x_i}, \tag{2.52}$$

where P_m is the loss map associated to aerodynamic losses and P_q the loss map associated to heat transfer within the flow. It is worth to notice that P_m also corresponds to the kinetic energy dissipation rate generally noted Φ in the literature.

As a result of the SLA, the study of loss maps P_m and P_q allows to locally identify the loss generation in a compressible anisothermal flow. This way, the overall work lost W_{lost} for the turbine can be retrieved from the integration of the time-averaged loss maps over the turbine volume $V_{turbine}$ (Eq. (2.12)) according to the following relation,

$$W_{lost} = \int_{V_{turbine}} \overline{\frac{T_0}{T} (P_m + P_q)} dV. \tag{2.53}$$

Since the definition of T_0 is not rigorous in the literature (as already discussed in Section 2.1), only loss maps P_m and P_q will be studied in the following of this work to identify and investigate the loss generation mechanisms. In the next section, the expressions of loss maps are extended to the LES formalism.

2.4.2 Second Law Analysis adapted to LES

In the context of LES, the loss maps are obtained from the fields resolved on mesh. In this context, the sub-grid fluxes, i.e, sub-grid Reynolds stresses τ_{ij}^t and sub-grid heat flux q_i^t need to be taken into account in the loss expressions so that,

$$P_m = (\tau_{ij} + \tau_{ij}^t) \frac{\partial \widehat{U_i}}{\partial x_j}, \tag{2.54}$$

$$P_q = \frac{(-q_i - q_i^t)}{\widehat{T}} \frac{\partial \widehat{T}}{\partial x_i}, \tag{2.55}$$

where $\widehat{\bullet}$ are the filtered quantifies. A Boussinesq assumption is used to model the sub-grid Reynolds stress tensor (Boussinesq, 1877) giving,

$$\tau_{ij}^t = 2\mu_t \left(\widehat{S_{ij}} - \frac{1}{3} \widehat{S_{ll}} \delta_{ij} \right) - \frac{2}{3} k_{SGS} \delta_{ij}, \tag{2.56}$$

where μ_t is the turbulent viscosity and k_{SGS} is the turbulent SGS kinetic energy. In this study, k_{SGS} is neglected. To close the sub-grid heat flux term, a turbulent conductivity λ_t (Pope, 2000) is introduced so that,

$$q_i^t = -\lambda_t \frac{\partial \widehat{T}}{\partial x_i}. \tag{2.57}$$

Note that λ_t is deduced from a sub-grid Prandtl number $Pr_{sgs} = \frac{\mu_t C_p}{\lambda_t}$ taken as constant and equal to 0.6. If re-injecting Eq. (2.56) and Eq. (2.47) in Eq (2.54) as well as Eq. (2.57) and Eq. (2.48) in Eq (2.55), the expressions for the resolved loss maps read as:

$$P_m = 2(\mu + \mu_t)\left(\widehat{S_{ij}} - \frac{1}{3}\widehat{S_{ll}}\delta_{ij}\right)\widehat{S_{ij}}, \tag{2.58}$$

$$P_q = \frac{(\lambda + \lambda_t)}{\widehat{T}}\frac{\partial \widehat{T}}{\partial x_i}\frac{\partial \widehat{T}}{\partial x_i}. \tag{2.59}$$

In the following, the filtering notation $\widehat{\ }$ will be omitted to simplify the expressions of the loss maps. From these loss map expressions, aerodynamic losses P_m are expected to be generated in regions of high sheared flows such as boundary layers or wakes. On the other hand, mixing losses P_q are expected to be produced in regions of high temperature gradients such as shocks or mixing regions taking place between two streams of different temperature. It is worth to note that the sub-grid scale (SGS) model is expected to drive the loss terms in the flow regions where $\mu_t >> \mu$ and $\lambda_t >> \lambda$. The choice of the SGS model and of the sub-grid Prandtl Pr_{sgs} is then expected to impact the loss terms, especially in the near wall flow region. Nevertheless, the impact of the SGS model on the loss maps will not be studied in this work but could be investigated in future studies.

With such an approach, both loss maps P_m and P_q are built from the resolved quantities obtained from a LES simulation. As a consequence, the losses can be investigated through the study of the loss maps to identify the loss generation locations and mechanisms. Indeed in the literature, this methodology has been mainly used to identify the losses for uncooled vanes as in (Zlatinov, 2011; Wheeler and al., 2016; Lin et al., 2017; Jin et al., 2017; Lengani et al., 2018; Fiore, 2019). To illustrate this approach, an example of an entropy generation map issued from the work of (Lin et al., 2017) is shown on Fig. 2.12. These numerical studies showed that losses are mainly generated in boundary layer and wake regions. Although these regions were expected to generate losses, SLA is shown to locally give access

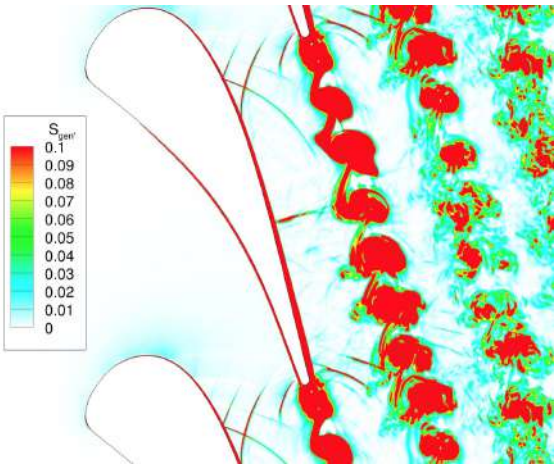

Figure 2.12 – Entropy generation map S_{gen} $[W/m^3/K]$ from (Lin et al., 2017).

to the loss sources for a compressible anisothermal flow, not only from a qualitatively point of view but also quantitatively. To the author's knowledge, SLA has not yet been used to study the losses for cooled turbine vanes. As a result, the SLA approach will be adopted to identify the loss generation mechanisms for the configurations investigated in this PhD work.

2.5 Chapter conclusions

As a consequence of this chapter, 1D loss models here presented were developed for isothermal flows of simple geometries and suffer from strong hypothesis on the flow physics. These models are then not adequate for the loss evaluation in the context of turbine vane cooling where the flow is naturally non-isothermal and complex, i.e: 3D, viscous and turbulent. To overcome the limitations inherent in these loss models and to identify the loss generation mechanisms, two high-fidelity approaches will be adopted in the following of the PhD work: entropy variation between two stations of the flow will be first evaluated through total variable 1D balance equations by using the mass flow average operator $\widetilde{\bullet}_S$. To identify the loss generation mechanisms within the flow, loss maps P_m and P_q obtained from LES will be then investigated by the use of SLA. These loss maps will be further analysed to link the flow physics with the losses. Finally, the capacity of the SLA approach to evaluate and quantify the losses for cooled turbine vanes will be discussed.

Part II

LES of academic blades

Outline of Part II

This part addresses the LES predictions for the academic T120 and T120D cascade blades. The uncooled T120 blade is designed to be highly loaded for which a recirculation bubble is present on the pressure side while the film-cooled academic T120D cascade blade presents a coolant film. The main objective of the present part is to validate the capacity of LES to predict the blade load distribution and the adiabatic wall temperature for both academic blades. After validations of the LES predictions, the loss generation locations and mechanisms issued by the flow aerodynamics and coolant film are investigated using the different approaches introduced in Chapter 2 i.e, through the use of total variable balances and Second Law Analysis (SLA). First, the uncooled T120 cascade blade is addressed in Chapter 3. In this chapter, the prediction of the flow structure and load distribution along the blade is first explored and validated. Then, only aerodynamic losses are addressed for this isothermal configuration. Afterwards, the anisothermal film-cooled T120D cascade blade is addressed in Chapter 4. In this chapter, the prediction of the blade load distribution and adiabatic film effectiveness is first assessed. Then, the losses issued by the flow aerodynamics and by the coolant film are investigated. From these analyses, the capacity of SLA to evaluate the losses and to identify the mechanisms associated to the loss generation for cooled high-pressure blades is finally discussed.

Chapter 3

Loss prediction of the academic uncooled T120 blade

Contents

3.1 Review of the T120 academic blade **70**
3.1.1 Introduction of the AITEB II project 70
3.1.2 Experimental set up and operating point 71
3.1.3 Aerodynamic measurements 72
3.1.4 CFD prediction of the T120 uncooled blade 75
3.2 Methodology and numerics **78**
3.2.1 Methodologies to inject fluctuations at the inlet of a LES computation 78
3.2.2 Numerical set up and LES modelling 80
3.3 LES predictions of the uncooled blade T120 . . . . . **84**
3.3.1 Validation of the synthetic turbulence injection 84
3.3.2 Impact of freestream turbulence on the flow prediction and validations 86
3.3.3 Investigation of the boundary layers 95
3.3.4 Investigation of losses 107
3.4 Chapter conclusions **121**

This chapter addresses the WRLES prediction for the academic uncooled T120 cascade blade presenting a bubble recirculation on the pressure side of the blade. The objectives of this chapter are first to validate LES predictions for such highly loaded blade and secondly investigate the aerodynamic losses using the different methodologies introduced in Chapter 2. To do so, the study is organized as follows. First, the T120 design, experimental operating point and available experimental database are described in Section 3.1. A review of existing numerical predictions of the uncooled T120 blade is provided to highlight the positioning of this work. From this review, freestream turbulence is shown to be a crucial parameter for flow

prediction of the T120 blade. To evaluate the impact of freestream turbulence on the flow prediction, wall resolved LES are performed with and without turbulence injection at the inlet of the computational domain. The impact of freestream turbulence on the flow prediction is assessed from the comparison between the two LES. The methodology adopted to inject turbulence and numerics are presented in Section 3.2. Then, the LES predictions are detailed and compared in Section 3.3. The impact on the mean flow organization and near wall flow region is explored and detailed. Next, the LES predictions are validated through the comparison to experimental results. After validations, aerodynamic losses and associated loss generation mechanisms are investigated. Finally, conclusions issued from the study are given in Section 3.4. Note that this specific part of the manuscript has been published in the proceedings of the international Turbo Expo conference (ASME):

- *M. Harnieh, L. Gicquel, and F. Duchaine. Sensitivity of large eddy simulations to inflow condition and modeling if applied to a transonic high-pressure cascade vane. In Proceedings of the ASME Turbo Expo 2017: Turbine Technical Conference and Exposition, GT2017-64686, Charlotte, USA, 2017.*
- *M. Harnieh, L. Gicquel, and F. Duchaine. Large eddy simulations of a highly loaded transonic blade with separated flow. In Turbomachinery Technical Conference and Exposition 2018, GT2018-75730, Oslo, Norway, 2018.*

Both publications can be found in Appendix D and Appendix E.

3.1 Review of the T120 academic blade

In this section, the T120 blade design issued from the AITEB II project is presented. First, the context of the project is recalled in Section 3.1.1. Then, the T120 blade design, experimental set up and operating point are described in Section 3.1.2. Next, available experimental database is provided in Section 3.1.3. Finally, a review of numerical predictions of the uncooled T120 blade is presented in Section 3.1.4.

3.1.1 Introduction of the AITEB II project

Reduction of engine size and weight leads to a reduction of the number of blades per stage and size of individual blades (Gomes and Niehuis, 2009). The flow deviation while reducing the blade size inevitably yields to highly curved blades. The strong curvature of the blade generates high adverse pressure gradient regions on both sides of the blade. Such pressure gradients yield easier the separation of boundary layers and creation of recirculation bubbles (Schlichting, 1955). The load for recent blades is then highly increased. To investigate the flow structure of such highly loaded blades, the academic high-pressure turbine T120 blade was designed and studied at the High-speed Cascade Wind Tunnel of the Institute of Jet Propulsion at the Armed Forces University Munich in the AITEB project (Haselbach and Schiffer, 2007). In the following, the design of the blade and experimental set up are introduced.

3.1.2 Experimental set up and operating point

The design of the T120 blade is presented in Fig. 3.1. The geometric specifications are presented in Table 3.1 (Gomes and Niehuis, 2013). The true chord length of the blade l is $120mm$ while the axial chord length c is 76 mm. The blade is highly curved on both suction and pressure sides to represent typical design of recent high pressure blades, Fig. 3.1 (a). The blades are investigated in a cascade form in the instrumented wind tunnel of Institute of Jet Propulsion of the German Armed Forces University Munich (Sturm and Fottner, 1985). In the experiment facility, the flow passes through a compressor to reach the desired operating point. A Pitot tube and resistance thermometers measure the inlet total pressure $P_{t,1}$ and inlet total temperature $T_{t,1}$ upstream the cascade, Fig. 3.1 (b). Note that the inflow is not aligned with the cascade and exhibits an inlet flow angle β_1 of 138.6°. The inflow is disturbed by a turbulence grid located upstream the cascade (not shown here). The corresponding turbulence intensity is measured with a hot wire

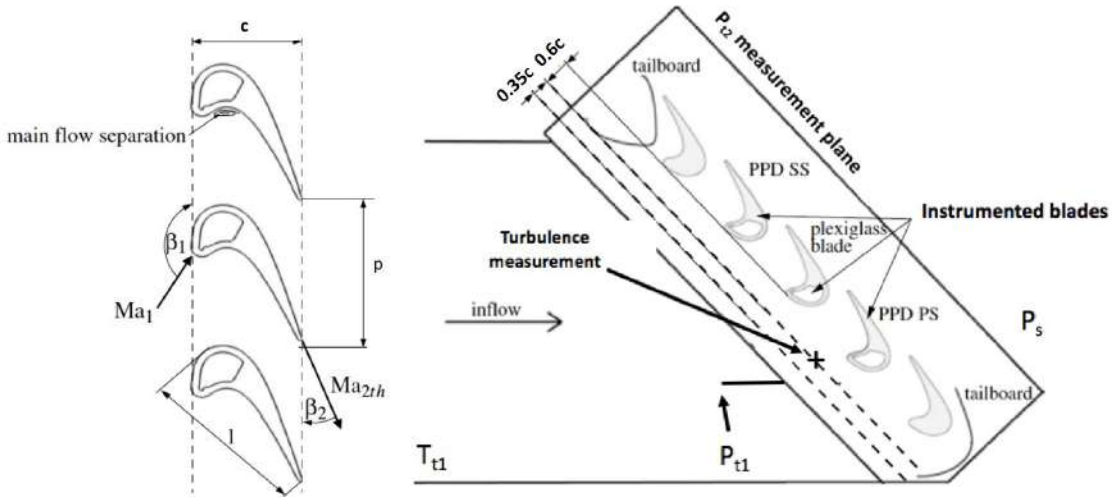

(a) (b)

Figure 3.1 – T120 blade cascade design on left (a) and scheme of the test rig on right (b). Extracted from (Gomes and Niehuis, 2013) and (Harnieh and Duchaine, 2017).

Feature	Symbol	Value
True chord length	l	120 mm
Axial chord length	c	76 mm
Blade height to chord ratio	h/l	1.5 [-]
Pitch to chord ratio	p/l	1.007 [-]
Inlet angle	β_1	138.6°
Turning	$\Delta\beta$	120°

Table 3.1 – Geometric characteristics of the T120 blade.

probe located $0.6c$ upstream the cascade in the middle of the passage between two blades. Downstream the cascade, a large tank is pressurized at the static pressure P_2 by a second compressor.

The operating point of the blade is specified at the exit of the cascade by the isentropic Mach number and Reynolds number respectively noted Ma_2 and Re_2. The isentropic Mach number Ma_2 is given by,

$$Ma_2 = \sqrt{\frac{2}{\gamma - 1}\left[\left(1 + \frac{q_2}{P_2}\right)^{\frac{\gamma-1}{\gamma}} - 1\right]}, \tag{3.1}$$

where $q_2 = P_{t,1} - P_2$ is the dynamic pressure in the tank downstream the cascade. The Reynolds number Re_2 is based on the inlet total temperature so that,

$$Re_2 = \sqrt{\frac{\gamma}{R}}\frac{l}{\beta_S}\frac{Ma_2.P_2\left[T_{t,1}.\frac{1}{1+\left(\frac{\gamma-1}{2}\right)Ma_2^2} + S\right]}{\left[T_{t,1}.\frac{1}{1+\left(\frac{\gamma-1}{2}\right)Ma_2^2}\right]}, \tag{3.2}$$

assuming a Sutherland law for the temperature dependent viscosity and R is the gas constant of perfect gases. Experimentally, 3 operating points have been investigated yielding different value of Re_2 and Ma_2 as summarised in (Gomes and Niehuis, 2013). For all experiments, the exit Mach number ranges from 0.87 to 0.95 to retrieve operating conditions of industrial blades while the tested Reynolds number are 390,000 and 800,000. In this work, the chosen operating point corresponds to the following couple: $Ma_2 = 0.87$ and $Re_2 = 390,000$.

3.1.3 Aerodynamic measurements

The aerodynamic of the uncooled T120 blade is experimentally characterized by the load of the blade, the wall shear stress as well as loss profiles downstream the cascade.

Load distribution on the blade surface measurement

In the experiment, the pressure distribution on the blade surface is obtained using static pressure taps located at mid-span of the cascade on the pressure side of one blade and on the suction side of another blade of the cascade. From the pressure taps, the static pressure P is recorded and time-averaged. Then, the axial evolution of the time-averaged static pressure $\overline{P}$ is normalized to build the isentropic Mach number Ma_{is} along the blade so that,

$$Ma_{is}(x/c) = \sqrt{\frac{2}{\gamma - 1}\left[\left(\frac{P_{t,1}}{\overline{P}(x/c)}\right)^{\frac{\gamma-1}{\gamma}} - 1\right]}, \tag{3.3}$$

where x/c the normalized axial distance along the blade and γ is the heat capacity ratio taken at 1.4. The axial evolutions of Ma_{is} for the 3 operating points are

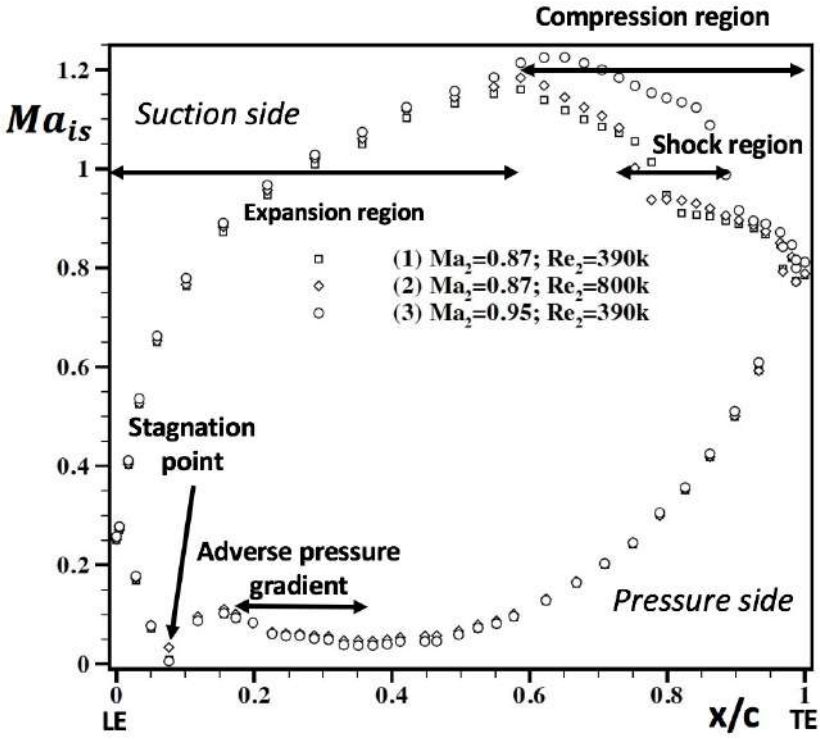

Figure 3.2 – Experimental distribution of the isentropic Mach number Ma_{is} [-] for different operating points. Taken from (Gomes and Niehuis, 2013). The leading edge (LE) is located at $x/c = 0$ and the trailing edge (TE) is located at $x/c = 1$.

given on Fig. 3.2. The stagnation point is located at $x/c = 0.05$ and does not correspond to the leading edge due to the inflow angle β_1. On the pressure side of the blade, Ma_{is} increases from $x/c = 0.05$ to $x/c = 0.15$. Next, the decrease of Ma_{is} between $x/c = 0.15$ and $x/c = 0.40$ indicates a region of adverse pressure gradient. This interval corresponds to the observation of a recirculation bubble on the pressure side (Gomes and Niehuis, 2013). From $x/c = 0.40$, Ma_{is} strongly increases which indicates a strong expansion and acceleration of the flow. On the suction side, the flow also exhibits a strong expansion between the leading edge to $x/c = 0.55$. From this axial position, the decrease of Ma_{is} indicates a compression region. Downstream, the rapid decrease of Ma_{is} at $x/c = 0.75$ for the targeted operating point highlights a shock.

Quasi-wall shear stress measurement

To evidence the wall shear stress on the blade surface, the blades are painted with a special oil mixture sensitive to skin friction. Due to the flow friction on the blade surface, the remaining oil concentration on the surface gives an indication on the level of local wall shear stress. For the targeted operating point, the time-averaged experimental oil flow on the unwrapped blade surface is shown on Fig. 3.3. Note that white color corresponds to low shear stress region. The stagnation line is represented by the white line at the leading edge of the blade located at $x/c = 0.05$.

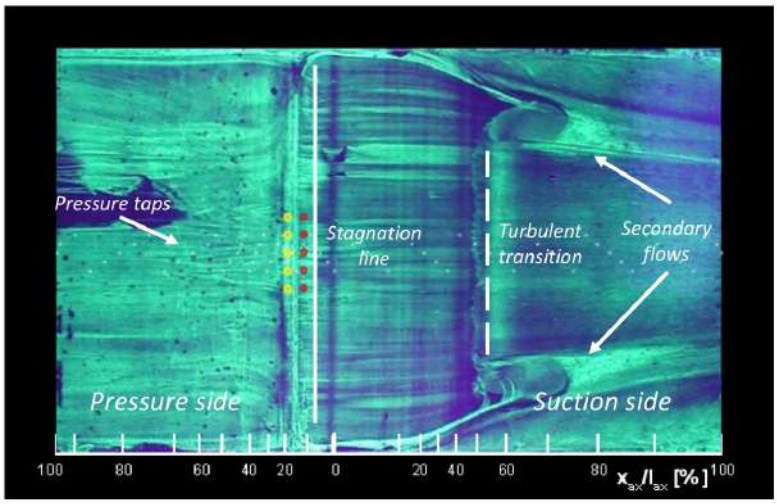

Figure 3.3 – Experimental oil flow visualization to evidence the wall shear stress on the unwrapped blade surface. Extracted from (Homeier et al., 2004).

On the suction side of the blade at $x/c = 0.5$, the dark zone evidences a turbulent transition of the boundary layer. Note that this transition occurs at the beginning of the deceleration meaning that the transition is probably induced by the adverse pressure gradient region. On the pressure side, no drastic change of the wall shear stress is noticed. Near the end-walls, vortices are observed and correspond to secondary flow structures. To avoid the impact of such secondary flows on the measurements, static pressure taps are exclusively located at mid-span.

Loss measurement

To experimentally evaluate the losses, total pressure variation is measured between the inlet total pressure $P_{t,1}$ and the axial plane located $x/c = 0.4$ downstream the cascade, i.e, in the wake of the blade as shown on Fig. 3.4. In this axial plane, local value of the total pressure is measured with a five probe hole along the local coordinates u and z corresponding respectively to the blade to blade and span directions, Fig. 3.4 (a). Then, the total pressure difference is normalized by the dynamic pressure q_2 to build the loss coefficient ξ so that,

$$\xi = \frac{P_{t,1} - \overline{P}_{t,2}(u,z)}{q_2}. \tag{3.4}$$

Loss profile is shown on Fig. 3.4 (b). The mark of the secondary flows on loss coefficient map is noticed between $z/h = -0.4$ and $z/h = -0.2$. On the center-line at $z/h = 0$, the shape of the loss coefficient corresponds to the wake developing downstream the blade. Such map also evidences that the flow field is independent of the span-wise direction (z) near mid-span of the blade for $-0.1 < z/h < 0.1$. Taking this property into account, numerical predictions for this blade can be performed on a limited span-wise domain using periodicity conditions.

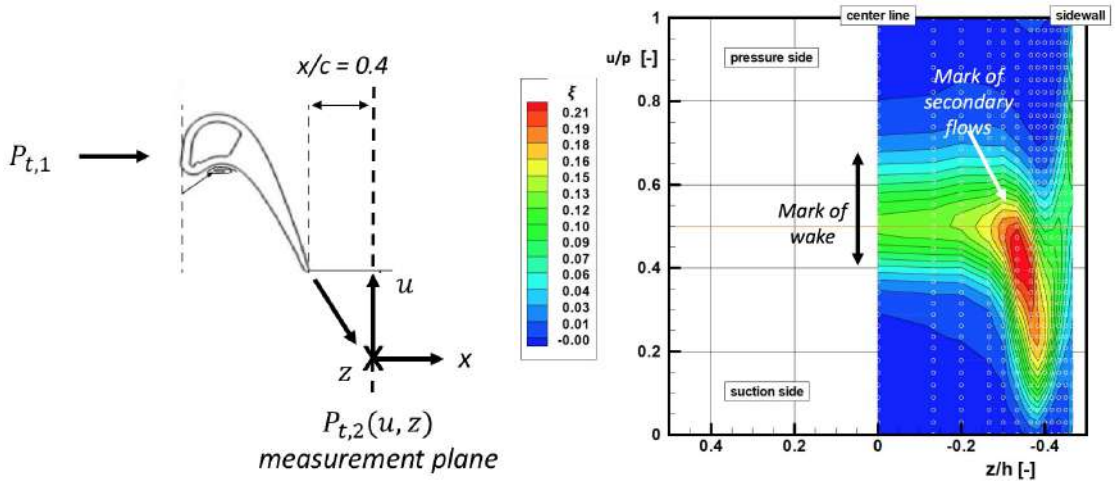

(a) (b)

Figure 3.4 – Scheme of the measurement loss plane (a) and experimental loss map $\xi = \frac{P_{t,1} - \overline{P}_{t,2}(u,z)}{q_2}$, [-] downstream the trailing edge in the axial plane at $x/c = 0.4$ (b). Taken from (Homeier et al., 2004).

To investigate the flow structure and flow expansion for such a highly loaded blade, CFD predictions were performed and are detailed hereafter.

3.1.4 CFD prediction of the T120 uncooled blade

In the literature, the T120 blade has been numerically investigated. Due to high Reynolds number value (390.000), no DNS has been performed for this blade to the author's knowledge. In the following, numerical predictions obtained with RANS and LES are detailed to establish a state of the art on this configuration.

RANS computations of the T120 blade

To study the flow aerodynamics, RANS has been first performed by (Homeier et al., 2004) and later by (Gomes and Araujo, 2010; Gomes and Niehuis, 2013). As discussed earlier, to exclude the effect of the observed secondary flows, a limited span domain of 16 mm containing one blade is represented using periodic boundary conditions. The mesh contains 150.000 nodes and mesh resolution is enforced near the blade wall to obtain a normalized wall units y^+ near 1. For these simulations, turbulence was modelled with the model $k-\omega$ SST transition model (Menter et al., 2004). Total pressure, temperature, turbulent kinetic energy and turbulent dissipation rate obtained from the experiment probes at the inlet are imposed at the inlet of the domain. The distribution of the isentropic Mach number obtained from this work is compared to experiment data on Fig. 3.5. Overall, RANS results reproduce fairly the experimental distribution except on the pressure side. In the RANS computation, the large plateau located in the interval between $x/c = 0.15$ and $x/c = 0.5$ evidences a large recirculation bubble (Gaster, 1967; Arena and Mueller, 1980; Lee et al., 2014). Despite the fine resolution in

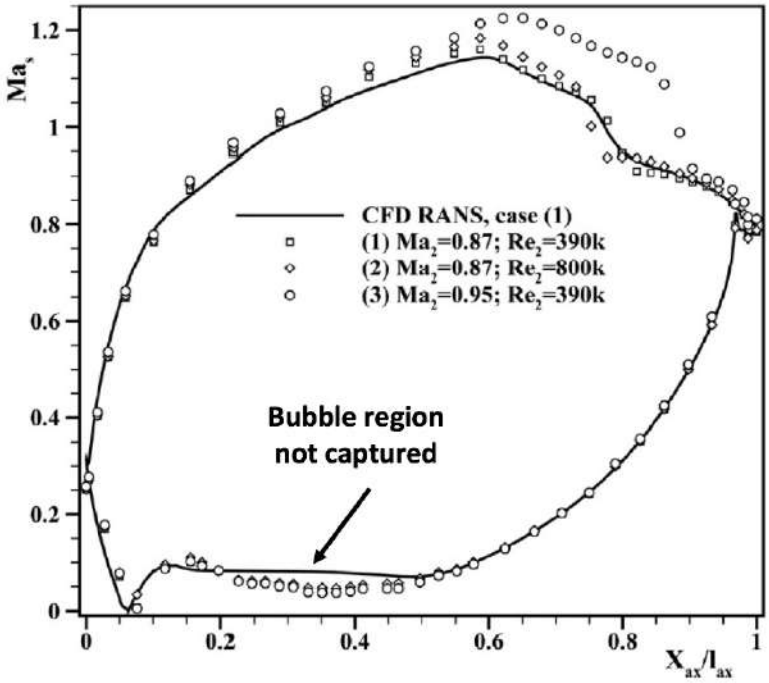

Figure 3.5 – Isentropic Mach number Ma_{is} [-] distribution along the blade between the experimental and RANS. Taken from (Gomes and Niehuis, 2013).

the near flow regions, RANS does not recover the load distribution in the bubble region. To improve the prediction, different turbulent models like the $k-\epsilon$ or Spalart Almaras models have been tested but no improvement has been noticed for this region (Homeier et al., 2004). On the suction side, although Ma_{is} is underestimated, the expansion and compression regions are correctly predicted. Strong sensitivity to turbulence models has been pointed out for the turbulent transition of the suction side boundary layer (Homeier et al., 2004).

This specific study illustrates the limit of RANS to predict unsteady phenomena such as bubble separation or turbulent transition of the boundary layer. Although solutions may exist in this context, the complexity of all mechanisms and their coupling makes the exercise quite difficult to be generalizable as of today.

LES computations of the T120 blade

LES of the academic T120 blade was first performed *A. Corpron*, a trainee employed at *Safran Helicopter Engines* (Pau, France) in 2008. Note that this work is the property of *Safran Helicopter Engines* and the associated full report is not public. Only the numerics and blade load distribution can be presented. The LES mesh contains 6 million of tetrahedra with a near wall resolution of $y^+ \sim 40$ at walls. Same steady inlet conditions as RANS without turbulence specifications is imposed at the inlet. The sub-grid scale turbulence was modelled using the sub-grid turbulence WALE model (Nicoud and Ducros, 1999) to recover the correct behaviour of the turbulence modelling at wall. The obtained isentropic Mach

number distribution along the blade is compared to experimental data on Fig. 3.6. The stagnation point is shifted compared to experiment indicating a deviation of the inlet angle with the experiment. On the pressure side of the blade, the level of the isentropic Mach number is over-estimated in the bubble region from $x/c = 0.05$ and $x/c = 0.55$ as the RANS computation presented above. From $x/c = 0.55$, the isentropic Mach number is well predicted on the pressure side. On the suction side, the distribution of Ma_{is} is well captured from the leading edge to $x/c = 0.4$. Downstream, the isentropic Mach number is under-estimated from $x/c = 0.4$ to $x/c = 0.8$ indicating a potential deficit of the expansion level and mass flow rate with the experiment. As a result, such LES set up was not able to predict the adverse pressure gradient regions. Later (Gomes and Niehuis, 2013) performed a new LES to study the bubble separation topology on the pressure side. The flow region near the pressure side was refined to reach a normalized wall unit y^+ between 1 and 3. Same numerics, boundary conditions and turbulence model as the previous LES have been used. However, the bubble size issued from this LES work was also found to be too large compared to experimental data. More details on the results can be found in (Gomes and Niehuis, 2013). Such differences can be explained by the fact that the wall mesh is not sufficiently refined leading to a bad prediction of the wall shear stress. Indeed wall resolved LES require a wall unit y^+ near 1 (Tyacke and Tucker, 2014). Likewise, flow with separation and bubble regions are known to be highly sensitive to near wall mesh resolution as well as freestream turbulence in DNS / LES (Burgmann and Schroder, 2008; ZAKI et al., 2010; Wheeler and al., 2016; Cadieux et al., 2014; Uzun and Malik, 2017). None of which was adequately taken into account in discussed LES.

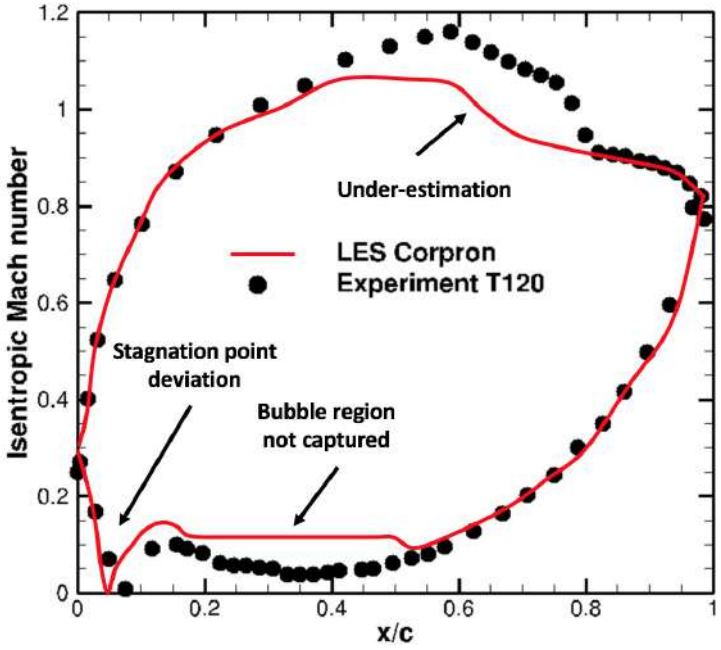

Figure 3.6 – Isentropic Mach number Ma_{is} [-] distribution along the blade. Red line – are LES data from *Corpron* and black circles • experimental data.

Although not fully extensive, the previous discussion indicates that no existing numerical approach was able to recover the full experimental distribution of the isentropic Mach number for the T120 blade. RANS is too sensitive to turbulence models and attempted LES's were not able to predict the bubble region so far. Since the separation is known to be sensitive to the freestream turbulence, one solution is to inject turbulence at the inlet of the LES computational domain. To evaluate the impact of freestream turbulence on the flow prediction, the adopted strategy is presented in the next section.

3.2 Methodology and numerics

To evaluate the impact of freestream turbulence on the flow prediction, wall resolved LES are performed with and without synthetic turbulence injection at the inlet and are compared. Both cases will be respectively refer as *laminar inlet* and *turbulent inlet* cases. Prior to the application of such strategy to the T120 blade, a quick review of the different methodologies to inject turbulence in LES is first presented in Section 3.2.1. Then, the numerics and LES modelling retained for this work are presented in Section 3.2.2.

3.2.1 Methodologies to inject fluctuations at the inlet of a LES computation

The specification of turbulence at the inlet of a computational domain is a complex issue since no analytical expression exists to specify a turbulent field, i.e, a field that satisfies the filtered Navier-Stokes equations and that includes unsteady as well as spatially fluctuations. In the following, two methodologies, presented in Fig. 3.7 and recently developed around the AVBP LES solver are introduced:

- Synthetic turbulence injection: This method consists in building a fluctuating signal at the inlet which approaches a specific turbulent signal generally issued by a Homogeneous Isotropic Turbulence (HIT). One example of such synthetic turbulence injection for the *LS89 blade* issued from the work of (Segui Troth, 2017) is shown on Fig. 3.7. To do so, a pseudo turbulent signal is built to recover the modelled analytical energy spectrum distribution of Passot-Bouquet (Passot and Pouquet, 1987; Smirnov et al., 2000). By construction, this model is not a solution of the filtered Navier-Stokes equations and adaptation of the injected fields are needed for the proper physics to establish. Indeed, the turbulent structures injected at the inlet were shown to be partially dissipated (as shown on Fig. 3.7 (a)) because of adaptation to mesh resolution and due to non-physical turbulent energy spectrum imposed at inlet. This method furthermore requires to specify a turbulent intensity and an integral length scale to scale the signal. The turbulent intensity is generally obtained from experimental data but the integral length scale is generally unknown. One solution proposed in the literature (Wheeler and al., 2016) is to simply impose the integral length scale to enter in the span-wise

extent domain and adjust the value to match experimental turbulent specifications. However, the value of the integral length scale is known to strongly affect the turbulent dissipation rate (Sreenivasan, 1998; Pope, 2000). Verifications of the decay of the turbulent signal between the inlet and the leading edge of the blade are then mandatory to ensure that turbulent structures injected at the inlet reach the leading edge of the blade.

- Precursor computation (Eswaran and Pope, 1988): This method couples the inlet of the domain to a precursor computation representing a turbulent channel or a HIT box. Turbulent fields are extracted from the precursor domain and interpolated at the inlet of the domain as shown on Fig. 3.7 (b). Since this methodology requires two LES computations, the CPU cost is then higher compared to the previous approach. This methodology has been implemented and validated in the thesis of (Segui Troth, 2017).

Both approaches have been tested at the inlet of a LES computation of the *LS98 blade* in the work of (Segui-Troth et al., 2017). To evaluate both approaches, a Power Spectral Density (PSD) of the temporal signal at the inlet plane and decay of the turbulent kinetic energy between the inlet and the leading edge are plotted on Fig. 3.8. Clearly, the -5/3 slope of the HIT turbulence is better predicted with the precursor approach than the synthetic turbulence approach, Fig. 3.8 (a). If the decay of the turbulent kinetic energy is compared to the analytical model using the Taylor hypothesis (Sagaut and Cambon, 2008), Fig. 3.8 (b), the decay of turbulent kinetic energy is better predicted with the precursor approach. Indeed and contrary to synthetic turbulence injection, the turbulent fields imposed from the precursor approach originate from numerical resolution of the filtered Navier-

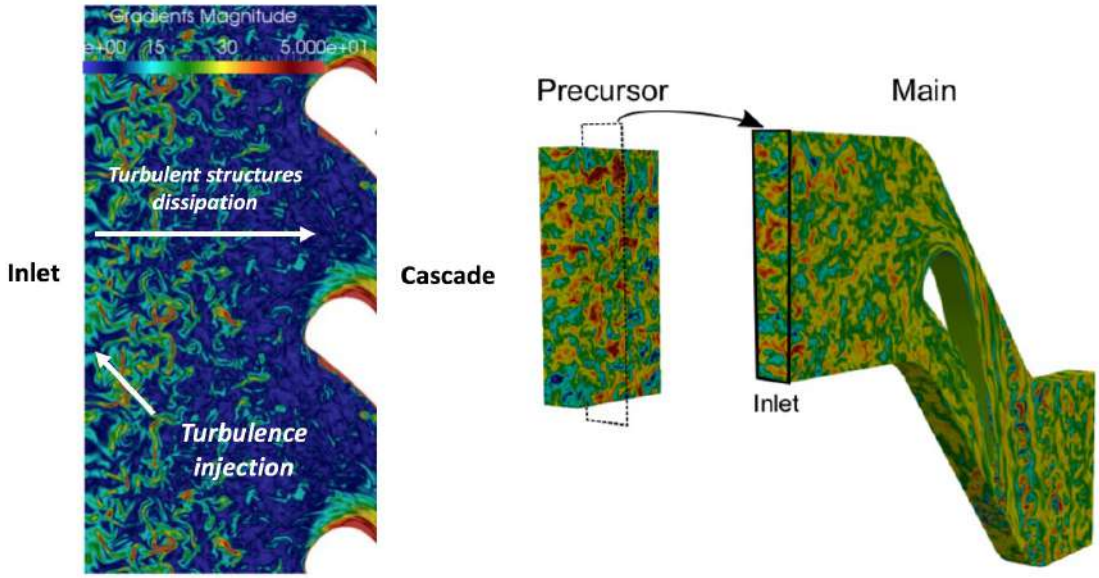

(a) (b)

Figure 3.7 – Example of a synthetic turbulence injection at the inlet on left (a) and using a precursor on right (b). Taken from (Segui-Troth et al., 2017).

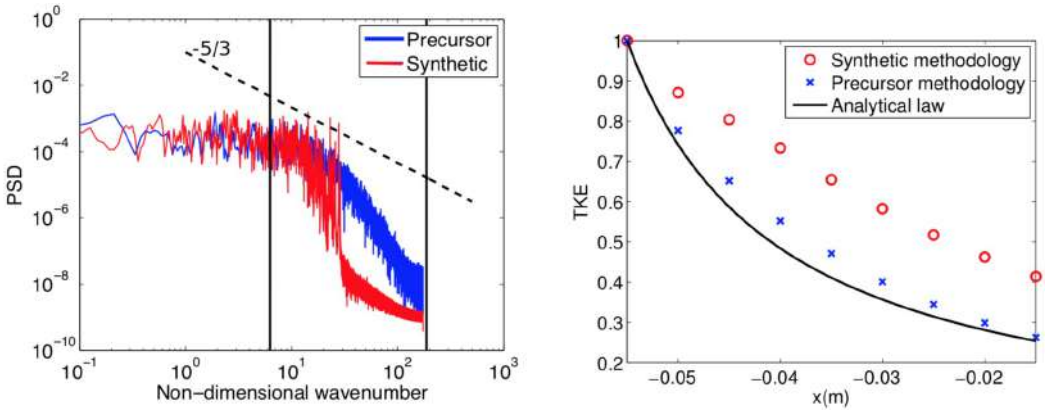

(a) (b)

Figure 3.8 – Power Spectral Density (PSD) of the signal at the inlet plane on left (a) and turbulent kinetic energy (TKE) decay between the inlet and the leading edge on right (b) for the synthetic turbulence approach (red) and precursor approach (blue). Extracted from (Segui-Troth et al., 2017).

Stokes equations. As a result, no adaptation is needed when imposed at the inlet of the computational domain. Although superior, difficulties in correctly injecting turbulence in the LES make the precursor approach complex and still function of parameters as the turbulent length scale. To avoid the CPU cost of a precursor LES computation, synthetic turbulence injection approach is chosen for this work.

3.2.2 Numerical set up and LES modelling

In this section, the numerics and LES modelling of *laminar inlet* and *turbulent inlet* cases are presented. First, the computational domain extent and the mesh are introduced. Then, numerics and LES modelling are provided. Finally, boundary conditions and inlet turbulent specifications are addressed for both cases.

Computational domain

The computational domain represents one blade of the cascade and is presented on Fig. 3.9. The span-wise domain extent is limited to 8 mm, i.e, 3 % of the blade span and 10% of the axial chord length to reduce the span-wise length of the domain allowing grid refinement in the near wall flow regions. Periodic conditions are applied in the y and z directions to represent only one single blade. One chord length is taken in the front part of the domain to avoid interactions between acoustic and potential effect of the blade at the inlet of the computational domain. Three chord lengths have been chosen between the blade and the outlet to dissipate the wake as well as acoustic waves prior to the outlet boundary condition.

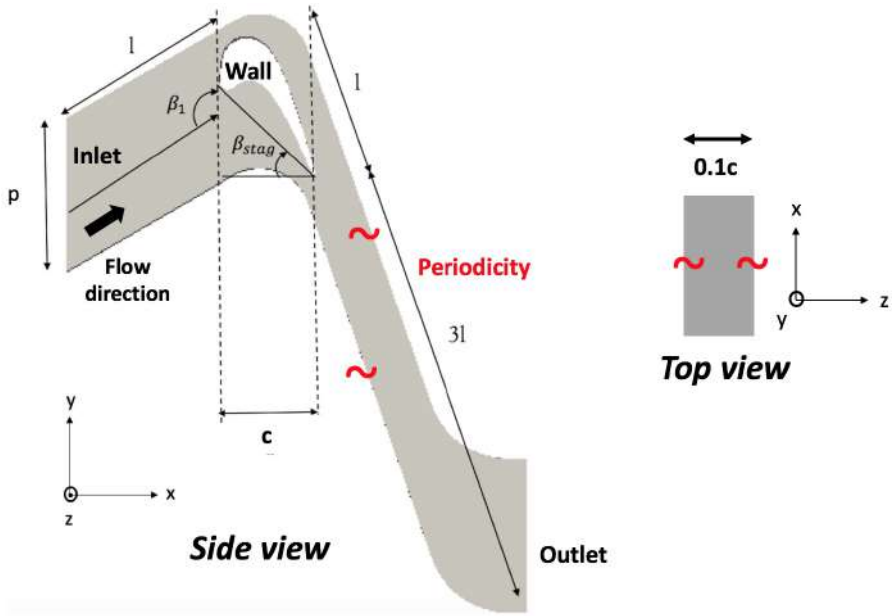

Figure 3.9 – Computational domain of the T120 blade. True chord length l, axial chord length c and pitch distance between 2 blades p are defined in Table 3.1.

Mesh

The unstructured mesh is composed of 24 million of tetrahedra and 10 million of prisms corresponding to a total number of vertices of about 9.3 millions. As shown on Fig. 3.10, the mesh is refined on the pressure side, suction side and wake regions to capture strong gradients and near wall flow structures on mesh. Ten layers of prisms at the blade surface are used to reduce the simulation computational cost while complying with a wall resolved approach. Indeed, the normalized wall unit, y^+, plotted on Fig. 3.11, remains below 2 along the blade except near the leading

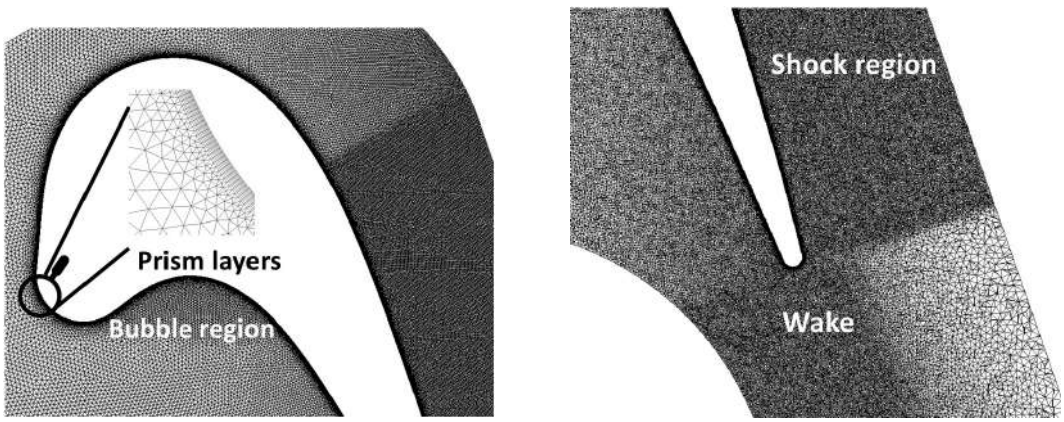

(a) (b)

Figure 3.10 – Mid-cut of the mesh in the near leading edge on left (a) and trailing edge on right (b).

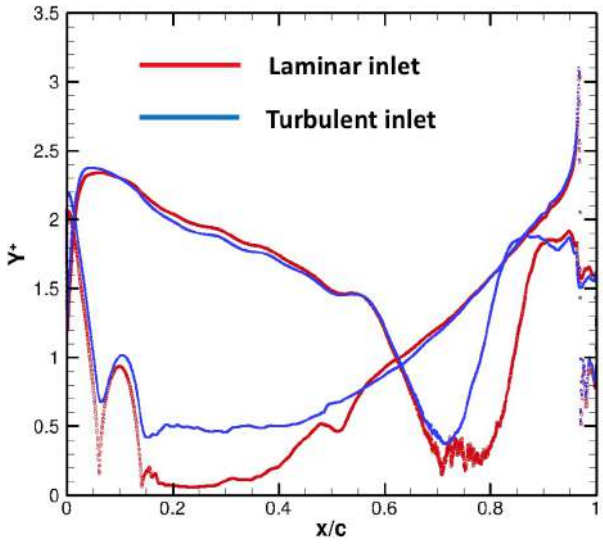

Figure 3.11 – y^+ [-] distribution along the blade. Red line - represents the laminar inlet case while blue line - is the turbulent inlet case.

and trailing edges. Although y^+ is partially superior to 1 along the blade, the designed mesh is in full agreement with requirements for a wall resolved LES (Tucker, 2013; Tyacke and Tucker, 2014) and is therefore expected to predict the wall shear stress in the viscous sub-layer of the boundary layer. The wall surface is meshed with isotropic triangles, i.e, $x^+ \approx z^+$. The aspect ratio of the prisms is limited to 5 along the blade, i.e, $x^+ \approx 5y^+$. Finally, cell volume jump at the interface between tetrahedron / prism is by construction imposed to 3 to ensure proper numerics in this part of the associated hybrid mesh.

Numerical scheme

The LES compressible equations (Garnier et al., 2009; Poinsot and Veynante, 2011) are numerically resolved for all simulations. The convective terms are integrated with the high order scheme TTGC (Colin and Rudgyard, 2000), i.e, 3rd order in time and space. This numerical scheme has good spectral properties and does not dissipate the smallest length scale flow structures resolved on mesh and thus is well adapted for LES (Colin and Rudgyard, 2000). The diffusive terms are integrated with a 2nd order finite element scheme.

LES modelling

The WALE sub-grid scale model is used to comply with the correct wall behaviour of the turbulent viscosity (Nicoud and Ducros, 1999).

Targeted operating point and boundary conditions

As a reminder, the chosen operating point of the blade for this work is defined by the doublet $(Re_2; Ma_2) = (390,000; 0.87)$ for both laminar and turbulent in-

Patch	Variable	Value
Inlet	$P_{t,1}$	26720 Pa
	$T_{t,1}$	333 K
	Inlet angle	138.6 °
Outlet	P_2	16307 Pa
Wall		Adiabatic no slip

Table 3.2 – Boundary conditions used in the computations.

let cases. In the computation, the inflow specifications are imposed by the total pressure $P_{t,1}$, total temperature $T_{t,1}$ and the inlet angle. The static pressure P_2 is imposed at the outlet. The corresponding boundary condition targeted values are summarized in Table 3.2 to match numerically the experimental operating point. To impose the targeted values on boundary conditions, the *NSCBC* formalism (Poinsot and Lele, 1992; Odier et al., 2018) is used to deal with acoustic treatment. With this approach, the instantaneous values on the boundary conditions are temporally relaxed towards the targeted values. The laminar and turbulent inlet cases are built by imposing different inflow specifications and this specific point is hereafter addressed.

Test cases and turbulence injection

To assess the effect of the inlet turbulent injection on the flow structure, different LES are established by differing the boundary inflow specifications as detailed in Table 3.3. For the turbulent inlet case, synthetic turbulence is injected at the inlet following the method of (Smirnov et al., 2000) presented in Section 3.2.1. The integral length scale l_t imposed at the inlet is adjusted at $6mm$ to enter in the span-wise domain ($8mm$). The obtaining integral length scale to chord ratio is then $\frac{l_t}{c} = 0.08c$ and corresponds to the same order of magnitude used in wall resolved LES of academic blades (Wheeler and al., 2016; Segui Troth, 2017). The inlet turbulence intensity is adjusted at 20% to comply with the experimental measurement obtained with the hot-wire probe located $x/c = 0.6$ upstream the cascade in the mid-flow passage between 2 blades.

Case	Inlet turbulent intensity
LAMINAR INLET	0%
TURBULENT INLET	20%

Table 3.3 – Test case matrix.

3.3 LES predictions of the uncooled blade T120

In this section, the impact of freestream turbulence on the flow prediction is evaluated through the comparison between the *laminar inlet* and *turbulent inlet* cases. To do so, the injection of synthetic turbulence at the inlet of the computational domain is first validated in Section 3.3.1. Then, the comparison between both laminar an turbulent inlet cases is detailed in Section 3.3.2. The impact on the near wall flow region is specifically addressed in Section 3.3.3. Finally, losses are investigated in Section 3.3.4.

3.3.1 Validation of the synthetic turbulence injection

To ensure that structures are generated at the inlet and transported to the blade, an instantaneous view of the iso-surface of Q-criterion taken from the turbulent inlet case is shown between the inlet and the blade on Fig. 3.12. Unsteady structures are clearly identified at the inlet of the computational domain. The decreasing of the number of structures when propagating evidences the dissipation of the synthetic turbulence between the inlet and the blade. It is important to note that structures are not fully dissipated when reaching the leading edge of the blade. To

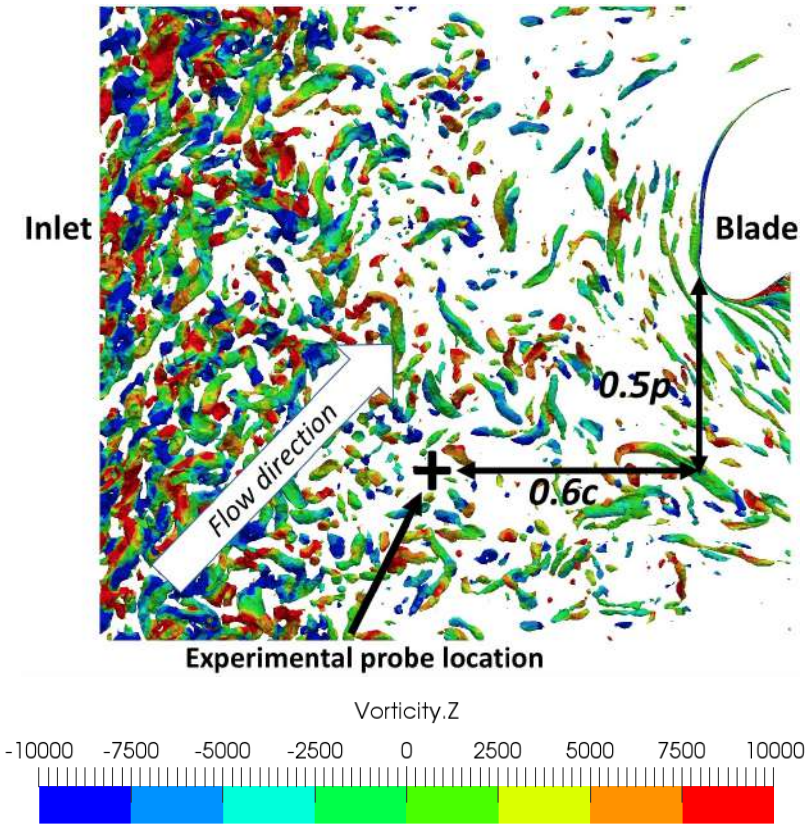

Figure 3.12 – Instantaneous view of an iso-surface of Q-criterion equal to $Q_{crit} = 4.10^7\ s^{-2}$ coloured by the span vorticity $\omega_z\ [s^{-1}]$ between the inlet and the blade.

evaluate the synthetic turbulence injected at the inlet, the signal of the velocity fluctuation located at the experimental probe (represented in Fig. 3.12) and decay of turbulent kinetic energy from the mean flow are shown in Fig. 3.13. At the experimental probe location, the signal of the velocity fluctuation is recorded during $4ms$ with a sampling frequency of $2.10^5 Hz$. From this signal, the Power Spectral Density is computed and shown on Fig. 3.13 (a). The -5/3 slope corresponding to the spectra of homogeneous turbulence is recovered for the middle range frequency between $2.10^3 Hz$ and $2.10^4 Hz$. The behaviour of the signal for higher frequencies ($> 2.10^4 Hz$) is coherent with observations of (Segui-Troth et al., 2017). Then, the decay of the turbulent kinetic energy between the inlet and the leading edge is compared to an analytical model in Fig. 3.13 (b). The model results from the decay of an homogeneous isotropic turbulent field (Sagaut and Cambon, 2008). For such a flow, the turbulence can be described by the initial turbulent kinetic energy k_0 and the initial turbulent dissipation rate ϵ_0. From such hypotheses, time evolution of the turbulent kinetic energy k then reduces to,

$$k(t) = k_0 \left(1 + (C_\epsilon - 1)\,\frac{t}{\tau_0}\right)^{\left(-\frac{1}{C_\epsilon - 1}\right)}, \tag{3.5}$$

with $\tau_0 = \frac{k_0}{\epsilon_0}$ and $C_\epsilon = 1.92$. From the integral length scale imposed at the inflow and from dimensional relations, the initial turbulent dissipation rate ϵ_0 is estimated at $\epsilon_0 = 3.78.10^6\ m^2 s^{-3}$. Using the Taylor hypothesis (Sagaut and Cambon, 2008), the temporal evolution can be recast into a spatial evolution x along a streamline so that $x = u_0 * t$ as long as the mean flow velocity u_0 is not affected by non-linear effects. The decay rate of turbulent kinetic energy is observed to be stronger than the model in part attributed to the unphysical spectrum imposed at the inflow

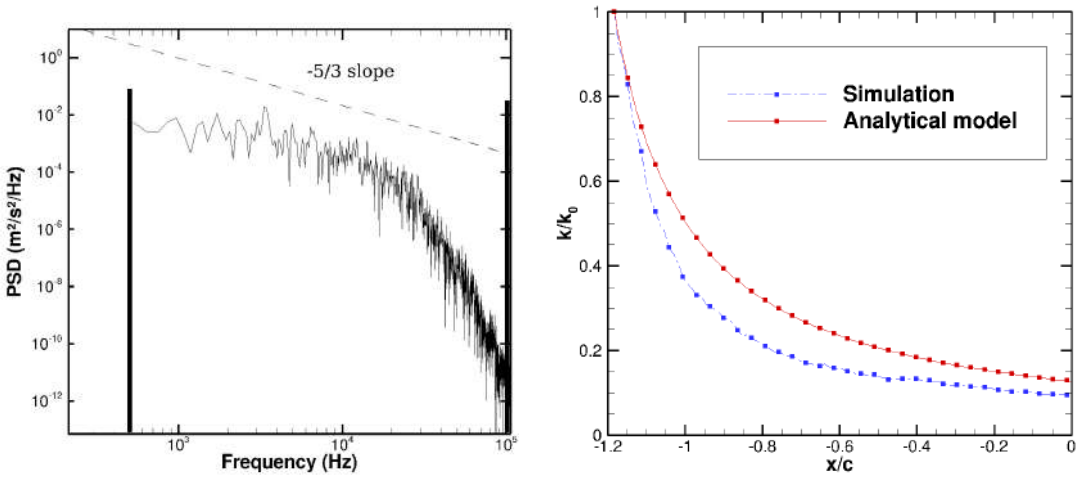

(a) (b)

Figure 3.13 – Power Spectral Density (PSD) of the axial velocity signal taken at the probe located at $x/c = -0.6$ in the mid flow passage (a) on left. Frequency limitations are given by the duration of the signal and the sampling frequency. Decay of the turbulent kinetic energy k $[m^2/s^2]$ from the inlet to the leading edge along a streamline passes in the mid-passage (b) on right.

Case	Turbulence intensity
Experiment	5%
LES	5.23%

Table 3.4 – Turbulence intensity measured at $x/c = 0.6$ upstream the leading edge in the mid-flow passage. Experimental value taken in (Gomes and Niehuis, 2009).

as observed by (Segui-Troth et al., 2017). Finally, to validate the turbulence injection, the turbulence intensity is extracted at the probe location represented in Fig. 3.12 and compared with the value measured in the experiment in Table 3.4. At this specific location, a good agreement is found with the experiment which validates the level of turbulence intensity upstream the blade.

After validation of the synthetic turbulence injection, both *laminar inlet* and *turbulent inlet* cases are compared in the next section to assess the impact of freestream turbulence on LES flow prediction.

3.3.2 Impact of freestream turbulence on the flow prediction and validations

Prior to compare both LES predictions, the numerical operating point should be verified and compared to targeted operating point for both LES cases. Then, the impact of freestream turbulence on instantaneous and mean field predictions are described. More specifically, the impact of freestream turbulence on the recirculation bubble on the pressure side and on the boundary layer turbulent transition on the suction side is addressed. Finally, the prediction of the wall stresses for both LES cases is evaluated through the comparison with experimental results.

Numerical operating points

To check the numerical operating point, mass flow rate Q_m and expansion ratio $P_2/P_{t_{LE}}$ for both cases are compared to experimental data in Table 3.5. The expansion ratio represents the ratio between static pressure at the outlet P_2 over the spatial averaged total pressure at the leading edge plane $P_{t_{LE}}$. Although both LES cases target the same experimental operating point, the expansion ratio

Case	$P_2/P_{t_{LE}}$ (-)	Q_m (g/s)
EXPERIMENT	0.61	-
LAMINAR INLET	0.6103	18.08
TURBULENT INLET	0.6109	18.07

Table 3.5 – Expansion ratio $P_2/P_{t_{LE}}$ and mass flow rate Q_m for both cases and experiment. Note that no data of mass flow rate from the experiment is available.

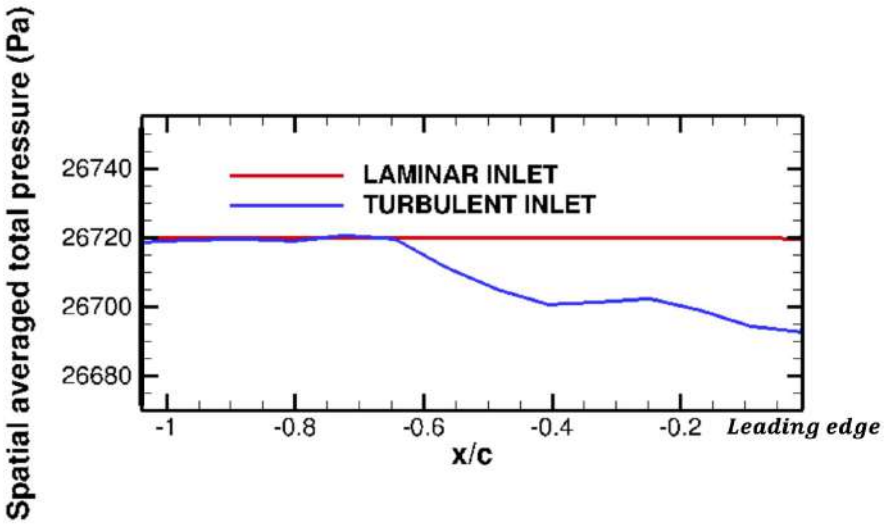

Figure 3.14 – Spatial averaged total pressure between the inlet and the leading edge axial plane.

slightly differs between both cases. Indeed, despite the outlet static pressure P_2 is imposed by the outlet boundary condition, $P_{t_{LE}}$ is not fully monitored by the inlet boundary condition and results from total pressure loss between the inlet and the leading edge. To verify this last statement, the axial evolution of the spatial averaged total pressure between the inlet and the blade is plotted on Fig. 3.14. For the laminar inlet case, the total pressure remains constant. For the turbulent inlet case, the spatial averaged total pressure decreases from $x/c = 0.6$ to the leading located at $x/c = 0$. This region corresponds to the dissipation of the turbulent structures in agreement with Fig. 3.12. The dissipation generates losses which decreases total pressure between the inlet and the leading edge of the blade. As a result, the expansion ratio for the turbulent inlet case is then necessary higher than the laminar inlet case. Note that this specific point will be later addressed more in details in the loss investigation section. If looking at the mass flow rate, no strong deviation is observed between both cases. Such differences remain negligible and then 0D values can be considered equivalent between both cases. In the next section, the impact of freestream turbulence on instantaneous large scale flow is addressed.

Impact of the turbulence injection on large scale flow structure

The large scale flow structure for both LES predictions is presented by providing an instantaneous view of the vorticity magnitude map extracted at mid-span of the blade on Fig. 3.15. The flow structure is first described for the laminar inlet case, Fig. 3.15 (a). On the pressure side, a recirculation bubble, evidenced by the white isocontour of zero axial velocity, is observed. The bubble originates from near the stagnation point region and then reattaches to the blade wall. The shape of the bubble and levels of vorticity on the white isocontour indicates that unsteady structures are generated at the edge of the bubble. On the suction side,

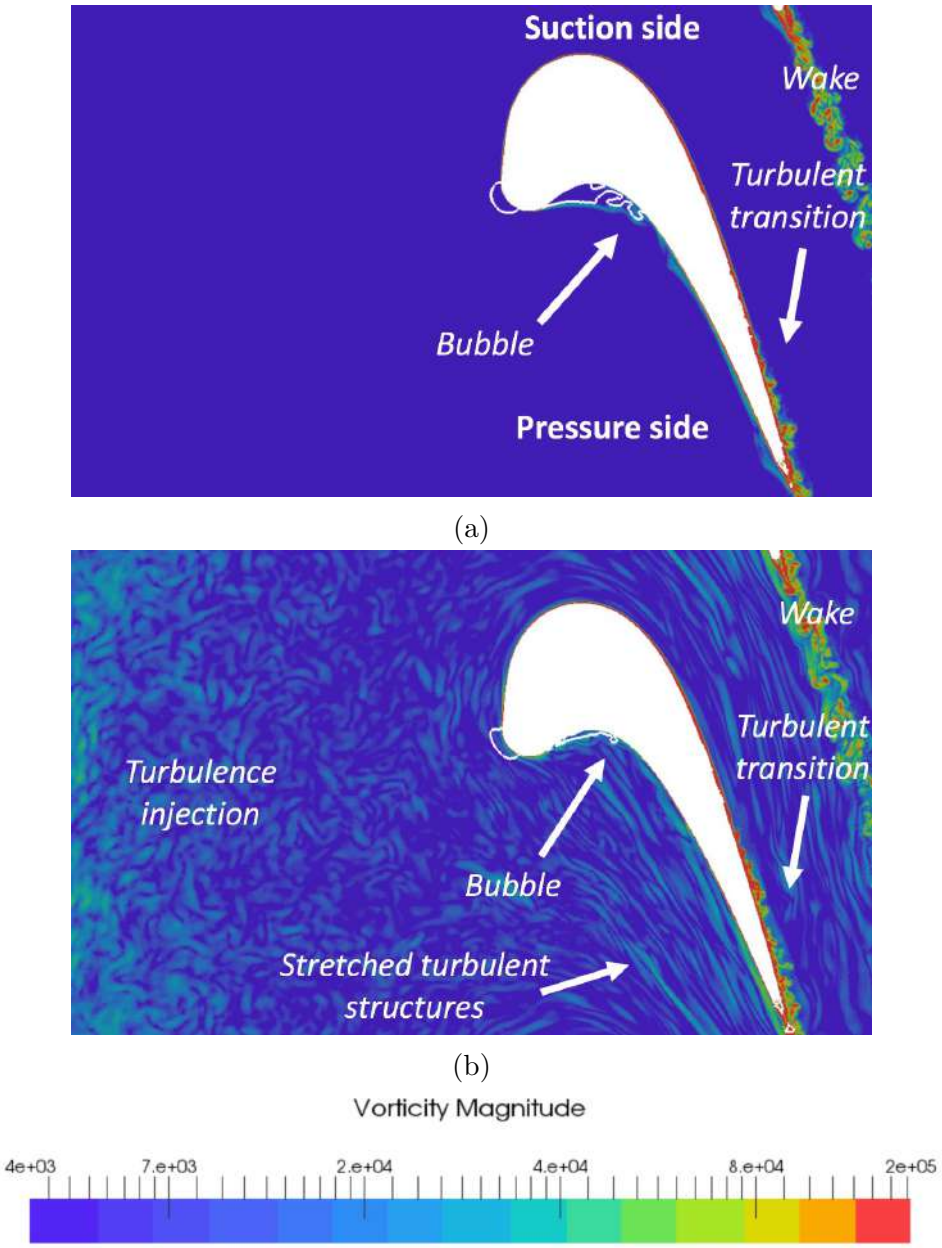

Figure 3.15 – Instantaneous map of vorticity magnitude $\|\omega\|$ $[s^{-1}]$ at mid-span of the blade. White isocontour corresponds to zero axial velocity. Laminar inlet case at top (a) and turbulent inlet case at bottom (b).

the boundary layer develops along the blade and exhibits a turbulent transition. Downstream the trailing edge, a turbulent wake presenting coherent structures is observed. For the turbulent inlet case, Fig. 3.15 (b), turbulent structures injected at the inlet propagates from the inlet to the blade. From the leading edge, turbulent structures are stretched by the acceleration of the flow. If compared both LES predictions, the bubble and turbulent transition positions and topologies differ. A closer look in these two regions is hereafter provided.

A closer look of the near wall flow region on the suction side of the blade for both cases is shown Fig. 3.16. For the laminar inlet case, Fig. 3.16 (a), a supersonic region is evidenced by the white sonic lines $\overline{M} = 1$. To discriminate potential shock waves, a numerical Schlieren visualization is shown at mid-span of the blade. Downstream this supersonic region, multiple unsteady shock-waves are observed and tend to move upstream. Such shock-waves, called shocklets, have been described in (Handa et al., 1999) and appear when the flow is weakly supersonic, i.e, when the Mach number Ma satisfies $1 < Ma < 1.1$. It is noted that the shocklet intensity is weaker in the turbulent inlet case in comparison with the laminar inlet case. Downstream the shocklets, a turbulent transition of the boundary layer occurs for both cases. Indeed, turbulent structures as hairpin vortices are observed along the suction side of the blade. If compared to the turbulent inlet case, Fig. 3.16 (b), the position of the turbulent transition position moves upstream in comparison with the laminar inlet case. Such effects of the impact of freestream turbulence on the position of turbulent transition of boundary layers have already been observed in LES / DNS (Brandt et al., 2004; Segui Troth, 2017; Wheeler et al., 2017). Finally, the turbulent wake is observed downstream the trailing edge for both cases.

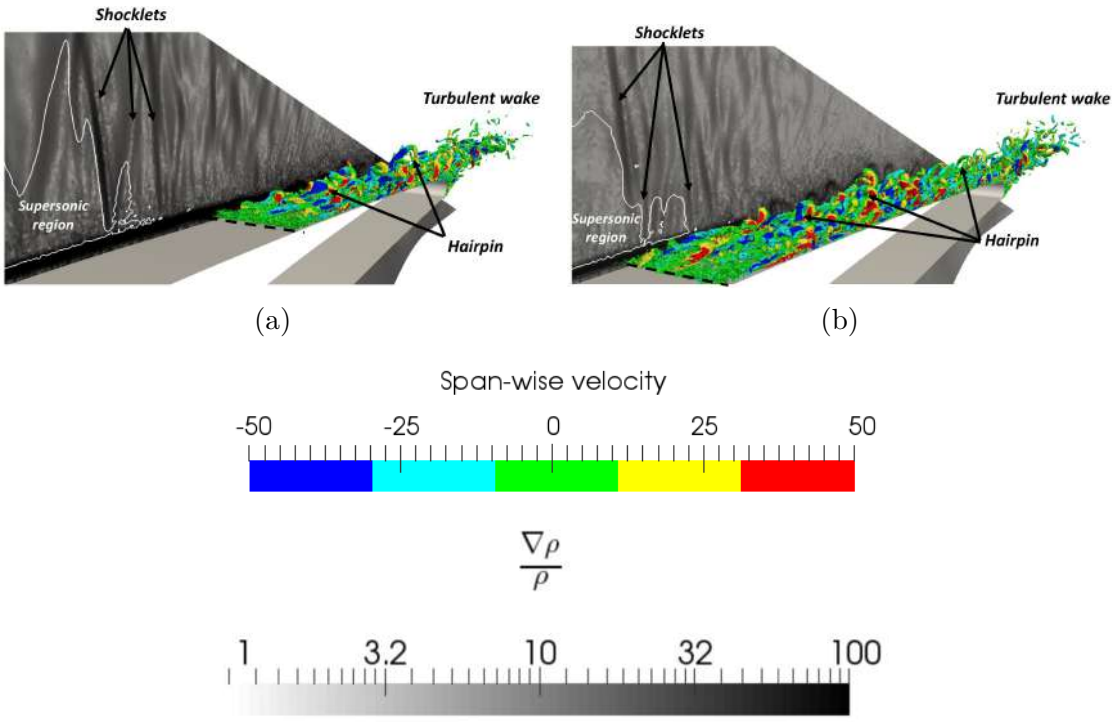

Figure 3.16 – Instantaneous view of an iso-surface of Q-criterion coloured by the span velocity w $[m/s]$, $Q_{crit} = 1.10^9$ s^{-2} in the near wall flow region on the suction side. Numerical Schlieren $\frac{\|\nabla\rho\|}{\rho}$ $[m^{-1}]$. White sonic lines $\overline{Ma} = 1$. Laminar inlet case on left (a) and turbulent inlet case on right (b). Dashed lines represent the position of the turbulent transition of the boundary layer.

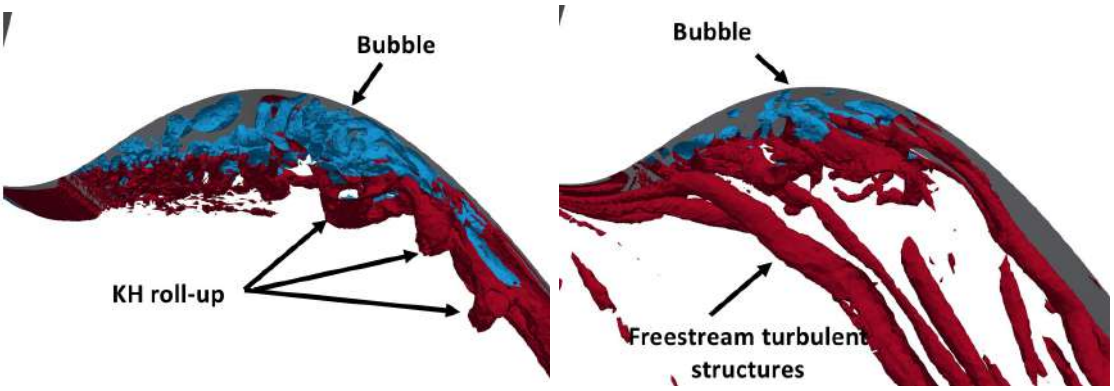

(a) (b)

Figure 3.17 – Instantaneous view of an iso-surface of Q-criterion, i.e $Q_{crit} = 1.10^5\ s^{-2}$, in the bubble region coloured by the axial velocity u. Red represents positive axial velocity $u > 0$ and blue negative axial velocity $u < 0$. Laminar inlet case on left (a) and turbulent inlet case on right (b).

On the pressure side of the blade, a closer look at the bubble structure is shown by plotting an instantaneous view of the iso-surface of Q-criterion coloured by the axial velocity in Fig. 3.17. For the laminar inlet case, Fig. 3.17 (a), Kelvin-Helmholtz (KH) roll-up are produced at the edge of the recirculation bubble which are transported and stretched by the acceleration of the flow. In the recirculation bubble, i.e, blue part, coherent structures are also evidenced. For the turbulent inlet case, Fig. 3.17 (b), the bubble structure is quite different and interacts with freestream turbulent structures at the edge of the bubble in the red part. Although coherent structures are still noticed in the bubble, no KH structure is observed at the edge of the bubble. Finally, the size of the bubble is strongly reduced in the turbulent inlet case.

To go further in the analysis, a statistical description of the flow is adopted. To do so, the flow fields are time-averaged on 4 flow time passages defined as a time for a fluid particle to go from the inlet to the outlet of the computational domain. Such a convergence time is sufficient to ensure that the flow statistics (mean + RMS) are converged. The mean flow organization is hereafter addressed.

Impact of the turbulence injection on the mean flow

The time-averaged pressure fields issued by both simulations are provided at mid-span in Fig. 3.18. The laminar inlet case is first described, Fig. 3.18 (a). On the pressure side of the blade, the recirculation bubble is retrieved on the mean flow evidenced by the black isocontour $\overline{u} = 0$. On the suction side, a strong expansion of the flow is observed leading to a supersonic region identified by the white iso-contour sonic line $\overline{Ma} = 1$. Downstream, a compression region is observed. When compared to the turbulent inlet case, Fig. 3.18 (b), the bubble size is strongly reduced. The spatial distribution of the static pressure between pressure and suction sides is also observed to be impacted by freestream turbulence.

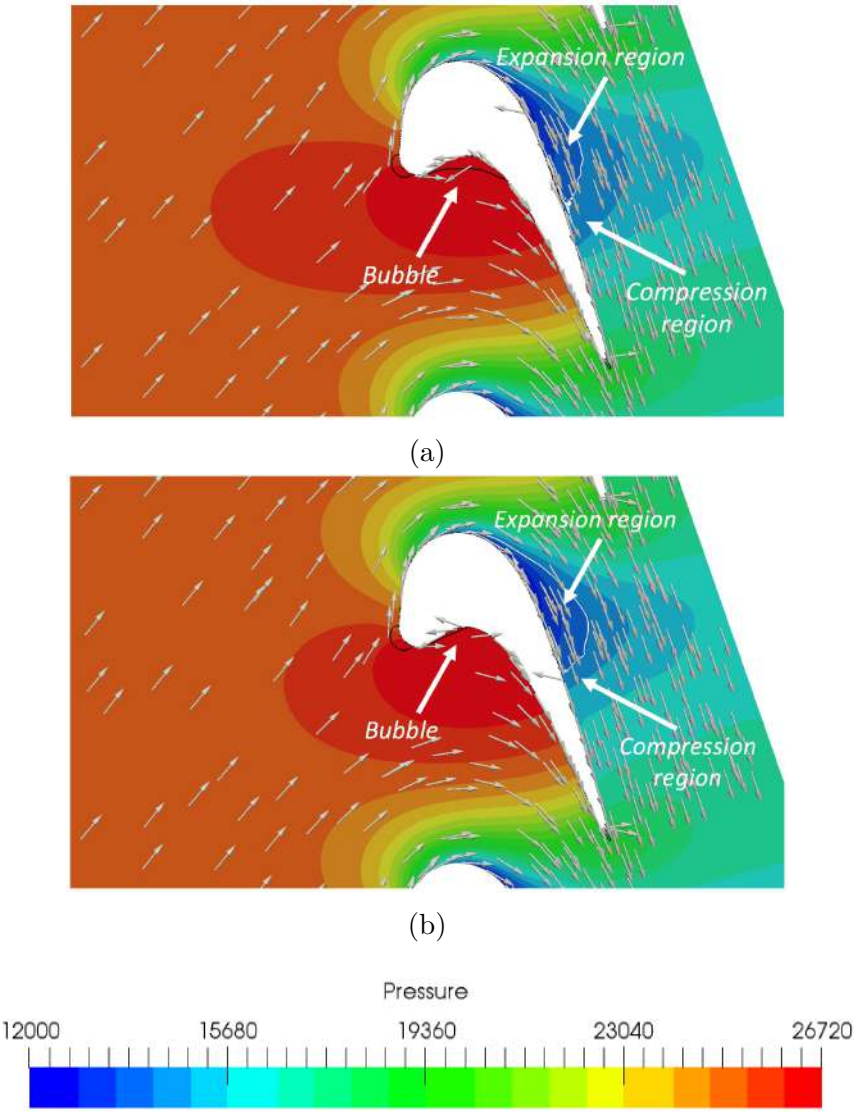

Figure 3.18 – Time-averaged pressure $\overline{P}$ $[Pa]$ map at mid-span. Black isocontour is null axial velocity $\overline{u} = 0$ and white isocontour is sonic line $\overline{Ma} = 1$. Velocity vectors are represented by arrows. Laminar inlet case at top (a) and turbulent inlet case at bottom (b).

To evaluate the impact of freestream turbulence on the static pressure distribution in the passage between both pressure and suction sides, time-averaged axial momentum profiles $\overline{\rho u}$ are extracted on different axial cuts in the passage along the blade as shown on Fig. 3.19. It is worth to recall that $\overline{\rho u}$ represents the spatial distribution of mass flux in the passage between the blades. Note that the current paragraph focuses on the passage between pressure and suction sides excluding the boundary layer regions. The boundary layer region will be specifically investigated later in this chapter. Axial cut positions are represented in Fig. 3.19 (a). Note that $y = 0$ corresponds to the suction side wall and $y = L$ to the pressure

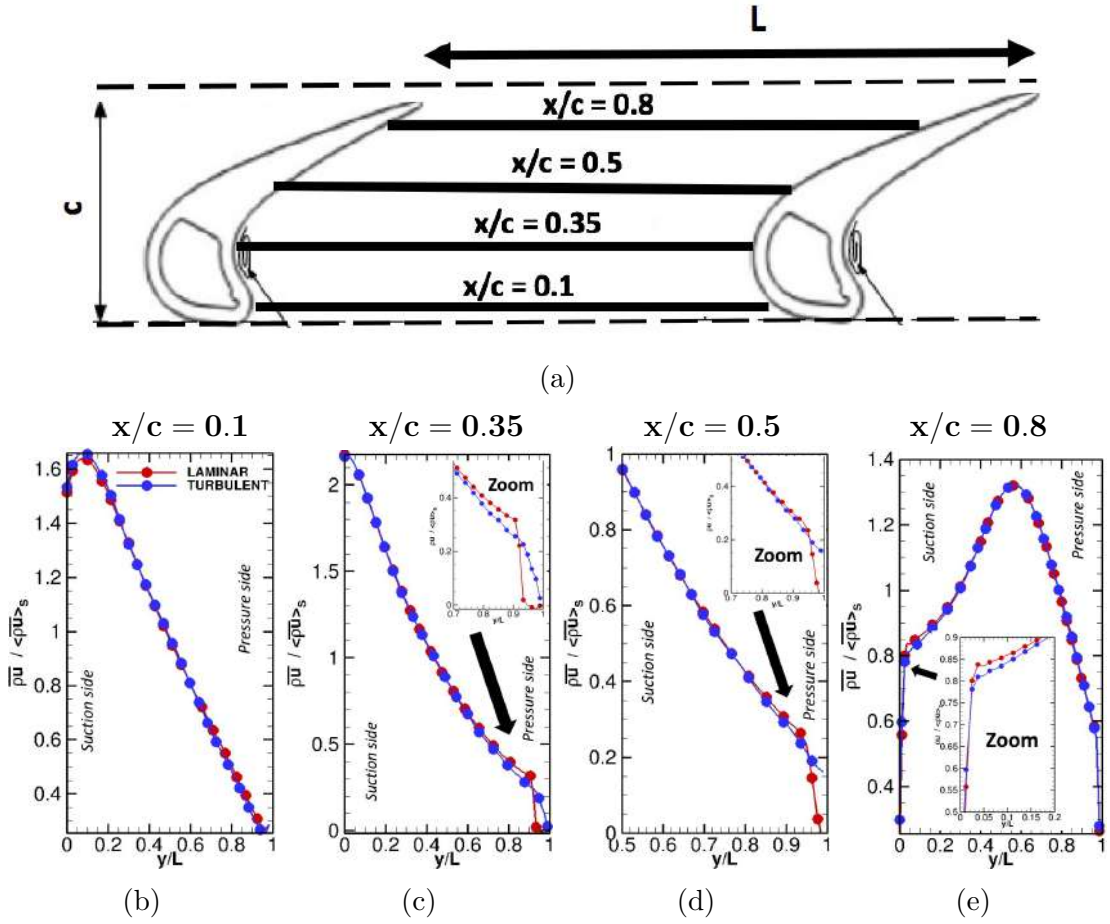

Figure 3.19 – Mass flow rate by surface unit normalized by the surface averaged mass flow $\overline{\rho u}/ < \overline{\rho u} >_S$ [-] along the passage at different axial position indicated on left (a). From left to right, $x/c = 0.1$ (b), $x/c = 0.35$ (c), $x/c = 0.5$ (d), $x/c = 0.8$ (e). $y = 0$ corresponds to the suction side wall and $y = L$ the pressure side wall. L is the distance between the blade walls. Red line represents the laminar inlet case and blue the turbulent inlet case.

side wall where L is the distance between the blades. Note that L remains constant along the axial coordinate for such a cascade configuration. Near the leading edge at $x/c = 0.10$, Fig. 3.19 (b), no deviations between both profiles are noticed. This confirms that same mean inflow impacts the blade between both cases. At $x/c = 0.35$, Fig. 3.19 (c), axial momentum is higher near the pressure side for the turbulent inlet case. Indeed, since the bubble is reduced in that case, more flow can passes near the pressure side of the blade. At $x/c = 0.5$ and $x/c = 0.8$, Fig. 3.19 (d) & (e), a deficit of axial momentum appears near the suction side in the turbulent inlet case in comparison with the laminar inlet case. Since the mass flow rate is ensured to be the same for both LES predictions, the additional mass flow rate observed on the pressure side necessary yields to a deficit of mass flow rate on the suction side to preserve the conservation of the integrated mass flow rate $\int_S \overline{\rho u} dS$ through the axial cuts. This redistribution of mass flux between

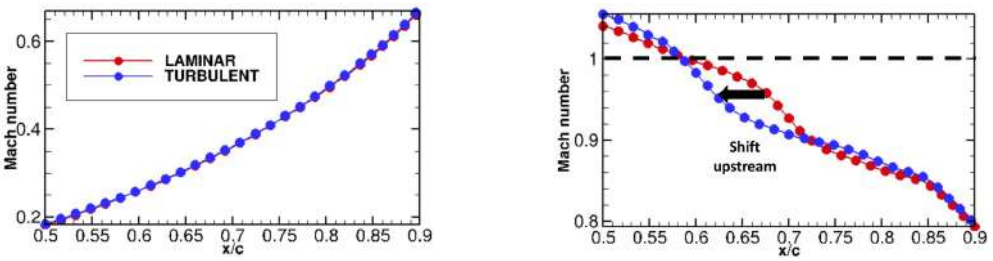

(a) (b)

Figure 3.20 – Mach number profiles $\overline{Ma}$ [-] along a streamline from $x/c = 0.5$ to $x/c = 0.9$ located at a wall normal distance of $0.2L$ on pressure side on left (a) and suction side on right (b). Red line represents the laminar inlet case and blue line the turbulent inlet case. Dashed line represents the sonic value.

the pressure and suction sides results in a different flow speed and expansion in the passage between both cases. To confirm, time-averaged Mach number $\overline{Ma}$ is extracted along a streamline from $x/c = 0.5$ to $x/c = 0.9$ located at a wall normal distance of $0.2L$ on both sides of the blade and shown on Fig. 3.20. On the pressure side, Fig. 3.20 (a), Mach number distribution does not differ. On the suction side, Fig. 3.20 (b), profiles deviate in the interval between $x/c = 0.6$ and $x/c = 0.7$ which corresponds to the compression region on the suction side. This compression region corresponds to the shocklet region and is observed to be shifted upstream in presence of freestream turbulence.

As a consequence of the previous discussions, freestream turbulence is found to affect the flow expansion around the blade. The wall normal and shear stresses are then expected to be also impacted and are hereafter investigated.

Skin friction and load distribution on the blade surface

In this paragraph, the impact of freestream turbulence is quantified on the normal and shear stresses on the blade surface. In the following, the wall shear stress is represented by the friction coefficient C_f by,

$$C_f = \frac{\tau_w}{0.5\rho_1 v_1^2} \tag{3.6}$$

where τ_w is the wall shear stress, ρ_1 and v_1 are respectively the density and inlet velocity. It is worth to recall that for separated flow, C_f is negative in the recirculation bubble. Separation (S) and reattachment (R) points of the bubble are defined for $C_f = 0$ and the distance between these two specific points represents the bubble size. C_f is extracted along on both sides of the blade for both cases and compared to experimental results in Fig. 3.21. The pressure side of the blade, Fig. 3.21 (a), is first described and discussed. From $x/c = 0.1$, C_f decreases and cancels at $x/c = 0.15$ for the laminar inlet case and $x/c = 0.14$ for the turbulent inlet case. This specific position corresponds to the separation of the boundary layer and the creation of the recirculation bubble. The reattachment point of the

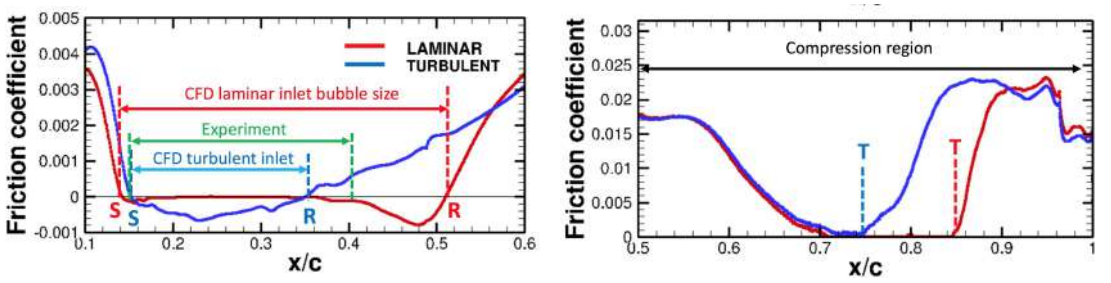

(a) (b)

Figure 3.21 – Friction coefficient C_f [-] evolution along the pressure side on left (a) between $x/c = 0.1$ and $x/c = 0.6$ as well as along the suction side on right (b) between $x/c = 0.5$ and $x/c = 1$. Laminar inlet case is represented by the red line and the turbulent inlet case by the blue line. The bubble size is indicated and compared with the experiment extracted from (Homeier et al., 2004). Separation point (S) and reattachment point (R) are indicated when $C_f = 0$ and turbulent transition position (T) is also indicated when the minimum value of C_f is reached on the suction side.

boundary layer is located at $x/c = 0.5$ for the laminar inlet case while it is located at $x/c = 0.35$ for the turbulent inlet case. In the bubble region and for the laminar inlet case, the absolute value of C_f is near 0. This indicates a region of very low velocity in the bubble (Gaster, 1967; Arena and Mueller, 1980; Lee et al., 2014). If compared the bubble size obtained from both LES to experimental data, the bubble is clearly too large in the laminar inlet case while the prediction is improved for the turbulent inlet case. A view of the axial evolution of C_f is presented on the suction side of the blade, in the compression region defined between $x/c = 0.5$ and $x/c = 1$, Fig. 3.21 (b). Due to the deceleration of the flow in this region, C_f decreases from $x/c = 0.5$ to $x/c = 0.75$ for both cases. From this latter position, both cases deviate. Indeed, for the laminar inlet case, C_f remains near 0 and then strongly increases at $x/c = 0.85$. Such an increase combined with observed turbulent structures on Fig. 3.16 confirm a transition to turbulence of the boundary layer (Schlichting, 1955). This transition occurs upstream in the turbulence inlet case at $x/c = 0.75$. Downstream the transition position, C_f decreases.

Normal stresses on the blade surface are represented by the pressure distribution on the blade surface. Pressure distribution is here given by the Isentropic Mach Number Ma_{is} computed with Eq. 3.3. Axial evolution of Ma_{is} is shown at mid-span of the blade and compared to the experimental results on Fig. 3.22. For the laminar inlet case and on the pressure side of the blade, the bubble region presents a plateau of Ma_{is} between $x/c = 0.15$ and $x/c = 0.5$ and differs from the experiment in agreement with previous findings (Gomes and Niehuis, 2013). For the turbulent inlet case, the prediction of the isentropic Mach number profile in the bubble is clearly improved and allows to recover the experimental results. On the suction side, the acceleration of the flow in the interval between $x/c = 0.$ and $x/c = 0.4$ is well captured in both cases. In the compression region, the sharp

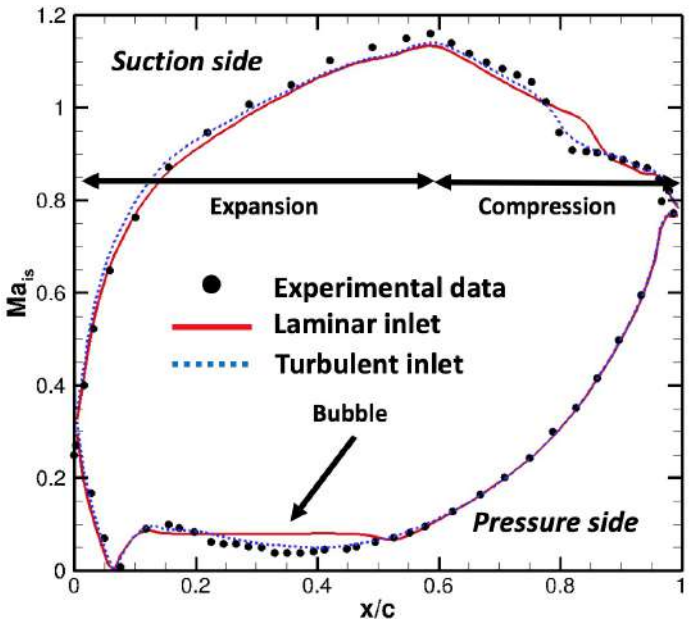

Figure 3.22 – Effect of the turbulence injection on the isentropic Mach number Ma_{is} [-] along the blade: •, experiment (Gomes and Niehuis, 2009); Red – LES laminar inlet case; Blue - - LES turbulent inlet case.

decrease of Ma_{is} corresponds to the shock region which is not well predicted in the laminar inlet case while the prediction is improved for the turbulent inlet case.

To sum up this section, freestream turbulence is found to affect the bubble size on the pressure side of the blade, which changes the mass flow distribution in the passage impacting also the suction side. At the end of the day, freestream turbulence allows to fully recover the load distribution for the T120 blade. To the author's knowledge, this is the first LES study able to recover the blade load distribution for this blade. Clearly, such results confirm the importance of the inflow turbulence specification for blades presenting recirculation bubbles. The impact of freestream turbulence on separated flows has been confirmed in experimental and numerical investigations (Burgmann and Schroder, 2008; ZAKI et al., 2010; Wheeler and al., 2016; Cadieux et al., 2014; Uzun and Malik, 2017). Since the near wall flow region was observed to be strongly changed by freestream turbulence, the following section focuses on boundary layer regions.

3.3.3 Investigation of the boundary layers

In this section, the impact of freestream turbulence on boundary layer properties is studied. To investigate the near wall flow region, boundary layers must be extracted from LES predictions. To do so, available methodologies to extract numerically this specific region are first introduced. Then, the validity of the boundary layer assumptions in the context of the T120 blade is discussed. Finally, boundary layer profiles and evolutions of integral properties are investigated.

Extraction of the boundary layer in turbomachinery The thickness of boundary layer hereafter noted δ is commonly defined when the tangential velocity component u_{tan} along the wall normal distance n reaches (Schlichting, 1955),

$$u_{tan}(n = \delta) = 0.99U_{\infty}, \tag{3.7}$$

where U_{∞} is the tangential freestream velocity located outside of the boundary layer. This definition suits well for flow on flat plates, where U_{∞} is easily defined. However, for turbomachinery applications, freestream velocity is affected by freestream pressure gradient and varies along the blade. To alleviate this issue, the definition of δ must be adapted. Alternative propositions exist and some of which are detailed afterwards.

One solution is to reconstruct the freestream velocity from the isentropic Mach number Ma_{is} and the local speed of sound c_{sound} assuming that there is no loss in the freestream flow region. Using this method, δ can be defined as the location where the tangential velocity satisfies,

$$u_{tan}(n = \delta) = 0.99Ma_{is} * c_{sound}. \tag{3.8}$$

However, this solution is limited to freestream laminar flow featuring no loss which is not satisfied in the context of synthetic turbulence injection.

A second solution is to use a functional f defined as $f = n^a \left|\frac{\partial u}{\partial n}\right|^b$ where a, and b are constants (W. Stock and Haase, 1999). This way, δ is built from the maximum of the functional f_{max} so that,

$$\delta = \epsilon f_{max}, \tag{3.9}$$

where ϵ is a threshold value. This method relies on the constants a and b chosen from correlations (not presented here) and is then highly dependent on the test case studied.

A last solution is to use the magnitude of vorticity $\|\omega\|$, here noted ω for simplicity, which is known to be high in the boundary layer region. In this case, δ is based on the minimum and maximum vorticity evolution along normal profiles to the wall, respectively noted ω_{min} and ω_{max}. Proposed by (Michelassi et al., 1998), the obtaining thickness satisfies,

$$\omega(n = \delta) = \omega_{min} + (\omega_{max} - \omega_{min}) * 0.01. \tag{3.10}$$

This definition suits well to our study and will be therefore used in the following.

The boundary layer investigation presented in this study requires that the near wall flow region complies with the boundary layer hypothesis (Schlichting, 1955). In the following, the validity of such hypotheses is checked for the T120 blade.

Validations of the boundary layer hypothesis The boundary layer assumptions are recalled here (Schlichting, 1955):

- The thickness of the boundary layer δ is negligible compared to the characteristic length of the wall L, i.e, $\frac{\delta}{L} << 1$.
- The curvature radius R_c is assumed large against the characteristic length of the wall L,i.e, $\frac{R_c}{L} >> 1$.

The validity of such hypotheses in the context of the T120 uncooled blade is discussed. Indeed, the first hypothesis is generally verified if the Reynolds number is sufficiently high (Schlichting, 1955). The latter hypothesis which involves curvature needs to be here discussed. Indeed, if curvature can not be neglected, the centrifugal force leads to a normal pressure gradient to the wall in the boundary layer. This effect is generally omitted in the boundary layer model equations. The effect of curvature on boundary layer equations was first studied by (Murphy, 1953) in the particular case of incompressible flow. With a dimensional analysis, (Murphy, 1953) showed that the effect of curvature can be estimated from the local ratio $\frac{\delta}{R_c}$. If $\frac{\delta}{R_c} << 1$, the curvature is not "viewed" by the boundary layer and the curvature effect in the boundary layer equations can be neglected. For the T120 case, axial evolutions of $\frac{\delta}{R_c}$ and $\frac{\delta}{c}$ are plotted along the blade for both pressure and suction side on Fig. 3.23 for the laminar inlet case. Note that oscillations observed on both sides between $x/c = 0.8$ and $x/c = 1.0$ originate from small defaults in the CAD of the blade. If taking the characteristic length of the wall L as its axial chord length, i.e, $L = c$, the thickness of the boundary layer on both sides remains two order of magnitudes below c. This confirms the first hypothesis of the boundary layer approximations, i.e, $\frac{\delta}{L} << 1$. Regarding the second hypothesis, the boundary layer thickness on the suction side remains one order of magnitude below the local radius curvature away from the bubble

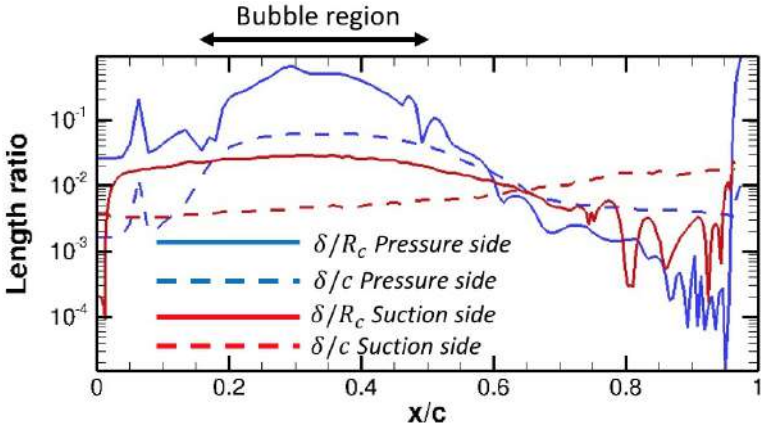

Figure 3.23 – Evolution of the local ratio $\frac{\delta}{R_c}$ [-] and $\frac{\delta}{c}$ [-] for the pressure and suction sides of the T120 blade for the laminar inlet case. Solid lines represent $\frac{\delta}{R_c}$ and dashed lines $\frac{\delta}{c}$. Blue represents the pressure side and red represents the suction side.

region. Indeed, in the bubble region, i.e, in the interval between $x/c = 0.15$ and $x/c = 0.5$, the thickness approaches the curvature radius of the blade. In this specific region, the effect of the curvature should then be considered for boundary layer investigation. As a result, the boundary layer profiles can be gauged against boundary layer model equations on both sides of the blade. Note nevertheless that the bubble region will be excluded from the boundary layer investigation.

Flow boundary layer evolutions The axial evolution of boundary layer thickness δ relying on Eq. (3.10) and associated freestream velocity U_∞ for both LES are plotted on Fig. 3.24. On the pressure side of the blade, Fig. 3.24 (a), δ smoothly increases from the stagnation point located at $x/c = 0.05$ to $x/c = 0.15$. From $x/c = 0.15$, δ suddenly grows which corresponds to the separation of the boundary layer and creation of the bubble. In the bubble region, the maximum of δ is higher in the laminar inlet case because the bubble is larger in comparison with the turbulent inlet case. The boundary layer then reattaches at different positions depending on the cases. Downstream at $x/c = 0.7$, δ remains constant due to the flow acceleration which stretches the boundary layer as confirmed in the experiment (Gomes and Niehuis, 2009). Freestream velocity U_∞, Fig. 3.24 (c), also smoothly increases from the stagnation point located at $x/c = 0.05$ to the boundary layer separation point located at $x/c = 0.15$. In the bubble region, U_∞ remains constant for the laminar inlet case while it decreases in the turbulent inlet case.

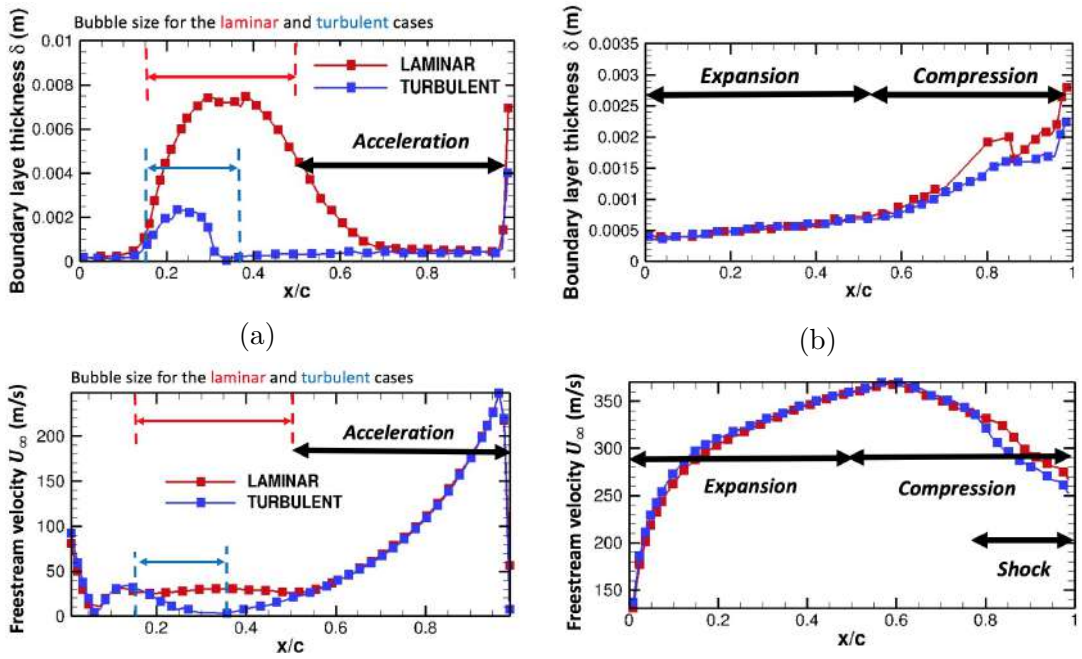

Figure 3.24 – Boundary layer thickness δ $[m]$ at top (a) & (b) and freestream velocity U_∞ $[m/s]$ at bottom (c) & (d) evolutions along the blade. Pressure side on left (a) & (c) and suction side on right (b) & (d). Red line represents the laminar inlet case and blue line turbulent inlet case.

Indeed and since the bubble is large for the laminar inlet case, the flow dynamic in the bubble is low which weakly impacts U_∞. Downstream the bubble, both cases converge towards same levels of freestream velocity. On the suction side, Fig. 3.24 (b), δ grows slowly from the leading edge to $x/c = 0.6$. At this location, δ increases more rapidly due to the compression induced by the adverse pressure gradient region in both cases. The freestream velocity, Fig. 3.24 (d), strongly accelerates from the leading edge to $x/c = 0.55$ due to the strong flow expansion on the suction side. From $x/c = 0.60$, U_∞ suddenly decreases corresponding to the compression and shock regions. To go further in the analysis, normal profiles to the wall of tangential velocity u_{tan} in the boundary layer are extracted at different axial positions on both sides and represented on Fig. 3.25: i.e, near the separation point at $x/c = 0.1$, in the bubble at $x/c = 0.3$, at $x/c = 0.7$ and near the trailing edge at $x/c = 0.9$. Time-averaged velocity normal profiles in the boundary layer are plotted on Fig. 3.26 and compared to analytical Blasius and turbulent power law profiles (Schlichting and Gersten, 2000). The turbulent power law profile corresponds to an empirical profile for the mean flow assuming no pressure gradient and expressed as $\frac{u_{tan}}{U_\infty} = \left(\frac{n}{\delta}\right)^{\frac{1}{7}}$. The effect of the pressure gradient on boundary layer profiles can then be deduced from the deviations between LES and analytical profiles. For each extracted boundary layer profiles, only the most suitable analytical profile is plotted, i.e: Blasius profile for laminar boundary layer and turbulent profile for turbulent boundary layer. It is worth to note that 11 points of the mesh are located in the boundary layer thickness on the pressure side, i.e, from $n/\delta = 0$ to $n/\delta = 1$. On the suction side, normal profiles are discretized with between 10 to 20 points depending on the axial position. First, the boundary layer profiles are described along the suction side, i.e, Fig. 3.26 (a)&(b)&(c)&(d). At $x/c = 0.1$, Fig. 3.26 (a), the profile is laminar and the deviation with the Blasius profile evidences a favourable pressure gradient due to the flow expansion in this region. No deviation is observed between both cases. At $x/c = 0.3$, Fig. 3.26 (b), no deviations is also found. At $x/c = 0.7$, Fig. 3.26 (c), profiles exhibit an inflexion point which highlights an adverse pressure gradient in this region. No strong deviation

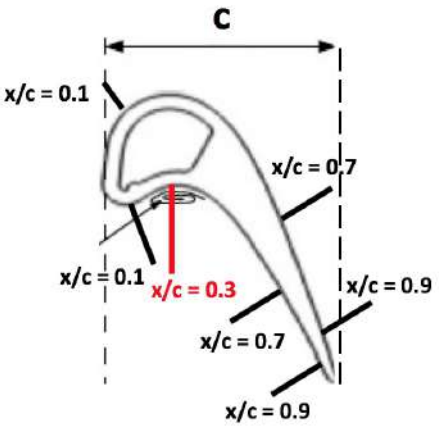

Figure 3.25 – Positions of the investigated boundary layer normal profiles. Bubble position is indicated in red.

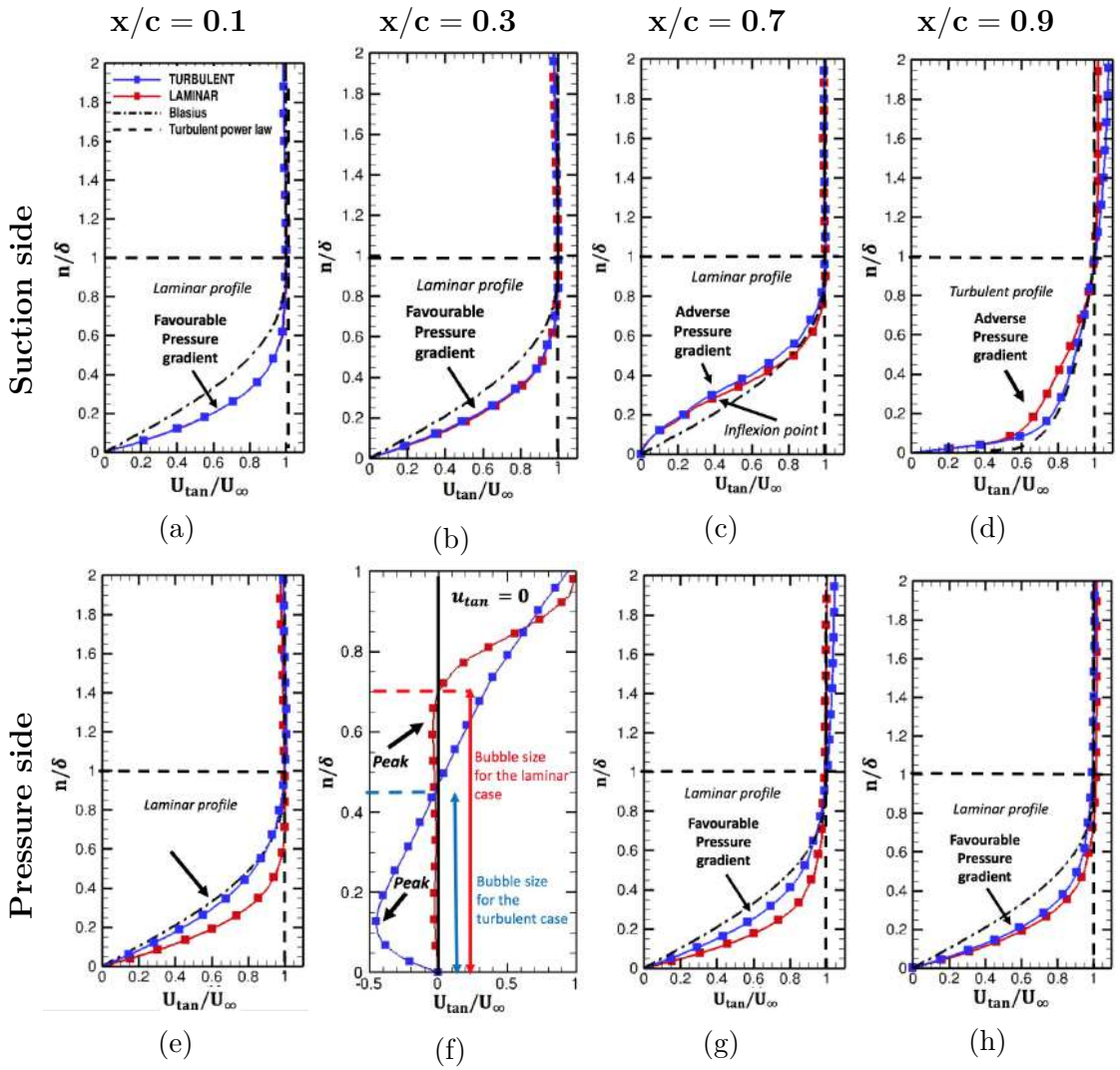

Figure 3.26 – Boundary layer normal mean velocity profiles. From left to right, $x/c = 0.1$, $x/c = 0.3$, $x/c = 0.7$, $x/c = 0.9$. Top, suction side and bottom, pressure side. n/δ [-] is the normalized wall distance and u_{tan}/U_∞ [-] the normalized tangential velocity. Red line represents the laminar inlet case and blue the turbulent inlet case. Black dot dashed line represents a Blasius profile without pressure gradient and dashed line the turbulent power law profile $\frac{u_{tan}}{U_\infty} = \left(\frac{n}{\delta}\right)^{\frac{1}{7}}$.

is also noticed between both cases. At $x/c = 0.9$, Fig. 3.26 (d), both profiles are clearly turbulent since this station is located downstream the turbulent transition. For this station, the profile in the laminar inlet case deviates from the analytical profile which indicates a streamwise pressure gradient in the boundary layer. The turbulent inlet case profile is found to recover the analytical turbulent profile. As a result, freestream turbulence is found to decrease the adverse pressure gradient for this axial position. Afterwards, the boundary layer profiles are described along the pressure side of the blade, i.e, Fig. 3.26 (e)&(f)&(g)&(h). At $x/c = 0.1$, Fig. 3.26 (e), profiles are laminar for both cases. Contrary to the laminar inlet case, the

turbulent inlet profile recovers the Blasius profile. This shows that the favourable pressure gradient at this station is then reduced by the freestream turbulence. At $x/c = 0.3$, Fig. 3.26 (f), no comparison with analytical boundary layer profiles can be done because the boundary layer hypotheses do not hold in the bubble. For this station, the profiles differs between the cases. The deviations here noticed are due to the difference of U_∞ between the cases. Indeed, since U_∞ was found to be much smaller in the turbulent inlet case (Fig. 3.24 (c)), profiles of normalized velocity $\frac{u_{tan}}{U_\infty}$ are also expected to strongly differ between the two cases. Despite this scaling difference, the profile in the bubble is found to be greatly impacted by freestream turbulence as confirmed in numerical studies (Lee et al., 2014; Cadieux et al., 2014; Zilli et al., 2017). Looking more in details these profiles, negative peaks are observed at $n/\delta = 0.14$ in the laminar inlet case while it is located further in the bubble at $n/\delta = 0.60$ in the turbulent inlet case. These peaks result from the development of an "intern boundary layer" which originates from the reattachment point by the reversed flow in the bubble. Since the bubble was shown to be larger in the laminar inlet case, this "intern boundary layer" in the bubble develops and extents more in the bubble region than for the turbulent inlet case. At $x/c = 0.7$, Fig. 3.26 (g), profiles remain laminar and admit a favourable pressure gradient due to the flow acceleration in this region. The deviations between both cases shows again that the pressure gradient is reduced in the turbulent inlet case. At $x/c = 0.9$, Fig. 3.26 (h), the profiles remain laminar and present a favourable pressure gradient. Finally, no strong deviation is here observed between both cases.

As a consequence of the previous discussion, freestream turbulence is found to impact boundary layer profiles and to decrease the effect of pressure gradients in this region. Such impacts of freestream turbulence are consistent with the theory of laminar and turbulent boundary layer (Schlichting and Gersten, 2000). From the boundary layer profiles, one can build the integral properties of the boundary layers which are hereafter described.

Boundary layer integral properties investigation From the boundary layer profiles, the displacement and momentum thickness noted respectively, δ^* and θ, can be built and are defined for compressible boundary layer (Schlichting, 1955) by the following expressions:

$$\delta^* = \int_0^\delta \left(1 - \frac{\rho u_{tan}}{\rho_\infty U_\infty}\right) dn, \tag{3.11}$$

$$\theta = \int_0^\delta \left(1 - \frac{u_{tan}}{U_\infty}\right) \frac{\rho u_{tan}}{\rho_\infty U_\infty} dn, \tag{3.12}$$

where u_{tan} is the local tangential velocity, n the wall normal distance and the subscript ∞ refers to freestream condition. It is important to note that the superior integration bound is limited to δ and does not tend to infinity to exclude the freestream region and potential flow effects on the computation of integral properties. $\rho_\infty U_\infty \delta^*$ and $\rho_\infty U_\infty^2 \theta$ respectively gives the deficit of mass and momentum fluxes for a span unit due to the presence of the boundary layer. From

these integral values, the shape factor H is built so that,

$$H = \frac{\delta^*}{\theta}. \tag{3.13}$$

The value of H gives an indication about the state of the boundary layer when no pressure gradient is present: i.e, the boundary layer is laminar around 2 - 2.5 and turbulent around 1.5 (Schlichting, 1955).

The displacement and momemtum thickness's are plotted on both sides and for both LES cases on Fig. 3.27. Note that values in the bubble region are not shown in both cases. On the pressure side of the blade, Fig. 3.27 (a), δ^* rapidly grows near the separation point and the creation of the recirculation bubble located at $x/c = 0.15$. Downstream the bubble region, δ^* decreases for the laminar inlet case while it remains constant for the turbulent inlet case and both converge to the same local values at $x/c = 0.6$. From this location, δ^* remains constant due to the flow acceleration which stretches the boundary layer. Regarding the momemtum thickness on the pressure side, Fig. 3.27 (c), the shape of profiles are very similar

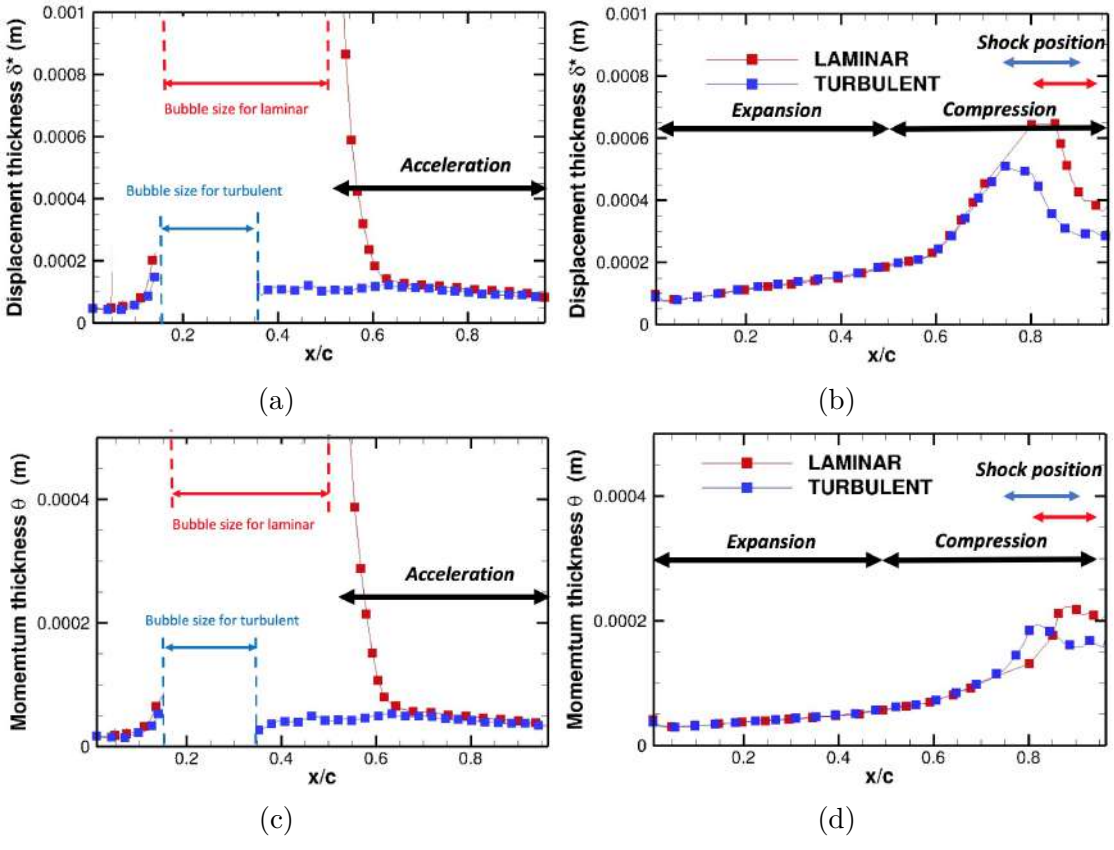

Figure 3.27 – Displacement thickness δ^* $[m]$ at top (a) & (b) and momemtum thickness θ $[m]$ at bottom (c) & (d) evolutions along the blade. Pressure side on left (a) & (c) and suction side on right (b) & (d). Bubble size is indicated for both LES and no values are shown in the bubble region. Red line represents the laminar inlet case while blue line corresponds to the turbulent inlet case.

to displacement thickness, Fig. 3.27 (a). On the suction side, Fig. 3.27 (b), δ^* increases from the leading edge to $x/c = 0.6$. At this location, δ^* increases more rapidly from $x/c = 0.60$ to $x/c = 0.75$ due to the adverse pressure gradient present in this region. Downstream the shock positions, δ^* decreases to the trailing edge in both cases. Same conclusions hold for the evolution of the momemtum thickness on the suction side, Fig. 3.27 (d). Shape factor axial evolutions for both LES cases are plotted on Fig. 3.28 . On the pressure side, Fig. 3.28 (a), H strongly increases from 2.5 to 3 upstream the bubble region in both cases. Such values of H indicate a strong effect of the adverse pressure gradient which can potentially cause a separation of the boundary layer (Schlichting, 1955; Greitzer., 2004). Downstream the bubble and for the laminar inlet case, H decreases to 1.5 at $x/c = 0.6$ corresponding to the turbulent transition of the boundary layer. Downstream this location, H increases and remains around 2.5. This means that the boundary layer relaminarizes due to the strong acceleration of the flow as pointed in the experiment (Gomes and Niehuis, 2009). This confirms the presence of laminar boundary layer profiles downstream the bubble as previously depicted on Fig. 3.26. For the turbulent inlet case, H remains around 2.5 downstream the bubble. This means that the boundary layer on the pressure side remains laminar along the blade. Indeed, the bubble is supposed to be too short to exhibit a turbulent transition in this case. Downstream the bubble region, H is clearly lower for the turbulent inlet case to $x/c = 0.6$. As a result, freestream turbulence tends to reduce the shape factor in this region. A smaller shape factor results into a reduction of the adverse pressure gradient and favors the resistance of the boundary layer to separation (Schlichting, 1955; Greitzer., 2004). Such effects of freestream turbulence on H have been observed in numerical investigations (Wheeler and al., 2016; Segui Troth, 2017; ZAKI et al., 2010; Uzun and Malik, 2017). On the suction side, Fig. 3.28 (b), H increases from the leading edge to $x/c = 0.6$. At this location, H increases more rapidly due to the adverse pressure gradient in the compression region to $x/c = 0.8$. Downstream the shock position, H decreases to 1.5 which is consistent with typical values found for turbulent boundary layers. In

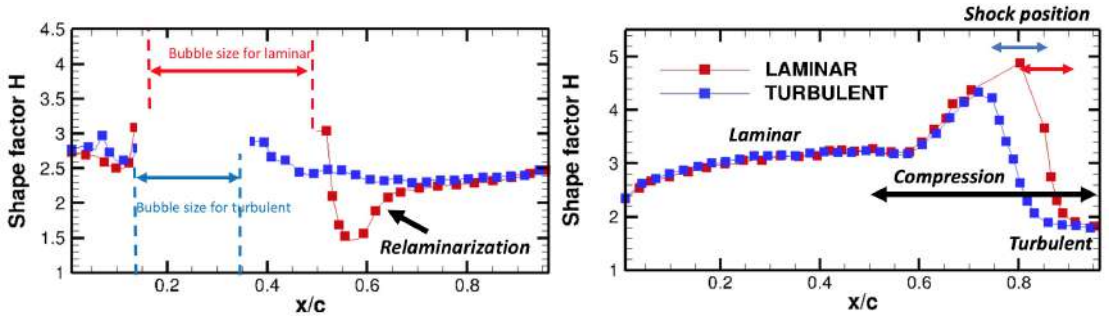

(a) (b)

Figure 3.28 – Shape factor H [-] evolution along the boundary layers. Pressure side on left (a) and suction side on right (b). Bubble size is indicated for both LES and no value is shown in the bubble region. Red line represents the laminar inlet case while blue ones corresponds to the turbulent inlet case.

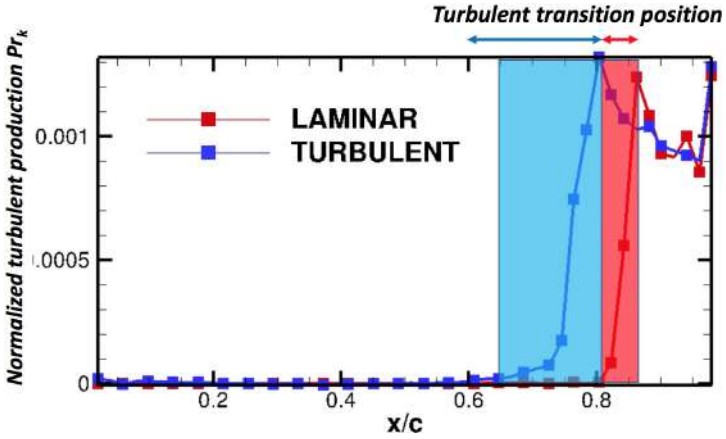

Figure 3.29 – Normalized integrated turbulent kinetic energy production Pr_k [-] (Eq. (3.14)) for the suction side boundary layer. Red line represents the laminar inlet case and blue the turbulent inlet case.

the turbulent inlet case, the decrease of H is shifted upstream in comparison with the laminar inlet case. This confirms that the transition to turbulence is shifted upstream with the presence of freestream turbulence. To confirm this finding, the integrated normalized production term of turbulent kinetic energy Pr_k in the boundary layer can be evaluated through (Wheeler et al., 2017),

$$Pr_k = \frac{1}{U_{\infty}{}^3} \int_0^{\delta} P_k dn, \tag{3.14}$$

where $P_k = -\overline{u_i' u_j'} \frac{\partial \overline{U_i}}{\partial x_j}$ is the turbulence production term, $\overline{u_i' u_j'}$ is the velocity correlation tensor and $\overline{U_i}$ is the time-averaged velocity. Pr_k is plotted on the suction side of the blade for both cases in Fig. 3.29. The turbulent kinetic energy production remains low for $x/c < 0.60$ in both cases. From this location, Pr_k strongly increases up to a peak. For the laminar inlet case, the peak is located at $x/c = 0.86$ while is located at $x/c = 0.80$ for the turbulent inlet case. This peak corresponds to the transition to turbulence. Downstream, the decrease of the turbulent production corresponds to the non-equilibrium region of the turbulent transition (Bradshaw, 1967; Wheeler et al., 2017).

The axial evolution of integral values in a general case is given by a momemtum balance in the boundary layer using the boundary layer assumptions for steady compressible flow is given by the following expression (Schlichting, 1955) ,

$$\frac{d\theta}{dx} + \left(H + 2 - M_{\infty}^2\right) \frac{\theta}{U_{\infty}} \frac{dU_{\infty}}{dx} = \frac{C_f}{2}. \tag{3.15}$$

where M_{∞} is the freestream Mach number and C_f is the friction coefficient. The first term of the LHS represents the momemtum thickness spatial rate, the second term is the normalized pressure gradient term while the RHS represents the skin friction at wall. To quantify the impact of freestream turbulence on the pressure gradient in the boundary layer, the axial evolution of the second term on

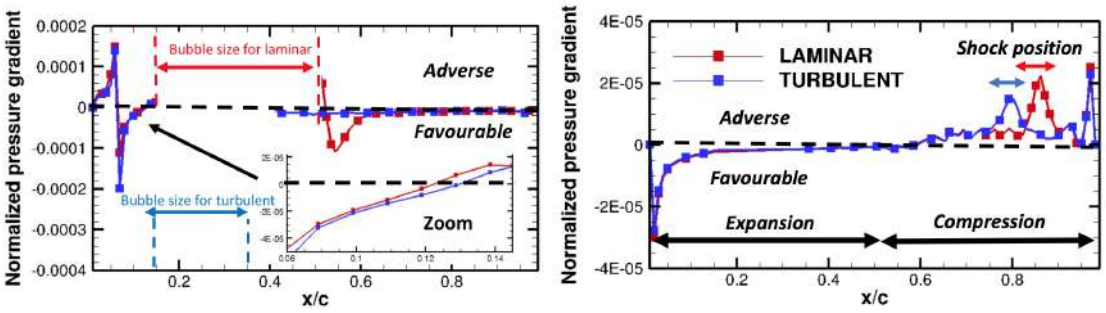

(a) (b)

Figure 3.30 – Normalized pressure gradient term $(H + 2 - M_\infty^2)\,\frac{\theta}{U_\infty}\frac{dU_\infty}{dx}$ [-] along the boundary layer blade. Pressure side on left (a) and suction side on right (b). A zoom is shown upstream the separation point indicated by the arrow. Red line represents the laminar inlet case and blue the turbulent inlet case. Favourable and adverse pressure gradients zone are indicated.

the LHS of Eq. (3.15), i.e,$(H + 2 - M_\infty^2)\,\frac{\theta}{U_\infty}\frac{dU_\infty}{dx}$, is plotted on both sides for both LES cases on Fig. 3.30. By definition, a favourable pressure gradient corresponds to negative values while an adverse pressure gradient yields positive values. If zooming upstream the bubble region on the pressure side, Fig. 3.30 (a), the normalized pressure gradient is shown to be adversed to the flow. This confirms the presence of the separation of the boundary layer at this region. When comparing both predictions, the adverse pressure gradient is reduced in the turbulent inlet case. This confirms that the boundary layer is more resistant to separation with freestream turbulence. Downstream the bubble, the normalized pressure gradient remains smaller with the presence of freestream turbulence and helps the flow to reattach to the wall. On the suction side, Fig. 3.30 (b), a favourable normalized pressure gradient is observed in the expansion region. Downstream, the normalized pressure gradient becomes adverse in the compression region for both cases. The normalized pressure gradient term is stronger in the shock regions and reduced in the turbulent inlet case.

Finally, the evolution of kinetic energy thickness θ^* along the blade is investigated and is expressed for a steady compressible flow by (Schlichting, 1955),

$$\theta^* = \int_0^\delta \left(1 - \frac{u_{tan}^2}{U_\infty^2}\right) \frac{\rho u_{tan}}{\rho_\infty U_\infty} dn. \tag{3.16}$$

θ^* gives the deficit of kinetic energy induced by the presence of the boundary layer. The axial evolution of θ^* along the blade is plotted for both cases on Fig. 3.31. On the pressure side of the blade, Fig. 3.31 (a), θ^* increases from the stagnation point located at $x/c = 0.05$ to the bubble region located at $x/c = 0.15$ for both cases. Downstream the bubble region, both cases converge towards similar values at $x/c = 0.6$. On the suction side, Fig. 3.31 (b), θ^* smoothly increases from the leading edge to $x/c = 0.6$. From this location, θ^* increases more rapidly corresponding to the turbulent transition region for each case. As a result, more

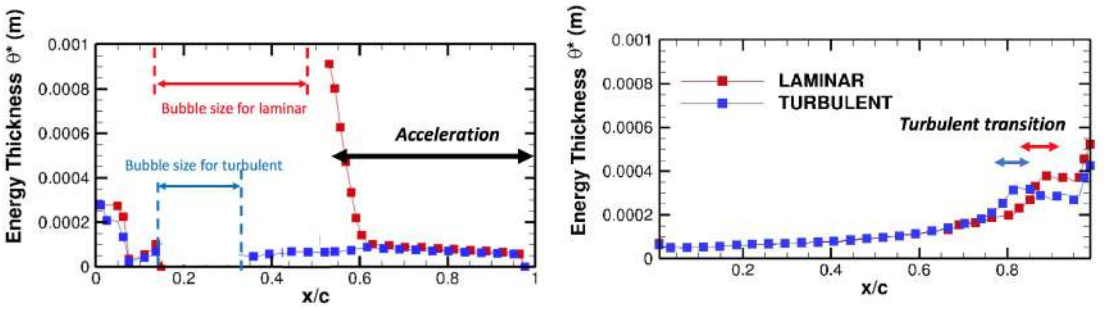

(a) (b)

Figure 3.31 – Energy thickness evolution θ^* $[m]$ along the blade on the pressure side on left (a) and suction side on right (b). Red line represents the laminar inlet case and blue line is the turbulent inlet case.

kinetic energy is lost in the turbulent transition of the boundary layer. Using the boundary layer assumptions and performing a kinetic energy balance in the boundary layer, the axial evolution of θ^* for a steady compressible flow is given by the following expression (Schlichting, 1955; Greitzer., 2004),

$$\frac{d\theta^*}{dx} + \left(3 - M_\infty^2\right) \frac{\theta^*}{U_\infty} \frac{dU_\infty}{dx} = \frac{(s^*T)_{BL}}{\rho_\infty U_\infty^3}. \tag{3.17}$$

The first term on the LHS gives the spatial rate of θ^*, the second term represents the work of the pressure gradient while the RHS represents the integrated loss production $(s^*T)_{BL}$ in the boundary layer. The axial evolution of θ^* then results from the work of pressure gradient and entropy production in the boundary layer. This confirms that losses are generated in the boundary layers and that loss generation is strongly impacted by separations and by boundary layer turbulent transitions as shown on Fig. 3.31. The investigation of losses in boundary layers will be later addressed in this work.

To conclude the boundary layer investigation, freestream turbulence is found to reduce the adverse pressure gradient on both sides of the blade and enforced the resistance of the boundary layer to separation. This investigation corroborates that freestream turbulence strongly affects the near wall flow region of the blade which clearly improves the flow prediction if compared to experiment. As a result, turbulent inlet specification is a crucial parameter to recover the load for blades presenting separated flows with wall resolved LES. Note that detailed analysis of the T120 blade sensitivity flow response to operating point uncertainties was studied in a conference paper of Turbo Expo in 2017 which can be found in Appendix D. In the next section of the study, the loss generation issued from the aerodynamics of the T120 blade is investigated. From the comparison of both LES cases, the impact of freestream turbulence on loss generation will be also addressed.

3.3.4 Investigation of losses

The mechanisms by which losses are produced for the T120 uncooled blade are investigated in this section. To do so, the losses are first evaluated using total variable balance equations introduced in Chapter 2. Losses are then analysed using the Second Law Analysis to identify the source of the loss generation process. Advanced decompositions of the loss maps are introduced to link the loss maps to flow physics. A particular attention will be finally paid to boundary layer regions and to the impact of the turbulent transition on losses.

Assessment of the loss distribution using total quantities

The losses are first evaluated using balance of total energy, total pressure and entropy. To perform such a balance, the notion of control volume must be first off all defined. In this section, the control volume is bounded by an axial section S_1 located at $x/c = 1$ upstream the leading edge and a moving axial section $S_x(x)$ associated to the normal n_i as represented on Fig. 3.32. To retrieve an axial dependency, $S_x(x)$ will move from S_1 to 1.3 axial chords downstream the trailing edge. Total energy balance equation is first applied to the control volume. In Chapter 2, total energy balance equation is shown to be reduced to the total temperature balance assuming $C_p = cst$ and reads as,

$$\underbrace{Q_m C_p \left(\widetilde{T}_{t,S_x} - \widetilde{T}_{t,S_1}\right)}_{\text{Total temperature balance}} = \underbrace{\iint_{S_x} \overline{U_i \tau_{ij}} n_j dS}_{\text{Viscous flux}} - \underbrace{\iint_{S_x} \overline{q_j} n_j dS}_{\text{Heat flux}}, \tag{3.18}$$

where $\iint_{S_x} \overline{U_i \tau_{ij}} n_j dS$ is the viscous flux, $\iint_{S_x} \overline{q_j} n_j dS$ the heat flux though S_x, Q_m the mass flow rate and $\widetilde{\bullet}_S$ is the mass flow average operator. The LHS represents the 1D variation of total energy. The first term in the RHS represents the viscous flux induced by shear forces on S_x. The second term represents the heat flux on S_x induced by temperature gradients if assuming a Fourier law. Note that fluxes

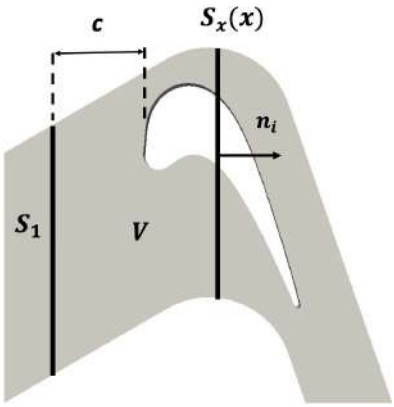

Figure 3.32 – Control volume bounded by an axial section S_1 located at $x/c = 1$ upstream the leading edge and a second axial section S_x defined by the normal n_i.

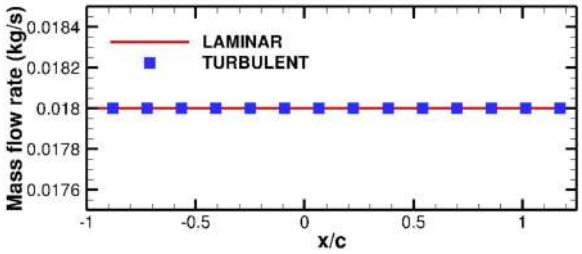

Figure 3.33 – Axial evolution of mass flow rate $Q_m(x)$ along the blade. Red line represents the laminar inlet case and blue squares the turbulent inlet case.

at the periodic boundaries conditions necessary cancel and are omitted in the balance. Since such a balance is only applicable to a statistically converged flow, the convergence of the mean field needs first to be checked. To do so, axial evolution of mass flow rate $Q_m(x)$ is plotted on Fig. 3.33 for both cases. The value of the mass flow rate keeps unchanged along the blade for both cases which recovers the mass flux conservation for a statistically converged flow. As a result, potential variations in total temperature will necessarily result from the flow dynamics. To study the balance, axial evolution of the total temperature term $(Q_m C_p \left(\widetilde{T}_{t,S_x} - \widetilde{T}_{t,S_1}\right))$ is plotted on Fig. 3.34 for both cases. For the laminar inlet case, the total temperature remains constant along the computational domain, except near the trailing edge located at $x/c = 1$. At this point, the total temperature slightly decreases. This weak variation remains negligible and is probably due to numerical errors generated at the trailing edge of the blade, where a strong velocity gradient is expected. For the turbulent inlet case, the evolution is clearly different. From $x/c = -1$ to $x/c = 0$, the total temperature increases. This interval corresponds to the dissipation of the turbulent structures injected at the inlet. Freestream turbulence generates gradients of velocity and temperature on section S_1 which activates the viscous fluxes corresponding to the LHS of Eq. (3.18). Between the

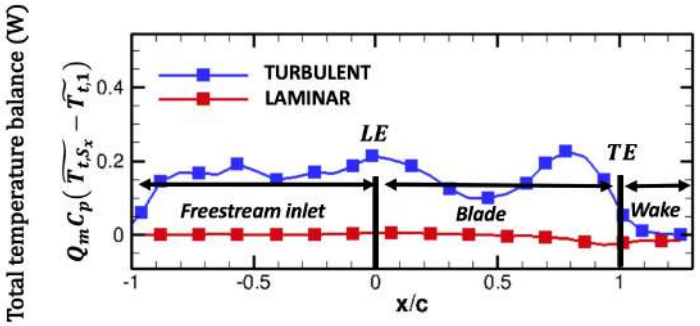

Figure 3.34 – Balance of total temperature between the axial section S_1 located $x/c = 1$ upstream the leading edge and $S_x(x)$. The origin of the normalized axial distance is set at the leading edge, i.e, $x/c = 0$. Red line with square represents the laminar inlet case while blue line with square represents the turbulent inlet case. Leading edge (LE) and trailing edge (TE).

leading and trailing edges, i.e from $x/c = 0$ to $x/c = 1$, the total temperature changes. This variation shows that freestream turbulence affects the viscous and heat fluxes along the blade. As a result, the 1D evolution of total temperature is not necessary constant in presence of freestream turbulence. However, this effect is generally neglected and omits in the literature. Indeed, the maximum of total temperature variation in the turbulent inlet case is located at $x/c = 0.8$ and is limited at $0.01K$. Finally and in the wake, the total temperature decreases and the associated variation tends to zero since the flow tends to be uniform downstream the blade. Indeed in this region, viscous effects tend to dissipate the velocity and temperature gradients which decreases the viscous fluxes in Eq. (3.18). Downstream the blade, the total temperature balance then closes which recovers 1D thermodynamic analysis for adiabatic static blades (Greitzer., 2004).

The losses are hereafter evaluated using entropy balance equation assuming $C_p = cst$ by combining Eq. (2.40) with Eq. (2.43), giving the following relation:

$$\underbrace{Q_m C_p(\widetilde{Ln(T_t)}_{S_x} - \widetilde{Ln(T_t)}_{S_1})}_{Q_m C_p \Delta\widetilde{Ln(T_t)}} \underbrace{-Q_m r(\widetilde{Ln(P_t)}_{S_x} - \widetilde{Ln(P_t)}_{S_1})}_{-Q_m r \Delta\widetilde{Ln(P_t)}} = \underbrace{\int_{V(x)} \frac{\overline{P_m + P_q}}{T} dV}_{\text{integrated losses}} . \tag{3.19}$$

The LHS represents the entropy balance between S_1 and S_x and is split into a total temperature contribution and total pressure contribution, hereafter respectively noted, $Q_m C_p \Delta\widetilde{Ln(T_t)}$ and $-Q_m r \Delta\widetilde{Ln(P_t)}$. The RHS represents the integrated source term of entropy in the control volume expressing from the loss maps P_m and P_q. Note again that fluxes at the periodic boundaries conditions and on the walls necessary cancel and are omitted in the balance. The total quantity contributions in the entropy balance, i.e, $Q_m C_p \Delta\widetilde{Ln(T_t)}$ and $-Q_m r \Delta\widetilde{Ln(P_t)}$ are plotted on Fig. 3.35 along the blade for both cases. The different contributions

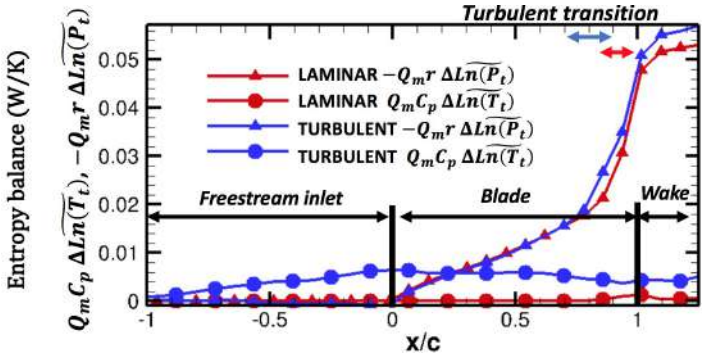

Figure 3.35 – Total temperature and pressure balances in the control volume defined between the axial section S_1 located $x/c = 1$ downstream the leading edge and $S_x(x)$. Red line represents the laminar inlet case and blue the turbulent inlet case. Lines with triangles show the total temperature term while lines with circles show the total pressure term. Leading edge (LE) and trailing edge (TE).

are first described in the freestream region, i.e, between $x/c = -1$ and $x/c = 0$. In this interval and for the laminar inlet case, both total temperature and pressure contributions cancel. For the turbulent inlet case, both total temperature and pressure vary due to the dissipation of freestream turbulence injected at the inlet as previously observed in Fig. 3.34. In the interval between $x/c = 0$ to $x/c = 1$ and for the laminar inlet case, the total temperature variation remains near zero. In the turbulent inlet case, the total temperature remains almost constant while total pressure variation increases in the blade region. Indeed, total pressure loss in the blade region is induced by losses generated in boundary layers (Denton, 1993). A change of slope for the profiles is noted from $x/c = 0.8$ corresponding to the turbulent transition of the boundary layer on the suction side. Indeed, the transition to turbulence has been shown to increase the loss of total pressure (Denton, 1993). In the wake, i.e, from $x/c = 1$ to $x/c = 1.3$, the total temperature variation converge towards the same value between both cases. In this interval, the total pressure loss still increases due to losses produced in the wake. If compared both total quantities contributions, total pressure variation clearly dominates total temperature variation. As a result, if neglecting total temperature variation, the integrated entropy production can be measured using only total pressure variation for this adiabatic case. To validate the total pressure loss, the loss coefficient profile ξ is extracted in the axial cut located at $x/c = 0.4$ downstream the trailing edge at mid-span and compares with the experimental profile in Fig. 3.36. The loss profile is represented against the y direction (blade to blade direction as represented on Fig. 3.9 and normalized by the spacing between the periodicity patches L_p. Although both LES cases are in gross agreement with experimental measurements, the loss profile

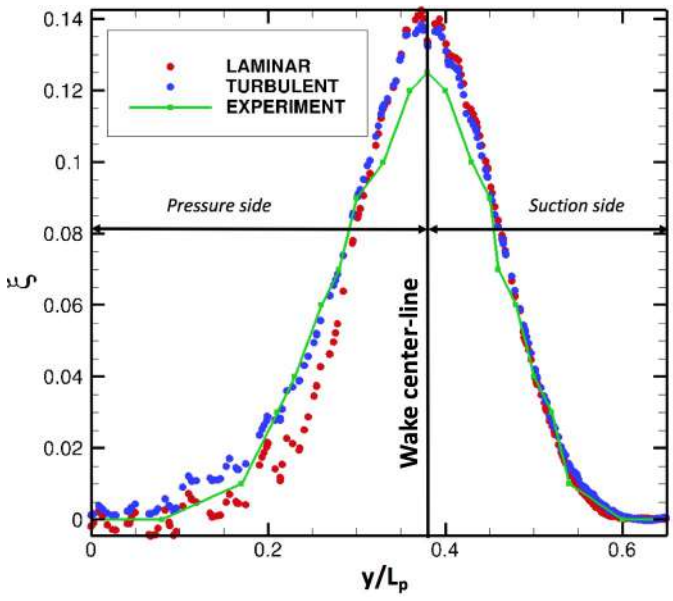

Figure 3.36 – Loss coefficient ξ [-] profiles at the mid-span located at $x/c = 0.4$ downstream the trailing edge along the y direction normalized by the spacing between the periodicity patches L_p.

is over-estimated at the wake center-line located at $y/L = 0.38$ in comparison with the experimental data. One can notice that the prediction is improved near the pressure side for $y/L < 0.38$ in the turbulent inlet case in comparison to the laminar inlet case. From Eq. (3.19), such total pressure loss in the wake originates from the integrated entropy source term in the considered control volume. To evaluate the losses generated upstream the wake for both cases, the RHS of Eq. (3.19) is integrated in the control volume defined between S_1 and the axial cut $S_x(x/c = 1.4)$ in Table 3.6. Note that the integrated entropy production is normalized by the entropy flux at the inlet of computational domain $Q_m\widetilde{s_1}$ where $\widetilde{s_1}$ is the mass flow averaged entropy on S_1. As expected, injecting freestream turbulence at the inlet increases the global loss generation within the computational domain. To evaluate the loss axial distribution along the blade, the axial evolution of the time-averaged integrated entropy production in the control volume defined between S_1 and the moving axial cut $S_x(x)$ is plotted on Fig. 3.37. Note that the time-averaged integrated entropy production $\int_{V(x)} \frac{\overline{P_m+P_q}}{T} dV$ is normalized by the entropy flux at the inlet of computational domain $Q_m\widetilde{s_1}$. In the freestream inlet region, i.e, between $x/c = -1$ to $x/c = 0$, no entropy is generated for the laminar inlet case. For the turbulent inlet case, a weak quantity of entropy is generated due to the dissipation of turbulent structures in this region. In the interval between $x/c = 0$ to $x/c = 1$, entropy is mainly produced in boundary layer regions (Denton, 1993). Again, a

CASE	$\frac{\int_{V(x/c=1.4)} \frac{\overline{P_m+P_q}}{T} dV}{Q_m\widetilde{s_1}}$ (-)
LAMINAR INLET	0.00073
TURBULENT INLET	0.00083

Table 3.6 – Integration of the entropy production in the control volume defined by S_1 and $S_x(x/c = 1.4)$ and normalized by the entropy flux at the inlet $Q_m\widetilde{s_1}$.

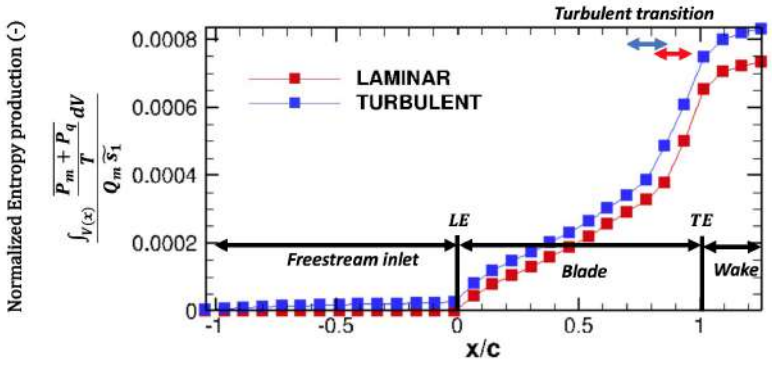

Figure 3.37 – Axial evolution of the normalized integrated entropy production between the axial section S_1 located $x/c = 1$ downstream the leading edge and $S_x(x)$. Red line represents the laminar inlet case and blue the turbulent inlet case. Leading edge (LE) and trailing edge (TE).

change of slope in the profiles is observed near the turbulent transition position. In the wake, entropy is still generated from viscous effects taking place in this region (Denton, 1993). If comparing both cases, more losses are generated for the turbulent inlet case with respect to laminar inlet case. However, such balances do not provide further informations on the loss generation mechanisms within the computational domain. To identify the loss generation mechanisms, loss maps are hereafter investigated thanks to the Second law Analysis.

Investigation of the loss maps using *Second Law Analysis*

In this section, time-averaged loss maps $\overline{P_m}$ $\overline{P_q}$ are investigated. As already stated in Chapter 2, these maps give access to loss generation local terms within the computational domain. Aerodynamic loss $\overline{P_m}$ and mixing loss $\overline{P_q}$ maps are shown at mid-span on Fig. 3.38 for both laminar inlet and turbulent inlet cases. For

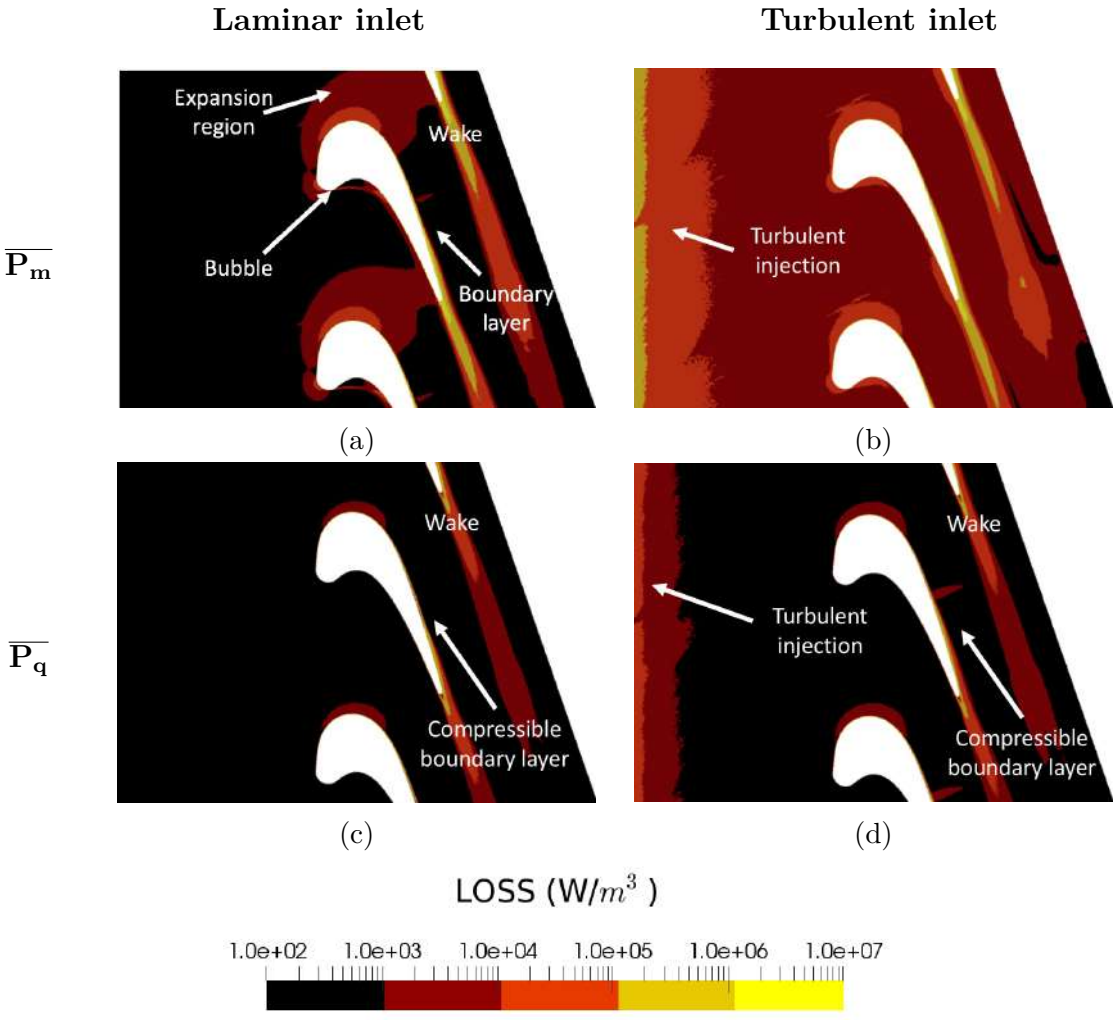

Figure 3.38 – Loss contributions at mid-span. Aerodynamic loss contribution $\overline{P_m}$ at top (a) & (b) and mixing loss contribution $\overline{P_q}$ at bottom (c) & (d). Laminar inlet case is shown on left (a) & (c) and turbulent inlet case on right (b) & (d).

the laminar inlet case, Fig. 3.38 (a), $\overline{P_m}$ is found to be mainly produced in the boundary layer and in the wake of the blade. Aerodynamic losses are also found to be generated in the sheared region at the edge of the recirculation bubble. In the freestream region near the leading edge, $\overline{P_m}$ also activates due to the strong flow expansion in this region. Indeed, the flow expansion induces a streamwise and transverse velocity gradient activating $\overline{P_m}$. Near the inlet, no loss is produced in the laminar inlet case because the fields imposed at the inlet are uniform for this case. For the turbulent inlet case, Fig. 3.38 (b), $\overline{P_m}$ is generated in the same regions described for the laminar inlet case. However, levels are higher confirming that more losses are generated in the turbulent inlet case. Indeed, the dissipation of freestream turbulence involves both laminar and SGS viscous effects in the expression of $\overline{P_m}$, Eq. (2.58). Mixing contribution $\overline{P_q}$, Fig. 3.38 (c), is observed to be only activated in the wake and boundary layer on the suction side of the blade. These regions are shown to be associated with high compressibility effects due to high levels of Mach number in these regions. Indeed, compressibility effects generate temperature gradients which are involved in the expression $\overline{P_q}$, Eq. (2.59). For the turbulent inlet case, Fig. 3.38 (d), the mark of the turbulent dissipation on $\overline{P_q}$ is noticed near the inlet. Indeed, the injection of turbulence also induces temperature gradients due to compressibility effects. If comparing the two LES predictions, $\overline{P_m}$ is found to clearly dominate the loss generation process. As a result, only the time-averaged field $\overline{P_m}$ is considered in the following.

From the loss maps, the contribution of the different regions of the flow to the global loss production can be evaluated. To do so, $\overline{P_m}$ is integrated in 4 volumes representing each region of the flow as displayed in Fig. 3.39. Local volumes are built to represent the boundary layer, the wake, the region upstream the blade and the rest of the computational domain here called freestream region. Note that the wake volume is extracted downstream the trailing edge when the magnitude of the vorticity satisfies $\omega < \omega_{crit}$ where $\omega_{crit} = 0.01\omega_{max}$ is a threshold value determined with the maximum of the vorticity ω_{max} downstream the blade. Integration results

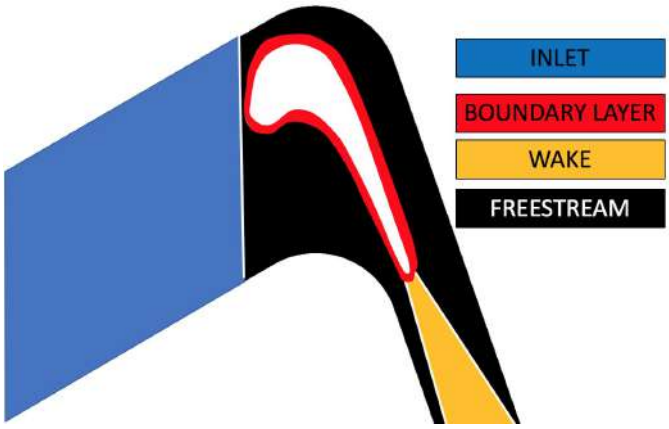

Figure 3.39 – Local control volume for integration of the losses.

	Contribution of $\int_V \overline{P_m} dV$ with respect to the total losses	
CASE	**LAMINAR**	**TURBULENT**
INLET	-	-
FREESTREAM	10 %	8 %
BOUNDARY LAYER	70 %	74 %
WAKE	20 %	18 %

Table 3.7 – Summary of the contribution of each zone on the overall loss production for the laminar and turbulent inlet cases.

are normalized by the integrated loss production in the computational domain to quantify the contribution of each region. Integration results for both LES predictions are shown in Table 3.7. Since losses generated upstream the blade are not induced by the presence of the blade, the contribution of the inlet region regarding to global loss generation is excluded. The first contributor to the loss generation is the boundary layer region for both cases. Indeed, almost $3/4^{th}$ of losses are produced in the boundary layer. The second contributor is the wake region. Finally, the third contributor is the freestream region. Although no turbulence is present in the freestream region for the laminar inlet case, the flow expansion is sufficient to generate losses. Note that this loss distribution is coherent with the ones found in the literature (Mee et al., 1992; Curtis et al., 1997). If comparing both LES predictions, the presence of freestream turbulence impacts and increases the losses produced in each volume.

The wake and the boundary layers generate most of losses for this blade and are known to present high vorticity levels. Indeed and in the literature, losses are shown to be linked to the vorticity field ω_i assuming adiabatic, incompressible and inviscid flow by the Crocco's theorem (here written in vectorial form for simplicity),

$$T\boldsymbol{\nabla} s = \boldsymbol{u} \quad \wedge \quad \boldsymbol{\omega}, \tag{3.20}$$

where $\boldsymbol{u}$ the velocity vector, $\boldsymbol{\omega}$ the vorticity vector, $\boldsymbol{\nabla} s$ the gradient of entropy and $\wedge$ the vectorial product. However, this expression does not hold for compressible and anisothermal flows. To alleviate this limitation, the Bobyleff-Forsyth formula (Serrin, 1959) generalises the Crocco's theorem to compressible flows. This expression links aerodynamic losses P_m to enstrophy defined as the squared of vorticity magnitude ω^2 so that,

$$P_m = 2\mu \frac{\partial \left(U_i \frac{\partial U_j}{\partial x_i} - U_j \vartheta \right)}{\partial x_j} + \mu\omega^2 + \mu \frac{4}{3} \vartheta^2, \tag{3.21}$$

where $\frac{\partial U_i}{\partial x_j}$ is the velocity gradient tensor, $\vartheta = \frac{\partial U_i}{\partial x_i}$ the divergence term and μ the laminar viscosity. The full demonstration of the formula can be found in (Wu et al., 1999; Buresti, 2012). On the RHS, the first term represents the flow deformation

due to the flow expansion and can be positive or negative. The second term on the RHS is linked to the enstrophy and the third term represents compressibility effects, these terms being necessarily positive. This means that any region of the flow presenting non zero vorticity and dilatation necessary generates losses. It is important to note that, even if the first term can be negative, the sum of the 3 contributions should be positive to ensure that P_m is positive. Adapted to the LES framework, the SGS viscosity should be included in Bobyleff-Forsyth formula so that,

$$P_m = \underbrace{2\left(\mu+\mu_t\right)\frac{\partial\left(U_i\frac{\partial U_j}{\partial x_i}-U_j\vartheta\right)}{\partial x_j}}_{\text{Deformation term}} + \underbrace{\left(\mu+\mu_t\right)\omega^2}_{\text{Vorticity term}} + \underbrace{\frac{4}{3}\left(\mu+\mu_t\right)\vartheta^2}_{\text{Dilatation term}}. \tag{3.22}$$

The second and third terms of the RHS hereafter respectively noted *vorticity term* and *dilatation term* and P_m are plotted at mid-span on Fig. 3.40 from instantaneous solutions. For the laminar inlet case, Fig. 3.40 (a), the vorticity term activates in the boundary layer on both sides of the blade, in the wake and at the edge of the bubble. All these regions are known to present high vorticity levels. If focusing on the boundary layer on the suction side of the blade, the vorticity term is observed to be strongly activated by the turbulent transition of the boundary layer. For the turbulent inlet case, Fig. 3.40 (b), in addition to regions previously described, the vorticity term is also activated by freestream turbulence. The dilatation term, Fig. 3.40 (c)&(d), activates in shocklets and in the wake for both laminar and turbulent inlet case. If comparing both vorticity and dilatation terms to the loss map P_m, Fig. 3.40 (e)&(f), the vorticity term is shown to dominate the loss generation for both cases. To confirm this finding, P_m, vorticity and dilation terms are integrated in the computational domain and integration results are given in Table 3.8. Integration values confirm that the vorticity term dominates the loss generation. It is noted that the integrated deformation term is negative meaning that this term limits the loss generation. If neglecting the deformation and dilatation terms, the integration of Eq. (3.22) in a control volume gives a simple link between the entropy production and enstrophy so that,

$$\int_V P_m dV = \int_V \left(\mu+\mu_t\right)\omega^2 dV. \tag{3.23}$$

Note that Eq. (3.23) is mainly used in the literature to estimate the integrated loss generation in a control volume for incompressible flows (Buresti, 2009).

	Deformation term	Vorticity term	Dilatation term
LAMINAR INLET CASE	-1.4 W	12.7 W	0.01 W
TURBULENT INLET CASE	-3.4 W	19.0 W	0.03 W

Table 3.8 – Integration of the Bobyleff formula terms in the computational domain for both cases.

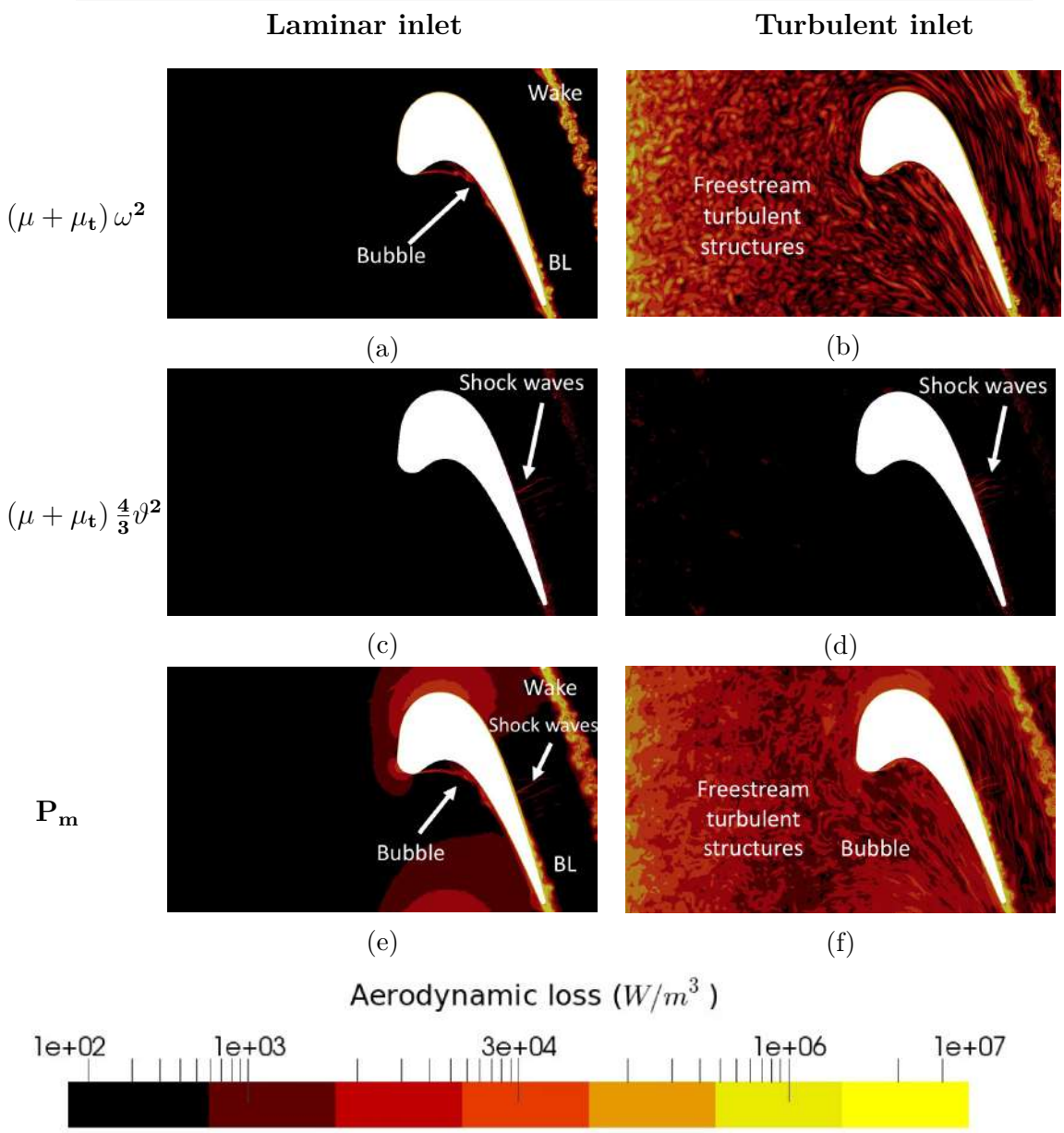

Figure 3.40 – Vorticity contribution at top (a) & (b). Dilatation contribution in the middle (c) & (d). Total aerodynamic loss generation at bottom (e) & (f). Laminar inlet case on left and turbulent inlet case on right extracted at mid-span.

From the previous observations and discussions, the loss maps are observed to be strongly activated in unsteady regions of the flow. In that case, it is of interest to discriminate the mean flow contribution from purely unsteady effects. To do so, the Reynolds decomposition is introduced on the resolved shear stress tensor, i.e, $S_{ij} = \overline{S_{ij}} + S'_{ij}$ where $\overline{\bullet}$ is the time-averaged operator and $\bullet'$ the temporal

fluctuation. Introducing the Reynolds decomposition in Eq. (2.58), one obtains,

$$\overline{P_m} = \underbrace{2(\overline{\mu}+\overline{\mu_t})\left(\overline{S_{ij}} - \frac{1}{3}\overline{S_{ll}}\delta_{ij}\right)\overline{S_{ij}}}_{\text{Loss due to mean field}} + \underbrace{\overline{2(\mu+\mu_t)\left(S'_{ij} - \frac{1}{3}S'_{ll}\delta_{ij}\right)S'_{ij}}}_{\text{Loss due to unsteady field}},$$

$$+ \underbrace{\overline{2(\mu+\mu_t)\left(2\overline{S_{ij}}S'_{ij} - \frac{1}{3}\overline{S_{ll}}\delta_{ij}S'_{ij} - \frac{1}{3}S'_{ll}\overline{S_{ij}}\delta_{ij}\right)}}_{\text{Loss due to mean / unsteady field interactions}}. \tag{3.24}$$

In the RHS, the first term represents the loss generation from the mean field while the second term represents the loss generation from purely unsteady fields. The third term represents the loss generation from interactions between mean and unsteady fields. To simplify Eq. (3.24), one can assume that the temporal correlations between $(\mu+\mu_t)$ and S'_{ij} are negligible to cancel the third term on the RHS. If neglecting also the compressibility effects on the loss generation, i.e, $S_{ll} \approx 0$, Eq. (3.24) reduces to the following expression:

$$\overline{P_m} = \underbrace{2(\overline{\mu}+\overline{\mu_t})\overline{S_{ij}}\overline{S_{ij}}}_{P_m^{mean}} + \underbrace{2\overline{(\mu+\mu_t)S'_{ij}S'_{ij}}}_{P_m^{turb}}. \tag{3.25}$$

The first term on the RHS will be hereafter noted P_m^{mean} and the second term P_m^{turb}. P_m^{mean} can be reconstructed from a time-averaged solution and P_m^{turb} can be evaluated from the difference between $\overline{P_m}$ and P_m^{mean}. Note that in RANS, only P_m^{mean} can be obtained from the mean flow while P_m^{turb} needs to be modelled. In the LES context, no modelling is needed because P_m^{turb} is directly obtained from the turbulence resolved on mesh. Mean and turbulent contributions are shown at mid-span in Fig. 3.41 for both cases. For the laminar inlet case, Fig. 3.41 (a), P_m^{mean} dominates in the laminar boundary layer, in the flow expansion region and in the bubble, where laminar shear stress is expected. For the turbulent inlet case, Fig. 3.41 (b), P_m^{mean} level is mainly reduced in the bubble because its size is much more smaller for this case. Regarding the turbulent contribution P_m^{turb} for the laminar inlet case, Fig. 3.41 (c), the turbulent contribution mainly activates in the wake, in the turbulent transition of the boundary layer and near the reattachment point of the bubble. Indeed, transition to turbulence of the flow in the bubble was previously observed and discussed in Section 3.3.3 for the laminar inlet case. Finally and for the turbulent inlet case, Fig. 3.41 (d), the mark of the turbulence injection at the inlet is clearly identified in the freestream region. Indeed, P_m^{turb} can be also assimilated to the dissipation rate of resolved turbulent kinetic energy. If comparing levels of both mean and turbulent contributions, P_m^{turb} is observed to clearly dominate P_m^{mean} in the boundary layers and in the wake. Since unsteady effects are shown to produce most of losses, the effect of the boundary layer turbulent transition on the loss generation is specifically hereafter addressed.

The following focuses on the losses generated by the turbulent transition of the suction side boundary layer. To quantify the loss generation in the boundary

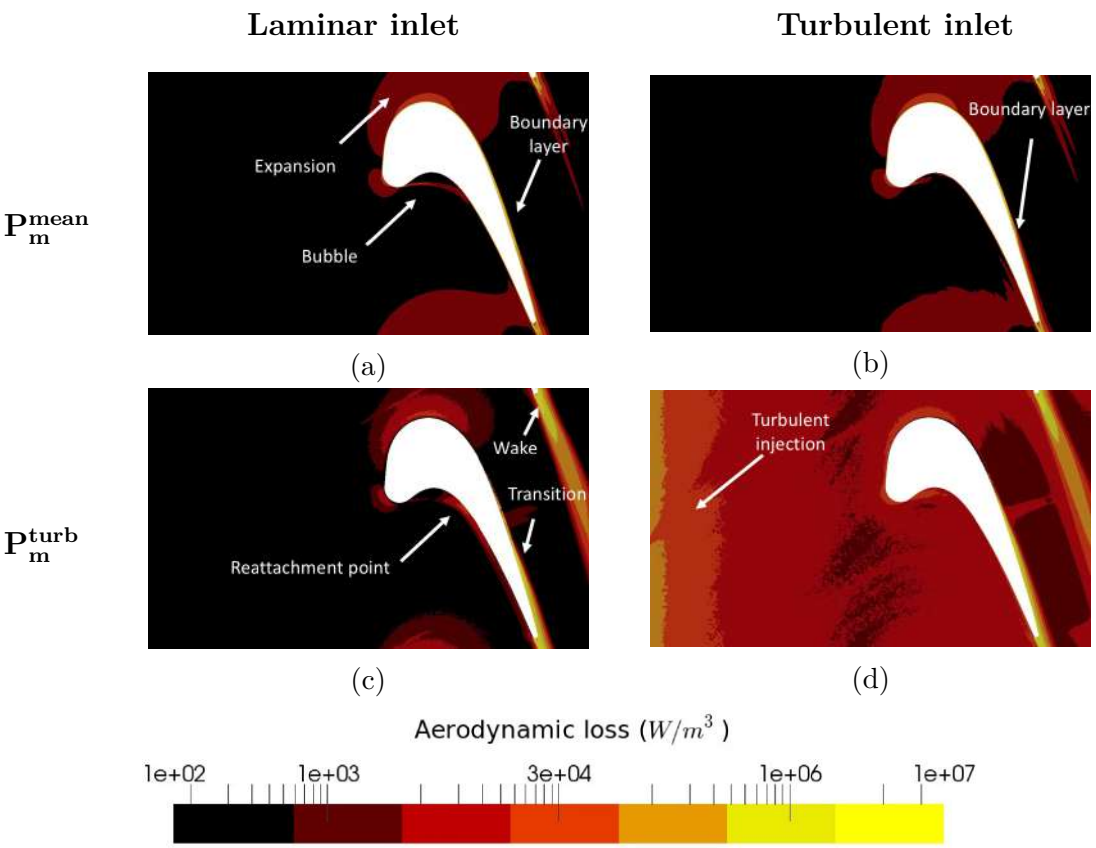

Figure 3.41 – Mean P_m^{mean} at top (a) & (b) and turbulent P_m^{turb} at bottom (c) & (d) contributions to the loss generation at mid-span. Laminar inlet case is shown on left (a) & (c) and turbulent inlet case on right (b) & (d).

layer, the integrated loss production in the layer noted $(s^*T)_{BL}$ is given by,

$$(s^*T)_{BL} = \int_0^\delta \overline{P_m} dn, \tag{3.26}$$

where n is the wall normal distance. Then, $(s^*T)_{BL}$ is normalized by the flux of kinetic energy at the edge of the boundary layer $\rho_\infty U_\infty^3$ to obtain the dissipation coefficient C_d defined as (Denton, 1993),

$$C_d = \frac{(s^*T)_{BL}}{\rho_\infty U_\infty^3}. \tag{3.27}$$

It is worth to recall that C_d also corresponds to the kinetic energy thickness rate in Eq. (3.17). The axial evolution of C_d is plotted for both cases on the suction side of the blade on Fig. 3.42. From the leading edge to $x/c = 0.7$, i.e, in the laminar part of the boundary layer, C_d decreases. No difference is observed between the LES predictions. Indeed, this region was shown not to be affected by freestream turbulence in Section 3.3.3. From the position of the turbulent transition, C_d is observed to strongly increase similarly as the turbulent production previously described in Fig. 3.29. This confirms that the transition to turbulence increases the

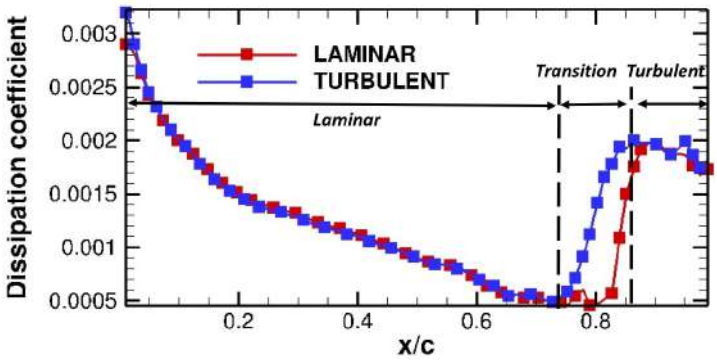

Figure 3.42 – Dissipation coefficient C_d [-] evolution in the boundary layer on the suction side of the blade. Red line represents the laminar inlet case while blue line is the turbulent inlet case.

loss generated by the boundary layer as already observed in experiments and numerical studies (Wheeler and al., 2016; Wheeler et al., 2017; Lengani et al., 2018). Finally, C_d decreases from $x/c = 0.9$ to the trailing edge. This specific evolution of C_d through a turbulent transition is consistent with numerical investigations found in the literature (Denton, 1993; Greitzer., 2004; Wheeler et al., 2017).

To understand the behaviour of the loss production in laminar and turbulent boundary layers, normal loss profiles to the wall are extracted from the laminar part of the boundary layer on the suction side at $x/c = 0.5$ and from the turbulent part at $x/c = 0.9$. At this position, the boundary layer was shown to be turbulent in both LES predictions in Section 3.3.3. For the turbulent boundary layer, the different sub-layers (viscous, transitional and log) are indicated on the profiles according to values of normalized wall distance y^+. Then, P_m^{mean} and P_m^{turb} are plotted against the wall normal distance normalized by the boundary layer thickness n/δ on Fig. 3.43. For the laminar boundary layer, Fig. 3.43 (a), the mean contribution P_m^{mean} increases and reaches a peak when approaching the wall. This peak is directly linked to the time-averaged wall shear stress τ_w. Indeed, if taking Eq. (2.58) and using boundary layer hypotheses, P_m^{mean} is given by,

$$(P_m^{mean})_{(n/\delta)=0} = \frac{\tau_w^2}{\mu}. \tag{3.28}$$

P_m^{turb} rapidly decreases toward zero for $n/\delta < 0.8$ because no turbulent fluctuation is expected within the laminar boundary layer. If comparing both LES predictions, no impact of freestream turbulence on the mean contribution is observed. Freestream turbulence only increases the penetration of P_m^{turb} in the boundary layer but still converge toward zero for $n/\delta < 0.8$. As a result, laminar boundary layer is not affected by freestream turbulence which confirms findings found in Section 3.3.3. For the turbulent boundary layer, Fig. 3.43 (b), P_m^{mean} increases when approaching the wall and rises faster from the translational sub-layer for $n/\delta < 0.15$. P_m^{turb} also increases when approaching the wall to a peak located at the edge between the transitional and viscous sub-layers at $n/\delta < 0.05$. For

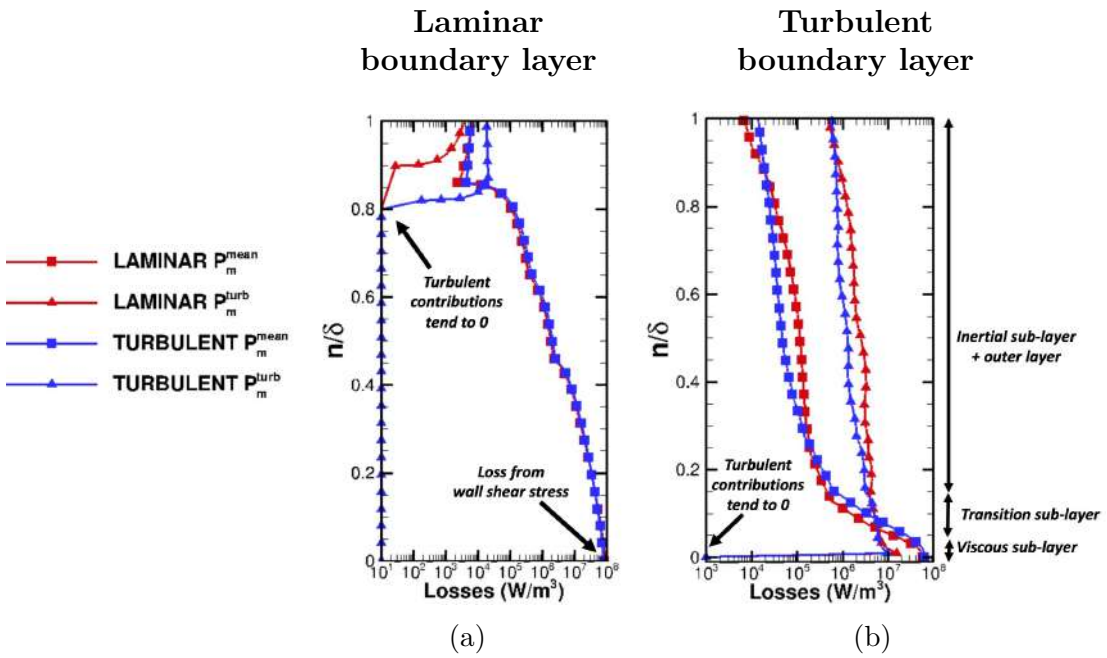

Figure 3.43 – Mean P_m^{mean} and turbulent P_m^{turb} normal loss profiles on the suction side of the blade at the axial positions $x/c = 0.5$ on left (a) and $x/c = 0.9$ on right (b). Red line represents the laminar inlet case while blue is the turbulent inlet case. Filled square is P_m^{mean} and filled triangle is P_m^{turb}.

this normal position, P_m^{turb} decreases and converges to zero at wall. Indeed, since no turbulent fluctuations is expected in the viscous sub-layer, P_m^{turb} necessarily cancels at wall. If comparing both contributions, P_m^{mean} is observed to dominate P_m^{turb} for $n/\delta < 0.1$ while P_m^{turb} is higher than P_m^{mean} for $n/\delta => 0.1$. No impact of freestream turbulence on loss profiles is noticed. Finally, to evaluate the contributions of the different sub-layers on the loss generation, P_m^{mean} and P_m^{turb} are integrated into each sub-layers for the turbulent inlet case and results are provided on Fig. 3.44. The loss production is found to be distributed between the

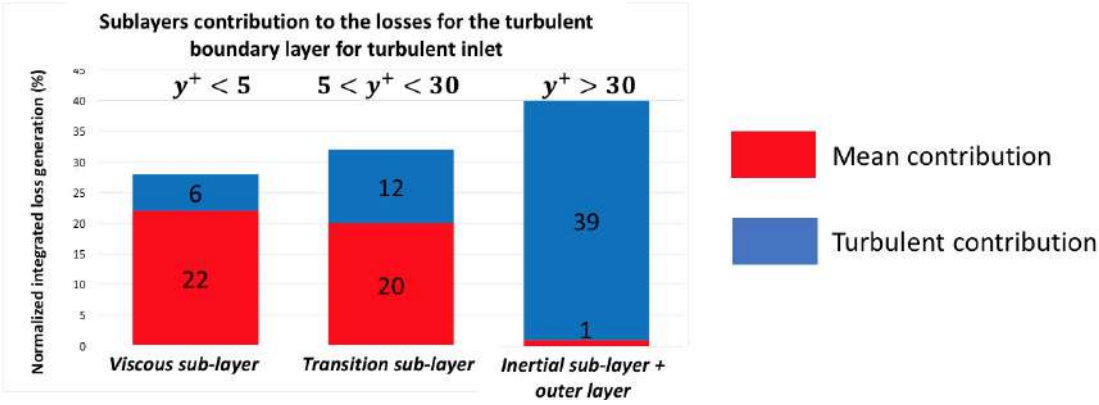

Figure 3.44 – Integrated mean and turbulent loss contributions in sub-layers of the turbulent boundary layer located at $x/c = 0.9$ for the turbulent inlet case.

viscous sub-layer ($\approx$ 28%), transitional sub-layer ($\approx$ 32%) and inertial / outer layers ($\approx$ 40%). In the viscous and transitional sub-layers, the mean contribution is more important than the turbulent contribution because turbulent fluctuations are less present in these regions. In the inertial sub-layer and outer layer, the loss generation is clearly dominated by the turbulent contributions.

3.4 Chapter conclusions

In this chapter, the capacity of LES to predict the blade load distribution for the T120 cascade blade presenting a recirculation bubble was first validated. To do so, wall resolved LES were performed with and without synthetic turbulence injection at inlet and compared. The injection of synthetic turbulence at the inlet is found to recover the experimental bubble size. The investigations of boundary layers profiles show that freestream turbulence reduces the pressure gradient in the boundary layer which makes the boundary layer more resistant to separation. The resulting distribution of mass flow on both pressure and suction sides is shown to be changed. Indeed, since the separation is reduced, more mass flow passes near the pressure side of the blade and then less mass flow passes near the suction side to conserve the integrated mass flow rate. This allows to recover the experimental load of the blade with turbulence injection. Afterwards, the losses are evaluated using methodologies introduced in Chapter 2. Total quantity balance equations confirm that total pressure variation dominates total temperature variation and measure the integrated entropy generated in the computational domain. Investigations of the loss maps through the use of SLA show that boundary layers produce the most of the losses followed by the wake. Advanced analyses of loss maps confirm that the loss generation occurs mainly in zones of high vorticity and compressibility. Introducing the Reynolds splitting in the loss expressions evidences that unsteady contributions of losses dominate the mean ones. Investigations of the loss generation in the boundary layer show that the turbulent transition of the boundary layer generates more losses than the laminar boundary layer. Local integration of the losses in the turbulent boundary layer shows that the mean contribution dominates the viscous and transitional sub-layers while turbulent contribution dominates the inertial and outer layers. Finally, freestream turbulence increases the loss generation in the log and outer layers while the viscous sub-layer is not impacted.

To conclude this chapter, LES has shown its capacity to predict the blade load distribution for the highly loaded T120 blade. Aerodynamic loss generation mechanisms were clearly identified for the T120 blade thanks to the Second Law Analysis (SLA). Indeed, SLA is found to be an efficient approach to identify the loss generation mechanisms for compressible anisothermal flows contrary to total temperature and total pressure 1D balances. In the next chapter, the complexity of the configuration is increased by investigating the cooled blade T120D presenting a coolant film on the pressure side. For this cooled blade, losses issued by both flow aerodynamics and by the coolant film are investigated.

Chapter 4

Loss prediction of the academic cooled blade T120D

Contents

4.1 Review of the T120D academic cooled blade **124**
4.1.1 Introduction of the T120D blade 124
4.1.2 Cooling system and operating condition 124
4.1.3 Available experimental measurements 127
4.1.4 CFD predictions of the T120D blade 131
4.2 Methodology and numerics **133**
4.3 LES prediction of the T120D cooled blade **137**
4.3.1 LES results and validations 137
4.3.2 Investigation of the mixing process in the film 157
4.3.3 Investigation of the losses 162
4.4 Chapter conclusions **175**

This chapter addresses the WRLES prediction for the academic cooled T120D blade. In this chapter, the capacity of LES to predict the blade load distribution and adiabatic film effectiveness for T120D blade is validated. After validations, losses issued by the flow aerodynamics and by the coolant film are investigated using the methodologies introduced in Chapter 2. To do so, the study is organized as follows. First, the cooling system of the T120D blade and the experimental operating point are presented in Section 4.1. To highlight the contribution of this work, a review of the existing CFD predictions is provided. Next, numerics and LES modelling are detailed in Section 4.2. Then, the LES prediction is presented in Section 4.3. The instantaneous flow structure and mean flow organization are first described. Then, LES results are validated through the comparison of the blade load distribution and adiabatic film effectiveness to experimental results. Afterwards, the loss generation mechanism is explored. Finally, conclusions of this study are recalled in Section 4.4.

4.1 Review of the T120D academic cooled blade

In this section, the T120D blade configuration is presented. First, the context of the T120D blade design is recalled in Section 4.1.1. Then, the cooling system of the blade is presented and the experimental operating point is introduced in Section 4.1.2. Available experimental database is presented in Section 4.1.3. Finally, a review of numerical predictions is detailed in Section 4.1.4.

4.1.1 Introduction of the T120D blade

As already described in Chapter 3, the T120 blade exhibits a recirculation bubble on its pressure side which impacts not only the flow aerodynamic but also the thermal stress on the blade wall. Indeed in a real engine, hot streams trapped in this recirculation bubble lead to a high temperature region near the blade wall (Gomes and Niehuis, 2013). To avoid such a phenomenon, ejection of coolant in the bubble helps in reducing the bubble size and heat transfer at wall (Deinert and Hourmouziadis, 2004; Gomes and Niehuis, 2011). However pressure variations in freestream flow can lead to oscillations of coolant mass flow rate in coolant pipes and produce re-ingestion of hot flows (Deinert and Hourmouziadis, 2004). To avoid such a re-ingestion process, coolant has to be injected at a pressure much higher than the pressure within the bubble. As a consequence, jets have a strong penetration which leads to a detachment of jets off the wall. For high Reynolds number flows, interactions between the detached jets and the main stream generate turbulent activity. This turbulent activity induces a turbulent diffusive process of cold temperature present in jets with the wall enhancing the film effectiveness at wall (Zhang and Moon, 2007; Polanka et al., 2000; Gomes and Niehuis, 2011). Indeed, turbulence was numerically observed to impact the film effectiveness in a complex way (Ekkad et al., 1997; Drost and Bocs, 1998; Polanka et al., 2000). A second point of coolant ejection is the increase of the momentum flux present in the bubble which helps in reducing its size and associated aerodynamic losses (Gomes and Niehuis, 2013). As a result, the prediction of flow aerodynamics and adiabatic wall temperature for such cooled blades is highly complex and still remains a challenge today. The academic cascade T120D cooled blade of the AITEB II project is the typical configuration for which all effects previously described can be investigated. Since the T120D blade was experimentally investigated with the same test rig than the T120 blade, the experimental set up will not be here recalled (Cf. Chapter 3). In the following, the design of the cooling system of the T120D blade is presented.

4.1.2 Cooling system and operating condition

The T120D blade relies on the T120 geometry (Cf. Chapter 3) for which 3 rows of coolant pipes are added on the pressure side of the blade. A detailed view of the pipes is displayed in Fig. 4.1. Each row contains 21 holes uniformly distributed along the span of the blade (z direction) and separated by a distance of $t_{fc} = 8$ mm. Geometric details of the cooling pipes are provided in Table 4.1. The first

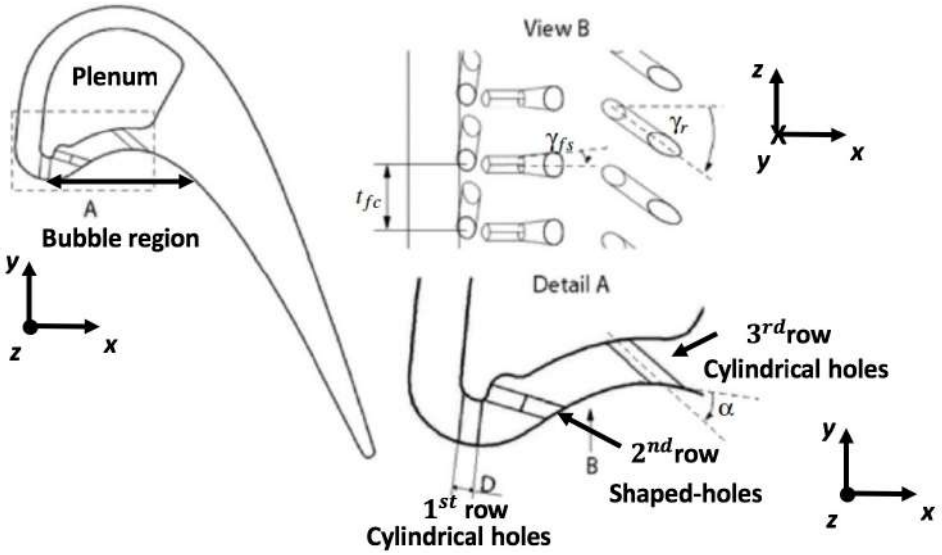

Figure 4.1 – Detailed view of the cooling system of the T120D blade. Adapted from (Gomes and Niehuis, 2011).

Symbol	Row 1	Row 2	Row 3
x/c	0.077	0.198	0.35
$(t/D)_{fc}$	4	4	4
α	84.2°	56.2°	35.1°
γ_r	37.2°	0°	30°
γ_{fs}	0°	7.5°	0°

Table 4.1 – Geometric details for the T120D blade. t_{fc} is the distance between holes of each row, D the diameter of holes, α, γ_r and γ_{fs} are geometric angles defined on Fig. 4.1.

row is composed of cylindrical holes of diameter $D = 2mm$ and locates near the stagnation point of the blade. The second row is composed of shaped-holes which locates in the bubble region of the blade to reduce the separation length. Finally, the last row is composed of cylindrical holes presenting a transverse angle with respect to the freestream flow direction.

The pipes are fed by a plenum located inside the blade at a constant total pressure $P_{t,c}$ and total temperature $T_{t,c}$ controlled by a compressor. The coolant temperature is set at 303 K while the main flow total temperature $T_{t,1}$ is set at 333 K. The temperature difference between the hot and coolant streams is then 30 K. The cooling operating condition is defined by the ratio between the coolant total pressure $P_{t,c}$ to the inlet total pressure $P_{t,1}$. In the experiment, 3 ratios have been studied: i.e, 1.03, 1.09 and 1.12. In this study, the intermediate ratio, i.e, $\frac{P_{t,c}}{P_{t,1}} = 1.09$ is arbitrary chosen. The coolant mass flow rate $Q_{m,c}$ injected in the plenum results from the total to total pressure ratio $\frac{P_{t,c}}{P_{t,1}}$ as well as from pressure

losses in the pipes. Such losses are experimentally evaluated by a global discharge coefficient C_D so that,

$$C_D = \frac{Q_{m,c}}{Q_{m,ideal}}, \tag{4.1}$$

where $Q_{m,ideal}$ is the ideal coolant mass flow rate in case of an ideal flow, i.e, through an isentropic process. As a result, $Q_{m,ideal}$ can be evaluated assuming an isentropic expansion from the total coolant pressure $P_{t,c}$ to the local span averaged static pressure P at the hole locations on the blade using the following expression,

$$Q_{m,ideal} = A_{fc}\left(\frac{P}{P_{t,c}}\right)^{\frac{1}{\gamma}} \frac{P_{t,c}}{\sqrt{rT_{t,c}}}\sqrt{\frac{2\gamma}{\gamma-1}\left(1-\left(\frac{P}{P_{t,c}}\right)^{\frac{\gamma-1}{\gamma}}\right)}, \tag{4.2}$$

where A_{fc} is the film cooling section at the exit of the pipes, r the perfect gas constant and γ the heat capacity ratio fixed at 1.4. From the coolant mass flow rate and freestream conditions, each pipe is characterized by its density ratio DR and blowing ratio M defined by Eqs. (1.4)&(1.5). To compute the blowing ratio M, one must know the coolant mass flow $\rho_c U_c$ through the ejection surface of holes as well as the local freestream mass flux $\rho_\infty U_\infty$. Since the plenum was designed to be sufficiently large, the coolant mass flow distribution between the cooling pipes can be considered uniform along the height of the blade (Gomes and Niehuis, 2011). As a consequence, equal mass flow distribution between the 21 holes for each row is assumed, i.e:

$$\rho_c U_c = \frac{Q_{m,ideal}}{21 * 3 * S_{hole}}, \tag{4.3}$$

where S_{hole} is the ejection surface for the considered hole. To evaluate the local freestream mass flow $\rho_\infty U_\infty$ near the holes, an isentropic expansion of the main stream from the inlet total pressure $P_{t,1}$ to the local static pressure P is also assumed so that,

$$\rho_\infty U_\infty = \sqrt{\frac{2\gamma}{(\gamma-1)rT_{t,1}}} P_{t,1}\left(\frac{P}{P_{t,1}}\right)^{1/\gamma}\sqrt{1-\left(\frac{P}{P_{t,1}}\right)^{\frac{\gamma-1}{\gamma}}}. \tag{4.4}$$

Using previous assumptions, the corresponding experimental values for DR, M and C_D for each row is given in Table 4.2. Note that the 1st, 2nd and 3rd row of pipes are respectively noted by the subscript 1, 2, 3. It is important to note that high blowing ratio does not necessary correspond to high coolant mass flow rate. For instance, the third row locates near the reattachment point of the bubble and then low values of $\rho_\infty U_\infty$ are expected which likely increase M (Gomes and Niehuis, 2013). For this coolant operating point, available experimental database is detailed in the next section.

DR	M_1	M_2	M_3	C_D
1.052	2.23	2.93	25.21	0.735

Table 4.2 – Coolant flow properties. Taken from (Gomes and Niehuis, 2011).

4.1.3 Available experimental measurements

In this section, available experimental aerodynamic and thermal measurements are provided. All presented experimental results correspond to the following operating point: $\frac{P_{t,c}}{P_{t,1}} = 1.09$ and $T_{t,1} - T_{t,c} = 30K$. The aerodynamic operating point corresponds to the one used in Chapter 3, i.e: $Ma_2 = 0.87$ and $Re_2 = 390,000$.

Aerodynamic measurements

The aerodynamic of the blade under investigation is experimentally characterized by the load distribution on the blade. The load distribution is experimentally obtained from pressure taps located near the mid-span of the blade. The time-averaged pressure distribution is then normalized to obtain the isentropic Mach number $Ma_{is}(x/c)$ distribution on both sides of the blade (Cf. Eq. (3.3)) and provided on Fig. 4.2. The flow expansion is found to be very similar to the uncooled T120 blade (Cf. Fig. 3.2). On the suction side of the blade, the flow exhibits a strong acceleration and becomes supersonic around $x/c = 0.3$. Downstream, a decrease of Ma_{is} from $x/c = 0.6$ evidences a compression region followed by a shock located at $x/c = 0.7$. On the pressure side, ejection of coolant changes the pressure distribution nearby the bubble region. At the coolant ejection locations (evidenced by straight vertical black lines), the local increase of Ma_{is} shows a local acceleration of the flow due to coolant ejection. Between $x/c = 0.4$ and $x/c = 0.5$, low velocities combined with coolant ejection from the third row of holes induce a local static pressure that is reported to be superior to the inlet total pressure. In

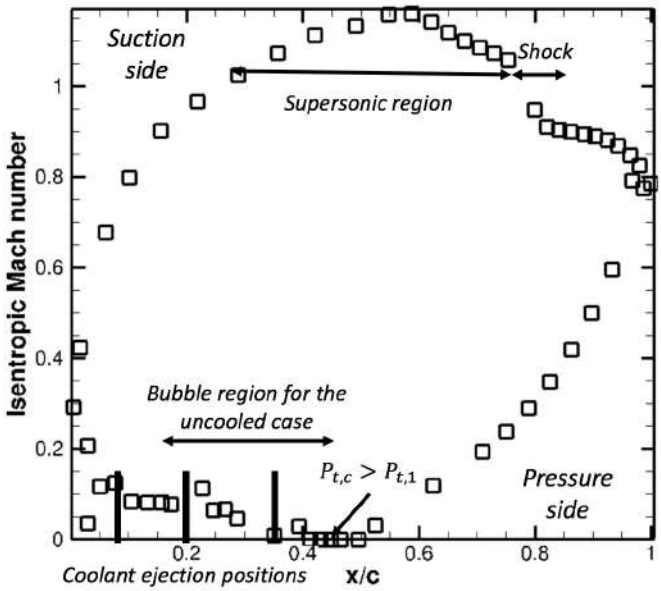

Figure 4.2 – Experimental Isentropic Mach number Ma_{is} [-] distribution of the T120D blade for the operating point $(Ma_2; Re_2) = (0.87; 390,000)$ and $\frac{P_{t,c}}{P_{t,1}} = 1.09$. Adapted from (Duchaine et al., 2009a). Coolant ejection locations are shown by straight vertical black lines.

this specific zone, Ma_{is} is therefore fixed at 0 to avoid non-physical values (Gomes and Niehuis, 2013). To evaluate more closely the flow dynamics in the coolant jets, the experimental local pressure coefficient C_P is experimentally evaluated at mid-span of the blade so that,

$$C_P(x/c) = \frac{\overline{P}(x/c) - P_2}{P_{t,1} - P_2}, \tag{4.5}$$

where $\overline{P}$ is the time-averaged static pressure on wall and P_2 the static pressure downstream the cascade. To evaluate the impact of coolant ejection on the load distribution, C_P profiles are then plotted on the pressure side between the leading edge and $x/c = 0.6$ for both cooled and uncooled cases on Fig. 4.3. Compared to the uncooled case, the flow expansion on the pressure side seems strongly impacted by the coolant ejection. Indeed and as expected, the flow accelerates at the coolant ejection positions: i.e, at $x/c = 0.08$, $x/c = 0.2$ and $x/c = 0.35$. Downstream the coolant ejections, C_P increases indicating a compression region of the flow which points potential jet detachments off the wall. Between $x/c = 0.4$ and $x/c = 0.5$, $C_P > 1$ because the local static pressure is superior to the inlet total pressure as previous discussed. The peak of C_P at $x/c = 0.45$ finally indicates that jets impact the wall in this concave part of the blade and then remain attached to the wall. Such a behaviour of coolant jets presenting a strong penetration in the main stream has already been observed in other experimental studies (Polanka et al., 2000; Colban et al., 2006).

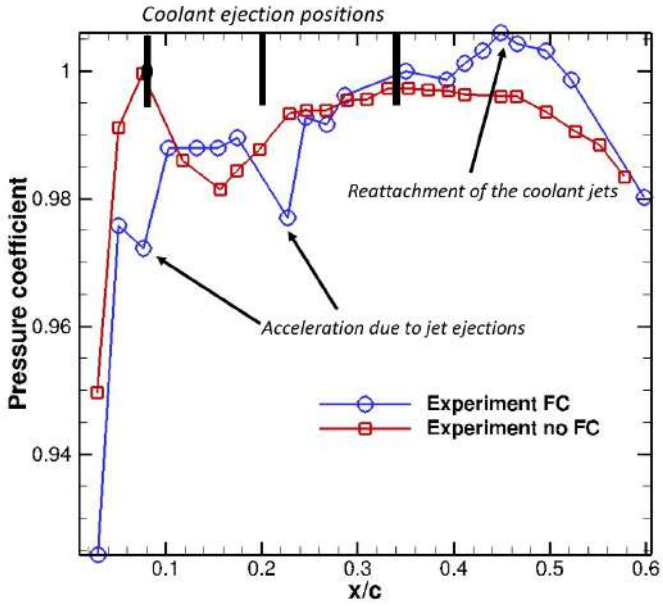

Figure 4.3 – Pressure coefficient C_P [-] on the pressure side of the T120D blade. Taken from (Gomes and Niehuis, 2011). With and without film cooling (FC).

Thermal measurements

In the experiment, the thermal environment of the blade is characterized by the adiabatic film effectiveness η along the pressure side of the blade and reads as,

$$\eta(x/c) = \frac{T_r(x/c) - T_{aw}(x/c)}{T_{t,1} - T_{t,c}}, \tag{4.6}$$

where T_{aw} is the measured wall adiabatic temperature at mid-span of the blade and T_r is the recovery temperature. T_r represents the wall temperature if the cooling flow would be injected at the same temperature than the main stream, i.e, at iso-energetic conditions (Goldstein, 1971). For incompressible flows, T_r is constant if walls are adiabatic and no work is done on the flow. However, for compressible flows, T_r is not constant along the blade due to compressibility effects. It thus must be taken into account introducing the recovery factor r_f (Goldstein, 1971) in the evaluation of T_r by,

$$T_r(x/c) = T_{t,1} + (r_f - 1)\frac{u_\infty(x/c)^2}{2C_p}, \tag{4.7}$$

where C_p is the heat capacity at constant pressure and u_∞ the local freestream velocity. The recovery factor r_f is defined as $r_f = Pr^{1/2}$ for laminar boundary layer and $r_f = Pr^{1/3}$ for turbulent boundary layer (Goldstein, 1971). In the experiment, wall temperature is measured using thermochromatic liquid crystals with a sensitivity of 1 K. Nonetheless and due to temperature difference between cooling and main stream, the blade is exposed to heat flux $\dot{q}$. To build the adiabatic wall temperature T_{aw}, the experimental wall temperature T_w must be corrected using a local heat transfer coefficient h yielding,

$$T_{aw}(x/c) = T_w(x/c) + \frac{\dot{q}}{h}. \tag{4.8}$$

The heat transfer coefficient h is obtained from dedicated heat transfer experiments where the walls are heated with a constant heat flux. Then, the heat equation is resolved for the solid blade using a Finite Element Analysis code to obtain the wall heat flux $\dot{q}$ of the experiment. As a result of the above discussion, experimental value of η suffers from uncertainties estimated around 5 - 8 % but can reach up to 30% for low values of η (Gomes and Niehuis, 2011). Experimental results of η on the pressure side of the blade are shown on Fig. 4.4 for one hole pattern, i.e, only one hole for each row is shown. Here, results are normalized with the maximum value of η reached on the pressure side. From such a map, η is observed to increase from $x/c = 0.1$ and $x/c = 0.15$ downstream the first hole. Although the coolant jet is detached from the wall, interactions with the main stream are suspected to generate a turbulent activity which diffuses the coolant temperature to the wall (Gomes and Niehuis, 2011). A small amount of coolant flow ejected through the second row is supposed to be brought back upstream due to the reversed flow present in the bubble (Deinert and Hourmouziadis, 2004). Around the second hole near $x/c = 0.2$, a region of low efficiency is observed because the coolant flow

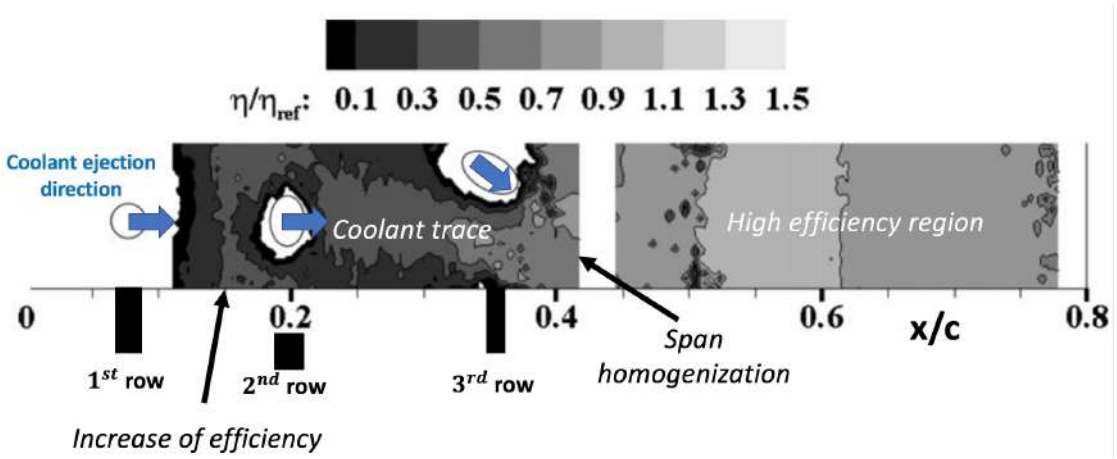

Figure 4.4 – Experimental map of the film effectiveness normalized by the peak value η/η_{ref} [-] for one hole pattern. Taken from (Gomes and Niehuis, 2011).

is supposed to be deviated by the jet issued from this hole. Downstream, the mark of the coolant is clearly evidenced between $x/c = 0.25$ and $x/c = 0.35$. Then, the film effectiveness is homogenized in span-wise direction which is explained by the deviation of the film by the jet issued from the third hole combined with strong turbulent diffusion (Gomes and Niehuis, 2011). Then, η increases to a peak located at $x/c = 0.55$. Finally from $x/c = 0.6$, η decreases because of mixing with the hot stream while the film remains attached to the wall (Gomes and Niehuis, 2011). Span-wise averaged results are given on Fig. 4.5. In agreement with the map of Fig. 4.4, the efficiency increases downstream the first hole. Between the second and third coolant holes from $x/c = 0.15$ to $x/c = 0.3$, the efficiency reaches a plateau. Regarding the map of Fig. 4.4, this plateau is not clearly observed and probably results from the span-average operation. From $x/c = 0.3$, the efficiency increases to a peak located at $x/c = 0.55$ and then decreases essentially due to mixing with the hot stream.

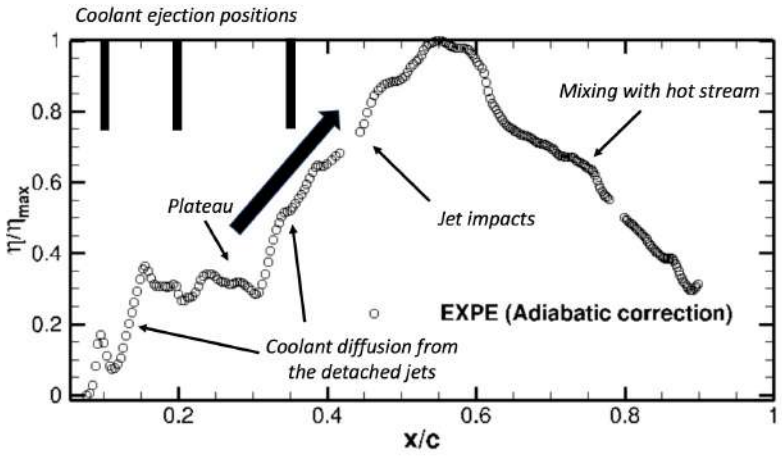

Figure 4.5 – Normalized adiabatic film effectiveness η/η_{max} [-] on the pressure side of the T120D blade. Taken from (Gomes and Niehuis, 2011).

Such a complex evolution of the film effectiveness results from complex interactions between the hot and coolant stream (Zhang and Moon, 2007; Polanka et al., 2000; Gomes and Niehuis, 2011). To investigate such interactions, CFD predictions for the T120D blade were performed and are hereafter detailed.

4.1.4 CFD predictions of the T120D blade

CFD predictions of the film effectiveness have been attempted although the prediction for such a configuration remains a challenge. To the author's knowledge, the only CFD prediction of the cooled blade T120D was performed by (Duchaine et al., 2009a). An adiabatic LES was performed with the compressible solver AVBP. The computational domain was based on a periodic domain in the span-wise direction representing only one hole pattern, i.e, one hole for each row was represented. The mesh was composed of 6.5 millions of tetrahedra. The wall unit y^+ was around 40 but was inferior to 5 in the region of jets. The sub-grid turbulence was WALE (Nicoud and Ducros, 1999). A noslip condition was applied in an attempt to produce a wall resolved LES although the wall unit y^+ was superior to 1. Note that no turbulence was injected at the inlet of the computational domain. A view of the coolant jet trajectories issued from the simulation is shown on Fig. 4.6. As discussed for the experiment, the jets issued from the first and second holes are shown to be detached from the wall. Note that coolant temperature iso-surface quickly vanishes as jets penetrate the main stream flow indicating a strong mixing process with the hot stream. The third jet slightly detaches from the wall but then impinges the wall near $x/c = 0.45$ as also observed in the experiment. Time-averaged isentropic Mach number obtained in the CFD prediction is compared to experimental results on Fig. 4.7. Overall, the prediction issued from the LES is satisfactory. On the pressure side of the blade, LES predicts well the load distribution. The stagnation point located at $x/c = 0.05$ is not perfectly positioned in the LES indicating a slight deviation of the inflow angle with the experiment. Local differences in the coolant ejection region suggest that the jet topologies are not exactly predicted. This is confirmed if focusing in the interval between $x/c = 0.4$

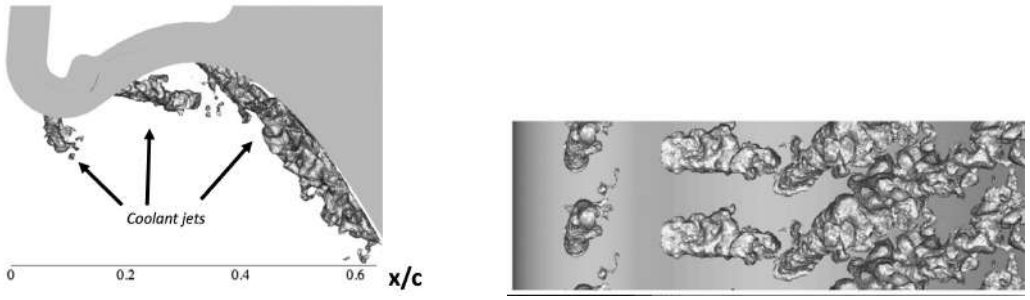

(a) (b)

Figure 4.6 – Isosurface of cold temperature. Side view (a) and pressure side view (b). Extracted from (Duchaine et al., 2009a).

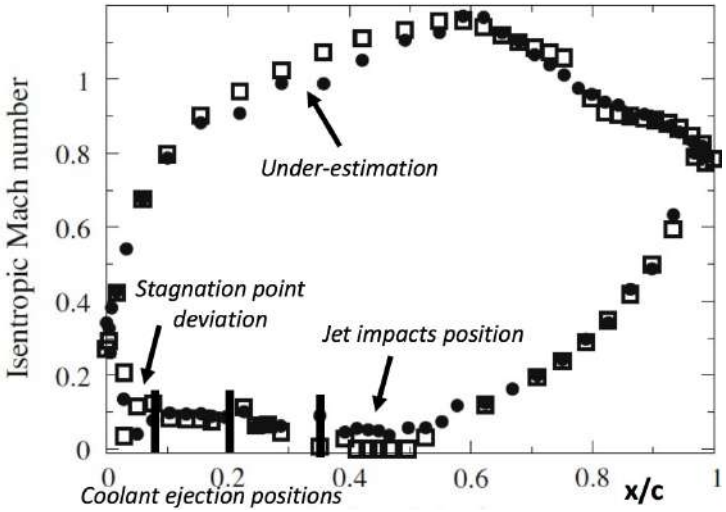

Figure 4.7 – Isentropic Mach number Ma_{is} [-] distribution along the blade between the experimental and LES. White squares • represent the experiment data and black squares □ the adiabatic LES from (Duchaine et al., 2009a).

and $x/c = 0.5$ where Ma_{is} is not null contrary to experimental data. One reason could be that the size of the predicted jet separations which probably differs with the experiment. On the suction side, a good agreement with the experiment is found despite a slight under-estimation observed between $x/c = 0.3$ and $x/c = 0.5$.

Film effectiveness on the pressure side is compared to the discussed adiabatic LES, experiment data and a RANS prediction using the $k - \omega$ / SST transition model (Menter et al., 2004) on Fig. 4.8. Note that experimental results do not take

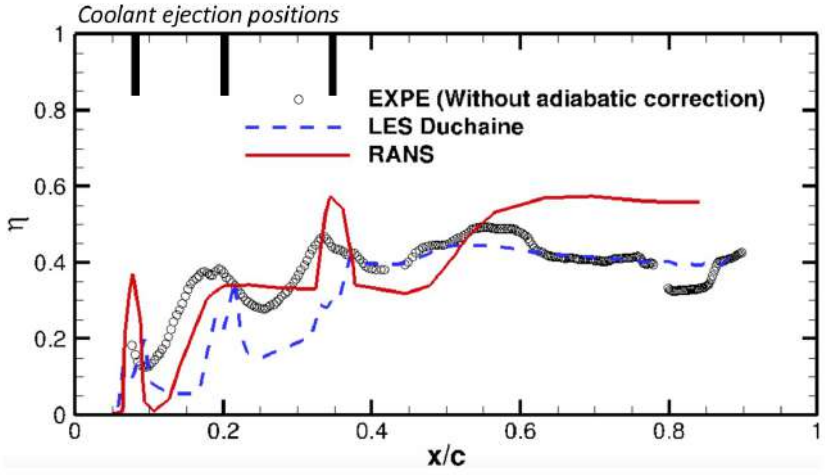

Figure 4.8 – Adiabatic film effectiveness η [-] on the pressure side of the blade. Extracted from (Duchaine et al., 2009a). Black circles O represent the experiment data, blue dashed lines −− the adiabatic LES and red solid line − the RANS (Gomes and Niehuis, 2011).

into account the adiabatic correction explained in Section 4.1.3 for the wall temperature. RANS was not able to recover the film effectiveness distribution along the pressure side. From $x/c = 0.5$, η is clearly over-estimated indicating that RANS under-estimates the mixing process between the coolant and hot streams. Indeed, the turbulent mixing is known to be greatly under-estimated with RANS (Dyson et al., 2012; Dickhoff et al., 2018). Although LES is observed to predict well the evolution of the efficiency, levels are also under-estimated along the pressure side. In the region of coolant ejection, i.e, from $x/c = 0.1$ to $x/c = 0.35$, the efficiency is also under-estimated. Such deviations between LES and experiment in this region could originate from the mesh which was not able to capture the turbulent mixing between coolant and hot streams. The limitation of the span-wise extent of the computational domain could also limit the interactions between coolant jets with hot stream. Indeed, and based on the return of experience of (Duchaine et al., 2009a), the first and the third coolant holes are partially oriented in the span-wise direction. Interactions between two rows of holes in this direction are then expected. The size of the span-wise extent is then expected to affect the flow in the region of the coolant holes.

As a result of the previous discussion, a new WRLES with a doubled span-wise extent is produced in this work while generating a finer mesh to comply with a wall resolved approach. To do so, numerics and LES modelling are described in the next section.

4.2 Methodology and numerics

In this section, numerics and LES modelling of the WRLES for the T120D blade are addressed. First, the computational domain and the mesh retained for this work are presented. Then, the numerical scheme and LES modelling are provided and justified. To reach the targeted operating point, the boundary conditions of the WRLES are finally presented.

Computational domain

The LES computational domain retained for the upcoming analysis is shown on Fig. 4.9. The domain is built from the one used for the computation of the uncooled blade T120 (Cf. Chapter 3) with a span-wise extent of $16mm$ (which is doubled with respect to the work of (Duchaine et al., 2009a)). This span-wise extent incorporates 2 span-wise pitches of hole pattern, i.e, 6 holes are represented in the domain as shown on Fig. 4.10. Although authors are aware of such reduced span-wise extent, only 2 span-wise pitches of hole pattern are retained for this work to allow grid refinement in the near wall flow regions while limiting the CPU effort of such a detailed simulation. Finally, periodic conditions are used in the span-wise (z) and blade to blade (y) directions to limit the computational domain to one single blade. In the experiment, coolant is fed by 2 endpoint boundaries of the plenum where a constant coolant pressure is applied. To numerically monitor

the coolant ejection in the computational domain, this plenum is represented in the computational domain and bounded by two inlets being located $16mm$, i.e, $\approx 0.1c$ away from the holes to avoid any interactions between the hole surfaces and the numerical coolant inlets.

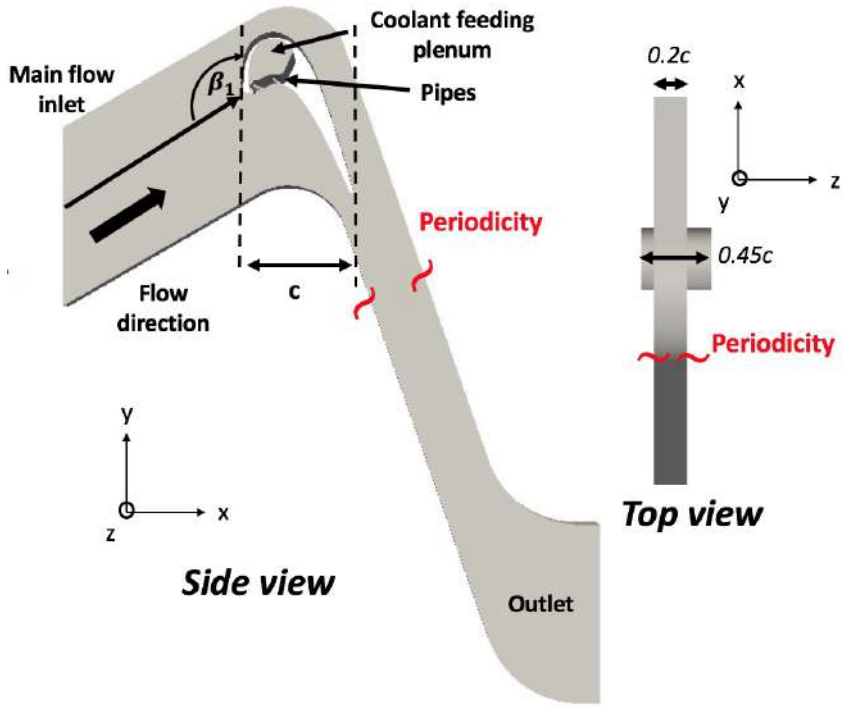

Figure 4.9 – LES computational domain. Span-wise domain is limited to $16mm$, i.e, 2 film cooling hole patterns. The inflow angle β_1 and the flow direction at the inlet are displayed. Periodicity boundary conditions are represented with $\sim$.

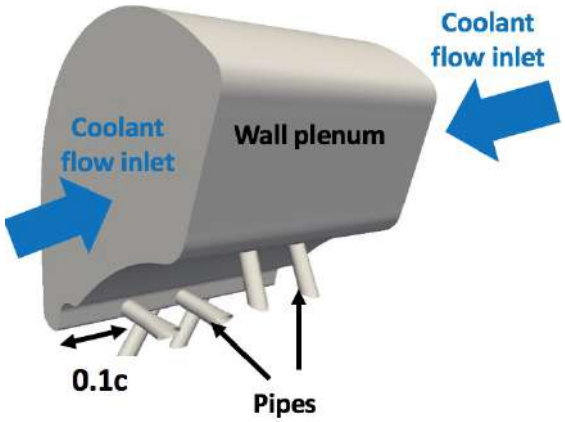

Figure 4.10 – Computational domain view of the plenum and holes.

Mesh

The mesh generated for this study is composed of 100 million of cells including 82 million of tetrahedra in the main stream and 18 million of prisms near walls as shown on Fig. 4.11. The blade surface is meshed with isotropic triangles, i.e, $x^+ \approx z^+$. The aspect ratio of the prism layer is by construction limited to 5 along the blade, i.e, $x^+ \approx 5y^+$. The cell volume jump at the interface tetrahedron / prism is by construction imposed at 3 to ensure proper numerics in this region. Meshing efforts have been furthermore focused on the mixing region between the hot and the coolant streams near the pressure side, Fig. 4.11 (a). The mesh is also refined near the suction side of the blade and in the wake to capture the strong gradients in these regions, 4.11 (b). To ensure the resolution of the flow in the cooling system, 10 million of cells are used to mesh the plenum and the pipes. The surface mesh of the pipes and plenum are displayed in Fig. 4.12. The mesh is refined near the wall of pipes, Fig. 4.12 (a). Note that meshing the corners between pipes and the blade wall were difficult to handle with prism layers. The diameter of each hole is meshed with 35 - 40 points as shown on Fig. 4.12 (b).

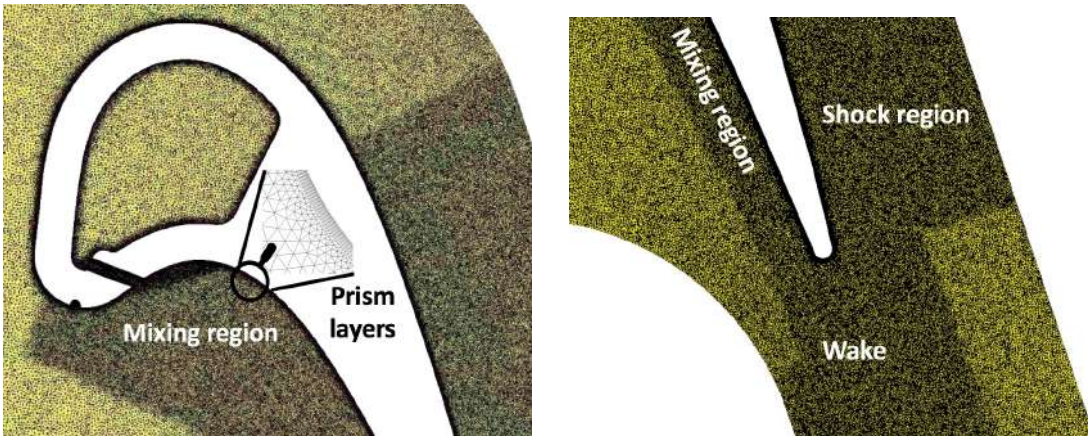

(a) (b)

Figure 4.11 – Mesh view at mid-span near leading edge (a) and trailing edge (b).

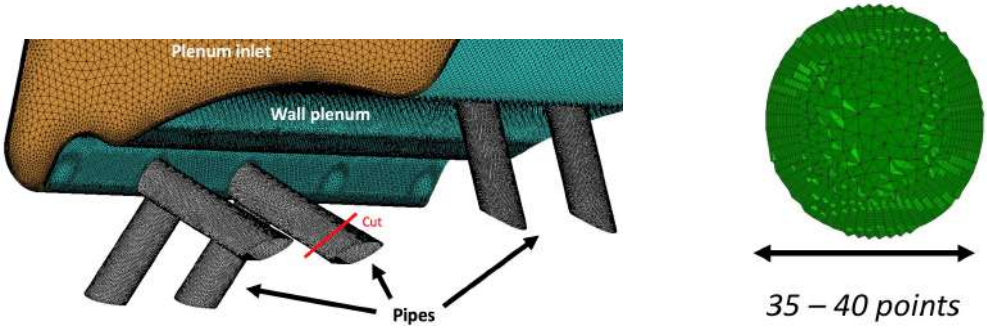

(a) (b)

Figure 4.12 – Surface mesh on the pipes on left (a) and mesh cut of one specific pipe on right (b). Red line represents the cut position.

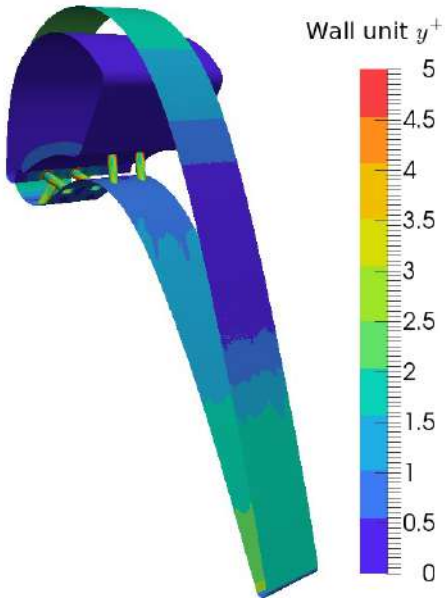

Figure 4.13 – Wall unit y^+ [-] on the walls of the computation domain.

The wall mesh resolution is checked a posteriori by showing the wall unit y^+ along both sides of the blade on Fig. 4.13. The wall unit y^+ is observed to be around 2 on the blade and around 3 in the pipes. Although y^+ is superior to 1 along the blade, the designed mesh is in full agreement with requirements for a wall resolved LES (Tucker, 2013; Tyacke and Tucker, 2014).

Numerical scheme

Similarly to Chapter 3, the compressible LES equations are numerically resolved with the code AVBP. The numerical scheme is the finite element scheme TTGC (Colin and Rudgyard, 2000), 3rd order in time and space. The diffusive terms are integrated with a 2nd order finite element scheme.

LES modelling

The sub-grid turbulence model is WALE (Nicoud and Ducros, 1999) to comply with the correct damping of the turbulent viscosity in the near wall flow region.

Targeted operating point and boundary conditions

The targeted operating point for this study corresponds to an outlet isentropic Mach number Ma_2 of 0.87 and a Reynolds number Re_2 of 390,000. The cooling operating condition corresponds to a difference of total temperature between the coolant and the hot flows of 30 K and the total to total pressure ratio between the coolant and the main flow is $\frac{P_{t,c}}{P_{t,1}} = 1.09$. To numerically reach this operating point, total pressure and temperature are imposed at all inlets of the computational domain. Note that no turbulence is injected at the inlet because it would require more convergence time and additional verifications which is not compatible

Patch	Variable	Value
Main flow Inlet	$P_{t,1}$	26720 Pa
	$T_{t,1}$	333 K
	Inlet angle	138.6 °
Coolant flow Inlet	$P_{t,c}$	29130 Pa
	$T_{t,c}$	303 K
	Inlet angle	90 ° (Normal to the patch)
Outlet	P_2	16307 Pa
Wall		Adiabatic no slip

Table 4.3 – Boundary conditions used in the computation.

with the PhD deadline. Note also that the coolant mass flow through the pipes is not imposed with such an approach but will result from the pressure ratio between the local static pressure at the hole exits and the coolant total pressure as well as pressure losses. Static pressure is specified at the outlet to produce the correct expansion ratio obtained from Ma_2. All boundary conditions are imposed using *NSCBC* formalism (Poinsot and Lele, 1992; Odier et al., 2018) to deal with acoustics and targeted values are summarized in Table 4.3. To track the coolant fluid, a passive scalar is injected at the coolant inlets so that it equals 1. The passive scalar is then transported with a simple convection-diffusion equation. For this passive scalar, the diffusion coefficient corresponds to a Schmidt number equal to 1. From this definition, the fictive species tracks the coolant and its value remains between 0 and 1. In the following, the value of the fictive species will be noted $Y_{coolant}$ and assimilated to the coolant mass fraction.

4.3 LES prediction of the T120D cooled blade

In this section, the LES flow prediction is investigated. First, the flow structure issued by the WRLES is detailed and validated in Section 4.3.1. Then, to investigate the evolution of the film effectiveness along the pressure side of the blade, the mixing process in the coolant film is specifically investigated in Section 4.3.2. Finally, losses are studied in Section 4.3.3.

4.3.1 LES results and validations

Prior to the description of the flow organization, both aerodynamic and coolant operating conditions are first verified while comparing 0D and 1D values with the experiment. Then, the large scale flow structures and mean flow organization are depicted. Afterwards, the near wall flow region is specifically addressed by studying boundary layer evolutions and compared to the uncooled T120 blade. Next, a detailed description of the mean flow structure in cooling pipes and in the coolant jet region is provided. Finally, wall stresses and temperature are addressed and validated through the comparison to experimental results.

Validation of the numerical operating point

First, the flow expansion induced by the presence of the blade is verified by comparing the span-averaged isentropic Mach number Ma_{is} on both sides of the blade to experimental results on Fig. 4.14. A good agreement is found between the WR-LES and experiment. However, it is noted that the stagnation point located near $x/c = 0.05$ is not perfectly positioned in the LES. A slight deviation of the inflow angle is then suspected with the experiment. On the suction side of the blade, the expansion and compression region are correctly predicted by the LES. The decrease of Ma_{is} near $x/c = 0.7$ is slightly shifted downstream in the LES. On the pressure side, the flow expansion is observed to slightly over-estimated by the LES between $x/c = 0.05$ and $x/c = 0.5$, corresponding to the coolant ejection region. To explain this deviation, it is important to recall that pressure tapping probes in the experiment are not perfectly located at mid-span of the blade due to the presence of the holes. As a result, the distribution of isentropic Mach number in the coolant ejection region given by experimental probes is not fully comparable with the span-averaged Ma_{is} given by the LES. Another reason of the deviation could be the absence of turbulence injection at the inlet of the LES which has been observed to impact this specific region of the flow in Chapter 3. Downstream this region, the acceleration of the flow from $x/c = 0.6$ to the trailing edge is well predicted by the LES. As a result of the previous discussion, LES results can be considered satisfactory.

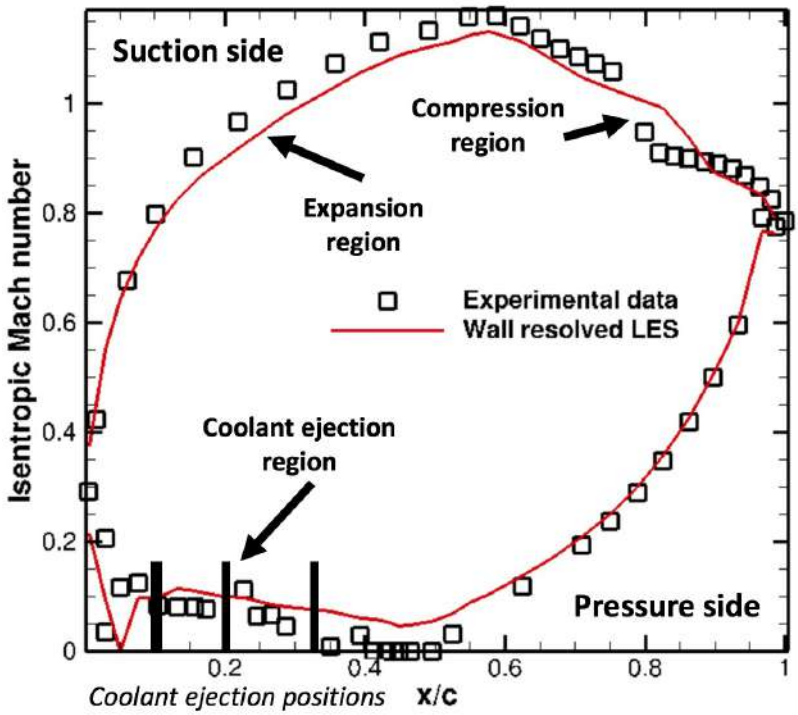

Figure 4.14 – Span averaged isentropic Mach number Ma_{is} [-]. Black squares represent the experiment data and red solid line – the WRLES.

	$Q_{m,c,1}$	$Q_{m,c,2}$	$Q_{m,c,3}$	M_1	M_2	M_3	DR	$Q_{m,c,t}$	C_D
LES	0.087	0.106	0.082	2.39	1.57	2.03	1.083	0.275	0.735
Experiment	-	-	-	2.23	2.93	25.21	1.052	0.260	0.715

Table 4.4 – Coolant operating condition. Mass flow rate $Q_{m,\bullet}$ values are given in g/s. Results are span-averaged for each row of holes. Experimental data are extracted from (Gomes and Niehuis, 2011). Experimental mass flow rate of each individual hole is not available.

The coolant operating condition is now addressed and needs also to be verified. To do so, the coolant mass flow rate $Q_{m,c}$, blowing ratio M for each row of holes as well as discharge coefficient C_D are compared to experimental values. To compute the blowing ratio M, equal repartition of the coolant flow through the pipes is assumed to be comparable with the experiment (Cf. Section 4.1.2). Span-averaged results are here given in Table 4.4. The mass flow rate distribution among the holes is found not to be perfectly equal. Indeed, the second row has a higher mass flow rate than the first and third rows. Since the 3 rows are supplied with the same coolant total pressure, the flow structure and associated losses probably differ in the pipes between the 3 rows. The resulting computation of the blowing ratio M is then expected to also differ with the experiment since not perfect equal repartition of coolant was found in the LES. Indeed, although M is correctly predicted for the first jet, M is under-estimated for the second and third jets. Nevertheless, if added the contribution of each hole, a good agreement with experiment is found on the total coolant mass flow rate $Q_{m,c,t}$, discharge coefficient C_D and density ratio DR.

Despite local deviations are observed for the distribution of the coolant mass flow rate among the holes, the flow expansion as well as the total coolant mass flow rate are well predicted by the LES. In the following, the instantaneous large scale flow structure is described.

Instantaneous view of large scale flow organization

To exhibit the large scale flow structure issued by the LES prediction, an instantaneous view of the numerical Schlieren $\frac{\nabla\rho}{\rho}$ map at mid-span of the CFD domain is shown on Fig. 4.15. On the pressure side of the blade, the mixing region between the hot and coolant exhibits a strong turbulent activity presenting unsteady structures of different sizes. Downstream this region, unsteady structures are found to be stretched by the flow acceleration. Downstream the trailing edge of the blade, a turbulent wake is noticed. On the suction side, a supersonic region (evidenced by the white sonic line) and followed by multiples shocklets are observed recovering the flow structure obtained for the uncooled T120 blade (Cf. Chapter 3). If looking at the near wall flow region, a turbulent transition of the boundary layer is also observed on the suction side of the blade. Detailed view of instantaneous flow structure in the near wall flow region are hereafter provided.

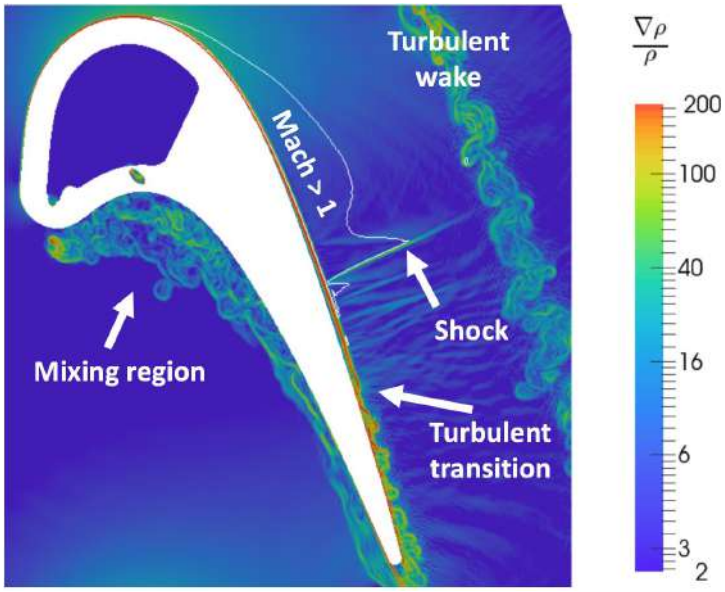

Figure 4.15 – Instantaneous view of the numerical Schlieren $\frac{\|\nabla\rho\|}{\rho}$ $[m^{-1}]$ at mid-span of the CFD domain. White isoline represents the sonic line $Ma = 1$.

A closer look to the near wall flow region on the suction side of the blade is shown on Fig. 4.16. The iso-surface of Q-criterion, Fig. 4.16 (a), evidences the presence of turbulent structures as hairpin vortices which appear and develop along the suction side of the blade. Smaller turbulent structures are also observed between the hairpin vortices confirming that the boundary layer transits to turbulence in this region. On the wall shear stress map, Fig. 4.16 (b), traces of turbulent structures are observed. On the pressure side of the blade, a new iso-surface of Q-criterion coloured by the coolant mass fraction $Y_{coolant}$ evidences the coolant jet structure on Fig. 4.17. Coherent structures are first observed within the pipes. These structures, shaped as rings, correspond to shear layer vortices produced from recirculation bubbles located in cooling pipes (Leylek and Zerkle, 1994; Lee et al., 2014). Then, in the jets, coherent structures shaped as rings are also observed. These specific structures are often observed in jets in cross flow (Fric and Roshko, 1994; New et al., 2003) and are here generated from the strong shear between the jets and the main cross stream. Downstream the jets, these coherent structures are observed to be dissipated and substituted by smaller turbulent structures. The effect of these turbulent structures on the mixing process is clearly identified by the strong spatial variation of $Y_{coolant}$ on the iso-surface. To investigate the effect of such a turbulent activity on the coolant film, instantaneous spatial distribution of coolant mass fraction is shown on Fig. 4.18. The film is observed to develop along the pressure side of the blade presenting a strong turbulent activity. Indeed, the spatial distribution of $Y_{coolant}$ illustrates a large range of turbulent eddies. This turbulent activity generates local segregations of the coolant, i.e, regions of high and low coolant concentrations are locally observed in the film. Such findings are coherent with existing experimental and numerical studies of coolant jet ejection (Leylek and Zerkle, 1994; Peet and Lele, 2008; Simiriotis, 2016; Bizzari, 2018).

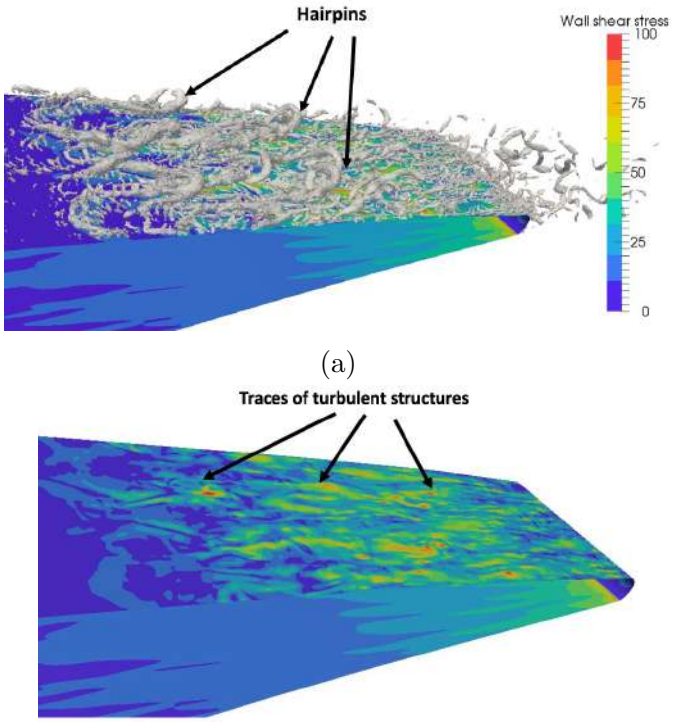

(a)

(b)

Figure 4.16 – Iso-surface of Q-criterion equal to $Q_{crit} = 2.10^{10} s^{-2}$ on the suction side of the blade at top (a) and wall shear stress τ_w $[Pa]$ at bottom (b).

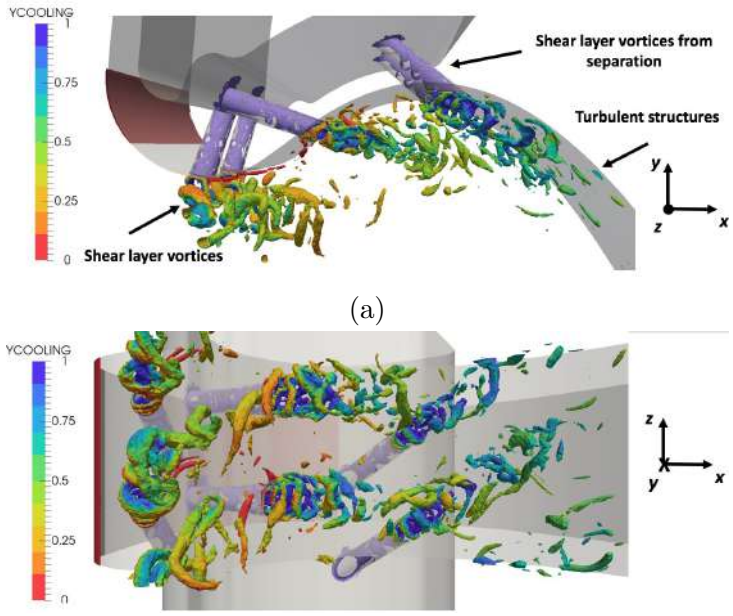

(a)

(b)

Figure 4.17 – Iso-surface of the Q-criterion equal to $Q_{crit} = 4.10^{9} s^{-2}$ on the pressure side coloured by the fictive species $Y_{coolant}$. Side view (a) and bottom view (b).

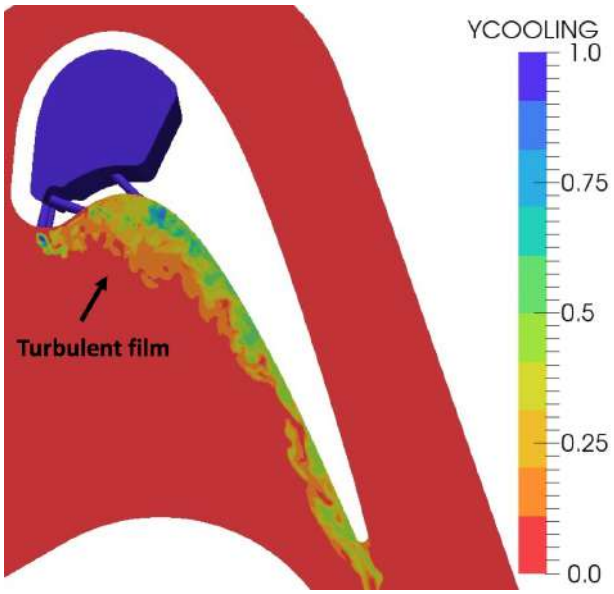

Figure 4.18 – Instantaneous view of the coolant mass fraction map $Y_{coolant}$ [-].

To go further in the analysis, a statistical description of the flow is adopted. To do so, the flow fields are time averaged on 3 flow time passages defined as a time for a fluid particle to go from the hot inlet to the outlet of the domain. Such a convergence time is sufficient to ensure that the flow statistics (mean + RMS) are converged. The mean flow organization is hereafter described.

Statistic description of the aerodynamic flow organization

Figure 4.19 shows the time-averaged static pressure and the turbulent kinetic energy k at mid-span of the CFD domain. The mean static pressure map, Fig. 4.19 (a), exhibits a region of flow expansion on the suction side of the blade followed by a supersonic region. In agreement with the distribution of isentropic Mach number shown on Fig. 4.14, the flow re-compresses downstream the supersonic region. On the pressure side, a compression region is also observed downstream the leading edge. In this region, the compression induces an adverse pressure gradient and leads to a small recirculation bubble evidenced by the black line. The turbulent kinetic energy k map, Fig. 4.19 (b), shows a production of turbulence in the near wall flow region on the suction side of the blade. This confirms the transition to turbulence of the boundary layer in this region. On the pressure side, turbulence is also evidenced in the coolant ejection region confirming that this region presents a turbulent activity. Downstream the trailing edge, k increases in the turbulent wake.

The mean flow structure of the T120D blade is found to be very similar to the T120 uncooled blade (Cf Chapter 3) except for the coolant ejection region on the pressure side of the blade. The near wall flow region is hereafter addressed through the investigation of boundary layers.

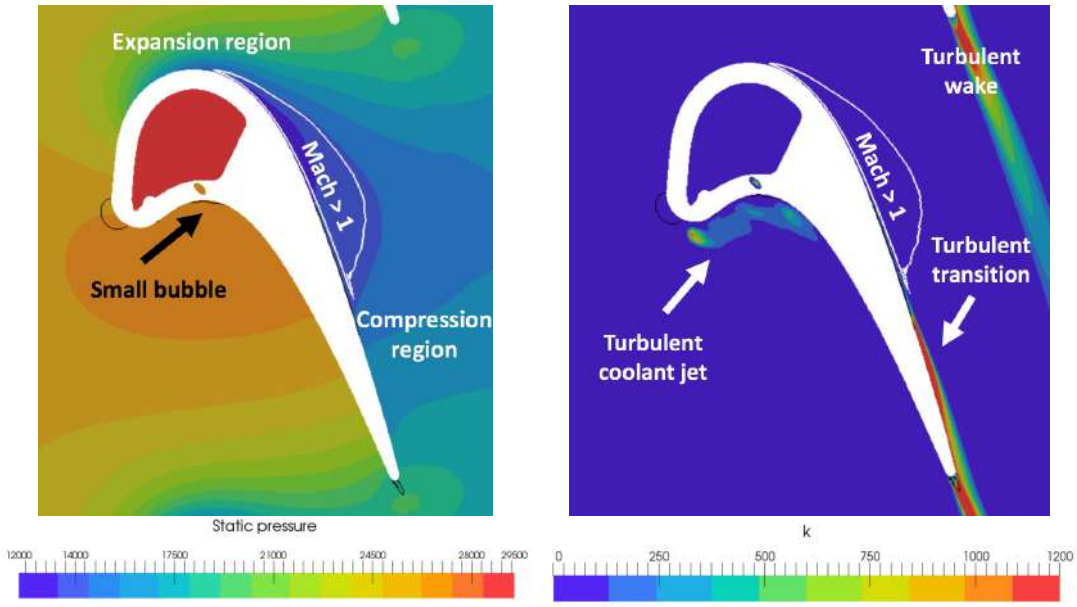

(a) (b)

Figure 4.19 – Time-averaged static pressure $\overline{P}$ $[Pa]$ on left (a) and turbulent kinetic energy k $[m^2/s^2]$ on right (b) at mid-span. Black iso-contour represents zero axial velocity $\overline{u} = 0$ and white iso-contour the sonic line $\overline{Ma} = 1$.

Near wall flow region and boundary layers

To evaluate the impact of coolant ejection on the near wall flow region, friction coefficient C_f and boundary layer evolutions are here provided and compared to results from the uncooled T120 blade without turbulent injection (Cf. Chapter 3). The friction coefficient is evaluated through Eq. (3.6) and extracted at mid-span of the CFD domain on both sides. Results are then plotted and compared to the uncooled T120 blade on Fig. 4.20. Note that the value $C_f = 0$ corresponds to the separation/reattachment of the boundary layer and negative values correspond to the presence of a recirculation bubble. On the pressure side, Fig. 4.20 (a), C_f

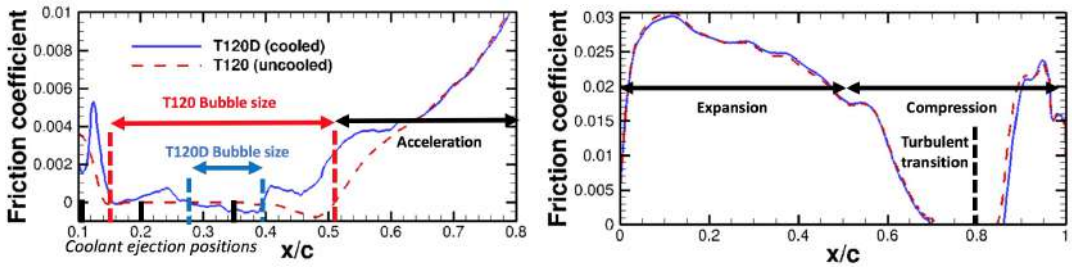

(a) (b)

Figure 4.20 – Friction coefficient C_f [-] at mid-span of the CFD domain for the cooled T120D blade (blue) and uncooled T120 blade (red) on the pressure side on left (a) and on the suction side on right (b).

differs between both blades near the coolant ejection positions from $x/c = 0.1$ to $x/c = 0.6$ as expected. At $x/c = 0.15$, a peak of C_f is observed for the T120D blade corresponding to the position of the first row of pipe. Downstream, C_f remains positive between $x/c = 0.1$ and $x/c = 0.25$ for the T120D blade while C_f is negative for the uncooled blade T120 in this interval. This confirms that the coolant ejection delays the separation of the boundary layer (Deinert and Hourmouziadis, 2004; Gomes and Niehuis, 2011). Downstream, C_f becomes negative in the interval between $x/c = 0.25$ and $x/c = 0.4$ for the T120D blade. This interval is shorter for the T120D blade compared to the T120 blade confirming that the bubble size is strongly reduced by the coolant ejection. From $x/c = 0.4$, the boundary layer reattaches and the flow accelerates which increases C_f. From $x/c = 0.6$, both cases converge to same values of C_f. On the suction side of the blade, Fig. 4.20 (b), the strong increase of C_f located at $x/c = 0.8$ corroborates the presence of a turbulent transition of the boundary layer. No strong deviations are observed between both cases. Thus, the coolant ejection only impacts the near flow region on the pressure of the blade as expected. To go further in the analysis, the boundary layer evolutions are investigated on both sides. To do so, the boundary layers are extracted using the methodology proposed by (Michelassi et al., 1998) based on the vorticity field (Cf. Chapter 3). The boundary layer thickness δ is extracted at mid-span of the CFD domain and compared to the T120 uncooled blade on Fig. 4.21. On the pressure side, Fig. 4.21 (a), the evolution of δ differs in the region of the bubble between both blades. Indeed, local peaks are observed for the T120D between $x/c = 0.1$ and $x/c = 0.6$ and correspond to local thickening of the boundary layer thickness due to local ejections of coolant. Indeed, since δ is built from the vorticity field, the value of δ in this region is necessary impacted by the vorticity generated in the coolant ejection region. Such an effect highlights that the approach to extract the boundary layer proposed by (Michelassi et al., 1998) should be improved in the context of coolant jet ejection. Nevertheless, this is out of the scope of this chapter and no improvement will be proposed in this work. Downstream the coolant ejection region for $x/c = 0.7$, no deviations are observed between both cases. On the suction side, Fig. 4.21 (b), no deviation is observed

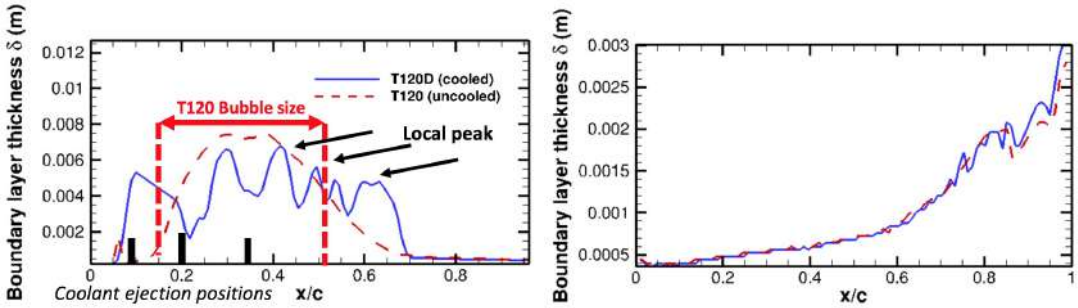

(a) (b)

Figure 4.21 – Boundary layer thickness δ $[m]$ at mid-span of the CFD domain for the T120D cooled blade (blue) and T120 uncooled blade (red) on the pressure side on left (a) and on the suction side on right (b).

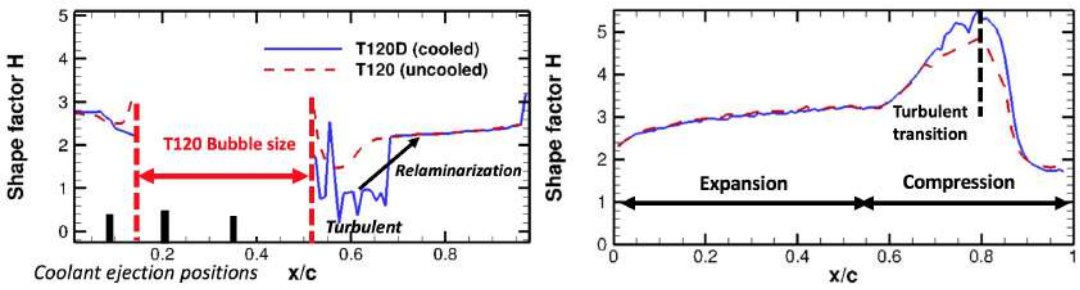

(a) (b)

Figure 4.22 – Shape factor H [-] at mid-span of the CFD domain for the T120D cooled blade (blue) and T120 uncooled blade (red) on the pressure side on left (a) and on the suction side on right (b). Values are omitted in the bubble.

confirming that the ejection of coolant only impacts the pressure side of the blade. The state of the boundary layer is now addressed by plotting the shape factor H on both sides on Fig. 4.22. Note that no values are plotted in coolant ejection region because the boundary layer hypotheses (Schlichting, 1955) are not verified in this region. On the pressure side of the blade, Fig. 4.22 (a), H is around 2.5 for $x/c < 0.15$ confirming that the boundary layer is laminar near the leading edge for both cases. Downstream the bubble region for $0.6 < x/c < 0.7$, H is below 2 for both cases meaning that the boundary layer transits to turbulence. For $x/c > 0.7$, H increases and reaches again a value around 2.5 in both cases corresponding to a relaminarization of the boundary layer as observed in the experiment (Gomes and Niehuis, 2013). Indeed, the strong flow acceleration downstream the bubble stretches and dissipates the turbulent structures as already discussed in Chapter 3. On the suction side, Fig. 4.22 (b), H increases from $x/c = 0.6$ for both cases in the region of adverse pressure gradient. This increase of H in the compression region is coherent with the literature of boundary layer (Schlichting, 1955; Greitzer., 2004). Downstream and from $x/c = 0.8$, H decreases to 1.5 confirming the transition to turbulence of the boundary layer on the suction side. Again, no strong deviations between both cases are observed on the suction side.

As a consequence of the previous discussion, the coolant ejection was observed to only affect the pressure side of the blade. In the following, the mean flow structure of jets is described.

Mean coolant jet flow structure

To evidence the mean flow structure of coolant jets, an iso-surface of the time-averaged coolant mass fraction equal to $\overline{Y_{coolant}} = 0.5$ is shown in the coolant jet region on Fig. 4.23. On the side view, Fig. 4.23 (a), the jets issued by the first and second rows are clearly observed to be detached from the wall. It is noted that these jets penetrate strongly in the main flow. The jet issued from the third row is found to be slightly detached to the wall as observed by (Duchaine et al., 2009a). If looking at the bottom view, Fig. 4.23 (b), the direction of the jets

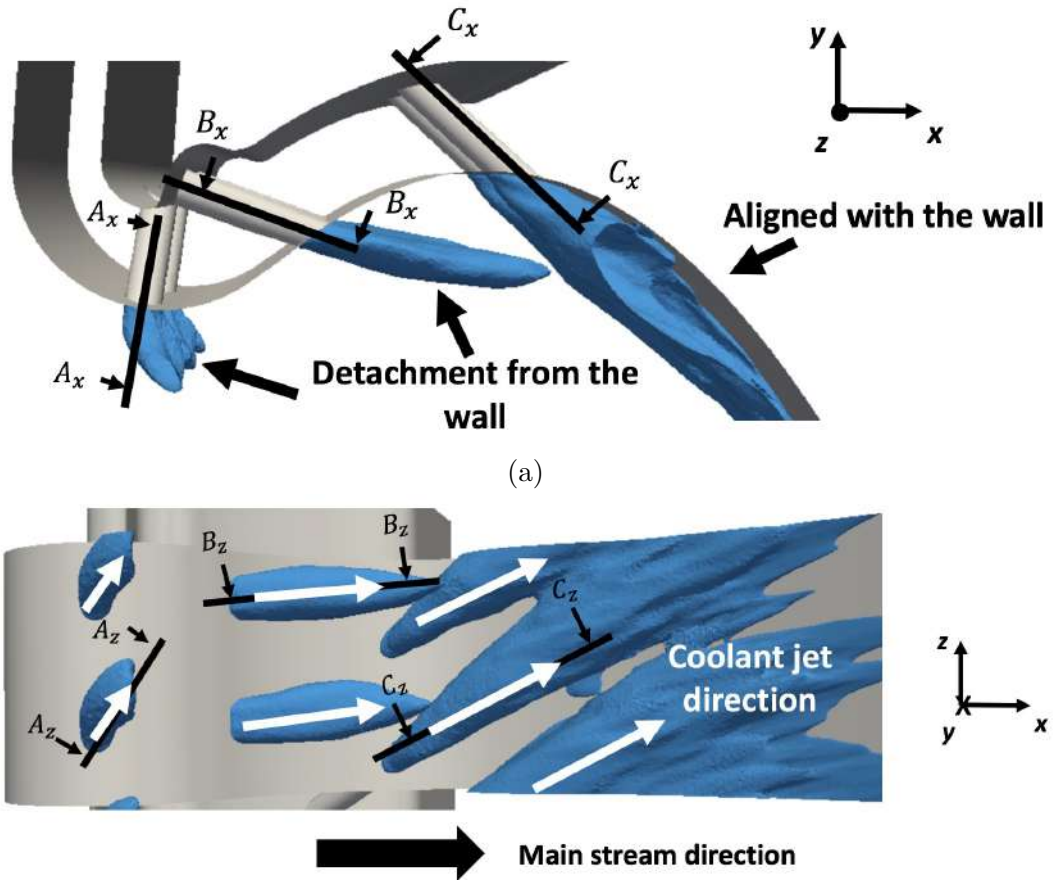

Figure 4.23 – Iso-surface of the time-averaged of the coolant mass fraction $\overline{Y_{coolant}} = 0.5$. Side view on left (a) and bottom view on right (b). White arrows show the direction of the coolant jets. Different cut planes are defined by A, B and C.

clearly differs from the main stream direction. Indeed, the coolant jets deviate in the span direction (z) because of the orientation of holes. The jets issued from the third row are observed to be strongly spread in the span direction as also noticed in the experiment (Gomes and Niehuis, 2011). This can indicate a strong mixing process with the hot flow downstream the holes.

The flow structure in the pipes is now addressed. To investigate the flow in the pipes, different cuts are performed for each row respectively noted A, B and C. These cuts are performed normal to the principal axes of the pipes respectively noted $\bullet_x$ and $\bullet_z$ as represented on Fig. 4.23 (a). On these cuts, time-averaged velocity magnitude $\overline{\mathbf{v}}$ and turbulent kinetic energy k are extracted. The cuts corresponding to the first row, i.e, cuts $A_x - A_x$ and $A_z - A_z$ are shown on Fig. 4.24. Note that streamlines are added for the cut $A_x - A_x$ to evidence potential recirculation bubbles. On the cut $A_x - A_x$, Fig. 4.24 (a), a low velocity region is observed in the pipe and is associated with a deviation of the streamlines. This low velocity region corresponds to a recirculation bubble created by the separation of the

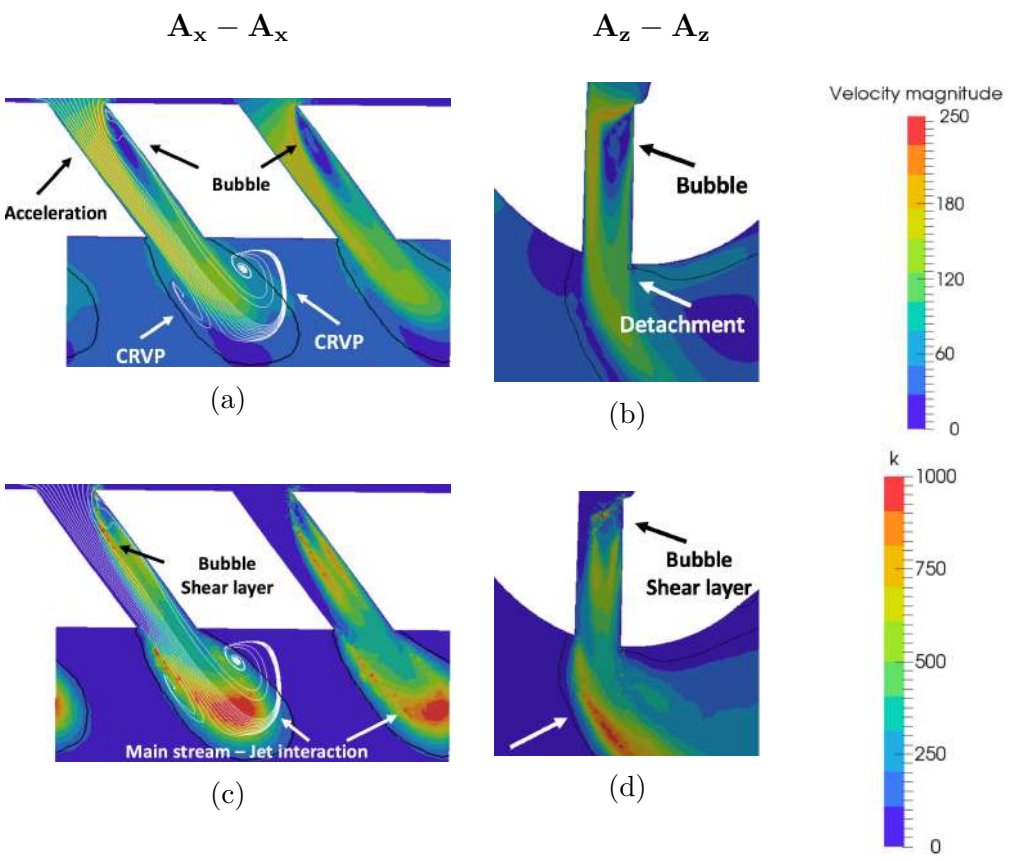

Figure 4.24 – Mean velocity magnitude $\overline{\mathbf{v}}$ $[m/s]$ at top (a)&(b) and turbulent kinetic energy k $[m^2/s^2]$ at bottom (c)&(d) on $A_x - A_x$ on left (a)&(c) and $A_z - A_z$ on right (b)&(d). White lines show the streamlines and black line iso-contour $\overline{Y_{coolant}} = 0.05$.

boundary layer at the corner between the pipe and the plenum walls (Leylek and Zerkle, 1994). The bubble reduces the passage section in the pipe leading to an acceleration of the flow. In the jets, Counter Rotating Vortex Pair (CRVP) are observed and are generated from the interaction between the coolant jet and the mainstream flow (Fric and Roshko, 1994; New et al., 2003). On the cut $A_z - A_z$, Fig. 4.24 (b), the bubble is retrieved meaning that the bubble has a 3D shape in the pipe. Downstream, the jets are clearly detached off the wall. If looking at turbulent kinetic energy k, Fig. 4.24 (c) & (d), turbulence is clearly produced by the strong shear present at the edge of the bubble and in the jets. Next, the flow in the second row of holes (shaped-holes) is shown on Fig. 4.25. On the cut $B_x - B_x$, Fig. 4.25 (a), large recirculation bubbles are also observed in the pipes. Contrary to the previous holes, the mean flow structure is observed to be symmetric with respect to the axis of the pipe. Bubbles reduce the flow passage and act as a venturi effect which accelerates the flow in-between. Downstream, the expansion part of the shaped-hole produces an adverse pressure gradient and generates small bubbles on the pipe wall. If looking at the cut $B_z - B_z$, Fig. 4.25 (b), bubbles are also retrieved. The jets issued from these holes are also found to be detached off the wall. If looking at turbulent kinetic energy k, Fig. 4.25 (c) & (d), turbulence

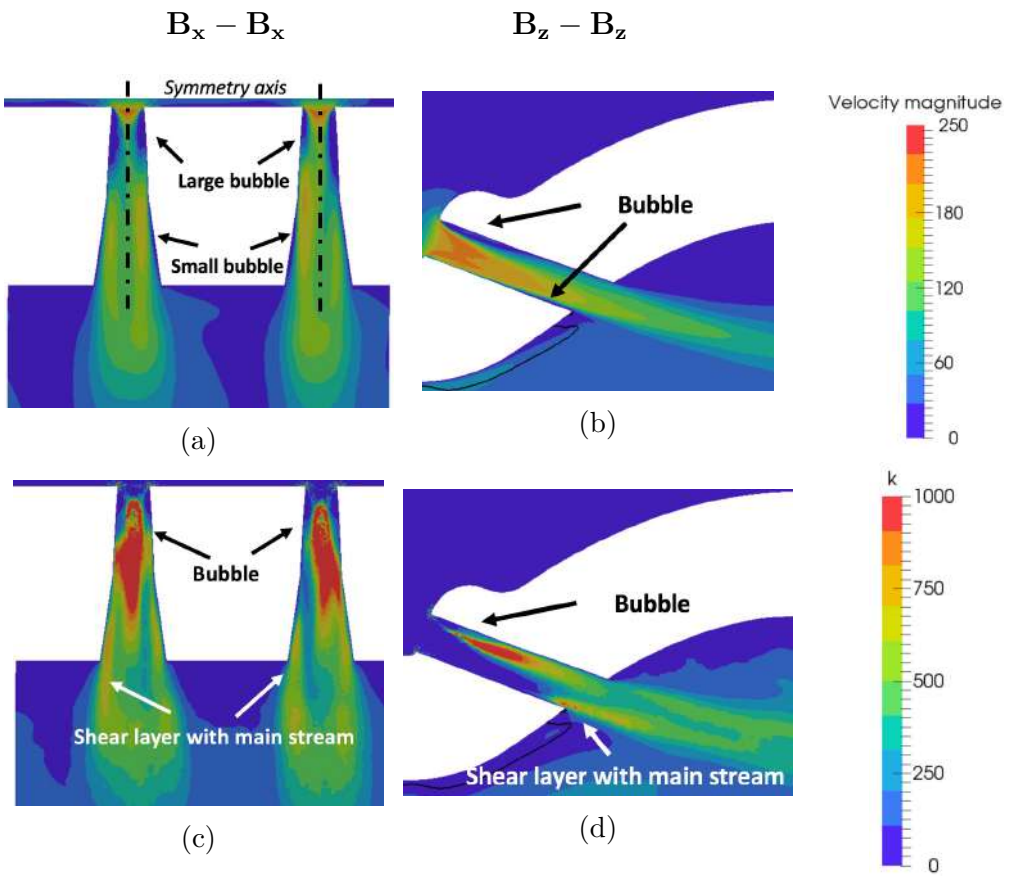

Figure 4.25 – Mean velocity magnitude $\overline{\mathbf{v}}$ $[m/s]$ at top (a)&(b) and turbulent kinetic energy k $[m^2/s^2]$ at bottom (c)&(d) on cuts $B_x - B_x$ on left (a)&(c) and $B_z - B_z$ on right (b)&(d). Black line shows iso-contour $\overline{Y_{coolant}} = 0.05$.

is confirmed to be generated at the edge of bubbles and in the jets as previously observed for the first row of pipes. Finally, the flow structure in the third row of pipes is shown on Fig. 4.26. The mean flow field and turbulent maps are found to be very similar as the first row and same conclusions are thus drawn. This specific flow structure described above corroborates experimental and numerical studies of (Leylek and Zerkle, 1994; Peet and Lele, 2008; Simiriotis, 2016; Bizzari, 2018). Such a flow structure in pipes is expected to yield non-symmetric flow field on the ejection surface at the exit of the pipes. To confirm, the time-averaged velocity magnitude and turbulent kinetic energy maps are extracted on the ejection surface for the three row of pipes and given on Fig. 4.27. Since no strong deviation was observed between the holes of each row, only one hole for each row of pipe is shown. For all jets, Figs. 4.27 (a) & (b) & (c), the mean flow has a horse-shoe pattern evidencing a strong sheared flow. The second jet issued from the shaped-hole presents a symmetric flow field with respect to a symmetric axis. These specific shapes corroborate profiles found in experimental and numerical studies (Leylek and Zerkle, 1994; Peet and Lele, 2008). If looking at the k maps, Figs. 4.27 (d) & (e) & (f), turbulence mainly localizes in the sheared region of the profiles underlying the potentially highly unsteady nature of jets.

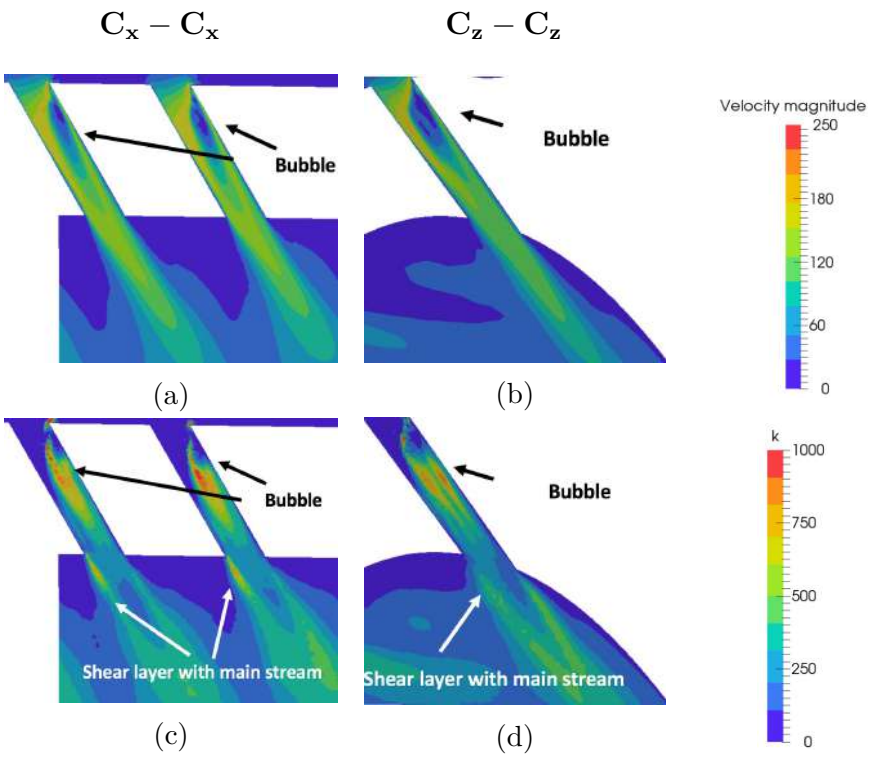

Figure 4.26 – Mean velocity magnitude $\overline{\mathbf{v}}$ $[m/s]$ at top (a)&(b) and turbulent kinetic energy k $[m^2/s^2]$ at bottom (c)&(d) on cuts $C_x - C_x$ on left (a)&(c) and $C_z - C_z$ on right (b)&(d).

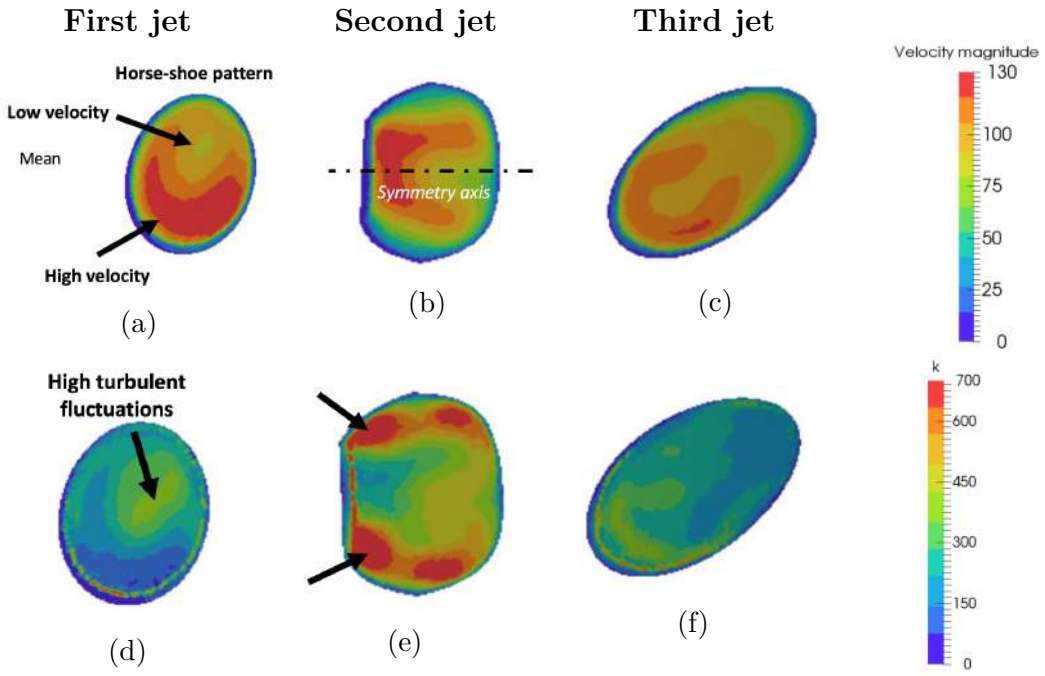

Figure 4.27 – Mean velocity magnitude $\overline{\mathbf{v}}$ $[m/s]$ at top and turbulent kinetic energy k $[m^2/s^2]$ at bottom for the three jets.

Such jet aerodynamic structures are expected to affect the coolant film development along the pressure side of the blade. In the following, the mean film development is specifically addressed.

Description of the coolant film

To investigate the film development along the pressure side of the blade, the film volume must be first extracted from the LES. Similarly to boundary layer extraction methodologies, the film thickness δ_f is defined as the wall normal distance for which the arbitrary value $\overline{Y_{coolant}} = 0.05$ is reached. With this definition, it is worth to note that δ_f represents the thickness of the mean film and does not necessary correspond to the mean of instantaneous film thickness. The mean film obtained through this approach is shown on Fig. 4.28. The film thickness is observed to increase from the hole positions. On the side view, Fig. 4.28 (a), traces of jets are observed in the film. Downstream the coolant ejection region, the film is observed to be stretched by the flow acceleration. If looking at the bottom view, Fig. 4.28 (b), traces of jets issued by the first row are clearly identified. From the drawn black line, all the span-extent of the blade wall is covered by the film. Downstream, an uniformization of the film thickness in span is observed. To quantify the axial evolution of the film thickness, δ_f is span-averaged and results are plotted on Fig. 4.29. From the position of the first row located at $x/c = 0.08$, δ_f increases due to the ejection of coolant to $x/c = 0.3$. It is noted that δ_f grows rapidly in this region. This effect is explained by the fact that the concave shape of the wall naturally increases the distance from the first jet. Then, δ_f presents a plateau between $x/c = 0.3$ and $x/c = 0.4$. This interval corresponds to the maximum penetration of the coolant jets in the main stream. From $x/c = 0.45$, δ_f decreases which indicates that the film reattaches to the wall. For $x/c > 0.6$, δ_f still decreases due to the flow acceleration which stretches the film.

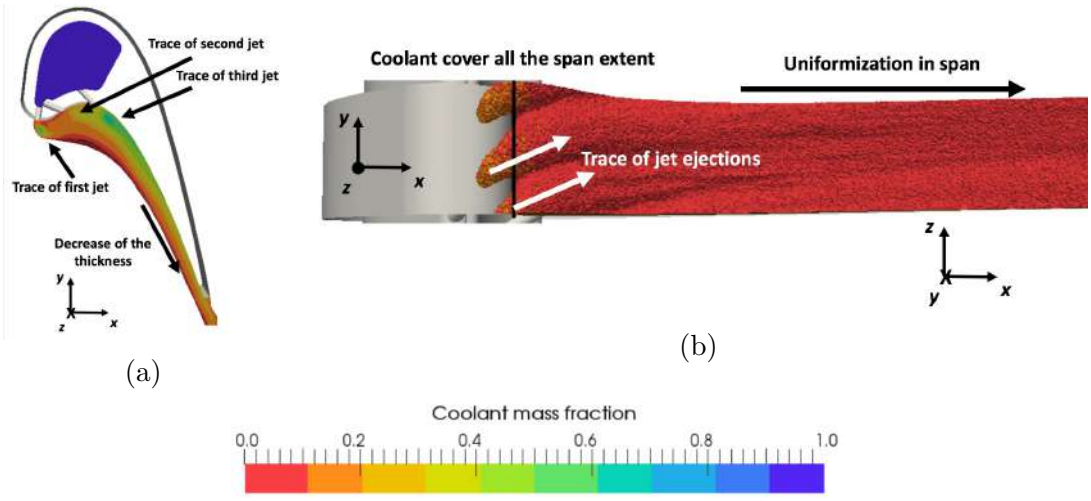

Figure 4.28 – Time-averaged coolant mass fraction $\overline{Y_{coolant}}$ [-] in the film thickness. Side view on left (a) and bottom view on right (b).

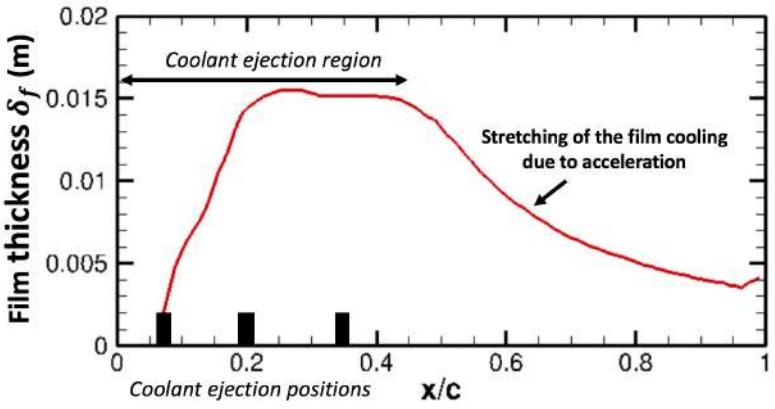

Figure 4.29 – Axial evolution of the span-averaged film thickness δ_f $[m]$.

The coolant mass fraction spatial distribution in the film is now investigated. To do so, a detailed view of the mean and RMS fields of $Y_{coolant}$ in the coolant ejection region is extracted on the cut $B_z - B_z$ and provided on Fig. 4.30. From the mean flow field, Fig. 4.30 (a), the jets issued from the first and second rows are observed to be detached off the wall confirming previous findings. This jet detachment leads to a coolant free region downstream the first jet. A low coolant concentration region is also observed downstream the second jet as observed in the experiment (Gomes and Niehuis, 2011). From the third jets, the coolant film reattaches to the wall. The RMS of $Y_{coolant}$, Fig. 4.30 (b), represents the impact of unsteady effects on the mixing process between the coolant and hot streams. Turbulent mixing is shown to be mainly activated in the jets. It is noted that levels of Y_{rms} are higher in the detached jets compared to the attached film region. Indeed, more turbulent activity was observed around the detached jets on Fig. 4.17. In the region where the film remains attaches to the wall, turbulent mixing is probably

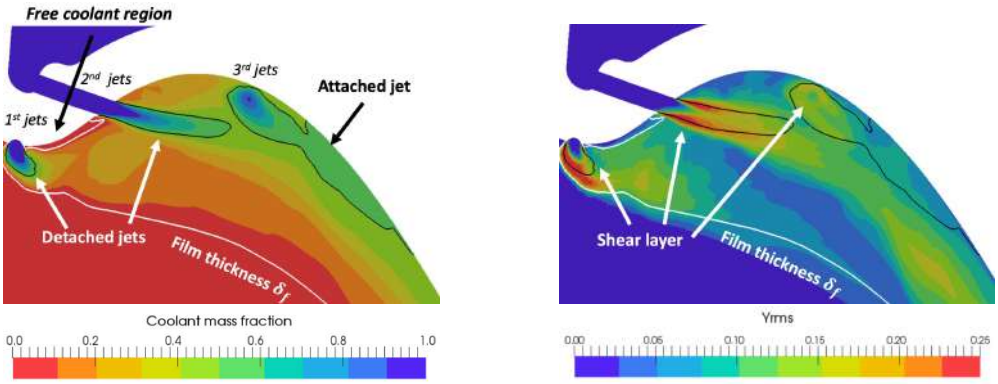

(a) (b)

Figure 4.30 – Time averaged coolant mass fraction $\overline{Y_{coolant}}$ [-] on left (a) and temporal Root Mean Square Y_{rms} [-] on right (b) on the cut $B_z - B_z$. White iso-line represents the film thickness δ_f and black iso-line the iso-contour $\overline{Y_{coolant}} = 0.5$.

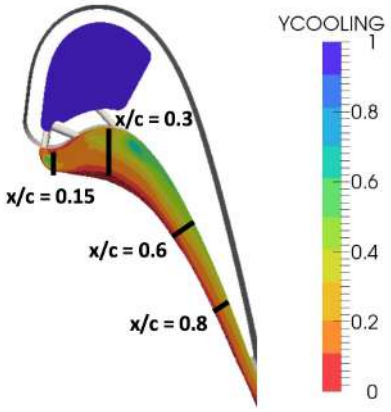

Figure 4.31 – Position of the extracted normal profiles of coolant mass fraction. White iso-line represents the thickness of the film δ_f.

the reason for the span uniformization previously observed on Fig. 4.28. To go further in the analysis, wall normal span-averaged profiles of $\overline{Y_{coolant}}$ and Y_{rms} are extracted at different axial positions in the film: i.e, downstream the first row of holes at $x/c = 0.15$, downstream the second row of holes at $x/c = 0.30$, downstream the reattachment point at $x/c = 0.60$ and finally at $x/c = 0.80$ as presented on Fig. 4.31. Normal profiles are plotted against the wall distance n normalized by the local film thickness $\delta_f(x/c)$ on Fig. 4.32. At $x/c = 0.15$, Fig. 4.32 (a), the passive scalar profile presents a peak at $n/\delta_f = 0.4$ corresponding to the maximum center-line value. If the detachment distance is defined as the wall normal distance where $Y_{coolant}$ is maximum, this peak confirms that the jets are detached from the wall for this axial position. The RMS profile also exhibits a peak near $n/\delta_f = 0.4$

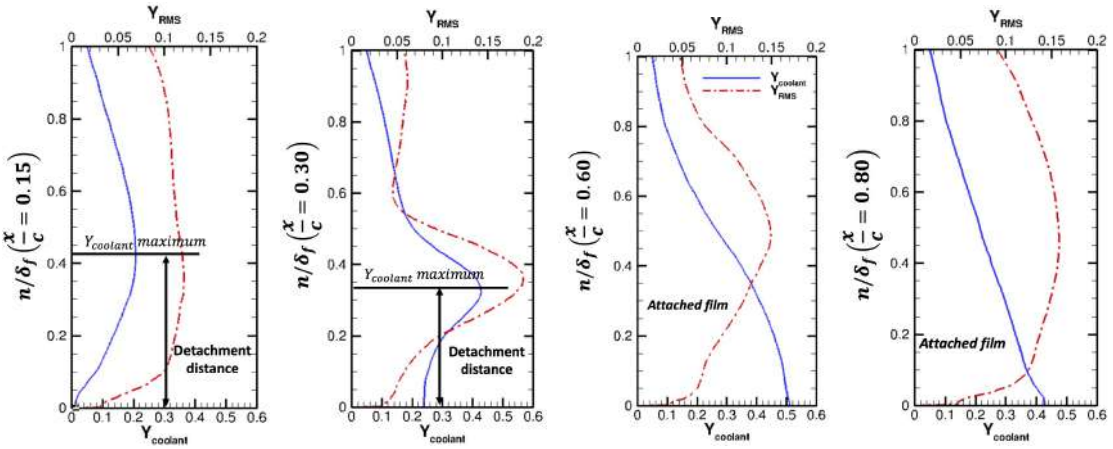

Figure 4.32 – Wall normal span-averaged profile of $Y_{coolant}$ [-] (solid blue line $-$) and Y_{rms} [-] (red dashed line $--$) located at $x/c = 0.15$, $x/c = 0.30$, $x/c = 0.60$ and $x/c = 0.80$ in the span-averaged film. n/δ_f represents the normal distance n to the wall normalized by the local film thickness $\delta_f(x/c)$.

and then decreases when naturally approaching the wall due to viscous effects when penetrating the boundary layer. At $x/c = 0.3$, Fig. 4.32 (b), the detachment distance is reduced compared to the previous position. Although the jets are still detached from the wall at this position, the level of $Y_{coolant}$ at the wall has increased thanks to turbulent mixing which spreads the coolant from the first detached jets to the wall. Indeed, the RMS profile reaches a peak corresponding to the detachment distance of jets, confirming that turbulent mixing mainly occurs in the detached jets. At $x/c = 0.60$, Fig. 4.32 (c), the coolant maximum value is located at wall confirming that the film is attached to the wall for this position. The RMS profile is located further from the wall near $n/\delta = 0.6$. At $x/c = 0.80$, Fig. 4.32 (d), the slope of the mean profile is lower than the previous position due to the effect of the mixing process on the spatial distribution of $Y_{coolant}$. Indeed, the level of the RMS profile shows that turbulent mixing process still occurs at this position.

As a result of the previous discussion, the coolant jet structure is complex presenting detachments and reattachments along the pressure side of the blade. The effect of such coolant flow structures on wall stresses and temperature is now investigated.

Effect of coolant jets on wall stresses and temperature

First, time-averaged wall shear stress $\overline{\tau_w}$ map is shown along the pressure side of the blade on Fig. 4.33. Zero wall shear stress iso-contour is added to evidence potential recirculation bubbles. The stagnation line is clearly identified by the zero wall shear stress iso-contour near the leading edge at $x/c = 0.06$. Downstream, a local increases of the wall shear stress is observed in-between the holes of the first row near $x/c = 0.08$. This effect is explained by the fact that jets issued from these holes probably act as an obstacle for the flow upstream which accelerates the main stream to by-pass the jets. Downstream the first row, a short recirculation bubble

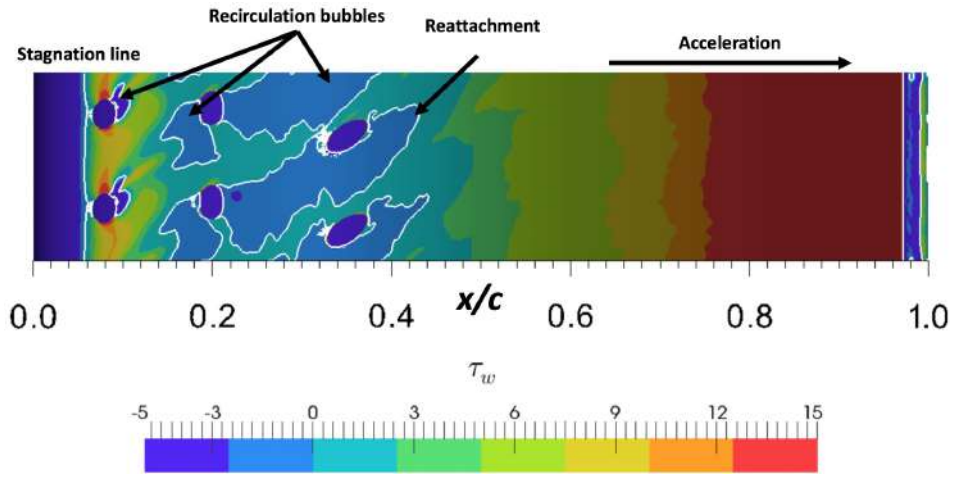

Figure 4.33 – Time-averaged wall shear stress $\overline{\tau_w}$ $[Pa]$ on the pressure side of the blade. White iso-line represents zero shear stress.

is observed near $x/c = 0.1$. Then, a second bubble is noticed upstream the second holes between $x/c = 0.15$ and $x/c = 0.2$. Downstream the second row, recirculation bubbles are also observed. These recirculation bubbles originate from the separation of the boundary layer due to coolant ejection. Indeed, the jets issued from these holes are assumed to have a strong potential effect on the upstream flow leading to an adverse pressure gradient and separation of the boundary layer. Downstream from $x/c = 0.45$, $\overline{\tau_w}$ becomes positive meaning that the boundary layer reattaches to the wall. For $x/c > 0.45$, the flow acceleration increases the wall shear stress. it is finally noted that $\overline{\tau_w}$ tends to be more uniform in span from this position corroborating previous findings.

The wall normal stress is now addressed and represented by the pressure distribution on the wall. To do so, the pressure coefficient C_P is plotted on Fig. 4.34 on the pressure side and compared to experimental results. Note that the plot is limited to the coolant ejection region from $x/c = 0$ to $x/c = 0.6$. The peak located at $x/c = 0.05$ corresponds to the stagnation point. In the interval between $x/c = 0.1$ and $x/c = 0.45$, C_P increases indicating a compression region. This compression region is then expected to induce an adverse pressure gradient which confirms the presence of recirculation bubbles observed in this region. At $x/c = 0.45$, the maximum value of C_P on the pressure side is reached and corresponds to the reattachment of the boundary layer and impact of jets on the wall (Gomes and Niehuis, 2011). For $x/c > 0.45$, C_P decreases confirming the acceleration of the flow downstream the holes. If comparing to experimental results, C_P is globally under-estimated. This means that the flow expansion and bubbles sizes are probably not perfectly predicted by the LES. To explain this deviation, it is worth to recall that bubbles are shown to be sensitive to freestream turbulence

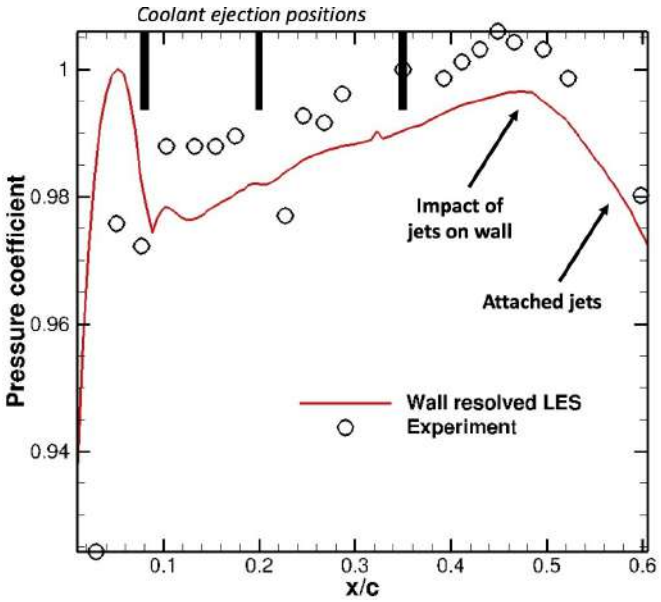

Figure 4.34 – Span averaged C_P [-] on the pressure side of the blade. Black circles **O** represent the experiment data and red solid line – LES results.

as shown in Chapter 3. As a result, deviations with the experiment could originate from the lack of turbulent injection at the inlets of the computation domain. Nevertheless, LES results can be considered satisfactory because deviations are included in the experimental uncertainty of 0.5% (Gomes and Niehuis, 2009).

The adiabatic wall temperature is now addressed. In the following, the wall temperature will be represented by the film effectiveness η defined by Eq. (4.6). Note that the value of the recovery factor r_f in Eq. (4.6) is adapted according to the state of the boundary layer to comply with the experimental methodology. Film effectiveness is provided along the pressure side of the blade on Fig. 4.35. The presence of cooling on the wall is evaluated by plotting the black iso-contour corresponding to $\overline{Y_{coolant}} = 0.01$. Downstream the first row of pipes, the coolant free region is retrieved due to the jet detachment from the wall between $x/c = 0$ and $x/c = 0.18$ and corresponds to zero film effectiveness. From $x/c = 0.18$, although jets are detached, the traces of jets can be identified and η increases. This is explained by the fact that the recirculation bubbles located between $x/c = 0.15$ and $x/c = 0.20$ probably bring back coolant from the second row of holes to this region. Furthermore, the turbulent mixing process observed in this region is supposed to diffuse the coolant to the wall increasing the film effectiveness. This specific effect of detached jets on film effectiveness has already been observed in experimental studies (Zhang and Moon, 2007; Polanka et al., 2000; Gomes and Niehuis, 2011). Near $x/c = 0.45$, the film effectiveness reaches its maximum value due to the impact of jets on wall at this position. For $x/c > 0.45$, the film effectiveness tends to be more uniform in the span direction due to the strong turbulent mixing process which homogenizes the wall temperature. The turbulent mixing process present in this region also mixes the cold with the hot flows which "re-heat" the film and decreases η. To be comparable to the experiment results, the film effectiveness is here span-averaged and normalized by its maximum values. Span-averaged results for the experiment, LES and RANS predictions are shown on Fig. 4.36. For the LES, film effectiveness begins to increase from $x/c = 0.15$. Downstream, the film

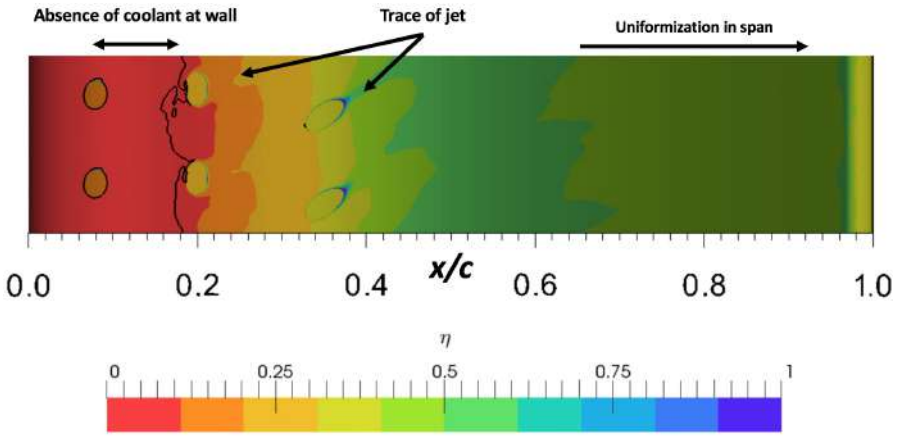

Figure 4.35 – Map of the film effectiveness η [-] along the pressure side of the blade. Black iso-contour represents the iso-contour $\overline{Y_{coolant}} = 0.01$.

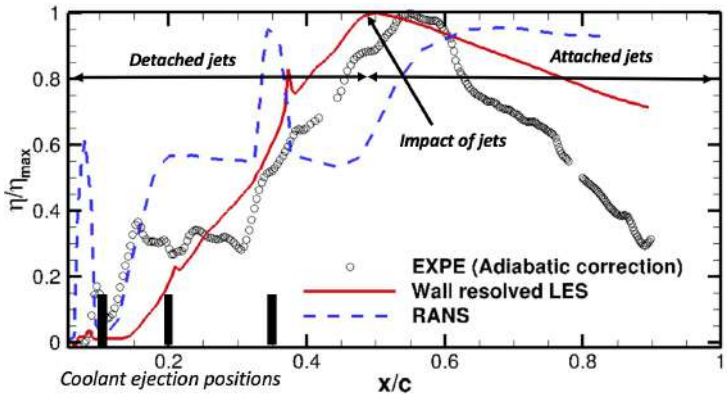

Figure 4.36 – Span-averaged film effectiveness axial evolution η/η_{max} [-] normalized by the peak value. Black circles O are the experiment data, red solid line – is the WRLES and blue dashed line – – – RANS (Gomes and Niehuis, 2011).

effectiveness increases almost linearly between $x/c = 0.15$ and $x/c = 0.45$. At this position, the maximum of efficiency is reached due to the impact of jets on wall. For $x/c > 0.45$, the film effectiveness decreases in agreement with the map of Fig. 4.35. If the LES prediction is compared to experimental results, deviations are mainly observed in the jet regions. However, it is important to recall that experimental data in this region suffer from strong uncertainties. Indeed, the recovery factor r_f of Eq. (4.7) is experimentally difficult to define in the jet regions because the boundary layer is partially separated from the wall. The comparison between results is then not relevant in the jet regions. Downstream, for $x/c > 0.45$, despite deviations are observed with the experiment, results are satisfactory. Deviations with the experiment suggest that the mixing process between the coolant and hot streams is not perfectly captured by the LES. Again, the lack of freestream turbulence could explain such differences with the experiment. Finally, when compared to RANS, LES clearly improves the prediction.

To conclude this section, the mean flow organization around the T120D blade is found to be very similar to the uncooled T120 blade. Indeed, similar flow structure and boundary layer evolutions are found between both configurations if excluding the coolant ejection region. On the pressure side of the blade, the jets are observed to be detached from the wall. The investigation of the flow field in the coolant pipes shows such jet structures originate from separations and recirculation bubbles present in the pipes. Such a flow structure in the pipe is found to generate a strong turbulent activity. This turbulent activity tends to increase the film effectiveness in the detached jets, by spreading the coolant from the jets to the wall. Downstream, when film is reattached to the wall, the coolant flow still mixes with the hot stream, decreasing the film effectiveness. Such a behaviour of film presenting detached jets is coherent with literature findings (Zhang and Moon, 2007; Polanka et al., 2000; Gomes and Niehuis, 2011). To further analyse the evolution of the film effectiveness along the pressure side of the blade, the mixing process in the coolant film is specifically investigated in the next section.

4.3.2 Investigation of the mixing process in the film

In this section, the mixing process in the coolant film is investigated. To simplify the investigation, the 3D time-averaged flow fields are first span-averaged to fall the dependency in span and to obtain a 2D view of the flow. To do so, different cuts are extracted at different height of the blade and interpolated on the mid-span mesh of the domain. Then, values obtained on the mid-span mesh are span-averaged. The resulting 2D mass fraction map obtained from this span-average is displayed in Fig. 4.37. The mark of jets is retrieved on the 2D view as well as the evolution of the film thickness. To ensure the continuity of the coolant mass fraction in the film thickness, the coolant free region located near the leading edge will be excluded from the following analysis. From such a 2D view, the coolant concentration in the film can be represented by the mass flow weighted film coolant mass fraction Y_{film} defined for each axial position x so that,

$$Y_{film}(x) = \frac{\int_0^{\delta_f(x)} \overline{\rho U_i n_i Y_{coolant}} dn}{\int_0^{\delta_f(x)} \overline{\rho U_i n_i} dn}, \tag{4.9}$$

where n is the wall normal distance, ρ the density, U_i the local velocity vector, n_i the normalized vector tangential to the wall and $\overline{\bullet}$ the time-averaged operator. The axial evolution of Y_{film} is provided along the pressure side of the blade on Fig. 4.38. Note that the profiles are taken sufficiently far from each other in the concave region of the blade to avoid any intersections between the wall normals. Y_{film} begins to increase from the hole positions for $x/c = 0.05$. Downstream, Y_{film} decreases from $x/c = 0.1$ to $x/c = 0.2$ meaning that less coolant is present in the

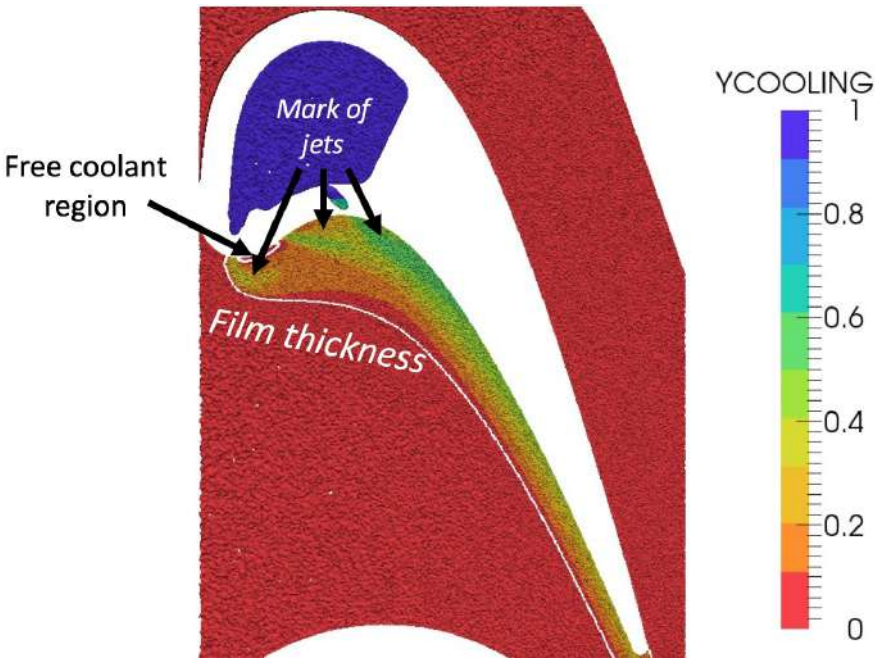

Figure 4.37 – Span-averaged $Y_{coolant}$ [-] 2D map shown on the mid-span mesh. White iso-line represents the film thickness δ_f.

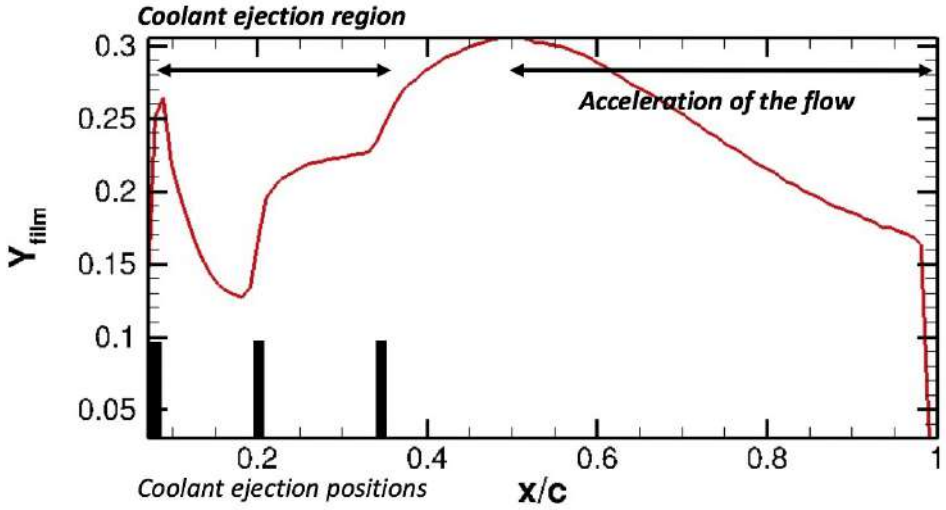

Figure 4.38 – Evolution of the mass flow weighted film coolant mass fraction Y_{film} [-] in the span-averaged film along the pressure side of the blade.

film. From this location at $x/c = 0.2$, Y_{film} increases again due to the coolant ejection from the second and third row of holes to a peak located at $x/c = 0.5$. From this location, Y_{film} decreases due to the mixing process with the hot stream. To investigate such an evolution of Y_{film} along the pressure side of the blade, a coolant mass balance is performed in the span-averaged film. To perform such a balance, a control volume must be wisely defined. The control volume retained for this work, here noted V_{film}, corresponds to the film volume bounded by the walls S_{wall}, by the ejection surfaces S_{cold}, by the film thickness S_δ and by a moving section $S_{film}(x)$ normal to the wall. The control volume is represented on Fig. 4.39. It is important to note that the control volume is built from the 2D map obtained from

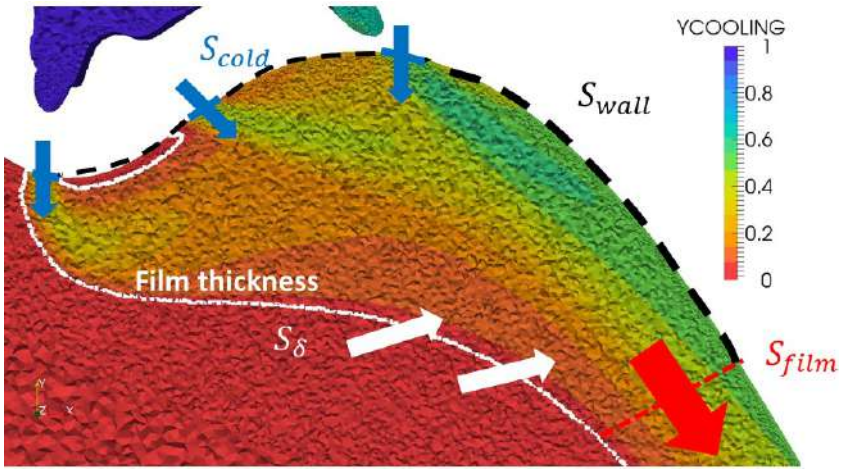

Figure 4.39 – Control volume V_{film} to apply the mass balance in the span-averaged film. The control volume is delimited by the sections corresponding to the ejection exit of the coolant pipes S_{cold}, the walls S_{wall}, the film thickness S_δ and the film section S_{film}.

the span-averaged process. Using such a control volume thus reduces the mass balance to a 2D space which makes the balance easier to apply. For a statistically converged flow, the mass balance of $Y_{coolant}$ in the control volume gives,

$$\overline{\int_{S_{film(x)}} \rho U_i Y_{coolant} n_i dS} = -\overline{\int_{S_{\delta(x)}} \rho U_i Y_{coolant} n_i dS} - \overline{\int_{S_{cold}} \rho U_i Y_{coolant} n_i dS}, \quad (4.10)$$

where ρU_i is the local mass flux, n_i is the surface normal pointing by definition out of the volume and $\overline{\bullet}$ the time-averaged operator. Equation (4.10) shows that the mass flux through $S_{film}(x)$ (LHS) depends on the coolant mass flux through the hole sections S_{cold} and through the film thickness $S_\delta(x)$ (RHS). To simplify the expression of Eq. (4.10), several hypotheses are hereafter introduced. First, since the balance is realized on a purely 2D flow, the section $S_{film}(x)$ exactly corresponds to the film thickness $\delta_f(x)$. Using Eq. 4.9, the first term on the RHS of Eq. (4.10) can be then replaced by $Q_{m,film} Y_{film}$ where $Q_{m,film}$ is the mass flow rate passing through S_δ. Assuming that the map of $Y_{coolant}$ on the coolant ejection surfaces S_{cold} is stationary, uniform and equal to 1, the second term of the RHS of Eq. (4.10) can be replaced by the coolant mass flow rate $Q_{m,cold}$. From the previous discussion, Eq. (4.10) is re-arranged to make appear the axial evolution of $Y_{film}(x)$ in the mass balance so that,

$$Y_{film}(x) = \frac{1}{Q_{m,film}} \left(Q_{m,cold} - \int_{S_{\delta(x)}} \overline{\rho U_i Y_{coolant}} n_i dS \right). \quad (4.11)$$

This last expression shows that the coolant concentration in the film $Y_{film}(x)$ depends on two contributions. The first contribution (first term on the RHS) corresponds to the coolant mass flux provided from the holes. This term is necessarily positive because no-reingestion of hot flow by the pipes was observed. The second contribution (second term the RHS) corresponds to the coolant mass flux through S_δ and its sign is a priori not known. Using the Reynolds decomposition and Favre (1969) averaging (denoted $\breve{\bullet}$), this last contribution can be split in a mean and turbulent contributions so that,

$$\int_{S_{\delta(x)}} \overline{\rho Y_{coolant} U_i} n_i dS = \underbrace{\int_{S_{\delta(x)}} \overline{\rho} \widetilde{Y_{coolant}} \breve{U}_i n_i dS}_{\text{Mean field contribution}} + \underbrace{\int_{S_{\delta(x)}} \overline{\rho} \widetilde{Y''_{coolant} U''_i} n_i dS}_{\text{Resolved turbulence contribution}} . \quad (4.12)$$

$\widetilde{Y''_{coolant} U''_i}$ corresponds to the resolved turbulent coolant mass diffusion and $''$ the temporal fluctuations with respect to the Favre averaging. The first term on the RHS represents the mass flux resulting from the mean flow topology and then depends on the alignment between the normal of S_δ and the mean velocity vector $\breve{U}_i$. When the film is attached and remains tangential to the wall, the velocity vector $\breve{U}_i$ can be considered aligned with the film thickness. As a result, $\breve{U}_i$ can be reasonably considered as normal to the normal of S_δ. From this hypothesis, the mean contribution in Eq. (4.12) is then neglected with respect to the resolved turbulence contribution. If combining Eq. (4.12) with Eq. (4.11), the mass balance

finally reads as,

$$Y_{film}(x) = \frac{1}{Q_{m,film}} \left(Q_{m,cold} - \underbrace{\int_{S_{\delta(x)}} \overline{\rho} \widetilde{Y''_{coolant} U''_i} n_i dS}_{\text{Turbulent mass flux}} \right). \tag{4.13}$$

As a consequence of the previous discussion, the axial evolution of $Y_{film}(x)$ results from the coolant mass flux from the pipes (first term on RHS) and from the turbulent mass flux through the external limit of the film (second term on RHS). To investigate this last turbulent contribution, axial evolution of the local turbulent mass flux $\overline{\rho} \widetilde{Y''_{coolant} U''_i} n_i$ and integrated value $\int_{S_{\delta(x)}} \overline{\rho} \widetilde{Y''_{coolant} U''_i} n_i dS$ along the film thickness are plotted on Fig. 4.40. From such a plot, $\widetilde{Y''_{coolant} U''_i} n_i$ is observed to rapidly grow to a peak located at the position of the first row and then decreases to $x/c = 0.4$. This confirms that the turbulent mixing process originates from the jets issued by the firs row of pipes. Then from $x/c = 0.45$ to $x/c = 0.7$, the local turbulent flux slightly increases corresponding to the reattachment region of the coolant film to the wall. Finally, the local turbulent flux stabilizes. It is worth to note that all along the film thickness, $\widetilde{Y''_{coolant} U''_i} n_i$ and its integral value remain positive. From Eq. (4.13), this confirms that the turbulent mass flux necessarily decreases the level of Y_{film} along the pressure side of the blade. To find the origin of this turbulent flux in the film, the second term on the RHS of Eq. (4.12) can be re-arranged using the Green-Ostrogradski theorem so that,

$$\underbrace{\int_{S_{\delta(x)}} \overline{\rho} \widetilde{Y''_{coolant} U''_i} n_i dS}_{\text{Turbulent flux through film thickness}} = \underbrace{\int_{V_{film}} \frac{\partial \left(\overline{\rho} \widetilde{Y''_{coolant} U''_i} \right)}{\partial x_i} dV}_{\text{Divergence term}} - \underbrace{\int_{S_{film}} \overline{\rho} \widetilde{Y''_{coolant} U''_i} n_i dS}_{\text{Turbulent flux on } S_{film}}. \tag{4.14}$$

This last expression shows that the turbulent mass flux through the film thickness S_δ results from the turbulent mass flux through S_{film} and from the turbulent mass

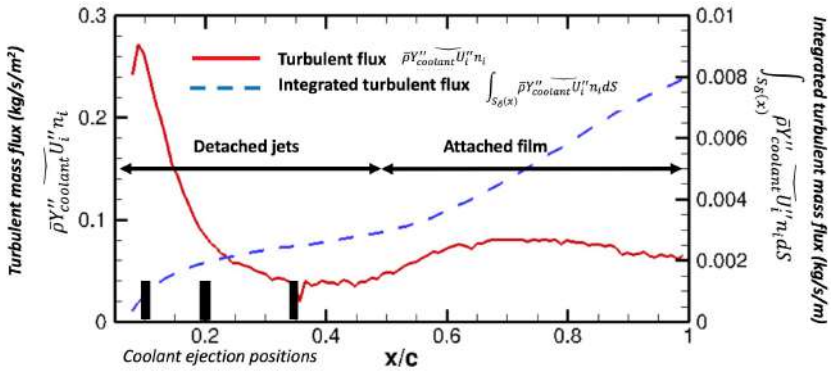

Figure 4.40 – Axial evolution of the turbulent flux $\widetilde{Y''_{coolant} U''_i} n_i$ $[kg/s/m^2]$ (solid red line $-$) and integrated value $[kg/s/m]$ (dashed blue line $--$) along the film thickness surface $S_{\delta(x)}$.

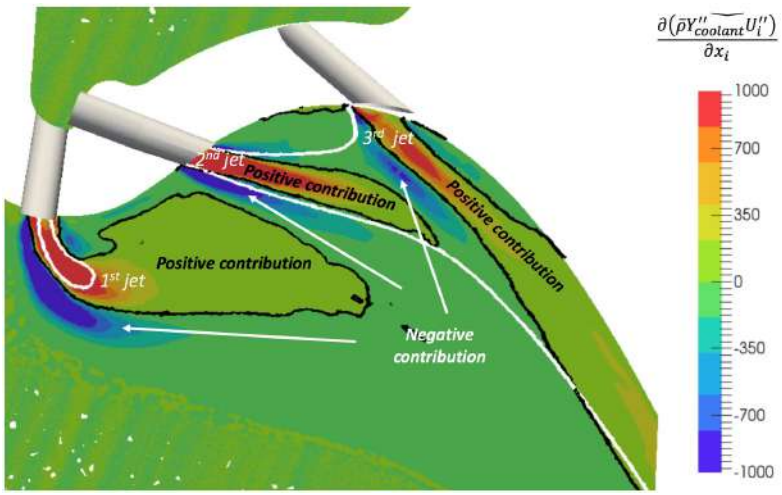

Figure 4.41 – Cross correlation divergence $\frac{\partial(\bar{\rho}\widetilde{Y''_{coolant}U''_i})}{\partial x_i}$ $[kg/s/m^3]$ map in the span-averaged film. White line represents the iso-contour $\overline{Y_{coolant}} = 0.3$ and black line the iso-contour $\frac{\partial(\bar{\rho}\widetilde{Y''_{coolant}U''_i})}{\partial x_i} = 0$.

flux divergence integrated in the film. Note that turbulent fluxes though the ejection pipe surfaces S_{cold} is zero because $Y_{coolant}$ was assumed to be stationary and uniform on S_{cold}. The study of the turbulent mass flux divergence within the film allows to identify regions which contribute to the turbulent mass flux taking place at the edge of the film. From Eq. (4.14), a positive divergence tends to increase the turbulent flux. To identity the regions which contribute to turbulent mass flux, the spatial distribution of the turbulent mass flux divergence $\frac{\partial(\bar{\rho}\widetilde{Y''_{coolant}U''_i})}{\partial x_i}$ in the film is shown on Fig. 4.41. To localize the regions of positive and negative contributions, a black iso-contour corresponding to $\frac{\partial(\bar{\rho}\widetilde{Y''_{coolant}U''_i})}{\partial x_i} = 0$ is added to the view. Note also that a white iso-contour corresponding to $\overline{Y_{coolant}} = 0.3$ is also added to the view to identify the jets. Positive regions are observed to be at the center of jets while negative regions are observed to be in the jet shear layers. It is also noted that the divergence term is stronger in absolute value in the region of detached jets issued from the first and second rows of pipes. This finding means that the turbulent flux on S_δ is mainly driven by the turbulent activity in the detached jets. Indeed, high levels of turbulent kinetic energy and Y_{rms} were observed in this region on Fig. 4.30. Finally, if looking downstream the jets, the divergence term is found to be also positive in the film confirming that turbulent mass flux through S_δ still occurs when the film is attached to the wall.

To conclude this section, a coolant mass balance was performed in the film to find the origin of the mixing process between the coolant and hot flows. The mixing process is found to mainly originate from the turbulent mixing in the region of detached jets. This is confirmed by the activation of Y_{rms} in the jets. This turbulent mixing is shown to mainly originate from the turbulence generated in the pipes and in the jets. This mixing process is also observed to affect the axial

evolution of adiabatic film effectiveness on the blade surface. Comparisons with the experiment shows that LES improves the prediction with respect to RANS. The quality of such LES results is then considered satisfactory to evaluate the losses in the next section.

4.3.3 Investigation of the losses

The mechanisms by which losses are produced for the T120D cooled blade are investigated in this section. To do so, the losses are first evaluated using total temperature and total pressure balance equations introduced in Chapter 2. Losses are then analysed using the Second Law Analysis to identify the sources of the loss generation. Similarly to Chapter 3, advanced decompositions of the loss maps are introduced to link the loss generation to flow physics. Finally, a particular attention will be finally paid to the losses generated in the film.

Assessment of the losses using balance of total variables

As already demonstrated and discussed, the losses can be evaluated using balances of the stagnation variables. To perform such a balance, again a control volume has to be introduced. In the following, the chosen control volume is bounded by the axial section S_{hot} corresponding to the axial section located at the leading edge of the blade, the coolant hole exit surfaces S_{cold} and a moving axial section $S_x(x)$ as presented on Fig. 4.42. To obtain an axial dependency of the balance, $S_x(x)$ will move from S_{hot} to 1.5 axial chords located downstream the trailing edge. First, total temperature balance is performed to capture the effects of multiple coolant

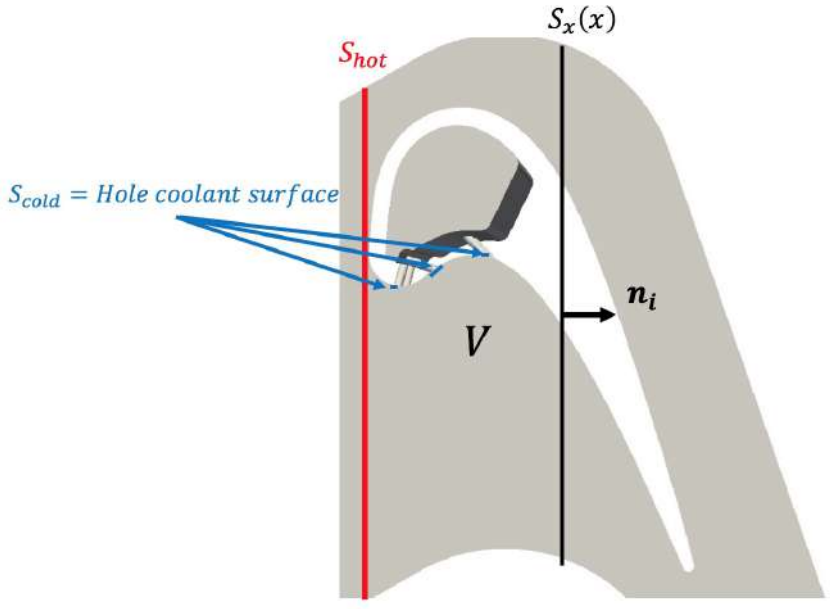

Figure 4.42 – Control volume used to perform total variables balances. The control volume is delimited by the hot flow inlet S_{hot}, the hole coolant sections S_{cold} and a moving axial section S_x.

ejections. Such a balance was derived in Chapter 2 for $C_p = cst$ and is adapted here for coolant ejection so that,

$$\underbrace{Q_m C_p \widetilde{T}_{t,S_x} - Q_{m,hot} C_p \widetilde{T}_{t,S_{hot}} - Q_{m,cold} C_p \widetilde{T}_{t,S_{cold}}}_{Q_m C_p \Delta \widetilde{T}_t} = \underbrace{\iint_{S_x} \overline{U_i \tau_{ij}} n_j dS}_{\text{Viscous flux}} - \underbrace{\iint_{S_x} \overline{q_j} n_j dS}_{\text{Heat flux}}, \tag{4.15}$$

where $Q_{m,hot}$ is the hot mass flow rate from the inlet, $Q_{m,cold}$ is the coolant mass flow rate, Q_m is the mass flow rate on $S_x(x)$ and $\widetilde{\bullet}_S$ is the mass flow average operator introduced in Chapter 2. The LHS of Eq. (4.15) corresponds to total temperature variation between $S_x(x)$, S_{hot} and S_{cold} and is here noted $Q_m C_p \Delta \widetilde{T}_t$ for simplicity. The first term on the RHS of Eq. (4.15) corresponds to viscous fluxes, while the second term corresponds to heat flux though S_x. Similarly to Chapter 3, fluxes at the periodic boundaries conditions necessary cancel and are omitted from the balance. Since such a balance is only applicable to a statistically converged flow, the convergence of the mean fields needs first to be checked. To do so, the mass flux conservation along the blade, i.e, $Q_m = Q_{m,cold} + Q_{m,hot}$ is verified on Fig. 4.43. Clearly, the mass balance closes which ensures that the mean flow is statistically converged. After this verification, balance of total temperature along the blade can be investigated. To do so, axial evolution of total temperature variation $Q_m C_p \Delta \widetilde{T}_t$ is plotted on Fig. 4.44. Upstream the blade, there is not variation because the imposed flow field from the inlet is almost uniform and laminar, i.e, with no turbulence injection. In the region of coolant ejection defined between $x/c = 0.08$ to $x/c = 0.35$, the term $Q_m C_p \Delta \widetilde{T}_t$ increases due to the activation of the flux terms contained in the RHS of Eq. (4.15). Indeed, the temperature difference between the hot and coolant flows necessarily induces a local heat flux. Downstream the coolant rows, i.e, for $x/c > 0.35$, the variation stabilizes around 1.5 W, corresponding to a total temperature variation of 0.1 K which is negligible. As a result and if neglecting this variation, the total enthalpy 1D balance necessary closes for the T120D cooled blade recovering the total enthalpy conservation. Nevertheless, the difference between the hot and coolant temperature is clearly under-estimated on this academic case if compared to real engine where heat flux is expected to be stronger.

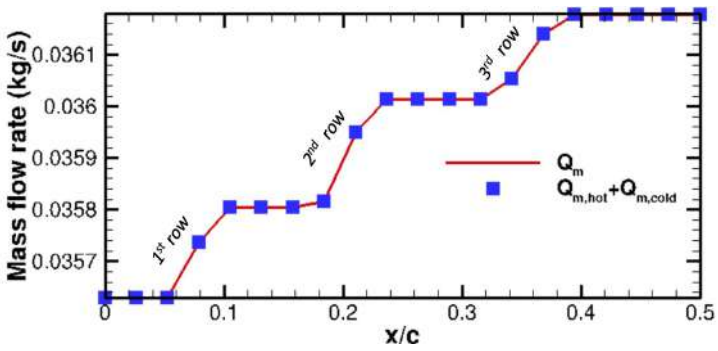

Figure 4.43 – Axial evolution of full mass flow rate Q_m in red line and of the sum of cold and hot mass flow rate $Q_{m,cold} + Q_{m,hot}$ in blue squares along the blade.

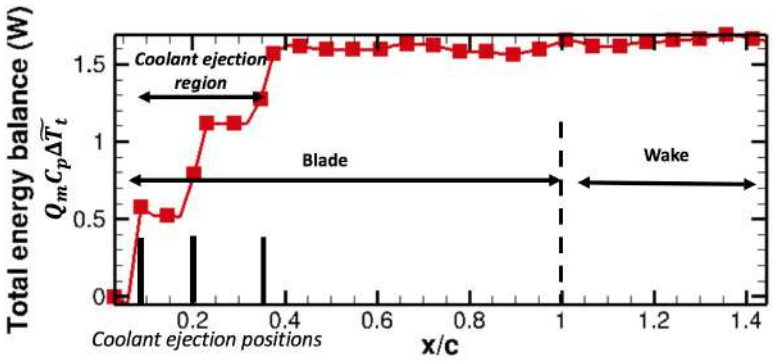

Figure 4.44 – Balance of the total temperature in the control volume defined between the axial section S_{hot} located at the leading edge and S_x a moving axial section from S_{hot} to 1.5 axial chords downstream the trailing edge.

The losses generated by such a system can be evaluated through entropy balance. Such an entropy balance was derived in Chapter 2 for $C_p = cst$ and is here adapted for coolant ejection so that,

$$\underbrace{Q_m C_p \widetilde{Ln(T_t)}_{S_x} - Q_{m,hot} C_p \widetilde{Ln(T_t)}_{S_{hot}} - Q_{m,cold} C_p \widetilde{Ln(T_t)}_{S_{cold}}}_{Q_m C_p \Delta \widetilde{Ln(T_t)}},$$

$$\underbrace{-r\left(Q_m \widetilde{Ln(P_t)}_{S_x} - Q_{m,hot} \widetilde{Ln(P_t)}_{S_{hot}} - Q_{m,cold} \widetilde{Ln(P_t)}_{S_{cold}}\right)}_{-Q_m r \Delta \widetilde{Ln(P_t)}},$$

$$= \underbrace{\int_{V(x)} \frac{\overline{P_m + P_q}}{T} dV}_{\text{Integrated losses}}. \tag{4.16}$$

The first term of the LHS here noted $Q_m C_p \Delta \widetilde{Ln(T_t)}$ represents the entropy variation from the total temperature contribution while the second term here noted $-Q_m r \Delta \widetilde{Ln(P_t)}$ results from total pressure variation. The RHS corresponds to the integration of the entropy source term in the control volume. Note again that fluxes at the periodic boundaries conditions necessary cancel and are omitted in the balance. The axial evolution of both total temperature and total pressure contributions are plotted on Fig. 4.45. From the coolant rows, total pressure contribution $-Q_m r \Delta \widetilde{Ln(P_t)}$ increases all along the axial extent of the blade. Indeed, in this interval, total pressure decreases due to the losses produced in boundary layers and mixing layers (Denton, 1993). From $x/c = 0.8$ to $x/c = 1$, an change of slope in the profile is noticed which corresponds to the turbulent transition of the boundary layer on the suction side of the blade as discussed in Chapter 3. In the wake for $x/c > 1$, the term still increases due to losses generated in the region. The axial evolution of total temperature term $Q_m C_p \Delta \widetilde{Ln(T_t)}$ is very similar to previous results and no new conclusions are drawn. If comparing levels of both terms in

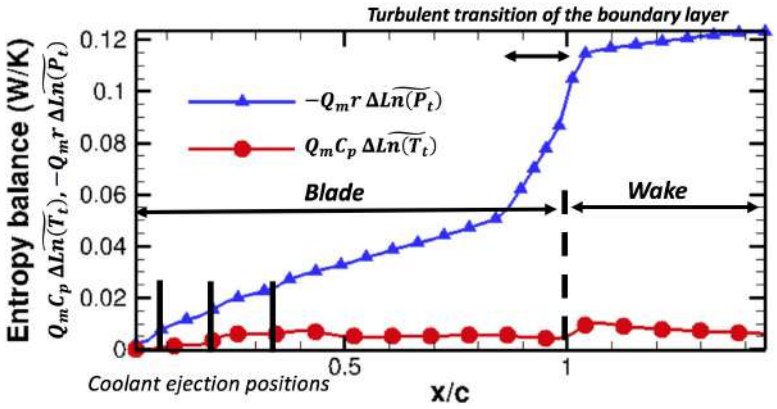

Figure 4.45 – Total temperature and pressure balances in the control volume defined between the axial section S_{hot} located at the leading edge and S_x a moving axial section from S_{hot} to 1.5 axial chords downstream the trailing edge. Red line with circle $-\bullet-$represents the total temperature contrition and blue line with triangle $-\blacktriangle-$ the total pressure contribution to the losses.

the coolant ejection region, total temperature contribution represents about 30% of the entropy balance. Contrary to the uncooled case, the integrated entropy production then results from both total pressure and temperature variations for such a system. As a result, investigating losses for cooled blades by only measuring total pressure (as mostly done in the literature) would omit the total temperature contribution and would provide a biased estimation of the losses. To alleviate such issues and avoid applying such complex balances, the losses can also be quantified by studying the RHS of Eq. (4.16), i.e, the entropy source term maps. In the next section, the losses are investigated through the study of the loss maps obtained from the Second Law Analysis (SLA) approach.

Investigation of the loss maps using *Second Law Analysis*

In this section, the time-averaged aerodynamic $\overline{P_m}$ and mixing $\overline{P_q}$ loss maps are investigated. As already stated in Chapter 2, these maps give access to the local loss generation within the computational domain. To evaluate the losses generated by the presence of the film, loss maps are compared to the ones obtained from the uncooled T120 case. Advanced diagnostics will be applied to the mixing loss $\overline{P_q}$ to link the flow physics to loss generation process. The losses generated by the boundary layer regions as well as by the film are finally addressed.

To identify the loss generation sources, time averaged loss maps are extracted on the cut B_z-B_z previously introduced in Section 4.3.1 and provided on Fig. 4.46. In the following discussions, the film thickness is added to the views to ease the localization of the film. Note that the choice of the cut position is expected to only impact the jet positions on the loss maps since the film rapidly homogenises downstream in the span-wise direction. When the loss maps for the T120D blade are compared to the T120 blade, Fig. 3.38, the same loss generation topology is

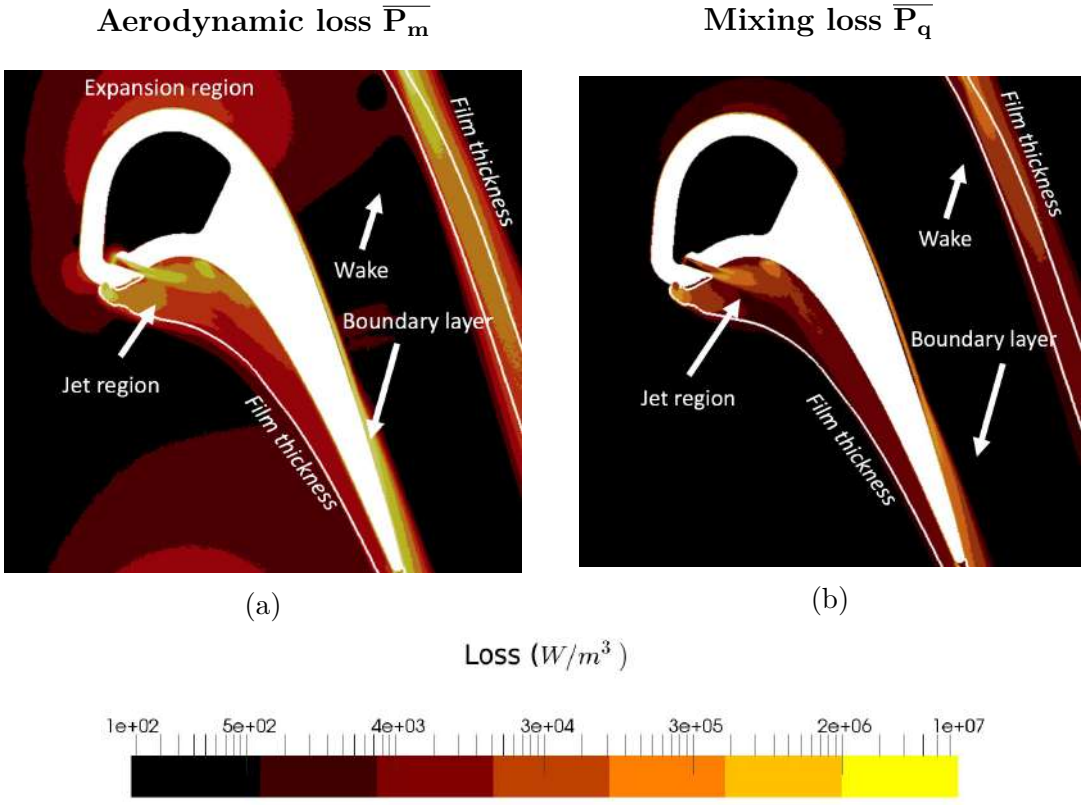

Figure 4.46 – Time-averaged loss maps on cut $B_z - B_z$. Aerodynamic loss $\overline{P_m}$ on left (a) and mixing loss $\overline{P_q}$ on right (b). White iso-line shows the film thickness.

recovered on the suction side of the blade. The main deviation is observed near the pressure side of the blade, where coolant is ejected for the T120D blade. The aerodynamic loss field $\overline{P_m}$, Fig. 4.46 (a), is first described. As expected, aerodynamic losses mainly occur in the boundary layer on the suction side of the blade, in the coolant film on the pressure side as well as in the wake downstream the blade. Indeed, these regions present highly sheared flows. On the suction side, the flow expansion region also evidences aerodynamic loss because of the strong flow acceleration present in this region. Note that no loss is generated in the freestream flow because no freestream turbulence was injected at the inlet. The mixing loss $\overline{P_q}$, Fig. 4.46 (b), mainly activates in the near wall flow region of the blade. On the suction side of the blade, the boundary layer generates mixing losses due to temperature gradients produced by compressibility effects as already discussed in Chapter 3. Mixing losses are observed to be also generated in the mixing region on the pressure side due to the temperature difference between the hot and coolant flows. It is noted that more losses are generated in the jets with respect to regions where the film is attached to the wall. Indeed, the mixing process was found to be mainly located in the detached jets in Section 4.3.1. If both loss maps are compared, $\overline{P_m}$ clearly dominates the loss generation in the domain. Nevertheless, the ratio between $\overline{P_q}$ and $\overline{P_m}$ is probably under-estimated for this academic configuration compared to real engine where temperature differences are much higher. From the loss maps, it is of interest to evaluate the contribution of each regions

	$\int_V \overline{P_m} dV$	$\int_V \overline{P_q} dV$
Coolant film	3.9 W (16 %)	0.5 W (23 %)
Profile losses (Wake, boundary layer)	20.0 W (84 %)	1.3 W (77 %)
Full domain (Excluding the pipes)	23.9 W	1.8 W

Table 4.5 – Integrated loss maps in each region of the flow normalized by the total loss generation in the domain excluding the plenum and pipes.

on the loss generation. To do so, the loss maps are integrated in different volumes corresponding to the film on the pressure side, the boundary layer on the suction side and the wake. To purely focus on the loss generation around the blade, the pipes are excluded from the integration domain. Integration results are provided and normalized in Table 4.5. Note that losses generated in the boundary layers and in the wake are gathered as *profile losses*. Integrated values confirm that aerodynamic losses dominate the loss generation in the domain. If looking at the contribution of each region, the profile losses clearly dominate the loss generation. Nevertheless, almost 25% of the mixing losses and 16 % of the aerodynamic losses are generated by the film. Since the most of losses are generated in the near wall flow region of the blade, the following discussion focuses on the loss generation in this specific region of the flow.

First, the losses generated by the suction side boundary layer are investigated and compared to results from the uncooled T120 blade. To do so, the dissipation coefficient C_d defined by Eq. (3.27) is plotted along the suction side of the blade and compared to the one obtained for the uncooled T120 blade on Fig. 4.47. Similarly to Chapter 3, C_d decreases in the laminar part of the boundary layer and then increases from $x/c = 0.8$ due to the boundary layer turbulent transition. No strong deviation is observed between both cases. As a result, same conclusions as the ones obtained in Chapter 3 can be drawn concerning the impact of turbulent transition on the losses. The loss generation in the coolant ejection region on the pressure

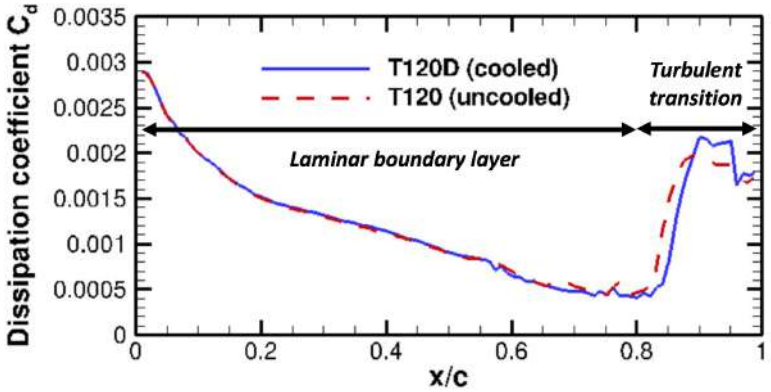

Figure 4.47 – Dissipation coefficient C_d [-] evolution along the suction side for the uncooled T120 blade (red) and cooled T120D blade (blue) at mid-span.

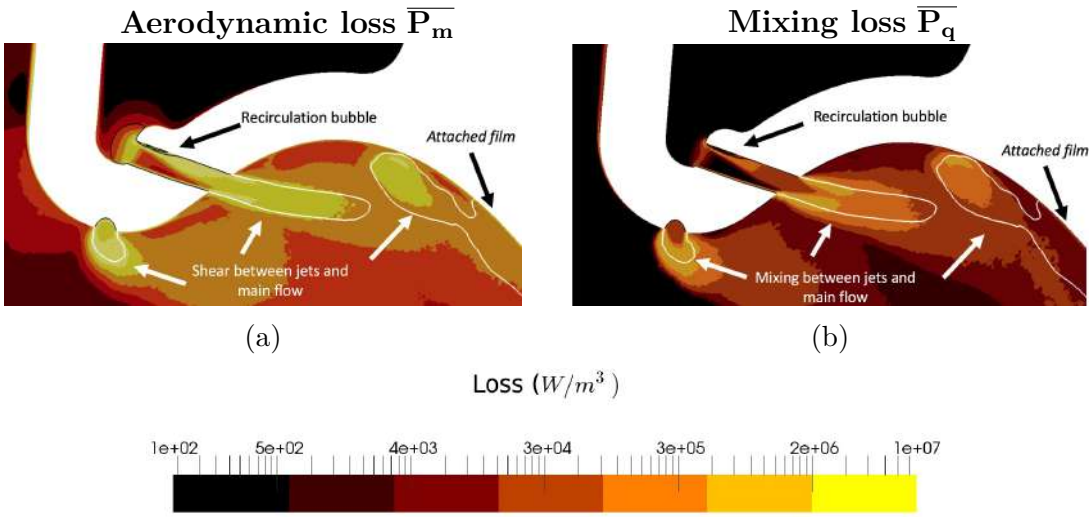

Figure 4.48 – Time-averaged loss maps in the jet regions on cut $B_z - B_z$. Aerodynamic losses $\overline{P_m}$ (a) and mixing losses $\overline{P_q}$ (b). White iso-contour represents $Y_{coolant} = 0.5$ and black iso-line $\overline{\mathbf{v}} = 20m/s$ where $\overline{\mathbf{v}}$ is the velocity magnitude.

side of the blade is now addressed. To do so, a detailed view of the loss maps in the coolant ejection region is provided on Fig. 4.48. For the following analysis, jets are highlighted by the white iso-contour $Y_{coolant} = 0.5$ and recirculation bubbles are evidenced by low velocity magnitude $\overline{\mathbf{v}}$ regions identified by the black iso-contour $\overline{\mathbf{v}} = 20m/s$. it is worth to note that the black iso-contour does not fully represent recirculation bubbles but only provides a rough view of its position in the pipes. The aerodynamic losses $\overline{P_m}$, Fig. 4.48 (a), are observed to be generated in the pipes, in the jets and in the attached film. It is noted that the detached jets generate more losses than the region where the film is attached to the wall. Indeed, the shear is expected to be stronger for detached jets. In the pipe, $\overline{P_m}$ is generated by the strong shear present at the edge of the recirculation bubble present in the pipe. The mixing losses $\overline{P_q}$, Fig. 4.48 (b), are generated in the mixing regions taking place between the jets and the hot flow. It is also noticed that, although no hot flow enters in the pipes, mixing losses are found to be also generated in the pipe. This can be explained by the compressibility effects induced by the flow acceleration in the pipe generates temperature gradients activating $\overline{P_q}$. To quantify the loss generation in the coolant film, film dissipation coefficients C_d^{film} can be defined for each loss contribution similarly to boundary layer dissipation coefficient C_d. In the following, aerodynamic film dissipation coefficient C_{d,P_m}^{film} and mixing film dissipation coefficient C_{d,P_q}^{film} are defined so that,

$$C_{d,P_m}^{film} = \frac{\int_0^{\delta_f} \overline{P_m} dn}{\rho_\infty U_\infty^3}, \tag{4.17}$$

$$C_{d,P_q}^{film} = \frac{\int_0^{\delta_f} \overline{P_q} dn}{\rho_\infty U_\infty^3}, \tag{4.18}$$

where ρ_∞ and U_∞ are respectively the density and velocity magnitude at the edge

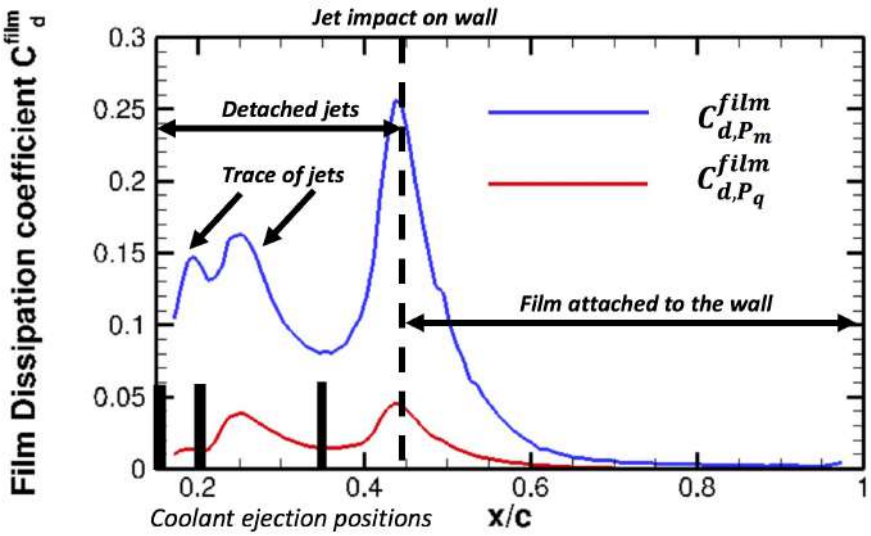

Figure 4.49 – Dissipation coefficient C_{d,P_m}^{film} [-] (red) and C_{d,P_q}^{film} [-] (blue) profiles extracted at mid-span of the T120D blade.

of the film thickness. The axial evolution of both film dissipation coefficients measured at mid-span of the blade are plotted on Fig. 4.49. Note that the jet positions on these profiles are expected to be shifted if another cut position is chosen. Nevertheless, the film rapidly homogenises along the blade and the choice of the cut position is then expected to weakly impact the loss profiles downstream the jets. From such profiles, the most of losses are clearly generated in the detached jet region confirming previous findings. Indeed, at $x/c = 0.2$ and $x/c = 0.3$, the effect of jets on losses are clearly identified for both loss coefficients. At $x/c = 0.45$, a peak is observed for both losses which corresponds to the impact of jets on the blade wall. For $x/c > 0.45$, both film dissipation coefficients decrease in the region where the film remains attached to the wall.

To link the flow physics to the losses, advanced diagnostics and decompositions of the loss maps are hereafter introduced. Similarly to the Bobyleff-Forsyth formula introduced in Eq. (3.22) for the aerodynamic loss generation, the mixing loss P_q can be decomposed into different contributions. To do so, the isentropic relation linking the static temperature T, total temperature T_t and Mach number Ma is introduced in Eq. (2.59) and after rearrangements of the terms, one can obtain,

$$P_q = \underbrace{\frac{\lambda+\lambda_t}{T}\frac{\partial T_t}{\partial x_j}\frac{\partial T_t}{\partial x_j}f(Ma)^{-2}}_{\text{Mixing term}} + \underbrace{\frac{\lambda+\lambda_t}{T}\frac{T_t^2}{f(Ma)^4}(\gamma-1)^2\frac{\partial Ma}{\partial x_j}\frac{\partial Ma}{\partial x_j}}_{\text{Compressibility term}}$$
$$\underbrace{-\frac{\lambda+\lambda_t}{T}\frac{\partial T_t}{\partial x_j}\frac{\partial Ma}{\partial x_j}\frac{T_t}{f(Ma)}(\gamma-1)}_{\text{Alignement term}}, \tag{4.19}$$

where λ and λ_t are respectively the laminar and turbulent thermal conductivity, γ the heat capacity ratio and $f(Ma) = 1 + \frac{\gamma-1}{2}Ma^2$. On the RHS, the first term

$\frac{\lambda+\lambda_t}{T}\frac{\partial T_t}{\partial x_j}\frac{\partial T_t}{\partial x_j}f(Ma)^{-2}$ $\frac{\lambda+\lambda_t}{T}\frac{T_t^2}{f(Ma)^4}(\gamma-1)^2\frac{\partial Ma}{\partial x_j}\frac{\partial Ma}{\partial x_j}$ $\frac{\lambda+\lambda_t}{T}\frac{\partial T_t}{\partial x_j}\frac{\partial Ma}{\partial x_j}\frac{T_t}{f(Ma)}(\gamma-1)$

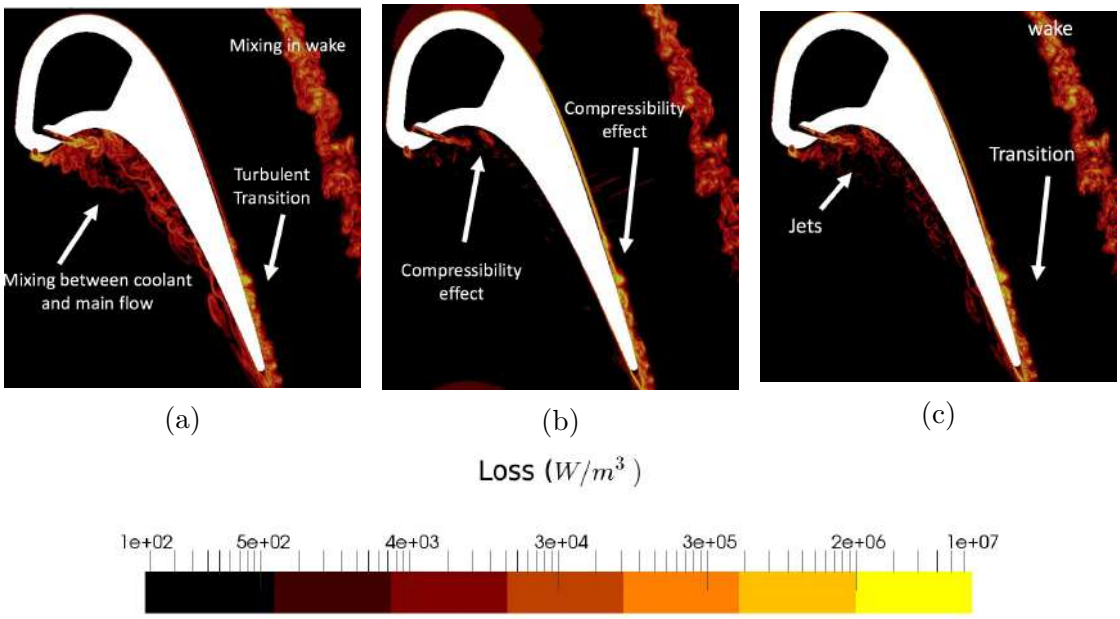

Figure 4.50 – Mixing term on left (a), compressibility term in the middle (b) and alignment term on right (c) on cut $B_z - B_z$.

represents the production of mixing losses due to non-zero total temperature gradients and will refer as *mixing term* in the following. The second term represents losses from Mach number gradients and tends to 0 if the Mach number is very small. As a result, this term represents the compressibility effects on the loss generation and will refer as *compressibility term*. Finally, the third term represents the alignment between the total temperature and Mach gradient and will be refer as *alignment term*. The mixing, compressibility and alignment terms are provided at mid-span on Fig. 4.50 for an instantaneous solution. As expected, the mixing term, Fig. 4.50 (a), dominates the mixing region on the pressure side of the blade taking place between the hot and coolant flows. It also appears on the suction side of the blade where turbulent transition of the boundary layer induces local total temperature gradients. The compressibility term, Fig. 4.50 (b), is mainly activated by compressibility effects on both sides of the blade. This term is found to also activate in the coolant jet region due to the difference of Mach number between the hot and coolant flows in this region. The alignment term, Fig. 4.50 (c), mainly activates in the near wall flow region of the blade. The reasons for which this term activates in such regions is not clearly understood by the author and would require more investigations. As a result of the previous discussion, it is confirmed that mixing losses are generated in regions of high temperature differences and high compressibility.

Similarly to Chapter 3, it is of interest to discriminate the mean flow contribution from purely unsteady effects for the time-averaged mixing loss generation $\overline{P_q}$. To do so, the Reynolds decomposition is introduced on the static temperature field, i.e, $T = \overline{T} + T'$ where $\overline{\bullet}$ is the time-averaged operator and $'$ the temporal fluctuation. Introducing the Reynolds decomposition in Eq. (2.59), one obtains,

$$\overline{P_q} = \overline{\frac{(\lambda + \lambda_t)}{\overline{T} + T'} \frac{\partial(\overline{T} + T')}{\partial x_i} \frac{\partial(\overline{T} + T')}{\partial x_i}},$$

or,

$$\overline{P_q} = \overline{\frac{(\lambda + \lambda_t)}{\overline{T} + T'} \left(\frac{\partial \overline{T}}{\partial x_i} \frac{\partial \overline{T}}{\partial x_i} + 2 \frac{\partial \overline{T}}{\partial x_i} \frac{\partial T'}{\partial x_i} + \frac{\partial T'}{\partial x_i} \frac{\partial T'}{\partial x_i} \right)}. \tag{4.20}$$

At this point of the demonstration, the time-averaged operator can not be distributed on the numerator and denominator because $\overline{\frac{(\lambda+\lambda_t)}{\overline{T}+T'}} \neq \frac{\overline{(\lambda+\lambda_t)}}{\overline{\overline{T}+T'}}$. To alleviate this issue, (Kock and Herwig, 2004) proposes to develop $\frac{1}{\overline{\overline{T}+T'}}$ in series using Taylor expansion around $T' \sim 0$ so that,

$$\frac{1}{\overline{\overline{T} + T'}} = \frac{1}{\overline{T}} - \frac{T'}{\overline{T}^2} + O(T'^2), \tag{4.21}$$

where $O(T'^2)$ is the Taylor expansion error. For the T120D academic blade, the temperature fluctuation T' is necessary greatly inferior to $\overline{T}^2$ whose the order of magnitude is around 10^5. Therefore if combining Eq. (4.21) with Eq. (4.20), the time-averaged operator can be distributed giving,

$$\overline{P_q} = \underbrace{\frac{(\overline{\lambda} + \overline{\lambda_t})}{\overline{T}} \frac{\partial \overline{T}}{\partial x_i} \frac{\partial \overline{T}}{\partial x_i}}_{\text{Loss due to the mean fields}} + \underbrace{\overline{\frac{(\lambda + \lambda_t)}{T} \frac{\partial T'}{\partial x_i} \frac{\partial T'}{\partial x_i}}}_{\text{Loss due to the unsteady fields}}. \tag{4.22}$$

The first term on the RHS represents the effect of the mean field while the second term represents unsteady effects on the mixing loss generation. Both contributions for both loss maps are extracted on the cut $B_z - B_z$ and provided on Fig. 4.51. As expected, the mean contribution of aerodynamic losses P_m^{mean}, Fig. 4.51 (a), dominates in highly mean sheared flow, i.e:boundary layer on the suction side and coolant jets on the pressure side. P_m^{mean} is also found to be activated in the flow expansion region on the suction side of the blade. The mean contribution of the mixing losses P_q^{mean} , Fig. 4.51 (b), mainly takes place in the mixing region on the pressure side due to the mean temperature difference between the coolant and the hot flow. Again, the compressibility effects in boundary layers contributes also to the mean mixing loss generation. The turbulent contribution of aerodynamic losses P_m^{turb}, Fig. 4.51 (c), mainly activates in the turbulent transition region of the boundary layer on the suction side and in the film on the pressure side of the blade. Indeed, in the film, P_m^{turb} activates in the region of jets which was observed to present a strong turbulent activity. Downstream the blade, P_m^{turb} also activates in the turbulent wake. Finally, the turbulent contribution of the mixing losses P_q^{turb}, Fig. 4.51 (d), also activates in the same regions as P_m^{turb}. More

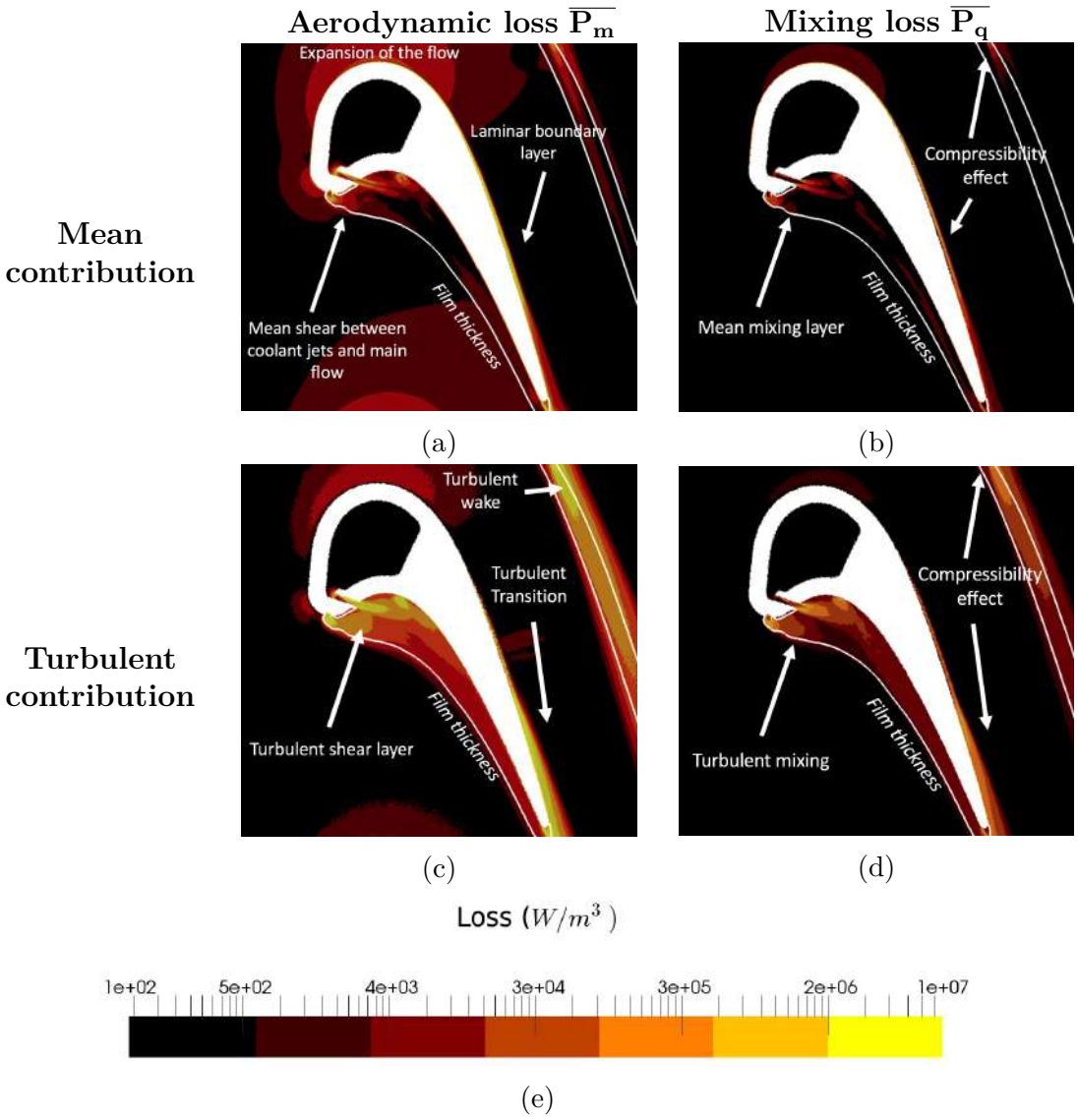

Figure 4.51 – Mean and unsteady loss contributions on cut $B_z - B_z$. Mean contribution, i.e, P_m^{mean} and P_q^{mean}, on the top (a) & (b) and unsteady contribution, i.e, P_m^{turb} and P_q^{turb}, on the bottom (c) & (d). Aerodynamic loss on the left (a) & (c) and mixing loss on the right (b) & (c). White iso-line represents the film thickness.

specifically in the jet region, P_q^{turb} is probably activated by the turbulent mixing taking place between the hot and coolant flows. If both mean and turbulent contributions are compared, unsteady effects clearly dominate the loss generation in the near wall flow region of the blade for both aerodynamic and mixing losses. Such findings are coherent with results obtained for the T120 blade, Fig. 3.41. To further investigate the loss generation in the jet region, a detailed view of previous maps in this specific region of the flow is provided on Fig. 4.52. The mean contributions P_m^{mean} and P_q^{mean}, Fig. 4.52 (a) & (b), are clearly linked to mean shear and mean mixing layers present in the jets evidenced by the white

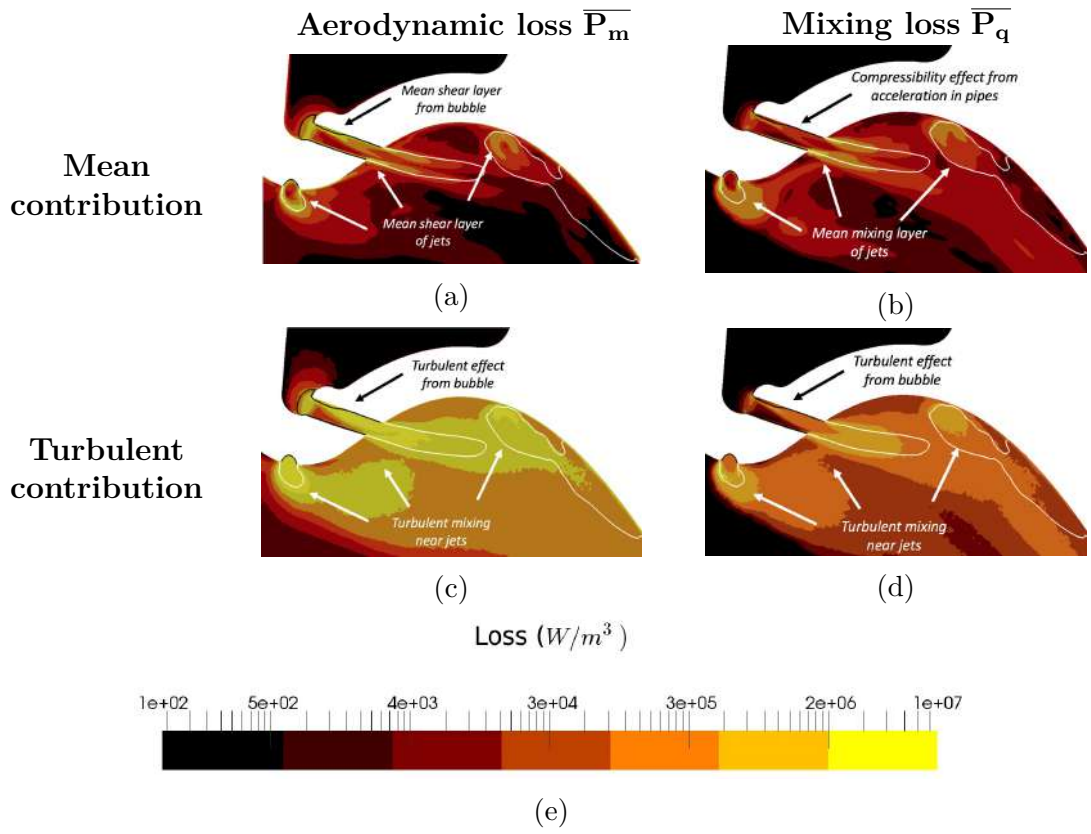

Figure 4.52 – Mean and unsteady loss contributions on cut $B_z - B_z$ in the jet region. Mean contribution, i.e, P_m^{mean} and P_q^{mean}, on the top (a) & (b) and unsteady contribution, i.e, P_m^{turb} and P_q^{turb}, on the bottom (c) & (d). Aerodynamic loss on the left (a) & (c) and mixing loss on the right (b) & (c). White iso-contour represents $Y_{coolant} = 0.5$ and black iso-line $\overline{\mathbf{v}} = 20m/s$.

iso-line. In the pipe, the mean contributions activate in the mean shear layer created at the edge of the recirculation bubble evidenced the black iso-line. The turbulent contributions P_m^{turb} and P_q^{turb}, Fig. 4.52 (c) & (d), are mainly generated inside the jets and in the pipes. Indeed, high levels of turbulent kinetic energy were previously observed in these regions. In the pipe, unsteady effects generated from the bubble also activate the turbulent contributions of the losses. To go further in the analysis of the losses generation in the film, wall normal loss profiles of mean and turbulent contributions are extracted at different axial positions along the pressure side of the blade, i.e,: at $x/c = 0.30$, i.e, where jets are detached off the wall and at $x/c = 0.80$ where the coolant film is attached to the wall. Results are then averaged in the span-wise direction and provided on Fig. 4.53. At $x/c = 0.3$, Fig. 4.53 (a) & (b), mean and turbulent contributions for both losses reach a peak located at $n/\delta = 0.33$. This distance corresponds to the detachment distance of the jets from the wall confirming that the detached jets generate large amounts of aerodynamic and mixing losses. When approaching the wall, P_m^{mean} increases due to the rise of shear in the boundary layer. Indeed, P_m^{mean} at wall was shown to be linked to the wall shear stress by Eq. (3.28). If looking at P_q^{mean}, the

mean contribution of mixing loss decreases when approaching the wall. Indeed, P_q^{mean} necessary tends to zero due to the adiabatic wall condition which cancels the temperature gradient. The turbulent contributions P_m^{turb} and P_q^{turb} also tend to zero when approaching the wall. Indeed, unsteady effects are expected to be dissipated by viscous effects when penetrating the laminar boundary layer. At $x/c = 0.8$, Fig. 4.53 (c) & (d), loss profile shapes differ from the previous position.

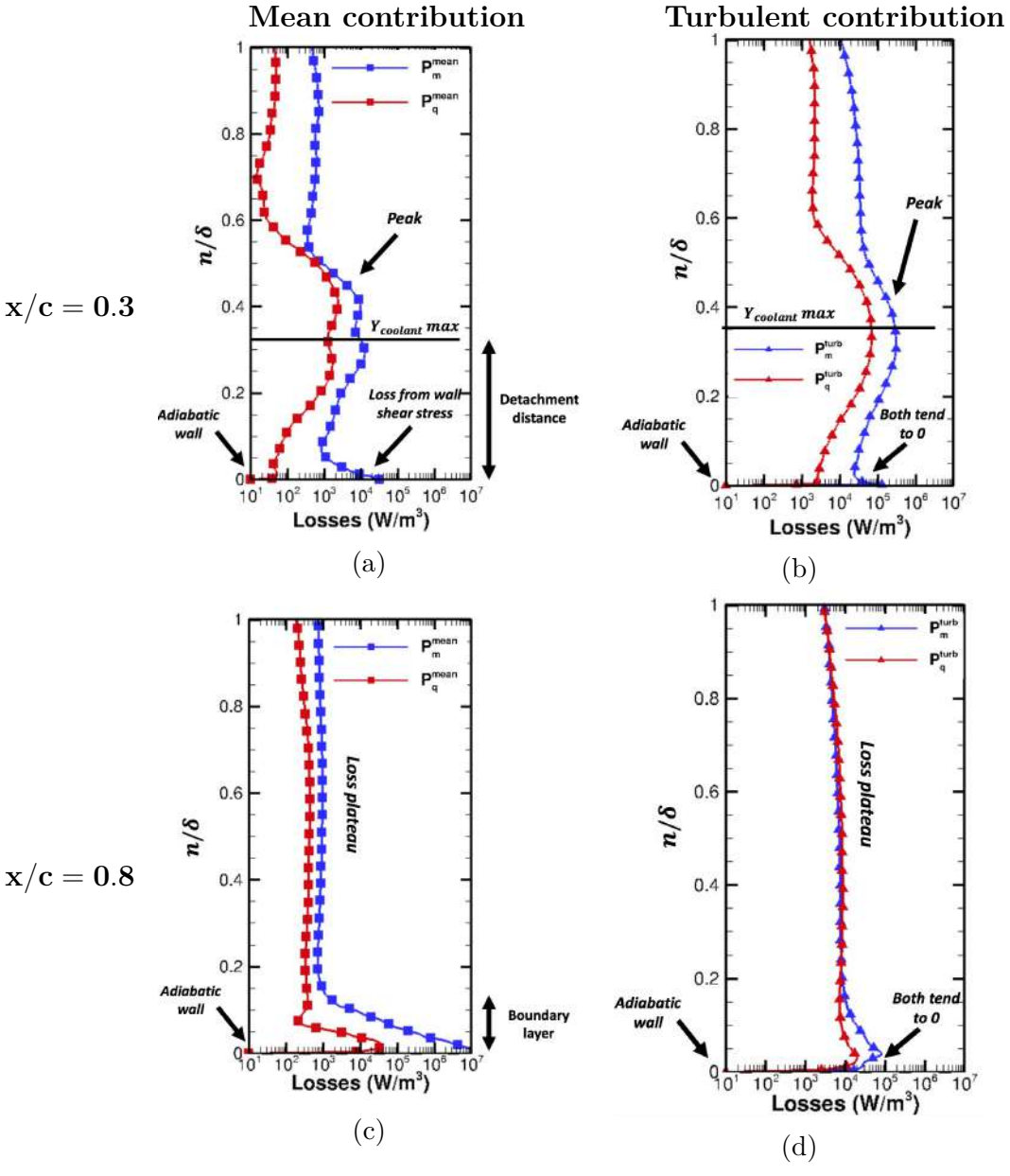

Figure 4.53 – Wall normal span-averaged loss profiles located at $x/c = 0.3$ at top (a) & (b) and at $x/c = 0.8$ at bottom (c) & (d). Mean contributions on left (a) & (c) and turbulent contributions on right (b) & (d). n/δ represents the wall normal distance normalized by the local thickness. Blue line represents aerodynamic loss profile $\overline{P_m}(n/\delta)$ and red line mixing loss profile $\overline{P_q}(n/\delta)$.

Away from the wall, a plateau in the profiles is observed for both losses and both contributions. This plateau is associated to the losses induced by the freestream flow. Since no freestream turbulence was injected at the inlet, the loss generation in the freestream is rather low and only induced by the freestream flow acceleration. When approaching the wall, P_m^{mean} again increases for $n/\delta < 0.15$ due to the rise of shear when penetrating the boundary layer and reaches a peak at the wall. Again, P_q^{mean} tends to zero due to the adiabatic wall condition. Finally and as the previous axial position, the turbulent contributions tend also to zero due to the dissipation of unsteady effects when penetrating the boundary layer.

4.4 Chapter conclusions

In this chapter, the capacity of LES to predict the blade load distribution and adiabatic film effectiveness for the T120D cooled blade was first evaluated. To do so, a wall resolved LES representing two span-wise pitches of holes was realized. From such a detailed simulation, the flow structure on the suction side of the blade is found to be very similar to the uncooled T120 blade. On the pressure side in the coolant ejection region, the instantaneous and mean flow organization are coherent with literature findings. Recirculation bubbles in pipes are observed to strongly alter the mean flow structure of jets and generate a strong turbulent activity. Jets are also found to be detached from the wall and to strongly penetrate the main stream. Then, jets are observed to reattach to the wall to produce an attached film along the pressure side of the blade. When adiabatic film effectiveness is compared to experimental results, deviations are mainly observed in the region of coolant jets but results are overall satisfactory. The LES prediction is expected to be improved if turbulence is injected at the inlets of the domain. Investigation of the mixing process in the coolant film shows that the turbulent mixing mainly occurs in the detached jet region. This mixing is shown to be induced by the unsteady effects produced in cooling pipes and from the jet interactions with the main stream. Finally, the losses were first investigated using methodologies introduced in Chapter 2. Results show that both total temperature and total pressure variations should be taken into account to evaluate the losses for non-isothermal flows. To identify the loss generation mechanism, loss maps were investigated through the use of Second Law Analysis. Aerodynamic losses are shown to be generated in highly sheared flow region while mixing losses are produced in the mixing region between hot and coolant flows. Again, the turbulent contributions to the losses dominate the mean ones in the near wall flow region of the blade. Integration of loss maps shows that the film has a great impact on the overall loss generation. Indeed, investigation of losses within the film shows that the peak of loss production occurs in the detached jets. When the film is attached to the wall, the peak of loss production is located nearby the wall and is mainly associated to wall shear stress and mixing process taking place between the cold and hot flows. The mixing losses are naturally found to tend to zero at wall due to the adiabatic wall condition.

To conclude this part, LES was shown to improve the prediction of the blade load distribution and adiabatic film effectiveness for the academic T120 and T120D blades with respect to RANS. Thanks to the Second Law Analysis (SLA), the loss generation sources and mechanisms were clearly identified for these academic blades not only from a qualitatively point of view but also quantitatively. Indeed, SLA is shown to discriminate aerodynamic losses from mixing losses for compressible anisothermal flows contrary to total variable 1D balances. Introducing advanced diagnostics, the loss generation process is shown to be mainly induced by unsteady effects. This last finding evidences the benefits of SLA to predict losses based on LES fields. Indeed, turbulent loss contributions are directly resolved on mesh with LES while it should be modelled in RANS. Nevertheless, the number of coolant holes and temperature differences for the academic configurations studied so far are greatly under-estimated with respect to real engines. As a result, in the next part, the loss generation issued by a 3D cooled blade including a high number of holes with realistic inlet conditions is addressed.

Part III

LES of an industry-oriented cooled vane

Outline of Part III

This part addresses the LES predictions for the industry oriented configuration corresponding to the high-pressure vanes of the FACTOR project. In this project, the migration of hot spots through combustion chambers and turbine vanes as well as their interactions with coolant flows are specifically addressed. The NGVs tested in this project are 3D vanes containing 171 coolant holes to form a film cooling around the vanes, the aerothermal environment of the vanes approaching real engine conditions. The main objective of the present part is to evaluate the capacity of LES to predict the vane load distribution, the adiabatic wall temperature and losses for such a complex configuration. To predict the flow of such a complex system, WMLES are performed on the NGV section of the FACTOR test rig. To deal with the coolant flow ejection on the vane surfaces, two approaches can be adopted, i.e:, the cooling system can be either included in the computational domain or the coolant can be directly ejected on the vane surfaces without meshing the cooling system through the use of a coolant ejection model. The main advantage of this last approach is to avoid the CPU effort inherent to the flow resolution in the cooling system of turbine vanes. To ease the use of LES for cooled turbine vanes in an industrial context, a new coolant ejection model is introduced in this work. To assess the coolant ejection model, both approaches are compared on the NGVs of FACTOR. To do so, a reference *hole-meshed LES* is first realized by meshing the cooling system while a *hole-modelled LES* is performed without meshing the cooling system using the proposed coolant ejection model. Finally, the model is assessed from the comparison of the *hole-modelled LES* to the *hole-meshed LES*. The reference *hole-meshed LES* is first presented in Chapter 5. From such a detailed simulation, LES prediction of flow aerodynamics and vane wall temperature is assessed through the comparison to experimental results. Then, losses are investigated using the methodologies introduced in Chapter 2. From this loss analysis, the capacity of SLA to evaluate and study the losses for complex configurations with LES is discussed. Afterwards, the *hole-modelled LES* is presented in Chapter 6. From the comparison between the *hole-modelled LES* and the *hole-meshed LES*, the capacity of the coolant ejection model to predict the flow aerodynamics, the vane wall temperature and the losses is finally discussed.

Chapter 5

Loss prediction for an industry-oriented geometry of high-pressure vanes

Contents

5.1 Review of the NGVs of the FACTOR project **182**
5.1.1 Presentation of FACTOR project and test rig 182
5.1.2 Design of the NGVs 183
5.1.3 Experimental operating point 185
5.1.4 Experimental measurements 187
5.1.5 Literature review of CFD prediction 189
5.2 Numerics and modelling **191**
5.3 LES results **196**
5.3.1 Flow description and validations 196
5.3.2 Investigation of the losses 214
5.4 Chapter conclusions **223**

This chapter addresses the *hole-meshed LES* prediction of the NGVs of FACTOR. For such a complex configuration, the capacity of LES to predict the vane load distribution, the adiabatic wall temperature as well as the losses is assessed. To do so, the *hole-meshed LES* is built by including the whole coolant pipes and feeding plena of the vanes in the computational domain. For the loss evaluation, the methodologies introduced in Chapter 2 are adopted. The capacity of the SLA to identify the loss generation mechanisms for such a complex geometry is specifically addressed and discussed. It is important to note that because of the configuration complexity, a global approach of losses is adopted. The chapter is organized as follows. First, the design of the high-pressure vanes of the FACTOR project and available experimental data are introduced in Section 5.1. At this occasion, existing CFD predictions are provided. Next, the numerical set up and

LES modelling of the *hole-meshed LES* are presented in Section 5.2. Then, the LES prediction is described in Section 5.3. The large flow structures and mean flow organization are first detailed. Then, the prediction of the vane load distribution as well as adiabatic wall temperature is assessed with respect to experimental results. After validation of LES results, losses are investigated. Finally, conclusions are provided in Section 5.4.

5.1 Review of the NGVs of the FACTOR project

In this section, the NGVs of the FACTOR project are presented. First, the context of the FACTOR project is briefly recalled in Section 5.1.1. Then, the design of the NGVs and the targeted experimental operating point are provided in Section 5.1.2. Next, the available experimental database is detailed in Section 5.1.4. Finally, a brief review of existing CFD predictions is shown in Section 5.1.5.

5.1.1 Presentation of FACTOR project and test rig

To reach the objective of NOx emission reduction, Rich Quench Lean (RQL) technology reached their limits and new combustor designs need to be introduced (Liu et al., 2017). Among the solutions, new lean combustor technologies tend to premix the reactive gases upstream the combustion chamber while removing the dilution holes. As a result, lower overall combustion temperatures are reached thereby reducing NOx production levels. Nonetheless, since more air is used in the combustion process, less air is available for cooling systems. This approach then leads to more temperature heterogeneities at the exit of the combustor. These temperature heterogeneities are then transported in the turbine which can locally increase the vane temperature to undesired levels as well as temperature gradients which are damageable for the vane material. To investigate such systems, the FACTOR project has been set up (Bacci et al., 2015; Battisti et al., 2012; Krumme et al., 2019) with the specific objectives of a better understanding of such interactions and better anticipate the effects of such design changes. To do so, this project experimentally and numerically investigates the migration of hot spots through combustion chambers and turbine vanes. The FACTOR project is experimentally conducted at the University of Florence (UNIFI) in Italy and at the Deutsches Zentrum fur Luft-und Raumfahrt (DLR) at Gottingen in Germany. The main test rig located at the DLR includes a swirler, a combustion chamber designed to reproduce an inlet velocity and temperature field for the turbines representative of new technologies and a high-pressure turbine stage. A scheme of the test rig is provided on Fig. 5.1. As a guideline, the different elements of the test rig are delimited by the axial planes defined on Fig. 5.1: i.e. P30, is the plenum entry feeding the swirling flow injection system of the combustor which ends at P40 which is the turbine entry plane. Downstream, P41 corresponds to the axial plane separating the stator and rotor while P42 corresponds to the exit plane of the turbine. The test rig is non-reactive and the flow is heated at the inlet of the test rig by an electrical device. To reproduce effusion cooling ejected in real

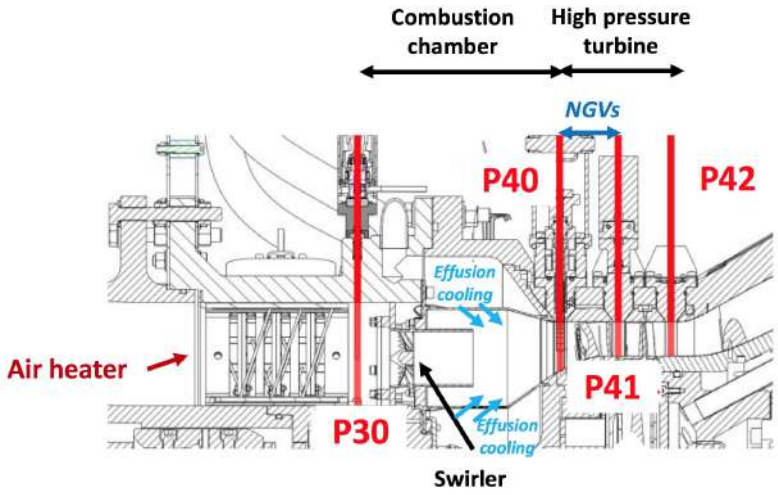

Figure 5.1 – Test rig scheme used at the DLR, Gottinger (Germany). P30 is the plenum entry feeding the swirling flow injection system of the combustor which ends at P40 which is the turbine entry plane. Downstream, P41 corresponds to the axial plane separating the stator and rotor while P42 corresponds to the exit plane of the turbine stage.

combustors, fresh gas is injected through liners in the combustor section of the test rig. In the following, the framework will be limited to the NGV section of the test rig which is delimited by the axial planes $P40$ and $P41$.

5.1.2 Design of the NGVs

An upstream view of the half angular sector of the NGV stage is provided on Fig. 5.2, the full angular sector containing 40 NGVs. One NGV angular sector

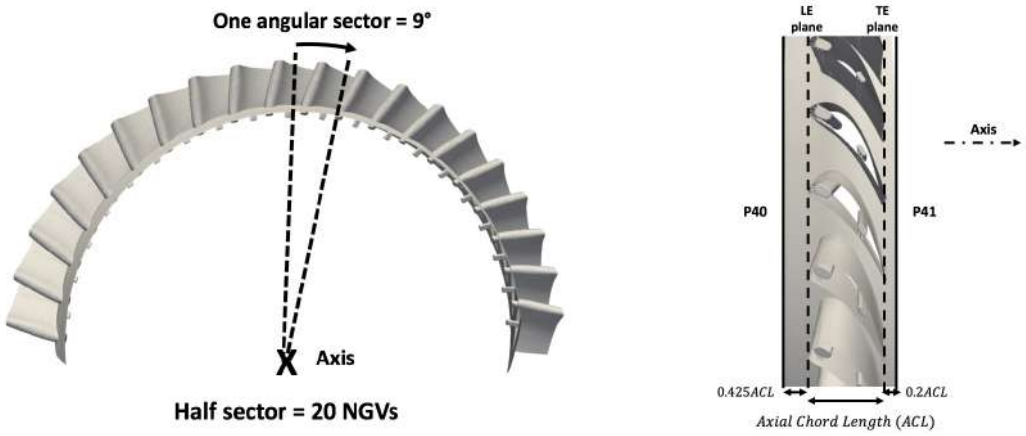

(a) (b)

Figure 5.2 – Upstream view of the half angular sector of the NGV stage in the direction of the engine axis on left (a) and radial view on right (b).

therefore corresponds to an angle of 9°, Fig. 5.2 (a). Each NGV has an Axial Chord Length (ACL) of 38.6 mm as detailed on the radial view of the stage in Fig. 5.2 (b). The axial plane $P40$ is located 0.425 ACL upstream the vanes while $P41$ is located 0.2 ACL downstream. It is important to note that one combustor angular sector corresponds to two NGV angular sectors. As a consequence, experimental data are given for an angular sector of 18° containing 2 NGVs denoted NGV1 and NGV2. To identify independently each vane, NGV1 is arbitrary chosen to be located before NGV2 in the clockwise rotation if looking downstream as shown on Fig. 5.3. Detailed views of one vane design is provided on Fig. 5.4. The vane is



Figure 5.3 – Relative position of NGV1 against NGV2 for an angular sector of 18°.

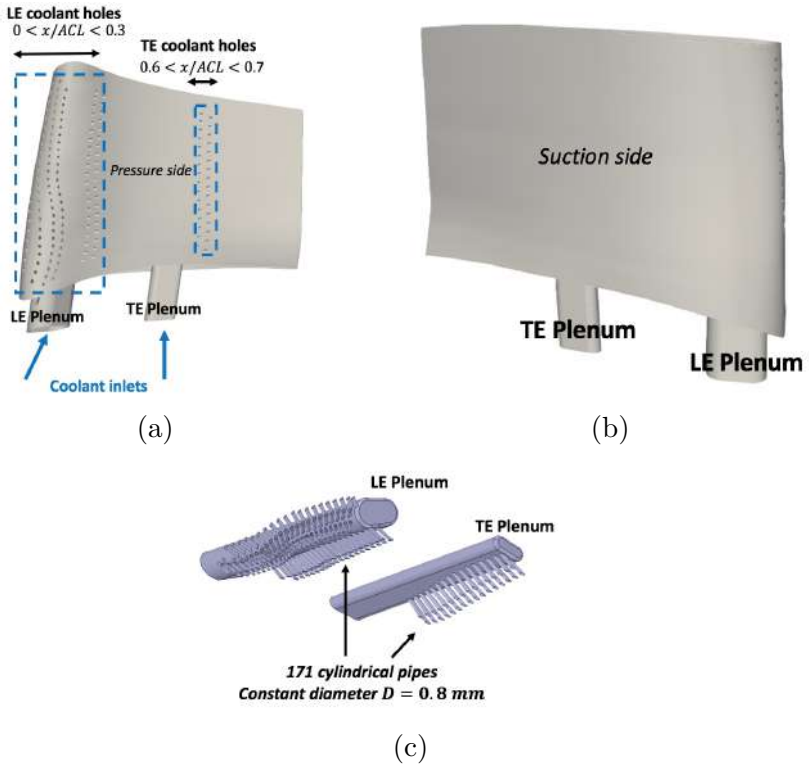

Figure 5.4 – Detailed upstream view of the design of the NGV. Pressure side view on left (a) suction side view on right (b) and coolant system at bottom (c).

designed to reproduce a similar expansion of the flow of real engines. To inject coolant, 171 holes are drilled on both sides of each vane as shown on Figs. 5.4 (a) &(b). The holes have a diameter of 0.8 mm and are distributed among 2 zones. The first zone is located near the leading edge of the vane and axially extends from $x/ACL = 0$ to $x/ACL = 0.3$. It is worth to specify that the radial distribution of these holes follows the radial distribution of the stagnation line. In the following, these coolant holes will be noted as *LE coolant holes*. The second zone is located on the pressure side and axially extends from $x/ACL = 0.6$ to $x/ACL = 0.7$. These coolant holes will be hereafter noted as *TE coolant holes*. A view of the internal cooling system is displayed in Fig. 5.4 (c). Note that the *LE coolant holes* are supplied by the plenum noted *LE plenum* while the *TE coolant holes* are supplied by the plenum noted *TE plenum*.

5.1.3 Experimental operating point

The targeted experimental operating point is the one of the UNIFI facility called *design point* (DP). This operating point is experimentally defined by the flow fields on $P40$ corresponding to 0D values for total temperature, total pressure and no-dimensional numbers provided in Table 5.1. As shown in Table 5.1, a strong swirled and turbulent flow originates from the combustor. To better characterize the flow on $P40$, 2D maps of velocity fields, total temperature and total pressure were experimentally measured and maps are shown on Fig. 5.5. The flow presents a hot spot located at the center of the plane, Fig. 5.5 (a), which is aligned with NGV1. A cold flow region coming from the effusion cooling ejected in the combustor is observed near the shroud. Such a temperature heterogeneity is expected to migrate through the vanes and will potentially interact with the coolant flow ejected around the high-pressure vanes. From total pressure map normalized by its mean spatial value, Fig. 5.5 (b), total pressure losses are mainly located at the plane center and are induced by the swirl. Radial and tangential velocities, Fig. 5.5 (c) & (d), confirm that the flow strongly rotates clockwise if looking downstream and is centred at the same position of the hot spot.

0D values on P40	
Reynolds number (based on ACL) [-]	111 000
Mach number [-]	0.112
Swirl number [-]	0.6
Mass flow rate for one angular sector $[kg/s]$	0.12
Spatial averaged of static temperature $[K]$	450
Spatial averaged of static pressure $[kPa]$	147

Table 5.1 – Design operating point for one angular sector (Koupper, 2015).

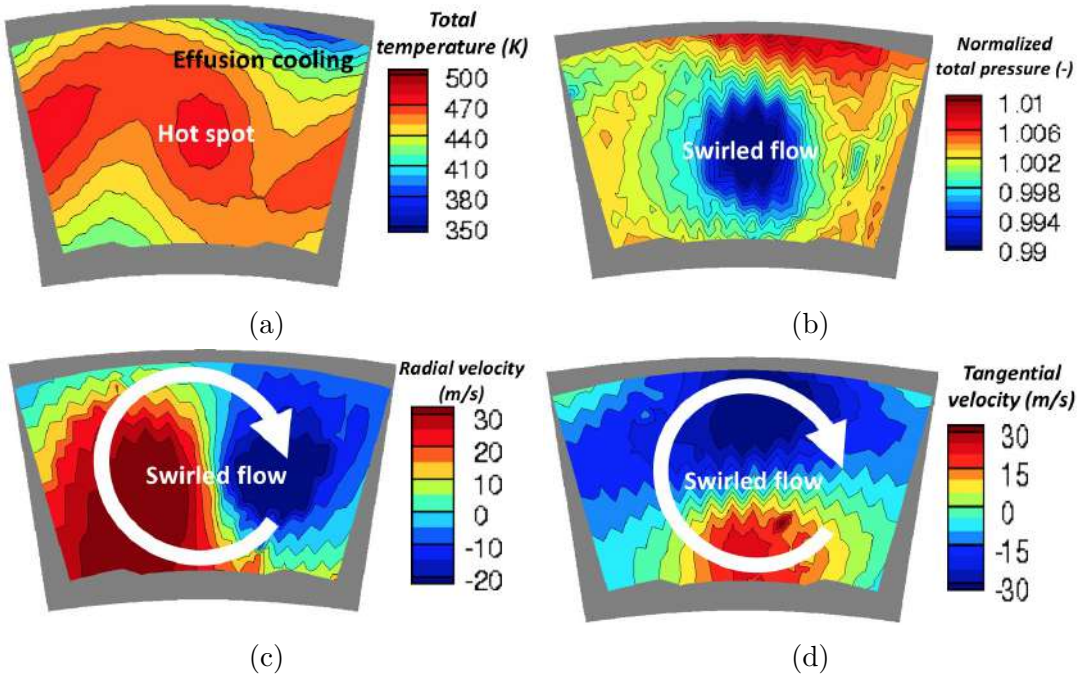

Figure 5.5 – Experimental data for the Design Point (DP). Total temperature (a), normalized total pressure (b), radial velocity (c) and tangential velocity (d) looking downstream. Taken from (Martin Thomas, 2017).

After description of the operating point, the experimental coolant operating point of the vanes is provided in Table 5.2. The spatial averaged temperature of the hot flow entering in the turbine is 450 K at $P40$ while the coolant is injected at 300 K. In this case, the ratio between the hot and coolant mass flow rate (for one angular sector) is fixed at 7.5%. Note that more coolant mass flow rate is injected in the LE plena to reduce the vane temperature near the stagnation line on the vane. Assuming an uniform repartition of the coolant mass flow rate among the coolant holes, the obtained blowing ratio M for each hole is around 1 and corresponds to typical values of turbine cooling systems (Han and Ekkad, 2001). For this specific operating point, the available experimental database is hereafter detailed.

NGV coolant	
Coolant temperature $[K]$	300
Coolant mass flow rate from LE Plenum $[kg/s]$	0.006
Coolant mass flow rate from TE Plenum $[kg/s]$	0.003
Coolant to hot mass flow rate ratio (One angular sector) [-]	7.5%

Table 5.2 – Coolant flow properties (Koupper, 2015).

5.1.4 Experimental measurements

The aerodynamics and the thermal environment of the NGVs were experimentally characterised by measuring the flow expansion along the vanes as well as the adiabatic film effectiveness on the vane surfaces. Details on the measurement set-up can be found in (Krumme et al., 2019). Both flow expansion and adiabatic film effectiveness measurements are hereafter described.

Flow expansion

The flow expansion through the vanes was measured at DLR from pressure taps located on the pressure side of NGV1 and on the suction side of NGV2. For all taps, the time averaged pressure distribution $\overline{P}(x/ACL)$ is obtained giving access to the spatial distribution along the axial position x. The pressure distribution is then normalized giving the isentropic Mach number $Ma_{is}(x/ACL)$ distribution following,

$$Ma_{is}(x/ACL) = \sqrt{\frac{2}{\gamma - 1}\left[\left(\frac{< P_t >_{P40}}{\overline{P}(x/ACL)}\right)^{\frac{\gamma-1}{\gamma}} - 1\right]}, \tag{5.1}$$

where $< P_t >_{P40}$ is the spatial averaged of the total pressure on P40 and γ is the heat capacity ratio equal to 1.4. The obtained experimental distribution of $Ma_{is}(x/ACL)$ at mid-height of the vanes is plotted on Fig. 5.6. Note that no pressure taps were present near the stagnation point of the vane near $x/ACL = 0$. On both sides of the vane, the flow accelerates along the axial direction. It is noted that on the suction side, the flow becomes supersonic after $x/ACL = 0.7$. From $x/ACL = 0.9$, Ma_{is} decreases indicating the presence of a shock region.

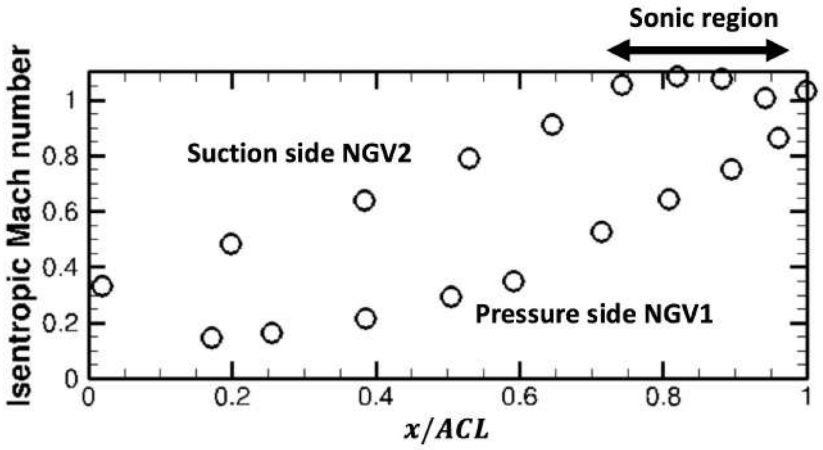

Figure 5.6 – Experimental isentropic Mach number Ma_{is} [-] distribution along the pressure side of NGV1 (bottom) and suction side of NGV2 (top).

Adiabatic film effectiveness

The adiabatic effectiveness η for this configuration is given by the following relation (Bacci et al., 2019),

$$\eta = \frac{\overline{T_{skin}} - T_{hot}}{T_{coolant} - T_{hot}}, \tag{5.2}$$

where $\overline{T_{skin}}$ is the time-averaged skin vane temperature, $T_{coolant}$ the total coolant temperature and T_{hot} the spatial averaged total temperature on $P40$. In the experiment, the film effectiveness is measured using the heat and mass transfer analogy (Han et al., 2000). To do so, a pressure sensitive paint (PSP) sensitive to oxygen concentration is applied to the vane surfaces. Then, pure CO2 is injected as cooling fluid, the main fluid being air. The concentration of oxygen on the vane is then measured using CCD cameras. Under the heat and mass transfer analogy (Bacci et al., 2019), the film effectiveness is obtain using,

$$\eta = \frac{\overline{C_{main}} - \overline{C_{wall}}}{\overline{C_{main}}}, \tag{5.3}$$

where $\overline{C_{main}}$ and $\overline{C_{wall}}$ are the time-averaged oxygen concentration respectively of the main flow and on the wall. The adiabatic film effectiveness distribution on both surfaces of NGV1 and NGV2 is provided on Fig. 5.7. One clearly notes that the film effectiveness is equal to 1 near all coolant holes suggesting that there is no re-ingestion of hot flow in coolant pipes for both NGVs. Overall, experimental spatial distribution of film effectiveness is highly heterogeneous and presents very localized patterns. Behind all coolant hole, traces of coolant on the vane surfaces are observed. Coolant free regions appear near the end-walls of the vane because of an absence of coolant ejection at these radial positions. On the suction side of NGV1, Fig. 5.7 (a), cooling is more efficient near the mid-height of the vane (denoted region 1 on Fig. 5.7). On the pressure side, Fig. 5.7 (b), a high coolant efficiency region is observed (denoted region 2). In the first third of the height of the vane, region 3, a lower coolant efficiency is noticed. Indeed, coolant radially migrates from the hub to the shroud because of the swirl (Bacci et al., 2019). Near the leading edge of the vane, region 4, film effectiveness rapidly decreases from the coolant ejection position suggesting a strong mixing with the hot flow downstream the holes. On the suction side of NGV2, Fig. 5.7 (c), cooling is more efficient near the middle and in the last third of vane height, region 1 and 2. On the pressure side, Fig. 5.7 (d), a region of high film effectiveness is observed in region 3. The strong variation along the radial direction of film effectiveness for both NGVs also suggests that the coolant mass flow rate distribution among the holes is not uniform.

Since such a film effectiveness distribution originates from the hot spot migration as well as complex interactions with the coolant flow (Koupper, 2015), CFD predictions were performed to understand all the interactions involved in such a complex geometry.

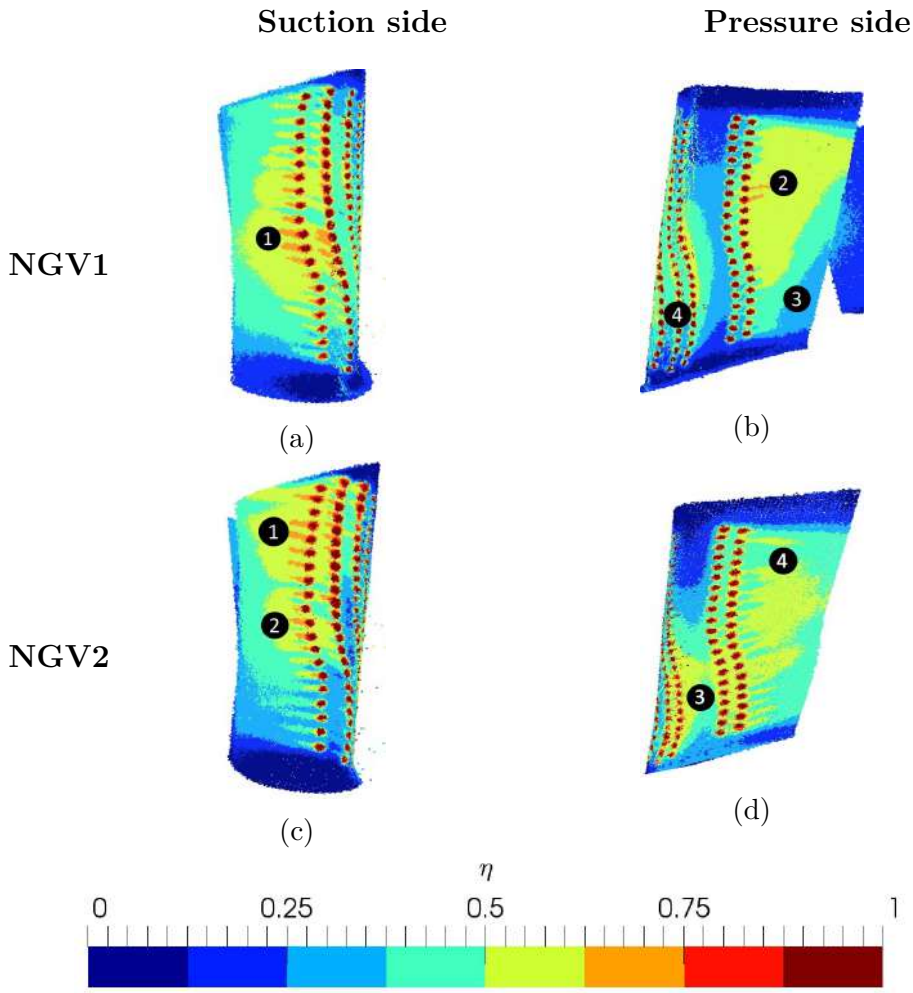

Figure 5.7 – Experimental film effectiveness η [-] for NGV1 at top (a) & (b) and for NGV2 at bottom (c) & (d). Pressure side on left (a) & (c) and suction side on right (b) & (d). The described regions are evidenced by numbers.

5.1.5 Literature review of CFD prediction

In the FACTOR project, several numerical investigations were performed to evaluate the CFD capacity to predict the aerothermal environment of the high-pressure turbine stage. Note that although multiples predictions of this test configuration exist (Koupper, 2015; Vagnoli et al., 2016; Cubeda et al., 2019; Duchaine et al., 2017; Thomas et al., 2018), only numerical works focusing on the prediction of the vane temperature are addressed in the following.

CFD predictions were first performed by (Koupper, 2015) to investigate the hot spot migration through the vanes and its impact on the vane surface temperature. In this original work, an adiabatic WMLES was performed representing an 18° angular sector of the combustor - NGVs section of the FACTOR test rig. Through such a LES, the transport of hot and cold flows issued from the combus-

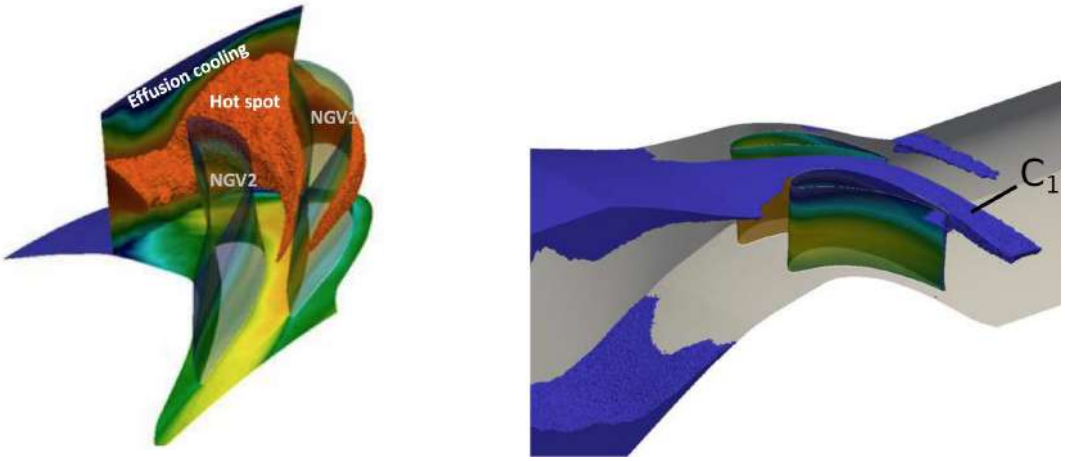

(a) (b)

Figure 5.8 – Iso-surface of the hot spot temperature (a) and iso-surface of the coolant temperature (b) of the time-averaged solution around the NGVs. Taken from (Koupper, 2015).

tor can be detailed by studying the mean fields presented on Fig. 5.8. As expected, the hot spot impacts NGV1 and splits in 2 parts, Fig. 5.8 (a). The hot spot is then stretched by the accelerating flow along the passage between the vanes. The effusion cooling exiting the combustor remains near the shroud (denoted noted C1 on Fig. 5.8 (b)), affecting the distribution of the vane surface temperature in the top region of NGV2 as shown on Fig. 5.9. The vane surface temperature for both NGVs is observed to be affected by the migration of the hot spot through the vanes. On NGV1, Fig. 5.9 (a), the hot spot impact marks both pressure and suction sides of the vane. On NGV2, Fig. 5.9 (b), hot temperature is also observed near the leading edge of the vane and on the downstream part of the vanes. Near the end-walls of NGV2, trace of coolant flow near the shroud (C1) is also clearly identified.

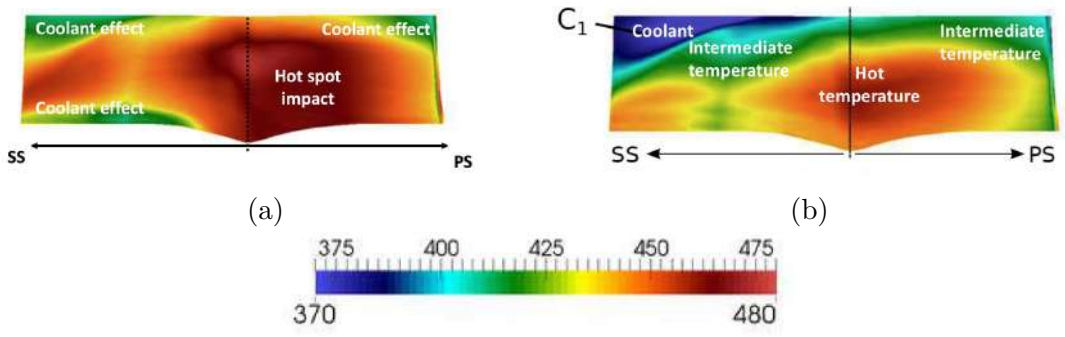

(a) (b)

Figure 5.9 – Vane surface temperature T_{wall} $[K]$ of NGV1 (a) and NGV2 (b). Taken from (Koupper, 2015).

Along with the work of *Koupper*, additional numerical investigations using RANS and LES have studied the impact of inlet specifications on the vane wall temperature (Vagnoli et al., 2016; Cubeda et al., 2019). The aim of these studies was to find best practices for inlet specifications to recover the turbulent activity as well as the temperature fluctuations when performing an isolated CFD of the stator domain. From such predictions, the hot spot migration through the vanes as well as vane wall temperature are shown to be highly sensitive to RANS modelling and inlet turbulent intensity.

Using LES predictions, the mixing process between the hot and coolant flows was confirmed to be sensitive to unsteady inlet specifications (Duchaine et al., 2017; Thomas et al., 2018). To inject unsteadiness at the inlet of an isolated adiabatic LES of the stator domain, the injection of synthetic turbulence was not however able to recover the turbulent activity as well as temperature fluctuations in the NGV passage (Duchaine et al., 2017). Finally, (Thomas et al., 2018) shows that the unsteady activity in the stator can be recovered in a large extent only if imposing the fully unsteady flow fields obtained from an integrated LES of the combustor and NGV section of the test rig.

As a consequence of the previous discussion, the temperature distribution on the vane surfaces is shown to be impacted by the inflow specifications and mixing process between the hot and coolant flows. To predict the vane wall temperature in this work, an isolated WMLES of the NGVs is built by including the cooling systems of the vanes in the computational domain. This WMLES will be hereafter named *hole-meshed LES*. Note that, to the author's knowledge, such a WMLES of such a complex geometry including the cooling system in the computational domain has not been performed in the literature. Details about the numerical set up are provided in the next section.

5.2 Numerics and modelling

In this section, the numerical set up and modelling of the *hole-meshed LES* are addressed. First, the computational domain and the mesh are presented. Boundary conditions and imposed fields are then provided and discussed. Finally, the numerical schemes and LES modelling are detailed.

Computational domain

The computational domain is based on the work of (Thomas, 2019) and is provided on Fig. 5.10. The computational domain is axially limited by the turbine inlet plane (P40) which is well numerically and experimentally characterized (Koupper, 2015; Thomas, 2019; Krumme et al., 2019). The domain represents a 18° periodic sector ($1/20^{th}$) of the full annular domain containing a pair of NGVs denoted NGV1 and NGV2. The outlet locates 6 $ACLs$ downstream the vanes to avoid interactions

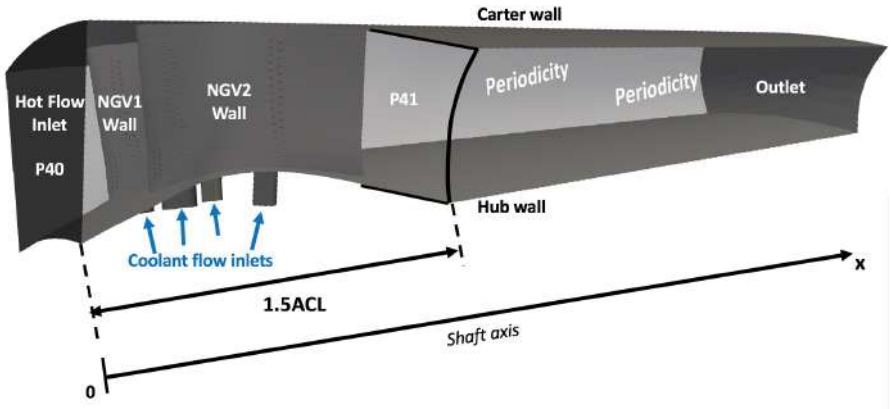

Figure 5.10 – Domain used for the study.

between the wakes of the vanes and the outlet boundary. As already indicated, the whole cooling system including the cooling pipes as well as the feeding plena are included in the computational domain. Coolant flow inlets coincide to the main inlets of the feeding plena.

Mesh

The mesh is purely composed of tetrahedra and contains 73 million of cells. Due to the high number of holes in the cooling system, half of the mesh cells are located in the coolant pipes and feeding plena. A view of the grid is provided at mid-height of vanes in Fig. 5.11. Meshing efforts have been made in the passage region between the vanes, in the near wall flow region as well as in the wake regions. To capture the flow dynamics in the cooling system, the cooling pipes are also refined to obtain 12-15 points to discretize each hole, Fig. 5.12. However, to ensure that the locally strong gradients induced by coolant ejection are properly captured by the

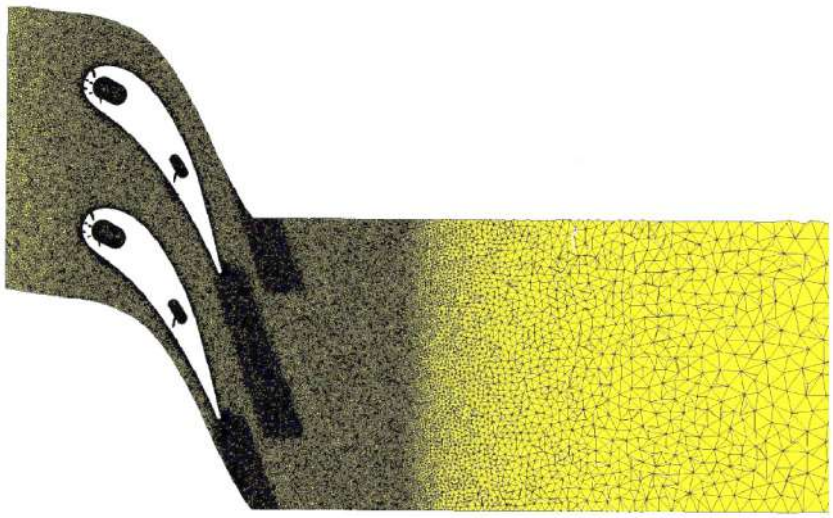

Figure 5.11 – View of the full tetrahedron mesh at mid-height of the vanes.

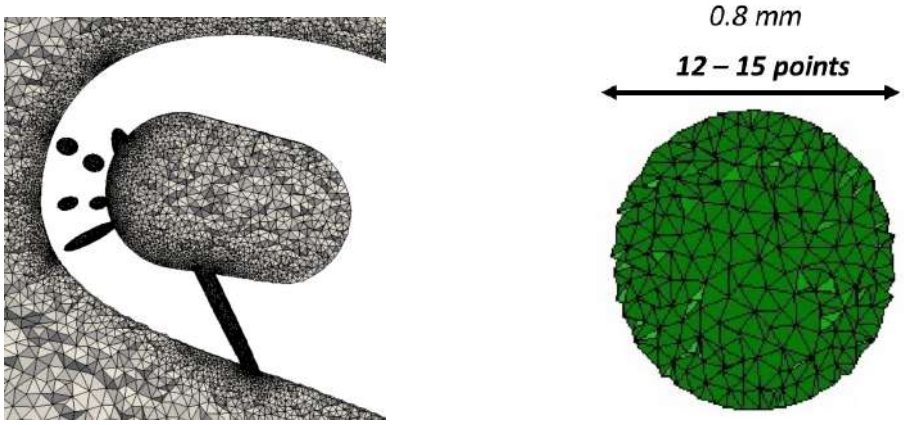

(a) (b)

Figure 5.12 – View of the mesh in the coolant pipes near the leading edge of NGV1 (a) and mesh cut in a pipe (b).

mesh, an adaptive mesh refinement process has been applied to refine the mixing regions between the main flow and coolant jets. The mesh refinement process is based on the MMG3D library (Dapogny et al., 2014; Daviller et al., 2017). The metric used to perform the automatic refinement is based on the loss maps $\overline{P_m}$ and $\overline{P_q}$ to identify regions of strong velocity and temperature gradients. Since coolant jets are expected to generate aerodynamic and mixing losses, the surface mesh is then refined along the coolant jet trajectories as shown on the surface mesh of NGV1 on Fig. 5.13. Note that the impact of the mesh adaptation process on the vane wall temperature and resolved turbulence can be found in Appendix F.

It is worth to note that such a mesh does not result in a purely academic LES in the sense that it does not respect the mesh resolutions of an academic problem. Nevertheless, using 15 points to discretize the diameter of each hole and the use of a wall-modelled approach is a good trade-off to deal with the capacity of mesh to capture flow dynamics while limiting the CPU effort of such a simulation.



(a) (b)

Figure 5.13 – Surface mesh on pressure side (a) and suction side (b) of NGV1.

Boundary conditions

Inflow and outflow boundary conditions are specified using the Navier-Stokes Characteristic Boundary Condition (NSCBC) formalism (Poinsot and Lele, 1992; Odier et al., 2018). To deal with the inlet specification, the corresponding 2D time-averaged mass flow rate $\overline{\rho U_i}$ and static temperature $\overline{T}$ maps obtained from the integrated computation combustor - NGVs realized by (Thomas et al., 2018) are extracted on $P40$ to be imposed as inflow for the isolated WMLES. To illustrate this inlet specification, the 2D steady map of temperature and associated velocity vectors are shown on Fig. 5.14. As expected, the hot spot locates at the center of the plane and aligns with NGV1. The cold flow issued from the effusion cooling ejected in the combustor is visible near the shroud in an anti-clockwise swirl. The coolant mass flow rates Q_{m1} and Q_{m2} corresponding respectively to coolant mass flow injected at the inlets of the LE plena and TE plena of both NGVs are set to comply with the experimental values with a static temperature of $T_{cold} = 300$ K. Note that to track the coolant, a fictive species $Y_{coolant}$ is also injected at the inlets of the plena. At the outlet, the surface averaged static pressure is imposed and adjusted to reach the experimental spatial averaged of static pressure on $P40$. Note that radial equilibrium is naturally obtained using the specific 3D NSCBC outlet boundary condition accounting for transversal terms as detailed by (Granet et al., 2010; Koupper et al., 2014). Note finally that all walls are treated as adiabatic condition. The imposed spatial averaged quantities are given in Table 5.3. It is important to note that, contrary to the work of (Thomas et al., 2018), the flow fields here imposed at the inlet are stationary. In other words, no turbulence is injected at the inlet to limit the CPU effort of such a complex simulation. Devia-

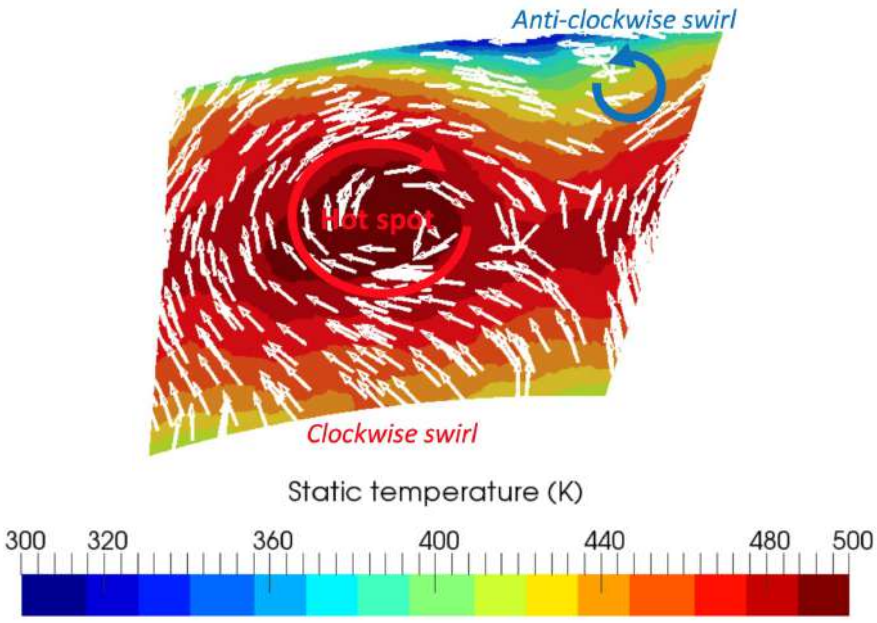

Figure 5.14 – 2D static temperature map T $[K]$ including a hot spot and swirled flow (evidenced by arrows) imposed at the inlet boundary condition.

Patch	Variable	Spatial mean value
Inlet	Q_m	0.240 $kg.s^{-1}$
•	T_{inlet}	455 K
Plena LE NGV1 & NGV2	Q_{m1}	0.0012 $kg.s^{-1}$
Plena TE NGV1 & NGV2	Q_{m2}	0.006 $kg.s^{-1}$
•	T_{cold}	300 K
Outlet	P_{outlet}	87000 Pa
Adiabatic Wall	-	-

Table 5.3 – Spatial mean values at the boundary conditions.

tions between LES prediction and experiment are then expected. Nonetheless, it is worth to recall that the *hole-meshed LES* presented in this chapter will be taken as the reference computation for the comparison with the *hole-modelled LES*. As a result, the lack of turbulence injection at the inlet has no impact on the main objective of this part.

LES modelling

The chosen sub-grid turbulence model is the WALE model (Nicoud and Ducros, 1999) because the Smagorinsky model (Smagorinsky, 1963) is known to be too dissipative for LES in turbomachinery (Collado, 2012; Papadogiannis, 2015; Koupper, 2015; Thomas et al., 2017).

More importantly, to avoid the overall cost of a WRLES for such a complex geometry, all walls are treated using an adiabatic wall law (Gourdain et al., 2009a; Tucker, 2011b; Tyacke and Tucker, 2014). In that case, the classical bilayer logarithm law of the wall is adopted (Von Karman, 1930). With this wall law, the switch from the log-law to sub-layer viscous linear part occurs when the normalized wall unit distance satisfies $y^+ = 11.445$. A view of the resulting cell size y^+ distribution is provided on Fig. 5.15. Clearly, the extent of wall unit value is large

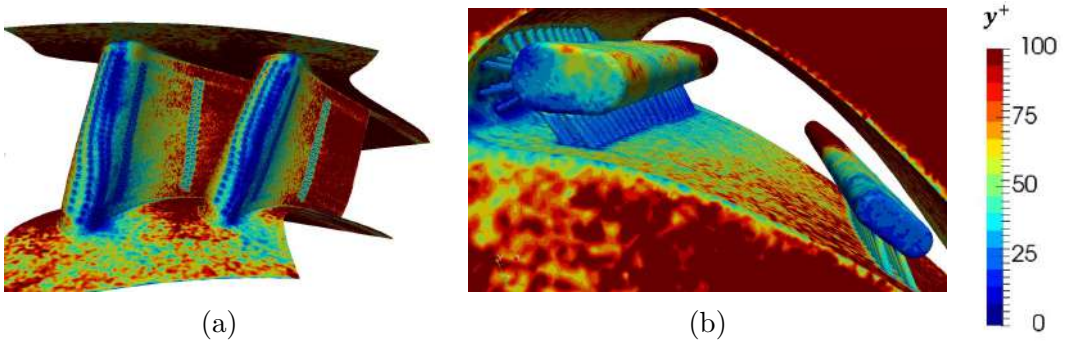

(a) (b)

Figure 5.15 – Normalized wall unit distance y^+ [-] near the leading edge of NGV1 (a) and in the cooling systems (b).

on the walls. Near the leading edge of the NGVs, Fig. 5.15 (a), the wall unit distance remains low, i.e, $y^+ < 10$. Downstream, y^+ rapidly increases and higher values are reached on the walls around the trailing edges of the vanes due to large velocities present in this region. In the cooling system of the vanes, a large extent of the walls is also observed to be in the viscous sub-layer, Fig. 5.15 (b). Although the author is aware of the limitations behind the chosen wall modelling (as the absence of pressure gradient), it is worth to recall that the aim of this work is to present the *hole-meshed LES* prior to the comparison with the *hole-modelled LES*. The effect of the wall law on the flow prediction is then out of scope of this work.

Numerical scheme

All simulations rely on the resolution of the LES compressible equations (Garnier et al., 2009; Poinsot and Veynante, 2011). The compressible equations are numerically integrated with the finite element numerical explicit scheme TTG4A, 3rd order in space and 4th order in time (Donea and Huerta, 2003).

5.3 LES results

In this section, the LES prediction of the above described configuration is presented. The instantaneous flow structure and mean flow organization are first described in Section 5.3.1. Since the migration of the hot spot and the mixing process with the coolant flow were shown to affect the vane wall temperature, these two points are specifically investigated. Following this investigation, the evaluation of the adiabatic film effectiveness on the vane surfaces are compared to experimental results. Finally, losses are investigated in Section 5.3.2.

5.3.1 Flow description and validations

Prior to the presentation of the flow organization, the numerical operating point of the vanes should be verified. This specific point is hereafter addressed.

Numerical operating point

To verify the numerical operating point of the vanes, the isentropic Mach number distribution obtained at mid-height of the vanes is compared to experimental results on Fig. 5.16. Based on this diagnostic, LES prediction and experiment data are found to be in very good agreement which validates the flow expansion through the vanes. Note that on both sides of the vanes, peaks are noticed in the profiles between $x/ACL = 0.05$ and $x/ACL = 0.15$ and on the pressure side near $x/ACL = 0.7$. These sudden changes of isentropic Mach values correspond to the local acceleration of the flow due to coolant ejection as already observed in Chapter 4.

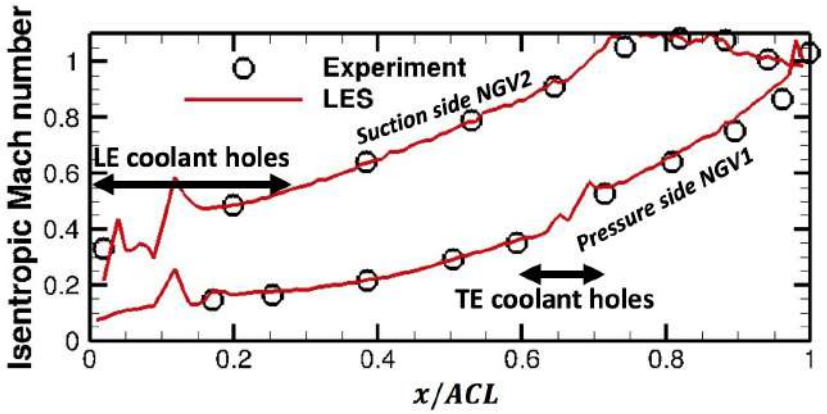

Figure 5.16 – Isentropic Mach number Ma_{is} [-] at mid-height of the vane on both sides. Red line – represents LES and black circle **O** the experimental data. Axial extents of the coolant rows are indicated.

Instantaneous view of the large scale flow structures

To evidence the large scale flow organization issued from the coolant jets, an instantaneous view of an iso-surface of Q-criterion equal to $Q_{crit} = 1.10^9 s^{-2}$ coloured by the vorticity is provided on Fig. 5.17. As expected, the wakes of the vanes are found to be turbulent. All the coolant jets also exhibit unsteady coherent structures. A closer look at the coolant jets in the region A is provided on Fig. 5.17. In this region, a pair of vortices is found to be issued from each hole and propagates along the jets. Such vortices correspond to the so-called Counter Rotating Vortex Pair (CRVP) and were reported in the literature of jets in cross-flows (Fric and Roshko, 1994; New et al., 2003). These structures are then stretched by the acceleration of the flow downstream. This stretching is naturally enforced near the trailing edge because of the strong flow expansion in this region. At the base of

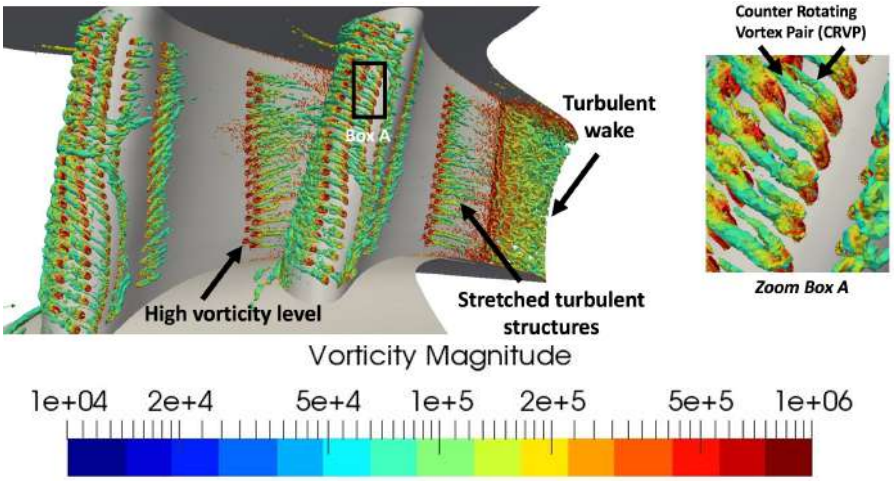

Figure 5.17 – Instantaneous view of an iso-surface of Q-criterion equal to $Q_{crit} = 1.10^9 s^{-2}$ coloured by the vorticity magnitude $\|\omega\|$ $[s^{-1}]$. A zoom in box A is shown.

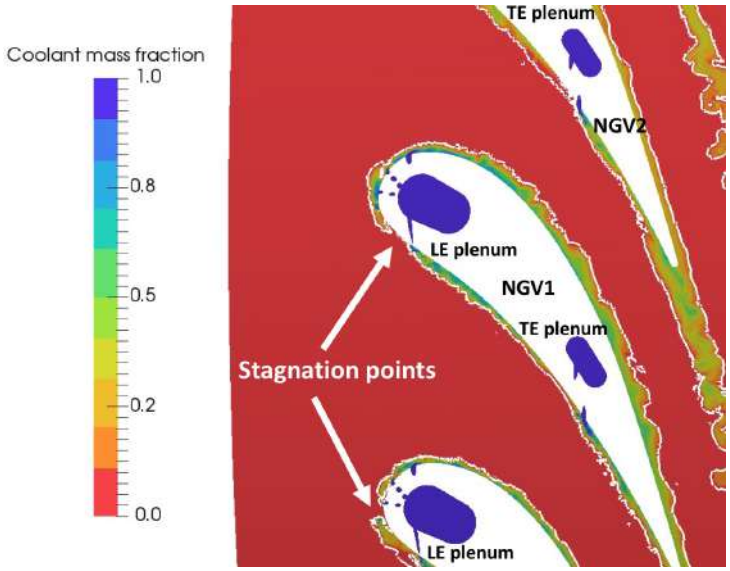

Figure 5.18 – Instantaneous view of coolant mass fraction map $Y_{coolant}$ [-] taken at mid-height. White iso-line represents the film thickness defined by $Y_{coolant} = 0.05$.

the coolant jets, high vorticity levels (red) are noticed due to the strong shear produced between coolant jet and main stream. To investigate the effect of all these unsteady structures on the coolant film, an instantaneous view of the coolant mass fraction map taken at mid-height is shown on Fig. 5.18. From this map, the film cooling thickness is built from the iso-contour value $Y_{coolant} = 0.05$. Clearly, the film covers both vanes except at the stagnation point. One also note that the thickness of the film strongly varies along both pressure and suction sides of vanes due to the unsteadiness present in the film. It is also noted that coolant mass fraction is highly segregated in the film and is characterized by regions of low and high concentrations due to unsteady structures.

For a clearer analysis and quantification, the flow fields are time-averaged through 4 flow time passages defined as the time taken by a fluid particle released at the inlet to reach the outlet of the computational domain. Such a convergence time is sufficient to ensure that the flow statistics (mean + RMS) are converged. From the time-averaged flow fields, the mean flow organization in the main stream as well as of coolant jets are hereafter described in more details.

Mean flow organization

In this section, the mean flow organization is described. First, the flow aerodynamics is discussed by studying the time-averaged Mach number maps extracted at different normalized heights h (by the height of the vanes H) on Fig. 5.19. To evidence supersonic regions, white iso-lines corresponding to unity Mach number are added to the views. First and despite the 2D fields imposed at the inlet, the flow acceleration is found to be very similar between NGV1 and NGV2. For all

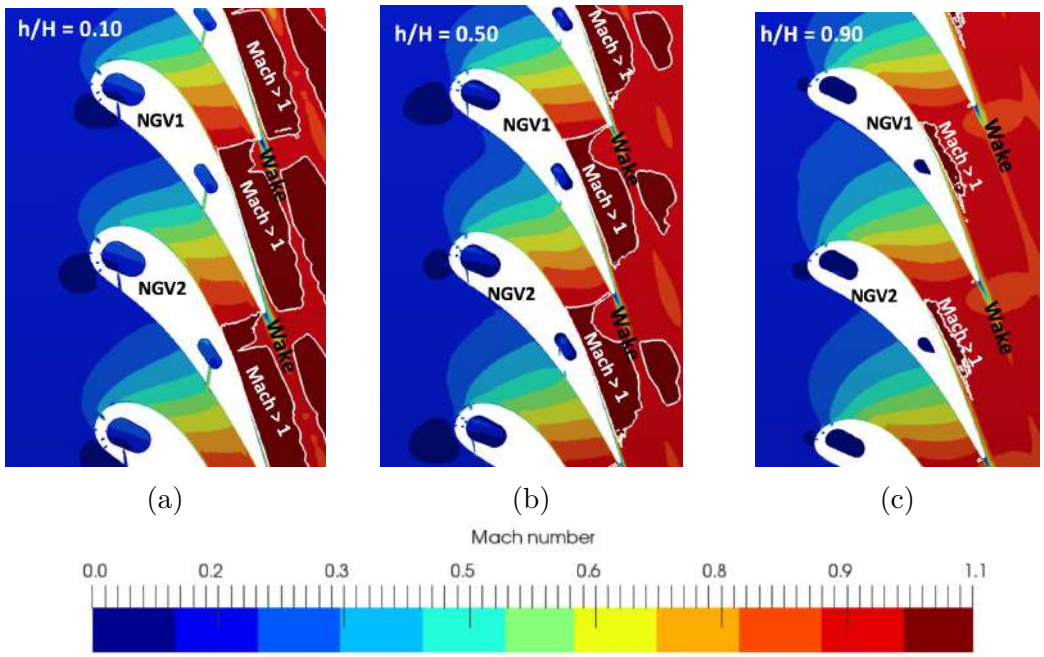

Figure 5.19 – Time-averaged Mach number maps $\overline{Ma}$ [-] at mid-height for $h/H = 0.50$ on left (a), near the hub for $h/H = 0.10$ in the middle (b) and near the shroud for $h/H = 0.90$ on right (c). White iso-line represents $\overline{Ma} = 1$.

heights, the flow is found to accelerate through the vanes, the white iso-contour of $\overline{Ma} = 1$ clearly evidencing a supersonic region located on the suction side of both vanes. On the contrary, very low Mach number, i.e, $\overline{Ma} < 0.3$ are found in the coolant feeding plena of the vanes. Clearly, a dependency of the flow acceleration appear and is in function of the radial position. Indeed, near the hub at $h/H = 0.10$, Fig. 5.19 (a), the acceleration of the flow is stronger compared to the mid-height cut, Fig. 5.19 (b). As a result, the supersonic region extends more in the NGV passage when approaching the hub. Near the shroud at $h/H = 0.90$, Fig. 5.19 (c), the opposite appears and only a small proportion of the suction side is supersonic. This radial dependency of flow expansion is recovered in all turbomachinery flows and is induced by the radial distribution of static pressure due to radial equilibrium (Smith Jr, 1966).

The thermal environment around the vanes is now addressed. To do so, the hot spot migration and the swirled flow through the vanes are investigated. In the following, the contour of the hot spot will be represented by the iso-surface of the total temperature T_t equal to 480 K. Indeed and since walls are adiabatic, the total temperature spatial distribution only depends on the transport of the hot spot and its mixing with the coolant flow. To get a first view of the migration of the hot spot as well as its interaction with the coolant flow, the iso-surface of the time-averaged total temperature $\overline{T_t} = 480K$ (in red) as well as of the coolant total temperature $\overline{T_t} = 300K$ (in blue) are shown on Fig. 5.20. Due to the initial

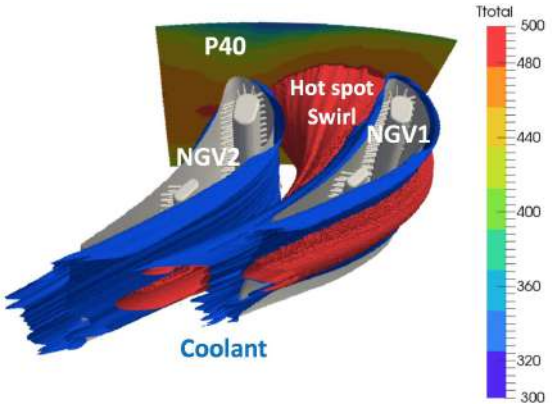

Figure 5.20 – Iso-surface of the time-averaged total temperature of 480 K in red as well as iso-surface of the coolant total temperature of 300 K in blue.

position of the hot spot on $P40$, the hot spot hits the pressure side of NGV1 and splits in 2 parts and propagates along both pressure and suction sides of NGV1 as described in (Koupper, 2015). The largest part of the hot spot remains near the pressure side of NGV1 due to flow inertial effects (Koupper, 2015; Cubeda et al., 2019; Li et al., 2019). Between the vanes, the hot spot is stretched by the flow acceleration. Coolant flow is found to cover both vanes and to interact with the hot spot mainly around NGV1. To investigate the hot spot migration along the vanes, different axial cuts represented on Fig. 5.21 are extracted from the computational domain. On these axial cuts, the total temperature field and swirled flow velocity vectors are shown on Fig. 5.22. Finally, the iso-contour $\overline{T_t} = 480K$ is added to the views to evidence the hot spot contour. To build the velocity vector of the swirled flow, a similar approach used to extract secondary flows found from the literature is adopted (Germain et al., 2007; Persico et al., 2009). This way, a reference flow direction is first defined for each axial cuts based on the 2D average direction of the flow at mid-height. Next, the local velocity vector is projected on this reference flow direction and this projection is then removed from the local velocity vector. Finally, the remaining velocity vector is projected onto axial cut to obtain the swirled flow velocity vector. In the following, swirled flow velocity vectors are normalized to obtain unit vectors and are represented by white arrows on the views. By construction, the field at the inlet, Fig. 5.22 (a), corresponds to the imposed field by the boundary condition and has already been discussed in

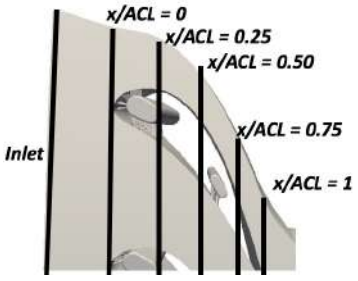

Figure 5.21 – Positions of the axial cuts in the computational domain.

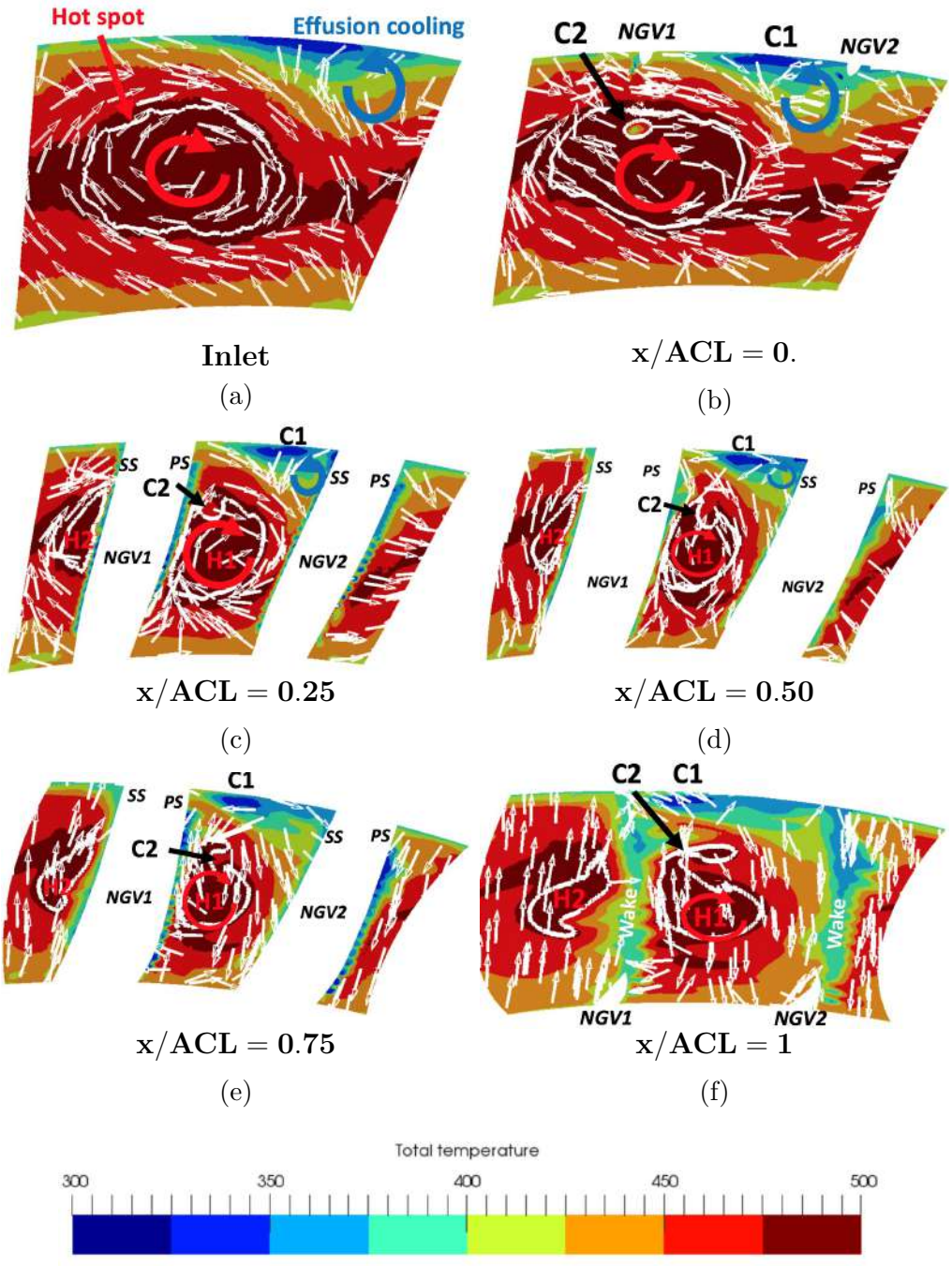

Figure 5.22 – Axial cuts of total temperature T_t $[K]$ at inlet (a), at leading edge for $x/ACL = 0.$ (b), at $x/ACL = 0.25$ (c), at $x/ACL = 0.50$ (d), at $x/ACL = 0.75$ (e) and at trailing edge for $x/ACL = 1.$ (f). View downstream. PS (pressure side) and SS (suction side). White iso-line represents $\overline{T_t} = 480K$. White arrows represent swirled flow velocity vectors.

Section 5.2. At the leading edge of both NGVs, Fig. 5.22 (b), the total temperature field as well as the hot spot boundary remain very similar compared to the inlet. The cold region located near the shroud is however pushed by the potential effect of NGV2 toward NGV1 (this cold region will be noted **C1** in the following). Another small cold region is observed to be surrounded by the hot spot and originates from the coolant ejected at the leading edge of NGV1 (this second cold region will be noted **C2**). At $x/ACL = 0.25$, Fig. 5.22 (c), the hot spot clearly splits in 2 parts. The part of the hot spot located near the pressure side of NGV1 is noted **H1** and the part located near the suction side of NGV1 is noted **H2**. Both parts **H1** and **H2** of the hot spot get smaller due to the reduction of the passage. The cold region **C1** lies at the corner between the shroud and the suction side of NGV2. The cold region **C2** locates near the pressure side of NGV1. Around both NGV1 and NGV2, the total coolant temperature is retrieved confirming that the coolant film covers both NGVs. At $x/ACL = 0.50$, Fig. 5.22 (d), the hot spot continues to shrink. Due to the swirled flow direction, the cold region **C2** moves away from NGV1 in the passage. Near the shroud, the cold region **C1** gets closer to NGV1. At $x/ACL = 0.75$, Fig. 5.22 (e), the part of the hot spot **H1** is distorted by the swirled flow. In parallel, size of cold region **C2** has grown. Indeed, one part of the coolant ejected on the pressure side of NGV1 is transported by the swirl from the near wall region of NGV1 to the passage between NGV1 and NGV2. At the trailing edge of the vanes, Fig. 5.22 (f), the part of the hot spot **H1** remains close to the pressure side of NGV1. This confirms that the trajectory of the hot spot is mainly driven by the flow inertial effects and is weakly impacted by the pressure gradient generated between pressure and suction of the vanes (Koupper, 2015; Cubeda et al., 2019; Li et al., 2019). At this station, the shape of the hot spot is highly distorted by the presence of cold region **C2**. The cold region **C1** on the other hand gets closer to the wake of NGV1 near the shroud. One finally notes that the total temperature in the wake of both NGVs lies between the hot spot and coolant total temperature. This indicates a strong mixing process taking place in the wakes between the hot and coolant flows. To investigate this last interaction between the hot spot and coolant flow, the mixing process between both flows is to be studied. To do so, turbulent mixing between the coolant and hot flows is studied by investigating the Root Mean Square (RMS) of the coolant mass fraction Y_{rms} at different axial cuts as previously described in Fig. 5.23. At the inlet, Fig. 5.23 (a), no turbulent mixing is observed because no coolant is ejected at the inlet of the computation domain. At the leading edge of both NGVs, Fig. 5.23 (b), turbulent mixing occurs near the coolant ejection position. This turbulent mixing is particularly strong in the cold region **C2** due to the presence of turbulent fluctuations in the jets. At $x/ACL = 0.25$, Fig. 5.23 (c), the mixing process mainly takes place in the near wall flow region of NGV1 and NGV2 due to the interaction between the hot and coolant flows in the film. At $x/ACL = 0.50$, Fig. 5.23 (d), the mixing process moves away from the pressure side NGV1 in the passage. This effect is probably induced by the transport of the coolant by the flow in the passage between the vanes. At $x/ACL = 0.75$, Fig. 5.23 (e), this last effect is strengthened. Finally, at $x/ACL = 1$, Fig. 5.23 (f), mixing regions are very extended in the wakes. This

confirms that the hot spot strongly mixes with the coolant film in the wakes. Mixing process is further spatially extended in the passage between both NGVs by the swirl. Note that turbulent mixing is also observed near the shroud due to the interaction between cold and hot flows in this region. To investigate the origin of mixing process, the coolant flow aerodynamic is detailed in the next section.

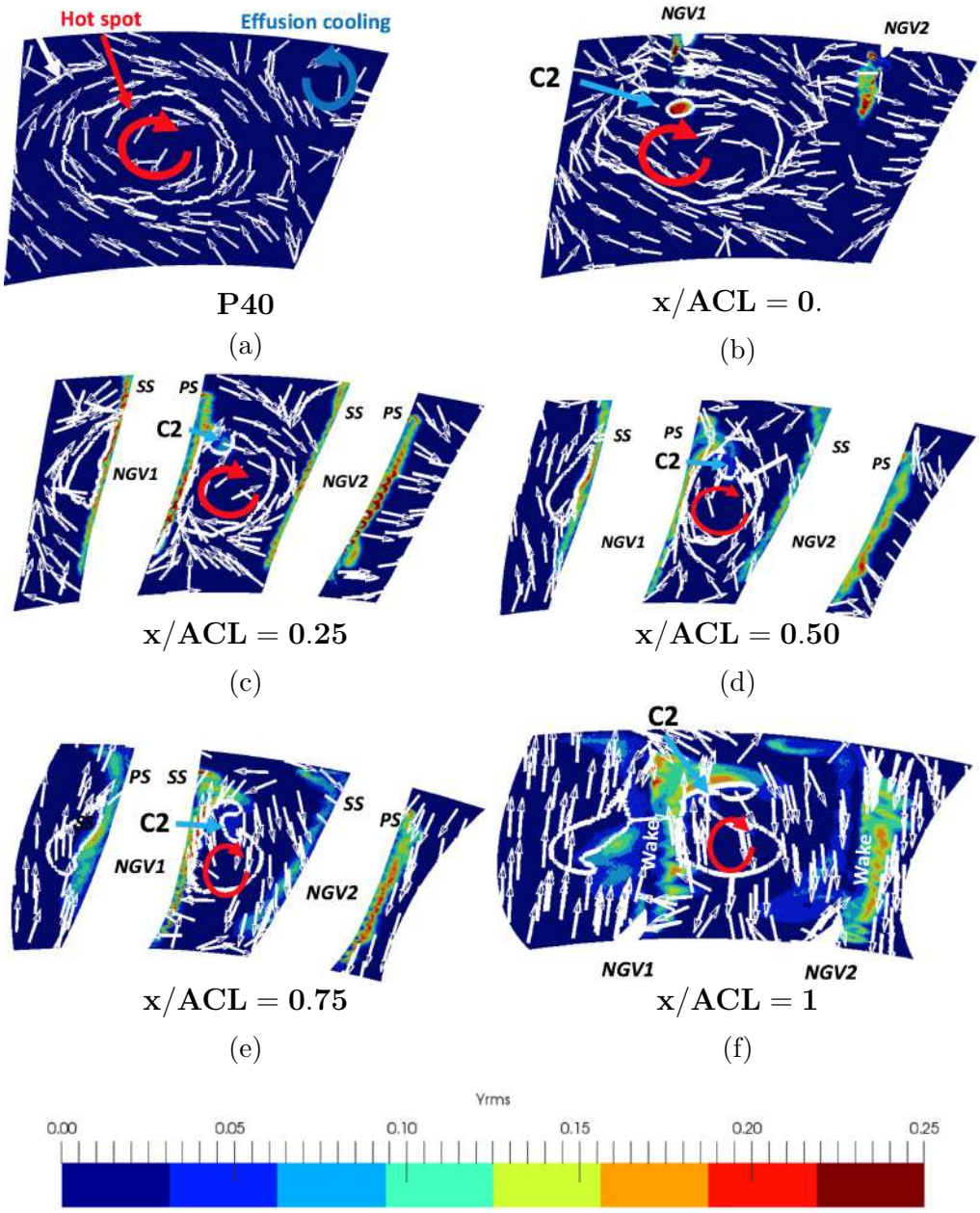

Figure 5.23 – Axial cuts of turbulent mixing represented by Y_{rms} [-]. Axial cuts correspond to the inlet (a), leading edge $x/ACL = 0$. (b) , $x/ACL = 0.25$ (c), $x/ACL = 0.50$ (d), $x/ACL = 0.75$ (e) and the trailing edge $x/ACL = 1$ (f). View downstream. White iso-line represents $\overline{T_t} = 480K$.

Mean structure of the coolant flow

In the following, the distribution of the coolant jets on both pressure and suction sides for both NGVs is presented. To do so, an iso-surface of the time-averaged coolant mass fraction equal to $\overline{Y_{coolant}} = 0.75$ is provided on Fig. 5.24. To discriminate the pressure from the suction side of both NGVs, white lines representing the identified stagnation lines on NGV1 and NGV2 are added to the views, the stagnation lines being deduced from a null iso-contour of wall shear stress. As seen on Fig. 5.24, both stagnation lines have a S shape which is explained by the swirl which implies a heterogeneous radial distribution of pressure. Note also that these stagnation lines are found to be different between NGV1 to NGV2 once gain because of the different respective position with respect to the inflow. To identify the coolant holes, the rows of holes are numbered from the leading edge to the trailing edge as shown on Fig. 5.24. From this notation, the stagnation line on NGV1 passes through the 4th row. The rows from 1 to 3 are therefore located on the suction side of the vane. On NGV2, the stagnation line passes though the 3rd and 4th rows. Only rows 1 and 2 are located on the suction side of the vane.

For all holes, a cold jet is ejected from the aperture confirming that there is no re-ingestion of hot gases through the coolant pipes. For rows 7th and 8th on both NGVs, the jet iso-surface is stretched by the strong flow acceleration in this region. It is noted for this value, the jet iso-surface remains near the vane wall and does not propagate in the passage. This confirms that the mixing process mainly takes place in coolant jets. To investigate the origin of this mixing process, the flow aerodynamic structure inside the coolant pipes is studied. To do so, time-averaged velocity magnitude and turbulent kinetic energy maps in the coolant pipes located near the leading edge at mid-height of NGV1 are given on Fig. 5.25. From Fig. 5.25 (a), strong sheared flow and horse-shoe pattern are observed in coolant pipes. Such coolant flow structure originates from the separation of the boundary layer at the inlet of the pipes as already observed in Chapter

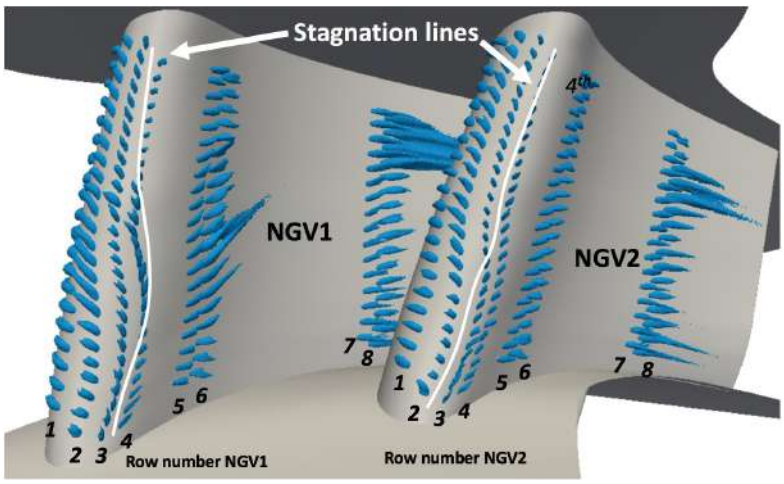

Figure 5.24 – Time-averaged coolant mass fraction iso-surface, $\overline{Y_{coolant}} = 0.75$.

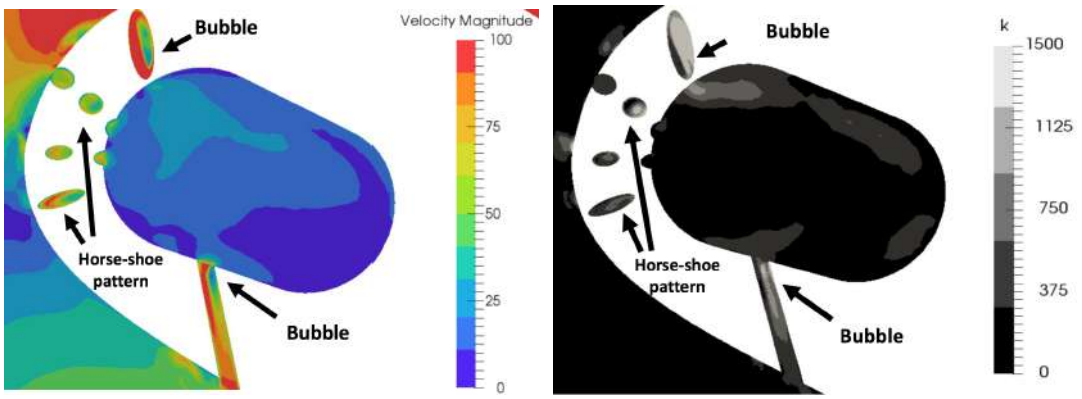

Figure 5.25 – Time-averaged velocity magnitude $\overline{\mathbf{v}}$ $[m/s]$ (a) and turbulent kinetic energy k $[m^2/s2]$ (b) maps at mid-height of the vanes in the pipes near the leading edge of NGV1.

4 and in the literature of coolant jets (Leylek and Zerkle, 1994; Peet and Lele, 2008; Simiriotis, 2016; Bizzari, 2018). These specific regions are observed to be associated with high levels of kinetic energy, Fig. 5.25 (b). Since no freestream turbulence is injected at the inlets of the coolant flow, the turbulence here evidenced necessary originates from the flow dynamics present in the plena and the pipes. Indeed and as observed in the literature, separations and horse-shoe patterns lead to a turbulent transition of the flow (Leylek and Zerkle, 1994; Peet, 2006). To study the impact of such a turbulence generation in the coolant pipes on the film dynamic, the turbulent kinetic energy k is shown at mid-height around both NGVs on Fig. 5.26. The edge of the coolant film defined by $\overline{Y_{coolant}} = 0.05$ is represented by the white iso-line. Since no freestream turbulence is injected at the inlets of the domain, turbulence levels observed in the film and in the cooling system (pipes + plena) necessary originate from the flow dynamics present in the cooling system.

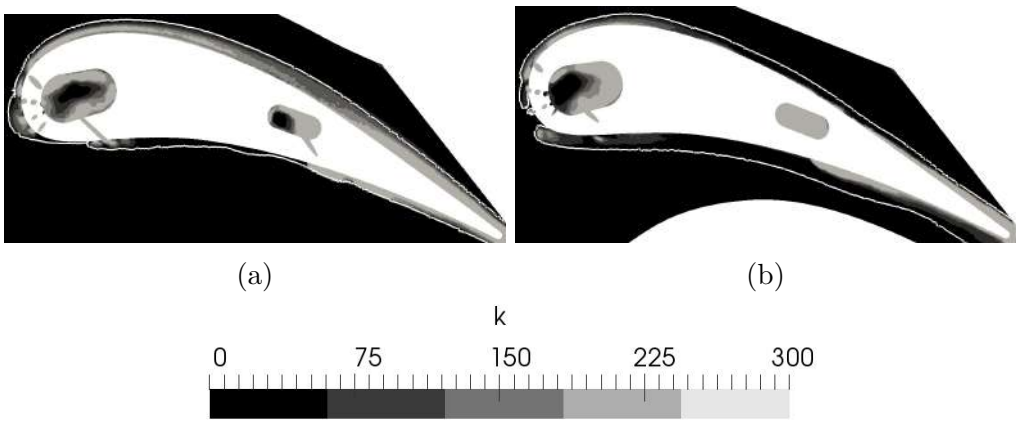

Figure 5.26 – Turbulent kinetic energy maps k $[m^2/s^2]$ on NGV1 on left (a) and NGV2 on right (b) at mid-height. White iso-line represents the thickness of the film cooling defined by the iso-value $Y_{coolant} = 0.05$.

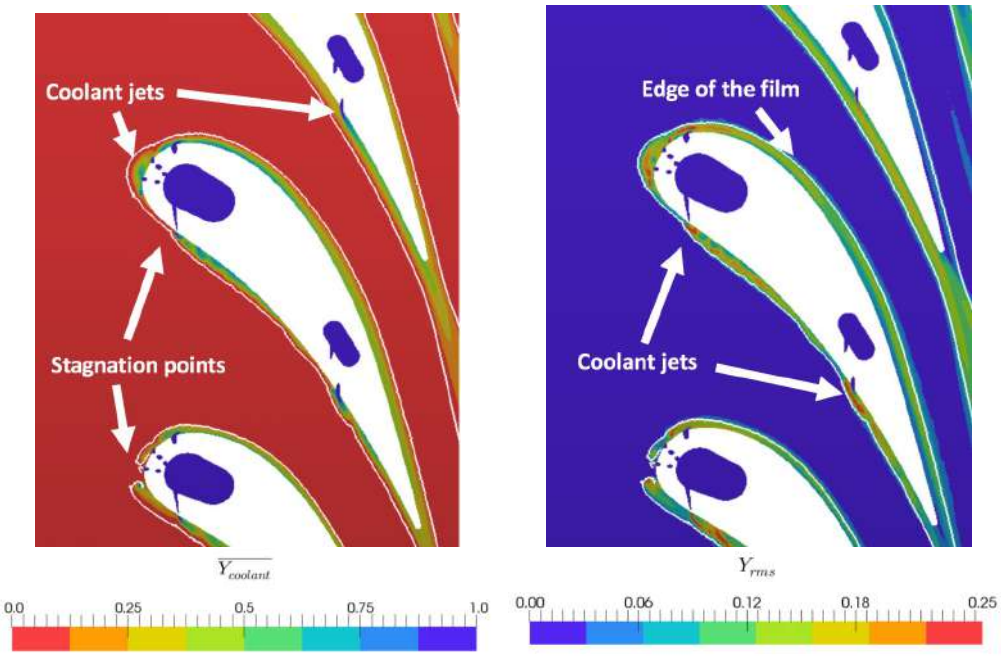

(a) (b)

Figure 5.27 – Time-averaged coolant mass fraction map $\overline{Y_{coolant}}$ [-] on left (a) and Y_{rms} [-] on right (b) at mid-height. White iso-contour represents $\overline{Y_{coolant}} = 0.05$.

To investigate the film development in more details, time-averaged coolant mass fraction $\overline{Y_{coolant}}$ as well as Y_{rms} at mid-height are shown on Fig. 5.27. The edge of the coolant film is added on the views for more clarity. Time-averaged coolant mass fraction $\overline{Y_{coolant}}$ map, Fig. 5.27 (a), shows that the mean film develops around both vanes except on the stagnation points. As for the film itself, spatial variations of $\overline{Y_{coolant}}$ is large. Indeed, $\overline{Y_{coolant}}$ approaches 1 near the coolant holes because of coolant ejection and then decreases when moving away from the wall due to the mixing process with the hot stream in the passage. Y_{rms} map, Fig. 5.27 (b), confirms that turbulent mixing only occurs in the film itself. Naturally, mixing is observed to be higher near the holes probably due to the higher temperature differences and flow dynamics in this region. Downstream the holes, Y_{rms} decreases indicating that turbulent mixing in the film reduces. Finally, turbulent mixing also activates in the wakes confirming that mixing process still occurs downstream the vanes. To quantify the development of the coolant film around the vanes, the thickness of the film δ_f is extracted from time-averaged maps. Similarly to Chapter 4, the film thickness δ_f is defined as the wall normal distance for which $\overline{Y_{coolant}} = 0.05$ along the vanes. Note that the following discussion is limited to the mid-height to exclude the effect of end-walls as well as secondary flows on the film development. Film evolutions are given on both sides of both NGVs on Fig. 5.28. From Fig. 5.28, δ_f equals zero at the stagnation point as expected. It is important to note that, since the origin of the plots is taken as the leading edge axial position, film evolutions for $x/ACL < 0.15$ for NGV1 and $x/ACL < 0.05$

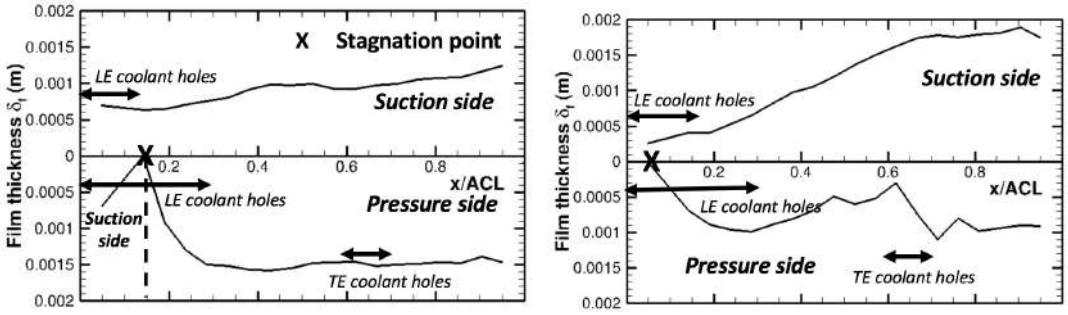

(a) (b)

Figure 5.28 – Axial evolution of the film thickness δ_f $[m]$ at mid-height of the vanes for NGV1 (a) and NGV2 (b). The axial extend of the coolant holes as well as the stagnation point for each NGVs are indicated.

for NGV2 correspond to suction side part of the vane. On the pressure side of NGV1, Fig. 5.28 (a), δ_f increases for the axial extent $0 < x/ACL < 0.4$ because of the coolant ejection through the holes located near the leading edge of the vane. For $x/ACL > 0.4$, δ_f stabilizes due to the flow acceleration in this region which stretches and reduces the film thickness. On the suction side, δ_f continuously increases along the vane due to the accumulation of coolant fluid injected through the holes located near the leading edge. Downstream the coolant holes, this increase of δ_f is expected to be mainly driven by the mixing process between the coolant and the hot streams. It is important to note that δ_f clearly evidences different evolutions for NGV2, Fig. 5.28 (b), with respect to NGV1. Such a deviation between both NGVs could originate from the 2D temperature map imposed at the inlet which naturally implies a different behaviour of the mixing process between both NGVs. On the pressure side of NGV2, δ_f increases at the axial positions where coolant is ejected, i.e, for $0 < x/ACL < 0.3$ and $0.6 < x/ACL < 0.7$. As for NGV1, δ_f then decreases downstream the coolant hole axial positions due to the flow acceleration stretching the film. On the suction side, δ_f continuously increases for $x/ACL > 0.2$ due to the accumulation of coolant fluid injected through the holes located near the leading edge as for NGV1. The swirled inflow is also expected to impact δ_f by radially drifting the coolant film.

From δ_f and similarly to Chapter 4, the axial evolution of coolant concentration along the vanes can be evaluated through the mass flow weighted film coolant Y_{film} so that,

$$Y_{film}(x) = \frac{\int_0^{\delta_f(x)} \overline{\rho U_i n_i Y_{coolant}} dn}{\int_0^{\delta_f(x)} \overline{\rho U_i n_i} dn}, \tag{5.4}$$

where n is the wall normal distance, ρ the density, U_i the local velocity vector, n_i the normalized vector tangential to the wall and $\overline{\bullet}$ the time-averaged operator. The axial evolution of Y_{film} is provided for both NGVs on Fig. 5.29. As expected, Y_{film} equals zero at the stagnation points. For both NGVs, Y_{film} increases for axial positions of where coolant is ejected, i.e, for $x/ACL < 0.3$ and $0.6 > x/ACL > 0.7$

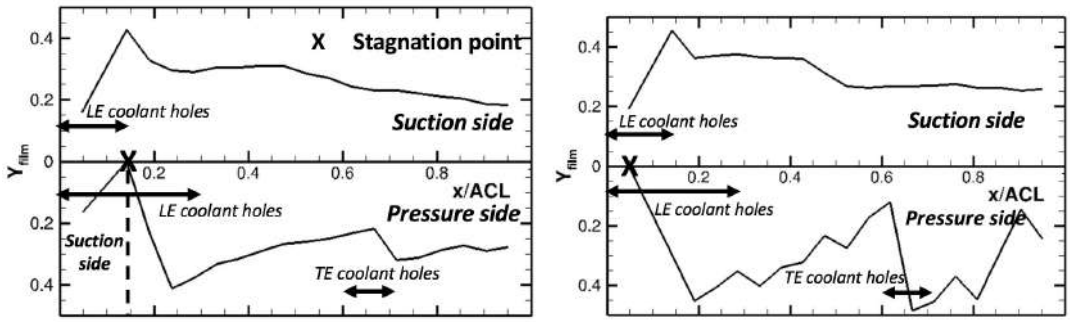

(a) (b)

Figure 5.29 – Axial evolution of the mass-flow averaged coolant mass fraction Y_{film} [-] at mid-height of the vanes for NGV1 (a) and NGV2 (b). The axial extend of the coolant holes as well as the stagnation point for each NGVs are indicated.

for the pressure side and $x/ACL < 0.15$ for the suction side. Downstream these positions, Y_{film} decreases because of the mixing process with the hot stream. Similar observations are drawn for NGV2, Fig. 5.29 (b).

To confirm the link between axial evolutions of Y_{film} and mixing process with the hot flow, a mass balance of the coolant flow can be performed as in Chapter 4. To perform such a balance, the control volume is defined at mid-height of the vane as shown in Fig. 5.30 and with the same notations of Chapter 4. Since the control volume is defined on a radial cut, the radial contribution of the coolant mass flux normal to the cut is omitted in the mass balance. Furthermore, since the flow is statistically converged, the same logic used in Section 4.3.2 can be here applied.

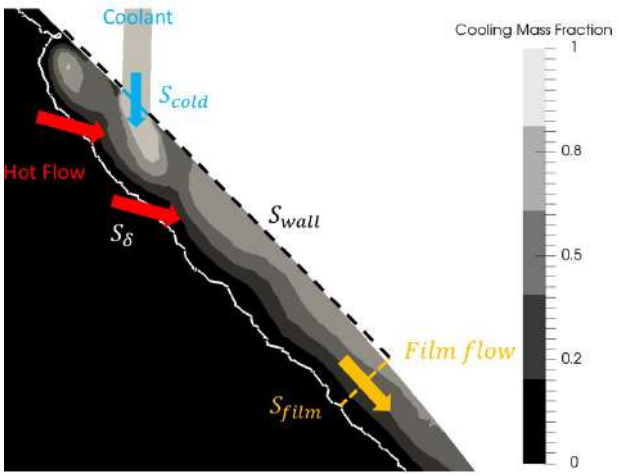

Figure 5.30 – Control volume at mid-height to apply the mass balance in the coolant film. The control volume is delimited by the ejection exit of the coolant pipes S_{cold}, the walls S_{wall}, the edge of the coolant film S_δ and the film section S_{film}.

As a result, the axial evolution of Y_{film} is retrieved by combining Eq. (4.11) with Eq. (4.12), giving:

$$Y_{film}(x) = \frac{1}{Q_{m,film}} \left(Q_{m,cold} - \underbrace{\int_{S_{\delta(x)}} \overline{\rho} \widetilde{Y''_{coolant} U''_i} n_i dS}_{\text{Turbulent mass flux}} \right), \tag{5.5}$$

where $Q_{m,film}$ is the mass flow rate passing through S_{film}, $Q_{m,cold}$ is the coolant mass flow rate injected through the coolant holes, $\overline{\bullet}$ is the time-averaged operator, $\widetilde{\bullet}$ is the Favre averaging and $''$ is the temporal fluctuations with respect to the Favre averaging. The second term on the RHS of Eq. (5.5) corresponds to the turbulent coolant mass flux through the edge of the coolant film. Note that the mean contribution of the mass flux is assumed to be small compared to the turbulent contribution and is thus omitted in Eq. (5.5). The axial evolution of the local turbulent mass flux $\overline{\rho} \widetilde{Y''_{coolant} U''_i} n_i$ on both sides of both NGVs is provided on Fig. 5.31. For both NGVs, it is important to note that turbulent mass flux is positive. According to Eq. (5.5), this means that turbulent mass flux necessary decreases the value of Y_{film} as expected. Turbulent mass flux is found to increase where coolant is ejected, i.e, for $0 < x/ACL < 0.3$ and $0.6 < x/ACL < 0.7$ confirming that turbulent mixing process mainly takes place in the coolant jets. Indeed, turbulent mixing was previously observed to be strong in these regions in Fig. 5.27. Downstream these axial positions, turbulent mass flux decreases. It is noted that at the trailing edge of the vanes, i.e, for $x/ACL = 1$, the value of turbulent mass flux is not zero confirming that mixing process still occurs in the wakes of the vanes.

In the following, the impact of the coolant film on time-averaged skin vane temperature is detailed.

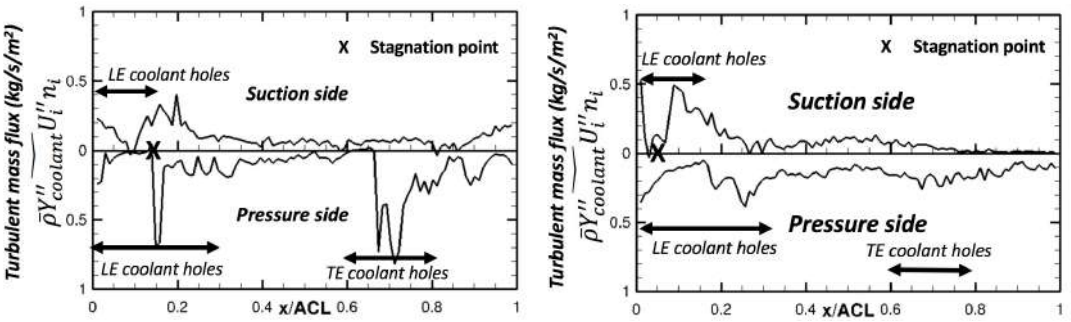

(a) (b)

Figure 5.31 – Axial evolution of the coolant turbulent mass flux $\overline{\rho} \widetilde{Y''_{coolant} U''_i} n_i$ $[kg/s/m^2]$ through the edge of the film at mid-height of the vanes for NGV1 (a) and NGV2 (b). The axial extend of the coolant holes as well as the stagnation point for each NGVs are indicated.

Time-averaged wall temperature and adiabatic film effectiveness

A 3D view of the time-averaged wall temperature is provided in Fig. 5.32. Time-averaged wall temperature field is observed to be highly non-uniform with large variation of temperature. On the hub, traces of hot spot are retrieved and seen to impact the pressure side of NGV1. On the shroud, the mark of the effusion cooling coming from combustor is also observed to migrate in the passage between the vanes. On the vane walls, a large range of temperature is also found. To better describe both sides, time-averaged wall temperature fields are unwrapped and results are shown on Fig. 5.33. For this view, radial coordinate h is normalized by the height of the vanes H taken at the trailing edge of the vanes. Note that this choice leads to negative values for the normalized radial coordinate h/H near the leading edge of the vane. Similarly, curvilinear coordinate s_c is normalized by the maximum curvilinear distance S_c for each sides of the vanes taken at $h/H = 0$ to ensure that $|s_c/S_c| < 1$ all along the vanes. Note also that normalized curvilinear coordinate s_c/S_c is arbitrary chosen to be positive on the pressure side and negative on the suction side. Using such a coordinate system, the LE coolant holes locate in the interval $-0.1 < s_c/S_c < 0.2$ while the TE coolant holes lie in the interval $0.6 < s_c/S_c < 0.7$. On NGV1, Fig. 5.33 (a), high levels of temperature ($> 400K$) and strong radial heterogeneity is observed near the leading edge of the vane for $0 < s_c/S_c < 0.2$, where the hot spot and swirl impact the vane. Downstream the coolant holes of the pressure side for $s_c/S_c > 0.2$, traces of coolant jets are clearly seen thanks to the temperature range from 300 K to 320 K. In the interval between $s_c/S_c = 0.2$ and $s_c/S_c = 0.5$, hot temperature ($> 400K$) are also observed in the first half of the height for $h/H < 0.5$ while colder temperatures ($< 400K$) concentrate on $h/H > 0.5$. Indeed, hot temperatures arise in-between the coolant holes for $s_c/S_c = 0.2$ and $h/H < 0.2$ indicating that one part of the hot flow passes in-between holes. This effect corresponds to the suction of the hot flow around the coolant holes due to the jet deviation as already observed in

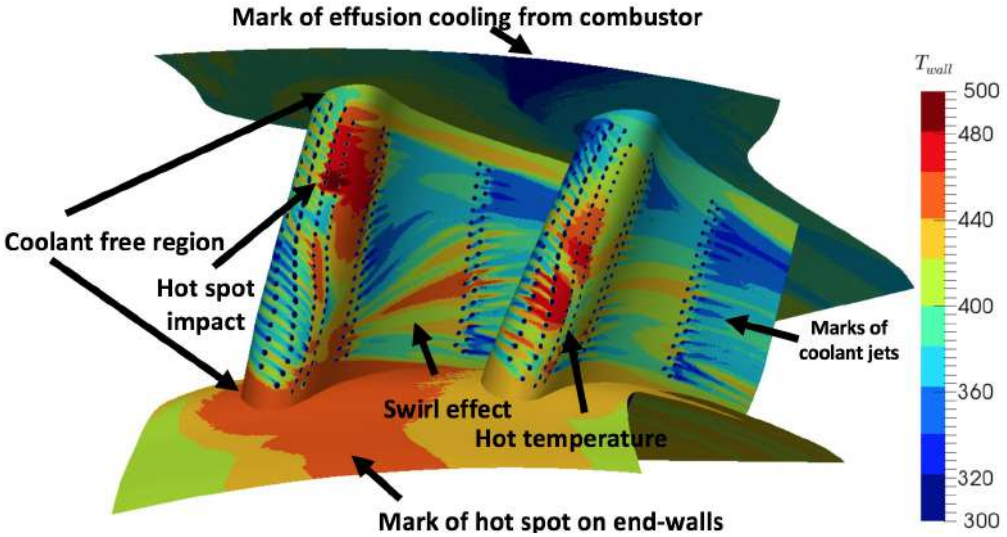

Figure 5.32 – 3D view of the time-averaged wall temperature T_{wall} $[K]$.

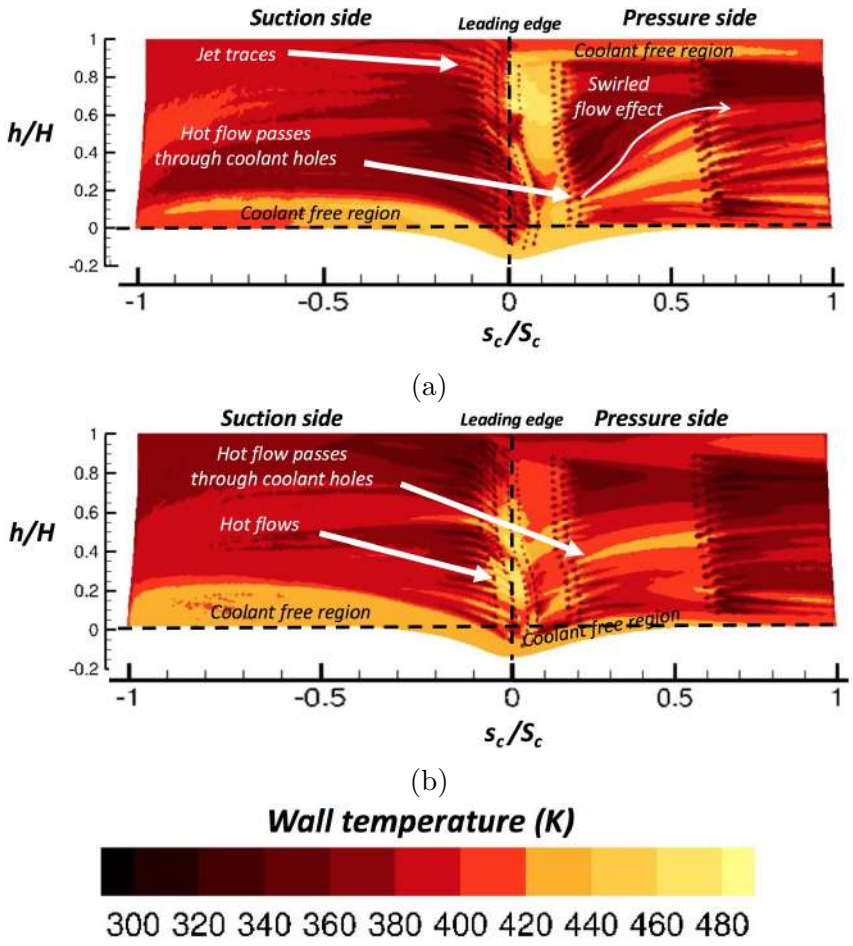

Figure 5.33 – Unwrapped time-averaged wall temperature, NGV1 (a) and NGV2 (b). Normalized radial coordinate h/H and curvilinear coordinate s_c/S_c.

Chapter 4 and in (Gomes and Niehuis, 2011). The temperature radial distribution on NGV1 is also to be linked to the radial drift of hot temperatures from $h/H = 0.2$ to $h/H = 0.6$ due to the effect of the swirl impacting NGV1. Downstream for $s_c/S_c > 0.7$, colder temperatures are observed because of the coolant ejection from the TE coolant holes which remains near the wall. On the suction side of NGV1 for $s_c/S_c < 0$, coolant jet traces are less marked compared to the pressure side which implies a more uniform temperature spatial distribution. This also indicates that a strong mixing process between the hot and coolant streams occurs in this region. Coolant free regions are finally observed near the end-walls for $h/H < 0.2$ and $h/H > 0.8$ due to the absence of coolant holes at these radial positions. On NGV2, Fig. 5.33 (b), temperature spatial distribution is found to differ from NGV1 because the inflow impacting the vane is different. Indeed, on the pressure side of NGV2, no strong radial drift of hot temperature is observed although similar local coolant flow patterns are found on both sides. For instance, hot temperature spots are also observed in-between the coolant holes for $h/H = 0.4$. On the suction side for $s_c/S_c < 0$, spatial temperature distribution is also found to be more uniform than on the pressure side as for NGV1.

To evaluate the efficiency of the film cooling with respect to the hot temperature, the adiabatic film effectiveness is computed using Eq. (5.2) for both vanes and compared to experimental results on Fig. 5.34. For both NGVs, LES fairly predicts the positions of high and low efficiency regions. Nevertheless, LES is observed to be more segregated with respect to the experiment. On the suction side of NGV1, Fig. 5.34 (a) & (b), the high film effectiveness spot located near the mid-height of the vane, denoted region 1, is well predicted by LES although coolant jet traces are more visible. On the pressure side, Fig. 5.34 (c) & (d), the radial deviation of the coolant flow, denoted by region 2, is also well predicted by LES. In regions 3 and 4 close to the hub on the pressure side, a lack of film effectiveness is noticed. On the suction side of NGV2, Fig. 5.34 (e) & (f), the positions of regions 1 and 2 featuring high levels film effectiveness are well captured by LES. As for NGV1, coolant jet traces are also more marked in the CFD prediction. On the pressure side, Fig. 5.34 (g) & (h), spatial distribution of the film effectiveness differs from the experiment in regions 3 and 4. Deviations with the experiment can be explained by the fact that the mixing process between the coolant and hot flow is probably under-estimated in LES. Such deviations can be explained by the lack of freestream turbulence at the inlets of the computational domain or insufficient mesh resolution in the mixing region between the hot and coolant flows. Another potential argument is that distribution of the coolant mass flow rate among the cooling pipes is probably different between LES and the experiment. Nevertheless, it is important to recall that such a validation is rare in the literature. Despite the deviations observed with the experiment, such results evidence that LES is able to capture the patterns and levels of the film effectiveness distribution for an industry-oriented configuration.

To sum up this section, the investigation of the flow aerodynamics evidences strong interactions between the hot spot migration and the coolant flow issued from the cooling system of the NGVs. The coolant flow issued from the coolant pipes develops near both sides of the NGVs while mixing process with the hot flow mainly takes place at the edge of the film. Investigation of the cooling film topology shows that the mixing process is mainly activated in the regions of coolant jets and originates from the turbulent fluctuations produced in the coolant pipes. By performing a coolant mass balance in the film, the mixing process is shown to decrease the level of coolant mass fraction in the film. As a result, the skin vane temperature is found to be highly affected by the mixing process between the hot and coolant flows. Indeed, traces of coolant flow are clearly identified on the vane temperature contours while downstream the coolant holes, the mixing process tends to homogenize the wall temperature. Comparisons with experiment shows that LES prediction fairly reproduces spatial distribution of adiabatic film effectiveness. The quality of the present LES results can hence be considered satisfactory to investigate the loss generation.

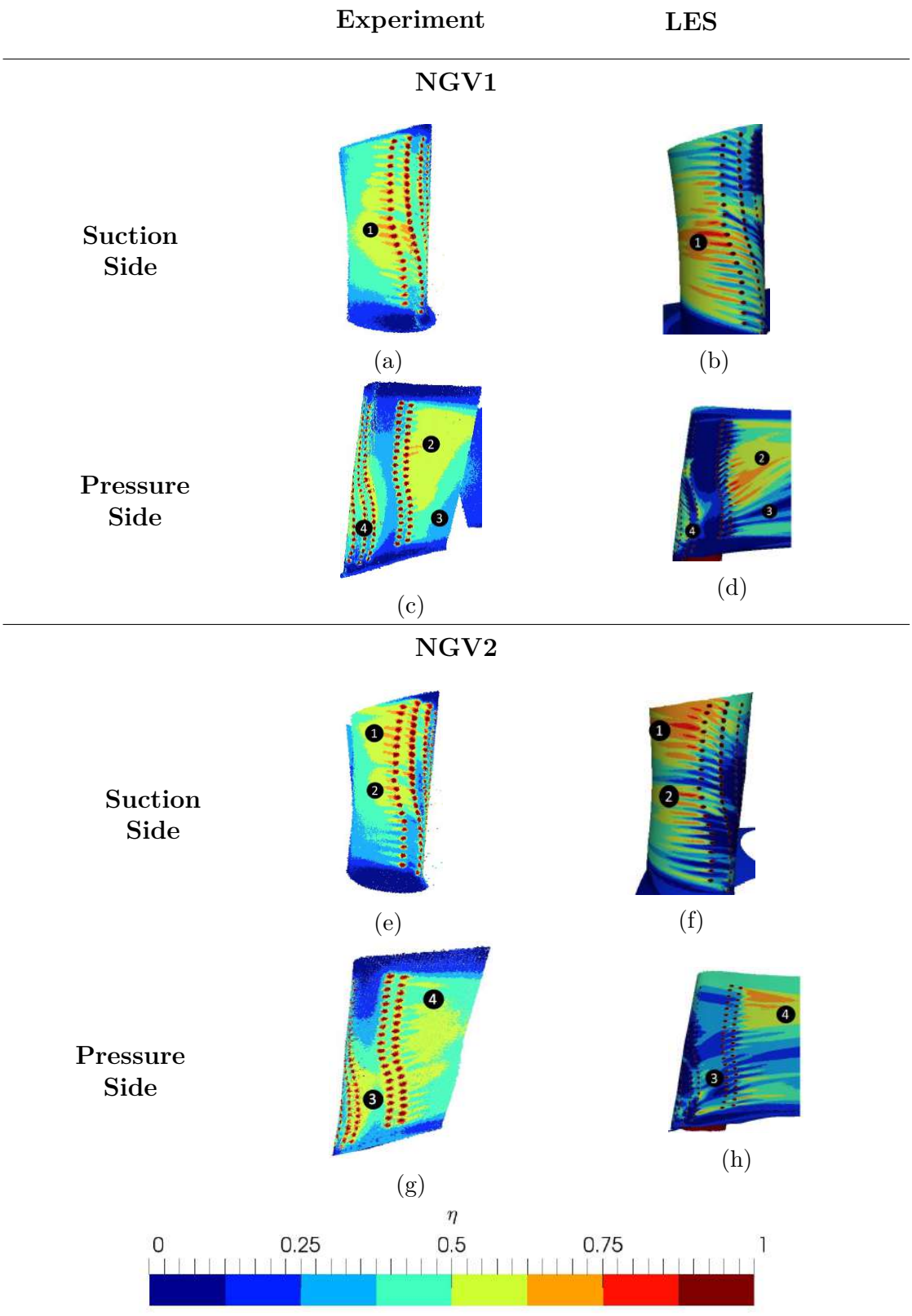

Figure 5.34 – Adiabatic film effectiveness η [-] on NGV1 at top and NGV2 at bottom for the experiment on left and LES on right.

5.3.2 Investigation of the losses

The mechanisms by which losses are generated for the cooled vanes of FACTOR are investigated in this section. More specifically, the losses generated by the flow aerodynamics and by the cooling systems are addressed. To identify the loss generation mechanisms, methodologies introduced in Chapter 2 are adopted, i.e: by using balance of total pressure and Second Law Analysis (SLA). It is important to recall that, contrary to academic T120 and T120D cascade blades investigated in previous chapters, the present configuration is a complex 3D geometry. As a result, the capacity of each methodology to predict the losses for such a strongly anisothermal configuration is discussed. To do so, losses are first evaluated using total pressure balance. To further investigate the losses, loss maps are then described through the SLA. Finally, advanced analyses of loss maps are performed to identify the dominant contributions behind the loss generation mechanisms.

Loss evaluation using balance of total pressure

First, the loss evaluation is based on a total pressure balance between two stations of the flow as usually performed in the industry. It is worth to recall that such a total pressure balance measures the losses generated between two stations of the flow only if total temperature variation is negligible with respect to total pressure variation as discussed in Chapter 4. Such an assumption is however not true if the coolant and hot streams are not fully mixed. Nevertheless, since balance is generally performed using a station crossing the wakes of the vanes, aerodynamic losses dominate and can be thus evaluated through total pressure balance. As a result in this work, total pressure variation is evaluated between the axial planes $P40$ and $P41$ (which is located in the wakes). Since the flow has a low velocity magnitude on $P40$, the reference total pressure in this plane was experimentally defined as the spatial averaged static pressure denoted $< P_S >_{P40}$. On $P41$, the spatial distribution of time-averaged total pressure $\overline{P_{t,41}(r,\theta)}$ is measured using five hole probe with respect to radial r and azimuthal θ coordinates. More details on the experimental set-up can be found in (Bacci et al., 2019). From the difference between the total pressure on $P40$ and $P41$, the loss coefficient ξ is obtained as,

$$\xi = \frac{< P_S >_{P40} - \overline{P_{t,41}(r,\theta)}}{P_{upstream} - < P_S >_{P41}}, \tag{5.6}$$

where $< P_S >_{P41}$ is the surface averaged static pressure on $P41$. The loss coefficient map obtained with LES is compared to experiment on Fig. 5.35. As expected, losses are mainly observed in the wakes of the vanes, Fig. 5.35 (a). High values are also observed near the end-walls (hub and shroud) which are probably induced by the presence of secondary flows developing along these walls. Advanced methodologies to extract secondary flows are hence needed as presented in (Germain et al., 2007; Persico et al., 2009) to confirm this last statement. Between the wakes, the loss coefficient also activates in the passage between the vanes. In this region, the losses are probably generated by the swirled flow. Compared to experimental results, Fig. 5.35 (b), the spatial extent of the wakes is well predicted by

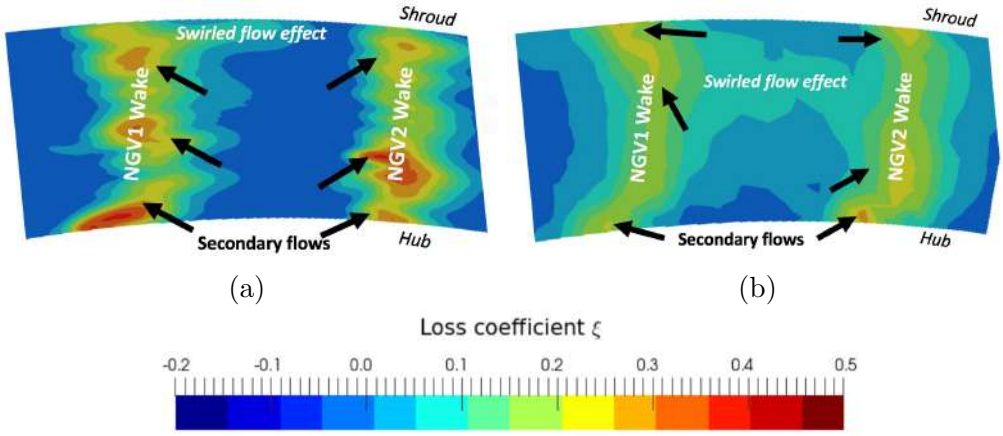

Figure 5.35 – Loss coefficient ξ [-] maps for experiment (a) and LES (b).

LES. Peaks located near the end-walls and in the wakes are also recovered. Note that relative differences in the positions of these peaks are found. This means that the secondary flow trajectories are most likely not fully reproduced by LES. These deviations are however to be affected by the unsteady inflow specification. Indeed, the true unsteady residual swirl exiting the combustor has been observed to largely affect secondary vortices in others numerical studies of the configuration (Duchaine et al., 2017; Thomas et al., 2018; Fiore, 2019).

To sum up, the loss evaluation from total pressure balance only highlights the wakes and secondary flows. Indeed, the balance performed here only evidences integrated losses generated upstream $P41$ without taking into account the coolant inlet contributions. Indeed, the coolant issued from the holes should be included in the balance of total pressure as shown in Chapter 4. However, the complexity of the vanes and the discrete positions of the jets make the balance difficult to apply. Finally and as already stated, such a balance does not allow to discriminate the aerodynamic losses from the mixing losses in the jets. As a consequence, total pressure balance may not be the most appropriate methodology to accurately evaluate the losses for such an anisothermal configuration. To further investigate the losses, loss maps obtained from SLA are hereafter studied.

Investigation of the loss maps using *Second Law Analysis*

In this section, time-averaged loss maps $\overline{P_m}$ and $\overline{P_q}$ are investigated. First, the overall loss generation can be estimated by integrating the loss maps. To limit the loss evaluation to external flow around the vanes, the internal cooling systems of the vanes are excluded from the integration and results are given in Table 5.4. In

$\int_V \overline{P_m} dV$	$\int_V \overline{P_q} dV$
509 W	264 W

Table 5.4 – Integrated loss values in the domain excluding the cooling system.

that case, aerodynamic losses are about twice as many as mixing losses suggesting that boundary layers and the wakes are responsible for the majority of losses. It is important to underline that the contribution of the mixing losses to the overall loss generation is high especially if compared to the academic T120D cascade blade (Table 4.5). Indeed, the present geometry contains more coolant holes and the temperature difference between hot and coolant flows is much higher than for the academic blade implying more interactions between these flows. This confirms that academic vanes are probably not fully representative of the loss generation of industrial cooled turbine vanes.

To obtain a better evaluation of the loss generation in the computational domain, an axial evolution of the integrated loss generation is studied by using a moving integration volume. To do so, the integration volume is defined between the axial plane $P40$ and an axial plane S_x moving from $P40$ to the axial plane $P41$. That way, an axial evolution of the cumulative losses is obtained. The axial evolution of the integrated losses is plotted on Fig. 5.36. Upstream the vanes for $x/ACL < 0$, no loss is generated because no freestream turbulence and coolant is injected at the inlet. From the leading of the vanes for $x/ACL > 0$, both aerodynamic and mixing losses begin to be generated. For both contributions, a first increase is observed between $x/ACL = 0$ and $x/ACL = 0.3$ and a second increase is observed between $x/ACL = 0.6$ and $x/ACL = 0.7$ which corresponds to the axial positions of the coolant holes. As a result in these regions, losses are probably generated in shear and mixing layers induced by the coolant ejection. It is worth to note that in these regions, integrated mixing losses are higher than aerodynamic losses due to the high temperature difference between the hot and coolant streams. Downstream the trailing edges for $x/ACL > 1$, both integrated losses increase mainly due to the wake evolutions. Since mixing process still occurs in the wakes, mixing losses are still generated downstream the vanes. This last

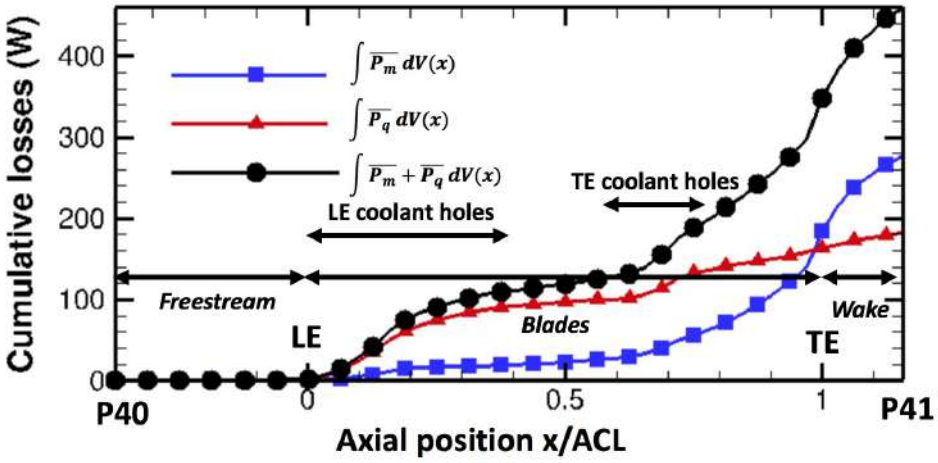

Figure 5.36 – Axial evolution of the integrated losses from $P40$ to $P41$. Leading edge (LE) and trailing edge (TE). Axial extents of the coolant holes are represented.

point indicates that the mixing contribution to the losses can not be neglected in the wakes for anisothermal configurations which is usually omitted in the literature. Nevertheless, more aerodynamic losses are generated in this region due to the strong shear present in the wakes and are seen to exceed mixing losses.

To better investigate the reported axial evolution of integrated losses, time-averaged loss maps are hereafter provided at mid-height on Fig. 5.37. To identify the film region, a white iso-line representing the iso-contour $\overline{Y_{coolant}} = 0.05$ is added to the views. Both aerodynamic losses (Fig. 5.37 (a)) and mixing losses (Fig. 5.37 (b)) are observed to be generated in the near wall flow region, in the wakes as well as in the passage between the vanes. It is observed that $\overline{P_q}$ dominates the film region while $\overline{P_m}$ dominates boundary layer and wake regions. In the passage between the vanes, the flow expansion and the swirl imposed at the inlet induce a streamwise velocity gradient activating $\overline{P_m}$ while mixing losses $\overline{P_q}$ are mainly activated due to the compressibility effects in high Mach number regions. In the wakes, aerodynamic losses are generated due to the strong shear present in this region while mixing losses are naturally generated from the mixing process. In the film, the coolant ejection induces a difference of velocity and temperature with the main stream, activating $\overline{P_m}$ and $\overline{P_q}$.

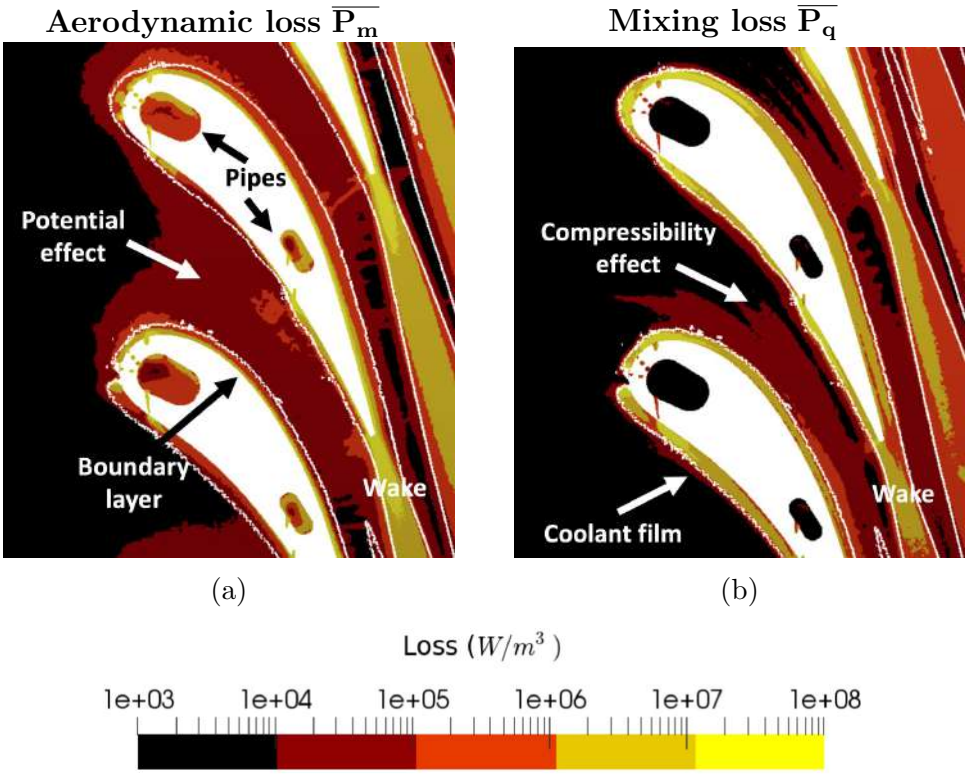

Figure 5.37 – Time averaged aerodynamic loss generation $\overline{P_m}$ (a) and mixing loss generation $\overline{P_q}$ (b) at mid-height of the vanes. The film thickness defined by $\overline{Y_{coolant}} = 0.05$ is represented by the white iso-line.

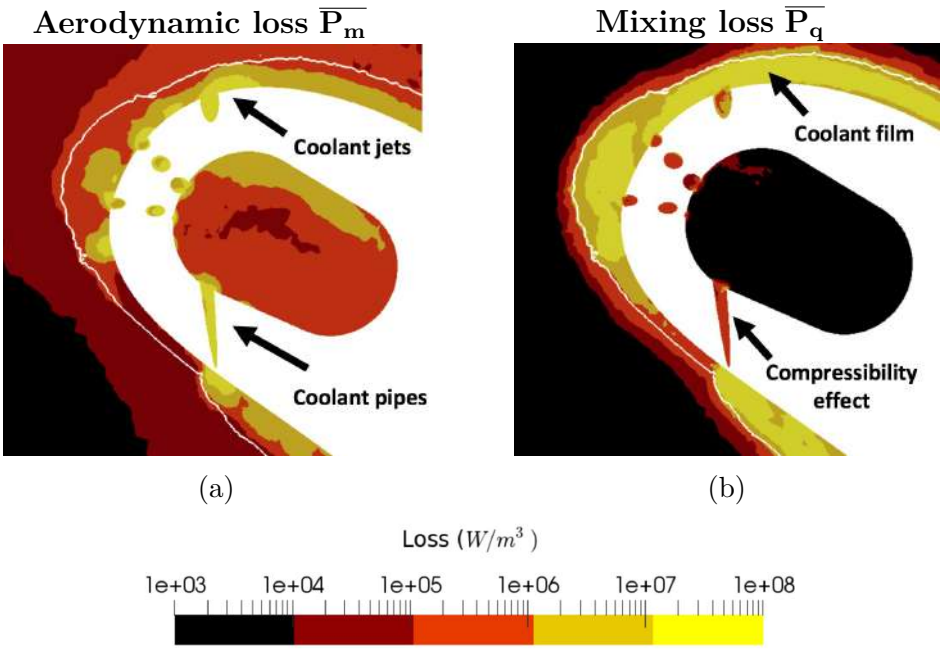

Figure 5.38 – Time averaged aerodynamic loss generation $\overline{P_m}$ (a) and mixing loss generation $\overline{P_m}$ (b) at mid-height of the vanes near the leading edge of NGV1. The film thickness defined by $\overline{Y_{coolant}} = 0.05$ is represented by the white iso-line.

A closer view of the loss maps in the coolant pipes near the leading of NGV1 is provided on Fig. 5.38. In this case, losses are observed to be mainly activated in coolant jets. A difference of behaviour is however observed between both contributions. Indeed, $\overline{P_m}$ mainly activates near the wall, i.e, in the boundary layer thickness and at the exit of coolant pipes while $\overline{P_q}$ mainly activates in the whole film thickness. This difference is partially explained by the fact that the mixing region between hot and coolant flows is probably thicker that the boundary layer developing around the vanes. The high temperature differences between the hot and cold streams could also explain that $\overline{P_q}$ dominates $\overline{P_m}$. In the coolant pipes, only aerodynamic losses are generated, Fig. 5.38 (a) because no re-ingestion of hot flows in the pipes was noticed. In this region, the low value of $\overline{P_q}$ is then only driven by compressibility effects.

To complement the previous view and eventually investigate the losses generated by the hot spot migration, time-averaged loss maps are extracted at different axial cuts represented on Fig. 5.39. Results are provided on Fig. 5.40.

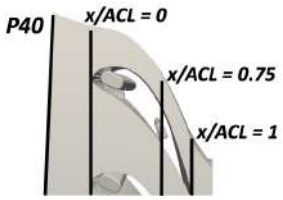

Figure 5.39 – Positions of the axial cuts in the computational domain.

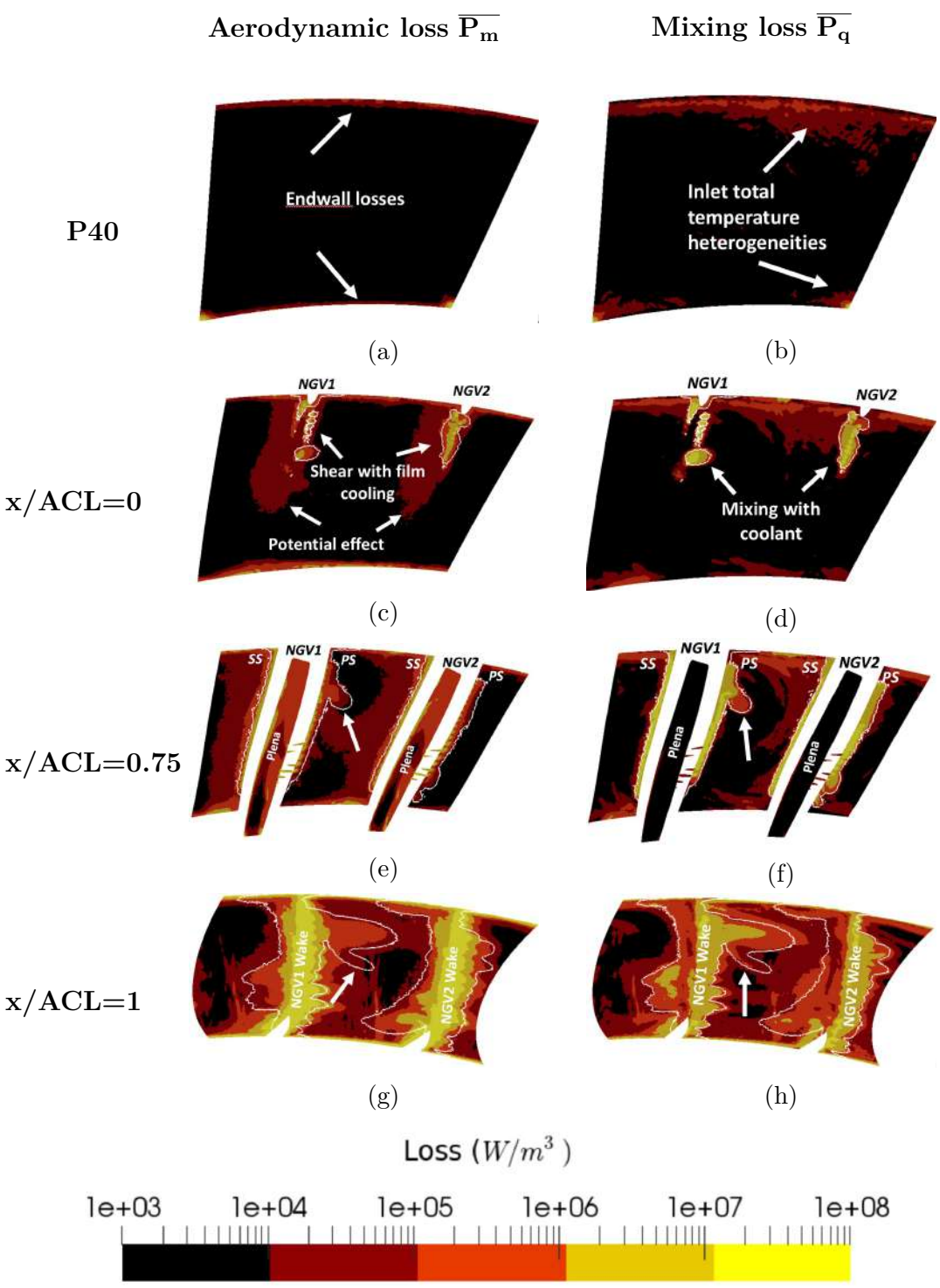

Figure 5.40 – Time averaged aerodynamic loss generation $\overline{P_m}$ on the left and mixing loss generation $\overline{P_q}$ on right. Axial cuts correspond to $P40$ (a) & (b), the leading edge $x/ACL = 0$. (c) & (d), $x/ACL = 0.75$ (e) & (f) and the trailing edge $x/ACL = 1$. (g) & (h). The film thickness defined by $\overline{Y_{coolant}} = 0.05$ is represented by the white iso-line.

At plane $P40$ corresponding to the inlet of the computational domain, Fig. 5.40 (a) & (b), no loss is generated at the center of the plane. Indeed, the fields imposed at the inlet are stationary and the mean velocity gradients are not sufficiently high to activate the loss terms. Nevertheless near the end-walls, aerodynamic losses are generated in boundary layers developing along these walls. A small quantity of mixing losses is also observed near the end-walls due to the temperature heterogeneities imposed at the inlet. Near the leading edge of the vanes, $x/ACL = 0$, Fig. 5.40 (c) & (d), both losses activate in the film. Note that a weak quantity of aerodynamic losses is also generated in the passage between the vanes. Near the shroud, mixing losses are also activated due to the presence of cold flow issued from the effusion cooling ejected in the combustor. At $x/ACL = 0.75$, Fig. 5.40 (e) & (f), both losses increase. A small region of mixing loss is noticed in the passage between the vanes as indicated by the white arrow. This region corresponds to the cold region **C2** which was observed to be extended in the passage by the swirl in Section 5.3.1, activating $\overline{P_q}$ in the passage. Finally, near the trailing edge, Fig. 5.40 (g) & (h), the swirled flow is found to contribute to the losses in the passage as indicated by the white arrow.

To sum up, the loss generation mainly locates in the regions of high shear and high temperature differences as already observed in Chapters 3 & 4. Detailed analyses of the loss generation in regions of interest like the film or boundary layers can be performed as presented in Chapters 3 & 4. Nevertheless, the boundary layers are difficult to extract on such a complex geometry. One remaining question which is addressed hereafter is the contribution of the mean and turbulent fields on the loss generation.

From the previous loss maps, the mean contributions P_m^{mean}, P_q^{mean} as well as the turbulent contributions P_m^{turb}, P_q^{turb} can be evaluated from Eqs.(3.25)&(4.22). These mean and turbulent contributions are first integrated in the computational domain excluding the cooling pipes and plena. Integrated value are provided in Table 5.5. Clearly, the turbulent contributions dominate the mean contributions for both losses in agreement with Chapters 3 & 4. To localize these contributions, mean and turbulent loss maps are shown at mid-height on Fig. 5.41. The mean aerodynamic contribution, Fig. 5.41 (a), mainly locates near the vane and in the wakes, where mean velocity gradients are expected. The mean contribution of mixing losses, Fig. 5.41 (b), only locates in the film, where mean temperature gradients are expected due to the mixing with hot and coolant flows. The turbu-

	Aerodynamic loss	**Mixing loss**
Integrated mean contribution	33 W	14 W
Integrated turbulent contribution	476 W	250 W

Table 5.5 – Integrated values of mean and turbulent contributions to the losses within the computational domain excluding the cooling pipes and plena.

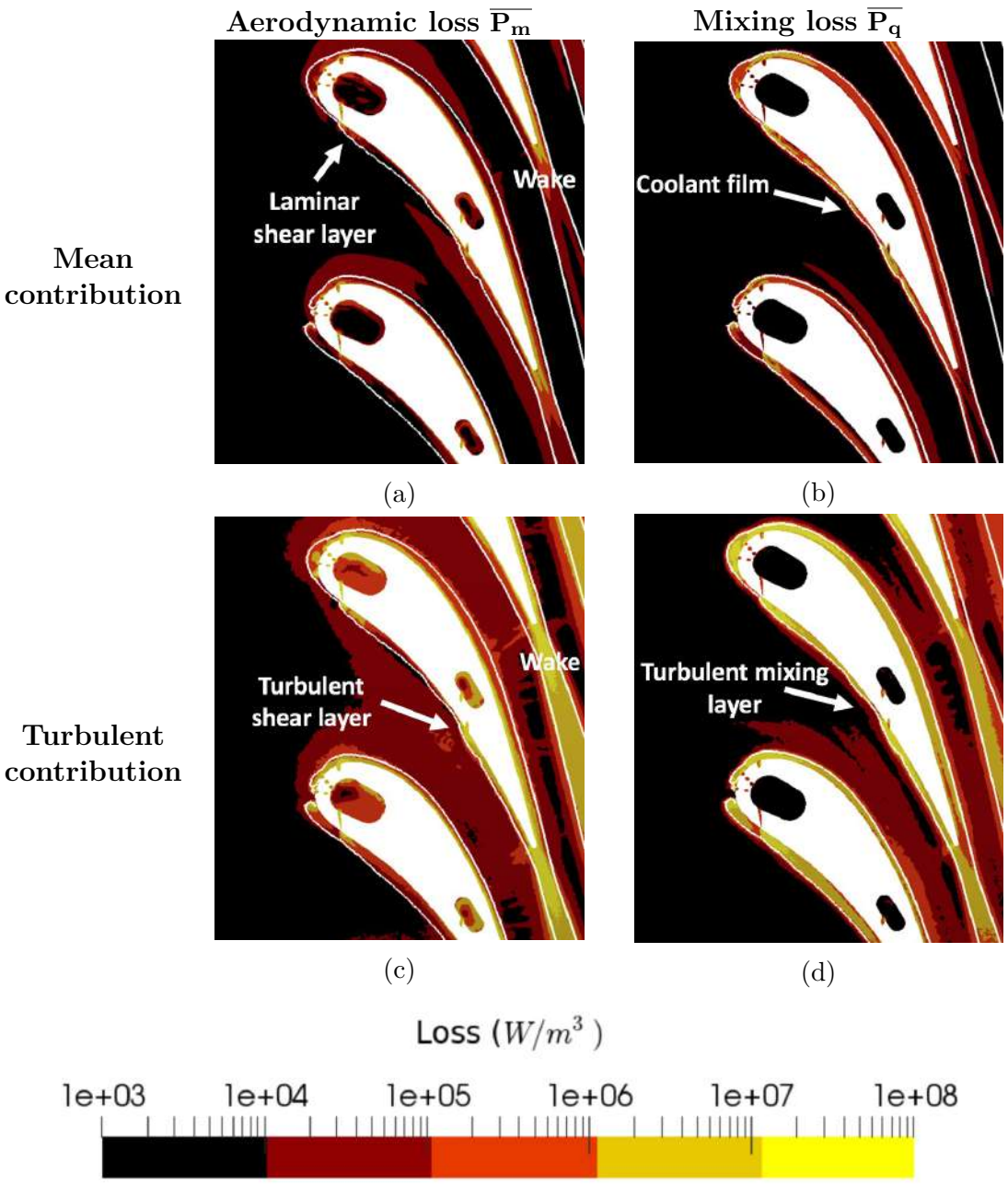

Figure 5.41 – Time averaged aerodynamic loss generation $\overline{P_m}$ (a) & (c) on left and mixing loss generation $\overline{P_q}$ (b) & (d) on right at mid-height of the vanes. Mean contributions at top (a) & (b) and turbulent contributions at bottom (c) & (d). The film thickness defined by $\overline{Y_{coolant}} = 0.05$ is represented by the white iso-line.

lent contribution of aerodynamic losses, Fig. 5.41 (c), occurs in the film and in the wakes, where high levels of turbulent kinetic energy have been observed in Section 5.3.1. Indeed, turbulent fluctuations are expected to correlate with unsteady velocity fluctuations activating P_m^{turb}. The turbulent contribution of mixing losses, Fig. 5.41 (d), activates in the regions where turbulent mixing occurs.

A closer view of the loss maps in the coolant pipes near the leading of NGV1 is provided in Fig. 5.42 confirms that for the cooling system, the turbulent contributions also dominate the mean ones. The mean contributions, Fig. 5.42 (a) & (b), are located in the boundary layer and in coolant jets. On the other hand, the turbulent contributions, Fig. 5.42 (c) & (d), only activate in the film. It is also noted that in the coolant pipes, the turbulent contribution P_m^{turb} also dominates the mean contribution P_m^{mean} due to strong turbulent activity in the cooling system.

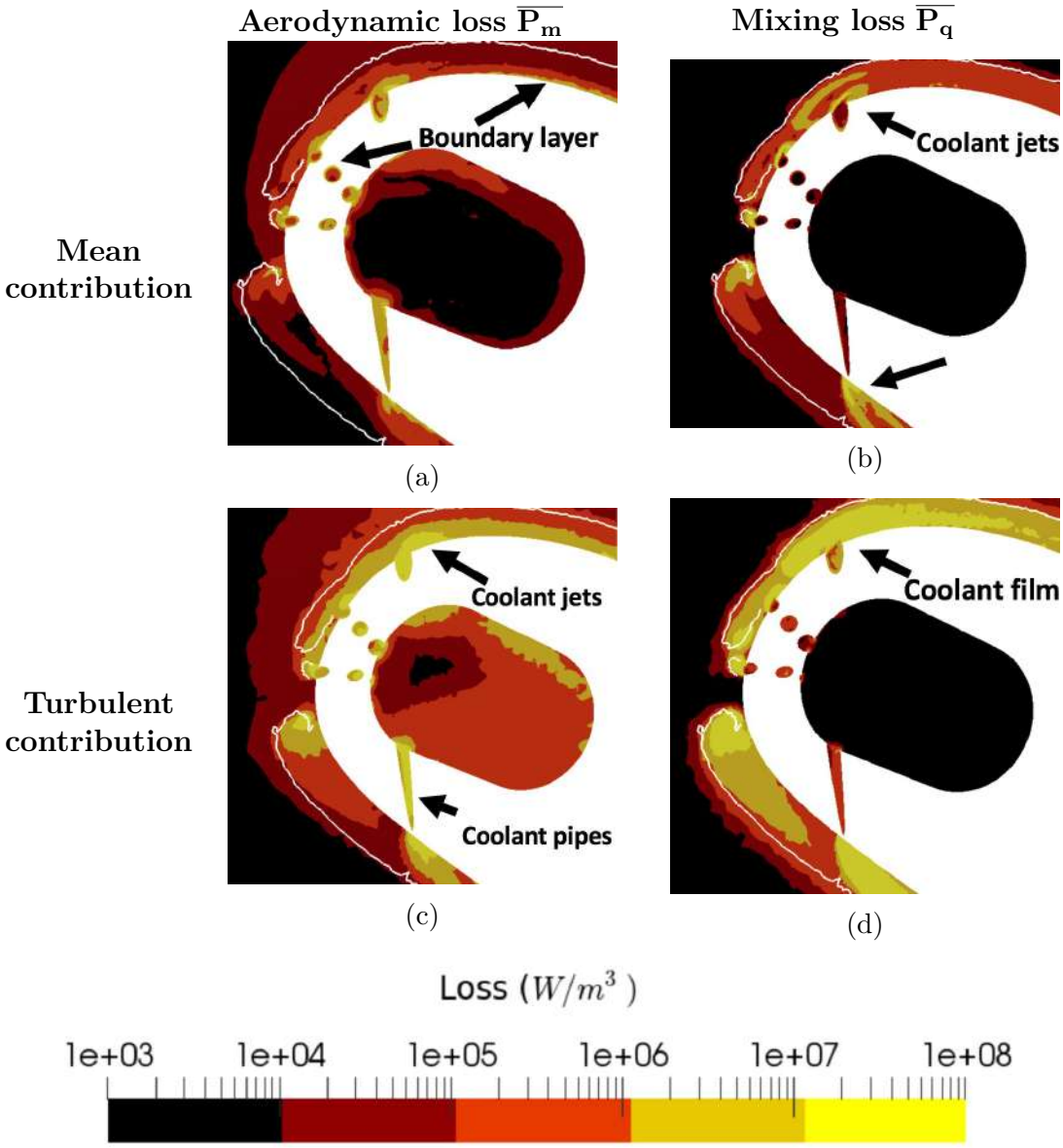

Figure 5.42 – Time averaged aerodynamic loss generation $\overline{P_m}$ (a) & (c) on left and mixing loss generation $\overline{P_q}$ (b) & (d) on right at mid-height of the vanes near the leading edge of NGV1. Mean contributions at top (a) & (b) and turbulent contributions at bottom (c) & (d). The film thickness defined by $\overline{Y_{coolant}} = 0.05$ is represented by the white iso-line.

5.4 Chapter conclusions

In this chapter, the capacity of LES to predict the vane load distribution, the adiabatic wall temperatures as well as the losses has been evaluated for the NGVs of the FACTOR project. To do so, a WMLES representing a pair of vanes has been performed meshing the whole cooling systems of the vanes. Results show that the vane load distribution is well predicted by LES. The thermal environment of the vane is found to be impacted by the hot spot migration and its mixing with the coolant flow. Indeed in the coolant film, a strong turbulent mixing process between coolant and hot flows was observed. As a result of the complex interactions between these flows, spatial distribution of time-averaged skin vane temperature is highly heterogeneous. Comparisons with experiment showed that LES prediction fairly reproduces spatial distribution of the adiabatic film effectiveness. Although levels are not fully reproduced, injection of unsteadiness at the inlets is expected to help to fully recover experimental results. Such results are then very encouraging and promising for the vane wall temperature prediction of complex configurations with LES. In the second part of the chapter, losses were investigated using balance of total pressure and Second Law Analysis (SLA). For the first methodology, total pressure variation only highlights the aerodynamic losses generated in the wakes of the vanes. Indeed, such a balance omits the contribution of mixing losses and is then not fully appropriated for this anisothermal configuration. To overcome this limitation, the loss generation mechanisms were identified thanks to the investigation of loss maps with SLA. Loss generation locations are coherent with the literature findings (Leggett, 2018; Fiore, 2019) and observations of Chapters 3 & 4. Again, turbulent contributions are shown to dominate the mean ones, encouraging the use of LES for the loss prediction. As a consequence of the results obtained in this chapter, SLA is found to be an appropriate methodology to evaluate and quantify the losses for complex configurations of cooled turbine vanes.

However, the loss prediction for such a complex geometry requires high CPU resources. Indeed and as shown in this chapter, resolving the internal cooling system results in a non negligible effort in terms of grid design since a major part of mesh cells is located in the cooling system. Cumulated to the fact that diameter of coolant holes are of the order of millimeter, small cell volumes are expected to locate there to ensure accurate flow predictions. As a consequence, the governing equations being fully compressible and explicitly integrated in time, very small time steps are required to satisfy numerical stabiltiy criterion increasing again the CPU effort of such LES. To overcome such limitations and better design use, one solution is to model the coolant injection on the vane surface. In the next and final chapter, a new coolant ejection model is hence introduced in the context of turbine vane cooling and assessed through the comparison between the *hole-modelled LES* and the *hole-meshed LES*.

Chapter 6

Develoment of a coolant model to perform LES of realistic NGVs

Contents

6.1 Review of coolant injection modelling **226**
6.2 Coolant ejection modelling in the context of turbine blade cooling **227**
6.3 Numerical set up of the hole-modelled LES **230**
6.4 Impact of the coolant model on the flow prediction **233**
6.4.1 Impact of the coolant model on operating point 233
6.4.2 Impact of the coolant model on large scale structures . 236
6.4.3 Impact of the coolant model on mean flow structure . 237
6.4.4 Adiabatic film effectiveness predictions 241
6.4.5 Analysis of the mixing process in the coolant film . . . 243
6.4.6 Impact of the coolant model on the loss prediction . . 249
6.5 Chapter conclusions **253**

This chapter addresses the evaluation of a coolant ejection model introduced in the context of turbine vane cooling. To assess the model, the coolant ejection model is applied on the NGVs of FACTOR to produce a so-called *hole-modelled LES*. Then, the capacity of the coolant ejection model to predict the flow aerodynamics, the adiabatic wall temperature and losses is evaluated through the comparison to the *hole-meshed LES* of Chapter 5. To do so, the chapter is organized as follows. First, a quick review of coolant injection modelling is provided in Section 6.1. Following this review, the mathematical formulation of the model is detailed in Section 6.2. Then, a specific discussion on coolant boundary condition deviations between the two LES is addressed in Section 6.3. Afterwards, the comparison between the *hole-meshed LES* and *hole-modelled LES* on the flow aerodynamics, adiabatic wall temperature and losses is described in Section 6.4. Finally, conclusions are given in Section 6.5. Note that this work has been carried

out in collaboration with *M. Thomas*, PhD student at CERFACS and has been published in international journals and conferences:

- *Harnieh, M., Thomas, M., Bizzari, R., Gicquel, L. Y. M. and Duchaine, F. (2018) Assessment of a coolant injection model on cooled high-pressure vanes in Large Eddy Simulation. 12th International Symposium on Engineering Turbulence Modelling and Measurements. Montpellier, France, 2018.*

- *Harnieh, M., Thomas, M., Bizzari, R., Gicquel, L. Y. M. and Duchaine, F. Assessment of a coolant injection model on cooled high-pressure vanes with Large Eddy Simulation. Flow Turbulence and Combustion (2019).*

6.1 Review of coolant injection modelling

To predict the flow aerodynamics and skin vane temperature for realistic cooled vanes, RANS has been mainly used in the industry (Tucker, 2011a). However to obtain accurate flow prediction, a great meshing effort is required to mesh the cooling system. To alleviate the CPU effort inherent to the flow resolution in the cooling system, coolant models have been first implemented in RANS solvers (Andrei et al., 2016; Andreini et al., 2013; auf dem Kampe and Volker, 2012). The aim of these models is to inject the coolant flow on the wall without meshing the cooling pipes. However if implemented in the context of RANS, the predictions still suffer from a lack of accuracy to predict mixing (Dickhoff et al., 2018; Ravelli and Barigozzi, 2017; Dyson et al., 2012) and resulting film effectivenesses remain highly sensitive to RANS closure as well as mesh resolution. With the constant increase of computational power, LES of turbomachineries is increasingly realized (Pichler et al., 2017; Tyacke and Tucker, 2014; Tucker, 2011b). However, when extended to cooled configurations, very few LES studies representing full span-wise extent of 3D cooled turbine vanes have been reported in the literature (Ravelli and Barigozzi, 2017; Ling and Guoliang, 2011). Indeed and similarly to RANS, resolving the flow in the coolant systems of cooled vanes requires large CPU resources when dealing with LES. The same situations are often encountered for LES predictions of multiperforated plates of aeronautical combustion chamber liners. In this last context, Mendez and Nicoud (Mendez and Nicoud, 2008) have proposed an homogeneous model with the objective to inject the coolant homogeneously on the wall conserving the integrated mass flow rate and tangential momentum fluxes. In this homogenisation process, the jet dynamics is lost and the mixing with the hot flow is under-estimated. While addressing this specific weakness, Bizzari *et al.* (2018) (Bizzari et al., 2018b) have proposed a *thickened hole LES model* to take into account the position of perforations as well as the capacity of the local mesh resolution to properly represent the jets issued from the perforations. An example of this new modelling approach is presented on Fig. 6.1 for the effusion cooling modelling in combustion chambers. In this approach, the cooling system is not meshed but represented on the wall allowing to save significant CPU resources. This modelling approach provides better results compared to the homogeneous

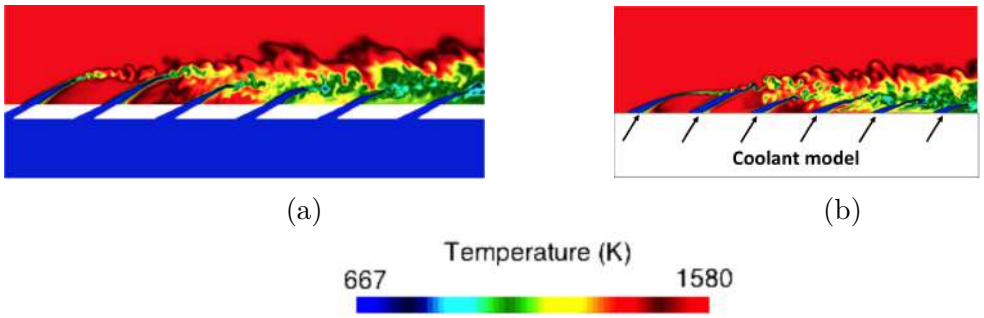

Figure 6.1 – Example of the use of the *thickened hole LES model* from (Bizzari et al., 2018b) in the context of effusion cooling in combustion chambers. (a) Hole-meshed simulation and (b) application of the coolant model.

model and more importantly the reproduction of jet dynamics as the mesh resolution increases (Bizzari, 2018; Bizzari et al., 2018a). In this work, this modelling approach is adopted and adapted to the context of turbine vane cooling.

6.2 Coolant ejection modelling in the context of turbine blade cooling

Prior to present the mathematical formulation of the model, the geometric parameters are first introduced in the context of blade cooling. The geometric parameters of holes present on vane surfaces are shown on Fig. 6.2. Note that the model only

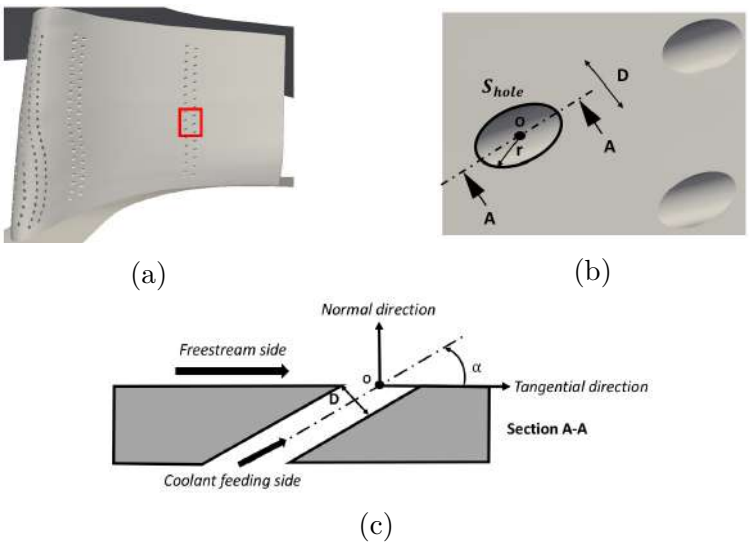

Figure 6.2 – Geometric definitions of holes. Example of the pressure side view of the FACTOR cooled vane (a). Normal blade view in the red square (b) and view of the A-A cut (c). O is the center of the hole, D the minimum diameter of the hole, r the local radial coordinate defined on the hole surface S_{hole} and α the inclination angle with respect to the wall.

deals with cylindrical holes. The hole surface is taken to be ellipsoidal and is thus defined by its minimum diameter D, its hole surface S_{hole} and its inclination angle to the blade surface α, Fig. 6.2 (a)&(b). A local radial coordinate r attached to the hole surface center O is introduced. In this case, the normal direction is defined at the center of the hole and the tangential direction is chosen to be aligned with the projection of the perforation axis vector on the wall, Fig. 6.2 (c).

Based on the above parameters, the main idea of the model is to inject the coolant on the wall surface without representing the cooling pipes in the computational domain but instead using an equivalent wall boundary condition. For NGVs, each perforation is considered independently and contributions of each hole are simply added when they belong to the same wall. To geometrically identify the hole extent on the wall boundary condition, an axi-symmetric normalized distribution function $f(r)$ centred on the hole center and defined on the total blade surface S_{tot} is considered so that,

$$f(r) = 0.5\left(1 - tanh\left(\frac{r - 0.5D_{num}}{\beta\,\Delta x}\right)\right), \tag{6.1}$$

where Δx is the local mesh size on the hole section, D_{num} is the numerical diameter used in the model and β a numerical constant to limit the sharpness of the distribution function on the mesh to avoid numerical stability issues. Bizzari et al. (Bizzari et al., 2018b) showed that $\beta = 0.1$ is a correct value to represent the distribution function on meshes usually used for combustor chamber liners while avoiding numerical problems of stability from the profile stiffness. A 1D plot of the distribution function $f(r)$ is provided in Fig. 6.3. The numerical diameter D_{num} depends on the thickening factor Γ following,

$$D_{num} = \Gamma D. \tag{6.2}$$

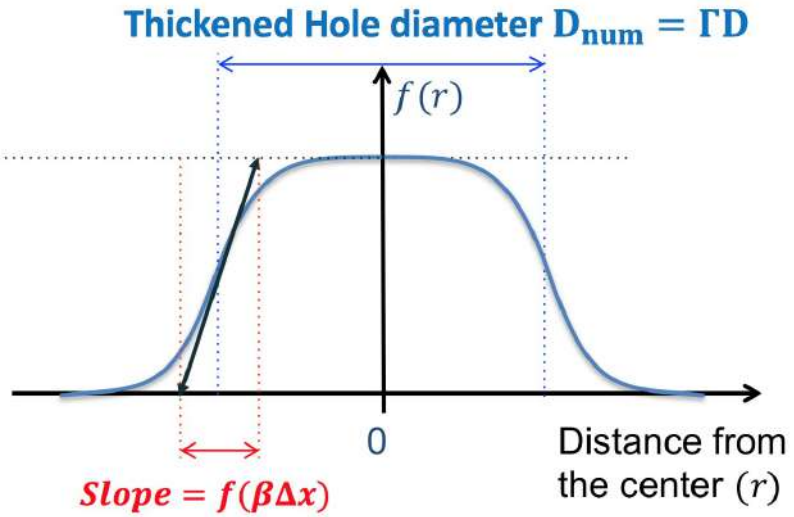

Figure 6.3 – Plot of the distribution function *f(r)* across a hole of diameter *D*.

The thickening factor Γ allows to thicken the hole diameter if the hole is under-resolved, i.e, $\frac{D}{\Delta x} < 3$ and is then expressed as,

$$\Gamma = Max\left(\frac{3\Delta x}{D}, 1\right). \tag{6.3}$$

This way, the radial extent of the distribution function covers the numerical diameter of the hole D_{num}. The normal and tangential velocity profiles on the hole section respectively noted V_n^{model} and V_t^{model}, are imposed by the model on the blade surface assuming a stationary state and following the expressions,

$$V_n^{model} = A_n f(r), \tag{6.4}$$

$$V_t^{model} = A_t f(r), \tag{6.5}$$

where A_n and A_t are constants of the model. Note that the distribution function $f(r)$ is used to impose the shape of the velocity profiles on the hole section. Note also that no turbulent fluctuation is imposed in the model, i.e, the velocity profile is stationary. To conserve mass and tangential momentum fluxes of the physical jet through the considered hole section S_{hole}, balances need to be addressed to evaluate the model parameters A_n and A_t. To do so, cited fluxes through the total surface of the blade S_{tot} only considering one hole are evaluated on the basis on the flux conservation between the physical and modelled jets so that,

$$\int_{S_{tot}} \rho V_n^{model} dS = \int_{S_{hole}} \rho V_n^{jet} dS, \tag{6.6}$$

$$\int_{S_{tot}} \rho V_n^{model} V_t^{model} dS = \int_{S_{hole}} \rho V_n^{jet} V_t^{jet} dS, \tag{6.7}$$

where V_n^{jet} and V_t^{jet} are the normal and tangential velocity profiles of the real jet if known and ρ is the density assumed uniform. Injecting the expressions of the modelled velocity profile in Eqs. (6.4)&(6.5) then gives,

$$\rho A_n \int_{S_{tot}} f(r) dS = \rho \int_{S_{hole}} V_n^{jet} dS, \tag{6.8}$$

$$\rho A_n A_t \int_{S_{tot}} f^2(r) dS = \rho \int_{S_{hole}} V_n^{jet} V_t^{jet} dS, \tag{6.9}$$

and rearranging the above expressions one gets,

$$A_n = \frac{< V_n^{jet} >_{S_{hole}} S_{hole}}{\int_{S_{tot}} f(r) dS}, \tag{6.10}$$

$$A_t = < V_t^{jet} >_{S_{hole}} \frac{\int_{S_{tot}} f(r) dS}{\int_{S_{tot}} f^2(r) dS}, \tag{6.11}$$

where $< \bullet >_S$ is the spatial averaged on the considered section S. Note that similarly to density, the temperature profile is also kept uniform on the hole extent. Further details on the mathematical derivations can be retrieved in (Lahbib, 2015; Bizzari, 2018). To apply the model in the context of turbine blades, one must know

a priori the mass flow rate of each hole $Q_{m,hole}$ to retrieve the surface averaged normal velocity. The jet angle needs also to be known to retrieve the surface averaged tangential velocity. In practice, the jet angle is assumed to be equal to the geometric angle α. This way, the expressions for the spatial averages of the velocity profiles follow,

$$< V_n^{jet} >_{S_{hole}} = \frac{Q_{m,hole}}{\rho S_{hole}}, \tag{6.12}$$

$$< V_t^{jet} >_{S_{hole}} = \frac{Q_{m,hole}}{\rho S_{hole} tan(\alpha)}. \tag{6.13}$$

Such a modelling approach was originally proposed in the context of multi-perforated liners so deviations are expected if used in the context of blade cooling and need to be discussed. Indeed, both systems operate at different coolant operating conditions. For combustion chamber liners, typical values for blowing ratio M and momentum ratio J are respectively $1 < M < 20$ and $30 < J < 90$ (Bizzari et al., 2018c) while for blade cooling systems, typical values are around 0.5 - 2 for both M and J (Han and Ekkad, 2001). The interactions between the jets and the external hot stream are also different between these two contexts. Indeed in combustion chambers, the external flow velocity remains relatively constant along the liners while it strongly accelerates along turbine vanes. Inter-hole distances are also quite different when comparing combustor liners with a NGV cooling system. Indeed, the overall number of holes are very different and their relative proximity strongly impacts the resulting film cooling dynamics. Jet physics are hence different depending on the context. Differences in flow responses as well as model sensitivities will thus arise. One objective of the following discussion is to highlight such changes and their potential importance in the context of a *hole-modelled LES* for realistic NGVs.

6.3 Numerical set up of the hole-modelled LES

To evaluate the applicability of the modelling approach described above, the coolant ejection model is applied on the NGVs of the FACTOR project to produce the *hole-modelled LES* which is thereafter compared to the *hole-meshed LES*. To purely evaluate the impact of the coolant model on the flow prediction, the hole *hole-modelled LES* is built from the *hole-meshed LES* while excluding the cooling system from the mesh and conserving same inflow/outflow boundary conditions, same numerics and LES modelling. In this section, details on numerics and coolant boundary conditions for both LES are provided.

As depicted above, the mesh uses the same mesh that is constructed for *hole-meshed LES* while excluding the plena and the pipes connecting the internal flow to the main flow. As a result, both simulations use the same freestream and vane surface meshes as shown on Fig. 6.4. For the *hole-modelled LES*, the cell number

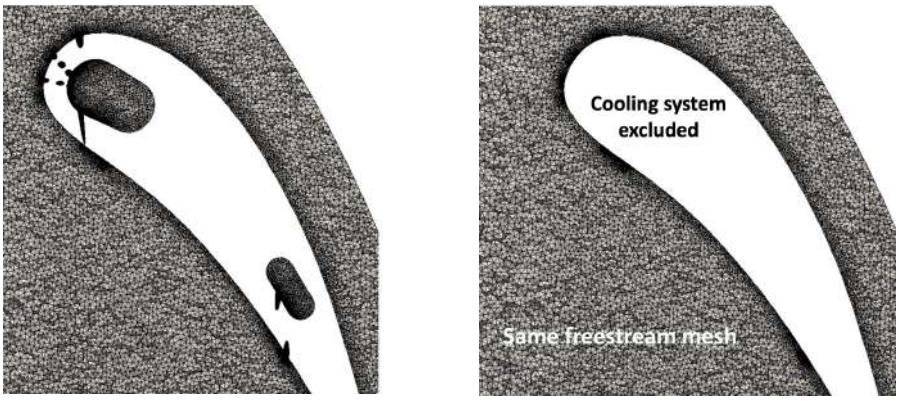

(a) (b)

Figure 6.4 – Mesh used in the *hole-meshed LES* (a) and in the *hole-modelled LES* (b) at mid-height of NGV1.

is reduced from 73 to 38 million tetrahedra (divided by 2 compared to the *hole-meshed LES*). At the exit of holes, it is worth to recall that 15 points are used to discretize the hole diameter. As a result, the value of the thickening factor given by Eq. (6.3) is then $\Gamma = 1$ meaning that the projected holes on the vane walls are not thickened in this context.

The coolant inlet condition is now addressed in the modelling approach. One requirement behind the hole-modelled approach is the knowledge of mass flow distribution through each hole considered by the model. For the *hole-modelled LES*, the distribution of coolant mass flow rate between holes to be imposed by the user is extracted from the *hole-meshed LES* to limit sources of differences between the two LES. As a result, the only deviation between the two LES predictions is the treatment of the coolant ejection. Note that to track the coolant flow, a fictive species $Y_{coolant}$ is injected at the coolant inlets similarly to Chapter 5. To illustrate the coolant ejection in the modelling approach, an instantaneous view of an iso-surface of coolant temperature in the near wall flow region is provided on Fig. 6.5. Coolant temperature iso-surfaces are observed to originate from the

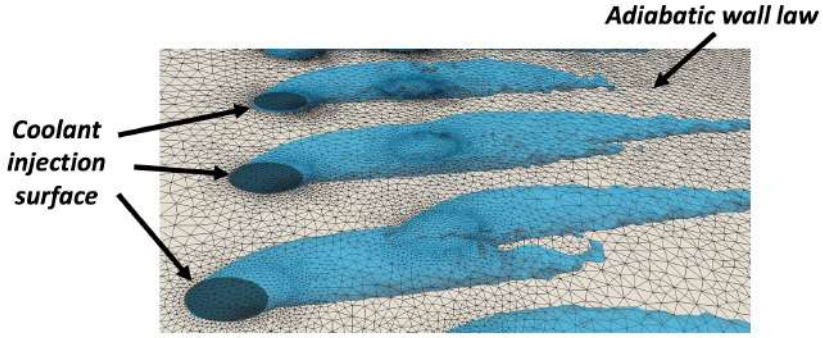

Figure 6.5 – Iso-surface of coolant temperature to evidence the jets in the *hole-modelled LES*.

coolant ejection surfaces and to penetrate in the freestream flow as expected. Away from the coolant ejection surfaces, the boundary condition switches to classical bi-layer logarithm law of the wall when the distribution function satisfies $f(r) < \epsilon$ where ϵ is a threshold value. On the coolant ejection surfaces, the fields to be imposed by the coolant model differ by construction from the fields obtained in the *hole-meshed LES*. Indeed, the model also assumes that the velocity profile at the exit of a coolant pipe is axi-symmetric and stationary which differs from real cooling hole features present in turbines (Peet and Lele, 2008). To illustrate these deviations between the two approaches, the time-averaged mass flux profile, $\overline{\rho U_i} n_i$ where n_i is the hole normal at the exit section of one specific hole of NGV1, is extracted in both LES predictions and presented in Fig. 6.6. In the *hole-meshed LES*, Fig. 6.6 (a), the mass flux profile is not axi-symmetric and presents a sheared flow pattern which is coherent with the literature (Fric and Roshko, 1994; New et al., 2003). In contrast, the profile imposed in the *hole-modelled LES*, Fig. 6.6 (b), clearly differs and is by construction uniform away from the wall. Unsteady activity evidenced by turbulent kinetic energy profiles k is also expected to differ as shown on Fig. 6.7. For the hole-meshed prediction, Fig. 6.7 (a), the turbulence intensity is around 5 % and unsteady activity is mainly located in the sheared region of the profile, a feature that is not taken into account by the hole-modelled approach, Fig. 6.7 (b). Indeed, no turbulent fluctuation is imposed with the model. Such deviations are expected to impact the coolant jet aerodynamics.

The main objective of the remaining discussion is the quantification of the modelling approach on mean flow prediction, aerodynamics of coolant jets as well as adiabatic film effectiveness in comparison to the *hole-meshed LES* prediction.

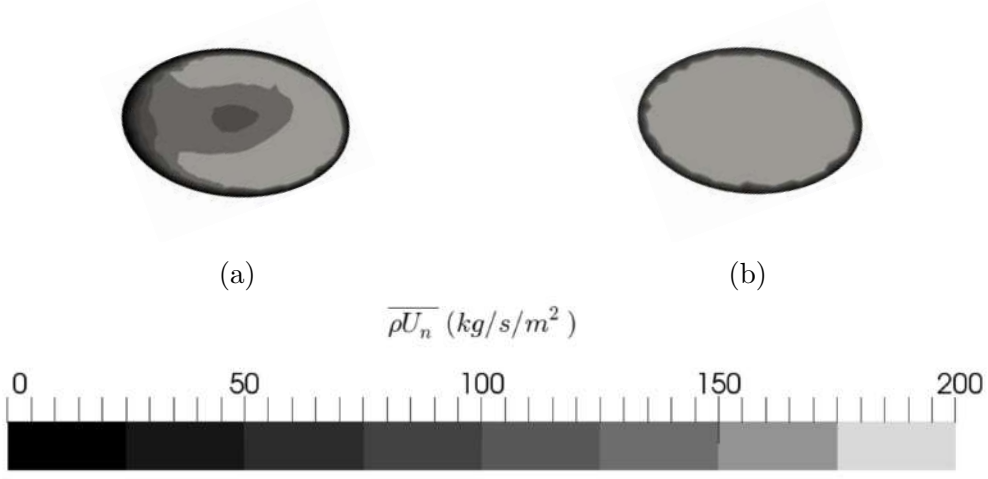

Figure 6.6 – Time-averaged normal profiles of the mass flux $\overline{\rho U_i} n_i$ of one specific hole of NGV1 for the hole-meshed (a) and hole-modelled (b) LES.

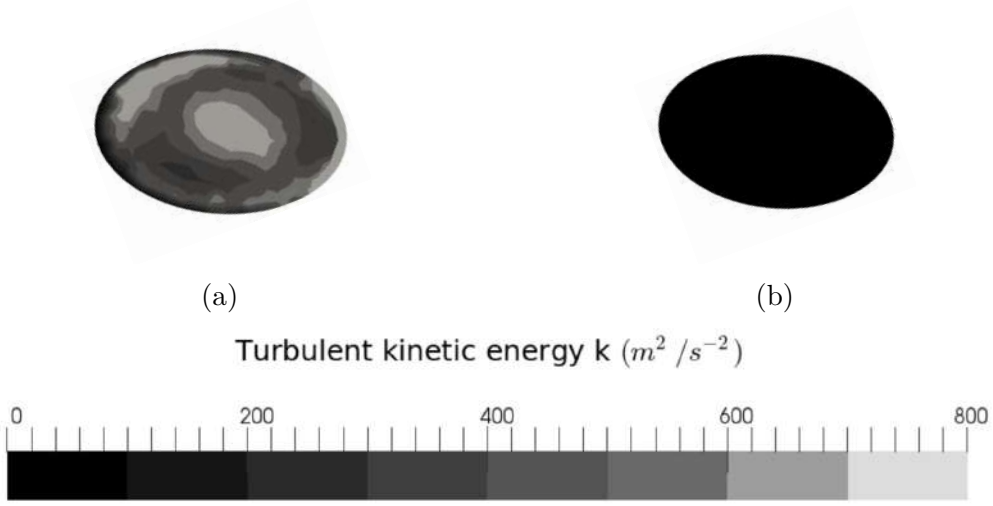

Figure 6.7 – Turbulent kinetic energy k profiles of one specific hole of NGV1 for the hole-meshed (a) and modelled (b) LES.

6.4 Impact of the coolant model on the flow prediction

In this section, detailed comparisons of both LES predictions are proposed so as to qualify the capacity of the hole-modelled approach to reproduce accurately the coolant ejection for complex NGV simulations. First, operating conditions obtained for the two LES predictions are verified to ensure the comparability of the computations. Then, the impact of the coolant model on unsteady large flow structure and mean flow organization is detailed. Next, the effect of the model on adiabatic film effectiveness is specifically discussed. Since the film effectiveness is sensitive to mixing process taking place within the film as shown in Chapter 5, the impact of the model on this mixing process is specifically investigated. Finally, the impact of the model on losses is addressed.

6.4.1 Impact of the coolant model on operating point

Wall temperature around a complex NGV geometry is the result of multiple tightly coupled factors. For uncooled NGVs and under adiabatic wall conditions, the wall temperature is governed by the aerodynamics induced by the presence of the vane and the impact of the hot spot generated in the combustor. For an anisothermal case: *i.e.* with cooling, the wall temperature is the result of more complex phenomena and is governed by the mixing process occurring between the hot and cold streams as well as the associated aerodynamics response of the flow. In the case of film cooling, the discrete nature of the cold stream ejection all around the vane boundary layer clearly hinders the analysis. As a consequence and prior to a deeper analysis of the hole-modelled approach, a verification of the overall operating condition and external flow aerodynamics provided by the two simulations is mandatory.

This specific point is here addressed by considering the overall mass flow rates going through the system, total temperature T_t and pressure P_t at the plane $P40$ to ensure that both LES ingest same inflow. Note that P_t and T_t are here mass-flow averaged on the considered planes. To get a first evaluation of the impact of the model on losses, the drop of T_t and P_t between the axial planes $P40$ and $P41$ is also evaluated through total enthalpy loss coefficient ξ_{ht} and total pressure loss coefficient ξ and compared between the LES predictions. To do so, the total enthalpy loss coefficient ξ_{ht} follows,

$$\xi_{ht} = \frac{T_{t40} - T_{t41}}{0.5 < V_{41}^2 >_S}, \tag{6.14}$$

where T_{t40} and T_{t41} are respectively the mass-flow averaged total temperature on the axial planes $P40$ and $P41$ and $0.5 < V_{41}^2 >_S$ is the surface averaged kinetic energy on $P41$. The total pressure loss coefficient ξ follows,

$$\xi = \frac{P_{t40} - P_{t41}}{P_{t41} - P_{41}}, \tag{6.15}$$

where P_{t40} and P_{t41} are respectively the mass-flow averaged total pressure on the axial planes $P40$ and $P41$ and P_{41} the surface averaged of the static pressure on the axial plane $P41$. It is worth to recall that a stationary swirled flow is injected at the main inlet of the computational domain. To ensure that the transport of the swirled flow is equivalent in both LES, the swirl number, noted $S_{w,S}$ and defined for a section S, is computed between planes $P40$ and $P41$. For this quantity, the definition from (Koupper et al., 2014) is retained,

$$S_{w,S} = \frac{1}{(R_{shroud} - R_{hub})} \frac{\int_S \overline{\rho} \overline{U_x}\, \overline{U_\theta} dS}{\int_S \overline{\rho} \overline{U_x}^2 + (\overline{P} - < \overline{P} >_S) dS}, \tag{6.16}$$

where $\overline{U_x}$ is the time-averaged of the axial velocity component, $\overline{U_\theta}$ the angular velocity component and $\overline{P}$ the static pressure. R_{shroud} and R_{hub} are respectively the radius of the hub and shroud. Global quantities are reported in Table 6.1. It is

CASE	**hole-meshed LES**	**hole-modelled LES**
Hot mass flow rate $[kg.s^{-1}]$	0.240	0.240
Cold mass flow rate $[kg.s^{-1}]$	0.018	0.018
T_{t40} $[K]$	443	443
P_{t40} $[Pa]$	149738	149619
$S_{w,40}$ [-]	0.19	0.19
$S_{w,41}$ [-])	21.2	20.3
ξ_{ht} [-]	≈ 0	≈ 0
ξ [-]	0.072	0.070

Table 6.1 – Global quantities on $P40$ and $P41$ and associated loss coefficients.

important to recall that total pressure and temperature at the inlet are not directly imposed by the boundary conditions but are the result of the flow aerodynamics in the domain. In that case, both LES present very similar global quantities at the inlet confirming that same inflow is injected at the main inlet of the domain in the two LES. Since the coolant mass flow only represents 7.5% of the total mass flow and no work is enforced on the fluid, the mass-flow averaged total enthalpy is conserved between $P40$ and $P41$ which leads to $\xi_{ht} \approx 0$. Total pressure loss coefficient ξ is found to be slightly lower for *hole-modelled LES* meaning that less losses are generated in the modelling approach. Since swirl number values at $P40$ and $P41$ between the two LES are very similar, the transport of the swirl through the vanes can be considered equivalent between the two LES. As a result of this discussion, the external flow passing through the vanes is comparable between the two LES and only minor and highly local deviations are expected between the hole-meshed and the *hole-modelled LES*. This is confirmed by looking at the flow expansion around the vanes. To do so, the isentropic Mach number profile obtained in the *hole-modelled LES* is compared to the *hole-modelled LES* on Fig. 6.8. For both NGVs, the flow expansion is well reproduced by the modelling approach. Nevertheless, a slight deviation is observed in the regions where the coolant is ejected. Indeed, since the jet velocity profile imposed by the model differs from the one obtained in the *hole-meshed LES*, this slight deviation was expected.

To sum up, global quantities as well as vane operating points between the two LES predictions are shown to be equivalent. Deviations induced by the modelling approach are then expected to be locally localized within the computational domain. In the following, unsteady flow structure and mean flow organization obtained from the two LES predictions are compared.

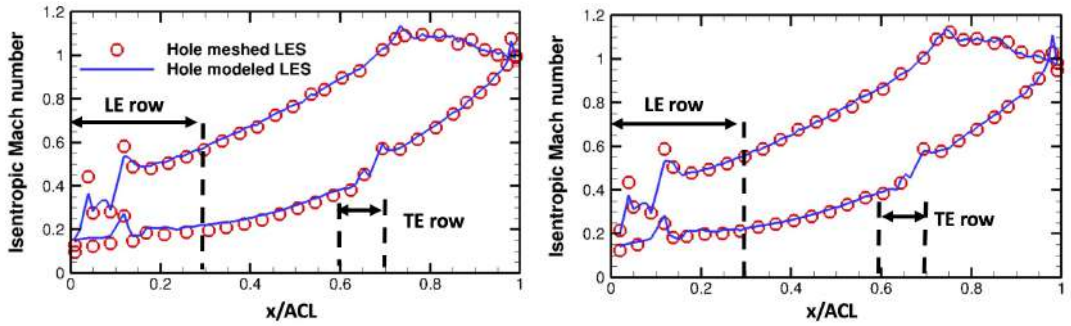

(a) (b)

Figure 6.8 – Isentropic Mach number Ma_{is} [-] along NGV1 (a) and NGV2 (b) at mid-height of the vanes. Red circles ∘ represent the *hole-meshed LES* and solid blue lines – represent the *hole-modelled LES*. Axial extent of coolant hole positions is indicated.

6.4.2 Impact of the coolant model on large scale structures

In this section, the impact of the coolant model on unsteady large scale flow structure in coolant jets is studied. To do so, a view of an iso-surface of Q-criterion equal to $Q_{crit} = 1.10^9 s^{-2}$ coloured by the vorticity magnitude in the coolant jet region of NGV1 is provided for both LES predictions in Fig. 6.9. Clearly, the model reproduces well the coolant jet trajectories as well as jet penetrations. In the *hole-meshed LES*, Fig. 6.9 (a), spatial fluctuations of the iso-surface are observed and originate from turbulent fluctuations generated in the coolant pipes as shown in Chapter 5. Shear layer rings are also retrieved in the jets as well as a pair of vortices propagating from each hole which corresponds to the Counter Rotating Vortex Pair (CRVP) (Fric and Roshko, 1994; New et al., 2003). The iso-surface obtained in the *hole-modelled LES*, Fig. 6.9 (b), also features such structures. However, jets seem to be smoother and more coherent than the one obtained in the *hole-meshed LES* due to lack of turbulent fluctuations injected at the coolant ejection surfaces in the modelling approach. As a result, the model partially reproduces the jet aerodynamics. Such a deviation is expected to affect the coolant film development around the vanes. To confirm this hypothesis, an instantaneous view of the coolant mass fraction map at mid-height of the vanes for both LES predictions is provided

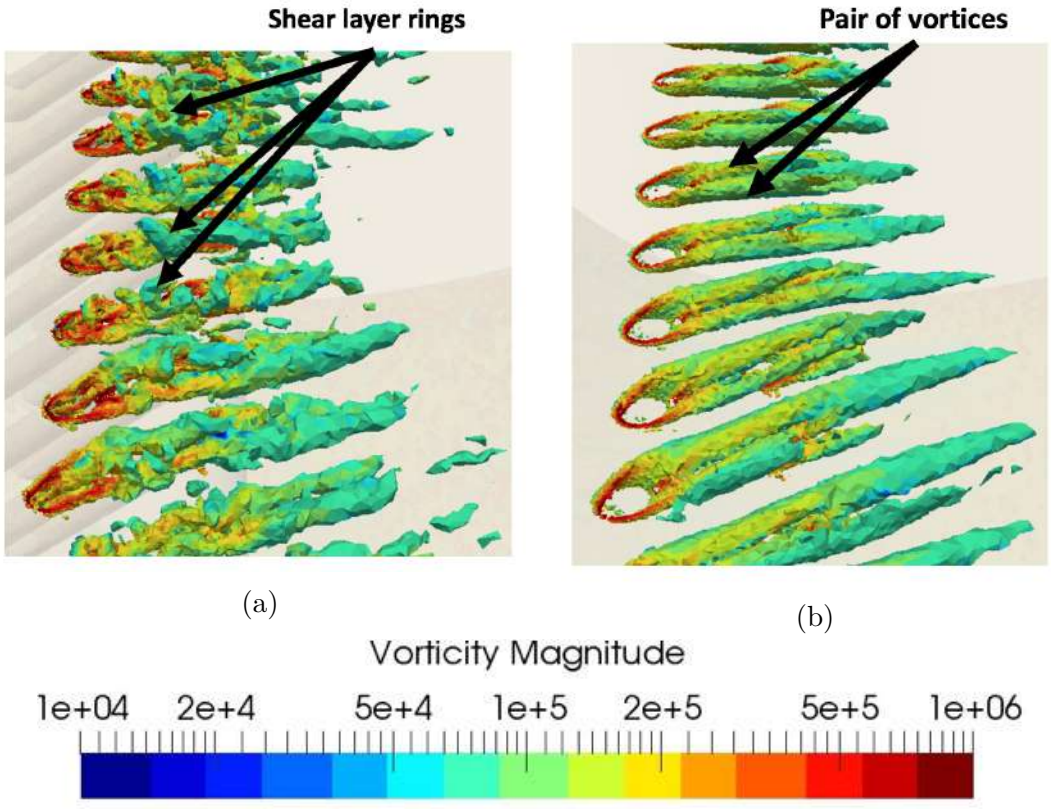

Figure 6.9 – Instantaneous view of an iso-surface of Q-criterion equal to $Q_{crit} = 1.10^9 s^{-2}$ coloured by the vorticity magnitude $\|\omega\|$ $[s^{-1}]$ near the surface vane of NGV1 for the hole-meshed case (a) and hole-modelled case (b).

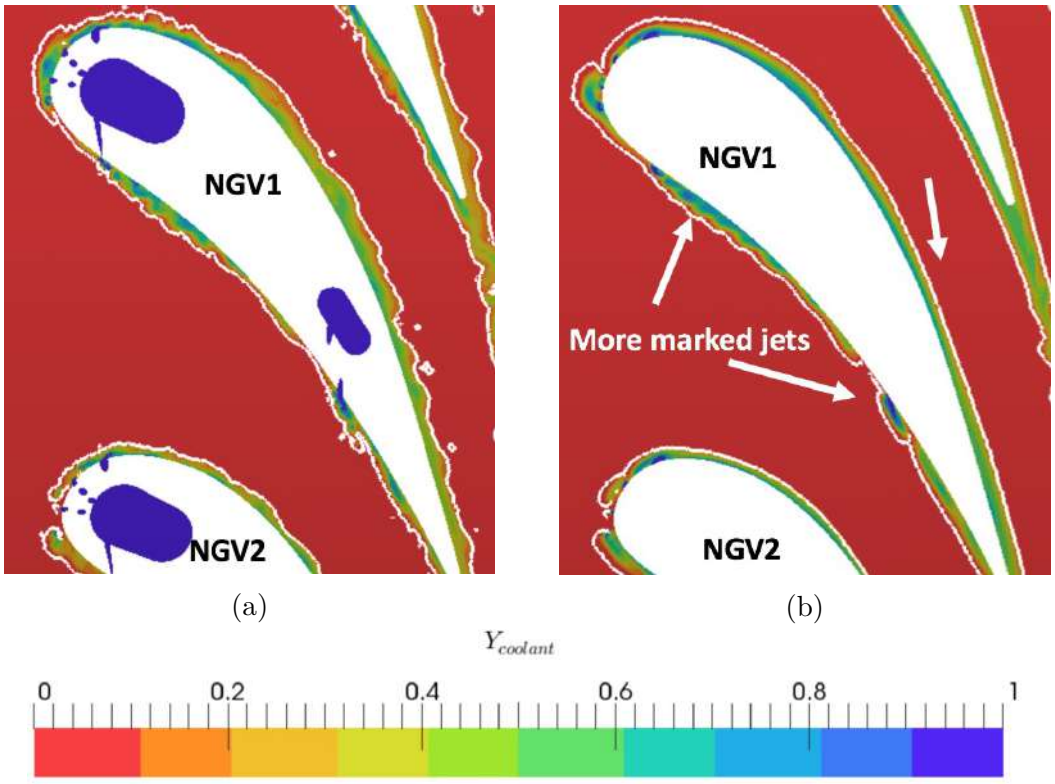

Figure 6.10 – Instantaneous view of the coolant mass fraction map $Y_{coolant}$ [-] at mid-height of the vanes for the hole-meshed case (a) and hole-modelled case (b). The edge of the film is represented by the white iso-contour $Y_{coolant} = 0.05$.

on Fig. 6.10. The edge of the coolant film is represented by the iso-contour $Y_{coolant} = 0.05$. The development of the film around both vanes is well reproduced by the model on both sides of the vanes. In the *hole-meshed LES*, Fig. 6.10 (a), the edge of the coolant film spatially varies in the jet regions and on the suction side of the vanes. Such spatial variations originate from turbulent activity present in the film as shown in Chapter 5. Within the film, local segregations of coolant mass fraction are observed. In the *hole-modelled LES*, Fig. 6.10 (b), the edge of the film is observed to be smoother and present less spatial variations due to the lack of turbulent activity. It is noted that jets are more marked in the *hole-modelled LES* indicating that the mixing process between the cold and hot streams is less efficient. To confirm this statement, the statistic descriptions of the two LES predictions need to be investigated and compared. To do so, the flow fields obtained with the *hole-modelled LES* are time-averaged on the same convergence time as the *hole-meshed LES*. Time-averaged and RMS fields obtained in the two LES predictions are then compared in the next section.

6.4.3 Impact of the coolant model on mean flow structure

In this section, the impact of the coolant model on mean flow aerodynamics as well as mean thermal environment is assessed. To evaluate the mean flow aerody-

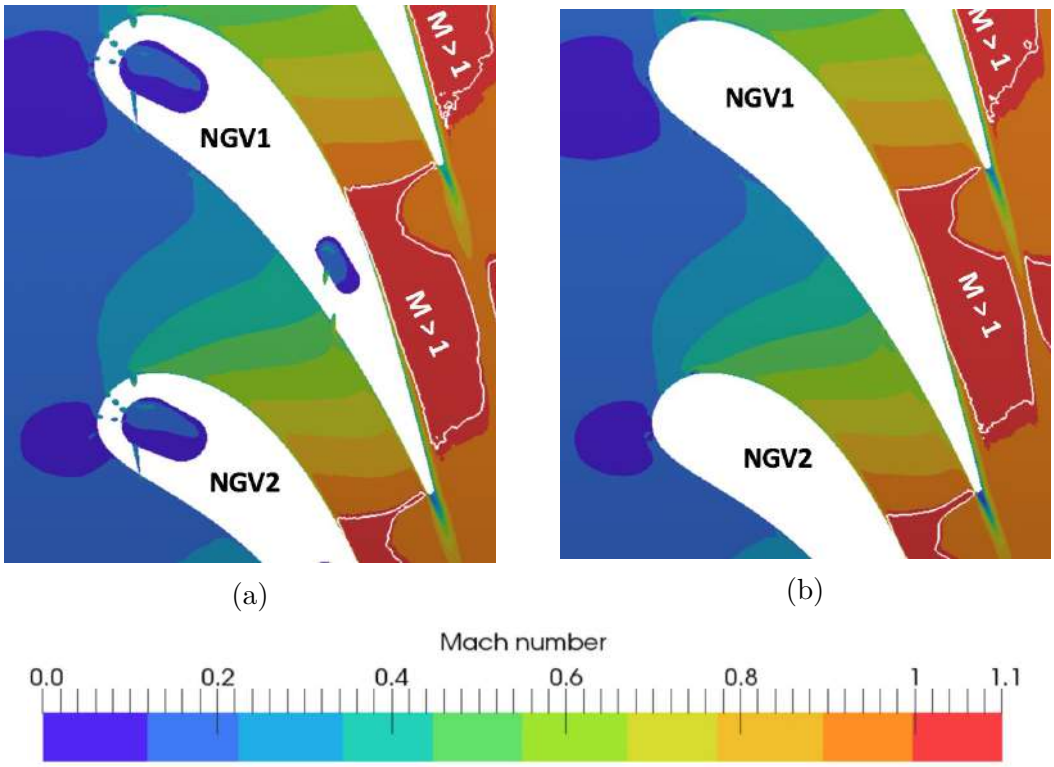

Figure 6.11 – Time-averaged Mach number map $\overline{M}$ [-] at mid-height of the vanes for the hole-meshed case (a) and hole-modelled case (b). White iso-line represents the iso-contour $\overline{M} = 1$.

namics within the passage, time-averaged Mach number maps at mid-height of the vanes for both LES predictions are shown on Fig. 6.11. Clearly, the Mach number maps between the two LES predictions are in full agreement. As anticipated, the stagnation point positions on the vanes are not impacted by the modelling approach because same inflow is imposed at the inlet for the two LES. The supersonic region located on the suction sides of the vanes is also well reproduced in the *hole-modelled LES*. As a result, the modelling approach does not impact the mean freestream flow in the passage between the vanes as expected. Deviations are then expected to be localized in the film. To evaluate the unsteady activity, turbulent kinetic energy map k are extracted at mid-height of the vanes for both LES predictions and displayed in Fig. 6.12. Results confirm that turbulent activity in the coolant film is strongly reduced in the *hole-modelled LES* compared to the *hole-meshed LES*. Indeed, in the *hole-meshed LES* (Fig. 6.12 (a)), turbulence is observed to be in the jets, in the film as well as in the wakes of the vanes. In the *hole-modelled LES* (Fig. 6.12 (b)), smaller values of k are found in the jets and in the film. Indeed and since the majority of turbulence is mainly generated in coolant pipes, these turbulence generation regions are then not represented in the mesh of the *hole-modelled LES*. Furthermore, since no turbulent activity is injected at the coolant ejection surfaces in the model, it results in a lack of turbulent activity in films.

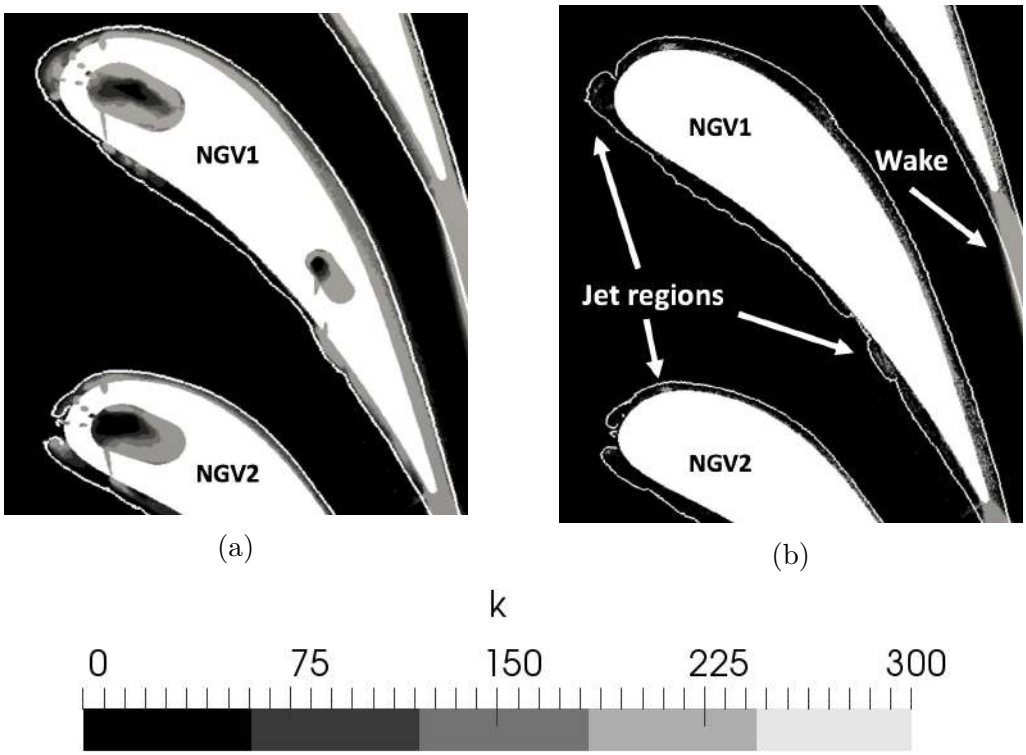

Figure 6.12 – Turbulent kinetic energy maps k $[m^2/s^2]$ for the *hole-meshed LES* on left (a) and *hole-modelled LES* on right (b) at mid-height of the vanes. The mean film thickness is represented by the white iso-line $\overline{Y_{coolant}} = 0.05$.

After comparisons of the mean flow organization, the mean thermal environment is now addressed by investigating the hot spot migration imposed at the main inlet of the computational domain. To assess the hot spot migration through the vanes, time-averaged total temperature fields are shown at mid-height of the vanes on Fig. 6.13. Total temperature maps appear very similar in both simulations. The hot spot, represented by the temperature range defined between $T_t = 480K$ and $T_t = 500K$ impacts NGV1 and migrates in the same way in both LES predictions. Deviations between the two LES are however observed in the region of the cooling flow near the blade surfaces. Indeed, as already observed, jets are more marked in the *hole-modelled LES* compared to the *hole-meshed LES*. Total temperature distribution near the leading edge of NGV1 is also observed to differ between the two LES. As a result, the model is shown to impact total temperature distribution in the film. To find the origins of these deviations, specific investigations of the mixing process in the coolant film will be later presented. To better assess the hot spot migration through the passage, mean total temperature field is further mass-flow averaged along the azimuthal direction on the axial planes $P40$ and $P41$ resulting in radial profiles plotted on Fig. 6.14. At plane $P40$, no difference is noticed between both LES confirming that same inflow is injected at the main inlet. At plane $P41$, profiles are very similar and differences only appear locally near the shroud (top section of the curves), between $0.6 < h/H < 0.8$ showing an impact of the model on the mixing process in the wakes.

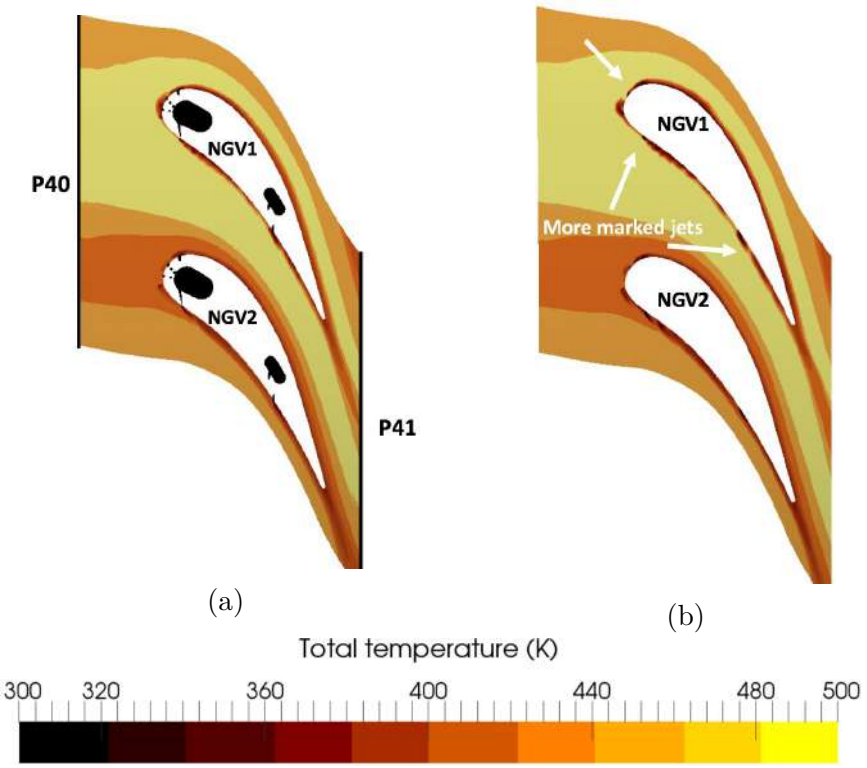

Figure 6.13 – Time-averaged total temperature fields T_t $[K]$ at mid-height of the vanes. (a) *hole-meshed* and (b) *hole-modelled LES*.

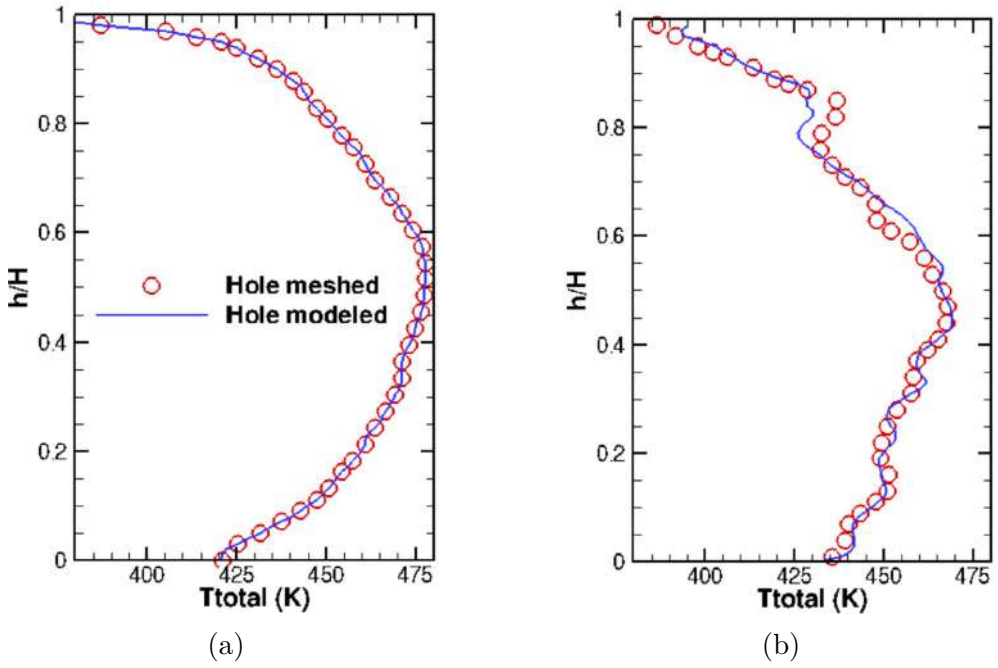

Figure 6.14 – Radial total temperature profiles T_t $[K]$ at the axial plane P40 (a) and P41 (b). Red circle ∘, *hole-meshed LES* and solid blue line −, *hole-modelled LES*.

To sum up, the mean flow aerodynamics and mean thermal environment are found to be equivalent between both LES with only minor differences localized in the coolant film. These findings underline the impact of coolant ejection treatment but at the same time highlight the suitability of the proposed approach for efficient LES use on such problems. Since the main objective in the industry is to predict adiabatic film effectiveness for film cooling design strategies, adiabatic film effectiveness profiles on both NGVs are analyzed in the following section.

6.4.4 Adiabatic film effectiveness predictions

Adiabatic film effectiveness η is obtained from Eq. (5.3) in both LES predictions and resulting profiles are shown on unwrapped NGV surfaces on Fig. 6.15. It is worth to recall that η corresponds to a normalization of the adiabatic wall temperature. As a result, the profiles of η present same spatial patterns of the wall temperature profiles described in Chapter 5. Only the deviations between the two LES predictions will be hereafter discussed. A good agreement between the two LES predictions for both NGVs is confirmed. Indeed, with both approaches all macroscopic patterns are present and equivalently positioned around the two vanes. Near the end-walls for $h/H > 0.8$ and $h/H < 0.2$, radial extents of the coolant free

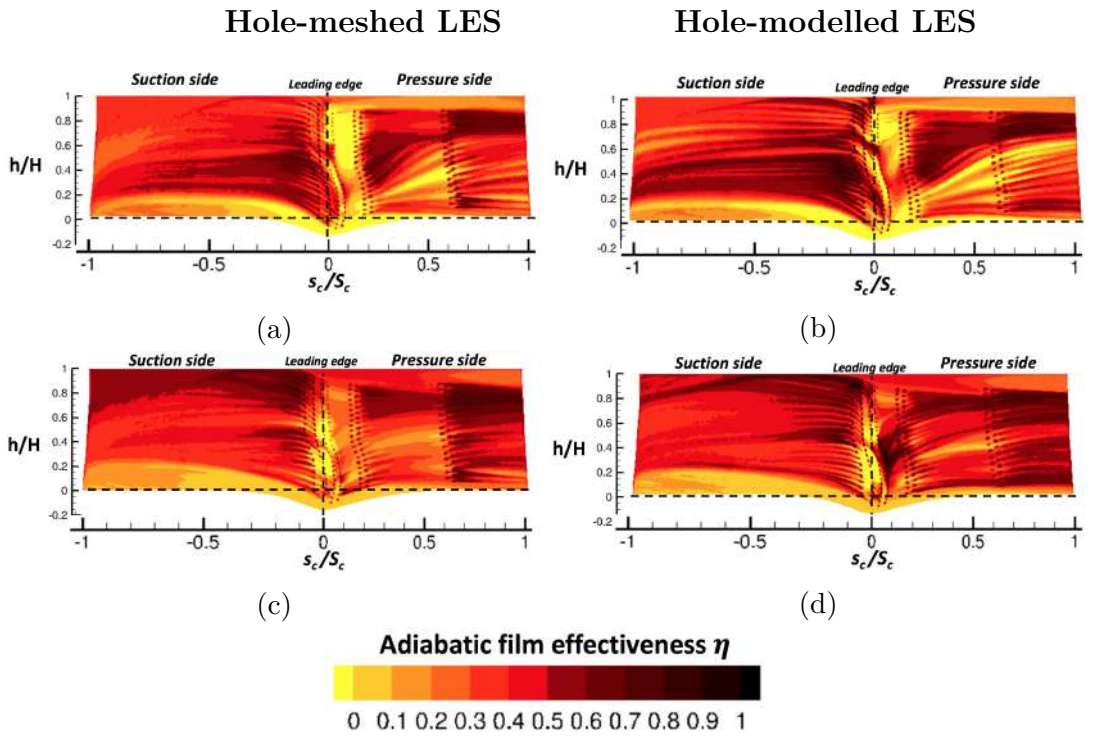

Figure 6.15 – Time-averaged adiabatic film effectiveness η [-] on both NGVs for both LES. Top (a) & (b), NGV1. Bottom (c) & (d), NGV2. Left (a) & (c), hole-meshed LES. Right (b) & (d), hole-modelled LES. Normalized radial coordinate h/H [-] and normalized curvilinear coordinate s_c/S_c [-].

regions and associated levels of film effectiveness are retrieved in the *hole-modelled LES*. Downstream the coolant holes on both sides for $s_c/S_c > 0.2$ and $s_c/S_c < 0$, traces of cold temperature on the wall surfaces (delimited by the iso-lines $\eta = 0.8$ and $\eta = 1$) are observed to be very similar between both approaches. Nonetheless, the *hole-modelled LES* exhibits more segregated values on both sides of the vanes. As anticipated, NGV1 profile, Fig. 6.15(a)&(b), is influenced by the swirled flow on the pressure side which radially deviates the cold flow on the vane surface. This effect is well reproduced in the modelling approach. Nevertheless, deviations appear on the pressure side of NGV1 near the leading edge for $s_c/S_c < 0.2$ where colder temperature are observed in the *hole-modelled LES* as previously noticed on Fig. 6.13. Since same coolant mass flow rate distribution is ejected in the two approaches, this specific deviation could originate from different jet detachments off the wall and jet angles between the two LES. Downstream the coolant holes for $s_c/S_c > 0.2$, traces of hot and cold temperatures are observed to be more marked in the *hole-modelled LES* compared to the *hole-meshed LES*. This confirms that the mixing process is less efficient in the modelling approach. On the suction side of NGV1, same conclusions are drawn. On NGV2, Fig. 6.15(c)&(d), patterns remain similar to the hole-meshed prediction but peak values are larger with the model. Similarly to NGV1, colder temperatures are observed near the leading edge of the vane. Again and similarly to NGV1 downstream the coolant holes for $s_c/S_c > 0.2$, traces of hot and cold flow are also observed to be more marked in the modelling approach on both sides of the vane. To quantify the impact of the model on adiabatic film effectiveness, profiles are mass-flow averaged along the azimuthal direction. Resulting radial profiles of η are plotted on Fig. 6.16. Overall, a good agreement is found between the two simulations. Nevertheless,

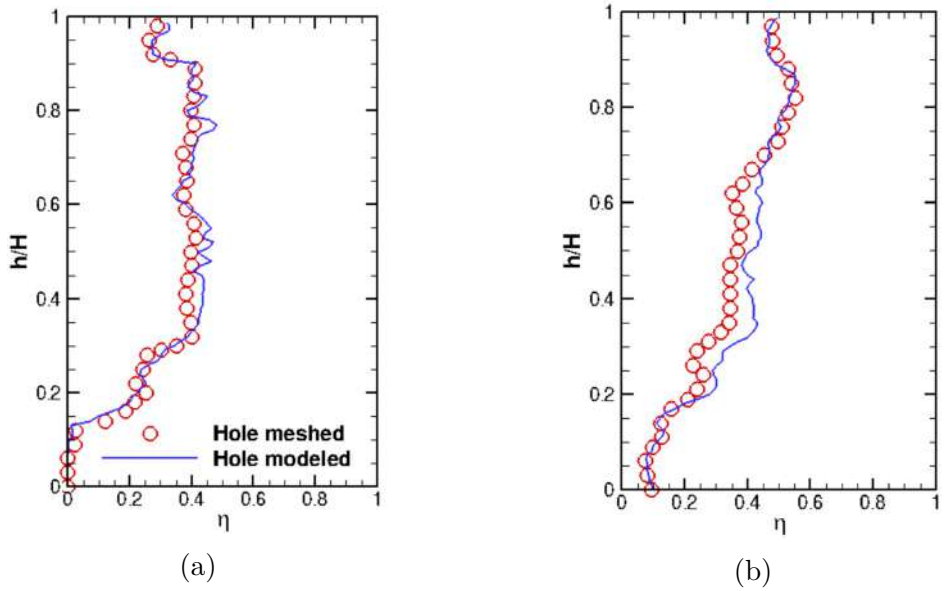

(a) (b)

Figure 6.16 – Radial profiles of adiabatic film effectiveness η [-] for NGV1 (a) and NGV2 (b). Red circle ∘ represents the *hole-meshed LES* and solid blue line − the *hole-modelled LES*.

profiles for the *hole-modelled LES* present more peaks than the *hole-meshed LES*. Indeed for NGV1, Fig. 6.16 (a), both approaches are very close and peaks are locally accentuated indicative of local colder or hotter streams. The differences are more important for NGV2 presenting a maximum deviation between the two approaches around 10 % reaching for a larger radial extent. As a result for both NGVs, the use of the modelling approach induces an efficiency that is slightly higher at mid-height. As expected, no impact is noticed near the hub and shroud where there is no coolant jets. Consequently and as expected, the *hole-modelled LES* does not fully recover the *hole-meshed LES* prediction indicating that the coolant film region is impacted by the coolant model. To find the origin of such defect near wall, the mixing process in the film is specifically investigated in the next section.

6.4.5 Analysis of the mixing process in the coolant film

A key feature differentiating the predictions of the *hole-meshed LES* from the modelled one is the coolant film development around the NGVs. Since the swirled flow is shown to be equivalent between both LES, the impact of the model is expected not to be impacted by the radial position in the computational domain. As a result, the following investigations only focus near mid-height plane of the vanes.

The impact of the model on the mean coolant jet topology is first evaluated. To do so, a view of an iso-surface of time-averaged coolant mass fraction $\overline{Y_{coolant}}$ located near the leading edge of NGV1 is shown on Fig. 6.17 for the two simulations. The shape of jets and their trajectories are shown to be well reproduced in the modelling approach. Nonetheless, iso-surfaces are observed to penetrate further in the freestream flow in the *hole-modelled LES*. This deviation could originate from a less efficient mixing process with the hot flow. Furthermore, jet angles are also

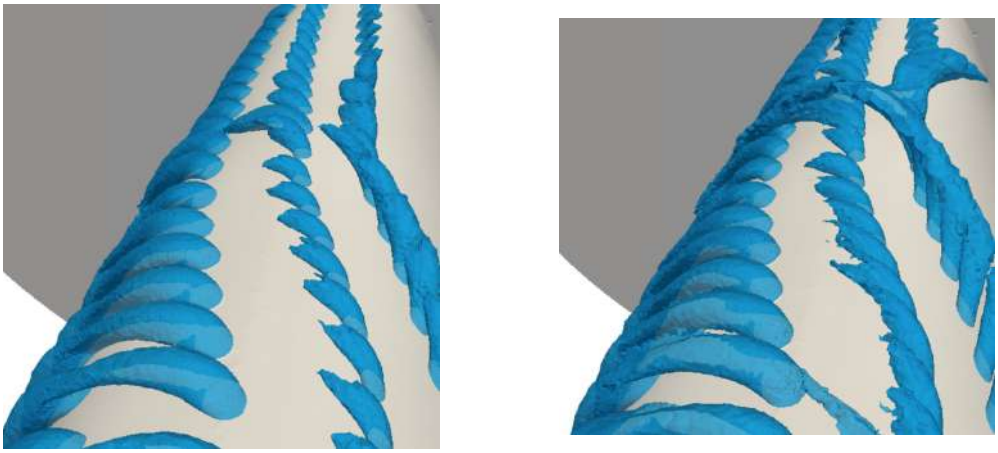

(a) (b)

Figure 6.17 – Iso-surface of time-averaged coolant mass fraction equal to $\overline{Y_{coolant}} = 0.65$ in the *hole-meshed LES* (a) and *hole-modelled LES* (b) near mid-height plane of the leading edge of NGV1.

observed to slightly differ between the two simulations. Indeed, it is important to recall that in the modelling approach, the jet angle is assumed to be equal to the geometric angle of holes. However, this is not necessary the case in the *hole-meshed LES*. Indeed, jet angles near the leading edge are expected to be strongly influenced by the inflow impacting the vane and then to deviate the jets from the geometric direction of the hole. As a consequence, deviations between the two LES are expected near the leading edge of the vanes.

The impact of the model on mean coolant film topology is now investigated. To do so, time-averaged coolant mass fraction $\overline{Y_{coolant}}$ is provided at mid-height on Fig. 6.18. Note that the mean edge of the coolant film is represented by the white iso-contour $\overline{Y_{coolant}} = 0.05$. The model reproduces correctly the mean coolant film topology around the vanes. Indeed, in the *hole-meshed LES*, Fig. 6.18 (a), the coolant film covers both sides of the vanes. If compared against the *hole-modelled LES*, Fig. 6.18 (b), the film topology is very similar but deviations are observed near the leading edge of NGV1, where the coolant film topology is clearly different. This specific deviation between the two LES originates from different jet angles as previously discussed. Coolant jets are furthermore observed to be more marked

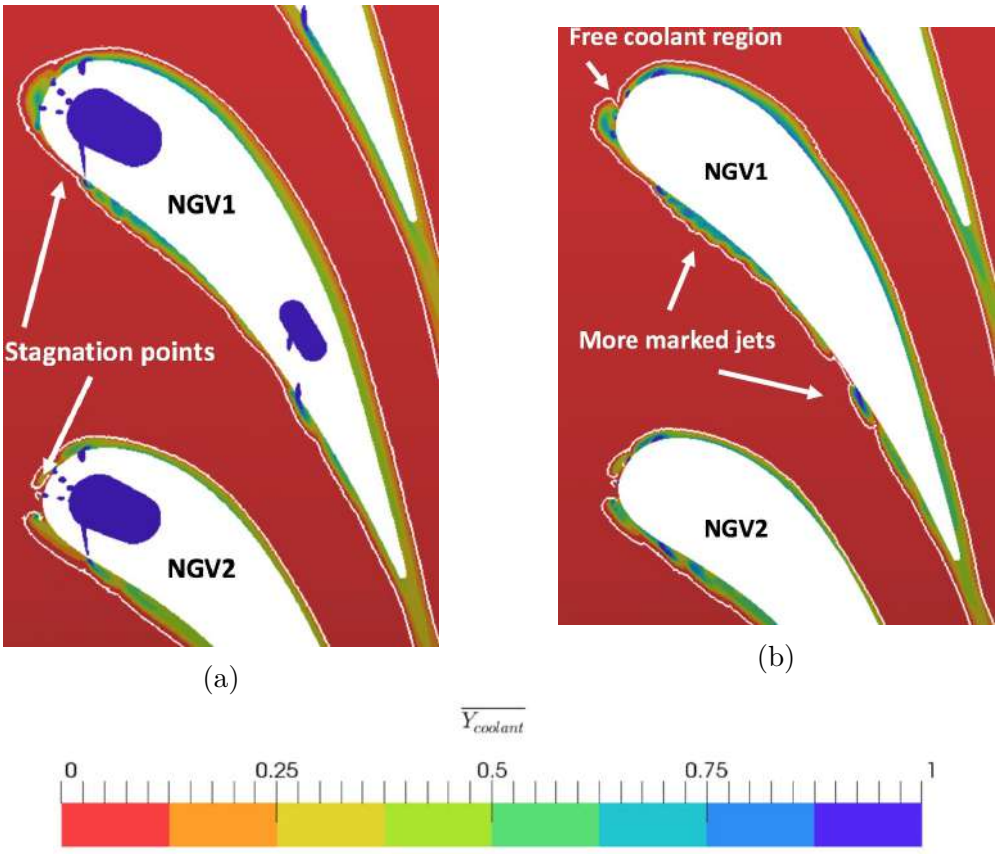

Figure 6.18 – Time-averaged coolant mass fraction map $\overline{Y_{coolant}}$ [-] at mid-height of the vanes for the hole-meshed case (a) and hole-modelled case (b). The mean film thickness is represented by the white iso-line $\overline{Y_{coolant}} = 0.05$.

in the regions where coolant is ejected in the *hole-modelled LES*. Indeed in this region, the mean coolant mass fraction is observed to be more segregated. This corroborates the fact that the mixing process between the jets and the hot streams is less efficient in the modelling approach. To confirm this statement, the mixing process between the cold and hot streams needs to be investigated. The effect of turbulent mixing on the coolant mass fraction can be evaluated from RMS fields of coolant mass fraction Y_{rms} maps plotted at mid-height of the vanes on Fig. 6.19. Turbulent mixing is found to be strongly reduced in the *hole-modelled LES*. In the *hole-meshed LES*, Fig. 6.19 (a), turbulent mixing mainly activates in the coolant jets, in the film and in the wakes. In the *hole-modelled LES*, Fig. 6.19 (b), lower values of Y_{rms} are found in the coolant jets and in the wakes. This finding is corroborated by lower levels of turbulent kinetic energy in the film in the *hole-modelled LES*, Fig. 6.12. To illustrate the difference of coolant distribution in the film between the LES predictions, the profile of $Y_{coolant}$ is extracted along the wall normal distance at mid-height of NGV1 on both sides and at different axial positions as represented on Fig. 6.20. Normal profiles obtained for LES predictions are then plotted on Fig. 6.21. Note that profiles are normalized by the local film thickness δ_f defined as the normal distance from the wall up to the arbitrary position where $\overline{Y_{coolant}} = 0.05$. Overall, both predictions remain equivalent and only local deviations in the profiles are observed. At $x/ACL = 0.25$, Fig. 6.21 (a), on the suction side, the passive scalar decreases monotonously away from the wall starting from a fixed value at the wall. On the pressure side, the behaviour is different, i.e. the

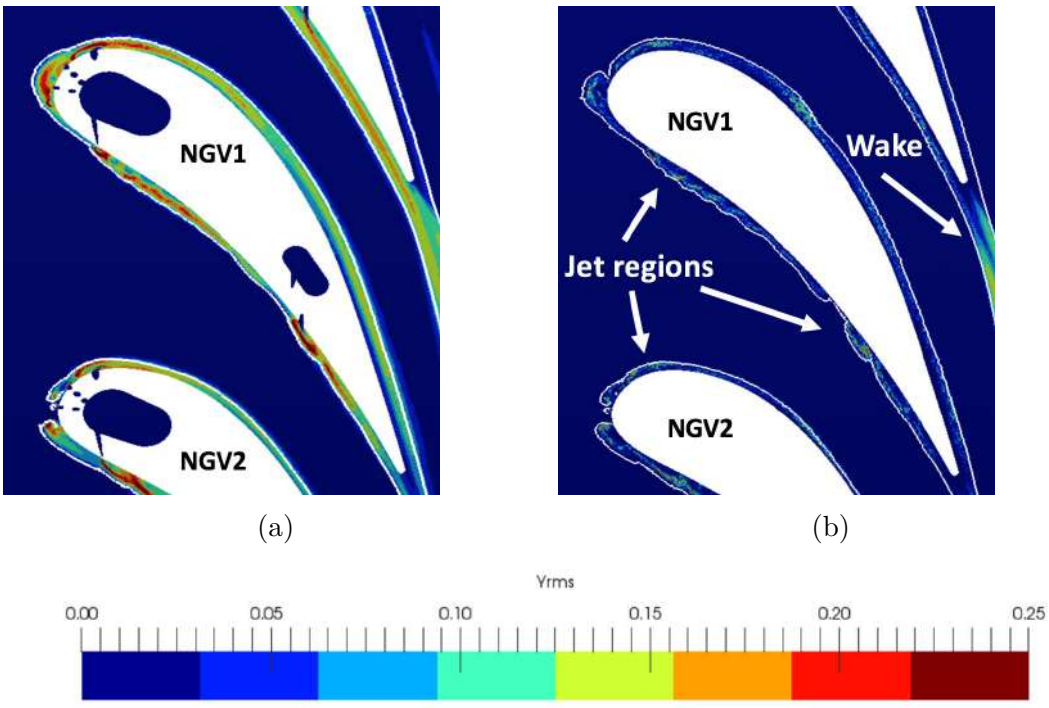

Figure 6.19 – Y_{rms} [-] maps for the *hole-meshed LES* on left (a) and *hole-modelled LES* on right (b) at mid-height of the vanes. The mean film thickness is represented by the white iso-line $\overline{Y_{coolant}} = 0.05$.

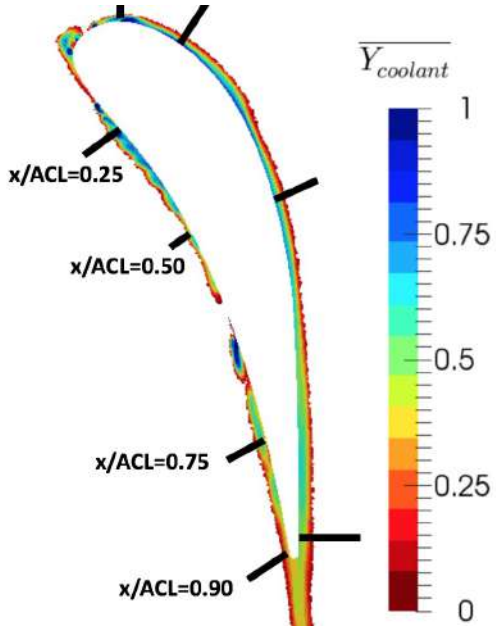

Figure 6.20 – Positions of the extracted normal profile to the wall.

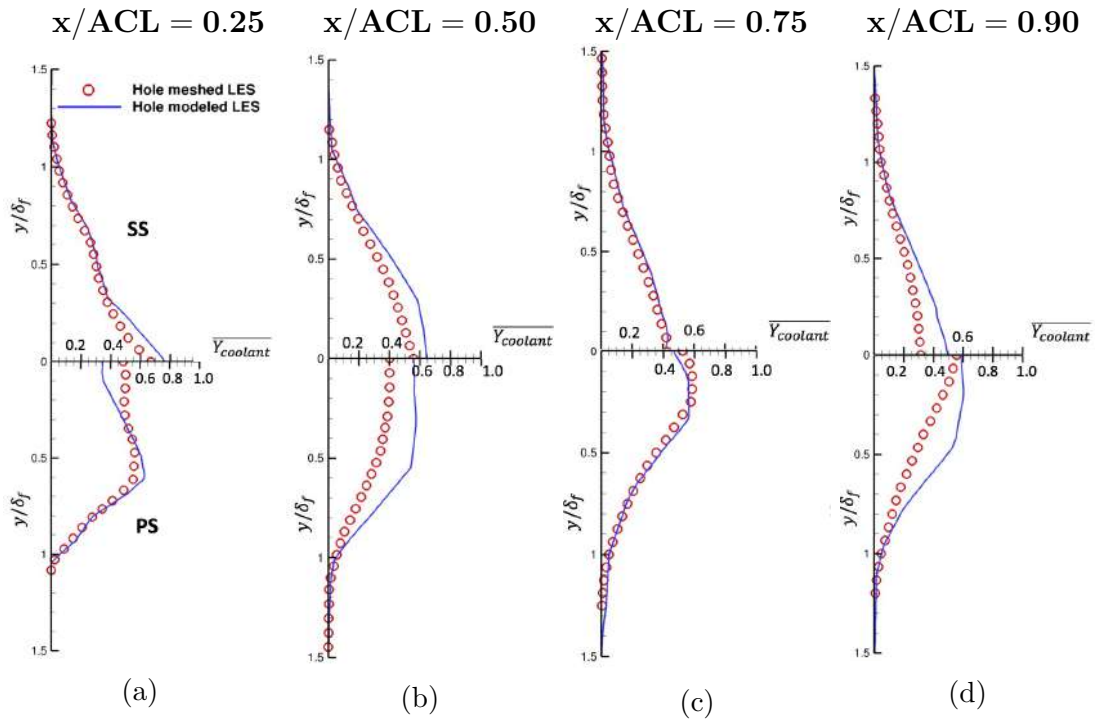

Figure 6.21 – Normal profile of coolant mass fraction $\overline{Y_{coolant}}$ [-] for different axial positions at (a) $x/ACL = 0.25$, (b) $x/ACL = 0.50$, (c) $x/ACL = 0.75$ and (d) $x/ACL = 0.90$ at mid-height along NGV1. Red circles ∘ represent the *hole-meshed LES* and the solid blue line – the *hole-modelled LES*. Pressure side (PS) is at the bottom and suction side (SS) at the top.

value of the passive scalar presents a maximum, not located at the wall, indicating that the coolant distribution in the film is complex and linked to the preceding local coolant ejection. Such observations are confirmed by the other positions, the pressure side film being more complex than the suction side film. When comparing the hole-meshed profiles to the hole-modelled one, differences are noticed near the walls where the coolant concentrations differs although both LES recover the same evolution when y approaches δ_f. At $x/ACL = 0.50$, Fig. 6.21 (b), the hole-modelled simulation over-estimates the value of the passive scalar if compared to the hole-meshed prediction. This indicates that the local concentration of coolant is higher in the film with the modelling approach. At $x/ACL = 0.75$, Fig. 6.21 (c), the two simulations are in very good agreement. It is important to recall that this specific station is located near the coolant holes located at $x/ACL = 0.7$. Thus in this region, the coolant distribution is then mainly dictated by the coolant mass flux injected through the holes which is consistent in both simulations. Finally and at $x/ACL = 0.90$, Fig. 6.21 (d), the local concentration of coolant is higher in the *hole-modelled LES* as already observed at the station located at $x/ACL = 0.50$. From these profiles, the axial evolution of the film thickness $\delta_f(x)$ is obtained and plotted along NGV1 and NGV2 on Fig. 6.22. Note that for the *hole-meshed LES*, a full description of the axial evolution of δ_f was provided in Chapter 5 and only deviations will be hereafter discussed. If comparing both LES, one observes that the hole-modelled formalism under-estimates the film thickness along both NGVs compared to the *hole-meshed LES*. For NGV1, Fig. 6.22 (a), the axial evolution of δ_f is well reproduced in the modelling approach while under-estimating levels on both sides of the vane. For NGV2, Fig. 6.22 (b), the axial evolution on the pressure side is also well reproduced. A larger deviation is however observed on the suction side of NGV2 where levels are also under-estimated. This indicates that coolant tends to remain in the film and lowly mixes with the hot stream in the modelling

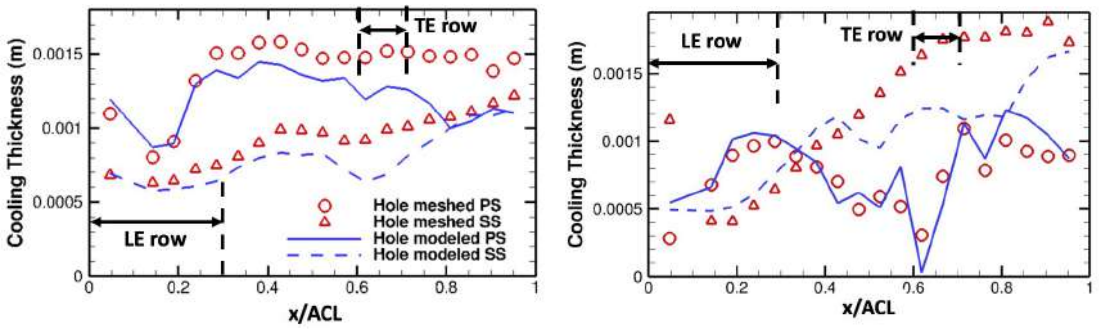

Figure 6.22 – Film thickness δ_f $[m]$ along the vanes for NGV1 (a) and NGV2 (b) at mid-height. Red circles ∘ represent the *hole-meshed LES* at the pressure side. Red triangles Δ represent the *hole-meshed LES* at the suction side. The solid blue line — represents the *hole-modelled LES* at the pressure side. The dashed blue line - - - represents the *hole-modelled LES* at the suction side. Cooling row axial locations are indicated.

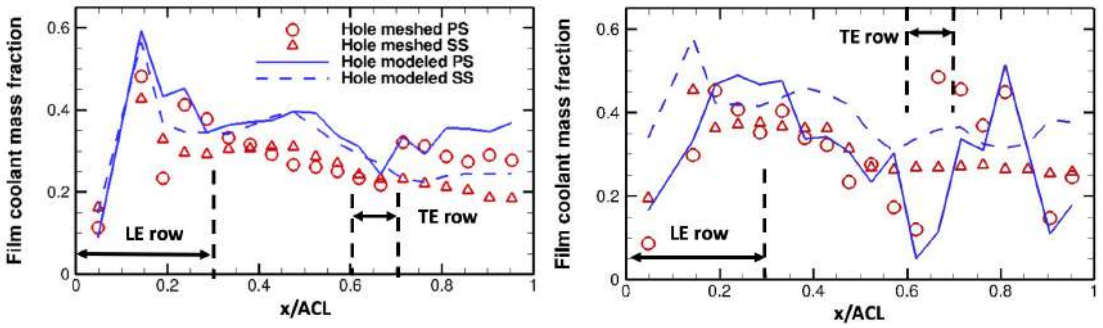

(a) (b)

Figure 6.23 – Film coolant mass fraction Y_{film} [-] along NGV1 (a) and NGV2 (b) at mid-height. Red circles ○ represent the *hole-meshed LES* at the pressure side. Red triangles Δ represent the *hole-meshed LES* at the suction side. The solid blue line – represents the *hole-modelled LES* at the pressure side. The dashed blue line - - - represents the *hole-modelled LES* at the suction side.

approach. From the above profiles, axial evolution of coolant concentration in the film along the vanes can be evaluated using the mass flow weighted film coolant fraction Y_{film} given by Eq. (5.4). Results are plotted on Fig. 6.23 for both NGVs and both LES. For both vanes, axial evolutions of Y_{film} are in good agreement in the two simulations. Nonetheless, levels of Y_{film} are over-estimated on both sides of the vanes in the modelling approach. This deviation confirms that more coolant is present in the film in the *hole-modelled LES*. Indeed for NGV1, Fig. 6.23 (a), levels are over-estimated along the vane on both sides. For NGV2 (Fig. 6.23 (b)), the *hole-modelled LES* follows the same evolution of Y_{film} as the *hole-meshed LES* along the vane while also over-estimating levels of coolant. Major differences are observed on the pressure side of the vane for $x/ACL = 0.65$ where δ_f was shown to be very low. As a result, this specific axial position is more sensitive to changes in the film. From this diagnostic, the coolant model leads to an over-estimation of Y_{film} for both vanes. This indicates that coolant mainly remains in the film because the mixing process with the hot stream is less efficient in the *hole-modelled LES*. To confirm this last statement, a mass balance of the passive scalar concentration is performed in the film region. Using the same control volume and same hypotheses adopted in Chapter 5, axial evolution of Y_{film} is given by Eq. (5.5) which is here recalled:

$$Y_{film}(x) = \frac{1}{Q_{m,film}} \left(Q_{m,cold} - \underbrace{\int_{S_{\delta(x)}} \overline{\rho} \widetilde{Y''_{coolant} U''_i} n_i dS}_{\text{Turbulent mass flux}} \right), \tag{6.17}$$

where $Q_{m,cold}$ is the coolant mass flow rate and $\int_{S_\delta(x)} \overline{\rho} \widetilde{Y''_{coolant} U''_i} n_i$ the turbulent mass flux through the edge of the film S_δ. Since the coolant mass flow rate distribution is consistent in the two LES predictions, the only deviation necessary originates from the turbulent mass flux through the edge of the film S_δ. The axial

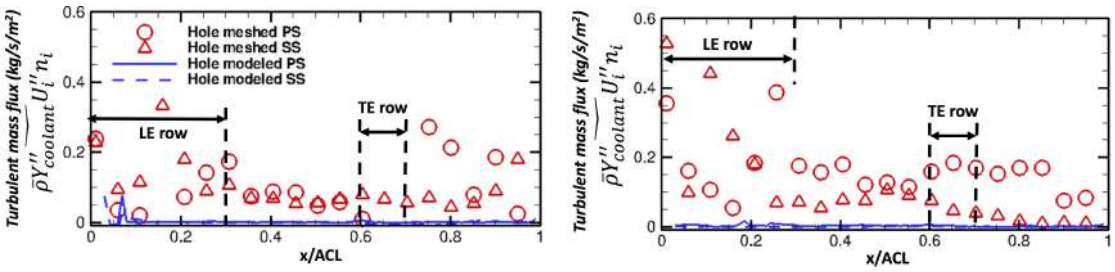

Figure 6.24 – Axial evolution of turbulent mass flux $\overline{\rho}\widetilde{Y''_{coolant}U''_i}n_i$ $[kg/s/m^2]$ through the edge of the film S_δ at mid-height of NGV1 (a) and NGV2 (b). Red circles ∘ represent the *hole-meshed LES* at the pressure side. Red triangles Δ represent the *hole-meshed LES* at the suction side. The solid blue line − represents the *hole-modelled LES* at the pressure side. The dashed blue line - - - represents the *hole-modelled LES* at the suction side.

profiles of local turbulent mass flux $\overline{\rho}\widetilde{Y''_{coolant}U''_i}n_i$ along $S_\delta(x)$ obtained for both LES predictions are provided in Fig. 6.24. First, it is worth to note that levels of $\overline{\rho}\widetilde{Y''_{coolant}U''_i}n_i$ remain strictly positive all along the coolant film. From Eq. (5.5), this shows that turbulent mass flux decreases levels of Y_{film} confirming previous findings. Clearly, turbulent mass flux is strongly reduced in the *hole-modelled LES* compared to the *hole-meshed LES* for both NGVs and values are near zero. This finding confirms that the lack of turbulent activity in the hole-modelling approach strongly reduces the mixing with the hot stream.

To conclude, the investigation of the impact of the model on the film effectiveness profiles shows that the vanes are slightly colder with the model. By performing a coolant mass balance in the near wall regions of the vanes, it can be deduced that there is more coolant in the film in the modelling approach. This is confirmed by the absence of turbulent fluctuations in the coolant film, reducing the mixing efficiency with the hot flow and thus keeping the film temperature near the cold injected temperature. The losses are thus expected to be also impacted by the model. This point is specifically addressed in the next section.

6.4.6 Impact of the coolant model on the loss prediction

An impact of the model on losses was already observed on the total pressure loss coefficient ξ in Table 6.1. Indeed, total pressure loss coefficient ξ was found to be lower for the *hole-modelled LES*, meaning that less losses are generated with the model. To find the origin of this deviation, time-averaged loss maps, $\overline{P_m}$ and $\overline{P_q}$ are compared between the two LES predictions. Note that a full description of the loss generation process was provided in Chapter 5 and only deviations between the LES predictions will be hereafter discussed. First, the integrated values of loss maps for both LES are provided in Table 6.2. To compare both LES predictions, the cooling system of the *hole-meshed LES* is excluded from the integration volume.

	hole-meshed LES	**hole-modelled LES**
$\int_V \overline{P_m} dV$	509 W	300 W
$\int_V \overline{P_q} dV$	264 W	171 W

Table 6.2 – Integrated loss values in the domain excluding the cooling system.

Overall loss generation is clearly reduced in the *hole-modelled LES* compared to the *hole-meshed LES*. Indeed, aerodynamic losses are reduced by 41% and mixing losses are reduced by 35 %. To study these deviations, loss maps are provided for both LES predictions at mid-height on Fig. 6.25. In the freestream flow, i.e, away from the film regions, the loss generation is not impacted by the model because no impact of the model has been observed on freestream flow. In contrast, the loss generation is reduced in the films with the model. Indeed, in the *hole-meshed LES*, aerodynamic losses, Fig. 6.25 (a), mainly takes place in the coolant jet regions. In the *hole-modelled LES*, Fig. 6.25 (b), same regions of loss generation are observed as the *hole-meshed LES* while under-estimating levels. Same conclusions are drawn for the mixing losses, Fig. 6.25 (c) & (d). To investigate the impact of the model on the loss generation process, the mean contributions P_m^{mean}, P_q^{mean} as well as turbulent contributions, P_m^{turb}, P_q^{turb} are hereafter studied. The different contributions for both losses are first integrated and results are provided in Table 6.3. Numbers show that the mean contributions are weakly impacted by the model. In contrast, the model strongly reduces the losses issued by turbulent fluctuations. To localize these deviations between the two LES predictions, the turbulent contribution maps for both losses P_m^{turb}, P_q^{turb} are provided at mid-height in Fig. 6.26. In the *hole-meshed LES*, Fig. 6.26 (a), turbulent contributions of aerodynamic losses are mainly located in coolant jets and in the wakes of the vanes, where high levels of turbulent kinetic energy were observed. In the *hole-modelled LES*, Fig. 6.26 (b), levels are clearly under-estimated. Same conclusions are drawn for the mixing losses, Fig. 6.26 (c)&(d). Turbulent contributions in the loss generation mechanism are then strongly reduced due to the lack of turbulent activity in the film in the hole-modelling approach.

	hole-meshed LES	**hole-modelled LES**
$\int_V P_m^{mean} dV$	33 W	31 W
$\int_V P_q^{mean} dV$	14 W	14 W
$\int_V P_m^{turb} dV$	476 W	269 W
$\int_V P_q^{turb} dV$	250 W	157 W

Table 6.3 – Integrated losses within the computational domain excluding the cooling system.

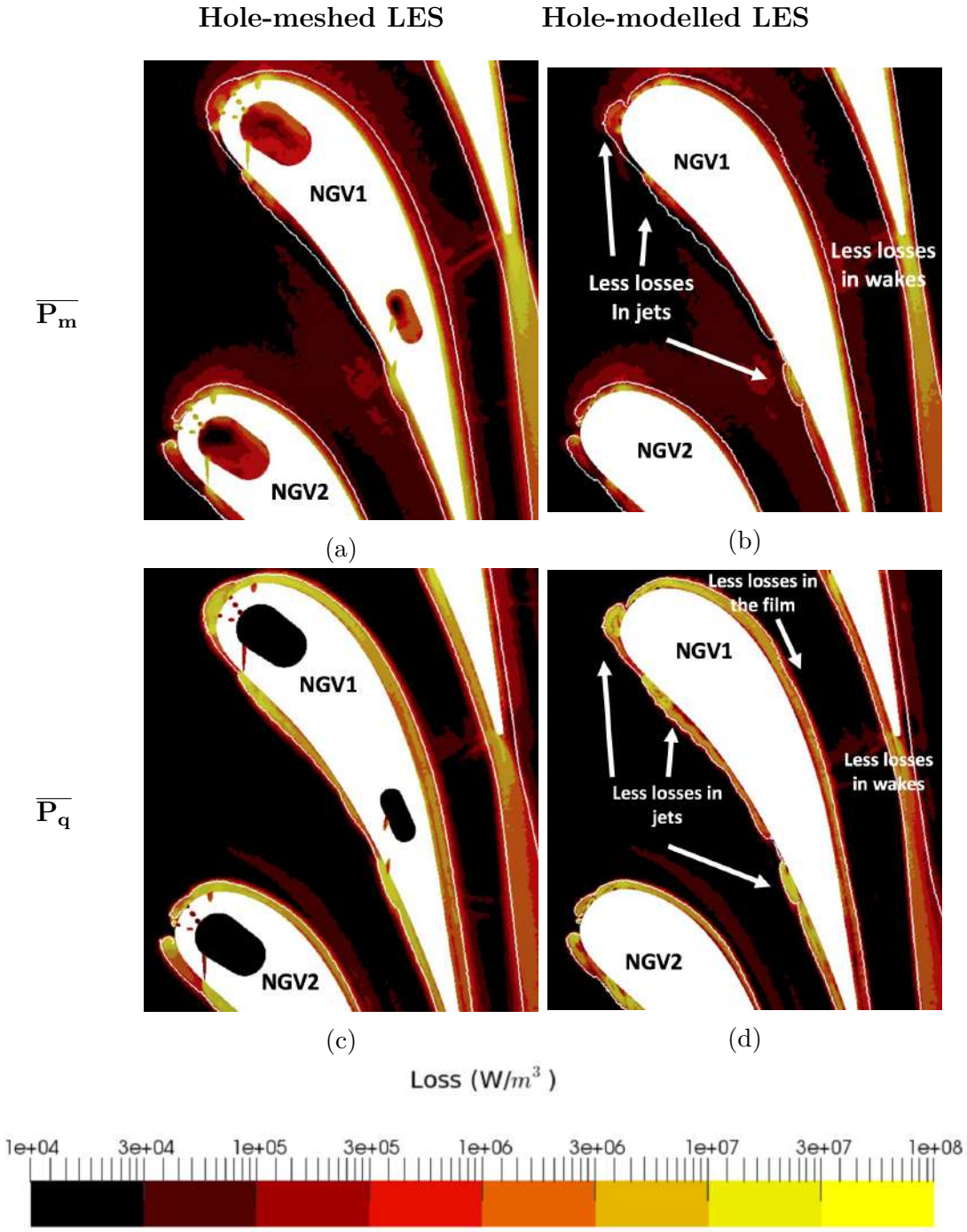

Figure 6.25 – Time-averaged loss maps at mid-height for the hole-meshed case on left (a)&(c) and hole-modelled case on right (b)&(d). Aerodynamic loss $\overline{P_m}$ at top (a)&(b) and mixing loss $\overline{P_q}$ at bottom (c)&(d). White iso-line represents the iso-contour $\overline{Y_{coolant}} = 0.05$.

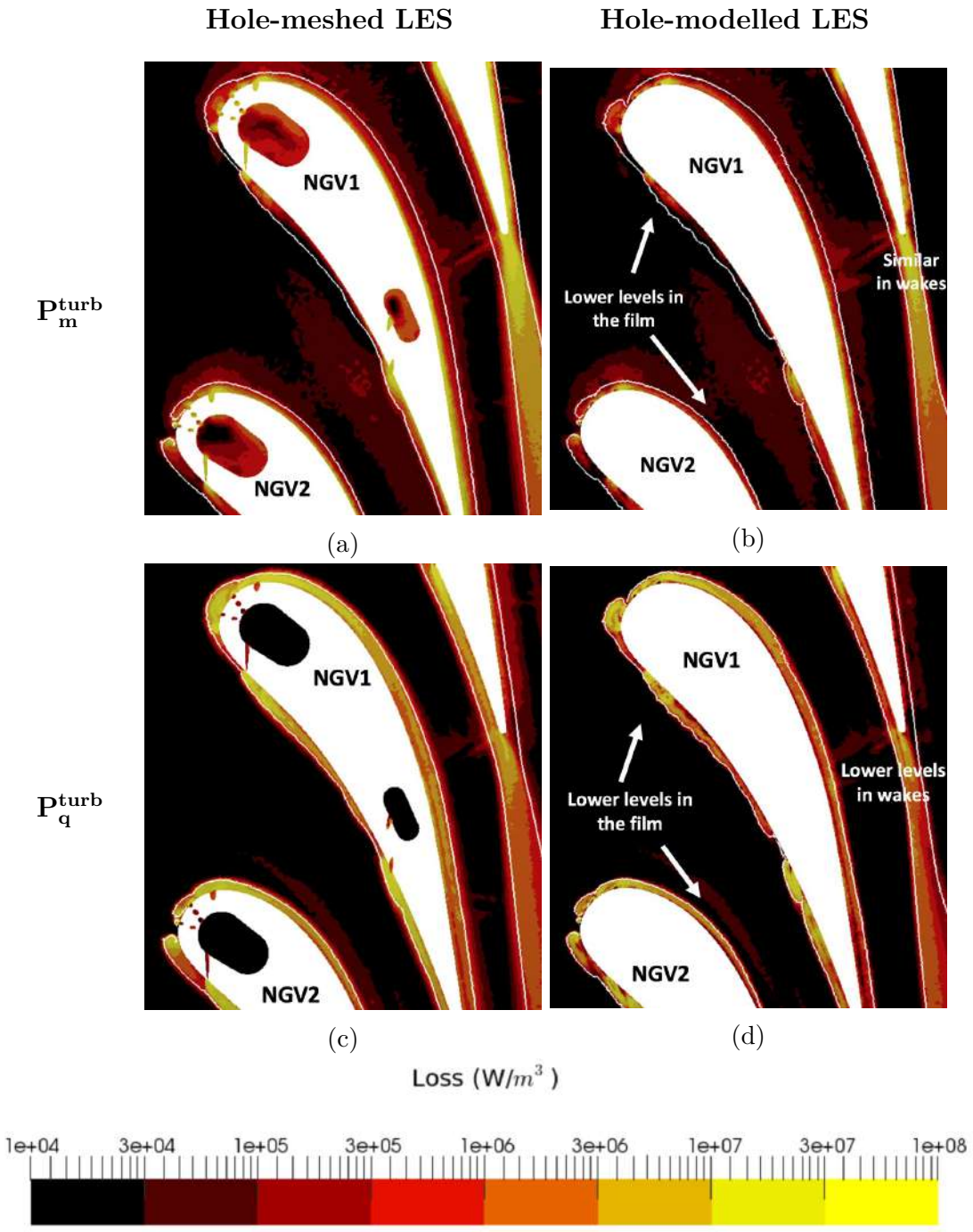

Figure 6.26 – Turbulent contribution P_m^{turb} at top (a)&(b) and P_q^{turb} at bottom (c)&(d) at mid-height for the hole-meshed case on left (a)&(c) and hole-modelled case on right (b)&(d). White iso-line represents the iso-contour $\overline{Y_{coolant}} = 0.05$.

6.5 Chapter conclusions

In the present study, the applicability of a coolant injection model to predict the adiabatic wall temperature for turbine vanes with LES has been assessed. The model derives from an existing coolant ejection model designed for combustion chamber liners and was adapted to turbine blade cooling. To evaluate the coolant model, the reference *hole-meshed LES* of Chapter 5 is compared to a so-called *hole-modelled LES* while conserving same inflow/outflow boundary conditions, same numerics and LES modelling. Results are very encouraging. The coolant jet trajectories and jet penetrations are well reproduced in the hole-modelling approach. In the *hole-modelled LES*, a very close distribution of the adiabatic film effectiveness is found compared to the *hole-meshed LES* with a maximum over-estimation of 10 % . Investigations of the coolant film show that the coolant concentration is higher in the *hole-modelled LES*. By performing a mass balance in the film region, turbulent mixing of the coolant with the hot flow is shown to be strongly reduced in the *hole-modelled LES*. Indeed, the evaluation of the turbulent fields shows that levels of turbulent kinetic energy and turbulent mixing are strongly reduced in the *hole-modelled LES*. Since turbulence is mainly produced in the cooling systems of the vanes which is omitted in the modelling approach, a lack of turbulent activity is observed in the film. The investigation of the loss maps confirms that turbulent contributions in the loss generation mechanism are reduced in the hole-modelling approach. As a result, the model needs to be improved to recover the flow dynamics in the film. Naturally, a path of improvement is the injection of synthetic turbulence at the exit pipe section with the model which needs to be tested in future studies. In terms of CPU effort, the model allows drastic saving of resources as presented in Table 6.4. Note that the CPU cost is estimated for one domain flow through time. Using the modelling approach, only one third of the original cost is needed to resolve the flow for these realistic cooled vanes. Indeed, the cooling system containing half of the mesh cells is removed from the computational domain decreasing the human work and time to produce CAD and mesh design of the vanes. As a result, the mesh refinement can be enforced around the vanes and in the mixing regions between hot and coolant streams thanks to the coolant ejection model. Finally, this coolant model also permits to test many layouts of coolant holes to improve and optimize future design of blade cooling for complex geometries with LES. To do so, the coolant mass flow distribution between holes can be estimated from RANS or analytical models based on flow physics in pipes.

CASE	**Number of cells**	**CPU cost (CPUH)**
Hole-meshed LES	73.10^6	50.000
Hole-modelled LES	38.10^6	15.000

Table 6.4 – Summary of the CPU costs to statistically converge the mean flow using the HPC ressources of IDRIS on the Blue Gene machine TURING [1].

[1]Further information on the machine can be found on http://www.idris.fr/eng/turing/.

General conclusions and Perspectives

To improve the engine efficiency while ensuring long time operation of high-pressure vanes in aeronautic engines, efficient and optimized cooling systems for turbine blades and vanes are required. To qualify turbine blade and vane designs, accurate predictions of wall temperature and losses are needed. In the industry, numerical predictions based on the Reynolds Average Navier-Stokes Simulations (RANS) formalism are mainly used. However, limitations have rapidly been encountered on the prediction of the mixing process between the hot and cold streams present in turbines of aeronautical engines. With the constant increase of CPU resources, Large Eddy Simulations (LES) has recently appeared as a potential substitute for the flow prediction in turbomachinery. Indeed, LES has proved its capacity to predict flow aerodynamics for turbine flows. However, very few LES studies of aerothermal configurations have been reported. From these observations, the capacity of LES to predict the flow aerodynamics, the blade wall temperature as well as the identification of the loss locations and mechanisms in the case of anisothermal configurations is considered in the present work.

To access and study the losses for these strong anisothermal flows, two high-fidelity methodologies are described in Chapter 2. In the first approach, losses are evaluated using entropy balance through the 1D evolution of total pressure and total temperature between two stations of the flow. This approach is quite standard and often used in the literature. The question addressed at this occasion rather focuses on the need to reduce the 3D unsteady LES data to 1D steady quantities. In that case, mass flow rate average is shown to be adequate since conservation properties of transport equations are preserved during the averaging process. Nevertheless, the main limitation of such a balance is that the loss generation process within the flow is not accessible. To access the loss generation location and mechanism, a second approach based on the Second Law Analysis (SLA) is adopted. In this approach, loss maps are constructed from the resolved entropy source terms. In this approach, loss maps are further split in an aerodynamic contribution and a mixing contribution. To evaluate the capacity of both approaches whenever used in the context of LES, academic and complex configurations of increasing complexity are investigated. For all cases addressed, the major conclusions are hereafter summarized:

Academic uncooled configuration T120 In Chapter 3, wall resolved LES are performed on the academic uncooled T120D blade studied in the framework of AITEB II project for which a recirculation bubble on the pressure side is present. For this specific problem, it is shown that injection of freestream turbulence at the inlet is needed to recover the pressure distribution around the blade. For this isothermal configuration, the total pressure drop measured between two stations is shown to give a good indication of the integrated loss value. To further investigate the process of loss generation, loss maps are investigated through the use of SLA. Most of the aerodynamic losses are observed to be generated in the wake, boundary layers and the freestream flow region when turbulence is injected at the inlet. More advanced analyses of these loss maps show that regions of strong unsteady fluctuations as well as high vorticity levels generate the majority of losses. The integration of loss maps in local volumes shows that the boundary layer is responsible for 70% of the loss generation. These loss generation locations are found to be coherent with the literature.

Academic film-cooled configuration T120D In Chapter 4, a wall resolved LES is performed on the academic blade T120D for which film cooling on the pressure side is present. When compared to experimental results, LES clearly improves the prediction of the pressure distribution as well as the adiabatic film effectiveness on the blade surface with respect to RANS. Nevertheless, jet separations and detachments are observed to be over-estimated in the LES compared to experimental results. Injection of freestream turbulence at the inlet could help to reduce these deviations with the experiment results and needs to be tested in future studies. Investigation of losses using entropy balance shows that both total pressure and total temperature should be taken into account to quantify the integrated value of losses between two stations. It is important to note that the contribution of total temperature is generally omitted in the literature and leads to an inaccurate estimation of loss levels for these anisothermal flows. To identify the loss location and mechanisms for these flows, SLA is shown to differentiate aerodynamic and mixing contributions of losses. It is shown that aerodynamics losses are generated in high sheared regions (boundary layer and shear layer of jets) while mixing losses are naturally produced in regions of mixing between the hot and coolant streams (film cooling and wake). Again, turbulent fluctuations are observed to dominate the overall loss generation process.

Industry oriented film-cooled configuration FACTOR In this part, the capacity of LES to predict the vane wall temperature and losses is assessed for the complex geometry of high-pressure vanes of the FACTOR project. To do so, WMLES are performed to avoid the CPU effort associated to the near wall flow resolution. A first *hole-meshed LES* is realized by meshing the whole coolant pipes and feeding plena and is presented in Chapter 5. Results show that LES captures the patterns and levels observed in the experiment of the adiabatic film effectiveness distribution on the vane surfaces. Again, the lack of unsteadiness injected at the inlet could explain the deviations with the experiment. A first evaluation of

losses is performed through the use of total variable balances and only evidences the aerodynamic losses generated in the wake. To access the loss generation mechanism for such a complex configuration, loss maps are further investigated using SLA. With this approach, the same loss generation locations and mechanisms observed for the academic configurations studied in Chapter 3 and Chapter 4 are found. However, resolving the flow in the cooling system of such a complex geometry requires a significant CPU effort. Indeed, half of the mesh cells are only dedicated to the cooling system for this case. To alleviate this CPU issue, the coolant can be directly ejected on the vane surfaces through the use of the coolant ejection model introduced in this work. To evaluate the coolant ejection model, a *hole-modelled LES* is realized by modelling the coolant ejection on the vane surfaces and is thereafter compared to the *hole-meshed LES* in Chapter 6. The model reproduces the coolant jet aerodynamics while over-estimating the adiabatic film effectiveness by 10%. Indeed, the mixing process between the hot and cold streams is observed to be strongly under-estimated in the *hole-modelled LES* because no turbulent fluctuation is imposed with the model. One natural consequence is that losses generated by turbulent fluctuations are also strongly reduced. To recover the dynamic of the flow, injection of freestream turbulence on the coolant ejection surfaces seems required and needs to be considered in futures studies. Finally, the CPU cost is divided by 3 with the model which reduces the lead time in industry.

From the above results and discussions, LES shows its capacity to predict the flow aerodynamics and blade wall temperature for complex non-isothermal configurations. Indeed, the prediction is clearly improved when compared to RANS which is the current industrial practise. It is further guaranteed if the mesh is sufficiently refined in highly dynamic regions and if unsteadiness are injected at the inlet boundary conditions especially for cases presenting separation bubbles. For more complex configurations, such high-fidelity simulations can be also performed through the use of the coolant ejection model introduced in this work. Such results are then very promising for the prediction of blade wall temperature of complex non-isothermal configurations with LES.

To evaluate the losses, SLA is shown to identify the loss generation locations and mechanisms for anisothermal complex configurations. Indeed, the main advantage of this approach is that loss maps are directly constructed from the LES resolved fields and does not require any averaging procedures contrary to total variable 1D balances. From these loss maps, SLA allows to discriminate aerodynamic losses from mixing losses. It is also shown that turbulent fluctuations dominate the loss generation mechanism. This finding highlights the benefits of SLA to predict the losses from LES fields. Indeed, turbulent contributions are directly resolved on mesh with LES while it should be modelled in RANS. Such a methodology coupled to the proposed analyses (integration of loss maps, Reynolds decomposition, links with the flow physics) is then very promising to accurately investigate the losses for highly turbulent, compressible and anisothermal flows in complex systems.

Note that the methodologies developed in this thesis were applied to an industrial cooled high-pressure vane supplied by Safran Helicopter Engine. Despite the existence of this work, it is not reported in the manuscript because of confidentiality reasons. However, very promising results were obtained.

Note finally that new developments have been implemented in the code AVBP to realize this work. First, the expressions of the loss maps for anisothermal compressible flows have been implemented to AVBP. Then, to impose a 2D map at the inlet of the periodic computation performed in Chapter 5, a specific tool has been designed. Afterwards, several post-processing tools have been created using Python to extract and analyse boundary layer and mixing regions for complex geometries. Finally, to comply with the variable heat capacity ratio formalism used in AVBP, new routines to compute the total pressure and temperature have been implemented and validated.

Perspectives

To improve the prediction of the blade wall temperature for complex geometries, several points need to be considered for futures studies. First, the injection of unsteady fluctuations at inlet of hot stream is expected to strongly impact the mixing process between the hot and cold streams and should hence be tested. Then, wall laws need to be improved in the context of turbine blade cooling to take into account radial and streamwise pressure gradients as well as mixing process between the hot and cold streams in the near wall flow region.

As a result of the present PhD work, different perspectives are foreseen for SLA when dealing with LES. First, SLA needs more validation. To do so, comparisons of loss maps obtained from academic configurations with LES to Direct Navier-Stokes Simulations (DNS) are needed since experimental access to such quantities remains difficult today. Last but not least, the impact of numerics and mesh resolution on loss maps needs also to be evaluated. Finally, the impact of sub-grid scale models and wall modelling needs also to be addressed.

For future industrial designs, optimization processes based on the loss maps can also be developed to minimize the losses. Loss maps can also be used to identify regions of strong velocity and temperature gradients in complex geometries to perform automatic mesh refinement as presented in (Daviller et al., 2017).

Finally and as a consequence of the present PhD work and perspectives, SLA coupled to LES is a very promising methodology to predict the flow aerodynamics and losses for the design of future geometries of industrial turbine vanes and blades.

Appendices

Appendix A

LES governing equations of non-reactive compressible flows

A.1 Governing equations of non-reactive compressible flows

The compressible non-reactive flow is governed by the Navier-Stokes equations. They constitute a set of three conservation laws which are detailed here using the Einstein's rule of summation for indices, considering no body forces nor radiative heat flux:

$$\frac{\partial \rho}{\partial t} + \frac{\partial}{\partial x_j}(\rho u_j) = 0 \tag{A.1}$$

$$\frac{\partial}{\partial t}(\rho u_i) + \frac{\partial}{\partial x_j}(\rho u_i u_j + P\delta_{ij} - \tau_{ij}) = 0 \tag{A.2}$$

$$\frac{\partial}{\partial t}(\rho E) + \frac{\partial}{\partial x_j}(\rho u_j E + u_i P\delta_{ij} + q_j - u_i \tau_{ij}) = 0 \tag{A.3}$$

In Eqs. (A.1), (A.2) and (A.3) respectively corresponding to the conservation laws for mass, momentum and total energy, the symbols $\tau_{ij}, f_i, E, q_j, Q_r$ denote respectively the viscous stress tensor, the body forces, the total energy, the heat flux vector and the radiative heat flux. The other symbols present in these equations were already introduced in this work and keep their meaning. In these equations, the pressure, temperature and density are linked by the equation of state of a perfect gas:

$$P = \rho r T \tag{A.4}$$

with $r = 287.0$ J/kg.K is the perfect gas constant for pure air. As air is a Newtonian fluid, the viscous stress tensor is linearly dependent on the strain rate which components read:

$$S_{ij} = \frac{1}{2}\left(\frac{\partial u_i}{\partial x_j} + \frac{\partial u_j}{\partial x_i}\right). \tag{A.5}$$

Using fluid particle isotropic considerations and Stokes' hypothesis one obtains the

following expression for the viscous stress tensor τ_{ij}:

$$\tau_{ij} = 2\mu \left(S_{ij} - \frac{1}{3} S_{kk} \delta_{ij} \right). \tag{A.6}$$

The dynamic viscosity μ is assumed to depend only on temperature because of the limited pressure level and variations found in the CS. The Sutherland law (valid from 100 K to 1900 K) is used at this purpose:

$$\mu = \mu_{ref} \left(\frac{T}{T_{ref}} \right)^{2/3} \frac{T_{ref} + 110.4}{T + 110.4}, \tag{A.7}$$

with $\mu_{ref} = 1.71 \times 10^{-5}$ kg/m.s and $T_{ref} = 273.15$ K.
Finally, for the monospecies flow of the CS, the heat flux vector reads:

$$q_i = -\lambda \frac{\partial T}{\partial x_i}, \tag{A.8}$$

where the thermal conductivity is expressed as:

$$\lambda = \frac{\mu C_p}{Pr} \tag{A.9}$$

with the molecular Prandtl number Pr =0.75 for air supposed as constant in time and space.

A.2 LES governing equations

LES are based on the hypothesis that the small turbulent structures are more universal in character and isotropic than the large eddies which are the real energy-carrying structures (Pope, 2000). Based on this separation of scales, the LES principle is to resolve the contribution of the large scales to the flow while modeling the effect of the small scales. The underlying concept of LES is therefore the filtering of the NS equations: any quantity ϕ is decomposed as a filtered quantity $\widehat{\phi}$ (resolved in the numerical simulation) and the SGS part ϕ'' due to the unresolved flow motion: $\phi = \widehat{\phi} + \phi''$. For a variable density ρ, a mass-weighted Favre filtering is introduced such as:

$$\breve{\phi} = \frac{\widehat{\rho\phi}}{\widehat{\rho}}. \tag{A.10}$$

Length-scale separation on any variable ϕ is achieved with the spatial Favre filtering operation:

$$\widetilde{\phi(\vec{x},t)} = \frac{1}{\widehat{\rho(\vec{x},t)}} \int_{-\infty}^{+\infty} \rho(\vec{x'},t)\phi(\vec{x'},t)G(\vec{x'}-\vec{x})d\vec{x'}, \tag{A.11}$$

where G is the filter function which determines the structure and size of the small scales based on the filter width and shape (tophat, Gaussian etc.). In most cases,

the filter width $\triangle$ is equal to the cubic root of the local cell volume. The balance equations for LES are obtained by filtering the NS equations (A.1), (A.2) and (A.3) yielding:

$$\frac{\partial \widehat{\rho}}{\partial t} + \frac{\partial}{\partial x_j}(\widehat{\rho}\,\breve{u_j}) = 0 \quad \text{(A.12)}$$

$$\frac{\partial}{\partial t}(\widehat{\rho}\,\breve{u_i}) + \frac{\partial}{\partial x_j}(\widehat{\rho}\,\breve{u_j}\,\breve{u_i} + \widehat{P}\delta_{ij} - \widehat{\tau_{ij}} - \widehat{\tau_{ij}}^{sgs}) = 0 \quad \text{(A.13)}$$

$$\frac{\partial}{\partial t}(\widehat{\rho}\,\breve{E}) + \frac{\partial}{\partial x_j}(\widehat{\rho}\,\breve{u_j}\,\breve{E} + \widehat{P}\,\breve{u_i}\,\delta_{ij} + \widehat{q_j} + \widehat{q_j}^{sgs} - \breve{u_i}(\widehat{\tau_{ij}} + \widehat{\tau_{ij}}^{sgs}) = 0 \quad \text{(A.14)}$$

The laminar filtered stress tensor and the filtered heat flux are respectively approximated by:

$$\widehat{\tau_{ij}} = 2\mu\left(\widehat{s_{ij} - \frac{1}{3}\delta_{ij}s_{kk}}\right) \simeq 2\widehat{\mu}\left(\breve{s_{ij}} - \frac{1}{3}\delta_{ij}\,\breve{s_{kk}}\right) \quad \text{(A.15)}$$

$$\widehat{q_i} = -\lambda\widehat{\frac{\partial T}{\partial x_i}} \simeq -\widehat{\lambda}\frac{\partial \breve{T}}{\partial x_i} \quad \text{(A.16)}$$

Due to non-linearity of the NS equations, Favre averaging introduces two new terms in these equations $(-\widehat{\tau_{ij}}^{sgs}, \widehat{q_j}^{sgs})$ which require to supply specific closures, i.e. ad-hoc modeling. The first term, also called Reynolds tensor is defined as:

$$\widehat{\tau_{ij}}^{sgs} = -\widehat{\rho}(\widetilde{u_i u_j} - \breve{u_i}\,\breve{u_j}). \quad \text{(A.17)}$$

Various methods of different complexity exist to model $\widehat{\tau_{ij}}^{sgs}$ One focuses here only on the so-called functional approach which supposes that the effect of the small scales on the larger ones is purely dissipative and models this influence by introducing a turbulent (SGS) viscosity ν_{sgs} in the LES equations. These models are able to represent the global dissipative effects of the small scales but they cannot reproduce the local details of the energy exchange, nor the backscatter process (energy transfer from small to large scales). Because of its reduced cost, effectiveness and robustness, this is the most common practice. The turbulent viscosity is thus expressed based on the Boussinesq eddy viscosity:

$$\widehat{\tau_{ij}}^{sgs} = 2\widehat{\rho}\nu_t\left(\breve{s_{ij}} - \frac{1}{3}\delta_{ij}\,\breve{s_{kk}}\right). \quad \text{(A.18)}$$

To close the turbulent viscosity term ν_t, the WALE model proposed by (Nicoud and Ducros, 1999) was adopted for all computations performed in this thesis. The second unclosed term is the SGS heat flux vector defined by:

$$\widehat{q_i}^{sgs} = \widehat{\rho}\left(\widetilde{u_i E} - \breve{u_i}\,\breve{E}\right), \quad \text{(A.19)}$$

and is modeled by introducing a SGS heat flux:

$$\widehat{q_i}^{sgs} = -\lambda_{sgs}\frac{\partial \breve{T}}{\partial x_i}, \quad \text{(A.20)}$$

which is driven by the SGS thermal conductivity λ_{sgs}:

$$\lambda_{sgs} = \frac{\nu_{sgs}\rho\widehat{C_p}}{Pr_{sgs}}. \tag{A.21}$$

where the SGS Prandtl number Pr_{sgs} is usually set to a constant value (about 0.6). When doing do, the SGS thermal conductivity shares the same properties as the turbulent viscosity in all the regions.

A.3 AVBP solver

The LES code used in this manuscript to is the AVBP code[1], today property of CERFACS and Institut Francais du Petrole Energies Nouvelles (IFPen). It was designed from the very beginning to be used for massively parallel computations on dedicated architectures, addressing all the issues associated with the High Performance Computing (HPC). The code solves the full compressible, multi-species, reactive NS equations, presented previously in the simplified mono-species and non-reactive form suitable for our study. The solver relies on the cell-vertex approach (data stored at mesh nodes) and finite volume method on unstructured or hybrid meshes which gives among other advantages a good robustness against mesh distortion. Temporal integration is performed by an explicit formulation which globally controls the time-step to respect the Courant Friedrichs Lewy condition (CFL). In AVBP, various numerical schemes are available from low to very high orders were used in this work:

TTGC is a version of the two-step Taylor-Galerkin schemes providing a third order discretization both in space and time (Colin and Rudgyard, 2000). It is known to be a good candidate for LES thanks to its good dissipation and dispersion properties (Lamarque, 2007). This numerical scheme was adopted for the flow prediction of the academic configurations T120 and T120D performed in Chapters 3 & Chapter 4.

TTG4A is a fourth order in time, third order is space scheme (Donea and Huerta, 2003) having better dispersion properties than TTGC but a worse dissipation behaviour (Lamarque, 2007). This numerical scheme is better use for complex geometry and was adopted for the flow prediction of the FACTOR configuration performed in Chapters 5 & 6.

In AVBP, the use of centered schemes with low dissipation requires the addition of artificial diffusion operator. Indeed, transport of high gradient may lead to the apparition of non physical oscillations. To help the diffusion operator in this task, artificial viscosity can be added locally in the field to remove numerical oscillations. A sensor specifically dedicated to unsteady turbulent flow can automatically detect numerical anomalies and increase local viscosity in the limitation of an user defined threshold.

[1] www.cerfacs.fr/~avbp

Appendix B

Effect of the formalism used for γ on the computation of the stagnation variables

Definition of P_t and T_t for γ variable

The stagnation state is a fictive state defined for each stations of the system. The stagnation or total state corresponds to the value of the temperature and pressure if the flow is stopped isentropically and is represented on the enthalpy - entropy diagram (Fig. B.1). The definition of the total temperature T_t is derived from the definition of the total enthalpy h_t. Assuming that the fluid is thermally perfect,

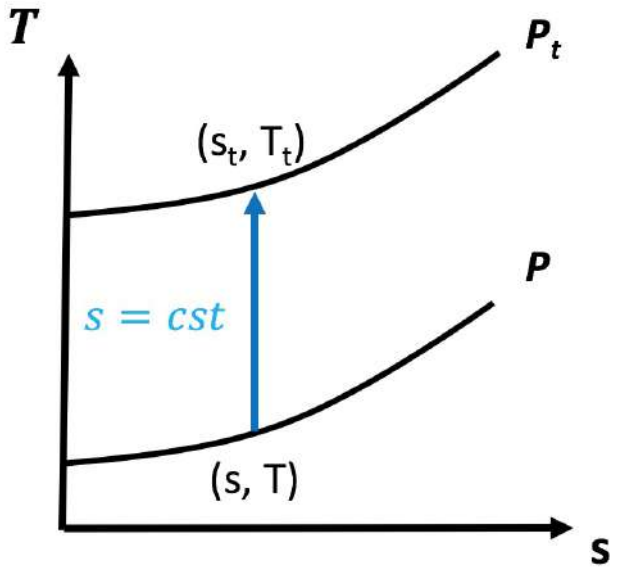

Figure B.1 – Relation static and total variables in the T - s diagram.

the enthalpy depends only on the temperature, i.e,

$$h(T) = h_0 + \int_{T_0}^{T} C_p dT, \tag{B.1}$$

where h_0 is the reference enthalpy taken at the reference temperature T_0. The specific heat capacity at constant pressure is C_p and in general depends on the temperature. In this study, the reference temperature and enthalpy taken for $T_0 = 0K$ and the C_p is tabulated every 100 K deduced from the JANAF tables. By inversing Eq. (B.1), the total temperature T_t in the most general case is given,

$$T_t = h^{-1}(h_t) = \int_0^{h^t} \frac{dh}{C_p} \tag{B.2}$$

where h^{-1} is the reciprocal function of the enthalpy.

The total pressure P_t is derived from the Gibbs equation, fundamental relation of thermodynamic so that,

$$ds = \frac{dh}{T} - r\frac{dP}{P}, \tag{B.3}$$

where r is the perfect gas constant. To do so, the Gibbs equation (Eq. (B.3)) is integrated between the static and stagnation variables giving,

$$\int_s^{s_t} ds = \int_T^{T_t} C_p \frac{dT}{T} - \int_P^{P_t} r\frac{dP}{P}. \tag{B.4}$$

Since the transformation between the static and stagnation variables is isentropic, i.e, $\int_s^{s_t} ds = 0$. The two terms on the RHS are then equal resulting in an expression for P_t that is,

$$P_t = Pe^{\phi_T}, \tag{B.5}$$

where $\phi_T = \int_T^{T_t} \frac{C_p}{r}\frac{1}{T}dT$.

Equations (B.2) and (B.5) gives the expressions of the isentropic relations if C_p depends on the temperature. Computing P_t and T_t therefore implies to know the evolution of C_p against the temperature and the reciprocal function h^{-1} or the integral ϕ_T are mandatory.

If the fluid is callorifically perfect, i.e, $C_p = cst$, the expressions are clearly simplified and the well known isentropic relations depending on the Mach number M are recovered,

$$T_t = T\left(1 + \frac{\gamma - 1}{2}M^2\right), \tag{B.6}$$

$$P_t = P\left(1 + \frac{\gamma - 1}{2}M^2\right)^{\frac{\gamma}{\gamma-1}}. \tag{B.7}$$

In the literature, the isentropic relations assuming $\gamma = cst$ is generally used. But the validity of this hypothesis depends on the evolution of the temperature within the flow. Figure B.2 shows the evolution of the specific heat ratio γ for air against

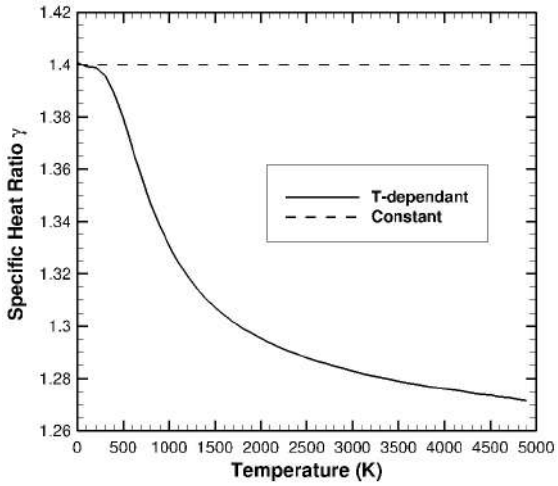

Figure B.2 – Evolution of the specific heat ratio for air against the temperature between 100 and 5000 K. Solid lines − represents the model where γ is tabulated every 100 K. Dashed lines −− represents the model where $\gamma = 1.4$.

the static temperature T assuming that γ is tabulated every 100 K deduced from the JANAF tables between 100 K and 5000 K. If the temperature is lower than 500 K, γ is almost constant and can be approximate at 1.4. However, for large values of temperature, γ evolves between 1.28 and 1.4. Since the computation of the stagnation variables involves γ in Eqs. (B.2) and (B.5), differences are expected on the computation of T_t and P_t. The effect of the formalism used to compute γ has been evaluated by (Zebbiche and Youbi, 2007) and is presented in the next section.

Impact of the formalism used for γ on the computation of stagnation variables

The computation of stagnation quantities T_t and P_t will depend on the formalism adopted for C_p. The objective here is to illustrate such effect for 2 operating points representative of 2 cases of application of the aeronautic flow context. The first operating point represents the external flow around a plane defined as : $T = 220K$ and $P = 25000Pa$ taken during cruise flight. The second operating point corresponds to the flow inside an engine, downstream the combustion chamber defined as : $T = 2000K$ and $P = 1.10^6 Pa$. The relative differences issued from a constant C_p formalism or variable while estimating T_t and P_t is plotted against the Mach Number on Fig. B.3 for both operating points. Results show that if the temperature remains low, i.e, near the ambient conditions, the error between both formalism is negligible and independent with respect to the Mach number. Otherwise, the effect of the variation of γ becomes significant if the temperature is higher than 2000 K and the Mach number approaches one. This leads to an error superior to 5% for the stagnation temperature and superior to 2.5% for the

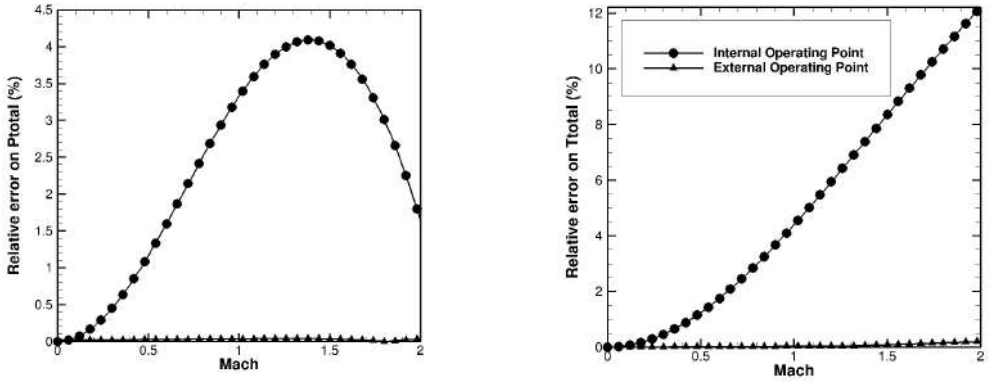

(a) (b)

Figure B.3 – Relative differences on the computation of P_t (a) and T_t (b) obtained for $\gamma = 1.4$ (▲) and the case where γ is temperature dependent (●).

stagnation pressure. This is not negligible compared to the accuracy searched in the industry. In this work, the investigated academic blades operate near ambient temperature. The effect of the variable C_p will be neglected on these specific cases. The isentropic relations using variable C_p have nevertheless been implemented in the AVBP code to evaluate the stagnation variables for industrial blades operating at real conditions.

Appendix C

Averaging operator to compute the balance of an extensive variable

Different averages are usually defined. The most common encountered in CFD is the time averaged that can be defined over a period T as follows,

$$\overline{\bullet} = \frac{\int_T \bullet dt}{\int_T dt}, \tag{C.1}$$

where $\bullet$ stands for any variable of interest. Time averaged is generally used to have access to the mean field yield by a turbulent flow. In this specific case, the mass flow time averaged can also be introduced and reads,

$$\widetilde{\bullet} = \frac{\int_T \rho U_i n_i \bullet dt}{\int_T \rho U_i n_i dt} = \frac{\overline{\rho U_i \bullet} n_i}{\overline{\rho U_i n_i}}, \tag{C.2}$$

where n_i stands for the normal of a section S, ρ the density and U_i the velocity component. To compare the fields from 3D simulation tools to 1D analytical model, a natural operator is the spatial averaging operator over the surface S as,

$$< \bullet >_S = \frac{\iint_S \bullet dS}{\iint_S dS}. \tag{C.3}$$

Taking into account the mass flow distribution over the section S, the spatial mass flow averaged naturally falls and writes,

$$< \bullet >_{\rho U_i S} = \frac{\iint_S \rho U_i n_i \bullet dS}{\iint_S \rho U_i n_i dS}. \tag{C.4}$$

The averaging operators defined previously are applied in the context of the transport equations. In our specific case, the objective is to preserve fundamental conservation properties while reducing 3D fields in 1D evolution.
Assuming that the variable ϕ is transported in a compressible turbulent flow, the transport equation follows,

$$\frac{\partial(\rho\phi)}{\partial t} + \frac{\partial(\rho U_i \phi)}{\partial x_i} = \dot{S}, \tag{C.5}$$

where $\dot{S}$ is the local source term. The time averaged operator $\overline{\bullet}$ applied on the Eq. (C.5) gives access to the transport equation of the mean flow. If this flow is statistically stationary and assuming the commutation between the averaging operator and the spatial derivative leads to,

$$\frac{\partial(\overline{\rho U_i \phi})}{\partial x_i} = \overline{\dot{S}}. \tag{C.6}$$

Integrating Eq. (C.6) over a control volume V yields,

$$\iiint_V \frac{\partial(\overline{\rho U_i \phi})}{\partial x_i} dV = \iiint_V \overline{\dot{S}} dV \tag{C.7}$$

In this specific case, the volume V is assumed to be bounded by an inlet S_1, an outlet S_2 and watertight surfaces S_w representing a wall or a streamsurface. Applying the theorem of Green-Ostrogradski reduces the divergence term into flux terms overs the bounded surface S_1 and S_2,

$$\iint_{S_1} (\overline{\rho U_i \phi}) n_i dS + \iint_{S_2} (\overline{\rho U_i \phi}) n_i dS = \iiint_V \overline{\dot{S}} dV. \tag{C.8}$$

At this point, the mass flow time averaged operator can be applied to get,

$$\iint_{S_1} \widetilde{\phi} \overline{\rho U_i} n_i dS + \iint_{S_2} \widetilde{\phi} \overline{\rho U_i} n_i dS = \overline{\dot{S}}. \tag{C.9}$$

Introducing the spatial mass flow averaged operator allows to rewrite Eq. (C.9) so that,

$$< \widetilde{\phi} >_{\rho U_i S_1} \iint_{S_1} \overline{\rho U_i} n_i dS + < \widetilde{\phi} >_{\rho U_i S_2} \iint_{S_2} \overline{\rho U_i} n_i dS = \iiint_V \overline{\dot{S}} dV. \tag{C.10}$$

The mass flow rate Q_m is recognised and it is by definition conserved between S_1 and S_2,

$$Q_m = \iint_{S_1} \overline{\rho U_i} n_i dS = - \iint_{S_2} \overline{\rho U_i} n_i dS \tag{C.11}$$

Finally, the balance reduces to,

$$Q_m (< \widetilde{\phi} >_{\rho U_i S_2} - < \widetilde{\phi} >_{\rho U_i S_1}) = \iiint_V \overline{\dot{S}} dV. \tag{C.12}$$

In Eq. (C.12), $< \widetilde{\phi} >_{\rho U_i S}$ represents the 1D value defined on each section by preserving the original conservation properties of Eq. (C.6). The evolution of $< \widetilde{\phi} >_{\rho U_i S}$ depends on the mass flow rate Q_m as well as the integrated source term within the control volume. Equation (C.12) can be generalized to N_{inlet} inlets and N_{outlet} outlets,

$$\sum_{k=1}^{N_{outlet}} Q_{m,k} < \widetilde{\phi} >_{\rho U_i S_k} - \sum_{k=1}^{N_{inlet}} Q_{m,k} < \widetilde{\phi} >_{\rho U_i S_k} = \iiint_V \overline{\dot{S}} dV. \tag{C.13}$$

In this PhD work, the notation of the mass flow averaging is simplified using $\widetilde{\bullet}_S$,

$$\widetilde{\bullet}_S = \frac{\iint_S \overline{\rho U_i} n_i \bullet dS}{Q_m}. \tag{C.14}$$

Finally, it worth noting that for no moving surfaces, the temporal and spatial averaged are commutative and can be applied in both orders.
From the above analysis, the final value of the averaged variable depends on the weighing used in the averaging operator. If the averaging operator is not weighted by the mass flow, the resulting balance introduces an error on the conservation properties whenever transforming the 3D field to the corresponding 1D value. To estimate this error, it is assumed that the variable ϕ can be split into the temporal averaged $\overline{\phi}$ and the temporal deviation ϕ',

$$\phi = \overline{\phi} + \phi'. \tag{C.15}$$

This splitting can then be introduced in the definition of the mass flow averaged operator to yield,

$$\widetilde{\phi} = \frac{\overline{\rho U_i \phi}}{\overline{\rho U_i}}, \tag{C.16}$$

$$\Rightarrow \widetilde{\phi} = \frac{\overline{\rho U_i}\ \overline{\phi}}{\overline{\rho U_i}} + \frac{\overline{(\rho U_i)'\phi'}}{\overline{\rho U_i}}, \tag{C.17}$$

$$\Rightarrow \widetilde{\phi} = \overline{\phi} + \frac{\overline{(\rho U_i)'\phi'}}{\overline{\rho U_i}}. \tag{C.18}$$

Equation (C.18) shows that the difference between averaging operators depends on the correlation between ϕ' and $(\rho U_i)'$. If the correlation $(\rho U_i)'\phi'$ is null, i.e, the temporal variation of the deviation ϕ' is independent of the variation of $(\rho U_i)'$, there is no difference between both averaging operators. From this analysis, an estimation of the correlation is given by the following expression,

$$\epsilon = \frac{\overline{(\rho U_i)^2}}{\overline{(\rho U_i)}^2}. \tag{C.19}$$

This demonstration can be also applied for spatial averaging. As a result, the weight used in the averaging operator will not impact the averaged value if the flow is uniform or stationary.

Appendix D

Sentivity of Large Eddy Simulations to the operating point of the T120 blade.

This appendix is extracted from the publication of (Harnieh and Duchaine, 2017).

Proceedings of ASME Turbo Expo 2017: Turbine Technical Conference and Exposition
GT2017
June 26-30, 2017, Charlotte, NC, USA

GT2017-64686

SENSITIVITY OF LARGE EDDY SIMULATIONS TO INFLOW CONDITION AND MODELING IF APPLIED TO A TRANSONIC HIGH-PRESSURE CASCADE VANE

Mael Harnieh *
CFD Team CERFACS
Toulouse, France
Email: harnieh@cerfacs.fr

Laurent Gicquel
Florent Duchaine
CFD team CERFACS
Toulouse, France

ABSTRACT

Large Eddy Simulation (LES) prediction of the flow around transonic high-pressure turbine cascade vanes is an active subject of research. For such problems, the flow topology is dictated by the geometry, inflow conditions and irreversibilities. When studied experimentally, input specifications necessarily suffer from uncertainties inherent to experimental measurement facilities. Such limits are also present in numerical applications. The following paper proposes to evaluate the relative importance of uncertainty sources in determining the adequate LES flow behaviour for the T120 transonic blade experimentally tested at UniBw (Munich) during the European project AITEB II. To do so, the nominal operating point is targeted and different simulations are obtained by changing inflow specifications with and without turbulence injection. As expected, changes in the static pressure ratio between the inlet and the outlet by more or less 4%, alter significantly the flow topology and the aerodynamic losses. Impact of turbulence injection at inlet is also addressed. Investigation of dissipation fields, including the laminar and sub-grid model contributions, allows the identification of the underlying mechanisms. Although irreversibilities have a smaller impact on the flow prediction relative to the static pressure ratio (and associated uncertainties), its relevance on the flow prediction and topology is found to be of primary importance.

NOMENCLATURE

Acronyms

$AITEB$	Aerothermal Investigation on Turbine Endwalls and Blades
CFD	Computational Fluid Dynamics
DNS	Direct Numerical Simulation
LES	Large Eddy Simulation
$RANS$	Reynolds Average Navier-Stokes
$TTGC$	Two-Step Taylor Galerkin C
$URANS$	Unsteady Reynolds Average Navier-Stokes
$WALE$	Wall Adaptative Local Eddy-viscosity

Greek letters

β_1	Inlet angle	$[-]$
β_S	Sutherland law constant	$[-]$
ϕ	Dissipation rate of the resolved kinetic energy	$[W.m^{-3}]$
ρ	Density	$[kg.m^{-3}]$
γ	Specific heat ratio	$[-]$
μ	Laminar viscosity	$[kg.m^{-1}.s^{-1}]$
μ_t	Turbulent viscosity	$[kg.m^{-1}.s^{-1}]$
τ_{ij}	Total viscous stress tensor	$[Pa]$
τ^l_{ij}	Laminar viscous stress tensor	$[Pa]$
τ^t_{ij}	Turbulent stress tensor	$[Pa]$
τ_w	Wall shear stress	$[Pa]$
ξ	Primary loss coefficient	$[-]$
ξ_{ke}	Kinetic loss energy coefficient	$[-]$

*Address all correspondence to this author.

Copyright © 2017 by ASME

Symbols

C_f	Skin friction coefficient	$[-]$
E_c	Resolved kinetic energy	$[kg.m^{-1}.s^{-2}]$
k	Subgrid-scale turbulent kinetic energy	$[m^2.s^{-2}]$
L	Integrated dissipation rate on volume	$[W]$
Ma	Mach number	$[-]$
Ma_{is}	Isentropic Mach number	$[-]$
Ma_2	Exit Isentropic Mach number	$[-]$
P	Local static pressure	$[Pa]$
P_s	Static pressure at the outlet	$[Pa]$
P_{t1}	Total pressure at the inlet	$[Pa]$
P_{t2}	Total pressure at the outlet	$[Pa]$
$P_{t_{LE}}$	Total pressure at the leading edge	$[Pa]$
q_2	Dynamic pressure at the outlet	$[Pa]$
Q_m	Flowrate	$[kg.s^{-1}]$
Re_2	Exit Reynolds number	$[-]$
S	Sutherland law constant	$[-]$
$\widetilde{s}$	Filtered entropy per unit mass	$[m^{-1}.s^{-2}.K^{-1}]$
S_{ij}	Symmetric part of the strain-rate tensor	$[s^{-1}]$
T_{t1}	Total temperature at inlet	$[K]$
$\widetilde{T}$	Filtered static temperature	$[K]$
$\widetilde{u_i}$	Resolved velocity	$[m.s^{-1}]$
U_1	Time averaged velocity at inlet	$[m.s^{-1}]$
U_2	Time averaged velocity at outlet	$[m.s^{-1}]$
V_{global}	Global volume	$[m^3]$
V	Specific volume	$[m^3]$
Y^+_{wall}	Dimensionless wall coordinate	$[-]$

INTRODUCTION

Understanding the behavior of flow around transonic high pressure vanes has been a key issue for researchers and engineers. Due to the geometry, high Reynolds number and compressible flow at the exit of the combustor, this flow topology is very complex and often unsteady. Experimental and numerical investigations are required to predict lift and drag coefficients as well as heat loads. Due to the increase in computational power, numerical approaches are increasingly used in turbomachinery design. The Reynolds Average Navier-Stokes (RANS) method is the most common method used for turbomachinery flows and blade load is usually well captured with an acceptable computation cost [1,2]. As RANS is a purely steady approach, limitations have been identified and it is known that all complex effects cannot be captured unless specific tuning or developments are applied [3]. To alleviate these limits, Direct Numerical Simulation (DNS) is possible but remains a costly method. Despite its computation cost, some academic test cases have been simulated in recent studies [4] . Large Eddy Simulation (LES) is another alternative to predict flow in turbomachinery. Resolving the most energetic scales while modeling the small ones allows the study of complex and unsteady effects [5–7]. Despite the high computation cost required compared to RANS and URANS approaches, this method has demonstrated capabilities to predict flows even in complex geometries [8–10].

Flow topology predictions in LES comes from complex interactions between boundary condition specifications, turbulent modeling and numerical handling. However, numerical inlet specification is generally given by experimental measurement which contains sources of uncertainties. The key issue addressed in this study concerns the effect of boundary condition uncertainties on flow predicted by LES. The aim is to demonstrate that uncertainties on inflow specifications can lead to strong variations of LES aerodynamic fields and whose origins are often ignored by experiments. To do so, LES is carried out on the T120 blade, tested experimentally at UniBw (Munich) during the European project AITEB II without film cooling. The nominal point is targeted to get a reference case. To evaluate the effect of uncertainties on boundary conditions, different simulations are tested by changing the static pressure ratio by more or less 4%. Injecting turbulence at the inlet is also tested.

The document is organized as follows. The experimental set up is presented in Section 2. Computational domain and numerical set up are described in Section 3. Then, numerical results are described and discussed in Section 4. The flow topology of the nominal point is presented in Section 4.1. The definition of the losses is introduced and applied for the nominal case in Section 4.2. Afterwards, the sensitivity to the inlet total pressure is discussed in Section 4.3. At last, the impact of turbulence injection on the irreversibilities is studied in Section 4.4.

EXPERIMENTAL SET UP

The experiments were conducted in the High-speed Cascade Wind Tunnel of the Institute of Jet Propulsion for AITEB II project [11, 12]. A wind tunnel operates continuously and is enclosed inside a tank. The pressure inside the vessel can be varied to obtain different Reynolds and Mach number combinations. The flow passes through a compressor before being accelerated inside a nozzle toward the test section. A turbulence grid with crossed rectangular plates is located at the entrance of a nozzle to increase the turbulence level of the freestream flow. Table 1 sums up the geometric features of the T120 blade.

Experimentally, the operating point is monitored by the static pressure P_s in the pressure tank and the dynamic pressure q_2 as well as total temperature T_{t1} measured at the inlet as represented on Fig. 1. Note that information on the turbulent field is experimentally characterized at a specific point located upstream the cascade in-between two blades. The total pressure downstream the cascade P_{t2} is monitored with a probe to estimate the total pressure loss between the inlet and the outlet. Due to uncertainty measurements, the inlet total pressure has an accuracy of +/- 1500 Pa. Dynamic pressure is computed using the inlet total

Copyright © 2017 by ASME

Feature	Symbols	Value
Chord length	l	120 mm
Axial chord length	l_{ax}	76 mm
Blade height	h	300 mm
Pitch to chord ratio	t/l	1.007
Stagger angle	β_{stag}	46.25 °

TABLE 1: Geometric features of the T120 blade.

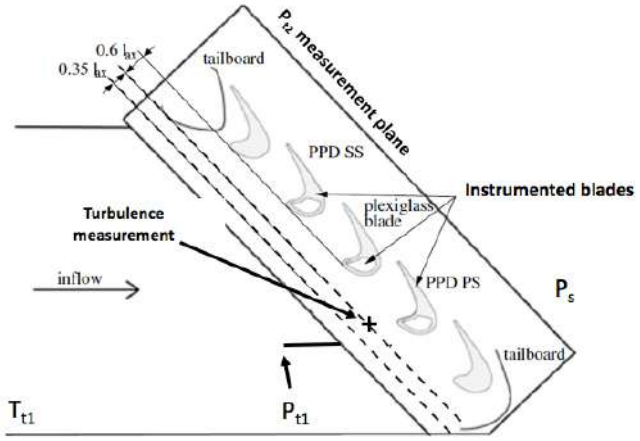

FIGURE 1: Scheme of the experimental set up extracted and adapted from [13] (Not to scale). Profile pressure distribution (PPD) measurements are carried out on the pressure side (PS) and the suction side (SS).

pressure P_{t1}, i.e:

$$q_2 = P_{t1} - P_s. \tag{1}$$

Operating point is then defined by the exit Mach number Ma_2 following:

$$Ma_2 = \sqrt{\frac{2}{\gamma - 1}\left[\left(1+\frac{q_2}{P_s}\right)^{\frac{\gamma-1}{\gamma}} - 1\right]}, \tag{2}$$

where γ is the heat specific ratio fixed at 1.4 for air. The exit Reynolds number Re_2 is defined as follows with Sutherland law for the temperature dependent viscosity,

$$Re_2 = \sqrt{\frac{\gamma}{R}}\frac{l}{\beta_S}\frac{Ma_2.P_s\left[T_t.\frac{1}{1+\left(\frac{\gamma-1}{2}\right)Ma_2^2}+S\right]}{\left[T_t.\frac{1}{1+\left(\frac{\gamma-1}{2}\right)Ma_2^2}\right]}, \tag{3}$$

where S and β_S are constants relative to Sutherland law: $S = 110.4$; $\beta_S = 1.458.10^{-6}$ for air. R is the gas constant of perfect gas.

NUMERICAL SET UP

Computational domain and mesh

The computational domain used for this work is displayed in Fig. 2. Only span-wise length of 8 *mm* (3% of total blade span) is represented in this domain. To avoid interaction between the inlet computational boundary condition and potential effect due to the blade, one chord length is taken between the inlet and leading edge. 3 chord lengths between the trailing edge and the outlet have been chosen to avoid strong wake effects on the outlet boundary condition. Wall resolved approach is used in the computation ($Y^+_{wall} \approx 1-2$).
A hybrid mesh composed of 24 millions tetrahedrons and 10 millions prisms is used (Fig. 3). The number of vertices is about 9.3 millions. Refinement of the grid is enforced near the blade pressure side wall to capture near wall flow physics and potential recirculation zones. Likewise, a fine mesh is used on the suction side to capture shock waves and vortex shedding. 10 layers of prism are chosen next to wall to reduce computational cost compared to a fully tetrahedral mesh (Fig. 4). Special care is taken to avoid big volume jump at the interface between prisms and tetrahedrons and to ensure proper numerics in these regions (average volume jump is about 0.8 - 0.9) .

Boundary conditions

To evaluate sensitivity of flow topology to inflow specification and associated uncertainties, different simulations are carried out around a nominal test case targeting the experimental nominal operating point: i.e. $Ma_2 = 0.87$ and $Re_2 = 390,000$. Table 2 describes the boundary conditions imposed in the simulation for the nominal case and enforced numerically through the mean local values by use of the NSCBC method [14]. Since the flow is compressible, special treatment is used to avoid acoustic reflection at inlet and outlet. It consists in relaxing the value of boundary conditions to the target values with a relaxation coefficient.
Table 3 shows the set of LES produced and considered to be representative of the experimental nominal case. Case 1 corresponds

Copyright © 2017 by ASME

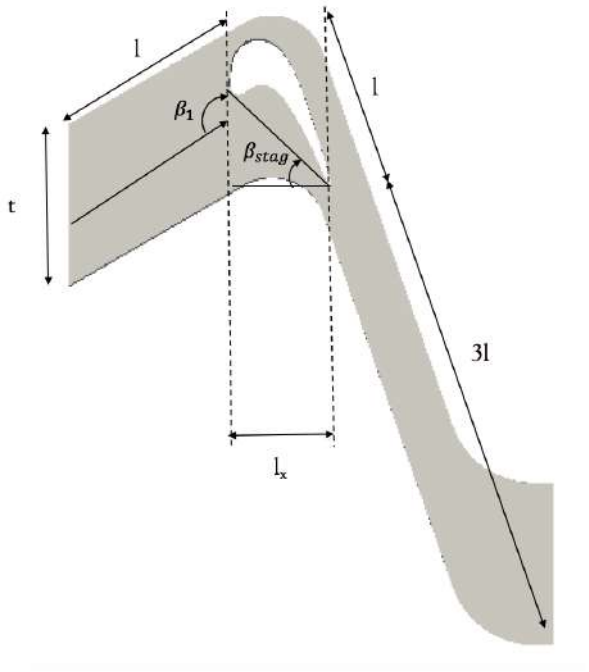

FIGURE 2: Computational domain with geometric features of the T120 blade. Span-wise length of 8 *mm* (3% of total span).

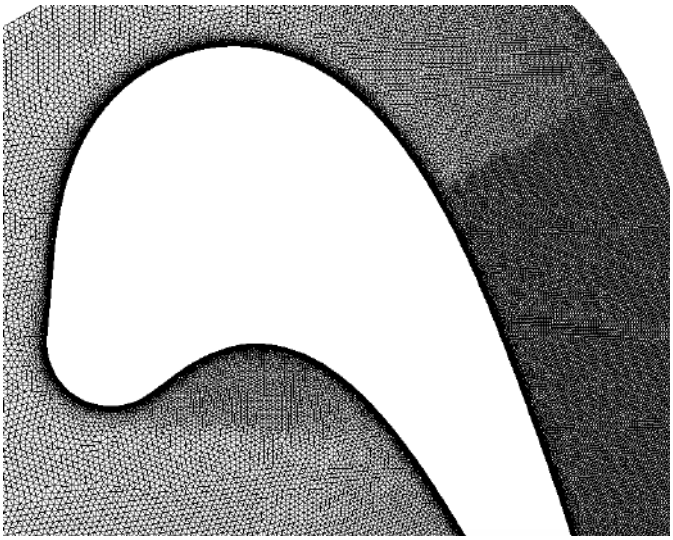

FIGURE 3: Global view of the mesh next to the leading edge.

to the nominal operating point. Case 2 and 3 are obtained by changing the inlet total pressure by 4% (which corresponds to change the pressure ratio P_s/P_{t1} between the inlet and the outlet by 3.6%) thereby coinciding with the known uncertainty on this

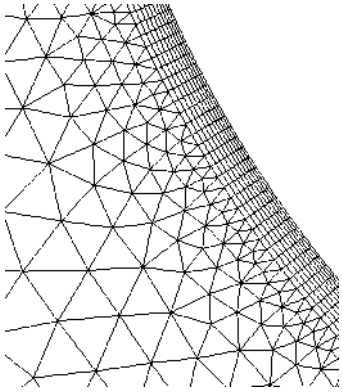

FIGURE 4: Wall view of the prism layers.

Patch	Variable	Value
Inlet	P_{t1}	26720 Pa
	T_{t1}	333 K
	β_1	138.6 °
	Turbulence injection	No
Outlet	P_s	16307 Pa
Wall		No slip adiabatic
Span		Periodicity

TABLE 2: Boundary conditions used in the computation for nominal operating point.

potential inflow specification. Case 4 considers the injection of turbulence on the top of case 1 reference conditions. Turbulence injection is done by imposing a turbulent fluctuation on velocity fields at the inlet [15].

Case name	P_{t1}	P_s/P_{t1}	Turbulence injection
Case 1	26720 Pa	0.61	No
Case 2	27720 Pa	0.59	No
Case 3	25720 Pa	0.63	No
Case 4	26720 Pa	0.61	Yes

TABLE 3: Set of LES produced.

Copyright © 2017 by ASME

Numerical scheme

All simulations are produced using TTGC finite element scheme [16] that is known for its good spectral properties. The WALE model [17] is used as sub-grid model to comply with a wall resolved approach which requires proper damping of the turbulent viscosity near wall. Finally, each simulation lasted long enough for the flow to pass through the solution domain 5 times. The time averaged flow fields were extracted and are discussed in the following section.

NUMERICAL RESULTS

Flow topology of the nominal case

The time averaged Mach number field is displayed in Fig. 5 for nominal case, i.e case 1. A recirculation zone is indicated

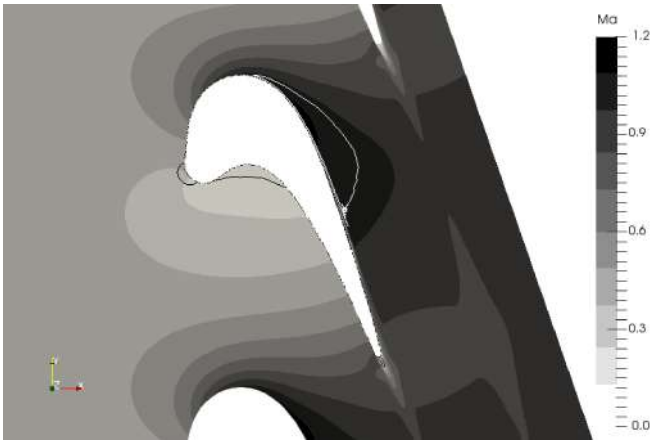

FIGURE 5: Time averaged of Mach number field at mid-span. Isocontour of $Ma = 1$ is plotted in white. Isocontour of null axial velocity is plotted in black.

on the pressure side by the black isocontour of zero axial velocity. This is created by the detachment of the boundary layer on the pressure side where the geometry presents a strong curvature and by the reattachment of the boundary layer downstream. On the suction side, a small supersonic zone is evidenced confirming that the flow is transonic. Thus, lot of activity of waves and shocks are expected. As exhibited on Fig. 6, acoustic waves are generated at the trailing edge due to temporal fluctuation of vortex shedding and are reflected on the suction side of the blade located below [18]. On the suction side, acoustic waves are observed to propagate upstream and merge generating weak shocks or shocklets. This behaviour has been already observed in a diffuser [19]. Note that no strong and stabilized shock arises: i.e, shocklets realign as they reach the sonic line (chocked region) where they disappear. This behavior is in agreement with weakly

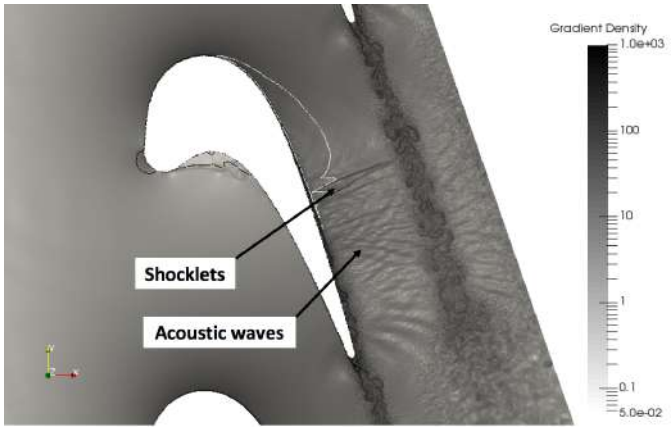

FIGURE 6: Instantaneous field of ρ gradient density at mid-span. Isocontour of $Ma = 1$ is plotted in white. Isocontour of null axial velocity is plotted in black.

transonic flows [20], i.e, $1.0 < Ma < 1.1$ at the throat.
A turbulent transition of the boundary layer is observed downstream the sonic line. This transition location can be evidenced by monitoring the skin friction coefficient $C_f = \frac{\tau_w}{\frac{1}{2}<\rho_1 U_1^2>}$ along the suction side wall for which ρ_1, U_1 are taken at the inlet and spatially averaged ($<>$) and τ_w stands for the local wall shear stress along the blade (Fig. 7). From this curve, the beginning of the transition is evidenced by an increase of C_f once a local minimum is reached. Naturally such a local change in flow topology is expected to impact the losses.

To validate the flow prediction, the isentropic Mach number is computed to compare with the experiment as follows,

$$Ma_{is} = \overline{\sqrt{\frac{2}{\gamma-1}\left[\left(1+\frac{P_{t1}}{P}\right)^{\frac{\gamma-1}{\gamma}}-1\right]}}, \qquad (4)$$

where P is the local static pressure and $\overline{\bullet}$ is the temporal average operator. Additional spanwise average is performed. Fig. 8 indicates that the overall result matches well the experiment. Slight differences can be noticed in the circulation zone on the pressure side, where the local time averaged static pressure is underestimated. The shock located on the suction side is not also correctly positioned. These differences have also been reported in some studies with LES [10, 21]. These two specific zones will be therefore of primary interest for the following discussion to assess the uncertainty effect on these two specific flow features and the capacity of LES to properly reproduce them. To detail the sensitivity of the flow, a loss indicator is constructed to evidence the most vulnerable zones of the computation.

Copyright © 2017 by ASME

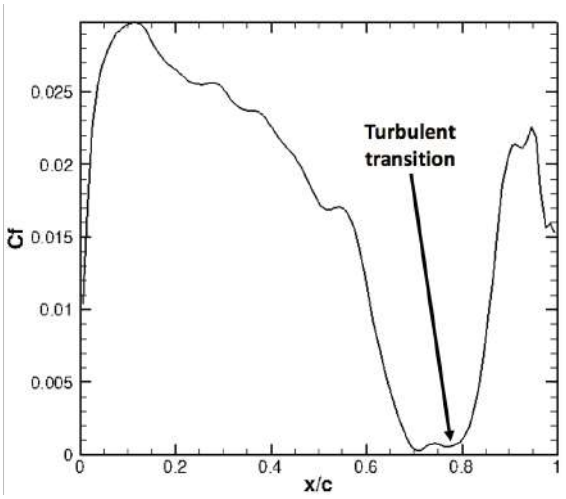

FIGURE 7: Time averaged of the skin friction coefficient C_f along the suction side. The turbulent transition of the boundary layer is evidenced by the sudden increase of the C_f profile once the local minimum has been reached.

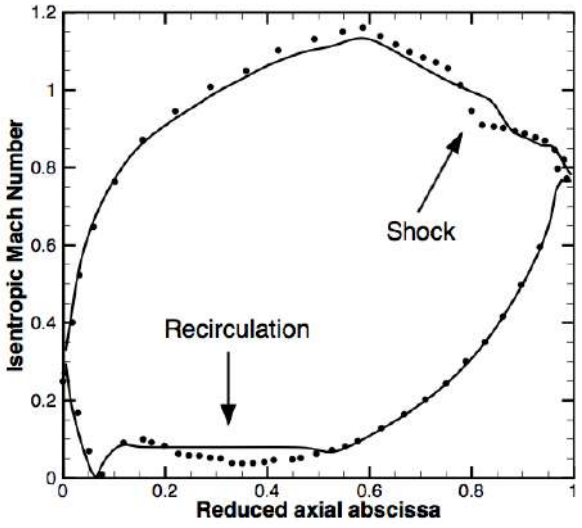

FIGURE 8: Isentropic Mach number along the blade: •, experiment; - LES nominal case.

Definition of the losses in the computation

To evaluate the losses within the flow, the local kinetic energy equation is written in the general context of LES compressible flow with no volume forces ([22]), i.e,

$$\frac{\partial E_c}{\partial t}+\frac{\partial E_c\widetilde{u_i}}{\partial x_i}=-\frac{\partial P\widetilde{u_i}}{\partial x_i}+\frac{\partial \tau_{ij}\widetilde{u_i}}{\partial x_j}+P\frac{\partial \widetilde{u_i}}{\partial x_i}-\tau_{ij}\frac{\partial \widetilde{u_i}}{\partial x_j} \quad (5)$$

where $E_c=\frac{1}{2}\overline{\rho}\widetilde{u_i}\widetilde{u_i}$ is the kinetic energy, $\overline{\rho}$ is the time averaged density and $\widetilde{u_i}$ is the resolved velocity. The total stress tensor τ_{ij} is divided into a laminar part τ^l_{ij} and a turbulent part τ^t_{ij}. Assuming that the fluid is Newtonian, the laminar part of the stress tensor is expressed as:

$$\tau^l_{ij}=2\mu\left(S_{ij}-\frac{1}{3}S_{ll}\delta_{ij}\right) \quad (6)$$

where $S_{ij}=\frac{1}{2}\left(\frac{\partial\widetilde{u_i}}{\partial x_j}+\frac{\partial\widetilde{u_j}}{\partial x_i}\right)$ is the symmetric part of the resolved strain-rate tensor and δ_{ij} the Kronecker symbol. The turbulent part τ^t_{ij} is modeled by a turbulent viscosity μ_t according to the Boussinesq assumption and a turbulent SGS kinetic energy k:

$$\tau^t_{ij}=2\mu_t\left(S_{ij}-\frac{1}{3}S_{ll}\delta_{ij}\right)-\frac{2}{3}k\delta_{ij} \quad (7)$$

Combining the different models for the total stress tensor τ_{ij}, the Eq. (5) is rewritten as:

$$\frac{\partial E_c}{\partial t}+\frac{\partial E_c\widetilde{u_i}}{\partial x_i}=-\frac{\partial P\widetilde{u_i}}{\partial x_i}+\frac{\partial(\tau^l_{ij}+\tau^t_{ij})\widetilde{u_i}}{\partial x_j}-P\frac{\partial\widetilde{u_i}}{\partial x_i}-\phi \quad (8)$$

where the last term ϕ is:

$$\phi=2(\mu+\mu_t)\left(S_{ij}-\frac{1}{3}S_{ll}\delta_{ij}\right)S_{ij}-\frac{2}{3}kS_{ll} \quad (9)$$

Likewise, the filtered entropy per unit mass $\widetilde{s}$ transport equation is written for adiabatic compressible flow [22]:

$$\frac{\partial\overline{\rho}\widetilde{s}}{\partial t}+\frac{\partial\rho\widetilde{u_i}\widetilde{s}}{\partial x_i}=\frac{1}{\widetilde{T}}\phi \quad (10)$$

The term ϕ appears in the Eq. (10) as a positive source term if the compressible effects are neglected (i.e. $S_{ll}\approx 0$ in Eq. (9)). So, the dissipation rate of the resolved kinetic energy, i.e.,

$$\phi=2(\mu+\mu_t)S_{ij}S_{ij} \quad (11)$$

is the unique irreversible process for adiabatic compressible flow. Since only time averaged fields are discussed in this study, the time averaged dissipation rate of the resolved kinetic energy will follow

$$\overline{\phi}=\overline{2(\mu+\mu_t)S_{ij}S_{ij}}. \quad (12)$$

Copyright © 2017 by ASME

A typical field of $\overline{\phi}$ is displayed in Fig. 9. The majority of losses occurs in the boundary layer, in the wake and the recirculation zone. The boundary layer at the suction side seems to produce more losses than the pressure side.

Contrary to this work, many studies evaluate the losses with a

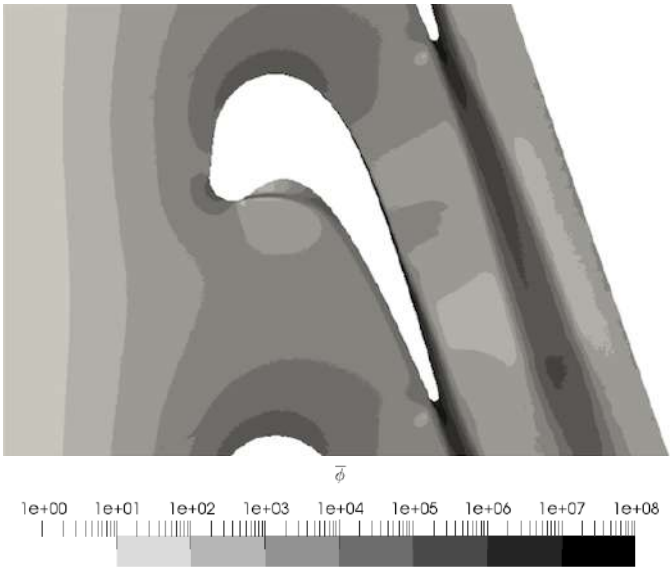

FIGURE 9: Local dissipation rate of the resolved kinetic energy $\overline{\phi}$ at mid-span for the nominal case.

global budget of the total pressure over a global volume [23, 24] by introduction of the primary loss coefficient, i.e.,

$$\xi = \frac{P_{t1} - P_{t2}}{q_2} \tag{13}$$

where the dynamic pressure q_2 is computed as Section 2. Hereafter, the global volume V_{global} is defined by the volume between the inlet of the computation and the plane measurement of P_{t2} used in the experiment to compare both numeric results and experiment data. Note that P_{t2} is extracted at midspan and a circumferential average is applied to both the numerical and experimental results. The primary loss coefficient is computed numerically considering V_{global} and is compared with the experimental value in table 4. Clearly the primary loss coefficient received from the simulation underestimates the experimental finding. To evaluate the origin of such differences, the losses in resolved flow kinetic energy are studied by use of volume partial integrations of $\overline{\phi}$ computed by

$$L = \int_V \overline{\phi} dV, \tag{14}$$

Case	P_s/P_{t1}	Q_m (g/s)	ξ
Numeric	0.61	18.08	2.67 %
Experiment	0.61	-	2.76 %

TABLE 4: Set of results for the nominal case. The primary loss coefficient is computed over V_{global}.

over the specific volumes V displayed in Fig. 10. Box a represents the boundary layer on the pressure side downstream the recirculation bubble. Box b refers to the turbulent boundary layer on suction side. Box c describes the recirculation zone. Box d exhibits the wake created by the blade. At last, box e illustrates the laminar boundary layer on suction side. The integrated dissi-

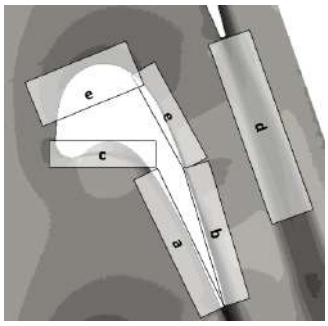

FIGURE 10: Location of partial integration volumes around the blade.

pation rate of the resolved kinetic energy L is normalized by the exit flux of the kinetic energy by the introduction of the kinetic energy loss coefficient ξ_{KE}:

$$\xi_{KE} = \frac{L}{\frac{1}{2} < U_2^2 > Q_m} \tag{15}$$

where $< U_2 >$ is the average magnitude of the time and spatial averaged velocity at the measurement plane P_{t2} used in the experiment. Note that coefficient does not depend on the mass flowrate due to the changes of the inlet specification.

Table 5 presents the results of the partial integrations over the specific volumes described before. The contribution of each specific volume is also presented. The dissipation rate of the resolved kinetic energy between the inlet and the measurement plane for P_{t2} represents 15.1 % of the exit energy flux. The major contributor of losses is the boundary layer at the suction side of the blade which represents almost 70 % of the total losses. The

Copyright © 2017 by ASME

turbulent part of the boundary layer produces more losses than the laminar one. Then, the second contributor is the vortex shedding. The laminar boundary layer at the pressure side has a minor impact on the losses. At last, the contribution of the recirculation zone is insignificant.

Zone	ξ_{KE}	Contribution
Pressure side BL (a)	1.5 %	9.9 %
Suction side turbulent BL (b)	6.1 %	40.4 %
Recirculation (c)	0.2 %	1.3 %
Vortex shedding (d)	3.1 %	20.5 %
Suction side laminar BL (e)	4.2 %	27.9 %
Total	**15.1 %**	

TABLE 5: Kinetic energy loss coefficient for specific volume V and the different contributions. The total dissipation rate of the resolved kinetic energy is computed over V_{global}.

This distribution of losses is similar to the literature [25]. As shown previously, the most critical zones in the domain are the turbulent boundary layer at the suction side and the wake. However if compared to the experiment (detailed in Section 4.1), the suction side pressure distribution and the bubble zone are observed not to be well captured. In the following, the effect of uncertainty of the inlet total pressure, i.e. case 2 and 3, and turbulence injection, i.e. case 4, are assessed on the LES aerodynamic fields and the losses.

Sensitivity of LES to the inlet total pressure

Figure 11 displays the time averaged Mach number field for cases 1, 2 and 3 where the flow exhibits clearly different mean flow topologies. The transonic zone enlarges for case 2. On the contrary, case 3 presents a transonic zone which moves upstream if compared to case 1. Note nonetheless that no change is noticed on the pressure side.

The operating point, flowrate and the losses are summarized in Table 6. As expected, the smaller the pressure ratio is, the larger the flowrate and the losses are. On the contrary, the smaller the pressure ratio is, the smaller are the loss coefficients , i.e, ξ and ξ_{KE}. The primary coefficient and the kinetic energy loss coefficient have the same trend when the flowrate increases. A more sensitive reaction of the kinetic energy loss coefficient can be noticed. To explain the trend, the kinetic energy loss coefficient is computed for each specific volume V described before in Table 7. The variation of ξ_{KE} over each specific volume between the cases is normalized by the kinetic energy loss coefficient computed over all the specific volumes for case 1. The most sensitive zone in the computational domain is the boundary layer at the suction side. Changing the inlet specification affects the freestream velocity and the Reynolds number which impacts the turbulent boundary layer losses. The position of the turbulent transition is different (Table 8). Since the turbulent transition occurs downstream for case 3, the turbulent boundary layer produce more losses along the blade. The wake and the boundary layer at the pressure side have a

Case	P_s/P_{t1}	Q_m (g/s)	L (W)	ξ	ξ_{KE}
Case 1	0.61	18.0	11.76	2.67 %	15.1 %
Case 2	0.59	18.8	12.52	2.63 %	14.4 %
Case 3	0.63	17.7	11.15	2.78 %	16.2 %

TABLE 6: Set of results for the inlet total pressure sensitivity. The different losses L, ξ and ξ_{KE} are computed over V_{global}.

	Case 2	Case 3
Pressure side BL (a)	- 0.6 %	+ 0.6 %
Suction side turbulent BL (b)	- 2.5 %	+ 3.8 %
Recirculation (c)	+ 0 %	+ 0.1 %
Vortex shedding (d)	+ 0.7 %	+ 0.5 %
Suction side laminar BL (e)	- 2.2 %	+ 2.3 %
Total	**- 4.6 %**	**+ 7.3 %**

TABLE 7: Absolute variation of ξ_{KE} over each specific volume for case 2 and case 3 compared to case 1 normalized by the kinetic energy loss coefficient computed over all the specific volumes for case 1.

Case	Case 1	Case 2	Case 3
Turbulent transition position	0.77	0.82	0.73

TABLE 8: Relative position of the turbulent transition of the boundary layer at the suction side. Position is determined with the method described in the Section 4.1.

Copyright © 2017 by ASME

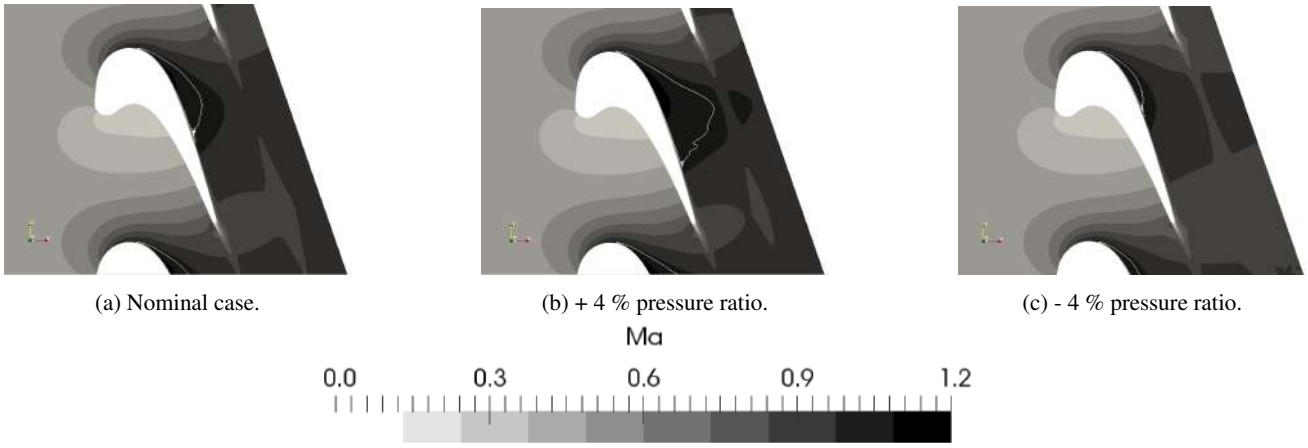

(a) Nominal case. (b) + 4 % pressure ratio. (c) - 4 % pressure ratio.

FIGURE 11: Effect of changing the pressure ratio on the time averaged Mach number field. Isocontour of $Ma = 1$ is plotted in white.

minor sensitivity.
Since the pressure distribution along the blade is affected by the losses, a more quantitative view is provided on Fig. 12 where the corresponding isentropic Mach number is plotted along the blade. In agreement with previous findings, the suction side

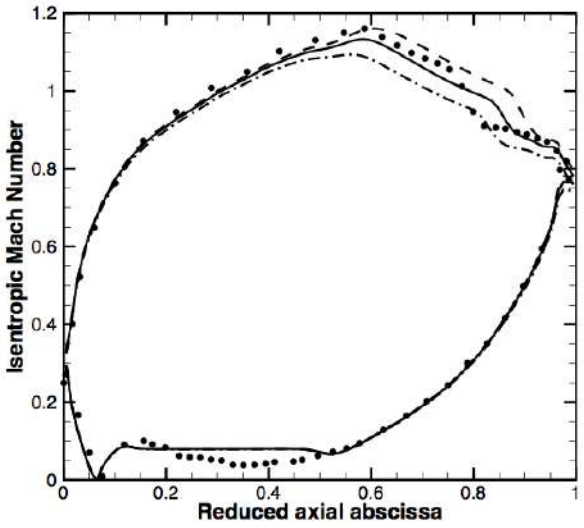

FIGURE 12: Effect of changing the pressure ratio on the isentropic Mach number along the blade: •, experiment; — LES nominal case; — —, LES + 4% pressure ratio; — · —, LES - 4% pressure ratio.

loads issued by all first three cases clearly differ as highlighted by the level of each curve downstream $x/c = 0.2$. The difference between case 2 and case 3 reaches up to 10% for the isentropic Mach number issued by these two simulations, which represents an overall difference of 11% on the local static pressure on the suction side. The pressure distribution is different because the inflow specification affects the flowrate, the losses and the turbulent transition position. Indeed, the larger the flowrate is, the larger the maximum Mach number is, which impacts the shock position. In contrast and as mentioned before, the pressure side is not affected compared to case 1.

At this point of this study, the response of the LES flow fields was discussed where only the static pressure ratio varied for the T120 test case. More specifically, a slight change of inlet specification produces significant changes of flow topology, especially on suction side. The expansion ratio is of primary importance. However, because of turbulent modeling and numerical handling, the losses are also known to be of primary importance to capture the load around a transonic blade. Flow losses are essentially issued by the boundary layer state and the blade wake. Indeed, the losses should only be perceived as a result issued by the prediction of the CFD tool. Flow losses are nonetheless known to be highly dependent on the turbulent modeling strategies in the flow field or near walls. These remarks partly explain the difficulties encountered by RANS / URANS modeling in adequately recovering proper flow behaviours outside the calibration range used for turbulent closure derivation. In that respect, since wall resolved LES theoretically diminishes the effect of turbulence modeling, it is expected to be more robust. The main question hence becomes which flow specifications and mechanisms highlighted previously are of importance for adequate predictions. The following part addresses the effect of the freestream turbulence on the mechanisms raised previously.

Copyright © 2017 by ASME

Sensitivity of LES to turbulence injection

As indicated early on, the T120 nominal case contains turbulence in the mean flow stream. It is taking into consideration in CFD computation by injecting turbulence at the inlet. In this section, the aim is to evaluate the sensitivity on the flow to turbulence injection. The turbulence intensity injected in the computation at the inlet is 20%. Going further downstream this turbulent field naturally decays and to compare with experimental findings at the same location, the measured numerical intensity is found to equal 5.0% which is in agreement with experimental findings: i.e. 5.23%. The inlet total pressure is affected by turbulence injection due to the kinetic energy added by the velocity fluctuation. To guaranty the same expansion between case 1 and 4, the total pressure at the leading edge $P_{t_{LE}}$ is retained in this section. Table 9 proves that the operating point is almost the same with a slight difference on flowrate inferior to 0.1%. On the contrary, one great difference between case 1 and case 4 is the flow induced losses in terms of L, ξ or ξ_{KE}. Irreversibilities are globally more important in case 4 than case 1 in the freestream as shown on Fig. 13. This is easily explained by the activation of the turbulent field of the sub-grid scale viscosity present in LES due to velocity gradient provided by turbulence. The effect of the freestream turbulence on the losses has been investigated in the literature, especially with a reciruclation bubble [18, 23, 24].

Case	$P_s/P_{t_{LE}}$	Q_m (g/s)	L (W)	ξ	ξ_{KE}
Case 1	0.6096	18.08	11.76	2.67 %	15.1 %
Case 4	0.6102	18.07	12.96	3.22 %	16.7 %

TABLE 9: Set of results for turbulence injection sensitivity.

The local contribution of turbulence is evaluated by the partial integration of losses over the same volumes presented in Section 4.2 and are reported in Table 10. The absolute variation of ξ_{KE} over each specific volume between the cases is normalized by the kinetic energy loss coefficient computed over all the specific volumes for case 1.

Major differences between case 1 and case 4 are situated in the turbulent boundary layer, in the wake and the laminar boundary layer. As expected, the turbulence injection increases the losses in the laminar boundary layer. This region produces more irreversibilities which affect the freestream flow. The turbulent transition occurs upstream for the turbulent case, which produces more losses (Table 11). A closer look at the recirculation displays important effects of the introduction of a turbulent field in the main stream. Such a difference is explained by clear different recirculation topologies as shown on Fig. 14. For case 4, the recirculation zone is smaller than in case 1. Turbulence helps in reattaching the boundary layer closer to leading edge. This behavior is similar to the flow around a cylinder where turbulence delays the detachment of the boundary layer [26].

Zone	**Case 4**
Pressure side BL (a)	+ 1.0 %
Suction side turbulent BL (b)	+ 5.2 %
Recirculation (c)	+ 0.4 %
Vortex shedding (d)	+ 2.4 %
Suction side laminar BL (e)	+ 1.6 %
Total	**+ 10.6 %**

TABLE 10: Absolute variation of ξ_{KE} over each specific volume between case 1 and case 4 normalized by the kinetic energy loss coefficient computed over all the specific volumes for case 1.

	Case 1	**Case 4**
Turbulent transition position	0.77	0.71

TABLE 11: Relative position of the turbulent transition of the boundary layer at the suction side. Position is determined with the method described in the Section 4.1.

Isentropic Mach number (Fig. 15) shows that the shock position is moved upstream the flow. Isentropic Mach number is larger at the suction side region, upstream the shock. At last and as underlined above, turbulence induced losses in the recirculation bubble located on the suction side is observed to allow the right recovery of the isentropic Mach profile in this specific region and if compared to experimental data.

To conclude, turbulence injection clearly implies a different evolution of losses in the T120 flow. It increases laminar boundary layer losses as well as moves the turbulent transition position. If compared to experiment, prediction from LES is improved. The boundary layer in the recirculation bubble is reattached upstream if compared with no turbulence injection. All in all, turbulence injection is found to provide LES predictions that better reproduce experimental findings.

Copyright © 2017 by ASME

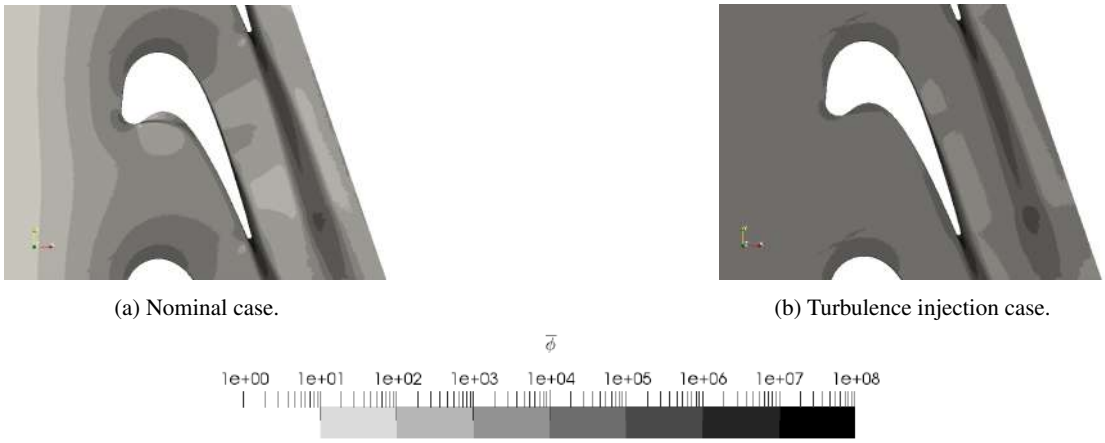

(a) Nominal case. (b) Turbulence injection case.

FIGURE 13: Effect of the turbulence injection on the local dissipation rate of the resolved kinetic energy $\overline{\phi}$ at mid-span.

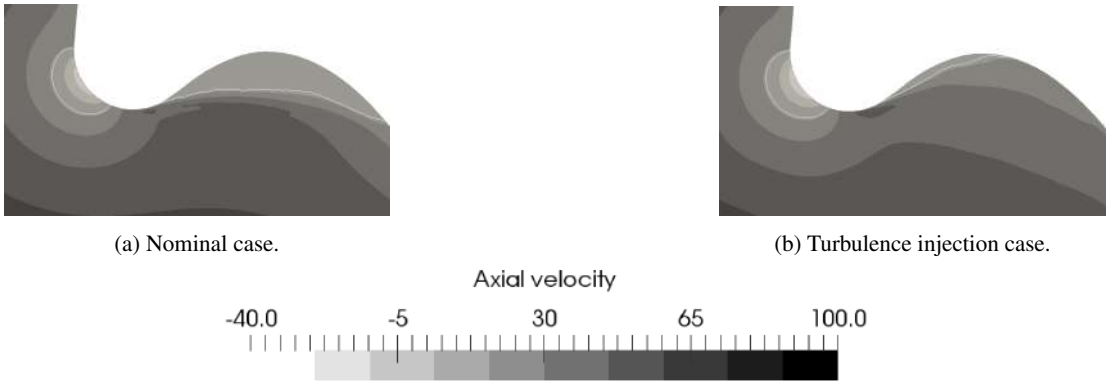

(a) Nominal case. (b) Turbulence injection case.

FIGURE 14: Effect of the turbulence injection on the recirculation zone at mid-span. Isocontour of null axial velocity is plotted in white.

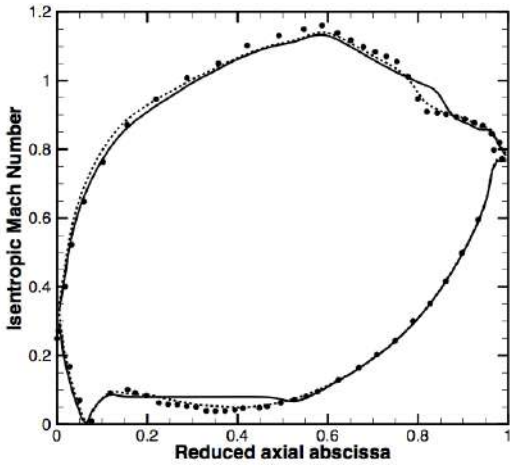

FIGURE 15: Effect of the turbulence injection on the isentropic Mach number along the blade: •, experiment; ⁃ LES nominal case; - - , LES turbulence injection case.

Copyright © 2017 by ASME

CONCLUSION

Uncertainties on inflow specifications are a key issue in LES. To evaluate the sensitivity of the flow topology to pressure ratio, different LES simulations were carried out. The losses were computed through L, ξ and ξ_{KE} to find the most vulnerable zone in the computational domain. The first set of simulations, i.e, case 1, 2 and 3 were obtained by changing the static pressure ratio by 4% to coincide with the experimental uncertainty compared to the nominal operating point. Investigation of dissipation field has proved that the majority of irreversibilities occurs in the turbulent boundary layer on suction side and the wake. Comparison of test cases shows a non linear interaction between the losses and the static pressure ratio. The pressure distribution around the blade is very sensitive to inflow specification. As a result, the response of LES depends on the capacity of the CFD tool to capture the correct losses within the flow since it is primary of interest as well as the pressure ratio.

The second set of LES concerns the effect of the turbulence injection on flow topology and dissipation field. Results show that prediction is improved in the recirculation zone by helping the boundary layer to reattach the blade wall. On suction side, both laminar and turbulent boundary layer produce more irreversibilities. As a result, mean flow topology in this region is very different and prediction is improved as well as shock position.

Future investigations are needed to compare the time averaged dissipation rate of the resolved kinetic energy $\overline{\phi}$ and the total pressure loss used in the literature [27] in the wake and in the boundary layer.

ACKNOWLEDGMENT

The authors wish to gratefully acknowledge the CASCADE project to provide funding for this work. Special thanks for the contributors of the AITEB II European project. The simulations presented here were performed using HPC resources from GENCI-IDRIS.

REFERENCES

[1] L. Homeier and F. Haselbach. Film cooling of highly loaded blades. In *XVIII International Symposium on Air Breathing Engines (ISABE)*, number AIAA-2005-1114, Munich, Germany, September 2005.

[2] Hosdon Popovic. Aerothermal impact of the interaction between hub leakage and mainstream flows in highly-loaded high pressure turbine blades. *Journal of Turbomachinery*, 135:061014–061014–11, 2013.

[3] Leschziner S. Lardeau. Unsteady rans modelling of wake-blade interaction: computational requirements and limitations. *Computer & Fluids*, 34:3–21, 2005.

[4] Sandberg Wheeler A.P.S. and al. Direct numerical simulations of a high-pressure turbine vane. *Journal of Turbomachinery*, 138:1–23, 2016.

[5] P. Sagaut. *Large Eddy Simulation for incompressible flows*. Scientific computation series. Springer-Verlag, 2000.

[6] K. Mahesh, G. Constantinescu, and P. Moin. A numerical method for large-eddy simulation in complex geometries. *Journal of computational physics*, 197(1):215–240, 2004.

[7] T. Poinsot and D. Veynante. *Theoretical and Numerical Combustion*. R.T. Edwards, 2nd edition, 2005.

[8] Matthieu Leyko, Ignacio Duran, Stephane Moreau, Franck Nicoud, and Thierry Poinsot. Simulation and modelling of the waves transmission and generation in a stator blade row in a combustion-noise framework. *Journal of Sound and Vibration*, 333(23):6090–6106, November 2014.

[9] C. Koupper, G. Caciolli, L.Y.M. Gicquel, F. Duchaine, G. Bonneau, L. Tarchi, and B. Facchini. Development of an engine representative combustor simulator dedicated to hot streak generation. *Journal of Turbomachinery*, 136(11):111007–111007–10, 2014.

[10] E. Collado Morata, N. Gourdain, F. Duchaine, and L.Y.M. Gicquel. Effects of free-stream turbulence on high pressure turbine blade heat transfer predicted by structured and unstructured les. *International Journal of Heat and Mass Transfer*, 55(21-22):5754 – 5768, 2012.

[11] W. Sturm and L. Fottner. The high-speed cascade wind-tunnel of the german armed forces university munich. In *8th Symposium on Measuring Techniques for Transonic and Supersonic Flows in Cascades and Turbomachines*, Genova, Italy, October 1985.

[12] R. A. Gomes and R. Niehuis. Film cooling effectiveness measurements with periodic unsteady inflow on higly loaded blades with mean flow separation. In *Proceedings of the ASME Turbo Expo 2009: Power for Sea, Land and Air*, Orlando, Florida, USA, 2009.

[13] Homeier et al. Aero-thermodynamic aspects of film cooling in regions of separated flow on the pressure side of a high-lift hpt blade. *ASME. Turbo Expo: Power for Land, Sea, and Air*, 5:277–286, 2004.

[14] T. Poinsot and S. Lele. Boundary conditions for direct simulations of compressible viscous flows. *Journal of computational physics*, 101(1):104–129, 1992.

[15] A. Smirnov, S. Shi, and I. Celik. Random flow simulations with bubble dynamics model. In *Proceedings of FEDSM00, ASME 2000 Fluids Egineering Division Summer Meeting*, volume FEDSM2000-11215, June 11-15, Boston, Massachusetts, USA, 2000.

[16] O. Colin and M. Rudgyard. Development of high-order taylor-galerkin schemes for unsteady calculations. *Journal of computational physics*, 162(2):338–371, 2000.

[17] F. Nicoud and F. Ducros. Subgrid-scale stress modelling based on the square of the velocity gradient. *Flow, Turbulence and Combustion*, 62(3):183–200, 1999.

Copyright © 2017 by ASME

[18] Elena Collado. *Impact of the unsteady aerothermal environment on the turbine blades temperature*. PhD thesis, Université de Toulouse - Institut National Polytechnique de Toulouse - Energétique et Transferts, 2012. PhD.

[19] Sanford S. Davis. On an invariance property of acoustic waveguides. *The Acoustical Society of America*, 59:264–266, 1976.

[20] T . Handa et al. Formation of multiple shocklets in a transonic diffuser flow. *Shock waves*, 11:423 – 430, 1999.

[21] F. Duchaine, A. Corpron, L. Pons, V. Moureau, F. Nicoud, and T. Poinsot. Development and assessment of a coupled strategy for conjugate heat transfer with large eddy simulation: Application to a cooled turbine blade. *International Journal of Heat and Fluid Flow*, 30(6):1129–1141, 2009.

[22] P. Chassaing. *Mécanique des fluides, Éléments d'un premier parcours*. Cépaduès-Éditions, 2000.

[23] R. Kiock H. Hoheisel. Influence of free stream turbulence and blade pressure gradient on boundary layer and loss behaviour on turbine cascades. Braunschweig, Germany, 1986.

[24] P. Ligrani Q. Zhang, D. Sandberg. Mach number and freestream turbulence effects on turbine vane aerodynamic losses. *Journal of Propulsion and Power*, 21:988–996, 2005.

[25] Baniegbhal et al. Development of blade profiles for low-pressure turbine applications. *Journal of Turbomachinery*, 119:531–538, 1997.

[26] Achenbach. Distribution of local pressure and skin friction around a circular cylinder in cross-flow up to re = 5 106. *Journal of Fluid Mechanics*, 34:625–639, 1968.

[27] J.D. Denton. Loss mechanisms in turbomachines. *Journal of turbomachinery*, 115:621–656, 1993.

Copyright © 2017 by ASME

Appendix E

LARGE EDDY SIMULATIONS OF A HIGHLY LOADED TRANSONIC BLADE WITH SEPARATED FLOW

This appendix is extracted from the publication of (Harnieh et al., 2018).

Proceedings of ASME Turbo Expo 2018: Turbine Technical Conference and Exposition
GT2018
June 11-15, 2018, Oslo, Norway

GT2018-75730

LARGE EDDY SIMULATIONS OF A HIGHLY LOADED TRANSONIC BLADE WITH SEPARATED FLOW

Mael Harnieh *
CFD Team CERFACS
Toulouse, France
Email: harnieh@cerfacs.fr

Laurent Gicquel
Florent Duchaine
CFD team CERFACS
Toulouse, France

ABSTRACT

Efficient design of highly loaded pressure blades often leads to the generation of a separation bubble on the pressure side of highly curved blades. For this specific region, fundamental, numerical and experimental studies have indicated the importance of the turbulence present in the main stream in determining the size of the bubble before its reattachment to the blade. Despite this important finding, many complex phenomena remain and are still present and can influence the overall flow response. In this paper, explorations of high-fidelity unsteady Large Eddy Simulations of a separated flow are studied for the high pressure T120 blade from the European project AITEB II (Aerothermal Investigation on Turbine Endwalls and Blades). For this investigation, simulations are carried out at the nominal operating point with and without synthetic turbulence injection at the inlet condition to comply with the specification from the experiment. Based on these predictions, the near wall flow structure and turbulent fields are specifically investigated in an attempt to identify the key mechanisms introduced by the turbulent main stream flow. Results show that the turbulence specification at the inlet enables the recovery of the correct pressure distribution on the blade surface contrary to the laminar inlet condition if compared to the experiment. Investigations of the boundary layer profiles show a strong impact of the freestream turbulence on the shape factor from the leading edge. As a consequence, the recirculation bubble located downstream on the pressure side is impacted and reduced when turbulence is injected. Due to this change in mean flow topology, the mass flow distribution in the passage appears strongly affected. Investigations of loss fields furthermore show that the freestream turbulence dramatically increases the loss production within the computational domain.

NOMENCLATURE

Acronyms

AITEB	Aerothermal Investigation on Turbine Endwalls and Blades
DNS	Direct Numerical Simulation
LES	Large Eddy Simulation
RANS	Reynolds Average Navier-Stokes
SLA	Second Law Analysis
TTGC	Two-Step Taylor Galerkin C
WALE	Wall Adaptative Local Eddy-viscosity

Greek letters

α	Deflection angle	$[-]$
β_S	Sutherland law constant	$[-]$
ε	Turbulent dissipation	$[m^2.s^{-3}]$
δ	Boundary layer thickness	$[m]$
γ	Specific heat ratio	$[-]$
λ	Thermal conductivity	$[W/(m.K)]$
λ_t	Turbulent thermal conductivity	$[W/(m.K)]$
μ	Laminar viscosity	$[kg.m^{-1}.s^{-1}]$
μ_t	Turbulent viscosity	$[kg.m^{-1}.s^{-1}]$
ρ	Density	$[kg.m^{-3}]$
τ_{ij}	Laminar viscous stress tensor	$[Pa]$
τ^t_{ij}	Turbulent stress tensor	$[Pa]$
ξ	Loss coefficient	$[-]$

*Address all correspondence to this author.

Copyright © 2018 by ASME

Symbols

c	Axial chord length	$[m]$
C_f	Friction coefficient	$[-]$
k	Resolved turbulent kinetic energy	$[m^2.s^{-2}]$
k_{SGS}	Subgrid-scale turbulent kinetic energy	$[m^2.s^{-2}]$
H	Shape factor	$[-]$
L	Blade to blade length	$[m]$
Ma_{is}	Isentropic Mach number	$[-]$
Ma_2	Outlet isentropic Mach number	$[-]$
P	Static pressure	$[Pa]$
P_t	Total pressure	$[Pa]$
P_k	Turbulent kinetic energy production	$[m^2.s^{-3}]$
P_m	Mechanical term of the losses	$[W.m^{-3}]$
P_q	Thermal term of the losses	$[W.m^{-3}]$
Pr	Normalized turbulent production	$[-]$
q	Thermal flux	$[W.m^{-2}]$
q_t	Turbulent thermal flux	$[W.m^{-2}]$
q_2	Dynamic pressure at the outlet	$[Pa]$
Q_{crit}	Q criterion	$[s^{-2}]$
Q_m	Flowrate	$[kg.s^{-1}]$
Re	Reynolds number	$[-]$
S	Sutherland law constant	$[-]$
S_{ij}	Symmetric part of the strain-rate tensor	$[s^{-1}]$
s^*	Resolved entropy source production	$[W.m^{-3}.K^{-1}]$
T_t	Total temperature	$[K]$
U_{inf}	Velocity at the edge of the boundary layer	$[s^{-1}]$
w	Vorticity	$[s^{-1}]$
$\widetilde{T}$	Filtered static temperature	$[K]$
$\widetilde{u_i}$	Resolved velocity	$[m.s^{-1}]$
x	Axial position	$[m]$
y	Blade to blade position	$[m]$
y^+	Dimensionless wall coordinate	$[-]$

Subscript

1	Inlet
2	Outlet
LE	Leading edge

INTRODUCTION

To comply with new environnemental regulations and reduce fuel consumption in aeronautics, the engine efficiency must be considerably improved. The Brayton cycle shows that the isentropic efficiency depends partly on the losses taking place in the turbine [1]. Recent turbine blade designs lead to highly loaded pressure blades for size and cost optimization [2]. The strong deviation of the flow in such cases can lead to high adverse pressure gradient and produce separation of the flow. If separation occurs, research has indicated that the size of the bubble is determined by the state of the boundary layer located upstream [3]. Experiments have indeed shown the influence of the inflow conditions on the separation [4]. Particularly, the freestream turbulence has been shown to play an important role in determining the size of the separation [5]. To predict the flow structure, different numerical studies have investigated the influence of the inflow condition on the flow structure. The Reynolds Average Navier-Stokes (RANS) consists in resolving the statistically mean flow while all the turbulence is modeled. With an acceptable CPU cost, RANS studies show that the prediction of the separation is sensitive to the turbulence modeling and mesh resolution [6]. However, such modeling tools have rapidly shown limitations and specific tunings and developments are required to capture complex flow structures [7]. An alternative is to use the Direct Numerical Simulation (DNS) where all the turbulence length scales are resolved on the mesh. Despite its high computational cost, recent studies realized on a limited span wise extent of academic blades show that the separation is strongly affected by the freestream turbulence [8,9]. Another alternative to predict complex flow structure is to use Large Eddy Simulations (LES). It consists in resolving the most energetic scales while modeling the small ones thereby offering access to much higher Reynolds number flows if compared to DNS [10–12]. Recent LES studies show the impact of the resolved freestream turbulence [13, 14] on the flow structure and particularly on the separation on simple test cases. But the impact on the pressure distribution of the blade have not sufficiently been studied in part because of the sub-grid modelling impact that may not be clear in such a context.

In this study, the effect of the inlet turbulent injection is assessed on the flow structure and on the operating point of a high pressure blade with separation. The question on the quantification of the losses is also addressed in this LES study due to its importance in engineering design. To realize this study, the T120 blade tested in the European project AITEB II (project number 2005-516113) is investigated with the compressible code AVBP [15]. One experimental operating point is targeted and the simulation is carried out with and without turbulent injection at the inlet. The investigation of the boundary layer state is done to understand the mechanism of the bubble separation in LES. The size of the bubble separation is assessed to explain the mass flow distribution in the passage. Lastly, the impact of the inlet turbulent injection has been evaluated on the loss distribution within the flow.

The document is organized as follows, the methodology and the numerical set up are explained in the first section. Then, the results are presented and discussed in the second section. The comparison of the operating point and the flow structure are here explained. To finish, the losses are evaluated in the third section.

METHODOLOGY AND SET UP

Computational domain and mesh

The features of the blade are summed up in Table 1. The computational domain is shown in Fig. 1. The span-wise do-

Copyright © 2018 by ASME

Feature	Symbols	Value
Chord length	l	120 mm
Axial chord length	l_x	76 mm
Blade height	h	300 mm
Pitch to chord ratio	t/l	1.007
Stagger angle	β_{stag}	46.25 °

TABLE 1: Geometric features of the T120 blade.

main extent is limited to 8 mm, i.e, 3 % of the height of the blade to allow fine mesh in the regions of interest. One chord length is taken in the front part of the domain to avoid acoustic interactions and potential effect of the blade on the inlet. Three chord lengths have been chosen between the blade and the outlet to damp the effect of the wake and the acoustic on the outlet boundary condition.

The unstructured mesh is composed of 24 million of tetrahedra

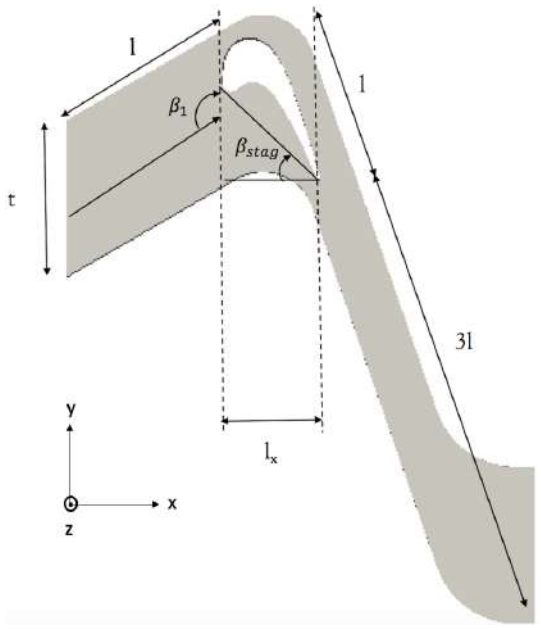

FIGURE 1: Computational domain of the T120 blade. The geometric features are summed up in Table 1.

and 10 million of prisms, i.e, the number of vertices is about 9.3 millions. Ten layers of prisms at the blade surface are used to reduce the simulation computational cost while complying with wall resolved approach. The normalized wall unit, y^+, is below 2 along the blade except near the leading and trailing edges as plotted in Fig. 2. The wall surface is meshed with isotropic triangles, i.e, $x^+ \approx z^+$. The aspect ratio of the prisms is limited to 5 along the blade except at the trailing edge, i.e, $x^+ \approx 5y^+$, and the cell volume jump volume at the interface tetrahedron / prism is by construction imposed to 3 to ensure proper numerics. As shown on Fig. 3, the mesh is refined on the pressure side, suction side and wake zone to capture strong gradients and near wall structures.

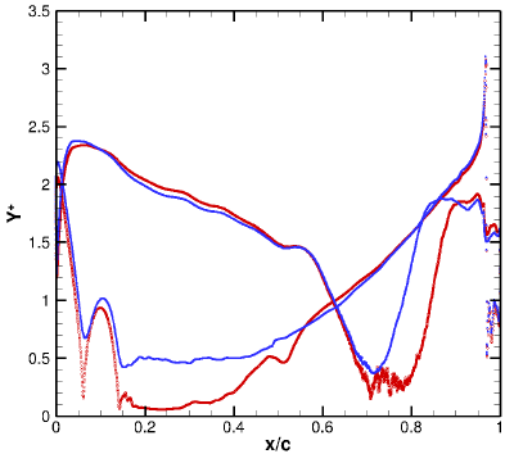

FIGURE 2: y^+ distribution along the blade. Red circle ∘ represents the laminar inlet case and blue circle ∘ the turbulent inlet case. Wall resolved approach is used for both cases.

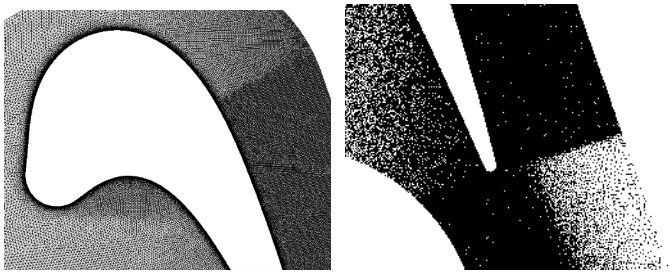

(a) Leading edge. (b) Trailing edge.

FIGURE 3: Mid-cut of the mesh in the near leading edge (a) and trailing edge (b). Refinement is done at the pressure side, suction side and wake zone.

Copyright © 2018 by ASME

Matching experimental operating point

The T120 blade was investigated in the High-speed Cascade Wind tunnel of the Institute of Jet Propulsion for AITEB II project [16–19]. The test bench is enclosed in a tank and the pressure inside the tank is monitored to get the desired operating point. A turbulence grid with cross rectangular plates is located upstream the blade to increase the turbulence level of the freestream flow. The turbulence level is measured with a hot wire probe upstream the cascade in the middle of the passage. The operating point is defined by the Reynolds number Re_2 and the outlet isentropic Mach number Ma_2 computed following,

$$Ma_2 = \sqrt{\frac{2}{\gamma-1}\left[\left(1+\frac{q_2}{P_2}\right)^{\frac{\gamma-1}{\gamma}}-1\right]}, \tag{1}$$

and monitoring the dynamic pressure q_2 given by the tank pressure P_2 and the inlet total pressure P_{t1},

$$q_2 = P_{t1} - P_2. \tag{2}$$

The Reynolds number is determined with the inlet total temperature T_{t1} following,

$$Re_2 = \sqrt{\frac{\gamma}{R}}\frac{l}{\beta_S}\frac{Ma_2.P_2\left[T_{t1}.\frac{1}{1+\left(\frac{\gamma-1}{2}\right)Ma_2^2}+S\right]}{\left[T_{t1}.\frac{1}{1+\left(\frac{\gamma-1}{2}\right)Ma_2^2}\right]}, \tag{3}$$

assuming a Sutherland law for the temperature dependent viscosity where the relative constants are : $S = 110.4$; $\beta_S = 1.458.10^{-6}$ for air and R is the gas constant of perfect gas.
To match numerically the experimental operating point, an iterative procedure is completed to compute P_{t1}, P_2 and T_{t1} to comply with the correct value of Re_2 and Ma_2. In the following, the operating point chosen is: $(Re_2; Ma_2) = (390,000; 0.87)$. The corresponding numerical boundary conditions are summed up in Table 2. Since a limited span-wise extent is computed, periodic conditions are applied in the span and y directions. To deal with acoustic treatment, the value of the boundary conditions are relaxed to the target values with NSCBC formalism [20].
To assess the inlet turbulent injection on the flow structure, the boundary conditions of the test cases are summed up in Table 3. The expansion ratio $P_2/P_{t_{LE}}$ computed with the total pressure at the leading edge $P_{t_{LE}}$ and the mass flow rate Q_m are assured to be the same for both simulations. The turbulence field is added to the mean flow at the inlet following the method of [21].

Patch	Variable	Value
Inlet	P_{t1}	26720 Pa
	T_{t1}	333 K
	Inlet angle	138.6 °
Outlet	P_2	16307 Pa
Wall		Adiabatic no slip

TABLE 2: Boundary conditions used in the computation to comply with $Re_2 = 390,000$ and $Ma_2 = 0.87$.

Case	$P_2/P_{t_{LE}}$	Q_m (g/s)	Inlet turbulent intensity
LAMINAR	0.6096	1.808	0%
TURBULENT	0.6102	1.807	20%

TABLE 3: Test case matrix. The expansion ration and the mass flow rate are equivalent for both simulations.

The inlet turbulent intensity is adjusted to comply with the experimental measurement at the probe location, i.e, the turbulence intensity is 5.23% at $0.6c$ upstream the cascade if c is the axial chord length [22]. The integral length scale imposed at the inlet is adjusted at $0.08c$ to be in the span-wise domain and corresponds to the typical value used in limited span-wise extent simulations [8].

Numerical scheme and averaging procedure

The finite element approach is used to run the simulations. The convective terms are integrated with the high order scheme TTGC [23], i.e, 3rd order in space and 3th order in time. This numerical scheme has good spectral properties and does not dissipate the smallest length scale flow structures present on the mesh. It is adapted for the Large Eddy Simulation [23]. The diffusive terms are integrated with a 2nd order finite element scheme. The WALE subgrid model is used to comply with correct wall behaviour of the turbulent viscosity [24].
The time average is based on 4 flow time passages and it is assured that the turbulent fields are sufficiently averaged based on the largest resolved time scale. The instantaneous and time averaged are extracted and discussed in the next section.

RESULTS: IMPACT OF THE INLET TURBULENT INJECTION ON THE FLOW STRUCTURE

In this section, the turbulent fields are first studied to show that the resolved turbulent structures reach the blade and are cor-

Copyright © 2018 by ASME

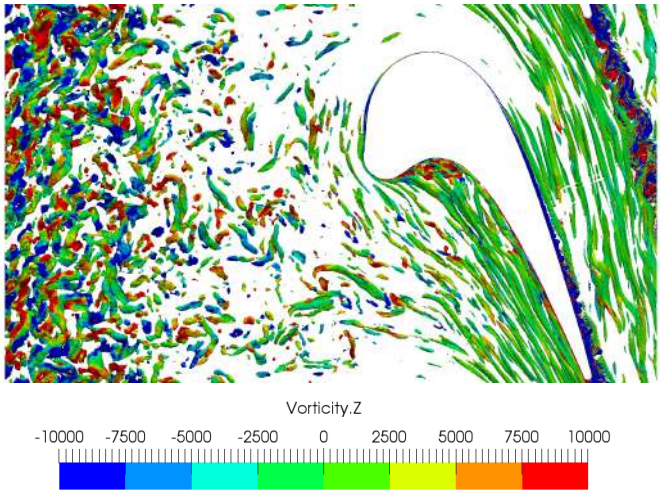

FIGURE 4: Iso-surface of Q criterion, i.e, $Q_{crit} = 4.10^7\ s^{-2}$, in the flow passage of the blade. The color indicates the span wise vorticity.

rectly transported. The iso-surface of Q criterion is plotted on Fig. 4 to discriminate the turbulent structures. Clearly, the turbulent structures are transported up to the leading edge of the blade and are then stretched in the flow passage. It is also evidenced through this view that structures are created at the pressure side and along the suction side of the blade. The spectra of the axial fluctuating velocity signal at $x/c = -0.1$ in the mid flow passage is displayed in Fig. 5. The -5/3 slope is well recovered corresponding to the spectra of homogeneous turbulence. The decay

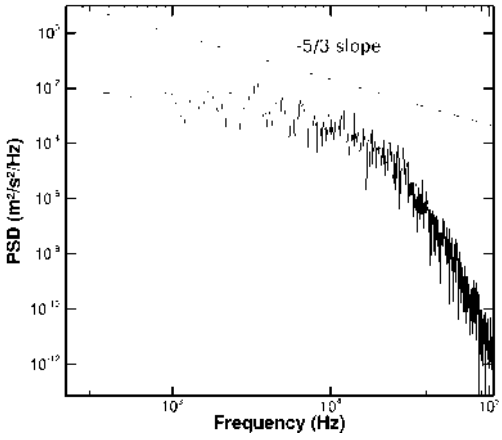

FIGURE 5: Power Spectral Density (PSD) of the axial velocity signal taken at the probe located at $x/c = -0.1$ in the mid flow passage. The -5/3 slope is plotted in dashed.

of turbulence is then compared to the analytical law resulting from the decay of an homogeneous isotropic turbulent field [25]. For such a flow, the turbulence can be described by the initial turbulent kinetic energy k_0 and the initial turbulent dissipation ε_0, the time evolution of k reducing to,

$$k(t) = k_0 \left(1 + (C_\varepsilon - 1)\,\frac{t}{\tau_0}\right)^{\left(-\frac{1}{C_\varepsilon - 1}\right)} \tag{4}$$

with $\tau_0 = \frac{k_0}{\varepsilon_0}$ and the analytical model constant $C_\varepsilon = 1.92$. From the integral length scale, the initial turbulent dissipation ε_0 is estimated at $\varepsilon_0 = 3.78.10^6\ m^2 s^{-3}$. The time evolution can then be transformed to a spatial evolution along a streamline using the Taylor hypothesis [25], i.e, $x = u_0 * t$ with u_0 the velocity at the inlet to be compared to the spatial prediction. Figure 6 shows the evolution from the inlet up to the leading edge of the blade. The decay of the turbulent kinetic energy is stronger than the model in part because of the unphysical spectrum used at the inflow. Despite this shortcoming both evolutions are in good agreement. Indeed, the turbulent intensity value at the experimental probe location is 5% and very similar to the experiment one, 5.23 %.

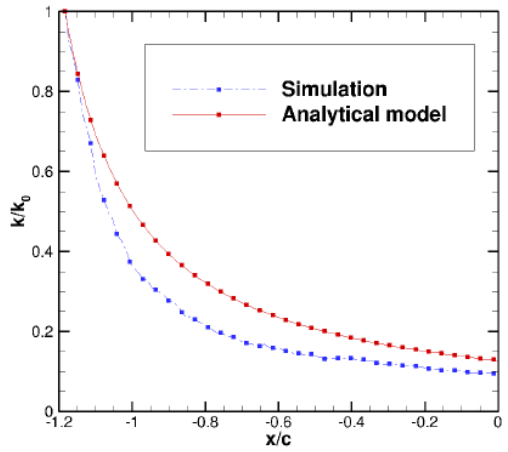

FIGURE 6: Turbulent kinetic energy decaying between the inlet and the leading edge of the blade along a streamline. Red solid line is the model and blue dashed line is the simulation.

Flow structures with and without turbulence injection

The time averaged pressure fields issued by both simulations, i.e. (a) without and (b) with turbulence injection, are plotted in Fig. 7 at mid-cut of the domain. The time averaged pressure fields are very similar. The flow structure is locally affected

Copyright © 2018 by ASME

by the freestream turbulence in the near wall region.

On the suction side, the sonic line shows that a shock is present

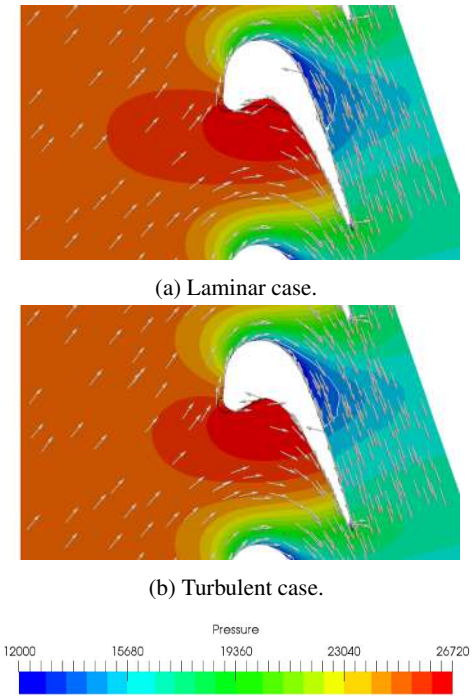

(a) Laminar case.

(b) Turbulent case.

FIGURE 7: Time averaged pressure field at mid-cut. Black line isocontour is null axial velocity. White line isocontour is sonic line. Velocity vectors are represented by arrows. (a) is the laminar case and (b) the turbulent case.

in this region. The turbulent transition of the boundary layer occurs on the blade as shown by Fig. 8. Turbulent structures, as hairpin vortices, are developed near the blade wall from the same position of the sonic line location. The transition mode is hence shock-induced. The position of the turbulent transition is different with the injection of the turbulence at the inlet and it is moved upstream when compared to the laminar case prediction.

On the pressure side, the flow exhibits a separation due to high adverse pressure gradient deduced by the null axial velocity iso-contour. The size of the bubble is smaller for the turbulent case. A closer look at the bubble structure is given in Fig. 9. For the laminar case, the shear produced by the bubble creates Kelvin-Helmholtz structures. The rolls are then transported and stretched downstream. For the turbulent case, the bubble structure is quite different. The freestream turbulence interacts with the bubble. The bubble does not fully vanish but its size is greatly diminished. The bubble size is estimated by extracting the friction coefficient C_f along the pressure side. The separation and

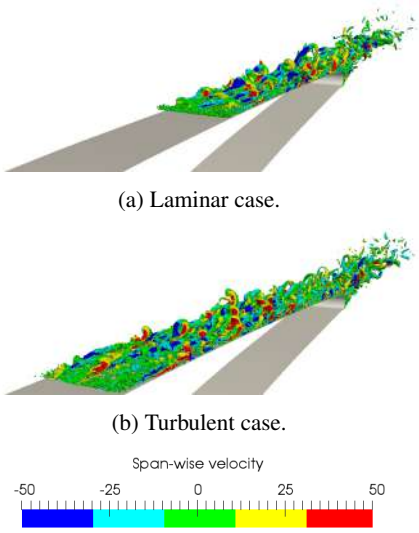

(a) Laminar case.

(b) Turbulent case.

FIGURE 8: Iso-surface of Q criterion, $Q_{crit} = 1.10^9\ s^{-2}$ in the near wall region on the suction side. The color indicates the span velocity. (a) is the laminar case and (b) the turbulent case.

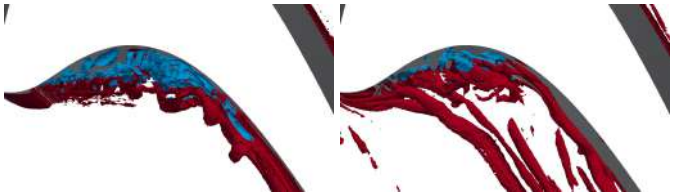

(a) Laminar case. (b) Turbulent case.

FIGURE 9: Iso-surface of Q criterion, i.e $Q_{crit} = 1.10^5\ s^{-2}$, in the bubble region. Red represents positive axial velocity and blue negative axial velocity. (a) is the laminar case and (b) the turbulent case.

reattachement points are defined when $C_f = 0$ and the bubble size is specified on Fig. 10 against the experimental results. For the laminar case, the bubble is clearly too large. For the turbulent case, the bubble size is reduced and improved. The impact of the freestream turbulence on the flow structure of high pressure blades, e.g, bubble size and turbulent transition of the boundary layer, has been studied in experimental and numerical investigations [5, 26]. Studies show that the state of the boundary layer along the blade needs to be investigated.

Copyright © 2018 by ASME

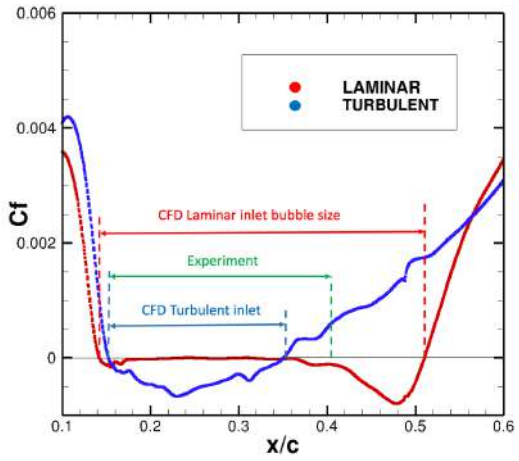

FIGURE 10: Friction coefficient evolution along the pressure side of the blade between $x/c = 0.1$ and $x/c = 0.6$ for the laminar, i.e, indicated by the red dots and the turbulent case, i.e, indicated the blue dots. The bubble size is indicated and compared with the experiment extracted from [19].

Boundary layer investigation

The boundary layer thickness δ is defined by the method of [27], i.e, based on the magnitude of the vorticity w. With this approach, the boundary layer thickness is defined when the magnitude of the vorticity satisfies,

$$w = w_{min} + (w_{max} - w_{min}) * 0.01, \tag{5}$$

where w_{min} and w_{max} are the minimum and the maximum of the vorticity magnitude along the wall normal cross section. The evolution of the different properties of the boundary layer, i.e, the displacement thickness $\delta*$ and the momentum thickness θ are then extracted along the blade. The evolution of the shape factor which is equal to $H = \frac{\delta*}{\theta}$ is plotted in Fig. 11. On the pressure side, the shape factor is near 2 all along the pressure side and the boundary layer remains laminar [3]. Downstream the reattachment point, the strong acceleration of the flow relaminarizes the boundary layer as pointed in the experiment [22]. The freestream turbulence affects the shape factor from the leading edge. Near the separation position, the shape factor is lower for the turbulent case. As shown by the theory of the boundary layer [3], the smaller is the shape factor, the more resistant is the boundary layer to detachment. For these two simulations, the turbulence injection clearly favors the boundary layer resistance to the separation. That is the reason why the bubble size is smaller in the turbulent case. On the suction side, the shape factor increases along the blade. The shape factor peak gives an indication on the strong pressure gradient term induced by the

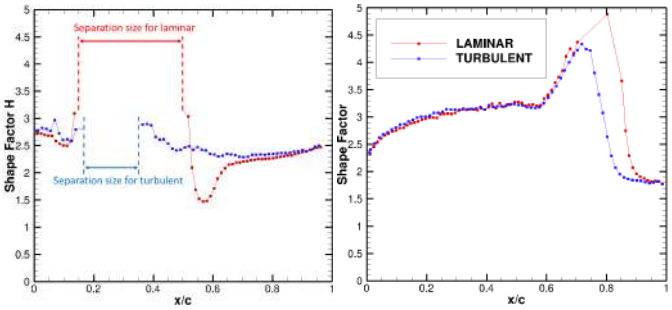

(a) Pressure side. (b) Suction side.

FIGURE 11: Shape factor evolution along the boundary layer blade. Suction side (a) and pressure side (b). Separation length is indicated for both LES and no points are plotted in the separation. Red line represents the laminar case and blue the turbulent case.

shock in the boundary layer theory [3]. Downstream, the shape factor dramatically decreases down to the typical value of the turbulent boundary layer, i.e 1.5.

To estimate the turbulent transition position, the normalized production term of the turbulent kinetic energy Pr is integrated in the boundary layer on the suction side of the blade,

$$Pr = \frac{1}{U_{inf}^3} \int_0^{\delta} P_k dy, \tag{6}$$

where $P_k = -\overline{u_i' u_j'} \frac{\partial \overline{U_i}}{\partial x_j}$ where $\overline{u_i' u_j'}$ is the time averaged velocity correlation tensor and $\overline{U_i}$ the time averaged velocity. The production term Pr is plotted in Fig. 12. The turbulent kinetic energy

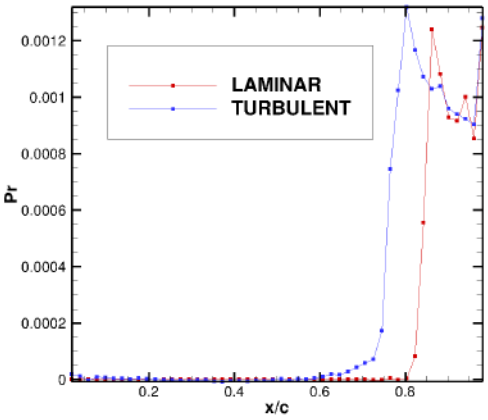

FIGURE 12: Normalized turbulent kinetic energy production Pr integrated in the boundary layer at the suction side of the blade. Red line represents the laminar case and blue the turbulent case.

Copyright © 2018 by ASME

production remains low in the first part of the boundary layer, i.e, $x/c < 0.60$ for both cases. The peak at $x/c = 0.86$ indicates the turbulent transition position of the boundary layer followed by the non-equilibririum region [28]. When the turbulence is injecting at the inlet, the transition moves upstream at $x/c = 0.80$. The impact on the position of the turbulent transition has been observed in numerical studies [26].

Impact on the pressure distribution

The mass flow distribution in a flow passage is affected by the flow structure. In this part, the impact of the inlet turbulent injection on the mass flow distribution is assessed. The mass flow rate by unit surface distribution on axial surfaces is plotted in Fig. 13 at different axial positions. The distribution is not affected

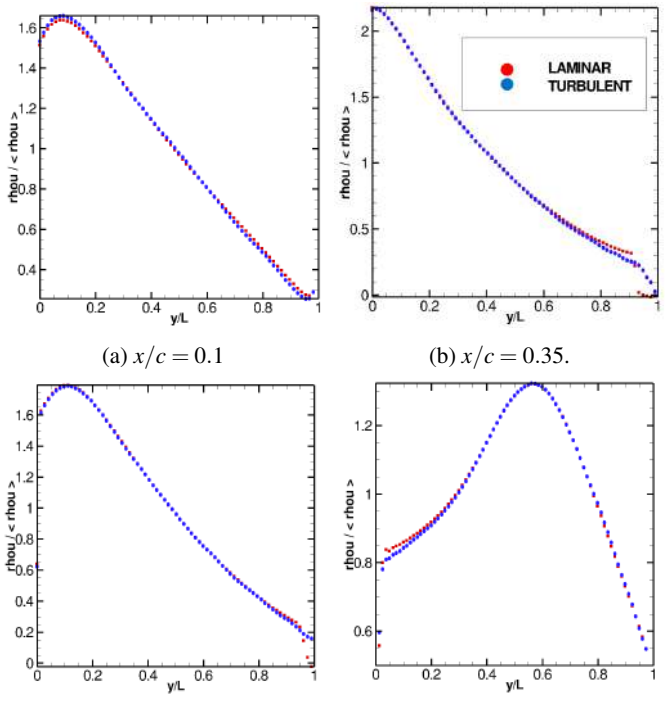

(a) $x/c = 0.1$ (b) $x/c = 0.35$.

(c) $x/c = 0.5$ (d) $x/c = 0.8$

FIGURE 13: Mass flow rate by surface unit normalized by the surface average mass flow $< rhou >$ along the flow passage at different axial locations. $y = 0$ corresponds to the suction side wall and $y = L$ the pressure side wall. L is the distance between the blade walls. Red dots represents the laminar case and blue dots the turbulent case.

near the leading edge at $x/c = 0.10$. The major differences are presented at the position of the separation, on the suction side, and at the turbulent transition, i.e, at $x/c = 0.35$, $x/c = 0.5$ and

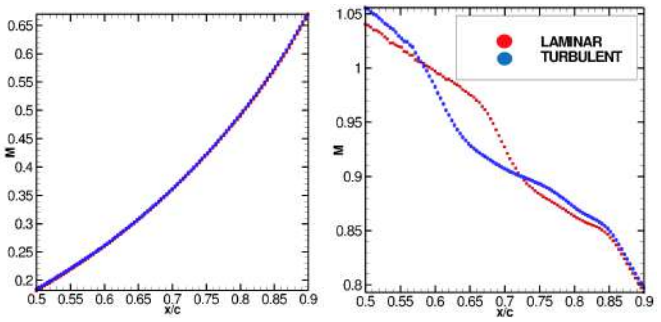

(a) Pressure side streamline. (b) Suction side streamline.

FIGURE 14: Mach number profile along the streamlines at the edge of the boundary layer from $x/c = 0.5$ to $x/c = 0.9$ on both pressure and suction side. s is the streamline coordinate. Red dots represents the laminar case and blue dots the turbulent case.

$x/c = 0.8$. At $x/c = 0.35$, the mass flow is more important near the pressure side for the turbulent case. Since the bubble size is lower for the turbulent case, more mass flow can pass in this region. At $x/c = 0.5$ and $x/c = 0.8$, a deficit of mass flow appears on the suction side for the turbulent case. Since the mass flow rate is the same for both test cases, the additional mass flow on the pressure side results in a deficit of mass flow on the suction side to preserve the integrated mass flow in a section. This results in a different Mach number distribution along the streamlines at the edge of the boundary layer from $x/c = 0.5$ to $x/c = 0.9$ on pressure and suction sides as proved by Fig. 14. On the pressure side, the Mach number is not impacted by the turbulent injection. On the suction side, the profiles are very different. For the turbulent case, the position of sonic line, i.e, $M = 1$ is moved upstream.

The impact of the freestream turbulence on the flow structure, i.e, at the pressure and suction side affects directly the pressure distribution on the blade surface displayed by the Isentropic Mach Number computed by,

$$Ma_{is} = \sqrt{\frac{2}{\gamma - 1}\left[\left(1 + \frac{P_{t1}}{P}\right)^{\frac{\gamma-1}{\gamma}} - 1\right]}. \qquad (7)$$

where $\overline{\bullet}$ is the time averaged operator. Compared to the experimental results (Fig. 15), the bubble size in the laminar case evidenced by the Ma_{is} plateau is too large. The position of the shock, represented by a decrease of the isentropic Mach number on the suction side is located downstream the experimental one. Turbulence injection at the inlet enables to recover the pressure distribution on the pressure and suction sides.

Copyright © 2018 by ASME

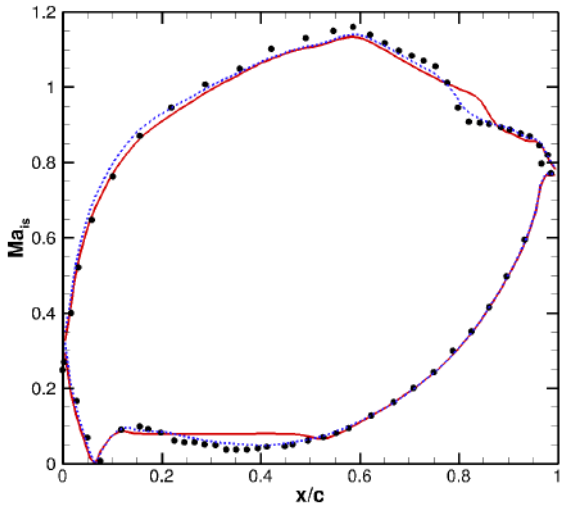

FIGURE 15: Effect of the turbulence injection on the isentropic Mach number along the blade: •, experiment [22]; Red – LES laminar case; Blue - - LES turbulence injection case.

Partial conclusion

To sum up this section, the inlet turbulent specification is assessed on the flow structure. The inlet turbulent injection affects strongly the leading edge boundary layer. The boundary layer profiles show an impact of the turbulence on the shape factor. The boundary layer on the pressure side remains laminar. It is then more resistant to the separation and the bubble size is reduced. The turbulent transition of the boundary layer on the suction side is also impacted and moved upstream. The mass flow distribution in the flow passage along the blade is then strongly affected. The comparison with the experiment shows that the inlet turbulent injection enables to recover the correct pressure distribution on the blade wall.

The first part of this study shows that the flow structure and the mass flow distribution in a section are different by injecting the same mass flow rate at the inlet but with different turbulent inlet specifications. The pressure and the suction side of the blade are coupled. One side can not be predicted without the other side. Comparisons with the experiment show that the prediction is improved if turbulence is injected at the inlet. In the next section, the impact of the inlet turbulent specification will be assessed on the losses.

INVESTIGATION OF THE LOSSES

In the litterature, the losses are usually defined with loss coefficients [1, 29] and the deflection angle α of the flow between the inlet and the outlet. Figure 16 compares with the experimental results the total pressure loss coefficient $\xi = \frac{P_{t_{LE}} - P_{t2}}{q_2}$ where P_{t2} is the total pressure measured at $x/c = 0.4$ downstream the trailing edge. Both LES are in agreement with the wake loss profiles reported experimentally. The loss coefficient in the middle of the wake, i.e, $y/L = 0.4$ is under-estimated for both LES simulations. Differences between the two LES appear on the pressure side although they remain close to the experimental findings. The deflection angle is computed as the angle between the surface averaged velocity vector at the outlet and the inlet. Looking at the flow deflection angle, Table 4, when turbulence is injected the prediction is improved.

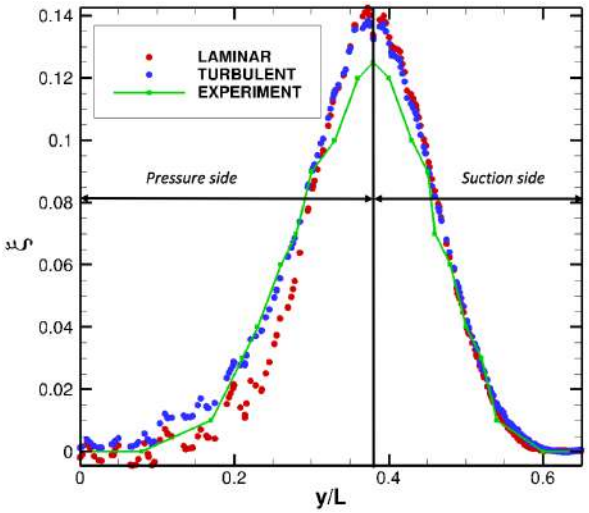

FIGURE 16: Loss coefficient profiles at the mid-cut located at $x/c = 0.4$ downstream the trailing edge along the y direction normalized by the spacing between the periodicity patches L. Red dots represents the laminar case, blue dots the turbulent case and green line the experimental data.

CASE	α
EXPERIMENT	60.60°
LAMINAR INLET SIMULATION	60.44°
TURBULENT INLET SIMULATION	60.56°

TABLE 4: Summary of the deflecting angle α for the experiment and simulations.

However, loss coefficients are generally based on the variation of total pressure and temperature from basic thermodynamic mod-

Copyright © 2018 by ASME

els assuming perfect fluid. As demonstrated by [30], the evolution of the total pressure and temperature does not measure rigorously the losses, e.g, the total pressure can increase between 2 sections of the flow passage due to viscous effect.
In this study, the Second Law Analysis (SLA) is used to quantify the losses, initially developped by [31] to optimize thermal systems. Following this method, the entropy source terms represent the losses and are directly assiciated with the detorioration of the isentropic efficency. The entropy source terms are locally identified within the flow to discrimanate the zones responsible for the losses. This method has already been used in turbulent flows for aeronautic applications with RANS [32], DNS [33] and LES [34, 35]. In the following, the definition of the loss terms is explained and detailed for a compressible viscous flow of perfect gas adapted to the LES. According to [34], the entropy production s^* is divided into 2 contributions, i.e, P_m and P_q,

$$s^* = \frac{P_m + P_q}{T}. \tag{8}$$

The first term of Eq. (8) is a momentum diffusion contribution,

$$P_m = (\tau_{ij} + \tau^t_{ij}) \frac{\partial \widetilde{U_i}}{\partial x_j}, \tag{9}$$

where τ_{ij} and τ^t_{ij} are respectively the filtered viscous stress tensor and the sub-grid Reynolds tensor. The second contribution is an energy diffusion term,

$$P_q = \frac{(-q_i - q^t_i)}{T} \frac{\partial \widetilde{T}}{\partial x_i}, \tag{10}$$

where q_i and q^t_i are respectively the filtered heat flux and the sub-grid turbulent heat flux. In the following, the expressions of P_m and P_q are expressed as resolved quantities.

Mechanical loss P_m

Assuming that the fluid is Newtonian, the filtered viscous stress tensor is modelled as,

$$\tau_{ij} = 2\mu \left(S_{ij} - \frac{1}{3} S_{ll} \delta_{ij} \right), \tag{11}$$

where μ is the dynamic viscosity, $S_{ij} = \frac{1}{2}\left(\frac{\partial \widetilde{u_i}}{\partial x_j} + \frac{\partial \widetilde{u_j}}{\partial x_i} \right)$ is the symmetric part of the resolved strain-rate tensor and δ_{ij} the Kronecker symbol. A Boussinesq assumption is used to model the sub-grid Reynolds stress tensor [36],

$$\tau^t_{ij} = 2\mu_t \left(S_{ij} - \frac{1}{3} S_{ll} \delta_{ij} \right) - \frac{2}{3} k_{SGS} \delta_{ij}, \tag{12}$$

where μ_t is the turbulent viscosity and k_{SGS} the turbulent SGS kinetic energy. In this study, the last term is neglected since it is not present in the sub grid model. According to the Eqs. (11) and (12), the mechanical term is given by,

$$P_m = 2(\mu + \mu_t) \left(S_{ij} - \frac{1}{3} S_{ll} \delta_{ij} \right) S_{ij}. \tag{13}$$

The mechanical term P_m is explicitly expressed as resolved quantities in Eq. (13).

Thermal loss P_q

Assuming that the heat flux follows the Fourier law,

$$q_i = -\lambda \frac{\partial \widetilde{T}}{\partial x_i}, \tag{14}$$

the turbulent flux is related a turbulent diffusivity λ_t [37],

$$q^t_i = -\lambda_t \frac{\partial \widetilde{T}}{\partial x_i}. \tag{15}$$

According to the Eqs. (14) and (15), P_q is given by,

$$P_q = \frac{(\lambda + \lambda_t)}{T} \frac{\partial \widetilde{T}}{\partial x_i} \frac{\partial \widetilde{T}}{\partial x_i}. \tag{16}$$

The thermal contribution P_q is also explicitly expressed as resolved quantities in Eq. (16).

Sensitivity of the losses to the turbulent injection

The time averaged losses map, i.e, $\overline{P_m}$ and $\overline{P_q}$ are shown on Fig. 17. The majority of the losses is produced in the boundary layer and the wake. The mechanical contribution is superior to the thermal one. By injecting turbulence at the inlet, the losses produced are overall dramatically increased. The losses are then integrated over the domain volume and normalized by the total enthalpy flux at the inlet defined as $F_{ht} = Q_m * C_p * T_{t1}$ in Table 5 where C_p is the heat capacity. The integrated mechanical term dominates the loss production within the global volume. The integrated thermal term is low because the boundary conditions are adiabatic and does not impose strong temperature gradient. For the turbulent case, the losses produced are more important due to the activation of the turbulent viscosity by injecting freestream turbulence at the inlet.
To evaluate the losses produced by each zone of the domain, the losses are integrated in 5 local volumes V_{local} of the domain. The local volume are displayed in Fig. 18. The wake

Copyright © 2018 by ASME

CASE	Contribution of $\int_V \overline{P_m} dV$ with respect to F_{ht}	Contribution of $\int_V \overline{P_q} dV$ with respect to F_{ht}	Overall contribution of the losses with respect to F_{ht}
LAMINAR	1.94 %	0.12 %	2.06 %
TURBULENT	2.53 %	0.16 %	2.69 %
RELATIVE DIFFERENCE	+ 30 %	+ 33 %	+ 31 %

TABLE 5: Global integration of the losses normalized by the total enthalpy flux at the inlet F_{ht}.

is extracted from the computation downstream the trailing edge when the magnitude of the vorticity satisfies $w < w_{crit}$ where $w_{crit} = 0.01 w_{max}$, a threshold value determined with the maximum of the vorticity w_{max} downstream the blade. Only the mechanical term P_m is integrated and investigated since it dominates the losses. Table 6 sums up the contribution of each zone for the turbulent injection case and the loss production is compared to the laminar case. Note that the inlet volume is not taken into account to compute the contributions since the inlet dissipation is not induced by the blade. The boundary layer on the blade produces the most of the losses. The turbulent boundary layer produces more losses than the laminar one. The second contributors of the loss production are the wake and the inlet domain.

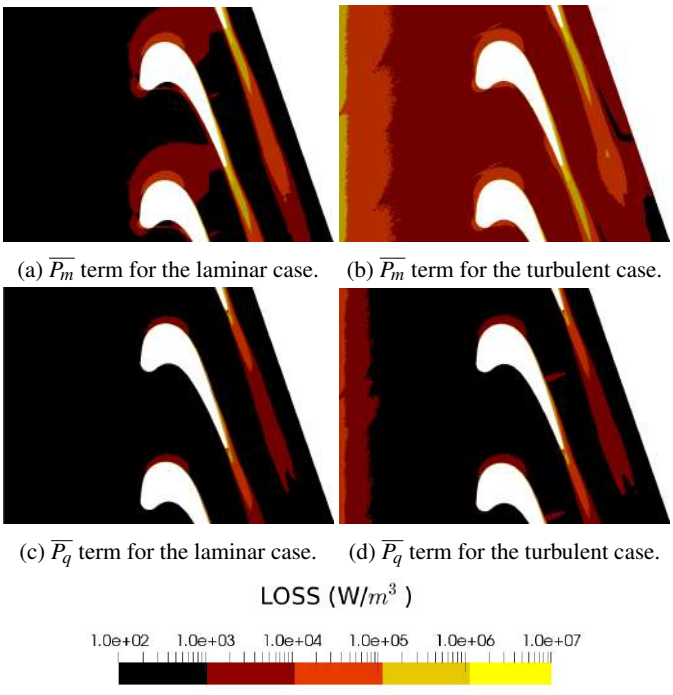

(a) $\overline{P_m}$ term for the laminar case. (b) $\overline{P_m}$ term for the turbulent case.

(c) $\overline{P_q}$ term for the laminar case. (d) $\overline{P_q}$ term for the turbulent case.

FIGURE 17: Loss contributions within the flow. Laminar case are plotted on (a) and (c) and turbulent case on (b) and (d).

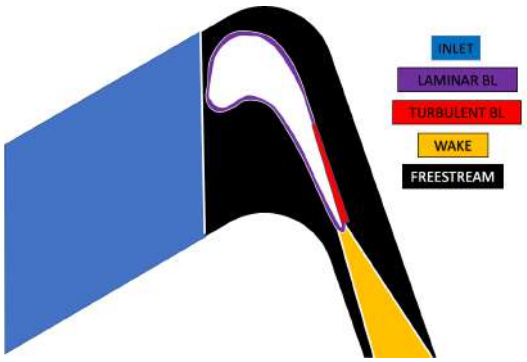

FIGURE 18: Local control volume for integration of the losses.

	Contribution of $\int_V \overline{P_m} dV$ with respect to F_{ht}		Contribution of $\int_V \overline{P_m} dV$ with respect to the total losses	
CASE	**LAMINAR**	**TURBULENT**	**LAMINAR**	**TURBULENT**
INLET	0 %	0.39 %	-	-
FREESTREAM	0.18 %	0.31 %	10 %	8 %
BOUNDARY LAYER	1.45 %	1.60 %	70 %	74 %
LAMINAR BL	0.60 %	0.69 %	29 %	32 %
TURBULENT BL	0.85 %	0.91 %	41 %	42 %
WAKE	0.385 %	0.39 %	20 %	18 %

TABLE 6: Summary of the integrated loss in each zone normalized by the total enthalpy flux at the inlet F_{ht}. The contribution of each zone on the overall loss produced is computed for the laminar and turbulent case.

Within the inlet domain, the losses correspond only to the turbulent dissipation because the time averaged velocity field injecting at the inlet is uniform. That is the reason why there is no loss produced for the laminar injection case. The distribution of the losses are very similar to high pressure turbine numerical studies [35, 38]. Injecting turbulence at the inlet affects the most the freestream flow by the turbulent dissipation. The freestream turbulence impacts also the losses produced in the laminar and turbulent boundary layer.

To sum up this section, the method of SLA is used to identify the loss location production within the flow. The integrated mechanical term dominates the integrated thermal term within the domain. Injecting freestream turbulence at the inlet changes the distribution of the loss map and increases the loss production.

Copyright © 2018 by ASME

CONCLUSION

In this paper, the effect of the inlet turbulent injection is studied on a high pressure loaded blade with separation. The freestream turbulence injected as fluctuations on the mean flow at the inlet propagates up to the leading edge and affect strongly the boundary layer. The boundary layer is more resistant to the separation which reduces the bubble size on the pressure side. Then, the mass flow distribution in a passage section is affected and increased in the near pressure side region. The supersonic pocket on the suction side is then moved upstream with the shock position. At the end, the pressure distribution on the blade wall is strongly affected and recovers the experimental results. This study shows that one side of the blade can not be predicted without the other side.

The losses were first measured with loss coefficients and give a good agreement with the experiment. The loss prediction is improved if turbulence is injected at the inlet. Then, the losses were identified within the flow with the Second Law Analysis method. The entropy source term are found to be located mainly in the boundary layer and in the wake of the blade. The turbulent boundary layer produces more losses than the laminar one. The injection of turbulence at the inlet increases the global loss produced within the flow and affects the loss map.

Future investigations are needed to evaluate the contribution of the sub-grid turbulent kinetic energy on the separation bubble and on the flow structure. The contribution of the sub-grid scale modelling on the entropy source terms needs also to be evaluated.

ACKNOWLEDGMENT

The authors gratefully acknowledge the CASCADE project for funding this study. The computations were run using the CPU resources of GENCI-IDRIS under the allocation 2017-x20172a6074. Special thanks to all contributors of the AITEB-2 consortium funded by Europe, FP6, contract number "AST4-CT-2005-516113", for providing the experimental results.

REFERENCES

[1] J.D. Denton. Loss mechanisms in turbomachines. *Journal of turbomachinery*, 115:621–656, 1993.

[2] Schiffer Haselbach. Aerothermal investigations on turbine endwalls and blades(aiteb). In *ASME. Turbo Expo: Power for Land, Sea, and Air*, volume 3, pages 67–76, Vienna, Austria, 2004.

[3] H. Schlichting. *Boundary layer theory*. McGraw-Hill, New York, 1955.

[4] Jacob Zilli, David M. Sutton, and Philippe Lavoie. Effect of freestream turbulence on laminar separation bubbles and flow transition on an sd7003 airfoil at low reynolds numbers. In *55th AIAA Aerospace Sciences Meeting*, Stockholm, Sweden, 08 2017.

[5] Sebastian Burgmann and W Schrder. Investigation of the vortex induced unsteadiness of a separation bubble via time-resolved and scanning piv measurements. *Experiments in Fluids*, 45:675–691, 10 2008.

[6] Daniele Cappelli and Nagi N. Mansour. *Performance of Reynolds Averaged Navier-Stokes Models in Predicting Separated Flows: Study of the Hump Flow Model Problem*. American Institute of Aeronautics and Astronautics, 2017/10/25 2013.

[7] Leschziner S. Lardeau. Unsteady rans modelling of wake-blade interaction: computational requirements and limitations. *Computer & Fluids*, 34:3–21, 2005.

[8] Sandberg Wheeler A.P.S. and al. Direct numerical simulations of a high-pressure turbine vane. *Journal of Turbomachinery*, 138:1–23, 2016.

[9] Zaki et al. Direct numerical simulations of transition in a compressor cascade: the influence of free-stream turbulence. *Journal of Fluid Mechanics*, 665:5798, 2010.

[10] P. Sagaut. *Large Eddy Simulation for incompressible flows*. Scientific computation series. Springer-Verlag, 2000.

[11] K. Mahesh, G. Constantinescu, and P. Moin. A numerical method for large-eddy simulation in complex geometries. *Journal of computational physics*, 197(1):215–240, 2004.

[12] T. Poinsot and D. Veynante. *Theoretical and Numerical Combustion*. R.T. Edwards, 2nd edition, 2005.

[13] Ali Uzun and Mujeeb R Malik. Wall-resolved large-eddy simulation of flow separation over nasa wall-mounted hump. In *55th AIAA Aerospace Sciences Meeting*, page 0538, 2017.

[14] Francois Cadieux, Julian A. Domaradzki, Taraneh Sayadi, and Sanjeeb Bose. Direct numerical simulation and large eddy simulation of laminar separation bubbles at moderate reynolds numbers. *Journal of Fluids Engineering*, 136(6):060902, 04 2014.

[15] T. Schønfeld and M. Rudgyard. Steady and unsteady flows simulations using the hybrid flow solver avbp. *AIAA Journal*, 37(11):1378–1385, 1999.

[16] W. Sturm and L. Fottner. The high-speed cascade wind-tunnel of the german armed forces university munich. In *8th Symposium on Measuring Techniques for Transonic and Supersonic Flows in Cascades and Turbomachines*, Genova, Italy, October 1985.

[17] R. A. Gomes and R. Niehuis. Film cooling effectiveness measurements with periodic unsteady inflow on higly loaded blades with mean flow separation. In *Proceedings of the ASME Turbo Expo 2009: Power for Sea, Land and Air*, Orlando, Florida, USA, 2009.

[18] F. Duchaine, A. Corpron, L. Pons, V. Moureau, F. Nicoud, and T. Poinsot. Development and assessment of a coupled strategy for conjugate heat transfer with large eddy simulation: Application to a cooled turbine blade. *International Journal of Heat and Fluid Flow*, 30(6):1129–1141, 2009.

Copyright © 2018 by ASME

[19] Homeier et al. Aero-thermodynamic aspects of film cooling in regions of separated flow on the pressure side of a high-lift hpt blade. volume 5, pages 277–286, 2004.

[20] T. Poinsot and S. Lele. Boundary conditions for direct simulations of compressible viscous flows. *Journal of computational physics*, 101(1):104–129, 1992.

[21] A. Smirnov, S. Shi, and I. Celik. Random flow simulations with bubble dynamics model. In *Proceedings of FEDSM00, ASME 2000 Fluids Egineering Division Summer Meeting*, volume FEDSM2000-11215, June 11-15, Boston, Massachusetts, USA, 2000.

[22] R.A. Gomes and R. Niehuis. Film cooling effectiveness measurements with periodic unsteady inflow on highly loaded blades with main flow separation. In *Proceedings of ASME Turbo Expo 2009: Power for Sea, Land and Air*, Orlando, Florida, USA, June 2009.

[23] O. Colin and M. Rudgyard. Development of high-order taylor-galerkin schemes for unsteady calculations. *Journal of computational physics*, 162(2):338–371, 2000.

[24] F. Nicoud and F. Ducros. Subgrid-scale stress modelling based on the square of the velocity gradient. *Flow, Turbulence and Combustion*, 62(3):183–200, 1999.

[25] Pierre Sagaut and Claude Cambon. *Homogeneous turbulence dynamics*, volume 10. Cambridge University Press Cambridge, 2008.

[26] Richard Pichler, Richard D. Sandberg, Gregory Laskowski, and Vittorio Michelassi. High-fidelity simulations of a linear hpt vane cascade subject to varying inlet turbulence. In *Turbo Expo: Power for Land, Sea, and Air*, number 50787, page V02AT40A001, 2017.

[27] Vittorio Michelassi, F Martelli, R Dénos, T Arts, and CH Sieverding. Unsteady heat transfer in stator-rotor interaction by two equation turbulence model. In *ASME 1998 International Gas Turbine and Aeroengine Congress and Exhibition*, page V001T01A058. American Society of Mechanical Engineers, 1998.

[28] Andrew P. S. Wheeler, Anthony M. J. Dickens, and Robert J. Miller. The effect of non-equilibrium boundary layers on compressor performance. In *Turbo Expo: Power for Land, Sea, and Air*, number 50794, page V02BT41A040, 2017.

[29] L. E. Brown. Axial flow compressor and turbine loss coefficients: A comparison of several parameters. *Journal of Engineering for Power*, 94:193–201, 1972.

[30] D.M. Williams, Dmitry Kamenetskiy, and Philippe Spalart. On stagnation pressure increases in calorically perfect, ideal gases. *InternationalJournalofHeatandFluidFlow*, 58:40–53, 04 2016.

[31] A. Bejan. *Entropy Generation through Heat and Fluide Flow*. John Wiley and Sons: New York, NY, USA, 1982.

[32] Yan Jin, Juan Du, Zhiyuan Li, and Hongwu Zhang. Second-law analysis of irreversible losses in gas turbines. *Entropy*, 19(9):470, Sep 2017.

[33] Ries et al. Thermal transport and entropy production mechanisms in a turbulent round jet at supercritical thermodynamic conditions. *Entropy*, 19(8):404, Aug 2017.

[34] Mehdi Safari, M. Reza H. Sheikhi, Mohammad Janbozorgi, and Hameed Metghalchi. Entropy transport equation in large eddy simulation for exergy analysis of turbulent combustion systems. *Entropy*, 12(3):434444, Mar 2010.

[35] Harnieh et al. Sensitivity of large eddy simulations to inflow condition and modeling if applied to a transonic high-pressure cascade vane. In *In Proceedings of the ASME Turbo Expo 2017: Turbine Technical Conference and Exposition*, Charlotte, USA, 2017.

[36] J. Boussinesq. Théorie de l'écoulement tourbillant. *Mém. Présentés par Divers Savants. Acad. Sci. Inst. Fr.*, 23:46–50, 1877.

[37] S. B. Pope. *Turbulent flows*. Cambridge University Press, 2000.

[38] Baniegbhal et al. Development of blade profiles for low-pressure turbine applications. *Journal of Turbomachinery*, 119:531–538, 1997.

Copyright © 2018 by ASME

Appendix F

Sensitivity of resolved turbulence and wall temperature to mesh adaptation process

In the present study, a mesh adaptation process has been performed to accurately refine the regions of mixing between the hot and coolant streams in Chapter 5. To do so, an user-defined mesh is first created. Then, an automatic mesh adaptation is performed based on the entropy source terms obtained from the user-defined mesh to identify regions of strong velocity and temperature gradients and refine these regions. The properties of the two meshes are summarized in Table F.1. To only refine the freestream and the near wall flow regions of the vanes, the

	User-defined mesh	**Adapted mesh**
Cells (millions)	60	73 (+ 21%)
Cells in the cooling system (millions)	35	35 (+ 0%)
Cells in the freestream region (millions)	25	38 (+ 52%)

Table F.1 – Number of cells for the user-defined mesh and adapted mesh.

mesh in the cooling system including coolant pipes and plena is frozen during the mesh adaptation process. As a result, the number of cells only increases in the freestream region by 52%. To localize the refined regions, a view of the two meshes at mid-height of the vanes are provided on Fig. F.1. The mesh is observed to be mainly refined in the near wall flow region of the vanes. The impact of the mesh adaptation on resolved turbulence is now addressed. To quantify the resolution of turbulence on mesh, the criteria of Pope (2000) is studied through the evaluation of M_E defined so that,

$$M_E = \frac{k_{res}}{k_{res} + k_{sgs}}, \tag{F.1}$$

where k_{sgs} is the sub-grid turbulent kinetic energy, $k_{res} = 0.5(u_{rms}^2 + v_{rms}^2 + w_{rms}^2)$ is the resolved turbulent kinetic energy and u_{rms}, v_{rms}, w_{rms} are the RMS of velocity fields. For the above relation, a closure for k_{sgs} is needed. To close k_{sgs}, the

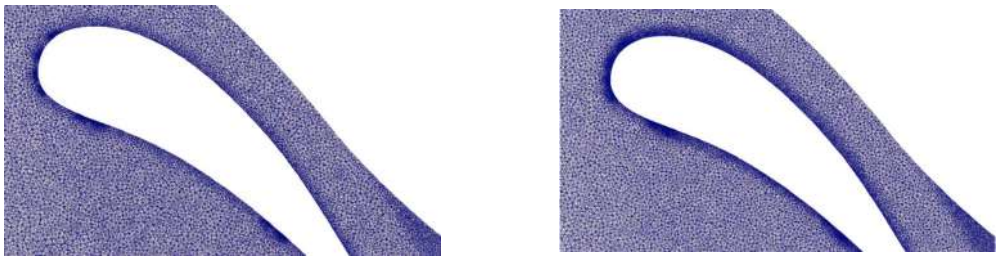

(a) (b)

Figure F.1 – View of user-defined mesh (a) and adapted mesh (b) at mid-height of NGV1.

following relation is used Smagorinsky (1963):

$$\nu_t = C_m V^{\frac{1}{3}} \sqrt{k_{sgs}}, \tag{F.2}$$

where ν_t is the turbulent viscosity, V the node volume and C_m a constant of the model. To operate suitability of LES, near 80% of the turbulence should be resolved on mesh according to Pope (2000). The map of M_E is provided at mid-height of the vanes on Fig. F.2 for the two meshes. To evidence the regions where more than 80% of turbulence is resolved on mesh, an iso-line equal to $M_E = 0.8$ is added to Fig. F.2. For the user-defined mesh, Fig. F.2 (a), turbulence in the

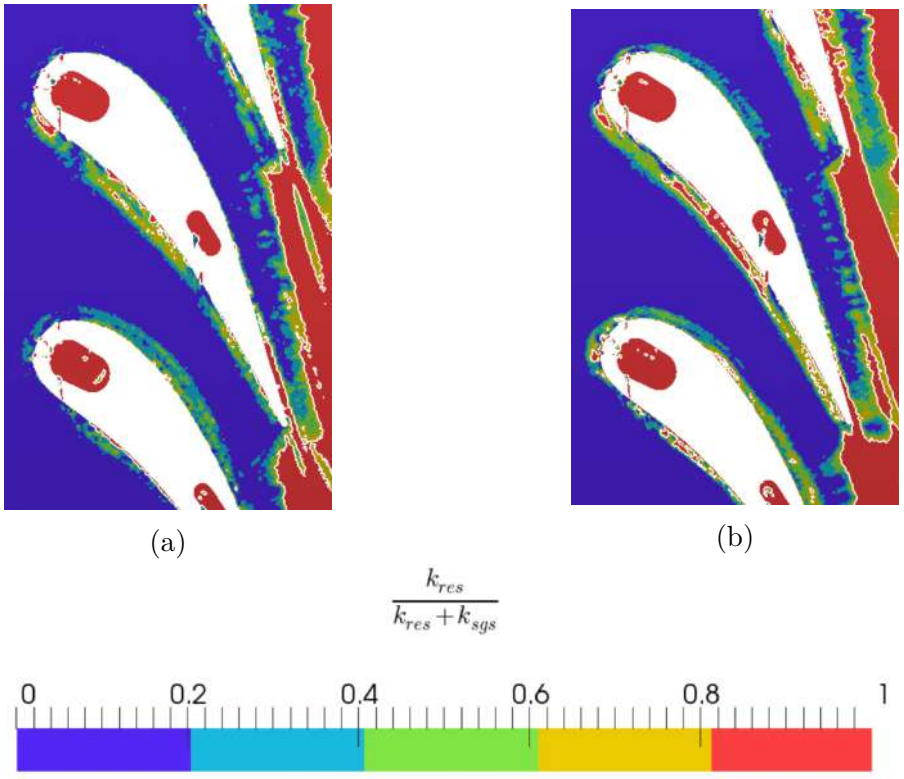

(a) (b)

Figure F.2 – M_E [-] map at mid-height of the vanes. White iso-line represents $M_E = 0.8$. User-defined mesh (a) and adapted mesh (b).

film region of the vanes is clearly under-resolved. Nevertheless in the wakes of the vanes, turbulence is observed to be sufficiently resolved. For the adapted mesh, Fig. F.2 (b), the resolution of turbulence is clearly improved in the film region and locally reaches 80% of the overall turbulence. The resolution of turbulence is also improved in the wakes of the vanes. In the coolant pipes, a good resolution of turbulence is also observed featuring more than 80% of resolution. The impact of the increasing mesh resolution on the prediction of time-averaged adiabatic wall temperature is shown on Fig. F.3. For the user-defined mesh, Fig. F.3 (a), a large

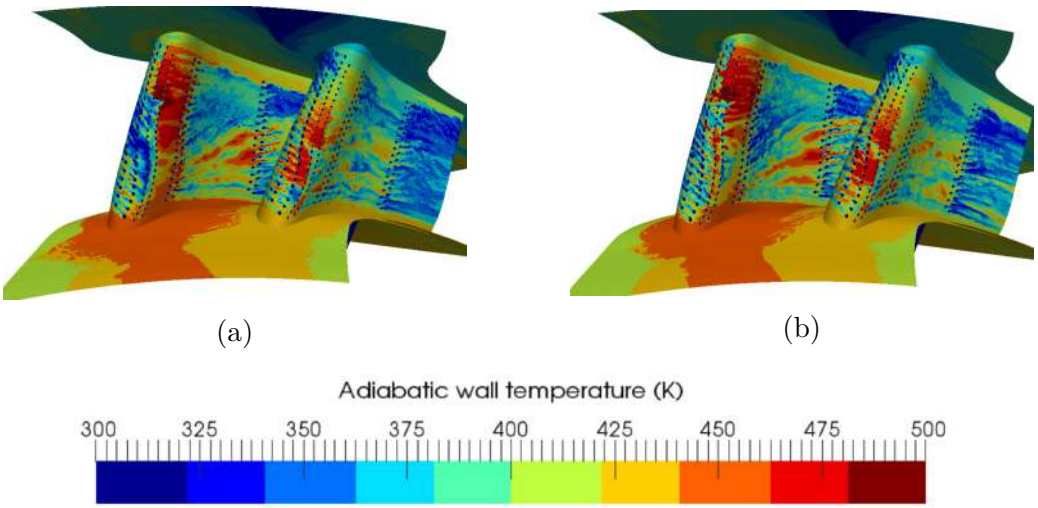

Figure F.3 – Impact of mesh adaptation on adiabatic wall temperature T_{wall} $[K]$. User-defined mesh (a) and adapted mesh (b).

range of temperature is observed on the vane surfaces and local patterns of hot and cold temperature are observed. For the adapted mesh, Fig. F.3 (b), the wall temperature is more segregated compared to the user-defined mesh. Indeed, finer patterns of hot and cold temperatures are observed on the vane surfaces because a finer turbulence is resolved on the adapted mesh.

As a consequence of the previous discussion, the mesh adaptation process has improved the resolution of turbulence in the film region of the vanes. Although turbulence resolution remains locally inferior to 80% around the vanes, the adapted mesh allows to capture very fine patterns of hot and cold temperature on the vane surfaces.

Bibliography

Honda engine from general electric. URL https://www.gehonda.com/engine/explore.html.

Dart engine from rolls-royce. URL https://airandspace.si.edu/collection-objects/rolls-royce-dart-mk-520-turboprop-engine-cutaway.

Ardiden egnine from safran helicopter engine. URL https://www.youtube.com/watch?v=zpHJOYHtnTo.

On board a sustainbale future report, 2016. URL https://www.icao.int/environmental-protection/Documents/ICAO%20Environmental%20Report%202016.pdf.

Global market forecast report, 2018. URL https://www.airbus.com/content/dam/corporate-topics/financial-and-company-information/GMF.pdf.

B. Abu-Ghannam and R. Shaw. Natural transition of boundary layers—the effects of turbulence, pressure gradient, and flow history. Journal of Mechanical Engineering Science, 22(5):213–228, 1980.

P. Aillaud. Simulations aux grandes echelles pour le refroidissement d'aubages de turbine haute-pression. PhD thesis, 2017. URL http://www.theses.fr/2017INPT0108. These de doctorat dirigee par Gicquel, Laurent et Duchaine, Florent Energetique et Transferts Toulouse, INPT 2017.

D. Ainley, G. Mathieson, and A. R. C. Ministry of Supply. An Examination of the Flow and Pressure Losses in Blade Rows of Axial-flow Turbines. ARC technical report. H.M. Stationery Office, 1951. URL https://books.google.fr/books?id=VujttgAACAAJ.

J. Amecke. Evaluation of wake measurements in twodimensional cascades. AVA, 1967.

L. Andrei, L. Innocenti, A. Andreini, B. Facchini, and L. Winchler. Film cooling modeling for gas turbine nozzles and blades: Validation and application. Journal of Turbomachinery, 139:011004–011004–9, 2016. URL http://dx.doi.org/10.1115/1.4034233.

A. Andreini, R. Da Soghe, B. Facchini, L. Mazzei, S. Colantuoni, and F. Turrini. Local source based cfd modeling of effusion cooling holes: Validation and application to an actual combustor test case. Journal of Engineering for Gas Turbines and Power, 136(1):011506–011506–11, 10 2013. URL http://dx.doi.org/10.1115/1.4025316.

A. Arena and T. Mueller. Laminar separation, transition, and turbulent reattachment near the leading edge of airfoils. AIAA journal, 18(7):747–753, 1980.

M. S. Attia, S. Manoharan, V. Shulman, and L. Lachmann. Elimination of the horse shoe vortex in axial turbine vane cascades via airfoil shape optimization. In 49th AIAA/ASME/SAE/ASEE Joint PropulsionConference, page 3952. 2013.

T. auf dem Kampe and S. Volker. A model for cylindrical hole film cooling part ii: Model formulation, implementation and results. Journal of Turbomachinery, 134(6):061011, 2012.

T. Bacci, G. Caciolli, B. Facchini, L. Tarchi, C. Koupper, and J.-L. Champion. Flowfield and temperature profiles measurements on a combustor simulator dedicated to hot streaks generation. In ASME Turbo Expo 2015: Turbine Technical Conference and Exposition, pages V05CT17A001–V05CT17A001. American Society of Mechanical Engineers, 2015.

T. Bacci, R. Becchi, A. Picchi, and B. Facchini. Adiabatic effectiveness on high-pressure turbine nozzle guide vanes under realistic swirling conditions. Journal of Turbomachinery, 141(1):011009, 2019.

J. Bardina, J. H. Ferziger, and W. C. Reynolds. Improved turbulence models based on large-eddy simulation of homogeneous, incompressible, turbulent flows. Technical Report TF-19, Department of Mechanical Engineering, Stanford University, 1983.

C. Battisti, F. Kost, N. Atkins, W. Playford, M. Orain, G. Caciolli, L. Tarchi, M. Mersinligil, and J. Raffel. Full aerothermal combustor turbine interaction research. Proceedings of 2nd EASN WORKSHOP on Flight Physics, 2012.

A. Bejan. Entropy Generation through Heat and Fluide Flow. John Wiley and Sons: New York, NY, USA, 1982.

A. Bejan. Entropy generation minimization: the method of thermodynamic optimization of finite-size systems and finite-time processes. CRC press, 2013.

R. Bizzari. Aerodynamic and thermal modelling of effusion cooling in LES. Phd thesis, Université Fédérale de Toulouse, INPT - Ecole doctorale MEGeP., 11 2018.

R. Bizzari, M. Férand, A. Dauptain, G. Staffelbach, S. Richard, J.-D. Mueller, T. Ogier, G. Exilard, and F. Nicoud. Mesh local refinement to enhance effusion cooling models; invited conference. In ERCOFTAC, edi-

tor, 12th International Symposium on Engineering Turbulence Modelling and Measurements (ETMM12), Montpellier (France), 9 2018a.

R. Bizzari, D. Lahbib, A. Dauptain, F. Duchaine, L. Gicquel, and F. Nicoud. A thickened-hole model for large eddy simulations over multiperforated liners. Flow Turbulence and Combustion, Online First Articles:1–13, 2018b. ISSN 1573-1987 (Online). doi: 10.1007/s10494-018-9909-3. URL https://doi.org/10.1007/s10494-018-9909-3.

R. Bizzari, D. Lahbib, A. Dauptain, F. Duchaine, S. Richard, and F. Nicoud. Low order modeling method for assessing the temperature of the multi-perforated plates. Submitted to International Journal of Heat and Mass Transfer, 2018c.

H. Blasius. Boundary layers in fluids with small friction. Z. Math. Phys. , 56:1–37, 1908.

J. Bodart and J. Larsson. Wall-modeled large eddy simulation in complex geometries with application to high-lift devices. Annual Research Briefs, Center for Turbulence Research, Stanford University, pages 37–48, 2011.

J. P. Bons, C. D. MacArthur, and R. B. Rivir. The effect of high free-stream turbulence on film cooling effectiveness. Journal of Turbomachinery, 118(4): 814–825, 1996.

J. Boussinesq. Théorie de l'écoulement tourbillant. Mém. Présentés par Divers Savants. Acad. Sci. Inst. Fr., 23:46–50, 1877.

M. P. Boyce. 2 - theoretical and actual cycle analyses. In Gas Turbine Engineering Handbook (Fourth Edition), pages 89 – 137. Butterworth-Heinemann, Oxford, fourth edition edition, 2012. ISBN 978-0-12-383842-1. doi: https://doi.org/10.1016/B978-0-12-383842-1.00002-0. URL http://www.sciencedirect.com/science/article/pii/B9780123838421000020.

P. Bradshaw. The turbulence structure of equilibrium boundary layers. Journal of Fluid Mechanics, 29(4):625–645, 1967.

D. Brandt and R. Wesorick. Ge gas turbine design philosophy. GER-3434, General Electric, 1994.

L. Brandt, P. Schlatter, and D. S. Henningson. Transition in boundary layers subject to free-stream turbulence. Journal of Fluid Mechanics, 517:167–198, 2004.

L. E. Brown. Axial flow compressor and turbine loss coefficients: A comparison of several parameters. Journal of Engineering for Power, 94:193–201, 1972. doi: 10.1115/1.3445672.

G. Buresti. Notes on the role of viscosity, vorticity and dissipation in incompressible flows. Meccanica, 44(4):469, 2009.

G. Buresti. Elements of fluid dynamics, volume 3. World Scientific Publishing Company, 2012.

S. Burgmann and W. Schroder. Investigation of the vortex induced unsteadiness of a separation bubble via time-resolved and scanning piv measurements. Experiments in Fluids, 45:675–691, 10 2008.

F. Cadieux, J. A. Domaradzki, T. Sayadi, and S. Bose. Direct numerical simulation and large eddy simulation of laminar separation bubbles at moderate reynolds numbers. Journal of Fluids Engineering, 136(6):060902–060902–5, 04 2014.

P. Caron and T. Khan. Evolution of ni-based superalloys for single crystal gas turbine blade applications. Aerospace Science and Technology, 3(8):513–523, 1999.

M. Catchirayer, J.-F. Boussuge, P. Sagaut, M. Montagnac, D. Papadogiannis, and X. Garnaud. Extended integral wall-model for large-eddy simulations of compressible wall-bounded turbulent flows. Physics of Fluids, 30(6), 2018. ISSN 065106. doi: 10.1063/1.5030859.

T. Cebeci and P. Bradshaw. Momentum Transfer in Boundary Layers. McGraw-Hill, New-York, 1977.

P. Chassaing. Mécanique des fluides, Éléments d'un premier parcours. Cépaduès-Éditions, 2000.

R. Ciorciari, T. Schubert, and R. Niehuis. Numerical investigation of secondary flow and loss development in a low-pressure turbine cascade with divergent endwalls. International Journal of Turbomachinery, Propulsion and Power, 3:5, 02 2018. doi: 10.3390/ijtpp3010005.

W. Colban, A. Gratton, K. Thole, and M. Haendler. Heat transfer and film-cooling measurements on a stator vane with fan-shaped cooling holes. Journal of Turbomachinery, 128(1):53–61, 2006.

O. Colin and M. Rudgyard. Development of high-order taylor-galerkin schemes for unsteady calculations. Journal of computational physics, 162(2):338–371, 2000.

E. Collado. Impact of the unsteady aerothermal environment on the turbine blades temperature. PhD thesis, Université de Toulouse - Institut National Polytechnique de Toulouse - Energétique et Transferts, 2012. PhD.

S. Cubeda, L. Mazzei, T. Bacci, and A. Andreini. Impact of predicted combustor outlet conditions on the aerothermal performance of film-cooled high pressure turbine vanes. Journal of Engineering for Gas Turbines and Power, 141(5): 051011, 2019.

N. Cumpsty and J. H. Horlock. Averaging non-uniform flow for a purpose. Journal of Turbomachinery-transactions of The Asme - J TURBOMACH-T ASME, 128, 01 2006. doi: 10.1115/1.2098807.

E. Curtis, H. Hodson, M. Banieghbal, J. Denton, R. Howell, and N. Harvey. Development of blade profiles for low-pressure turbine applications. Journal of Turbomachinery, 119(3):531–538, 1997.

C. Dapogny, C. Dobrzynski, and P. Frey. Three-dimensional adaptive domain remeshing, implicit domain meshing, and applications to free and moving boundary problems. Journal of computational physics, 262:358–378, 2014.

G. Daviller, M. Brebion, P. Xavier, G. Staffelbach, J.-D. Müller, and T. Poinsot. A mesh adaptation strategy to predict pressure losses in les of swirled flows. Flow, Turbulence and Combustion, 99(1):93–118, 2017.

W. Dawes. A comparison of zero and one equation turbulence modelling for turbomachinery calculations. In ASME 1990 International Gas Turbine and Aeroengine Congress and Exposition, pages V001T01A093–V001T01A093. American Society of Mechanical Engineers, 1990.

M. Deinert and J. Hourmouziadis. Film cooling in unsteady flow with separation bubble. In ASME Turbo Expo 2004: Power for Land, Sea, and Air, pages 55–66. American Society of Mechanical Engineers, 2004.

J. Denton. Loss mechanisms in turbomachines. Journal of turbomachinery, 115: 621–656, 1993.

J. Denton and L. Xu. The trailing edge loss of transonic turbine blades. Journal of Turbomachinery, 112(2):277–285, 1990.

J. Dickhoff, K. Kusterer, S. K. Bhaskar, and D. Bohn. Cfd simulations for film cooling holes: Comparison between different isotropic and anisotropic eddy viscosity models. (51081):V05AT12A008–, 2018. URL http://dx.doi.org/10.1115/GT2018-75543.

S. Dixon and C. Hall. Chapter 1 - Introduction: Basic Principles. Butterworth-Heinemann, Boston, sixth edition edition, 2010. ISBN 978-1-85617-793-1. doi: https://doi.org/10.1016/B978-1-85617-793-1.00001-8. URL http://www.sciencedirect.com/science/article/pii/B9781856177931000018.

J. Donea and A. Huerta. Finite Element Methods for Flow Problems. John Wiley & Sons Inc, New York, 2003.

E. R. V. Driest. Turbulent boundary layer in compressible fluids. J. Aeronaut. Sci. , 18(3):145–160, 216, 1951.

U. Drost and A. Bocs. Investigation of detailed film cooling effectiveness and heat transfer distributions on a gas turbine airfoil. In ASME 1998 International Gas Turbine and Aeroengine Congress and Exhibition, pages V004T09A003–V004T09A003. American Society of Mechanical Engineers, 1998.

F. Duchaine, A. Corpron, L. Pons, V. Moureau, F. Nicoud, and T. Poinsot. Development and assessment of a coupled strategy for conjugate heat transfer with large eddy simulation: Application to a cooled turbine blade. Int. J. Heat Fluid Flow , 30:1129–1141, 2009a.

F. Duchaine, A. Corpron, L. Pons, V. Moureau, F. Nicoud, and T. Poinsot. Development and assessment of a coupled strategy for conjugate heat transfer with large eddy simulation: Application to a cooled turbine blade. International Journal of Heat and Fluid Flow, 30(6):1129–1141, 2009b.

F. Duchaine, J. Dombard, L. Gicquel, and C. Koupper. Integrated large eddy simulation of combustor and turbine interactions: Effect of turbine stage inlet condition. In ASME Turbo Expo 2017: Turbomachinery Technical Conference and Exposition, pages V02BT41A014–V02BT41A014. American Society of Mechanical Engineers, 2017.

T. E. Dyson, D. G. Bogard, and S. D. Bradshaw. Evaluation of cfd simulations of film cooling performance in the showerhead region of a turbine vane including conjugate effects. (45233):1977–1986, 2012. URL http://dx.doi.org/10.1115/IMECE2012-88386.

S. V. Ekkad, J.-C. Han, and H. Du. Detailed film cooling measurements on a cylindrical leading edge model: effect of free-stream turbulence and coolant density. In ASME 1997 International Gas Turbine and Aeroengine Congress and Exhibition, pages V003T09A032–V003T09A032. American Society of Mechanical Engineers, 1997.

H. Emmons. The laminar-turbulent transition in a boundary layer-part i. Journal of the Aeronautical Sciences, 18(7):490–498, 1951.

V. Eswaran and S. B. Pope. Direct numerical simulations of the turbulent mixing of a passive scalar. Phys. Fluids , 31:506, 1988.

A. Favre. Statistical equations of turbulent gases. In Problems of hydrodynamics and continuum mechanics, pages 231–266. SIAM, Philadelphia, 1969.

M. Fiore. Influence of inter-disc cavity flow on turbine aerodynamics. Phd thesis, Universite de Toulouse - Institut Superieur de l'Aeronautique et de l'Espace (ISAE), 5 2019.

R. Fransen. LES based aerothermal modeling of turbine blade cooling systems. PhD thesis, 2013. URL http://www.theses.fr/2013INPT0037. These de doctorat dirigee par Gicquel, Laurent et Arts, Tony Energetique et Transferts Toulouse, INPT 2013.

T. F. Fric and A. Roshko. Vortical structure in the wake of a transverse jet. J. Fluid Mech. , 279:1–47, 1994.

E. Garnier, N. Adams, and P. Sagaut. Large Eddy Simulation for Compressible Flows. 01 2009. doi: 10.1007/978-90-481-2819-8.

M. Gaster. The structure and behaviour of laminar separation bubbles. TIL, 1967.

T. Germain, M. Nagel, and R. Baier. Visualisation and quantification of secondary flows: Application to turbine bladings with 3d-endwalls. In Paper ISAIF8-0098, Proc. of the 8th Int. Symposium on Experimental and Computational Aerothermodynamics of Internal Flows, Lyon. Citeseer, 2007.

M. Germano. Turbulence: the filtering approach. J. Fluid Mech. , 238:325–336, 1992.

L. Y. M. Gicquel, G. Staffelbach, and T. Poinsot. Large eddy simulations of gaseous flames in gas turbine combustion chambers. Prog. Energy Combust. Sci. , 38 (6):782 – 817, 2012.

R. Goldstein, E. Eckert, and F. Burggraf. Effects of hole geometry and density on three-dimensional film cooling. International Journal of heat and mass transfer, 17(5):595–607, 1974.

R. J. Goldstein. Film cooling. In Advances in Heat Transfer, volume 7, pages 321–379. Academic Press, New York, 1971.

R. Gomes and R. Niehuis. Film cooling effectiveness measurements with periodic unsteady inflow on highly loaded blades with main flow separation. In Proceedings of ASME Turbo Expo 2009: Power for Sea, Land and Air, Orlando, Florida, USA, June 2009.

R. A. Gomes and M. Araujo. On Aerothermal Effects of Film Cooling on Turbine Blades with Flow Separation. Verlag Dr. Hut, 2010.

R. A. Gomes and R. Niehuis. Film cooling effectiveness measurements with periodic unsteady inflow on highly loaded blades with main flow separation. Journal of Turbomachinery, 133(2):021019, 2011.

R. A. Gomes and R. Niehuis. Film cooling on highly loaded blades with main flow separation—part i: Heat transfer. Journal of Turbomachinery, 135(1):011043, 2013.

N. Gourdain, L. Gicquel, M. Montagnac, O. Vermorel, M. Gazaix, G. Staffelbach, M. Garcia, J. Boussuge, and T. Poinsot. High performance parallel computing of flows in complex geometries: I. methods. Comput. Sci. Disc., 2:015003, 2009a.

N. Gourdain, L. Gicquel, G. Staffelbach, O. Vermorel, F. Duchaine, J.-F. Boussuge, and T. Poinsot. High performance parallel computing of flows in complex geometries - part 2: applications. Comput. Sci. Disc., 2(1):28pp, January-December 2009b.

V. Granet, O. Vermorel, T. Leonard, L. Gicquel, , and T. Poinsot. Comparison of nonreflecting outlet boundary conditions for compressible solvers on unstructured grids. AIAA J. , 48(10):2348–2364, 2010.

Greitzer. Internal flow: Concepts and Applications. Cambridge University Press, 2004.

M. Gritsch, A. Schulz, and S. Wittig. Adiabatic wall effectiveness measurements of film-cooling holes with expanded exits. Journal of Turbomachinery, 120(3): 549–556, 1998.

T. Grosnickel. Large Eddy Simulations to predict internal turbine blade cooling flows. Phd thesis, Institut National Polytechnique de Toulouse - Ecole doctorale MEGeP, 2 2019.

F. Hammer, N. D. Sandham, and R. D. Sandberg. The influence of different wake profiles on losses in a low pressure turbine cascade. International Journal of Turbomachinery, Propulsion and Power, 3(2):10, 2018.

J. Han, S. Dutta, and S. Ekkad. Gas Turbine Heat Transfer and Cooling Technology. Taylor & Francis, New York, NY, USA, 2000.

J.-C. Han and S. Ekkad. Recent development in turbine blade film cooling. International Journal of Rotating Machinery, 7(1):21–40, 2001.

J.-C. Han and A. Rallabandi. Turbine blade film cooling using psp technique. Frontiers in Heat and Mass Transfer (FHMT), 1(1), 2010.

T. Handa, Y. Miyazato, M. Masuda, and K. Matsuo. Formation of multiple shocklets in a transonic diffuser flow. Shock waves, 11:423 – 430, 1999.

L. Harnieh, Gicquel and F. Duchaine. Sensitivity of large eddy simulations to inflow condition and modeling if applied to a transonic high-pressure cascade vane. In In Proceedings of the ASME Turbo Expo 2017: Turbine Technical Conference and Exposition, Charlotte, USA, 2017.

M. Harnieh, L. Gicquel, and F. Duchaine. Large eddy simulations of a highly loaded transonic blade with separated flow - invited conference. In Turbomachinery Technical Conference and Exposition 2018, pages GT2018–75730, Oslo, Norway, 6 2018. ASME International Gas Turbine Institute.

S. Harrison. Secondary loss generation in a linear cascade of high-turning turbine blades. Journal of Turbomachinery, 112(4):618–624, 1990.

F. Haselbach and P. Schiffer. Aiteb - an european research project on aero-thermodynamics of turbine endwalls and blades. Int. J. of Therm. Sci. , 13 (2):97–108, 2007.

L. Homeier, E. Lutum, E. Janke, and F. Haselbach. Aero-thermodynamic aspects of film cooling in regions of separated flow on the pressure side of a high-lift hpt blade. In ASME Turbo Expo 2004: Power for Land, Sea, and Air, pages 277–286. American Society of Mechanical Engineers Digital Collection, 2004.

J. Horlock, D. Watson, and T. Jones. Limitations on gas turbine performance imposed by large turbine cooling flows. Journal of engineering for gas turbines and power, 123(3):487–494, 2001.

J. H. Horlock. Advanced gas turbine cycles: a brief review of power generation thermodynamics. Elsevier, 2013.

L. Howarth. Concerning the effect of compressibility on lam inar boundary layers and their separation. Proceedings of the Royal Society of London. Series A. Mathematical and Physical Sciences, 194(1036):16–42, 1948.

A. R. Howell. Fluid dynamics of axial compressors. Proceedings of the Institution of Mechanical Engineers, 153(1):441–452, 1945. doi: 10.1243/PIME_PROC_1945_153_049_02. URL https://doi.org/10.1243/PIME_PROC_1945_153_049_02.

P. G. Huang and P. Bradshaw. Law of the wall for turbulent flows in pressure gradients. AIAA J. , 33(4):624–632, April 1995.

P. G. Huang and G. N. Coleman. Van driest transformation and compressible wall-bounded flows. AIAA J. , 32(10):2110–2113, 1994.

Y. Jin, J. Du, Z. Li, and H. Zhang. Second-law analysis of irreversible losses in gas turbines. Entropy, 19(9):470, Sep 2017. ISSN 1099-4300. doi: 10.3390/e19090470. URL http://dx.doi.org/10.3390/e19090470.

M. Kampa and E. Castanas. Human health effects of air pollution. Environmental pollution, 151(2):362–367, 2008.

F. Kock and H. Herwig. Local entropy production in turbulent shear flows: a high-reynolds number model with wall functions. International journal of heat and mass transfer, 47(10-11):2205–2215, 2004.

A. N. Kolmogorov. The local structure of turbulence in incompressible viscous fluid for very large reynolds numbers. C. R. Acad. Sci. , USSR, 30:301, 1941.

C. Koupper. Unsteady multi-component simulations dedicated to the impact of the combustion chamber on the turbine of aeronautical gas turbines. PhD thesis, 2015. URL http://www.theses.fr/2015INPT0035.

C. Koupper, G. Caciolli, L. Gicquel, F. Duchaine, G. Bonneau, L. Tarchi, and B. Facchini. Development of an engine representative combustor simulator dedicated to hot streak generation. Journal of Turbomachinery, 136(11):111007–111007–10, 2014.

C. Koupper, T. Poinsot, L. Gicquel, and F. Duchaine. Compatibility of Characteristic Boundary Conditions with Radial Equilibrium in Turbomachinery Simulations. AIAA Journal, 52, Dec. 2014. doi: 10.2514/1.J052915.

A. Krumme, M. Tegler, and G. S. Design, integration and operation of a rotating combustor-turbine-interaction test rig within the scope of ec fp7 project factor. Proceedings of 13th European Conference on Turbomachinery Fluid Dynamics & Thermodynamics ETC13, pages 1–13, 2019.

K. N. Kumar and M. Govardhan. Secondary flow loss reduction in a turbine cascade with a linearly varied height streamwise endwall fence.(research article)(report). International Journal of Rotating Machinery, 2011.

D. Lahbib. Modelisation aerodynamique et thermique des multiperforations en LES. PhD thesis, Universitee Montpellier II, 2015.

D. Laidlaw and A. Vilanova. New developments in the visualization and processing of tensor fields. Mathematics and visualization. Springer, Germany, 2012. ISBN 978-3-642-27342-1. doi: 10.1007/978-3-642-27343-8.

N. Lamarque. Schémas numériques et conditions limites pour la simulation aux grandes échelles de la combustion diphasique dans les foyers d'hélicoptère. Phd thesis, INP Toulouse, 2007.

D. Lee, S. Kawai, T. Nonomura, M. Anyoji, H. Aono, A. Oyama, K. Asai, and K. Fujii. Mechanisms of surface pressure distribution within a laminar separation bubble at different reynolds numbers. Phys. Fluids, 93601(10.1063/1.4894427): 26, 2014.

J. Leggett. Detailed investigation of loss prediction of an axial compressor cascade at off-design conditions in the presence of incident free-stream disturbances using large eddy simulations. PhD thesis, University of Southampton, 2018.

S. Lele. Compact finite difference schemes with spectral like resolution. Journal of computational physics, 103:16–42, 1992.

D. Lengani, D. Simoni, R. Pichler, R. Sandberg, V. Michelassi, and F. Bertini. Identification and quantification of losses in a lpt cascade by pod applied to les data. International Journal of Heat and Fluid Flow, 70:28 – 40, 2018. ISSN 0142-727X. doi: https://doi.org/10.1016/j.ijheatfluidflow.2018.01.011. URL http://www.sciencedirect.com/science/article/pii/S0142727X17308573.

J. H. Leylek and R. D. Zerkle. Discrete-jet film cooling: A comparison of computational results with experiments. Journal of Turbomachinery, 116:358–368, 1994.

Y. Li, X. Su, and X. Yuan. The effect of mismatching between combustor and hp vanes on the aerodynamics and heat load in a 1-1/2 stages turbine. Aerospace Science and Technology, 86:78–92, 2019.

D. Lin, X. Yuan, and X. Su. Local entropy generation in compressible flow through a high pressure turbine with delayed detached eddy simulation. Entropy, 19:29, 01 2017. doi: 10.3390/e19010029.

Z. Ling and W. Guoliang. Large eddy simulation on compound angle film cooling of turbine blades. In IEEE 2011 10th International Conference on Electronic Measurement & Instruments, volume 1, pages 282–287. IEEE, 2011.

Y. Liu, X. Sun, V. Sethi, D. Nalianda, Y.-G. Li, and L. Wang. Review of modern low emissions combustion technologies for aero gas turbine engines. Progress in Aerospace Sciences, 94:12 – 45, 2017. ISSN 0376-0421. doi: https://doi.org/10.1016/j.paerosci.2017.08.001. URL http://www.sciencedirect.com/science/article/pii/S037604211630118X.

e. a. Martin Thomas. Comparison of heterogeneous and homogeneous coolant injection models for large eddy simulation of multiperforated liners present in a combustion simulator. In ASME Turbo Expo 2017: Turbomachinery Technical Conference and Exposition. ASME, 2017.

J. D. Mattingly, W. H. Heiser, and D. T. Pratt. Aircraft engine design. American Institute of Aeronautics and Astronautics, 2002.

R. E. Mayle. The role of laminar-turbulent transition in gas turbine engines. Journal of Turbomachinery, 113:509–537, October 1991.

H. Mcdonald. The effect of pressure gradient on the law of the wall in turbulent flow. Journal of Fluid Mechanics, 35(2):311–336, 1969. doi: 10.1017/S0022112069001133.

K. T. McGovern and J. H. Leylek. A detailed analysis of film cooling physics: part ii—compound-angle injection with cylindrical holes. Journal of Turbomachinery, 122(1):113–121, 2000.

D. Mee, N. Baines, M. Oldfield, and T. Dickens. An examination of the contributions to loss on a transonic turbine blade in cascade. Journal of Turbomachinery, 114(1):155–162, 1992.

S. Mendez and F. Nicoud. Adiabatic homogeneous model for flow around a multiperforated plate. AIAA Journal, 46(10):2623–2633, 2008.

F. R. Menter, R. B. Langtry, S. R. Likki, Y. B. Suzen, P. G. Huang, and S. Volker. A correlation-based transition model using local variables—part i: Model formulation. Journal of Turbomachinery, 128(3):413–422, 03 2004. URL http://dx.doi.org/10.1115/1.2184352.

V. Michelassi, F. Martelli, R. Dénos, T. Arts, and C. Sieverding. Unsteady heat transfer in stator-rotor interaction by two equation turbulence model. In ASME 1998 International Gas Turbine and Aeroengine Congress and Exhibition, pages V001T01A058–V001T01A058. American Society of Mechanical Engineers, 1998.

R. J. Miller. Mechanical work potential. In ASME Turbo Expo 2013: Turbine Technical Conference and Exposition. American Society of Mechanical Engineers Digital Collection, 2013.

F. Montomoli, M. Massini, H. Yang, and J. Han. The benefit of high-conductivity materials in film cooled turbine nozzles. International Journal of Heat and Fluid Flow, 34:107–116, 2012.

J. S. Murphy. Some effects of surface curvature on laminar boundary-layer flow. Journal of the Aeronautical Sciences, 20(5):338–344, 1953.

T. New, T. Lim, and S. Luo. Elliptic jets in cross-flow. Journal of fluid mechanics, 494:119–140, 2003.

F. Nicoud and F. Ducros. Subgrid-scale stress modelling based on the square of the velocity gradient. Flow, Turbulence and Combustion, 62(3):183–200, 1999.

N. Odier, M. Sanjose, L. Gicquel, T. Poinsot, S. Moreau, and F. Duchaine. A characteristic inlet boundary condition for compressible, turbulent, multispecies turbomachinery flows. Computers and Fluids, 178:41–55, 2018. doi: 10.1016/j.compfluid.2018.09.014. URL https://doi.org/10.1016/j.compfluid.2018.09.014.

R. Pal. On the gouy–stodola theorem of thermodynamics for open systems. International Journal of Mechanical Engineering Education, 45(2):194–206, 2017.

D. Papadogiannis. Coupled Large Eddy Simulations of combustion chamber-turbine interactions. PhD thesis, 2015. URL http://www.theses.fr/2015INPT0049.

T. Passot and A. Pouquet. Numerical simulation of compressible homogeneous flows in the turbulent regime. J. Fluid Mech. , 181:441–466, 1987.

Y. Peet and S. Lele. Near field of film cooling jet issued into a flat plate boundary layer: Les study. Proceedings of the ASME Turbo Expo, 4, 01 2008. doi: 10.1115/GT2008-50420.

Y. V. Peet. Film cooling from inclined cylindrical holes using Large-Eddy Simulations. Phd thesis, Stanford University, 2006.

G. Persico, P. Gaetani, V. Dossena, G. D'Ippolito, and C. Osnaghi. On the definition of the secondary flow in three-dimensional cascades. Proceedings of the Institution of Mechanical Engineers, Part A: Journal of Power and Energy, 223 (6):667–676, 2009.

M. Pianko and F. Wazelt. Propulsion and energetics panel working group 14 on suitable averaging techniques in non-uniform internal flows. Technical report, ADVISORY GROUP FOR AEROSPACE RESEARCH AND DEVELOPMENT NEUILLY-SUR-SEINE (FRANCE), 1983.

R. Pichler, R. D. Sandberg, G. Laskowski, and V. Michelassi. High-fidelity simulations of a linear hpt vane cascade subject to varying inlet turbulence. In Turbo Expo: Power for Land, Sea, and Air, number 50787, pages V02AT40A001–, 2017.

T. Poinsot and S. Lele. Boundary conditions for direct simulations of compressible viscous flows. Journal of computational physics, 101(1):104–129, 1992. doi: 10.1016/0021-9991(92)90046-2.

T. Poinsot and D. Veynante. Theoretical and Numerical Combustion. Third Edition (www.cerfacs.fr/elearning), 2011.

M. D. Polanka, M. I. Ethridge, J. M. Cutbirth, and D. G. Bogard. Effects of showerhead injection on film cooling effectiveness for a downstream row of holes. In ASME Turbo Expo 2000: Power for Land, Sea, and Air, pages V003T01A048–V003T01A048. American Society of Mechanical Engineers, 2000.

S. B. Pope. Turbulent flows. Cambridge University Press, 2000.

L. Prandtl. Uber Flussigkeitsbewegung bei sehr kleiner Reibung. In Teubner, editor, Verhandlungen des dritten internationalen Mathematiker-Kongresses, pages 484–491, Leipzig, Germany, 1905.

S. Ravelli and G. Barigozzi. Comparison of rans and detached eddy simulation modeling against measurements of leading edge film cooling on a first-stage vane. Journal of Turbomachinery, 139(5):051005, 2017.

L. F. Richardson. Weather Prediction by Numerical Process. Cambridge University Press, cambridge edition, 1922.

L. S. Lardeau. Unsteady rans modelling of wake–blade interaction: computational requirements and limitations. Computer & Fluids, 34:3–21, 2005.

P. Sagaut. Large Eddy Simulation for incompressible flows. Scientific computation series. Springer-Verlag, 2000.

P. Sagaut and C. Cambon. Homogeneous turbulence dynamics, volume 10. Cambridge University Press Cambridge, 2008.

R. D. Sandberg, V. Michelassi, R. Pichler, L. Chen, and R. Johnstone. Compressible direct numerical simulation of low-pressure turbines—part i: Methodology. Journal of Turbomachinery, 137(5):051011, 2015.

C. Saumweber and A. Schulz. Effect of geometry variations on the cooling performance of fan-shaped cooling holes. Journal of Turbomachinery, 134(6):061008, 2012.

H. Schlichting. Boundary layer theory. McGraw-Hill, New York, 1955.

H. Schlichting and K. Gersten. Boundary layer theory. Springer-Verlag, 8th rev. edition, 2000.

L. Segui Troth. Multi-physics coupled simulations of gas turbines. Phd thesis, Universite de Toulouse, INP Toulouse Ecole doctorale MEGeP, 11 2017.

L. Segui-Troth, L. Gicquel, F. Duchaine, and J. de Laborderie. Les of the ls89 cascade: influence of inflow turbulence on the flow predictions. pages Paper ID: ETC2017–159, 2017.

J. Serrin. Mathematical principles of classical fluid mechanics. In Fluid Dynamics I/Strömungsmechanik I, pages 125–263. Springer, 1959.

A. H. Shapiro. The Dynamics and Thermodynamics of Compressible Fluid Flow, Vol. 1. John Wiley & Sons, 1953.

N. Simiriotis. Large eddy simulation of the film cooling flow system of turbine blades: Public shaped holes. working note, ISAE-SUPAERO, CERFACS, Toulouse, France, 2016.

J. Smagorinsky. General circulation experiments with the primitive equations: 1. the basic experiment. Mon. Weather Rev. , 91:99–164, 1963.

A. Smirnov, S. Shi, and I. Celik. Random flow simulations with bubble dynamics model. In Proceedings of FEDSM00, ASME 2000 Fluids Egineering Division Summer Meeting, volume FEDSM2000-11215, June 11-15, Boston, Massachusetts, USA, 2000.

L. Smith Jr. The radial equilibrium equation of turbomachinery. Journal of Engineering for Gas Turbines and Power, 1966.

P. Spalart, W.-H. Jou, M. Strelets, and S. Allmaras. Comments on the feasibility of les for winds, and on a hybrid rans/les approach. 1:4–8, 05 1997.

P. R. Spalart. Detached-eddy simulation. Annual review of fluid mechanics, 41: 181–202, 2009.

K. R. Sreenivasan. An update on the energy dissipation rate in isotropic turbulence. Physics of Fluids, 10(2):528–529, 1998.

H. Struchtrup and M. A. Rosen. How much work is lost in an irreversible turbine? Exergy, an international journal, 2(3):152–158, 2002.

W. Sturm and L. Fottner. The high speed cascade wind-tunnel of the german armed forces university munich. In 8th Symposium on Measuring Techniques for Transonic and Supersonic Flows in Cascades and Turbomachines, Genova, Italy, October 1985.

A. Terzis. Detailed heat transfer distributions of narrow impingement channels for integrally cast turbine airfoils. PhD thesis, 2014.

M. Thomas. Combustor-turbine interactions: Hot spot migration and thermal environment prediction for a better understanding and design of helicopter engines. PhD thesis, 2019.

M. Thomas, F. Duchaine, L. Gicquel, and C. Koupper. Advanced statistical analysis estimating the heat load issued by hot streaks and turbulence on a high-pressure vane in the context of adiabatic large eddy simulations. In ASME Turbo Expo 2017: Turbomachinery Technical Conference and Exposition, pages V02BT41A041–V02BT41A041. American Society of Mechanical Engineers, 2017.

M. Thomas, F. Duchaine, L. Gicquel, and C. Koupper. Impact of realistic inlet condition on les predictions of isolated high pressure vanes. In 12th International ERCOFTAC Symposium on Engineering Turbulence Modelling and Measurements (ETMM12), Montpellier, France, 9 2018.

P. Tucker. Computation of unsteady turbomachinery flows: Part 1 progress and challenges. Progress in Aerospace Sciences, 47(7):522 – 545, 2011a.

P. Tucker. Computation of unsteady turbomachinery flows: Part 2 LES and hybrids. Progress in Aerospace Sciences, 47(7):546 – 569, 2011b.

P. G. Tucker. Unsteady computational fluid dynamics in aeronautics, volume 104. Springer Science & Business Media, 2013.

J. Tyacke and P. Tucker. Future use of large eddy simulation in aeroengines. J. Turbomach., Published online December 01, 2014., 06 2014. doi: 10.1115/1.4029363.

A. Uzun and M. R. Malik. Wall-resolved large-eddy simulation of flow separation over nasa wall-mounted hump. In 55th AIAA Aerospace Sciences Meeting, page 0538, 2017.

S. Vagnoli, T. Verstraete, C. Koupper, and G. Bonneau. Assessment of rans against les for the aero-thermal behavior of high pressure turbine stages under realistic inlet conditions. In ASME Turbo Expo 2016: Turbomachinery Technical Conference and Exposition, pages V02CT39A023–V02CT39A023. American Society of Mechanical Engineers, 2016.

T. Von Karman. Mechanische ahnlichkeit und turbulenz. Nach. Ges. Wiss. Gottingen, Math. Phys. Klasse, pages 58–68, 1930.

H. W. Stock and W. Haase. Feasibility study of e transition prediction in navier-stokes methods for airfoils. AIAA Journal, Vol. 37:1187–1196, 10 1999. doi: 10.2514/2.612.

A. P. S. Wheeler, A. M. J. Dickens, and R. J. Miller. The effect of non-equilibrium boundary layers on compressor performance. In Turbo Expo: Power for Land, Sea, and Air, number 50794, pages V02BT41A040–, 2017.

S. Wheeler and al. Direct numerical simulations of a high-pressure turbine vane. Journal of Turbomachinery, 138:1–23, 2016. doi: 10.1115/1.4032435.

R. Wilcock, J. Young, and J. Horlock. The effect of turbine blade cooling on the cycle efficiency of gas turbine power cycles. Journal of Engineering for Gas Turbines and Power, 127(1):109–120, 2005.

D. Williams, D. Kamenetskiy, and P. Spalart. On stagnation pressure increases in calorically perfect, ideal gases. International Journal of Heat and Fluid Flow, 58:40–53, 04 2016.

J.-Z. Wu, Y. Zhou, and M. Fan. A note on kinetic energy, dissipation and enstrophy. Physics of Fluids, 11(2):503–505, 1999.

T. A. ZAKI, J. G. WISSINK, W. RODI, and P. A. DURBIN. Direct numerical simulations of transition in a compressor cascade: the influence of free-stream turbulence. Journal of Fluid Mechanics, 665:57–98, 2010. doi: 10.1017/S0022112010003873.

Y. Zang, R. L. Street, and J. R. Koseff. A dynamic mixed subgrid-scale model and its application to turbulent recirculating flows. Physics of Fluids A: Fluid Dynamics, 5(12):3186–3196, 1993.

T. Zebbiche and Z. Youbi. Effect of stagnation temperature on supersonic flow parameters application for air in nozzles. The Aeronautical Journal (1968), 111 (1115):31–40, 2007. doi: 10.1017/S0001924000001731.

L. Zhang and H.-K. Moon. Turbine blade film cooling study: the effects of film hole location on the pressure side. In ASME Turbo Expo 2007: Power for Land, Sea, and Air, pages 497–506. American Society of Mechanical Engineers, 2007.

J. Zilli, D. M. Sutton, and P. Lavoie. Effect of freestream turbulence on laminar separation bubbles and flow transition on an sd7003 airfoil at low reynolds numbers. In 55th AIAA Aerospace Sciences Meeting, STOCKHOLM, SWEDEN, 08 2017.

M. B. Zlatinov. Secondary air interaction with main flow in axial turbines. PhD thesis, Massachusetts Institute of Technology, 2011.